Transactions of the ASME®

Transactions of the ASME, Journal of Heat Transfer (ISSN 0022-1481) is published quarterly (Feb., May, Aug., Nov.) for $160.00 per year by The American Society of Mechanical Engineers, 345 East 47th Street, New York, NY 10017. Second class postage paid at New York, NY and additional *mailing offices. POSTMASTER: Send address* changes to Transactions of the ASME, Journal of Heat Transfer, c/o THE AMERICAN SOCIETY OF MECHANICAL ENGINEERS, 22 Law Drive, Box 2300, Fairfield, NJ 07007-2300.
CHANGES OF ADDRESS must be received at Society headquarters seven weeks before they are to be effective. Please send old label and new address.
PRICES: To members, $36.00, annually: to nonmembers, $160.00.
Add $15.00 for postage to countries outside the United States and Canada.
STATEMENT from By-Laws. The Society shall not be responsible for statements or opinions advanced in papers or . . . printed in its publications (B7.1, para. 3).

INDEXED by Applied Mechanics Reviews and Engineering Information, Inc.
Canadian Goods & Services Tax Registration #126148048

Journal of Heat Transfer

Published Quarterly by The American Society of Mechanical Engineers

VOLUME 113 • NUMBER 2 • MAY 1991

ANNOUNCEMENTS

TECHNICAL PAPERS

(Contents Continued)

TECHNICAL NOTES

Numerical Solution of One Case of Inverse Heat Conduction Problems

K. Kurpisz
Institute of Thermal Technology,
Technical University of Silesia,
Gliwice, Poland

This paper is concerned with a method for solving one case of inverse heat conduction problems. The solution is presented in terms of a series containing the derivatives of the temperature with respect to time and shows no explicit dependence on the initial temperature distribution. In order to solve the problem some temperature histories at the interior points should be known. The derivatives are calculated with the aid of the regularization method. The results of some test cases are presented. Errors due to data accuracy, time steps, Biot numbers, etc. are investigated. The paper focuses on problems that are numerically formulated.

Introduction

Inverse heat conduction problems are defined in different ways. Beck et al. (1985) and Beck and Blackwell (1988) considered the problems of the estimation of the surface heat flux history when one or more measured temperature histories inside a heat-conducting body are given. However, other authors call them the boundary inverse problems (e.g., Matzevity and Multanovsky, 1982; Kozdoba and Krukovsky, 1982). Kozdoba and Krukovsky (1982) defined the inverse problems as the problems where some results are known while all the reasons, such as boundary or initial conditions, are to be found. The case considered in this paper is slightly different. The objective is to find all the results when some of them are known and when some of the reasons may remain unknown. In particular, the temperature distribution inside the body is to be determined while the initial condition and some boundary conditions are unknown. In order to solve such a problem, temperature histories at some interior points should be known. The location of these points can be chosen in any way for one-dimensional problems but not for multidimensional problems. That is one of the limitations of the present method. The method can be applied when both transient and steady-state problems are considered (that are analytically or numerically formulated). However, this paper focuses only on numerical solutions of transient problems.

The solution is given in terms of a series containing the derivatives of the temperature or heat flux with respect to time. Such a solution is similar to one of the earliest exact solutions of the inverse heat condition problems given by Burggraf (1964). Burggraf approached the one-dimensional problem by assuming that both the temperature and heat flux were known at a sensor location. Such an approach was advanced by other authors, e.g., Temkin (1973), but it was finally given up because of its extreme sensitivity to data errors. However, the recent advance in the field of solving the ill-posed problems enables one to obtain values of derivatives that are accurate and stable enough (e.g., Tikhonov and Arsenin, 1977; Lazutchenkov and Shmukin, 1981). Nevertheless, the ill-posed nature of the solution remains and therefore, the word "estimation" should be used rather than the word "solution" in order to describe the results of the calculations.

Internal Response

Solving the inverse heat conduction problems is possible when information about temperatures or heat flux is known at some interior points of the body or, in other words, the solution of the heat conduction problem is known at those points. Such information is called an internal response. When considering transient problems the internal response is a temperature or heat flux history on a certain surface S_1 (see Fig. 1). However, only a temperature response will be taken into account in this paper.

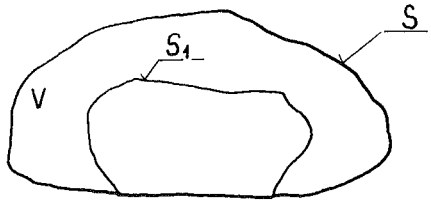

Fig. 1 Illustration of an inverse problem

Let us consider the transient problem described by Fourier–Kirchhoff's equation:

$$\frac{\partial T(\mathbf{r}, t)}{\partial t} = a\nabla^2 T(\mathbf{r}, t), \qquad \mathbf{r}\in V \tag{1}$$

where T = temperature, t = time, a = thermal diffusivity, $\mathbf{r}$ = space variable vector, V = volume of the body.

A temperature response $F_i(t)$ is a function that satisfies the equation

$$F_i(t) = T(\mathbf{r}, t), \qquad \text{for } \mathbf{r}\to\mathbf{r}_i\in S_1, \text{ and } 0\le t<\infty \tag{2}$$

In addition, the derivatives of the temperature response with respect to time should be limited

$$F_i^{(k)}(t) = d^k F_i(t)/dt^k < \infty,\ k=0, 1, 2, \ldots \text{ for } 0\le t<\infty \tag{3}$$

In particular, the surface S_1 can be the external surface of the body. Such a problem is not the inverse problem in the classical point of view but is often of great practical importance, e.g., when evaluating the temperature distribution inside an ingot heated in an industrial furnace or before plastic working. However, in this case the surface temperature cannot be an arbitrary function of time as in an ordinary boundary condition of the first kind but should satisfy equations (2) and (3).

General Description of the Method

The method uses some properties of the solution of the ordinary differential equation set, which is written in the form:

$$\frac{d\mathbf{T}}{dt} = \mathbf{C}\mathbf{T} + \sum_{i=1}^{L} F_i(t)\mathbf{B}_i \tag{4}$$

where $\mathbf{C}$ = a nonsingular N^*N matrix of constant known components, $\mathbf{B}_i$ = an N vector of constant known components, $F_i(t)$ = known functions that satisfy condition (3), $\mathbf{T}$ = an N vector of unknown functions.

Contributed by the Heat Transfer Division for publication in the JOURNAL OF HEAT TRANSFER. Manuscript received by the Heat Transfer Division May 18, 1989; revision received May 29, 1990. Keywords: Conduction, Numerical Methods, Transient and Unsteady Heat Transfer.

Numerical methods for solving heat conduction problems lead directly to equation (4) when discretization with respect to the time variable is not necessary. Such a form of the equation set can be obtained even if steady-state problems are considered in the case when one spatial variable (e.g., the x variable) is not to be discretized (see Kurpisz, 1988). The general form of the equation set after discretization is as follows:

$$\frac{d^2\mathbf{T}}{dx^2} = \mathbf{C}\mathbf{T} + \sum_{i=1}^{L} F_i(x)\mathbf{B}_i \tag{5}$$

Introducing a new variable

$$\mathbf{Z} = d\mathbf{T}/dx$$

we obtain the new differential equation set, which is similar to equation set (4). Analytical methods can lead to equation (4) when the integral transforms with respect to spatial variables are applied (see Kurpisz, 1983). Nevertheless, only the numerical solution of the transient problem is taken into consideration in this paper.

The solution of equation (4) is known and may be written in the form

$$\mathbf{T}(t) = e^{\mathbf{C}t}\mathbf{T}_o + e^{\mathbf{C}t}\sum_{i=1}^{L}\int_0^t F_i(s)e^{-\mathbf{C}s}\mathbf{B}_i ds \tag{6}$$

where $\mathbf{T} = \mathbf{T}_0$ for $t = 0$.

After integrating by parts infinite times the integral in equation (6) we obtain

$$\mathbf{T}(t) = e^{\mathbf{C}t}\mathbf{T}_o + \sum_{k=0}^{\infty}\sum_{i=1}^{L}\mathbf{\Phi}_{k,i}F_i^{(k)}(t) - e^{\mathbf{C}t}\sum_{k=0}^{\infty}\sum_{i=1}^{L}\mathbf{\Phi}_{k,i}F_i^{(k)}(1) \tag{7}$$

where the $\mathbf{\Phi}_{k,i}$ vectors satisfy the equation

$$\mathbf{\Phi}_{k,i} = -(\mathbf{C}^{-1})^{k+1}\mathbf{B}_i \tag{8}$$

In solution (7) the following term is neglected:

$$-\sum_{i=1}^{L} e^{\mathbf{C}t}(\mathbf{C}^{-1})^K \int_0^t F_i^{(K)}(s)e^{-\mathbf{C}s}\mathbf{B}_i ds \qquad \text{for } K\to\infty \tag{9}$$

This term may be neglected because the derivatives are assumed to be limited [equation (3)]. Besides, it can be proved (see Kurpisz and Skorek, 1987) that the absolute value of the least eigenvalue of the $\mathbf{C}$ matrix is greater than 1 if $F_i(t)$ is the temperature response and the vector $\mathbf{T}$ contains only temperatures at the interior points of a heat conducting body (not, e.g., an ambient temperature). It may be compared with eigenvalues for the appropriate Sturm–Liouville problem for the boundary problem with boundary conditions of the first kind (see Ozisik, 1968).

Therefore

$$(\mathbf{C}^{-1})^K \to \mathbf{0} \qquad \text{for } K\to\infty$$

A similar series appeared in Temkin (1973) and the problem of convergence was examined there in detail.

It can also be proved that if the $F_i(t)$ functions are the internal response and satisfy all the assumptions given in the previous section the following equation holds (see Kurpisz and Skorek, 1987):

$$\mathbf{T}_o = \sum_{k=0}^{\infty}\sum_{i=1}^{L}\mathbf{\Phi}_{k,i}F_i^{(k)}(0) \tag{10}$$

The proof is fairly easy but a little troublesome and is based on the spectral analysis of a matrix. The analysis starts with transforming equation (4) by introducing an eigenvector matrix that contains a set of eigenvectors of $\mathbf{C}$. As a result, instead of $\mathbf{C}$, a new diagonal matrix $\mathbf{C}^*$ with the eigenvalues of $\mathbf{C}$ along the principal diagonal is obtained. Thus, each equation of set (4) can be solved separately (similarly to the analytical problems when the integral transforms are applied). Also, equation (2) should be transformed in the same way. After short matrix algebra (see Korn and Korn, 1968) one can obtain equation (10).

Finally, the solution can be written in the form

$$\mathbf{T}(t) = \sum_{k=0}^{\infty}\sum_{i=1}^{L}\mathbf{\Phi}_{k,i}F_i^{(k)}(t) \tag{11}$$

The L number will be determined in the following section.

This solution is similar to that obtained by Burggraf (1964) or Temkin (1973) for problems that were analytically formulated, but is more general. In particular, multidimensional, numerically formulated problems can be solved here. Besides, no information about heat flux histories is necessary. The solution shows no explicit dependence on the initial temperature distribution inside the body. Therefore, one can estimate the temperature distribution inside the body starting the measurements at any time.

Solving Transient Heat Conduction Problems Numerically Formulated

As indicated previously, numerical methods for solving heat conduction problems lead directly to equation set (4) and its solution may be written in the form of equation (11). Any numerical method can be applied to obtain equation set (4). The method used here is the elementary balance method (or finite control volume procedure), which is described by Croft and Lilley (1977) or Kurpisz (1984). This method is similar to the finite difference method and is based on energy balances for each difference element. The difference elements result from the division of the whole domain. The nodal points are situated in the middle of the difference element.

For convenience the nodal points are divided into two groups: interior and external surface points. External surface points are situated on the external surface of the body. Their heat capacity and the thermal conductivity between them are assumed to be zero. Other points are called interior.

The problems that are considered herein can also be divided into two groups: internal and external. The problem is called

Nomenclature

a = thermal diffusivity
Bi = Biot number $= hd/\lambda$
d = size of body
F = temperature response
Fo = Fourier number $= at/d^2$
h = heat transfer coefficient
$\mathbf{r}$ = space variable vector
S = surface
t = time
T = temperature
x, y = Cartesian coordinates
Δx = space step
$\mathbf{A}$ = matrix containing coefficients of difference equation set
$\mathbf{B}$ = vector of known components, equation (4)
$\mathbf{C}$ = matrix of known components, equation (4)
$\mathbf{D}$ = matrix, equation (13)
$\mathbf{H}$ = matrix, equation (12)
$\mathbf{J}$ = vector containing indices of nodal points at which temperature is known
$\mathbf{P}$ = vector, equation (16)
$\mathbf{T}$ = vector of temperature at nodal points
$\mathbf{\Phi}$ = vector, equation (8)
$\mathbf{\Psi}$ = vector, equation (15)
α = regularization parameter
γ = random value
δ = maximum absolute error
λ = thermal conductivity

Subscripts

i = relative to nodal points
k = relative to order of derivative with respect to time

internal when all the nodal points at which the temperature is to be found are situated inside the surface S_1. In particular, when the surface S_1 is the external surface of the body, the problem looks like the direct problem with the boundary condition of the first kind. In fact, such a problem is quite different because the initial condition or even the moment when the transient process of heat conduction begins may remain unknown. The problem is called external when the solution is to be extrapolated from the surface S_1 to the external surface of the body. This is a classical inverse heat conduction problem.

Solution (11) is a little troublesome because any change in the selection of nodal points at which the temperature is measured requires rearranging the **C** matrix and $\mathbf{B}_i$ vectors. Therefore, in this section solution (11) is rewritten in a more convenient form.

Let us denote

N = the number of interior nodal points,
L = the number of external surface nodal points,
M = the total number of nodal points
$M = N+L$

The interior nodal points are numbered 1, 2, . . . , N, and the external surface points $N+1$, $N+2$, . . . , $N+L$.

Let us also denote

J = an L vector containing the indices of the nodal points at which the temperature history is known,
T = an M vector containing the temperatures at all the nodal points, also including the values of F_i (see equation (4)); L components of this vector must be known,
A = an N^*M matrix containing the coefficients of the difference equation set, including also the $\mathbf{B}_i$ vectors (see equation (4)).

Solving equation set (4) is possible if the number of equations is equal to the number of unknown functions. Equation set (4) consists of N equations. The total number of nodal points is equal to M. Therefore, $L=M-N$ temperature histories should be known. However, this conclusion holds for one-dimensional or internal problems only. For multidimensional external problems there are some limitations in selecting nodal points at which the temperature is measured. The same limitations were pointed out by Kozdoba and Krukovsky (1982). The problem will be discussed at the end of this section.

For convenience let us introduce an M^*M matrix called **H**, which consists of two submatrices **A** and **D**

$$\mathbf{H}=\begin{bmatrix}\mathbf{A}\\ \mathbf{D}\end{bmatrix} \tag{12}$$

The L^*M matrix called **D** is defined as follows:

$$D_{i,m}=1 \text{ for } m=J_i,\quad i=1, 2, \ldots, L\quad m=1, 2, \ldots, M$$

$$D_{i,m}=0 \text{ for } m\neq J_i,\quad i=1, 2, \ldots, L \qquad m=1, 2, \ldots, M \tag{13}$$

The final form of the solution can be written as

$$\mathbf{T}(t)=\sum_{k=0}^{K}\sum_{i=1}^{L}\Psi_{k,i}T_{J_i}^{(k)}(t) \tag{14}$$

where $\Psi_{k,i}$ are the M vectors that satisfy the equation

$$\mathbf{H}\Psi_{k,i}=\mathbf{P}_{k,i},\quad k=0, 1, 2, \ldots, K,\quad i=1, 2, \ldots, L \tag{15}$$

and

$$\begin{aligned}
&P_{0,i,m}=0 && \text{for } m\neq N+i,\quad i=1, 2, \ldots, L,\\
&&& \quad m=1, 2, \ldots, M\\
&P_{0,i,i+N}=1, && \text{for } i=1, 2, \ldots, L,\\
&P_{k,i,m}=\Psi_{k-1,i,m}, && \text{for } m=1, 2, \ldots, N,\\
&P_{k,i,m}=0, && \text{for } m=N+1, N+2, \ldots, M,\\
&&& \quad i=1, 2, \ldots, L,\\
&&& \quad k=1, 2, \ldots, K.
\end{aligned} \tag{16}$$

The temperature $T_{J_i}(t)$ stands for the temperature response at the nodal point denoted as J_i. The K number is equal to N for the external problems and tends to infinity for the internal ones. As indicated previously, there are some limitations in selecting nodal points at which the temperature is measured. In other words, it may happen that the solution cannot be obtained when the nodal points are selected improperly. The correctness of the selection of the nodal points can be checked by examination of the rank of the **H** matrix. The rank should be equal to M.

Calculating Derivatives

The inverse heat conduction problems belong to the ill-posed category, which means that their solutions are extremely sensitive to data errors. The ill-posed nature of the present method is revealed when the derivatives are calculated. Therefore, special techniques should be used in order to calculate derivatives and this problem needs a lot of attention. Some authors (e.g., Burggraf, 1964; Temkin, 1973) suggested that the value of derivatives that are stable and accurate enough can be obtained by using the difference approximations of high order. This conclusion is not true when data errors are substantial.

Much better results can be obtained by using the regularization method (Tikhonov and Arsenin, 1977; Lazutchenkov and Shmukin, 1981). The regularization method is a procedure that modifies the least-squares approach by adding factors that are intended to reduce excursions in the unknown function, such as the temperature. The procedure is specially adjusted to solving the ill-posed integral equations. Therefore, the problem of calculating derivatives is transformed into the problem of solving Volterra's integral equation of the first kind. Let us denote

$$Z=d^kF/dt^k$$

The Z variable is the solution of the integral equation

$$\int_{t_0}^{t}\frac{(t-s)^{k-1}}{(k-1)!}Z(s)ds=W(t) \tag{17}$$

where

$$W(t)=F(t)-\sum_{n=0}^{k-1}\frac{(t-t_0)^n}{n!}\frac{d^nF(t)}{dt^n}\bigg|_{t=t_0} \tag{18}$$

which can be proved by integrating by parts equation (17).

This integral equation can be solved with the aid of the regularization procedure. The regularization parameter that appears in the regularization method can be selected by the quasi-optimum algorithm (see Tikhonov and Arsenin, 1977; Honerkamp and Weese, 1990). However, the calculations prove that the influence of the regularization parameter selection on the results is usually not substantial. The integral in equation (17) can be determined by using the trapezium method, which is accurate enough for this purpose. Although the regularization method provides the values of derivatives that are usually stable enough, it is clear that the higher the order of the derivatives, the worse the accuracy. Therefore, the number of terms in the series described by equation (14) should be limited. That is the second main limitation of the present method.

Solving Overspecified Problems

The present method is applicable to overspecified problems. Any additional information can be employed due to a procedure called the coordinate of measuring results method or the equalization method (see, e.g., Szargut, 1984). This method is based on the least-squares approach and is widely used, e.g., in geodesy.

Any additional information may be written in the form of a condition

$$G_j(\xi_1, \ldots, \xi_I)=0,\quad j=1, 2, \ldots, r \tag{19}$$

where r is the number of conditions (19). This equation can be employed if it holds for each moment of time of a transient problem. Such conditions may correspond to additional temperature histories, information about boundary conditions, etc. The list of ξ_i variables may contain measured or calculated temperatures or parameters describing heat transfer. Because fluctuations in the derivatives affect the accuracy and stability of the solution, the list should also contain the derivatives of the thermal response.

After substituting the measured values of the temperatures and calculated values of the derivatives into equation (19) it may appear that due to data errors we obtain

$$G_j(\zeta_1, \ldots, \zeta_I) = -W_j, \quad j=1, 2 \ldots, r \tag{20}$$

where ζ_i stands for measured or calculated values of ξ_i and W_j is a discrepancy of the equation. The objective is to change the values of ζ_i by adding corrections in order to get

$$G_j(\zeta_1+\delta\zeta_1, \ldots, \zeta_I+\delta\zeta_I)=0 \tag{21}$$

and

$$\sum_{i=1}^{I}\frac{\delta\zeta_i^2}{\delta_i^2} \rightarrow \text{minimum} \tag{22}$$

where δ_i is the standard deviation of ζ_i.

To solve the optimization problem, equation (21) can be expanded in a Taylor series. For linear problems or for small values of $\delta\zeta_i$ the series can be truncated after two terms

$$G_j(\zeta_1+\delta\zeta_1, \ldots, \zeta_I+\delta\zeta_I) = G_j(\zeta_1, \ldots, \zeta_I) + \sum_{i=1}^{I}\frac{\partial G_j}{\partial \xi_i}\bigg|_{\xi_i=\zeta_i}\delta\zeta_i \tag{23}$$

or substituting equations (20) and (21)

$$\sum_{i=1}^{I}\frac{\partial G_j}{\partial \xi_i}\bigg|_{\xi_i=\zeta_i}\delta\zeta_i = W_j, \quad j=1, 2, \ldots, r \tag{24}$$

The problem, which consists of objective function (22) and constraints (24), can easily be solved using the Lagrangian multiplier method (see Pierre and Lowe, 1975).

As an example we can employ equation (14) as condition (19), if we know the temperature histories at additional points

$$G_j(\xi_i, \ldots, \xi_I) \equiv \sum_{k=0}^{K}\sum_{i=1}^{L}\Psi_{k,i,j}T_{j_i}^{(k)}(t_n) - T_j(t_n) = 0 \tag{25}$$

where the subscript j stands for the node number at which the temperature is additionally known and the subscript n stands for the nth moment of time. The list of ξ_i variables may contain the $(K+1)^*L$ values of $T_{j_i}^{(k)}$ and the temperature T_j. The procedure should be repeated for each moment of time.

Test Cases

Numerous examples were carried out in order to examine the advantages and disadvantages of the present method. The temperature histories necessary for solving the test cases were obtained from the direct problems of heat conduction. To make the cases more realistic, errors can be added to the exact temperatures. The simulated temperatures were given by

$$T_i(t) = \bar{T}_i(t) + (1-2\gamma)\delta \tag{26}$$

where $\bar{T}_i(t)$ = the exact temperature history, taken from the direct problem, δ = the maximum absolute error, γ = the random value produced by a random value generator of a uniform distribution in the range $[-1, 1]$. The results of two test cases are shown here.

The First Test Case. The first test case is for a two-dimensional plate shown in Fig. 2. The plate is divided into six difference elements. When considering the direct problem (in order to receive data for the inverse problem) the surfaces $x=0$ and $y=0$ are insulated (the condition of symmetry). The boundary condition of the third kind is prescribed for the other surfaces

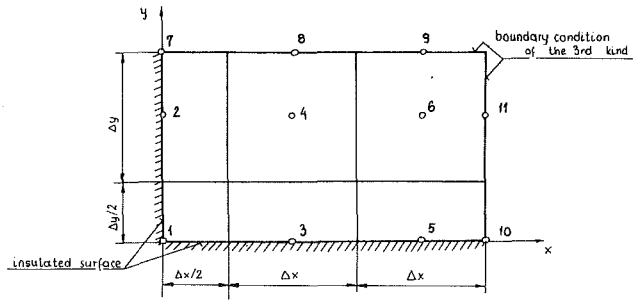

Fig. 2 The net of mesh for the two-dimensional test case

$$\frac{\partial T}{\partial X} + \mathrm{Bi}_x T = \mathrm{Bi}_x T_e, \text{ for } X=1$$

and

$$\frac{\partial T}{\partial Y} + \mathrm{Bi}_y T = \mathrm{Bi}_y T_e, \text{ for } Y=Y_e$$

where $X = x/d_x$, $Y = y/d_x$, $Y_e = d_y/d_x$ = dimensional space variables, T_e = an ambient temperature, and $\mathrm{Bi}_x = h_x d_x/\lambda$, $\mathrm{Bi}_y = h_y d_x/\lambda$ = the Biot numbers, where h_x, h_y = convective heat transfer coefficients along the x and y axes, respectively, d_x, d_y = the size of the plate in the x and y directions, respectively, λ = thermal conductivity.

The test cases were calculated for different Biot numbers, time steps, initial conditions, maximum errors, etc.

Let us consider the inverse problem when

$$N=6, \; L=5, \; M=N+L=11.$$

The N differential equations can be written for the N difference elements, e.g.,

$$\frac{dT_1}{dt} = A_{1,1}T_1 + A_{1,2}T_2 + A_{1,3}T_3$$

$$\frac{dT_2}{dt} = A_{2,1}T_1 + A_{2,2}T_2 + A_{2,4}T_4 + A_{2,7}T_7$$

.....

$$\frac{dT_6}{dt} = A_{6,4}T_4 + A_{6,5}T_5 + A_{6,6}T_6 + A_{6,9}T_9 + A_{6,11}T_{11}$$

The temperature should be measured at $L=5$ points (M values of temperatures, N equations, $L=M-N$ values should be known).

Let us consider the case when the temperature is known at points 1, 2, 3, 5, and 10. This is the external problem, but determining the temperature is impossible for this case. It is easy to understand when considering the equation for the first nodal point. All the temperatures are known in this equation and, therefore, the rank of the **H** matrix is lower than M. This is an example of a problem that cannot be solved using the present method due to one of its limitations.

The problem of determining the temperatures within the plate can be solved when the temperature histories are given at certain points, e.g., 1, 2, 7, 8, and 9. The **J** vector is defined as

$$\mathbf{J}^T = [1, 2, 7, 8, 9]$$

where $\mathbf{J}^T$ is the transpose vector of **J**, while the **D** matrix is defined as

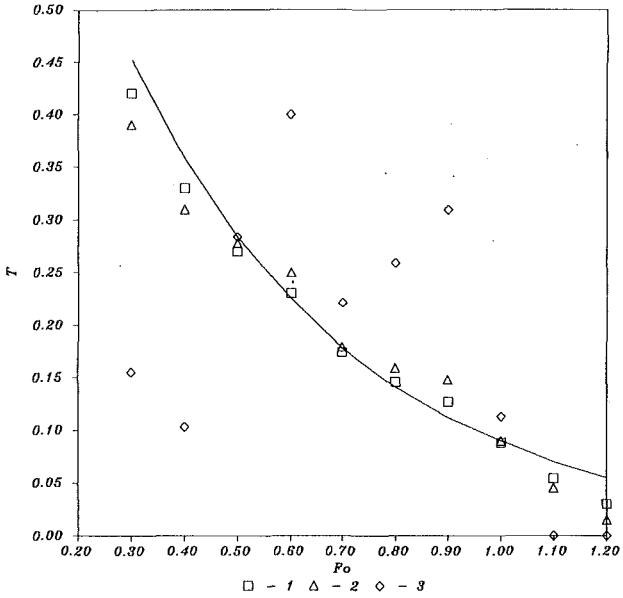

Fig. 3 Temperature history for the first test case (external problem)

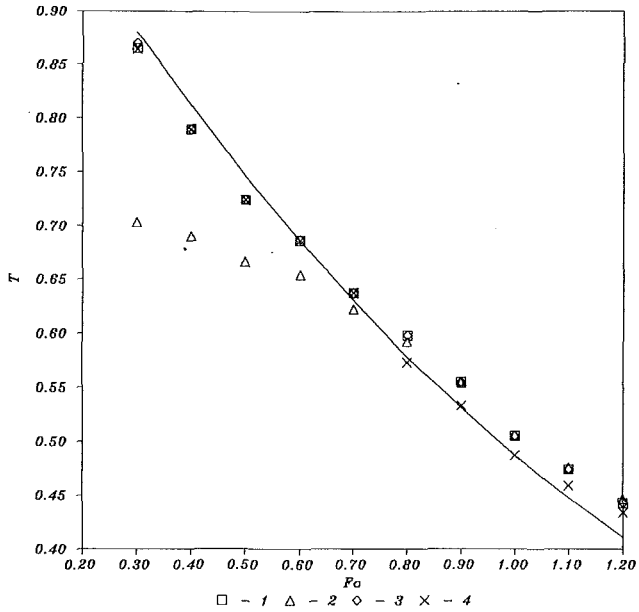

Fig. 5 Influence of the regularization parameter on the temperature history for $\delta = 0.05$

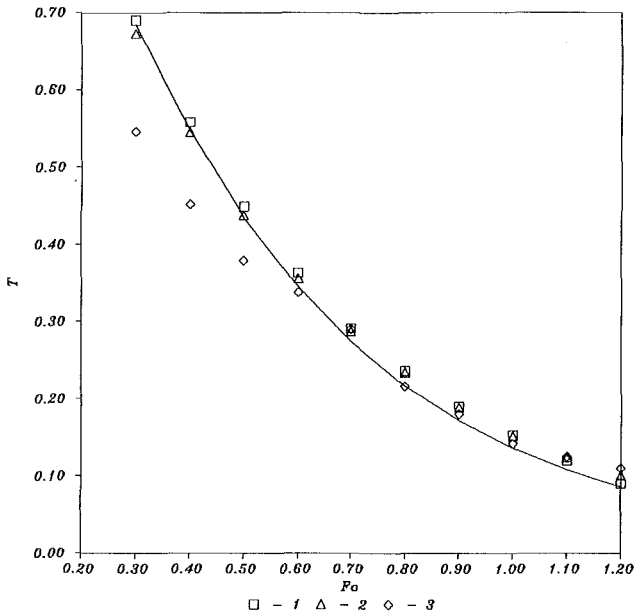

Fig. 4 Temperature history for the first test case (internal problem)

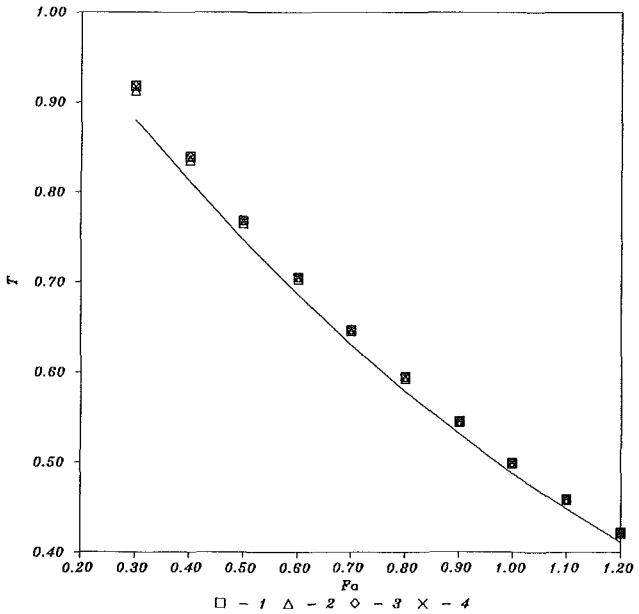

Fig. 6 Influence of the regularization parameter on the temperature history for $\delta = 0.005$

$$\mathbf{D} = \begin{bmatrix} 1 & 0 & 0 & 0 & 0 & 0 & 0 & 0 & 0 & 0 & 0 \\ 0 & 1 & 0 & 0 & 0 & 0 & 0 & 0 & 0 & 0 & 0 \\ \cdot & \cdot & \cdot & \cdot & \cdot & \cdot & \cdot & \cdot & \cdot & \cdot & \cdot \\ 0 & 0 & 0 & 0 & 0 & 0 & 0 & 0 & 1 & 0 & 0 \end{bmatrix}.$$

Some results for such an external problem are shown in Fig. 3. They refer to the case when $\mathrm{Bi}_x = \mathrm{Bi}_y = 2.0$, the initial distribution is uniform and equal to one, and the ambient temperature is assumed to be zero. The Fourier number is defined as

$$\mathrm{Fo} = at/d_x^2$$

The dimensionless time step is equal to $\Delta\mathrm{Fo} = 0.1$ and the temperature histories are recorded from $\mathrm{Fo} = 0.3$. At this moment the temperature distribution within the plate is not uniform at all.

The temperature history at node 5 is shown in Fig. 3. The solid line refers to the solution of the direct problems (exact results). The points denoted as No. 1 stand for $\delta = 0.005$; No. 2: $\delta = 0.01$; No. 3: $\delta = 0.05$. The results are stable and accurate enough except for the third case. However, for this case the differences between two successive values of temperatures are close to the values of the $(1 - 2\gamma)\delta$ component in equation (26).

Figure 4 displays results of the internal problem for the same data. The temperature histories have been taken at points 7, 8, 9, 10, and 11. The temperature history at node 1 is shown. It can be seen that the results are more accurate and stable than results for the external problem.

The calculations prove that the stability and accuracy of the results are dependent on the numerous parameters. The main ones are maximum errors that can be seen in Figs. 3 and 4, Biot numbers, and time steps. It proves that the greater the

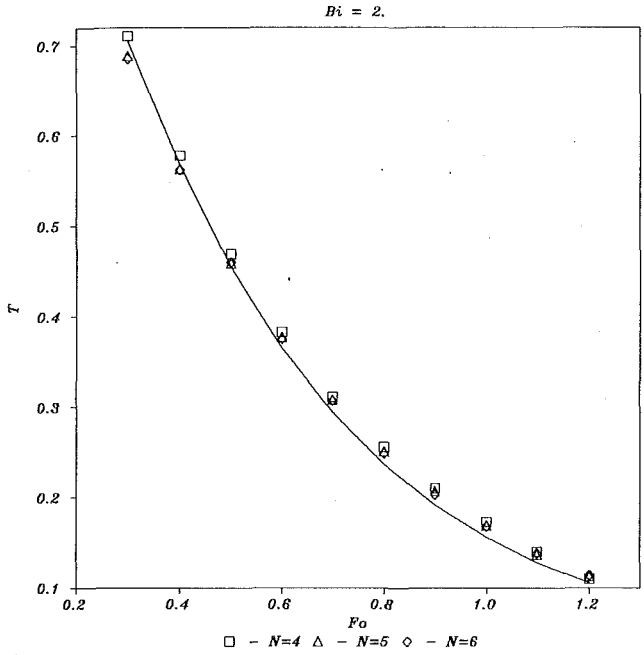

Fig. 7 Influence of the number of nodal points

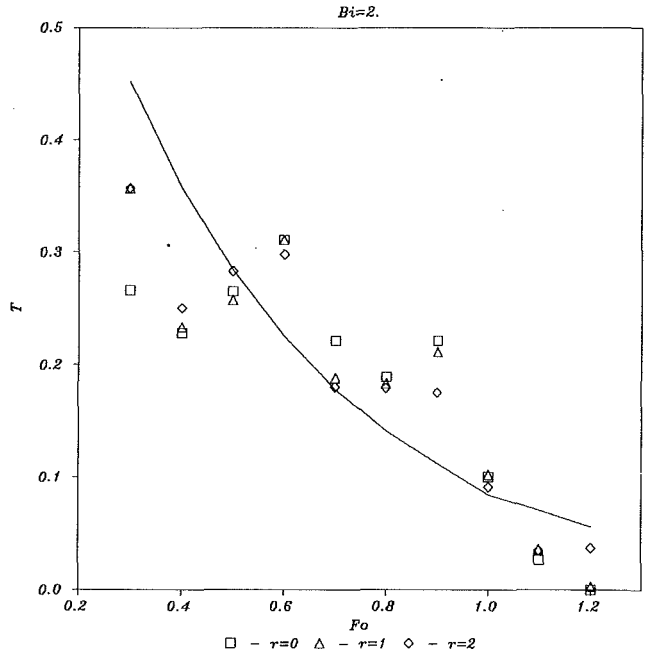

Fig. 8 Results of the overspecified problem

value of the Biot number, the less the accuracy and stability. For two-dimensional problems such as that shown in Fig. 2, stable results have been obtained until the Biot number equals approximately 4–6. The choice of time steps is more troublesome. The greater the errors, the greater the time steps should be. On the other hand, due to the increasing time steps, the approximation of the temperature history is much worse and the results can be inaccurate as well, especially for large Biot numbers. The numbers of satisfying accuracy have been obtained for the dimensionless time steps from a range of approximately 0.05–0.1.

The series described by equation (14) was truncated after the sixth term, which meant the derivatives were calculated up to the fifth order. That was because of their stability and accuracy. However, the calculations prove that when taking into account only four or five terms the present method provides satisfying results for Biot numbers, time steps, and maximum errors such as mentioned above. On the other hand, it is clear that there may be numerous problems when six terms of a series are not enough, especially for rapid changes of temperatures. The present method cannot be applied to such cases.

The influence of the regularization parameter on the results for cases that have been considered is not substantial. It is shown in Figs. 5 and 6, which display this influence for the internal problem described above. For both of them the Biot number was equal to 0.5. Figure 5 refers to $\delta = 0.05$, whereas Fig. 6 refers to $\delta = 0.005$. The solid lines refer to the exact solution. The points denoted as No. 1 stand for the following values of the regularization parameters (for four successive derivatives):

$$\alpha_1 = 100, \quad \alpha_2 = 100, \quad \alpha_3 100, \quad \alpha_4 = 100,$$

No. 2

$$\alpha_1 = 0.001, \quad \alpha_2 = 0.001, \quad \alpha_3 = 0.001, \quad \alpha_4 = 0.001,$$

No. 3

$$\alpha_1 = 100, \quad \alpha_2 = 10, \quad \alpha_3 = 0.1, \quad \alpha_4 = 0.1,$$

No. 4

$$\alpha_1 = 0.1, \quad \alpha_2 = 0.1, \quad \alpha_3 = 1.0, \quad \alpha_4 = 1.0,$$

It can be seen that the influence of the regularization parameter on the results of the calculations increases if the data errors increase, but for the large range of parameters it is not considerable. The influence also increases when Biot numbers increase and for small time steps, or in other words, for rapid processes of heat transfer. Figures 5 and 6 (the Biot number is equal to 0.5) confirm the conclusion that the smaller the Biot number, the better the accuracy (compare with Figs. 3 and 4 for Bi = 2.0).

Figure 7 shows the influence of the number of nodal points on the results for the internal problem ($Bi_x = Bi_y = 2.0$). The letter N stands for the number of nodal points along the x axis, whereas the number of nodal points along the y axis has not been changed. The temperature at node 1 is displayed. It can be seen that the number of nodal points has been chosen properly. However, it is worth pointing out that for a large number of nodal points the matrix **H** in equation (15) may become ill-posed.

Some results for the overspecified problem are shown in Fig. 8. They correspond to the same problem as shown in Fig. 3 for $\delta = 0.05$. The case $r = 0$ refers to the temperature histories, which have been taken at points 3, 4, 7, 8, and 9. The case $r = 1$ refers to the overspecified problem when the temperature has additionally been recorded at point 1. For the case $r = 2$ the temperature histories have been taken at points 1, 2, 3, 4, 7, 8, and 9. Although the value of the maximum absolute error is significant one can observe more accurate and stable results when employing additional information.

The Second Test Case. The second test case is thoroughly discussed by Beck et al. (1985). It is for heat flux, which varies in time in a triangular fashion. Before Fo = 0, the surface heat flux is zero. For Fo between zero and 0.6 it increases linearly with time, and for Fo > 0.6 the flux decreases linearly to zero at Fo = 1.2. The sensor is located at node 1 (see Fig. 9). Knowing the temperature history at node 1 (Fig. 9), the surface heat flux at node $N+1$ is to be determined. The simulated temperature measurements with errors added have been taken from Beck et al. (1985). The input temperature data have been divided into two groups: The first one contains 10 values for the subinterval Fo = 0.06–0.6, whereas the second one contains the other ten values for the subinterval Fo = 0.6–1.2. The inverse heat conduction problems corresponding to these two subin-

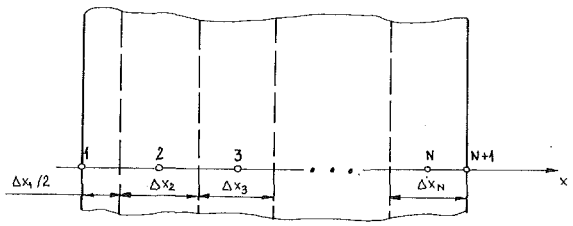

Fig. 9 The net of mesh for the second test case

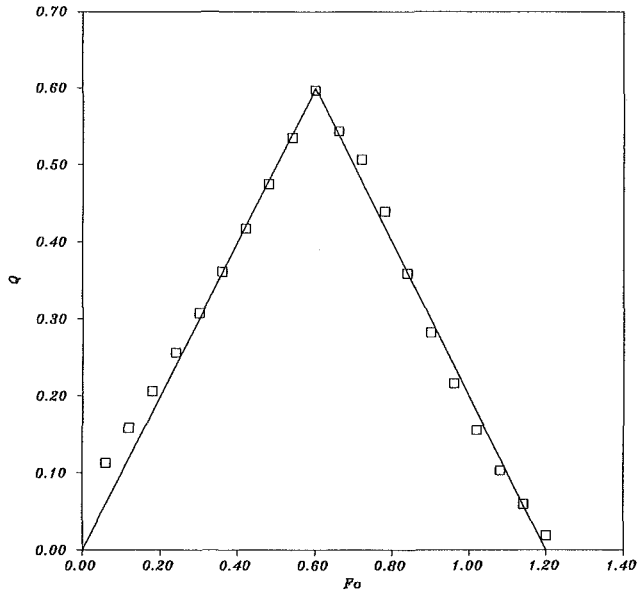

Fig. 10 Calculated heat flux for the triangular heat flux test case

tervals have been solved separately in order to examine the influence of the initial distribution on the results. The heat flux has been calculated from the energy balance for the N nodal point after calculation of the temperatures.

The results of the calculations are displayed in Fig. 10. The solid line refers to the exact solution. The dimensionless time step is equal to 0.06. The agreement with the exact heat flux is sufficient. The greatest difference between the exact and inverse solutions can be noticed at the first couple of time points. That is because the temperature rise at node 1 is very small for this period of time due to damping and lagging. The results are of similar accuracy to those shown by Beck et al. (1985). However, it is worth pointing out that solution (14) requires no information about the initial condition, contrary to the methods described by Beck.

Conclusions

Any practical application of the inverse problem requires an inverse scheme that remains stable when experimental data are used. The present method can produce results that are stable and accurate for a wide range of problems. The main limitations are connected with the number of derivatives in the solution and the time steps. As a result, when rapid processes of heat conduction are considered the method shows poor stability and convergence. The dimensionless time step should not be less than approximately 0.5 and the number of terms in the solution should be fewer than five to six.

The location of the temperature sensors is also the limitation for the external multidimensional problems. The correctness of the selection of the nodal points can be checked by examination of the rank of the **H** matrix. However, for the internal or one-dimensional problems the temperature sensor location may be chosen in any way.

Due to the ill-posed nature of the inverse problems the data errors should be as moderate as possible.

The present method can also be applied to nonlinear cases. In these cases the considered time interval should be divided into subintervals that are small enough to assume the constant thermal properties. Because of the independence from the initial distribution such an approach does not introduce any new trouble.

This method can also be applicable to the overspecified problems. Additional information can improve the stability and convergence of the solution considerably.

A major advantage of the present method is that the initial temperature distribution or even the moment when the transient process begins may remain unknown, which is different from most of the other methods. Another is that the method can be directly extended to multiple interior sensors and two- and three-dimensional cases. Moreover, quite different problems, which are governed by the equation set of type (4) or lead to equation (4), can be treated successfully. The limitations that are mentioned above are its major weakness. A statistical basis of the method is also not satisfying. In some cases other methods, such as the function specification and regularization methods (see Beck et al., 1985) can produce stable results for smaller time steps and greater measurement errors. Nevertheless, the proposed procedure gives the flexibility to treat a variety of inverse problems with sufficient accuracy.

References

Beck, J. V., Blackwell, B., and Clair, Ch. R., 1985, *Inverse Heat Conduction Problems*, Wiley-Interscience, New York.

Beck, J. V., and Blackwell, B., 1988, "Inverse Problems," in: *Handbook of Numerical Heat Transfer*, W. J. Minkowycz, E. M. Sparrow, G. M. Schneider, and R. H. Pletcher, eds., Wiley-Interscience, New York, pp. 787–834.

Burggraf, O. R., 1964, "An Exact Solution of the Inverse Problem in Heat Conduction — Theory and Applications," ASME JOURNAL OF HEAT TRANSFER, Vol. 86, pp. 373–382.

Croft, D. R., and Lilley, D. G., 1977, *Heat Transfer Calculations Using Finite Difference Equations*, Applied Science Publ., London, United Kingdom.

Honerkamp, J., and Weese, J., 1990, "Tikhonov's Regularization Method for Ill-Posed Problems," *Continuum Mechanics and Thermodynamics*, Vol. 2, No. 1, pp. 17–30.

Korn, A. G., and Korn, T. M., 1968, *Mathematical Handbook*, McGraw-Hill, New York.

Kozdoba, L. A., and Krukovsky, P. G., 1982, *Methods for Solution of Inverse Heat Conduction Problems* [in Russian], Naukova Dumka, Kiev, USSR.

Kurpisz, K., 1983, "Determining Temperature Fields in Solids When Initial and Some Boundary Conditions are Unknown" [in Polish], *Arch. of Thermodynamics (Poland)*, Vol. 4, pp. 301–316.

Kurpisz, K., 1984, "Numerical Methods," in: *Heat Conduction* [in Polish], S. J. Gdula, ed., Polish Scientific Publ., Warsaw, Poland, pp. 236–325.

Kurpisz, K., 1988, "Method for Determining Steady State Temperature Distribution Within Blast Furnace Lining by Measuring Temperature at Selected Points," *Trans. of ISIJ (Japan)*, Vol. 28, pp. 926–929.

Kurpisz, and Skorek, J., 1987, "Inverse Heat Conduction Problems," *Techn. Report of the Inst. of Thermal Technology* [in Polish], Technical University of Silesia, Gliwice, Poland, Rept. No. NB-300/RME-3/87.

Lazutchenkov, N. M., and Shmukin, A. A., 1981, "On Boundary Inverse Heat Conduction Problem for Two-Dimensional Domain" [in Russian], *Journal of Eng. Phys. (USSR)*, Vol. 40, No. 2, pp. 352–358.

Matzevity, J., and Multanovsky, A. M., 1982, *Identifying Heat Conduction Problems* [in Russian], Naukova Dumka, Kiev, USSR.

Ozisik, M. N., 1968, *Boundary Value Problems of Heat Conduction*, Int. Textbook, Scranton, PA.

Pierre, D. A., and Lowe, M. J., 1975, *Mathematical Programming Via Augmented Lagrangians*, Addison-Wesley Publ. Co., London, United Kingdom.

Szargut, J., ed., 1984, *Co-ordination of Measuring Results in Thermal Technology* [in Polish], Zak. Ossolinskich Publ., Wroclaw, Poland.

Temkin, A. G., 1973, *Inverse Methods in Heat Conduction* [in Russian], Energia, Moscow, USSR.

Tikhonov, A. N., and Arsenin, V. Y., 1977, *Solutions of Ill-Posed Problems*, V. H. Winston and Sons, Washington, DC.

Shape Sensitivities and Optimal Configurations for Heat Diffusion Problems: a BEM Approach

S. Saigal
Assistant Professor,
Department of Civil Engineering,
Carnegie Institute of Technology,
Carnegie Mellon University,
Pittsburgh, PA 15213
Mem. ASME

A. Chandra
Associate Professor,
Department of Aerospace
and Mechanical Engineering,
University of Arizona,
Tucson, AZ 85721
Mem. ASME

Design sensitivity analysis, along with the shape optimization of heat diffusion problems using the boundary element method (BEM), is presented in this paper. The present approach utilizes the implicit differentiation of discretized boundary integral equations with respect to the design variables to yield the sensitivity equations. A technique based on the response of an object to a constant boundary temperature is presented for the evaluation of singular terms in the thermal sensitivity kernels. A procedure for the design sensitivity analysis of a reduced system of equations obtained via substructuring and condensation is also presented. The BEM formulations are implemented for both two-dimensional and axisymmetric objects. A number of sample problems are solved to demonstrate the accuracy of the present sensitivity formulation and to obtain optimal configurations of some mechanical components of practical interest, which are subjected to different thermal environments.

Introduction

Design sensitivity analysis forms an important component of the shape optimization process. Design sensitivities represent the gradients of variables of interest with respect to change of shape. This information is used in nonlinear programming algorithms to search for the optimal direction in which to proceed in altering the existing design of an object as it evolves towards an optimal configuration. These algorithms change the configuration of the object incrementally and require a number of such increments or iterations to obtain the optimal shape. Inaccurate values of design sensitivities lead to an increased number of iterations and may even render the effort unsuccessful. The determination of accurate design sensitivities is thus of crucial significance and has attracted the attention of numerous researchers. A survey of these efforts has been given by, for example, Haug et al. (1986) and Adelman and Haftka (1986). From these surveys, it can be seen that most of the work in this area has been done using the finite element method.

The boundary element method (BEM) has gained importance as an analysis tool in recent years. This method has special advantages when applied to shape optimization of objects and these advantages have been pointed out by, among others, Barone and Yang (1988), Kane and Saigal (1988), and Mukherjee and Chandra (1989, 1990).

Two methods, namely the direct-differentiation approach (DDA) and the adjoint structure approach (ASA), emerge as the most significant ones for the evaluation of design sensitivities. Both of these approaches have recently been developed in the context of BEM for elastic systems. For examples, see the references by Barone and Yang (1988) and Saigal et al. (1990a) for two dimensional systems: Saigal et al. (1989) and Rice and Mukherjee (1990) for axisymmetric systems; Aithal et al. (1990) for three-dimensional systems; Mukhurjee and Chandra (1989, 1990) for problems involving materially nonlinear as well as geometrically nonlinear structural systems using the DDA; and Saigal and Aithal (1990) for two-dimensional structural systems using the ASA. The ASA has also been used recently for determining the design sensitivities of steady-state diffusion problems by Meric (1986), including optimal thermal insulation application; and by Park and Yoo (1988) for two-dimensional heat conduction problems. Recently, Chandra and Chan (1990) have presented a DDA for determining design sensitivities in steady-state conduction–convection problems without internal energy generation.

In this paper, the DDA using BEM is developed for steady-state heat diffusion problems including internal energy generation. The boundary integral equations for heat transfer are first discretized using a number of boundary elements. The sensitivity equations with respect to the design variables. A treatment for the sensitivities due to internal heat generation is presented using a particular integral approach similar to that given by Pape and Banerjee (1987) for two-dimensional elastic systems. A scheme based on substructuring and condensation for performing the sensitivity analysis on a reduced system of equations is also presented. This capability is of significance for those objects undergoing shape optimization that have only a portion of their boundary changing. The present heat transfer analysis and sensitivity analysis capabilities are linked to a numerical optimization algorithm. A number of examples are first solved to demonstrate the accuracy of the present sensitivity formulations. Three examples of heat diffusion problems that are of practical significance are then studied to obtain the optimal configurations in their respective thermal environments.

Boundary Integral Equations. The governing differential equation for steady-state diffusion in the presence of a heat source may be written as

$$k\nabla^2 T + f = 0 \tag{1}$$

where T is the temperature and f denotes the heat source term. The boundary conditions on the boundary $\Gamma = \Gamma_1 + \Gamma_2 + \Gamma_3$ are given as

$$\begin{aligned} T &= T_0 \text{ on } \Gamma_1 \\ \frac{\partial T}{\partial n} &= q_0 \text{ on } \Gamma_2 \text{ and} \\ T + C_1 \frac{\partial T}{\partial n} &= C_2 \text{ on } \Gamma_3 \end{aligned} \tag{2}$$

where n is the outward normal and T_0, q_0, C_1, and C_2 are specified values. The solution to equation (1) may be written as

$$T = T^c + T^p \tag{3}$$

Contributed by the Heat Transfer Division for publication in the JOURNAL OF HEAT TRANSFER. Manuscript received by the Heat Transfer Division October 17, 1989; revision received June 4, 1990. Keywords: Materials Processing and Manufacturing Processes, Numerical Methods.

where T^c and T^p are the complementary and particular integral solutions, respectively, satisfying the equations

$$\nabla^2 T^c = 0 \tag{4}$$

and

$$k\nabla^2 T^p + f = 0 \tag{5}$$

For the homogeneous differential equation (4), the boundary integral equation relating the temperature and the temperature gradient on the boundary is given as (Banerjee and Butterfield, 1981)

$$T^c(p) + \int_\Gamma T^c(p)\frac{\partial \psi^*}{dn}(p, Q)\, d\Gamma(Q) = \int_\Gamma \frac{\partial T^c}{dn}(p)\psi^*(p, Q)\, d\Gamma(Q) \tag{6}$$

where p and q denote interior source and field points; P and Q denote boundary source and field points. The function $\psi^*(p, Q)$ denotes the temperature at point p due to a unit point source applied at point Q. For two dimensions, ψ^* is given as

$$\psi^* = -\frac{1}{2\pi k} \ln \left| \frac{r}{r_0} \right| \tag{7a}$$

with r_0 constant such that $\psi^* = 0$ at $r = r_0$, where r is the distance between the points p and Q. To obtain the required boundary integral equation, the interior point p is taken to a boundary point P in equation (6). The boundary of the solid is next discretized using N boundary elements. The coordinated of points on the boundary, the temperatures, and the temperature gradients are each expressed using quadratic interpolation functions as ($m = 1, 3$ for a three-noded element)

$$x(\xi) = \sum_{i=1}^{m} N_i(\xi) x_i \tag{7b}$$

and similarly for $y(\xi)$, $T(\xi)$, and $dT(\xi)/dn$. The N_i denote the shape functions and ξ the nondimensional element coordinate. The transformation of the integration variable from Γ to ξ will lead to the Jacobian J as

$$J = \left[\left(\frac{\partial x}{\partial \xi}\right)^2 + \left(\frac{\partial y}{\partial \xi}\right)^2 \right]^{1/2} \tag{8}$$

where $\partial x/\partial \xi$ is obtained through the differentiation of equation (7) and similarly for $\partial y/\partial \xi$. Substituting equations (7) and (8) into the boundary form of equation (6) and taking each nodal point in turn as the source point P leads to a set of linear algebraic equations written as ($m = 1, 3$)

$$[A]\{T^c\} = [B]\left(\frac{dT^c}{dn}\right) \tag{9}$$

where

$$[A] = \sum_{k=1}^{N}\left[\sum_{i=1}^{m}\int_{-1}^{+1} \frac{d\psi^*(P, Q(\xi))}{dn} N_i(\xi)\, J(\xi)\, d(\xi)\right]_k \tag{10}$$

$$[B] = \sum_{k=1}^{N}\left[\sum_{i=1}^{m}\int_{-1}^{+1} \psi^*(P, Q(\xi))\, N_i(\xi)\, J(\xi)\, d(\xi)\right]_k \tag{11}$$

In equations (10) and (11) the summation over N elements denotes the assembly of the matrices of each element. Substituting $\{T^c\} = \{T\} - \{T^p\}$ from equation (3) into equation (9) gives

$$[A]\{T\} = [B]\left\{\frac{\partial T}{\partial n}\right\} + \{f\} \tag{12}$$

where

$$\{f\} = [A]\{T^p\} - [B]\left\{\frac{dT^p}{dn}\right\} \tag{13}$$

It is noted that the fundamental solution $d\psi^*/dn$ ($\nabla\psi^* \cdot n$) contains r_{PQ}, the distance between the points P and Q, in its denominator. When P lies on Q, $r_{PQ} = 0$; and thus, the integration shown in equation (10) is singular. These terms are evaluated using the fact that if a uniform distribution of temperature is applied at the boundary of any solution domain, the temperature is also uniform throughout the domain and the temperature gradient is zero everywhere on the boundary. Thus, equation (9) gives

$$[A]\{T\} = \{0\} \tag{14}$$

and the diagonal term can be written as

$$A_{ii} = -\sum_{\substack{j=1 \\ i \neq j}}^{\text{TNOD}} A_{ij} \text{ for } i = 1, 2, \ldots, \text{TNOD} \tag{15}$$

TNOD is the total number of nodes. The off-diagonal terms are all evaluated using the Gauss integration.

The analysis above pertains to two-dimensional situations. A procedure for axisymmetric cases can be similarly developed, resulting in equations of the form of equations (12) and (13). The $[A]$ and $[B]$ matrices for axisymmetric analysis are not derived here and may be found in, for example, the text by Banerjee and Butterfield (1981).

Design Sensitivity Analysis for Steady-State Diffusion

Sensitivity Equations. The design sensitivity analysis consists of determination of the variation in the response of an object with respect to a variation in the design variable X_L. In the present study only the geometric parameters are considered as design variables. To determine the sensitivity of a heat transfer system with respect to a design variable X_L, the implicit differentiation of equation (12) with respect to X_L is performed. This leads to the design sensitivity equation ($m = 1, 3$ for a three-noded element)

$$[A]\{T\}_{,L} = [B]\left\{\frac{dT}{dn}\right\}_{,L} + [B]_{,L}\left\{\frac{dT}{dn}\right\} - [A]_{,L}\{T\} + \{f\}_{,L} \tag{16}$$

Using equations (10) and (11), we get

$$[A]_{,L} = \sum_{k=1}^{N}\left[\sum_{i=1}^{m}\int_{-1}^{+1}\left\{\left(\frac{d\psi^*}{dn}\right)_{,L} N_i\, J + \left(\frac{d\psi^*}{dn}\right) N_i\, J_{,L}\right\} d\xi\right]_k \tag{17}$$

$$[B]_{,L} = \sum_{k=1}^{N}\left[\sum_{i=1}^{m}\int_{-1}^{+1}\left\{\psi^*_{,L} N_i\, J + \psi^*\, N_i\, J_{,L}\right\} d\xi\right]_k \tag{18}$$

$$\{f\}_{,L} = [A]\{T^p\}_{,L} + [A]_{,L}\{T^p\} - [B]_{,L}\left\{\frac{dT^p}{dn}\right\} - [B]\left\{\frac{dT^p}{dn}\right\}_{,L} \tag{19}$$

Here, $(*)_{,L}$ denotes the derivative of $(*)$ with respect to the design variable X_L. Equation (16) is used for the solution of temperature sensitivity and temperature gradient sensitivity. Some computational aspects concerning the evaluation of various terms in equation (16) and the efficiency of the design sensitivity analysis procedure using this equation are described below.

Evaluation of Singular Terms. The diagonal terms of $[A]_{,L}$ in equation (17) are singular for the case when P and Q coincide. Again, as in the case of heat transfer equation (9), the condition of constant boundary temperature applied to the surface is used in determining these terms. For the constant boundary temperature, we have

$$\left\{\frac{dT}{dn}\right\} = \{T^p\} = \left\{\frac{dT^p}{dn}\right\} = 0$$
$$\{T\}_{,L} = \left\{\frac{dT}{dn}\right\}_{,L} = \{T^p\}_{,L} = \left\{\frac{dT^p}{dn}\right\}_{,L} = 0 \tag{20}$$

These conditions, when used in equation (16), lead to

$$[A]_{,L}\{T\} = 0 \tag{21}$$

Since $\{T\}$ is constant in equation (21), it leads to an expression for the diagonal terms in terms of the off-diagonal terms:

$$A_{ii,L} = -\sum_{\substack{j=1 \\ i \neq j}}^{\text{TNOD}} A_{ij,L}, \quad i = 1, 2, \ldots, \text{TNOD} \tag{22}$$

The off-diagonal terms are nonsingular and are evaluated using Gauss quadrature.

Sensitivity for Internal Heat Generation. The effect of internal heat generation for determining the sensitivities is included in equation (16) through the term $\{f\}_{,L}$ defined in equation (19). As seen from equation (19), the evaluation of $\{f\}_{,L}$ requires the expression for the particular integral solution $\{T_p\}$, which satisfies equation (5). The internal heat generation term f in equation (5) may be expressed in a polynomial form by using the method of global shape function from Henry and Banerjee (1988) or by using the method of stepwise linear regression model of Saigal et al. (1990b). The particular integral solutions for this polynomial can then be determined using the method of undetermined coefficients. The derivatives of these solutions with respect to the design variables are now taken to yield the particular integral sensitivities $\{T^p\}_{,L}$ and $\{dT^p/dn\}_{,L}$. The term $\{f\}_{,L}$ representing the effect of internal heat generation in sensitivity computations can then be determined from this information.

Reduced Design Sensitivity Analysis. The process of numerical shape optimization involves beginning with an initial design and generating a sequence of improving designs in an iterative algorithm to obtain the final optimal shape. A reduction in the size of the model being iterated upon in this process would clearly increase the ability to treat presently untractable large systems. This may be accomplished by reducing the model to retain only the degrees of freedom representing the parts of the design that are allowed to change during the optimization procedure. The multizone BEM (Banerjee and Butterfield, 1981) is especially suited for condensation since the zones can be defined such that the degrees of freedom to be retained appear in separate zones. The rest of the zones can then be condensed to obtain a reduced system of equations.

Considering equation (12), its partitioned form can be written as

$$\begin{bmatrix} A_{MM} & A_{MC} \\ A_{CM} & A_{CC} \end{bmatrix} \begin{Bmatrix} T_M \\ T_C \end{Bmatrix} = \begin{bmatrix} B_{MM} & B_{MC} \\ B_{CM} & B_{CC} \end{bmatrix} \begin{Bmatrix} \left(\frac{dT}{dn}\right)_M \\ \left(\frac{dT}{dn}\right)_C \end{Bmatrix} + \begin{Bmatrix} f_M \\ f_C \end{Bmatrix} \tag{23}$$

where the subscripts M and C refer to the master and the condensed degrees of freedom, respectively. Equation (23) can be rearranged (Kane and Saigal, 1990) to obtain the reduced system of equations

$$[M_1]\{T_M\} = [M_2]\left\{\left(\frac{dT}{dn}\right)_M\right\} + [M_3]\left\{\left(\frac{dT}{dn}\right)_C\right\} + [M_4]\{f_C\} + \{f_M\} \tag{24}$$

where

$$\begin{aligned} [M_1] &= [A_{MM}] - [A_{MC}][A_{CC}]^{-1}[A_{CM}] \\ [M_2] &= [B_{MM}] - [A_{MC}][A_{CC}]^{-1}[B_{CM}] \\ [M_3] &= [B_{MC}] - [A_{MC}][A_{CC}]^{-1}[B_{CC}] \\ [M_4] &= -[A_{MC}][A_{CC}]^{-1} \end{aligned} \tag{25}$$

The solution of the master degrees of freedom can be obtained by solving the reduced system of equations (24). The remaining unknowns may be obtained from the expansion equations given as (Kane and Saigal, 1990)

$$\{T_C\} = [A_{CC}]^{-1}[B_{CM}]\left\{\left(\frac{dT}{dn}\right)_M\right\} + [A_{CC}]^{-1}[B_{CC}]\left\{\left(\frac{dT}{dn}\right)_C\right\} - [A_{CC}]^{-1}[A_{CM}]\{T_M\} + [A_{CC}]^{-1}\left\{\left(\frac{dT}{dn}\right)_C\right\} \tag{26}$$

For the reduced design sensitivity analysis of steady-state heat diffusion problems, the implicit differentiation of equation (24) with respect to the design variable is performed to yield

$$[M_1]\{T_M\}_{,L} = [M_2]\left\{\left(\frac{dT}{dn}\right)_M\right\}_{,L} + \{b_1\} \tag{27}$$

where

$$\{b_1\} = [M_2]_{,L}\left\{\left(\frac{dT}{dn}\right)_M\right\} + [M_3]_{,L}\left\{\left(\frac{dT}{dn}\right)_C\right\} + [M_3]\left\{\left(\frac{dT}{dn}\right)_C\right\}_{,L} + [M_4]_{,L}\{f_C\} + [M_4]_{,L}\{f_C\} - [M_1]_{,L}\{T_M\} + \{f_M\}_{,L} \tag{28}$$

The sensitivities of the $[M_i]$ matrices in equation (28) are obtained by the differentiation of their expressions given in equation (25). Equation (27) is then used for the determination of sensitivities corresponding to the master degrees of freedom for which the iterations are performed in an optimization loop. The sensitivities of the condensed degrees of freedom, if required, may be computed using the expression obtained by the differentiation of the expansion equations (26).

Solution Procedure. The boundary conditions of the diffusion problem treated in this study are: (*a*) prescribed temperature, (*b*) prescribed normal temperature gradient,and (*c*) prescribed relationship between temperature and normal temperature gradient. Any combination of these conditions may be prescribed on the entire boundary or on a portion of the boundary. These boundary conditions are applied to equation (12) for the solution of the steady-state diffusion problem. The following steps describe the solution procedure to obtain the design sensitivities in the diffusion problem:

- Step I: Equation (12) is rearranged such that all the unknowns are on the left-hand side and all the known quantities as per the prescribed boundary conditions are on the right-hand side.
- Step II: The resulting equation (12) is solved for the unknown values $\{T\}$ and $\{dT/dn\}$.
- Step III: The vectors $\{T\}$ and $\{dT/dn\}$ determined from the boundary conditions and Step II are substituted into equation (16).
- Step IV: Equation (16) is rearranged using boundary conditions [similar to the treatment of equation (12) in Step I].
- Step V: The resulting equation (16) is solved for the unknown values of $\{T\}_{,L}$ and $\{dT/dn\}_{,L}$.

It is noted that the left-hand-side coefficient matrix is the same in equations (12) and (16). Thus, the factorization of matrix $[A]$ (modified using boundary conditions) performed for the solution of equation (12) is saved for reuse in the solution of equation (16). This is an attractive feature of the implicit-differentiation process for design sensitivity analysis since it results in a substantial saving of computer time and storage

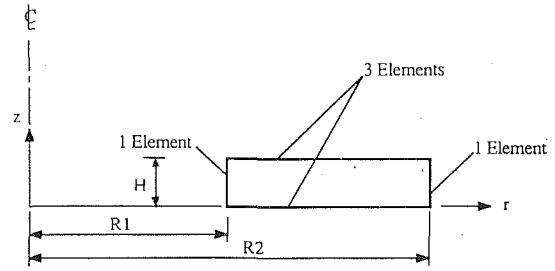

Fig. 1 Hollow cylinder with prescribed temperatures on the inner and outer surfaces

Table 1 Design sensitivity analysis of a hollow cylinder with prescribed temperatures on the inner and outer surfaces

Radius (inch)	Sensitivity					
	Temp. (10^{-2}) T		Temperature Gradient (10^{-1})			
			dT/dn		dT/dr[a]	
	Exact	This Study	Exact	This Study	Exact	This Study
3.0	0.0000	0.0000	1.4193	1.4184	-1.4193	-1.4184
3.5	6.0903	6.0916	0.0000	0.0000	-2.0017	-2.0021
4.0	8.1717	8.1735	0.0000	0.0000	-2.2667	-2.2675
4.5	7.8583	7.8605	0.0000	0.0000	-2.3711	-2.3720
5.0	6.0626	6.0638	0.0000	0.0000	-2.3904	-2.3908
5.5	3.3299	3.3301	0.0000	0.0000	-2.3639	-2.3641
6.0	0.0000	0.0000	-2.3126	-2.3128	-2.3126	-2.3128

[a] These values are obtained using the interior recovery solutions.

requirements. A similar procedure as explained above is used in conjunction with the reduced design sensitivity analysis.

Shape Optimization. The essential components of the shape optimization procedure include: (*a*) a shape definition system that controls the shape by a list of design variables that can be continuously modified without destroying the essential characteristics of that shape, (*b*) an accurate formulation for design sensitivities, and (*c*) a boundary element mesh generation system that includes the capability to allow the mesh to remain valid for a wide range of shape variations. Components (*a*) and (*c*) used in the present study were developed previously for the shape optimization of elastic systems and are described in detail by Saigal and Kane (1990a, 1990b). The sensitivity analysis was performed using the developments reported in this paper. Finally, the BEM analysis and the BEM sensitivity analysis were coupled to the numerical optimization code ADS (Vanderplaats, 1983) to generate optimal shapes in an iterative fashion.

Numerical Results

The developments presented in this paper are now applied to obtain numerical results, which are presented here in two parts. In the first part, the design sensitivity analysis is performed for various sample problems for which analytical solutions are available in the literature. The accuracy of the present formulations is demonstrated in these examples through a comparison of the numerical and analytical results.In the second part, optimal shapes for steady-state diffusion problems are obtained for some geometries that are of practical interest. The shape optimization code, ADS (Vanderplaats, 1983), is driven by the sensitivities computed using the present formulations to obtain optimal shapes.

Design Sensitivity Analysis Examples. The number of iterations required to generate the optimal shape starting from the initial design depends upon the accuracy of the design sensitivities used in the shape optimization algorithm. In this section, the accuracy of the present formulation is demonstrated through the solution of a number of example problems.

Hollow Cylinder With Prescribed Temperatures on the Inner and Outer Surfaces. A hollow cylinder of inner radius $R_1 = 3.0$ in., outer radius $R_2 = 6.0$ in., and height $H = 1.0$ in. is considered. The ends of the cylinder are thermally insulated and are thus at zero axial temperature gradient (flux). The inner and outer cylindrical surfaces are at prescribed temperatures of $T_1 = 5.0°C$ and $T_2 = 3.0°C$, respectively. The sensitivities of the temperature and temperature gradient along the radial direction with respect to variation in the inner radius R_1 are studied in this example.

A rectangular radial cross section of this cylinder is modeled using eight axisymmetric quadratic boundary elements. The mesh distribution used is shown in Fig. 1. The coordinates of the nodal points on the inner surface are parameterized in terms of the inner radius R_1 so that the sensitivities of the geometric quantities are directly obtained using analytical differentiation.

The analytical solution of the purely radial distribution of temperature is given as

$$T(R) = T_1 - \frac{T_1 - T_2}{\ln(R_2/R_1)} \ln\left(\frac{R}{R_1}\right) \tag{29}$$

The analytical solution for the sensitivities of the temperature and the temperature gradient with respect to the inner radius R_1 can then be written, respectively, as

$$\frac{\partial T(R)}{\partial R_1} = \frac{T_2 - T_1}{\left[\ln\left(\frac{R_2}{R_1}\right)^2\right]} \left\{ \left(\frac{\partial R}{\partial R_1}\frac{1}{R} - \frac{1}{R_1}\right) \ln\left(\frac{R_2}{R_1}\right) + \frac{\ln\left(\frac{R}{R_1}\right)}{R_1} \right\} \tag{30}$$

and

$$\frac{\partial}{\partial R_1}\frac{dT(R)}{dR} = \frac{T_1 - T_2}{R_2\left[\ln\left(\frac{R_2}{R_1}\right)\right]^2} \left[\ln\left(\frac{R_2}{R_1}\right)\frac{\partial R}{\partial R_1} - \frac{R}{R_1} \right] \tag{31}$$

The results of the present boundary element design sensitivity analysis for this case are shown in Table 1. The exact analytical sensitivities obtained from the expressions in equations (30) and (31) are also shown in Table 1 for comparison. Very good agreement of the sensitivities for both the temperature and the temperature gradient is obtained.

Hollow Sphere Under a Thermal Environment. A hollow sphere of inner radius $R_1 = 1.0$ in. and outer radius $R_2 = 2.0$ in. is studied. The inner surface is maintained at a constant temperature $T_1 = 3.0°C$, while the outer surface is in contact with a fluid whose temperature, remote from the sphere, is $T_0 = 5.0°C$. The boundary condition at the outer surface is given by

$$\frac{dT}{dn} = -h(T - T_0) \tag{32}$$

where h is the ratio of the heat transfer coefficient at the outer surface to the thermal conductivity of the material of the sphere. In this example, $h = 0.1$. The analytical solution for temperature distribution for this problem is given as

$$T = \frac{A}{R} + B \tag{33}$$

where

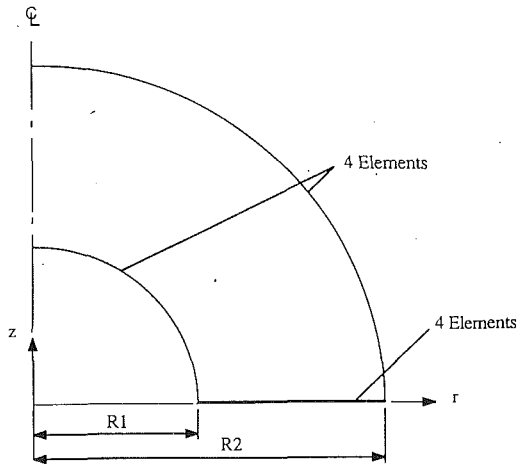

Fig. 2 Hollow sphere in a thermal environment

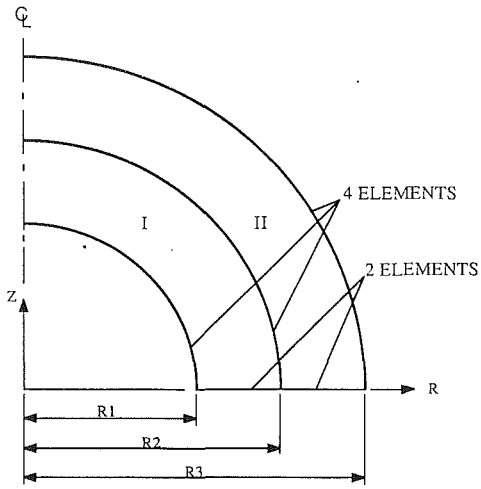

Fig. 3 Compound sphere with prescribed temperature on inner and outer surfaces

Table 2 Design sensitivity analysis of a hollow sphere in a thermal environment

Radius (inch)	Sensitivity: Temperature T		Sensitivity: Temperature Gradient dT/dn		Sensitivity: Temperature Gradient dT/dr[a]	
	Exact	This Study	Exact	This Study	Exact	This Study
1.0	0.0000	0.0000	-1.1111	-1.1111	1.1111	1.1111
1.25	-0.3022	-0.3037	0.0000	0.0000	0.3697	0.3698
1.50	-0.4444	-0.4462	0.0000	0.0000	0.0987	0.0988
1.75	-0.5170	-0.5188	0.0000	0.0000	0.0103	0.0103
2.0	-0.5555	-0.5577	0.0555	0.0557	0.0555	0.0557

[a]These values are obtained using the interior recovery solutions.

Table 3 Design sensitivity analysis of a compound sphere with prescribed temperatures on inner and outer surfaces

Radius (inch)	Sensitivity: Temperature T		Sensitivity: Temperature Gradient dT/dn		Sensitivity: Temperature Gradient dT/dr[a]	
	Exact	This Study	Exact	This Study	Exact	This Study
1.000	0.00000	0.00000	0.6400	0.6411	-0.6400	-0.6411
1.125	0.34370	0.34396	0.0000	0.0000	-2.1913	-2.1943
1.250	0.44800	0.44816	0.0000	0.0000	-2.8672	-2.8701
1.375	0.42050	0.42050	0.0000	0.0000	-3.1081	-3.1094
1.5 (inner)	0.32000	0.32001	-3.1289	-3.1294	-3.1289	-3.1294
1.5 (outer)	0.32000	0.32001	1.5644	1.5647	-1.5644	-1.5647
1.625	0.24994	0.25000	0.0000	0.0000	-1.5194	-1.5195
1.750	0.16980	0.16980	0.0000	0.0000	-1.4479	-1.4487
1.875	0.08533	0.08528	0.0000	0.0000	-1.3653	-1.3657
2.000	0.00000	0.00000	-1.2800	-1.2803	-1.2800	-1.2803

[a]These values are obtained using the interior recovery solutions.

$$A=\frac{R_1R_2(T_1-T_0)}{R^2+\left(\frac{R_1}{h}\right)-R_1R_2} \qquad B=\frac{T_1R_1\left(\frac{1}{h}-R_2\right)+R_2^2T_0}{R_2^2+\left(\frac{R_1}{h}\right)-R_1R_2} \tag{34}$$

The inner radius, R_1, is considered as the design variable in this example. The expression in equation (33) is differentiated with respect to the inner radius, R_1, to obtain the analytical expressions for the corresponding design sensitivities of temperature and temperature gradient as

$$\frac{\partial T(R)}{\partial R_1}=\frac{1}{R^2}\left(R\frac{\partial A}{\partial R_1}-A\frac{\partial R}{\partial R_1}\right)+\frac{\partial B}{\partial R_1} \tag{35}$$

$$\frac{\partial}{\partial R_1}\frac{dT(R)}{dR}=\frac{1}{R_3}\left(2A\frac{\partial R}{\partial R_1}-\frac{\partial A}{\partial R_1}R\right)+\frac{\partial B}{\partial R_1} \tag{36}$$

where

$$\frac{\partial A}{\partial R_1}=\frac{R_2^4(T_1-T_0)}{\left(R_2^2+\frac{R_1}{h}-R_1R_2\right)} \tag{37a}$$

$$\frac{\partial B}{\partial R_1}=\frac{(T_1-T_0)R_2^2}{\left(R_2^2+\frac{R_1}{h}-R_1R_2\right)^2}\left(\frac{1}{h}-R_2\right) \tag{37b}$$

A radial section of the sphere as shown in Fig. 2 is modeled using 12 quadratic axisymmetric boundary elements. The geometric sensitivities due to change in the inner radius, R_1, are analytically obtained for input into the program. The sensitivities of both the temperature and the temperature gradient along a radial direction are shown in Table 2. The exact analytical values of these sensitivities obtained from the expressions in equations (35) and (36) are also shown in Table 2. A comparison of the present boundary element result with the exact analytical results shows good agreement between the two results.

Compound Sphere With Prescribed Temperatures on Inner and Outer Surfaces. A compound sphere consisting of two thick-walled spheres perfectly bonded to each other with inner radius $R_1=1.0$ in. interface radius $R_2=1.5$ in. and outer radius $R_3=2.0$ in. is studied. The inner sphere has a thermal conductivity of $K_1=1.0$ 1/°C and the outer sphere has a thermal conductivity of $K_2=2.0$ 1/°C. The inner and outer surfaces are maintained at temperatures of $T_1=5.0$°C and $T_3=3.0$°C, respectively. The radial temperature distribution for this example can be analytically determined from the following expressions:

$$T_a(R)=\frac{A_a}{R}+B_a \qquad (R_1\le R\le R_2) \tag{38}$$

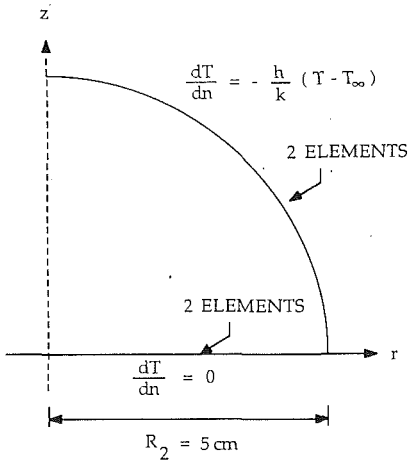

Fig. 4 Solid sphere with internal energy generation and convection boundary conditions

Table 4 Design sensitivity analysis of a solid sphere with energy generation and convection boundary conditions

Radius (inch)	Temperature Sensitivity		Temperature Gradient Sensitivity	
	Exact	This Study	Exact	This Study
0	8333.33	8333.5	--	--
1.25	8229.17	8229.3	--	--
2.50	7916.67	7916.8	--	--
3.75	7395.83	7396.0	--	--
5.00	6666.67	6666.6	-33333.3	-33333.0

$$T_b(R)=\frac{A_b}{R}+B_b \qquad (R_2\le R\le R_3) \tag{39}$$

where

$$A_a=\frac{R_1(R_1+R_3)(T_1-T_2)}{R_3-R_1} \quad A_b=\frac{R_3(R_1+R_3)(T_2-T_3)}{R_3-R_1} \tag{40}$$

$$B_a=\frac{T_3(R_1+R_3)(2R_1T_1)}{R_3-R_1} \quad B_b=\frac{2T_3R_3-T_2(R_1+R_3)}{R_3-R_1} \tag{41}$$

$$T_2=\frac{T_1-(T_1-T_3)(R_2-R_1)R_3K_2}{R_1(R_3K_1-R_3K_2-R_2K_1)+R_2R_3K_2} \tag{42}$$

The inner radius of the sphere, R_1, was considered as the design variable for this example. The exact analytical expression for sensitivities in this case can be obtained by differentiation of the expressions in equations (38) and (39) with respect to R_1 as

$$\frac{\partial T_a(R)}{\partial R_1}=\frac{1}{R^2}\left(\frac{\partial A_a}{\partial R_1}R-\frac{\partial R}{\partial R_1}A_a\right)+\frac{\partial B_a}{\partial R_1}$$

$$\frac{\partial}{\partial R_1}\frac{dT_a(R)}{dR}=\frac{1}{R^3}\left(2A_a\frac{\partial R}{\partial R_1}-\frac{\partial A_a}{\partial R_1}R\right) \tag{43}$$

$$\frac{\partial T_b}{\partial R_1}=\frac{1}{R^2}\left(\frac{\partial A_b}{\partial R_1}R-\frac{\partial R}{\partial R_1}A_b\right)+\frac{\partial B_b}{\partial R_1}$$

$$\frac{\partial}{\partial R_1}\frac{dT_b(R)}{dR}=\frac{1}{R^3}\left(2A_b\frac{\partial R}{\partial R_1}-R\frac{\partial A_b}{\partial R_1}\right)$$

and

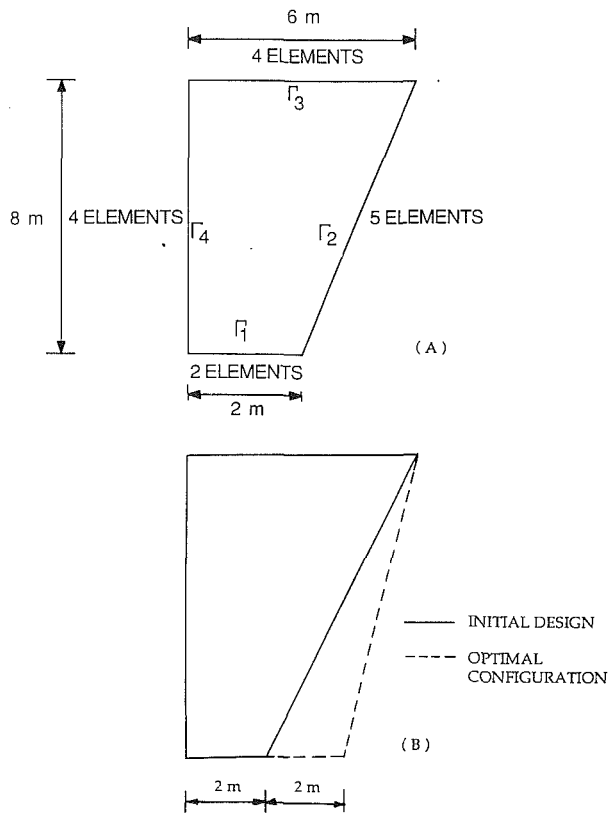

Fig. 5 A cooling fin: (*a*) model; (*b*) initial design and optimal configuration

$$\frac{\partial A_a}{\partial R_1}=\frac{T_1-T_2}{(R_3-R_1)^2}(2R_1R_3-R_1^2R_3^2)-\frac{R_1(R_1+R_3)}{(R_3-R_1)}\frac{\partial T_2}{\partial R_1}$$

$$\frac{\partial A_b}{\partial R_1}=\frac{T_2-T_3}{(R_3-R_1)^2}2R_3^2+\frac{R_3(R_1+R_3)}{R_3-R_1}\frac{\partial T_2}{\partial R_1}$$

$$\frac{\partial B_a}{\partial R_1}=\frac{T_2-T_1}{(R_3-R_1)^2}2R_3+\frac{R_1+R_3}{R_3-R_1}\frac{\partial T_2}{\partial R_1} \tag{44}$$

$$\frac{\partial B_b}{\partial R_1}=\frac{T_3-T_2}{(R_3-R_1)^2}2R_3-\frac{R_1+R_3}{R_3-R_1}\frac{\partial T_2}{\partial R_1}$$

Due to symmetry about the $z=0$ plane, only a quarter of the section of the compound sphere is modeled using 16 elements and 2 zones, as shown in Fig. 3. Zone 1 has 10 elements and was used to model the region of material 2. Across the zone interface, the temperatures are continuous, while the temperature gradients are discontinuous. The sensitivities of temperature and temperature gradient along the radial direction are obtained and are shown in Table 3. The exact analytical results obtained from equation (43) are also shown in Table 3 for comparison, and good agreement is seen.

Solid Sphere With Energy Generation and Convection Boundary Conditions. A solid sphere of radius $R_2=5$ cm is considered for sensitivity analysis. The sphere is heated uniformly at a rate of $g=2\times10^6$ W/m^3 and has a thermal conductivity $K=20$ W/(m°C). The heat is dissipated from the outer surface of the sphere by convection to ambient air at a temperature of $T_\infty=25$°C with a heat transfer coefficient $h=100$ W/(m^2 °C). The analytical expression for temperature distribution in the sphere can be obtained as

$$T(R)=\frac{g}{6K}(R_2^2-R^2)+\frac{gR_2}{3h}+T_\infty \tag{45}$$

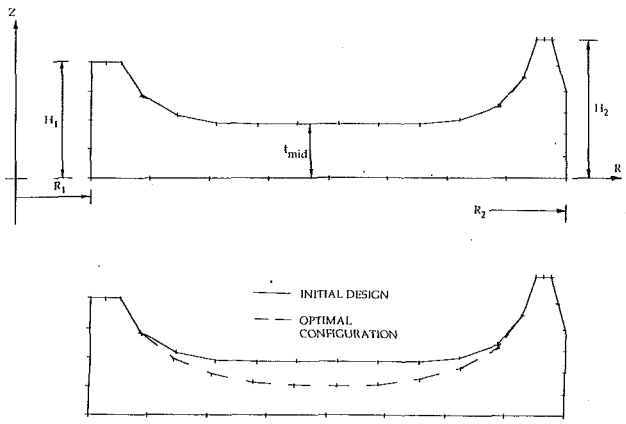

Fig. 6 A rotating disk: (*a*) model; (*b*) initial design and optimal configuration

Considering the radius of the sphere R_2 as the design variable, the analytical expressions for the sensitivities of temperature and temperature gradient, respectively, can be written as

$$\frac{\partial}{\partial R_2}(T(R)) = -\frac{g}{3K}\left(R_2 - R\frac{\partial R}{\partial R_2}\right) + \frac{g}{3h} \tag{46}$$

A radial cross section of the sphere is modeled using four axisymmetric quadratic boundary elements, as shown in Fig. 4. The particular solution for the boundary element analysis for this case is given as

$$T^p = -\frac{g}{6K}(r^2 + z^2) \tag{47}$$

$$\left(\frac{dT}{dn}\right)^p = -\frac{g}{3K}(rn_r + zn_z) \tag{48}$$

The corresponding sensitivities of the particular integral solutions can then be obtained through differentiation of the expressions in equations (47) and (48). The results of the present boundary element design sensitivity analysis are shown in Table 4. The temperature sensitivity and the temperature gradient sensitivity results along the sphere radius are compared in Table 4 with the corresponding exact values. Good agreement is observed.

Shape Optimization Examples. The numerical examples presented in the previous section demonstrate that the present BEM formulation determines the sensitivities accurately for steady-state heat diffusion problems. A number of shape optimization examples are solved next using these sensitivity formulations. Three representative examples for determining the optimal configuration for heat transfer are presented below.

Shape Optimization of a Fin Configuration. The initial geometry of the fin considered in this example is shown in Fig. 5(*a*). Face Γ_1 of the fin is subjected to a constant temperature of T_1. Convection into the ambient medium occurs on boundaries Γ_2 and Γ_3, and the face Γ_4 is insulated. These conditions are expressed as

$$T = T_1 \text{ on } \Gamma_1$$

$$\frac{\partial T}{\partial n} = -\frac{h}{K}(T - T_\infty) \text{ on } \Gamma_2 \cup \Gamma_3$$

$$\frac{\partial T}{\partial n} = 0 \text{ on } \Gamma_4$$

where T_∞ is the ambient temperature, K and h are the heat conduction coefficient and heat convection coefficient, and n denotes the outward normal. The data used for the present example are: $T_1 = 300°C$, $T_\infty = 50°C$, $K = 200$ W/(m °C), and

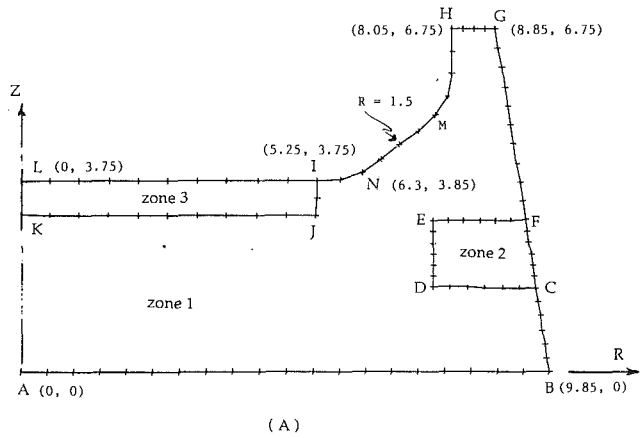

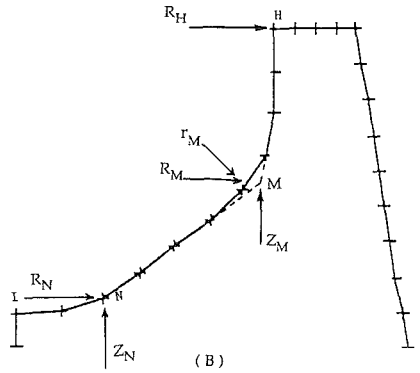

Fig. 7 Blast furnace hearth: (*a*) model; (*b*) design variables for the hearth geometry

$h = 10$ W/(m^2 °C). The physical objective of the shape optimization of the system is to find the shape of the fin domain that gives a uniform temperature of T_0 and Γ_3 under the maximum area constraint. Thus, the objective function and the constraint function respectively, are

$$\text{Objective Function: Minimize } (T_3 - T_0)$$

$$\text{Constraint Function: Volume} \le V_c$$

where $T_0 = 180°C$ and the volume $V_c = 44$ m^2, assuming a unit width. The fin is discretized using 15 two-dimensional quadratic boundary elements, as shown in Fig. 5(*a*). The length of the face Γ_1 is chosen as the design variable. Figure 5(*b*) shows the initial design (solid lines) and the optimal shape obtained in the present study (dotted lines). These designs correspond to a temperature on face Γ_3 of $T_3 = 133°C$ and $T_3 = 165.6°C$, respectively. The shape optimization procedure using the optimization code ADS required a total of 13 iterations to yield the optimal configuration.

Shape Optimization of a Rotating Disk. A rotating disk in a thermal environment is considered for shape optimization. The symmetric portion about the symmetry axis $z = 0$ of the axisymmetric cross section of the disk is shown in Fig. 6(*a*). The geometric data for the initial design are given as $R_1 = 20$ mm, $R_2 = 100$ mm, $H_1 = 20$ mm, $H_2 = 24$ mm, and $t_{mid} = 9.4$ mm. The half-thickness of the disk, t_{mid}, is considered as the design variable for this example. The disk is assumed to be rotating at an angular velocity $\omega = 10$ rad/s.

The disk is modeled using 17 axisymmetric quadratic boundary elements, as shown in Fig. 6(*a*). The inner face of the disk is maintained at a constant temperature of $T_2 = 700°C$. The condition $\partial T/\partial n = 0$ is imposed on the symmetry axes $z = 0$, and all the other surfaces have the convective boundary con-

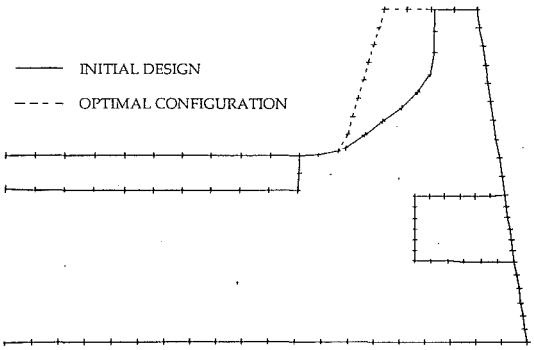

Fig. 8 Initial design and optimal configuration of a blast furnance hearth

dition $\partial T/\partial n = h(T - T_\infty)$, with the convection coefficient $h = 50$ W/(m^2 °C), and the ambient temperature $T_\infty = 50$°C.

The physical objective of shape optimization for this example is defined by the following functions:

$$\text{Objective Function: Minimize } \{\text{Volume } (T_3 - T_0)\}$$

$$\text{Constraint Function: } t_{\text{mid}} \geq 0.5$$

where T_3 is the temperature of the outer radius of the disk, $T_0 = 110$°C, and the requirement that the midthickness be at least 1 in. is imposed due to manufacturing considerations. The initial design and the final shape obtained using the optimization procedure are both shown in Fig. 6, with the final optimal shape denoted by dotted lines. This configuration produces a temperature $T_3 = 110$°C on the outer face and is obtained in 14 iterations of the optimization code.

Shape Optimization of a Blast Furnace Hearth. The axisymmetric section of the blast furnace hearth considered is shown in Fig. 7(*a*). A similar geometry was analyzed earlier by Yoshikawa and Tanaka (1982). The blast furnace hearth is made of ceramic or carbon refractories and is equipped with a cooling system to protect the refractories. The boundary conditions for the hearth are given as

$$\frac{\partial T}{\partial n} = h_1(T - T_{\infty 1}) \text{ on } \Gamma_{AB}$$

$$\frac{\partial T}{\partial n} = h_2(T - T_{\infty 2}) \text{ on } \Gamma_{BG}$$

$$\frac{\partial T}{\partial n} = 0 \text{ on } \Gamma_{GH} \text{ and } T = T_C \text{ on } \Gamma_{HL}$$

with $h_1 = 40.7$ W/(m^2 °C), $h_2 = 105$ W(m^2 °C), $T_{\infty 1} = 30$°C, $T_{\infty 2} = 30$°C, and $T_c = 300$°C. The hearth is comprised of three different refractories, each made up of a separate homogeneous material. The hearth is modeled using three zones and a total of 48 quadratic axisymmetric boundary elements, as shown in Fig. 7(*a*). The three zones represent the three refractories of the hearth. The thermal conductivities of the materials of the three refractories are $K_1 = 9.3$ W/(m °C) for zone 1, $K_2 = 14$ W/(m °C) for zone 2, and $K_3 = 3.49$ W/(M °C) for zone 3.

The physical objective of the optimization problem is to achieve a uniform distribution of temperature in the interior of zone 2 as close to the desired temperature of 390°C as possible. Only the portion HMNI of the initial design is allowed to be changed. This portion of the design is defined using six design variables, as shown in Fig. 7(*b*). In this figure, *R*, *Z*, and *r* denote the *r* coordinate,the *z* coordinate, and the arc radius, respectively. In addition, the conditions $R_N \geq R_{NI}$ and $Z_N \geq Z_{NI}$ also has to be satisfied, where the subscript *I* denoted the initial design. Since the changing portion of the boundary belongs solely to zone 1, zones 2 and 3 are condensed to allow optimization iterations on a smaller matrix. The initial design corresponds to a maximum temperature of 477°C in zone 2. The final design is obtained in 21 iterations of the optimization code ADS and corresponds to a maximum temperature of 390°C in zone 2. Both the initial design and the optimal shape obtained are shown in Fig. 8, with the optimal shape shown in dotted lines.

Concluding Remarks

An efficient approach for the design sensitivity analysis of two-dimensional and axisymmetric steady-state heat diffusion problems using the boundary element approach was presented. The present formulations are based on the implicit differentiation of the discretized boundary integral equations with respect to the design variable to obtain the sensitivity equations. This results in an efficient algorithm that eliminates the need for any new matrix factorization for the determination of design sensitivities. A procedure is presented for the design sensitivity analysis using a reduced system of equations based on substructuring and static condensation. Numerical algorithms and solution procedures are presented for obtaining the sensitivities of temperatures and temperature gradients. The accuracy of the present formulation is demonstrated through comparison of the sensitivity results for a number of example problems with their corresponding exact solutions. The shape optimization of a cooling fin, a rotating turbine disk, and a blast furnace hearth, each subjected to their respective thermal environment, are performed to show the practical utility of the present developments.

Acknowledgments

S. Saigal's contribution to this research is supported by Grant No. MSS-8996258 of the U.S. National Science Foundation and by General Dynamics, Electric Board Division, Groton, Connecticut. A. Chandra's contribution to this research is supported by Grant No. DMC-8657345 of the U.S. National Science Foundation. The authors gratefully acknowledge this financial support.

References

Adelman, H. M., and Haftka, R. T., 1986, "Sensitivity Analysis of Discrete Structural Systems," *AIAA J.*, Vol. 24, No. 5, pp. 823–832.

Aithal, R., Saigal, S., and Mukherjee, S., 1990, "Three-Dimensional Boundary Element Implicit-Differentiation Formulation for Structural Design Sensitivity Analysis," *Computers and Mathematics With Applications,* in press.

Banerjee, P. K., and Butterfield, R., 1981, *Boundary Element Methods in Engineering Science,* McGraw-Hill, New York.

Barone, M., and Yang, R. J., 1988, "Boundary Integral Equations for Recovery of Design Sensitivities in Shape Optimization," *AIAA J.,* Vol. 26, pp. 589–594.

Chandra, A., and Chan, C. L., 1990, "A BEM Formulation for Design Sensitivities in Steady-State Convection Problems," ASME *J. Appl. Mech.,* in press.

Haug, E. J., Choi, K. K., and Komkov, V., 1986, *Design Sensitivity Analysis of Structural Systems,* Academic Press, New York.

Henry, D. P., Jr, and Banerjee, P. K., 1988, "A New Boundary Element Formulation for Two- and Three-Dimensional Thermoelasticity Using Particular Integrals," *Int. J. Num. Meth. Engng.,* Vol. 26, pp. 2061–2077.

Kane, J. H., and Saigal, S., 1988, "Design Sensitivity Analysis of Solids Using BEM," *J. Engng. Mech.,* Vol. 114, No. 10, pp. 1703–1722.

Kane, J. H., and Saigal, S., 1990, "An Arbitrary Condensing, Non-condensing Solution Strategy for Large Scale, Multi-zone Boundary Element Analysis," *Computer Methods in Applied Mechanics and Engineering,* in press.

Meric, R. A., 1986, "Optimal Thermal Insulation by the Boundary Element Method," *Numerical Heat Transfer,* Vol. 9, pp. 163–182.

Mukherjee, S., and Chandra, A., 1989, "A Boundary Element Formulation for Design Sensitivities in Materially Nonlinear Problems," *Acta Mechanica,* Vol. 78, pp. 243–253.

Mukherjee, S., and Chandra, A., 1990, "A Boundary Element Formulation for Design Sensitivities of Problems Involving Both Geometric and Material Nonlinearities," *Computers and Mathematics With Applications,* in press.

Pape, D. A., and Banerjee, P. K., 1987, "Treatment of Body Forces in 2D Elastostatics BEM Using Particular Integrals," ASME *J. Appl. Mech.,* Vol. 54, pp. 866–871.

Park, C. W., and Yoo, Y. M., 1988, "Shape Design Sensitivity Analysis for

a Two-Dimensional Heat Transfer System Using the Boundary Element Method," *Comp. Struct.*, Vol. 28, pp. 543–550.

Rice, J. S., and Mukherjee, S., 1990, "Design Sensitivity Coefficients for Axisymmetric Elasticity Problems by Boundary Element Methods," *Engineering Analysis,* in press.

Saigal, S., and Aithal, R., 1990, "Adjoint Structure Approach for Shape Design Sensitivity Analysis Using BEM," ASME *J. Engng. Mech.*, in press.

Saigal, S., Borggaard, J. T., and Kane, J. H., 1989, "Boundary Element Implicit Differentiation Equations for Design Sensitivities of Axisymmetric Structures," *Int. J. Solids Struct.*, Vol. 25, No. 5, pp. 527–538.

Saigal, S. Aithal, R., and Kane, J. H., 1990a, "Conforming Boundary Elements in Plane Elasticity for Shape Design Sensitivity," *Int. J. Num. Meth. Engng.*, Vol. 28, pp. 2795–2811.

Saigal, S., Gupta, A., and Cheng, J., 1990b, "Stepwise Linear Regression Particular Integrals for Uncoupled Thermoelasticity With Boundary Elements," Int. J. Solids Struct., Vol. 28, No. 4, pp. 471–482.

Saigal, S., and Kane, J. H., 1990a, "A Boundary Element Shape Optimization System for Aircraft Components," *AIAA J.*, in press.

Saigal, S., and Kane, J. H., 1990b, "Design Sensitivity Analysis of Boundary Element Substructures," *AIAA J.*, in press.

Vanderplaats, G. N., 1983, *Numerical Optimization Techniques for Engineering Design,* McGraw-Hill, New York.

Yoshikawa, F., and Tanaka, M., 1982, "Boundary Elements in Axisymmetric Potential Problems," *Proceedings, Fourth International Seminar on Boundary Element Methods,* C. A. Brebbia, ed., Southampton, United Kingdom, pp. 101–110.

ERRATA

Errata for the technical paper "Investigation of High-Intensity Beam Characteristics on Welding Cavity Shape and Temperature Distribution," by P. S. Wei, T. H. Wu, and Y. T. Chow, JOURNAL OF HEAT TRANSFER, Vol. 112, pp. 163–169, February 1990.

In Fig. 14 on p. 168, the abscissa $u\sigma/\alpha_s$ should be replaced by $u\sigma/\sqrt{6}\alpha_s$ due to a scale error. The authors would like to thank Prof. W. H. Giedt of Sandia National Laboratories, Livermore, CA, for bringing this error to their attention.

Thermal Aspects of Grinding: Heat Transfer to Workpiece, Wheel, and Fluid

A. S. Lavine

T.-C. Jen

University of California, Los Angeles,
Los Angeles, CA 90024-1597

A model of heat transfer in grinding has been developed that considers heat removed from the grinding zone by the workpiece, abrasive grains, and grinding fluid. This model eliminates the need to specify the fraction of the total grinding power that enters the workpiece, or the convection coefficient due to the grinding fluid. The dependence of the workpiece temperature on the various grinding parameters has been explored.

Introduction

This paper addresses thermal aspects of the grinding process. In any grinding process, essentially all of the grinding power is dissipated as heat in the grinding zone, at the interface between the wheel and the workpiece (Outwater and Shaw, 1952). This heat causes the workpiece and wheel temperatures to rise, which may cause thermal damage. Thermal damage can take various forms, such as workpiece burning, softening of the surface layer with possible rehardening and embrittlement, thermal expansion, which can lead to unfavorable residual tensile stresses and reduced geometric accuracy, cracks, and accelerated wheel wear. Thermal damage is the main limitation to increasing removal rates while maintaining high-quality surfaces.

The grinding process is illustrated in Fig. 1. The grinding zone is the region of length l and depth b (into the page) over which the wheel contacts the workpiece. The wheel and workpiece are shown moving in the same direction. This is termed down grinding, since the wheel moves downward through the grinding zone. The analyses that follow are strictly only applicable to down grinding, since then the wheel, fluid, and workpiece all enter the grinding zone at the same point, $x=0$, and their temperatures all begin to increase from that same point. However, the results should be qualitatively applicable to upgrinding as well. Some typical grinding parameters are as follows. The wheel speed and diameter are on the order of $v_s=30$ m/s, $d=200$ mm. For conventional grinding the workpiece speed, depth of cut, and grinding zone length are on the order of $v_w=0.1$ m/s, $a=10$ μm, and $l=(ad)^{1/2}=1$ mm. For creep feed grinding, the workpiece speed is much lower and the depth of cut much higher, e.g., $v_w=1$ mm/s, $a=1$ mm, $l,=(ad)^{1/2}=10$ mm.

The heat generated in the grinding zone is removed from that region in a variety of ways: (*a*) It may conduct downward into the workpiece, where it is convected away by the motion of the workpiece; (*b*) it may conduct upward into the wheel, where it is convected away by the motion of the wheel, and then removed from the wheel (to some extent) by the surrounding air; (*c*) it may be removed by the grinding fluid; or (*d*) it may be carried away by the chips. However, this last contribution is typically not large, even for large material removal rates (Malkin, 1989), and will be neglected here. This assumption is least accurate in creep feed grinding.

There has been a substantial amount of research concerning heat transfer in grinding. Snoeys et al. (1978) and Malkin (1984a) present literature reviews. Only papers of direct concern to the present work will be mentioned here. Malkin (1974) and DesRuisseaux and Zerkle (1970a) calculated the peak workpiece temperature by considering three types of heat sources due to: (*a*) the distributed action of all grains cutting into the workpiece; (*b*) the shear plane due to an individual grain; and (*c*) the wear flat area of an individual grain (Malkin only). Kopalinsky (1984) performed a more complex calculation of the workpiece temperature distribution by assuming some random distribution of grains and superposing the temperature rise due to each one. DesRuisseaux and Zerkle (1970b) modeled the heat transfer from the workpiece to the fluid using a constant convection coefficient over the entire surface, which had to be specified. Sauer (1972) used a combined experimental and analytical approach to estimate the value of the convection coefficient.

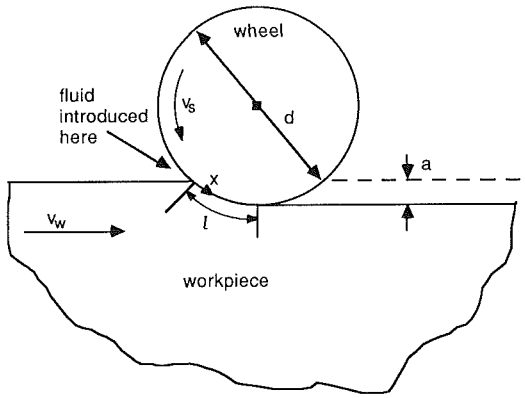

Fig 1 Grinding geometry

All of these previous analyses of heat transfer in the grinding process have addressed heat transfer in the workpiece only, with appropriate thermal boundary conditions at its surface. In particular, this requires specification of the fraction of the grinding energy that enters the workpiece, and the convection coefficient due to the grinding fluid. The intent of this paper is to eliminate the need to specify these quantities by analyzing the coupled heat transfer to the workpiece, wheel, and fluid. This work builds on the analyses presented by Lavine (1988), Lavine and Malkin (1990), and Lavine et al. (1989).

It should be noted that the subject of thermal contact conductance is also relevant to the problem of heat transfer between the abrasive grain and the workpiece. A recent review of this area is given by Yovanovich (1986). Kennedy (1984) reviews the topic of sliding contacts. Kuhlmann-Wilsdorf (1987) evaluates the temperature at the interface between two materials in sliding contact, due to frictional heating. Yuen (1988)

Contributed by the Heat Transfer Division and presented at the ASME Winter Annual Meeting, San Francisco, California, December 10–15, 1989. Manuscript received by the Heat Transfer Division December 14, 1989, revision received July 23, 1990. Keywords: Conduction, Materials Processing and Manufacturing Processes.

also evaluates the temperature distribution in two solids in relative motion when heat is generated at their interface.

Analysis

As an individual grain passes over the workpiece, heat is generated at three locations: the grain/workpiece interface, the grain/chip interface, and the shear plane between the workpiece and chip. The two mechanisms of heat generation are friction (at the grain/workpiece and grain/chip interfaces) and plastic deformation (at the shear plane and at the grain/workpiece interface due to "plowing," i.e., the grain pushing workpiece material aside without removing a chip (Malkin, 1974)). For simplicity, the heat will be thought of as being generated at the grain–workpiece interface, although this is not a precise description of the locations of heat generation. The rate at which heat is generated at a grain–workpiece interface (per unit area) is termed q''_{grind}. This heat instantaneously conducts into either the workpiece or the wheel (see Fig. 2). Thus, $q''_{\text{grind}} = q''_{wg} + q''_g$ where q''_{wg} is the heat flux into the workpiece at the grain location and q''_g is the heat flux into the grain.

Of the heat that is conducted into the workpiece, some remains in the workpiece and some is removed by convection to the fluid (see Fig.2). (Some also leaves with the chip, but as mentioned previously this will be neglected.) This can be expressed as follows: $q''_{wg} A_g = q''_{wb} A_{\text{tot}} + q''_f (A_{\text{tot}} - A_g)$, where $A_{\text{tot}} = lb$ is the area of the entire grinding zone and A_g is the area over which there is actual contact between the grains and the workpiece. Also, in this expression q''_{wb} is the heat flux that remains in the workpiece, which is assumed to be evenly distributed over the entire workpiece surface (more about this later), and q''_f is the heat flux into the fluid, assumed uniform over the area exposed to the fluid.

Now, separate models will be developed for heat transfer to the abrasive grain, the fluid, and the workpiece. These models will then be coupled to yield the temperature at the interface between the workpiece and wheel. This can be used as an indicator of whether thermal damage will occur.

Heat Transfer to Abrasive Grain. Consider a single grain moving along the workpiece surface with velocity v_s. Let the heat flux into the grain at the workpiece surface be q''_g. In the cylindrical coordinate system fixed to the grain (see Fig. 3), the grain temperature depends on r, z, and on the time t since the grain entered the grinding zone. (Note that t is related to the distance from the beginning of the grinding zone, $t = x/v_s$.) Due to the large thermal conductivity of the grain relative to the grinding fluid, it is reasonable to assume that the heat that enters the grain simply conducts further into the grain without being removed by the fluid. (This assumption has been investigated in detail and it was found that the convection heat transfer from the grain to the fluid was no more than 0.4 percent of the heat transfer into the grain.) It will at first be assumed that q''_g is independent of time (i.e., distance from the beginning of the grinding zone). Later, this assumption will be modified. The grain will be modeled as a frustum of a cone, so that the cross-sectional area is $A_c = \pi r_g^2 = \pi (r_o + \gamma z)^2$ where $\gamma = dr_g/dz \approx 1$ (since on the average the grains are as wide as they are high). Then there is an exact solution for $\bar{\theta}_g$, the radially averaged grain temperature rise relative to the

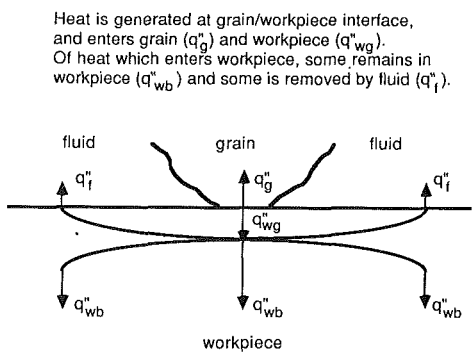

Fig 2 Heat transfer paths

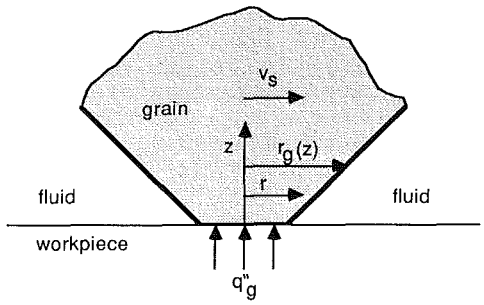

Fig 3 Model for heat transfer in abrasive grain

Nomenclature

A = fractional grain–workpiece contact area = A_g/A_{tot}
$A_c(z)$ = individual grain cross-sectional area
A_g = total grain–workpiece contact area
A_0 = individual grain–workpiece contact area
A_{tot} = grinding zone area = lb
b = grinding zone depth
c_p = specific heat
$f(\zeta)$ = function defined by equation (3)
h = heat transfer coefficient
I_1 = integral defined by equation (7)
I_2 = integral defined by equation (8)
I_3 = integral defined by equation (20)
k = thermal conductivity
l = grinding zone length
l_g = dimension of square heat source due to individual grain
L = $v_s\, l/\alpha_w$
L_g = $v_s\, l_g/\alpha_w$
q = heat transfer rate
q'' = heat flux
$r_g(z)$ = grain radius
r_o = radius of grain–workpiece contact area
v_s = wheel velocity
v_w = workpiece velocity
x = distance from beginning of grinding zone
$\hat{x}$ = coordinate along surface relative to grain heat source
z = coordinate normal to surface
α = thermal diffusivity
ζ = $(\pi\alpha_g\, x/A_o v_s)^{1/2}$
θ = temperature rise relative to ambient temperature
κ = defined by equations (22*a*) and (22*b*)
ρ = density
Φ = nondimensional temperature = $h_{wb}\theta_{wb,s}/q''_{\text{tot}}$

Subscripts

f = fluid
g = grain
grind = grinding power
s = surface (except in v_s)
tot = total
w = workpiece
wb = workpiece background
wg = workpiece under grain

ambient wheel temperature (Lavine et al., 1989). The surface temperature is given by

$$\bar{\theta}_g(z=0)=\frac{q_g'' r_o}{k_g}\left[1-\exp(\zeta^2)\operatorname{erfc}(\zeta)\right] \tag{1}$$

where

$$\zeta(x)=(\alpha_g x/r_o^2 v_s)^{1/2}=(\pi\alpha_g x/A_o v_s)^{1/2}, \text{ with } A_o=\pi r_o^2.$$

For the purpose of matching this solution to the solutions for the wheel and fluid, it will be useful to define a local heat transfer coefficient for the grain as follows:

$$h_g(x)=q_g''/\bar{\theta}_g(z=0)=\sqrt{\pi(k\rho c_p)_g v_s/4x}\, f(\zeta) \tag{2}$$

where

$$f(\zeta)=\frac{2}{\pi^{1/2}}\frac{\zeta}{1-\exp(\zeta^2)\operatorname{erfc}(\zeta)} \tag{3}$$

The function $f(\zeta)$ can be thought of as accounting for the fact that the cross-sectional area of the grain increases with z, so the heat "spreads out" as it conducts further into the grain, which increases the rate of heat transfer. The function $f(\zeta)$ increases slower than $x^{1/2}$, so that $h_g(x)$ decreases with x, but not as rapidly as $x^{-1/2}$.

Heat Transfer to Grinding Fluid. In analyzing the heat transfer from the workpiece to the fluid, it is helpful to recognize that the contact area between the workpiece and the grains is typically only a few percent of the total grinding zone area. Thus, over most of the grinding zone, the fluid comes into contact with the workpiece surface. There is assumed to be a heat flux q_f'' into the fluid from the workpiece surface. This heat flux will be assumed uniform over the grinding zone. Consistent with the model of the abrasive grain, the heat transfer between the grains and the fluid is neglected. It is assumed that the grinding fluid completely fills the space around the abrasive grains, to a depth greater than the thermal boundary layer thickness (Lavine, 1988), although this may not always be the case. It is further assumed that the fluid is at rest with respect to the wheel, so that the fluid moves past the workpiece with uniform velocity v_s. Then the fluid is simply a moving "semi-infinite solid," with a uniform heat flux at its surface. Finally, based on the large Peclet number (typically $v_s\, l/\alpha_f$ is on the order of 10^5 or greater), conduction in the direction of motion is neglected. The solution for the temperature distribution in the fluid is then the well-known error-function solution, and the local heat transfer coefficient for the fluid is given by

$$h_f(x)=q_f''/\theta_f(z=0)=\sqrt{\pi(k\rho c_p)_f v_s/4x} \tag{4}$$

This solution assumes that the fluid remains liquid. In reality, the fluid may boil under some conditions. This is discussed in more detail by Lavine and Jen (1991).

Heat Transfer to Workpiece. The temperature distribution in the workpiece is due to the action of many individual grains producing heat at discrete points of the workpiece surface. One method of calculating the workpiece temperature is to assume some distribution of heat sources, and superpose the temperature rises due to each heat source (Kopalinsky, 1984). A simpler method that has been used in the past (Hahn, 1956; Malkin, 1974; DesRuisseaux and Zerkle, 1970a) is to consider the temperature distribution to be the superposition of a "background" or "interference zone" temperature rise and an "individual grain" temperature rise. The background temperature rise is calculated by taking the heat generation at all grains and distributing it uniformly over the grinding zone. The workpiece moves relative to the grinding zone heat source with the workpiece velocity v_w. The individual grain temperature rise is calculated from a heat source at an individual grain–workpiece contact area, moving past the workpiece with the wheel velocity v_s.

Background Temperature Rise. To calculate the background temperature rise, the entire grinding zone is thought of as a distributed heat source, which causes a heat flux q_{wb}'' into the workpiece. This heat flux will be taken as uniform. The workpiece is then a moving semi-infinite medium with a uniform heat flux at its surface. If conduction in the direction of motion is neglected, the solution is exactly analogous to that for the fluid temperature. The Peclet number for the workpiece is *not* always large enough to justify neglecting conduction in the direction of motion; for "creep feed" grinding conditions, $v_w\, l/\alpha_w$ can be less than unity. However, for creep feed grinding heat transfer into the workpiece is not dominant, so that an error in heat transfer to the workpiece does not cause a substantial error in temperature prediction. For instance, the effect of axial conduction was assessed for one typical creep feed grinding case, and was found to change the temperature by only 3 percent. Therefore, conduction in the direction of motion can be neglected without significant error. Given this assumption, the local heat transfer coefficient corresponding to the workpiece background temperature is

$$h_{wb}(x)=q_{wb}''/\theta_{wb}(z=0)=\sqrt{\pi(k\rho c_p)_w v_w/4x} \tag{5}$$

Individual Grain Temperature Rise. An individual grain is modeled as a square heat source of dimension l_g moving with velocity $v_s-v_w\approx v_s$ relative to the workpiece surface, and causing a heat flux q_{wb}'' into the workpiece surface (see Fig. 4). A square heat source is used for convenience, even though the analysis of the grain assumed that the contact area between the grain and workpiece was circular. The heat flux will be assumed uniform over the heat source area, and unchanging as the grain moves through the grinding zone.

The grain first makes contact with the workpiece at the beginning of the grinding zone, $x=0$. For locations extremely close to $x=0$, the temperature rise in the workpiece due to the grain heat source depends on x. However, for larger x (greater than about 50 μm for typical grinding conditions) the temperature distribution becomes essentially independent of x, and depends only on the location measured relative to the heat source, $(\hat{x}, y, z)$ (see Fig. 4). Since the grinding zone is usually on the order of a millimeter or longer, it is reasonable to neglect the dependence on x. The temperature distribution can be calculated using moving heat source theory (Carslaw and Jaeger, 1947). The temperature distribution due to a point heat source is integrated over a square region to yield the following for the workpiece temperature rise due to an individual grain:

$$\theta_{wg}=\frac{q_{wg}''}{2\pi k_w}\int_0^{l_g}\int_0^{l_g}\frac{e^{-v_s[R-(\hat{x}-x_0)]/2\alpha_w}}{R}dx_0 dy_0 \tag{6}$$

where θ_{wg} is the temperature rise relative to the workpiece background temperature, and $R^2=(\hat{x}-x_0)^2+(y-y_0)^2+z^2$. Evaluating the temperature at the workpiece surface, $z=0$, and performing a change of variables, yields

$$\theta_{wg,s}=\frac{q_{wg}''}{2\pi(\rho c_p)_w v_s}\int_Y^{Y-L_g}\int_X^{X-L_g}\frac{e^{-[\sqrt{\xi^2+\eta^2}-\xi]/2}}{\sqrt{\xi^2+\eta^2}}d\xi d\eta \tag{7}$$

$$=\frac{q_{wg}''}{2\pi(\rho c_p)_w v_s}I_1(X, Y, L_g)$$

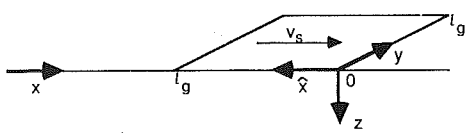

Fig 4 Model for individual grain heat source

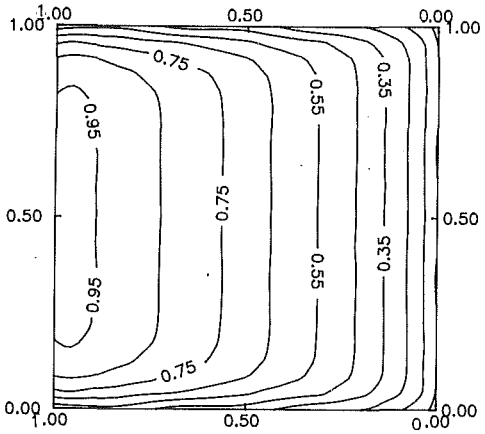

Fig 5 Isotherms for temperature under grain heat source (isotherms are normalized with respect to the maximum temperature)

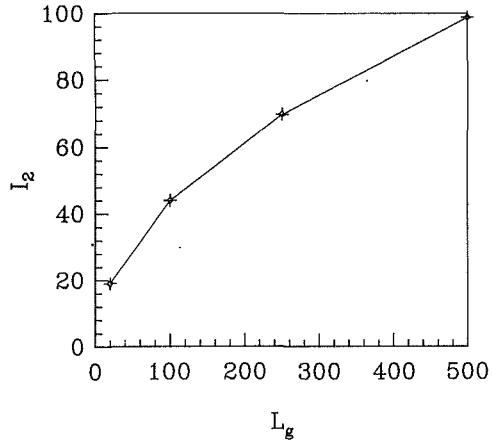

Fig 6 l_2 versus L_g

where $X=\frac{\hat{x}v_s}{\alpha_w}$, $Y=yv_s/\alpha_w$, and $L_g=\frac{l_g v_s}{\alpha_w}$. Figure 5 shows an isotherm plot of $\theta_{wg,s}$ directly underneath the heat source. The temperature has been normalized with respect to its maximum value, and the coordinates have been normalized with respect to l_g. The temperature at each point (X, Y) of an 82 × 82 grid was calculated by integrating over an 82 × 82 (x_0, y_0) grid using Simpson's rule. The temperature is seen to be maximum near the trailing edge of the heat source (the grain heat source moves to the right.)

It should be recalled that the analysis of heat transfer into the grain solved for the radially averaged grain temperature. Thus, it will not be possible to match the present solution for the *local* workpiece temperature under the grain to that earlier solution for the temperature of the grain. Instead, the average workpiece temperature under the grain will be matched to the average grain temperature. The average value of $\theta_{wg,s}$ is calculated by integrating equation (7) over the heat source area:

$$\bar{\theta}_{wg,s}=\frac{q''_{wg}}{2\pi(\rho c_p)_w v_s}\frac{1}{L_g^2}\int_0^{Lg}\int_0^{Lg} I_1(X,\ Y,\ L_g)\,dXdY \qquad (8)$$

$$=\frac{q''_{wq}}{2\pi(\rho c_p)_w v_s} I_2(L_g)$$

Note that the temperature rise $\bar{\theta}_{wg,s}$ is not a function of location, it is simply a constant for given grinding parameters. The quantity I_2 is shown in Fig. 6 as a function of L_g. This integral was calculated using Simpson's rule and the 82 × 82 (X, Y) grid. The result was compared to the results for a 61 × 61 grid, and differed by less than 9 percent, and to the results for a 121 × 121 grid and differed by less than 7 percent. A heat transfer coefficient for the individual grain heat source is defined as usual:

$$\bar{h}_{wg}=q''_{wg}/\bar{\theta}_{wg,s}=2\pi(\rho c_p)_w v_s/I_2(L_g) \qquad (9)$$

Coupling the Models. Now the models for the wheel, fluid, and workpiece will be coupled, by requiring that the surface temperatures match. In particular, it will be assumed that at a point on the workpiece surface that is *not* underneath a grain, the temperature rise is equal to the workpiece background temperature rise, $\theta_{wb,s}$, and this must equal the fluid temperature rise, $\theta_{f,s}$:

$$\theta_{wb,s}(x)=\theta_{f,s}(x) \qquad (10)$$

At a point on the workpiece surface that *is* underneath a grain, the grain temperature rise, $\bar{\theta}_{g,s}$, must equal the *sum* of the workpiece background temperature rise and the individual grain temperature rise:

$$\bar{\theta}_{g,s}(x)=\theta_{wb,s}(x)+\bar{\theta}_{wg,s} \qquad (11)$$

In writing these two equations, it has been assumed that the ambient temperatures are the same for the wheel, fluid, and workpiece. Making use of the heat transfer coefficients defined in equations (2), (4), (5), and (9), equations (10) and (11) become

$$\frac{q''_{wb}}{h_{wb}(x)}=\frac{q''_f}{h_f(x)} \qquad (12a)$$

$$\frac{q''_g}{h_g(x)}=\frac{q''_{wb}}{h_{wb}(x)}+\frac{q''_{wg}}{h_{wg}} \qquad (12b)$$

There are two additional relationships between the unknown heat fluxes, which were given earlier, namely

$$q''_{\text{grind}}=q''_{wg}+q''_g \qquad (13a)$$

$$q''_{wg}\,A_g=q''_{wb}\,A_{\text{tot}}+q''_f\,(A_{\text{tot}}-A_g) \qquad (13b)$$

If q''_{grind} in equation (13a) is assumed to be known, then equations (12a,b) and (13a,b) are four equations that can be solved for the four unknown heat fluxes. Unfortunately, at this point a contradiction becomes apparent. All heat fluxes were assumed to be constant. The heat transfer coefficients h_{wb} and h_f both vary as $x^{-1/2}$. Thus, equation (12a) can be satisfied. However, equation (12b) cannot be satisfied, because h_g varies as $x^{-1/2}f(\zeta)$, h_{wb} varies as $x^{-1/2}$, and $\bar{h}_{wg}$ is constant. In other words, the true solution to the coupled heat transfer problem does not have uniform heat fluxes into each of the various materials. Some or all of the heat fluxes will depend on x, regardless of whether or not q''_{grind} itself varies with x.

There are a variety of ways to resolve this problem. One would be to solve the actual coupled heat transfer problem and determine how the heat fluxes depend on x. However, the additional complexity of this approach would not be warranted, since the accuracy of the solution is limited by other factors. For instance, the x dependence of q''_{grind} is not accurately known to begin with, so that the x dependence of the other heat fluxes could not be accurately determined. Furthermore, there is substantial uncertainty in some of the parameters, such as A_g and l_g. An alternative and very simple approach would be to require that the temperatures match at only one point in the grinding zone, such as the midpoint or the hottest point ($x=l$). A third option, and the one that will be used here, is to insist that q''_{wb}, q''_f, and q''_{wg} be uniform, but to allow q''_g to vary with x in equation (12b) in such a way as to satisfy the equation at every point in the grinding zone. (Of course, then the solution that was derived for the temperature of the grain is no longer strictly valid. This will be discussed later.) If q''_g varies with x, then equation (13a) implies that q''_{grind} must vary with (x) as well, in a particular manner. Thus, rather than specifying q''_{grind} (x), only the total grinding power, q_{tot}, will be specified. This is actually preferable, since the total

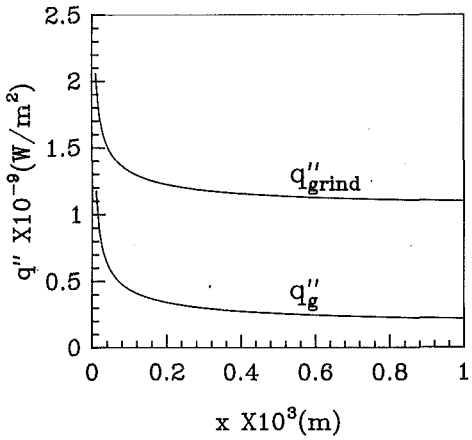

Fig 7 The x dependence of q''_g and q''_{grind}

grinding power can easily be measured experimentally, but not its x dependence. A fictitious x dependence of q''_{grind} will then be dictated by equation (13*a*). Finally, in equation (12*b*), q''_g will be replaced with $q''_g(x)$, and equation (13*a*) will be replaced with the integrated equivalent:

$$q_{tot} = \int_{A_g} q''_{grind}(x)\,dA_g = q''_{wg}\,A_g + \int_0^l q''_g(x)\,b\,dx\,\frac{A_g}{A_{tot}} \quad (14)$$

Equations (12*a*, *b*) and (13*b*) can be used to express $q''_g(x)$ and q''_{wg} in terms of q''_{wb}, and the result can be substituted into equation (14), to yield the following equation for q''_{wb}:

$$q''_{wb} = \frac{q''_{tot}}{[1+\frac{h_f}{h_{wb}}(1-A)]\,[1+\frac{\bar{h}_g}{h_{wg}}] + A\,\overline{(h_g/h_{wb})}} \quad (15)$$

where A is the *fractional* area of the grinding zone over which there is actual contact, i.e., $A = A_g/A_{tot}$, and q''_{tot} is the average grinding power flux based on the total grinding zone area, i.e., $q''_{tot} = q_{tot}/A_{tot}$. The two newly introduced functions $\bar{h}_g$ and $\overline{(h_g/h_{wb})}$ will be defined now and written out in greater detail later:

$$\bar{h}_g = \frac{1}{l}\int_0^l h_g\,dx \quad (16a)$$

$$\overline{(h_g/h_{wb})} = \frac{1}{l}\int_0^l (h_g/h_{wb})\,dx \quad (16b)$$

Now that q''_{wb} has been determined, all other heat fluxes are known. Examples of q''_g and q''_{tot} are plotted as functions of x in Fig. 7. It can be seen that they do not vary rapidly except for very near $x=0$. For $l>0.1$ mm, the variation in q''_g is less than 4 percent (i.e., $\Delta q''_g/\Delta l < 0.04\ q''_g$). If this variation in q''_g were accounted for in the solution for the grain (e.g., using Duhamel's Theorem), this would change the temperature by an amount on the same order as the variation in q''_g. Therefore, provided that the grinding zone is significantly longer than 0.1 mm (which it typically is), the assumption of constant q''_g in solving the heat transfer problem in the grain should not introduce much error in the temperature.

Workpiece Background Temperature. It has been shown experimentally (Malkin, 1974) that from the point of view of predicting thermal damage to the workpiece, it is the workpiece *background* temperature that is of interest, not the peak temperature that occurs under a grain. The reason for this is that the peak temperature occurs for a very short time, and thermal damage such as reaustenitization requires time to occur. For this reason, the rest of this paper will address the workpiece background temperature prediction

$$\theta_{wb,s}(x) = \frac{q''_{wb}}{h_{wb}(x)} = \frac{q''_{tot}/h_{wb}(x)}{[1+\frac{h_f}{h_{wb}}(1-A)]\,[1+\frac{\bar{h}_g}{h_{wg}}] + A\,\overline{(h_g/h_{wb})}} \quad (17)$$

This temperature will be put into nondimensional form as follows:

$$\Phi = \frac{h_{wb}(x)\theta_{wb,s}(x)}{q''_{tot}} = \frac{1}{[1+\frac{h_f}{h_{wb}}(1-A)]\,[1+\frac{\bar{h}_g}{h_{wg}}] + A\,\overline{(h_g/h_{wb})}} \quad (18)$$

Now Φ will be rewritten using the definitions of the heat transfer coefficients in equations (2), (4), (5), and (9). Before doing so, it is useful to note that ζ can be rewritten as follows, assuming $A_o = l_g^2$:

$$\zeta = (\pi\alpha_g x/A_o v_s)^{1/2} = (\pi\alpha_g\,x/l_g^2 v_s)^{1/2} = \pi^{1/2}(\alpha_g/\alpha_w)^{1/2}X^{1/2}/L_g \quad (19)$$

Then,

$$\frac{\bar{h}_g}{\bar{h}_{wg}} = \frac{1}{l}\int_0^l \frac{h_g(x)}{\bar{h}_{wg}}dx = \kappa_g I_2(L_g)\frac{1}{4\pi^{1/2}L}\int_0^L X^{-1/2}f(\zeta)dX$$

$$= \kappa_g I_2(L_g) I_3(L,\ L_g,\ \alpha_g/\alpha_w) \quad (20)$$

and

$$\overline{(h_g/h_{wb})} = \kappa_g(\frac{v_s}{v_w})^{1/2}\frac{1}{l}\int_0^l f(\zeta)\,dx$$

$$= \kappa_g(\frac{v_s}{v_w})^{1/2}\frac{1}{L}\int_0^L f\,[\pi^{1/2}(\alpha_g/\alpha_w)^{1/2}X^{1/2}/L_g]dX$$

$$= \kappa_g(\frac{v_s}{v_w})^{1/2}\bar{f}(L,\ L_g,\ \alpha_g/\alpha_w) \quad (21)$$

where

$$\kappa_f = \sqrt{(k\rho c_p)_f/(k\rho c_p)_w} \quad (22a)$$

$$\kappa_g = \sqrt{(k\rho c_p)_g/(k\rho c_p)_w} \quad (22b)$$

Thus, finally

$$\Phi = \left\{[1+\kappa_f(\frac{v_s}{v_w})^{1/2}(1-A)][1+\kappa_g I_2(L_g)I_3(L,L_g\ \alpha_g/\alpha_w)] + \kappa_g(\frac{v_s}{v_w})^{1/2}A\bar{f}(L,\ L_g,\ \alpha_g/\alpha_w)\right\}^{-1}$$

$$= \Phi(\kappa_g,\ \kappa_f,\ \alpha_g/\alpha_w,\ v_s/v_w,\ A,\ L,\ L_g) \quad (23)$$

The quantity of Φ is seen *not* to depend on x. It has two physical interpretations. It is the actual workpiece surface temperature divided by the maximum possible surface temperature that would occur if all of the grinding power went into the workpiece, i.e., $\Phi = \theta_{wb,s}/\theta_{max.\ poss.}$, where $\theta_{max.\ poss.} = q''_{tot}/h_{wb}$. It is also equal to the fraction of the total grinding power that ends up in the workpiece, since $\Phi = h_{wb}\theta_{wb,s}/q''_{tot} = q''_{wb}/q''_{tot}$. It can be seen that Φ depends on seven nondimensional parameters, as given in the last line in equation (23). The first three parameters depend only on material properties, and are fixed for a given workpiece, grain, and fluid. The last four parameters depend on material properties, operating conditions, and wheel geometry. The parameters v_s/v_w and L are typically accurately known (assuming elastic flattening of the wheel to be negligible), but the parameters A and L_g are usually not accurately known.

Table 1 Comparison to data of Yasui and Tsukuda (1983) for conventional grinding

q''_{tot}(W/mm^2)	a(μm)	l(mm)		$\theta_{max.exp}$	$\theta_{max.pred}$
12	5	1.0	water	30	32
			oil	60	62
14	10	1.4	water	40	45
			oil	90	88
18	30	2.5	water	70	80
			oil	160	156

$v_s = 20$ m/s, $v_w = 0.033$ m/s, A = 0.01, $l_g = 110$ μm, d = 205 mm, material properties from Table 3.

Table 2 Comparison to data of Ohishi and Furukawa (1985) for creep feed grinding

q''_{tot}(W/mm^2)	l(mm)		$\theta_{max.exp}$	$\theta_{max.pred}$
2.0	17.5	water	15	32
		oil	80	78
6.5	17.5	water	50	105
		oil	260	253
9.5	17.5	water	75	153
		oil	--- (burn)	369 (film boiling)

$v_s = 18$ m/s, $v_w = 0.6$ mm/s, A = 0.01, $l_g = 110$ μm, a = 1.0 mm, d = 305 mm, material properties from Table 3.

Table 3 Material properties and nondimensional parameters

	Water	Oil	Al_2O_3	CBN	Steel
k	0.65	0.15	46	1,300	60.5
ρ	1,000	820	4,000	3,450	7,854
c_p	4,180	2,000	770	506	434
κ_f	0.115	0.0345			
κ_g			0.829	3.32	
(α_g/α_w)			0.841	42.	

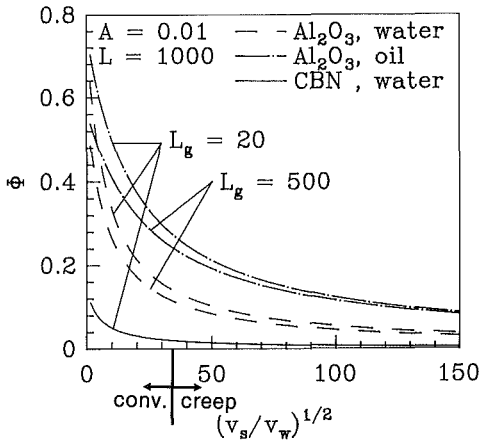

Fig 8 Φ versus $(v_s/v_w)^{1/2}$ for aluminum oxide wheel with oil and water, and for CBN wheel with water

Results and Discussion

Comparison to Experimental Data. The results of the model will now be compared to experimental data for conventional and creep feed grinding, using aluminum oxide wheels and both oil and water-based grinding fluids. The data are from papers by Yasui and Tsukuda (1983) and Ohishi and Furukawa (1985), and have been used previously for comparison with an earlier, simpler model of grinding temperature (Lavine, 1988). In both experiments the grinding power was varied in some manner, and the workpiece temperature was measured. The measured temperature would most likely correspond to the workpiece background temperature, because it is difficult to resolve the peak temperatures that occur under a grain, due to the large spatial and temporal gradients. The maximum workpiece temperatures were reported. This would correspond to the temperature at the end of the grinding zone, $x = l$.

The data of Yasui and Tsukuda (1983) are for conventional grinding (although the workpiece speed is lower than typical conventional grinding). Table 1 lists six of their data points (three each for water and oil). Lavine (1988) explains how these data were determined from the graphs given by Yasui and Tsukuda (1983). The various variables that determine the nondimensional parameters are also given in the table. The values of A and l_g had to be assumed, and the values used are typical of aluminum oxide grinding wheels. It will be shown in the next section that the temperature is not very sensitive to the choices of A and l_g. The theoretical predictions given by equation (17) (evaluated at $x = l$) are shown, and the agreement is seen to be excellent for oil and quite good for a water-based grinding fluid.

The data of Ohishi and Furukawa (1985) for creep feed grinding are given in Table 2. At the highest heat flux, "workpiece burn" occurs. This means that the grinding fluid underwent film boiling, and the workpiece temperature suddenly rose above the temperature at which thermal damage of the workpiece occurs. The parameter values are given in the table. The value of the ambient temperature had to be estimated because it was not given in the paper. This was done by extrapolating their graphs of temperature versus grinding power to zero grinding power. From the data presented, it appeared that the ambient temperature was approximately 25°C for water and 40°C for oil. This difference is not surprising since the wheel would tend to be hotter for oil than for water. The theoretically predicted temperature is also shown in the table. For oil the agreement is excellent, but for water the predictions are substantially too high. The reasons for this discrepancy are currently being investigated. The simpler model presented in Lavine (1988) showed better agreement with these data than the results presented here. However, it is important to note that the simpler model had adjustable constants that were used to fit the results to the data, whereas the present model does not.

The Effects of the Nondimensional Parameters. The dependence of Φ on the seven nondimensional parameters will now be investigated. Two values each for κ_g, α_g/α_w, and κ_f are considered, corresponding to aluminum oxide and CBN grains, and oil and water-based grinding fluids (see Table 3). The workpiece material properties are taken to be those of plain carbon steel (see Table 3). The remaining four parameters are allowed to vary over broad ranges.

All of the theoretical predictions will be presented as graphs of Φ versus $(v_s/v_w)^{1/2}$, because the velocity ratio has the strongest effect on Φ of any of the remaining four parameters. Several examples are shown in Fig. 8. It should be noted that typical values of the velocity ratio are lower in conventional than in creep feed grinding (see ranges indicated on abscissa of Fig. 8). Clearly, the larger the value of the velocity ratio, the lower

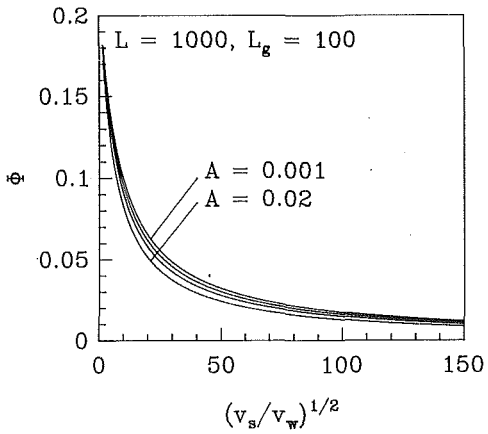

Fig 9 Φ versus $(v_s/v_w)^{1/2}$ for CBN wheel with water, effect of A

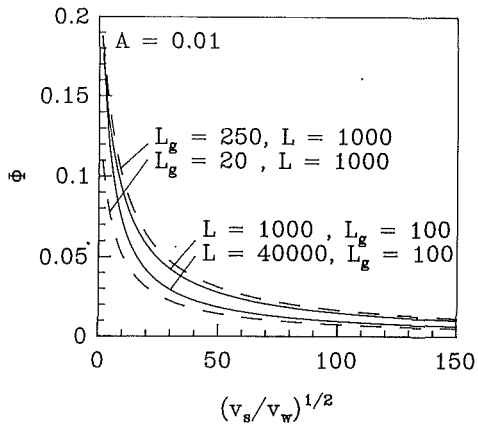

Fig 10 Φ versus $(v_s/v_w)^{1/2}$ for CBN wheel with water, effect of L and L_g

Φ will be, since more heat is removed by the wheel and fluid. (However, this should not be taken to mean that a larger value of the velocity ratio necessarily results in a lower temperature, since the actual dimensional temperature is also affected by the workpiece speed, with smaller workpiece speed contributing to higher temperatures.)

Results are given for an aluminum oxide wheel with oil as the grinding fluid, for an aluminum oxide wheel with a water-based grinding fluid, and for a CBN wheel with a water-based grinding fluid. Obviously, water results in lower Φ than oil because of its larger thermal conductivity, and similarly CBN results in a lower Φ than aluminum oxide. This figure also shows the effect of the parameter $L_g = v_s\, l_g/\alpha_w$, for the aluminum oxide wheel cases (CBN will be discussed momentarily). It is seen that a reasonably broad range of this parameter has a relatively minor effect on Φ for aluminum oxide grains. The two other parameters, A and $L = v_s\, l/\alpha_w$ were varied over the ranges $A = 0.001$ to 0.02 and $L = 1000$ to 40,000, and were found to have a smaller effect on Φ. However, for CBN grains the effect of these parameters is larger (see Figs. 9 and 10). Each of these parameters affects the heat transfer into the grain, and since the heat transfer into the grain is more significant for CBN wheels, these parameters are consequently more important. For instance, for $(v_s/v_w)^{1/2} = 15$, as L_g varies from 20 to 250, Φ varies from 0.038 to 0.078. For $(v_s/v_w)^{1/2} = 100$, over the same L_g range, Φ changes from 0.007 to 0.017. In both cases, the change in Φ is greater than 100 percent.

It is interesting to consider in which direction the parameters A, L, and L_g affect Φ. The effect of A is to increase heat transfer into the grains (with a corresponding minor decrease of the heat transfer into the fluid). Thus, an increase in A always causes a decrease in Φ (see Fig. 9 for CBN).

The effects of L and L_g are more complex. First, consider L_g. Referring to equation (18), L_g affects both $\bar{h}_g$ and $\bar{h}_{wg}$. Recall that the grain cross-sectional area increases with z, causing heat to spread out, thereby increasing the rate of heat transfer. This effect is more important for a smaller contact area, since then the area increase is a greater percentage of the contact area. Thus smaller L_g causes more efficient heat transfer into the grain (larger $\bar{h}_g$). But smaller L_g also causes larger $\bar{h}_{wg}$, because heat can conduct out from under a small heat source more efficiently than from a large heat source (the perimeter-to-area ratio is larger for a smaller heat source). Heat transfer into the grain is more important for CBN than for aluminum oxide, and it is seen that for CBN (Fig. 10), decreasing L_g causes a decrease in Φ due to the increased heat transfer into the grain, whereas for aluminum oxide (Fig. 8), decreasing L_g causes an increase in Φ due to the increased heat transfer into the workpiece.

Next, consider the effect of L. Referring to equation (18), the heat transfer coefficents h_f and h_{wb} both vary as $x^{-1/2}$, so their ratio is independent of x. However, h_g decreases more slowly than $x^{-1/2}$ (because of the moderating influence of heat spreading out into the larger grain cross-sectional area), and $\bar{h}_{wg}$ is constant. Thus, $h_g/\bar{h}_{wg}$ decreases with x, and h_g/h_{wb} increases with x. Therefore, as L increases, $\bar{h}_g/\bar{h}_{wg}$ decreases and $\overline{(h_g/h_{wb})}$ increases. These two competing effects result in Φ decreasing with increasing L for CBN (Fig. 10), and increasing with increasing L for aluminum oxide (not shown).

It should be noted that a decrease in Φ does not necessarily correspond to a decrease in actual dimensional temperature. For instance, as mentioned previously, decreasing the workpiece speed has the effect of decreasing Φ, but increasing $\theta_{wb,s}$. Furthermore, the effect of the grinding parameters on q_{tot} must be accounted for. For instance, increasing the wear flat area, A, decreases Φ, since more heat enters the wheel, but it also increases q_{tot} and would usually result in an increased workpiece temperature.

Film Boiling. As mentioned previously, when the maximum grinding zone temperature reaches approximately 100 to 120°C for water-based grinding fluid and 300°C for oil, the temperature of the workpiece suddenly increases. This phenomenon has been attributed to film boiling of the fluid. When film boiling occurs, the heat transfer coefficient of the fluid drops significantly. It is reasonable to assume that heat transfer to the fluid then becomes negligible compared to heat transfer to the wheel and workpiece. Thus, when film boiling occurs, the equations derived previously can be used, with h_f (or κ_f) set to zero. The effect of film boiling on the workpiece background temperature and occurrence of workpiece burn are discussed by Lavine and Jen (1991).

Conclusions

The goal of this work was to develop a theoretical prediction of the workpiece background temperature that does not require a priori specification of the fraction of energy entering the workpiece or the convection coefficient due to the grinding fluid. This goal has been accomplished by developing separate models of heat transfer into an abrasive grain, the grinding fluid, and the workpiece. The separate models are coupled by requiring that the temperatures match at the workpiece–fluid interface and the workpiece–grain interface. This model is an improvement over one of the authors' previous models (Lavine et al., 1989), because it takes into account the elevated temperature underneath a grain, which affects the fraction of the grinding energy that enters the grain and the workpiece.

The results were presented in terms of a nondimensional temperature, Φ, which depends on seven nondimensional pa-

rameters. Three of these (κ_f, κ_g, α_g/α_w) depend only on material properties, whereas the other four (v_s/v_w, A, L, L_g) depend on material properties, operating conditions, and wheel geometry. The quantity Φ was found to depend strongly on the fluid type and abrasive grain type. It also depends strongly on the velocity ratio v_s/v_w. Smaller effects were seen for A, L, and L_g.

The prediction of the workpiece background temperature has been compared to experimental data over a broad range of grinding conditions. The results are not excellent, but are reasonably good considering that no adjustable constants were used to match the predictions to experimental data.

The utility of such a theoretical model is twofold. First, a model that predicts the workpiece temperature as a function of the various parameters can be used to optimize the grinding process to achieve high material removal rates without thermal damage. Second, a predictive model can be used for adaptive control of the grinding process (Malkin, 1984). During grinding, the grinding power can be easily monitored. If the measured grinding power, when used as an input to the predictive model, indicates that the workpiece temperature is approaching a damaging level, then the grinding parameters can be automatically adjusted to reduce the temperature.

Acknowledgments

The support of the National Science Foundation, General Motors, General Electric, and Norton Co. is gratefully acknowledged.

References

Carslaw, H. S., and Jaeger, J. C., 1947, *Conduction of Heat in Solids*, Oxford University Press, London, United Kingdom.

DesRuisseaux, N. R., and Zerkle, R. D., 1970a, "Thermal Analysis of the Grinding Process," ASME *Journal of Engineering for Industry*, Vol. 92, pp. 428–434.

DesRuisseaux, N. R., and Zerkle, R. D., 1970b, "Temperature in Semi-infinite and Cylindrical Bodies Subjected to Moving Heat Sources and Surface Cooling," ASME JOURNAL OF HEAT TRANSFER, Vol. 92, pp. 456–464.

Hahn, R. S., 1956, "The Relation Between Grinding Conditions and Thermal Damage in the Workpiece," *Transactions of the ASME*, Vol. 78, pp. 807–812.

Kennedy, F. E., Jr., 1984, "Thermal and Thermomechanical Effects in Dry Sliding," *Wear*, Vol. 100, pp. 453–476.

Kopalinsky, E. M., 1984, "A New Approach to Calculating the Workpiece Temperature Distributions in Grinding," *Wear*, Vol. 94, pp. 295–322.

Kuhlmann-Wilsdorf, D., 1987, "Temperatures at Interfacial Contact Spots: Dependence on Velocity and on Role Reversal of Two Materials in Sliding Contact," ASME *Journal of Tribology*, Vol. 109, pp. 321–329.

Lavine, A. S., 1988, "A Simple Model for Convective Cooling During the Grinding Process," ASME *Journal of Engineering for Industry*, Vol. 110, pp. 1–6.

Lavine, A. S., Malkin, S., and Jen, T. C., 1989, "Thermal Aspects of Grinding With CBN Wheels," *CIRP Annals*, Vol. 38, No. 1, pp. 557–560.

Lavine, A. S., and Malkin, S., 1990, "The Role of Cooling in Creep Feed Grinding," *Int. J. Advanced Manufacturing Technology*, Vol. 5, pp. 97–111.

Lavine, A. S., and Jen, T. C., 1991, "Coupled Heat Transfer to Workpiece, Wheel, and Fluid in Grinding, and the Occurrence of Workpiece Burn," accepted for publication in *Int. J. Heat Mass Transfer*.

Malkin, S., 1974, "Thermal Aspects of Grinding. Part 2—Surface Temperatures and Workpiece Burn," ASME *Journal of Engineering for Industry*, Vol. 96, pp. 1184–1191.

Malkin, S., 1984a, "Grinding of Metals: Theory and Application," *J. Applied Metalworking*, Vol. 3, No. 2, pp. 95–109.

Malkin, S., 1984b, "In-Process Control of Thermal Damage During Grinding," Presented at the Int'l Grinding Conference, SME Paper No. MR84-532.

Malkin, S., 1989, *Grinding Technology, Theory and Applications of Machining With Abrasives*, Ellis Horward Ltd., Chichester, Wiley, New York.

Ohishi, S., and Furukawa, Y., 1985, "Analysis of Workpiece Temperature and Grinding Burn in Creep Feed Grinding," *Bulletin of JSME*, Vol. 28, No. 242, pp. 1775–1781.

Outwater, J. O., and Shaw, M. C., 1952, "Surface Temperatures in Grinding," *Transactions ASME*, Vol. 74, pp. 73–86.

Sauer, W. J., 1972, "Thermal Aspects of Surface Grinding," *Proc. of Int'l Grinding Conf.*, pp. 391–411.

Snoeys, R., Maris, M., and Peters, J., 1978, "Thermally Induced Damage in Grinding," *CIRP Annals*, Vol. 27, No. 2, pp. 571–581.

Yasui, H., and Tsukuda, S., 1983, "Influence of Fluid Type on Wet Grinding Temperature," *Bull. Japan Soc. of Prec. Engg.*, Vol. 17, No. 2, pp. 133–134.

Yovanovich, M. M., 1986, "Recent Developments in Thermal Contact, Gap and Joint Conductance Theories and Experiment," *Proc. Eighth Int'l Heat Transfer Conf.*, Vol. 1, pp. 35–45.

Yuen, W. Y. D., 1988, "Heat Conduction in Sliding Solids," *Int. J. Heat Mass Transfer*, Vol. 31, pp. 637–645.

Thermal Analysis of In-Situ Thermoplastic-Matrix Composite Filament Winding

M. N. Ghasemi Nejhad

R. D. Cope

S. I. Güçeri

Department of Mechanical Engineering,
University of Delaware,
Newark, DE 19716

In filament winding of thermoplastics, localized melting/solidification can reduce the residual stresses and allow for improved dimensional stability and performance. This paper presents a three-dimensional thermal analysis for melting and consolidating impregnated tows in the presence of a local heat source during filament winding of thermoplastic composites. The analysis is performed using an Eulerian approach. The anisotropy of the filament wound woven structure is modeled as an orthotropic domain employing the concept of angle-ply sublaminates. The effective orthotropic conductivity tensor incorporates the effect of winding angle. The governing equations are discretized in a nonuniform mesh domain and solved using a finite difference approach. The processing parameters, such as winding angle, winding speed, and heat input, as well as material properties, are incorporated into the analysis. The results show large thermal gradients in the vicinity of the consolidation point. The effects of winding speed and heat input are investigated, and the overall thermal characterization of the process is discussed. The accuracy of the numerical method is assessed by comparing the results of a test problem with an available analytical solution.

1 Introduction

With the development of high-temperature, advanced thermoplastic resins, the manufacture of various structures such as pressure vessels, pressure pipes, and structural beams using thermoplastic filament winding has received considerable attention (Egerton and Gruber, 1988, 1989; Chang and Lees, 1988; Winkel and Hurdle, 1988; Hollingsworth and Osment, 1987; Griffiths et al., 1988). In filament winding processes, thermoplastic composites open the possibility of combining the laydown, melting, and consolidation steps of the impregnated tows in a continuous process, thereby eliminating the curing steps of thermosetting materials and hence reducing the overall cost of in-situ thermoplastic filament winding (Beyeler et al., 1988). Moreover, since the parts consolidate as they are wound, the fiber buckling or fiber wave, often present in the case of autoclave curing of thermoset-matrix filament wound parts, can be minimized (a thorough analysis of the filament winding process for parts subjected to post-curing is given by Calius and Springer, 1988). While producing thick cross sections is very difficult for thermoset-matrix parts, due to their exothermic cure, there is conceptually no limit on the thickness of an in-situ consolidated thermoplastic part. An additional advantage of this process is the possibility of winding on highly nongeodesic paths as well as concave-convex surfaces (Wells and McAnulty, 1987).

It is well known (e.g., see Seferis, 1984; Seferis and Velisaris, 1986; Blundell et al., 1985) that for thermoplastic composites the resulting material properties and the performance characteristics depend strongly on the thermal history during processing. Furthermore, the assessments of the process-induced residual stresses, in general, and the range of nongeodesic winding capability, in particular, are possible only when the thermal characterization of the process is available.

In an in-situ thermoplastic filament winding process, a local heat source generates a molten region around the laydown point. The tow is consolidated through a melting diffusion process under the pressure of a consolidation roller and/or fiber tension. Solidification of the material occurs as a result of heat removal from the melt region as it consolidates and moves away from the laydown point. The temperature field is altered with the variation of the processing parameters, such as winding angle and speed, heat input, thermal boundary conditions, etc. A parametric study can be used to determine the processing window that indicates the bounds on the heat flux at any given manufacturing speed (Beyeler, 1987; Beyeler and Güçeri, 1988; Beyeler et al., 1988).

This paper presents a three-dimensional thermal analysis for melting and consolidating the impregnated tows in a continuous manufacturing process (in-situ) of thermoplastic filament winding in the presence of a localized heat source. Analytical models, solved using a numerical technique, are presented to predict the temperature distribution (in the anisotropic composite and the isotropic mandrel), the resulting heating/cooling rates, and the processing window. For verification, the analytical solution obtained for a modeled in-situ thermoplastic tape laying process is compared with the results obtained using the numerical method employed for the in-situ thermoplastic filament winding. The primary objective of this phase of the study is to identify the important processing parameters and their effects on thermal history as well as the overall feasibility of in-situ thermoplastic filament winding.

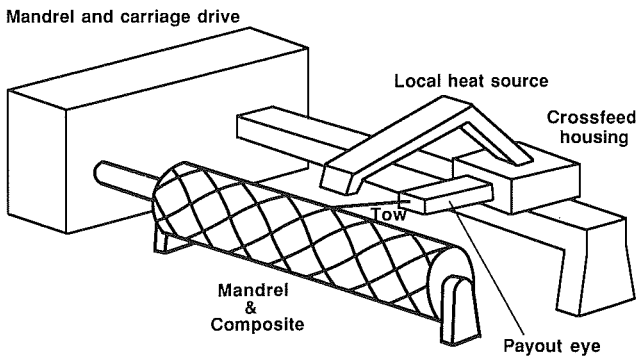

Fig. 1 A schematic view of a typical in-situ filament winding machine

Contributed by the Heat Transfer Division for publication in the JOURNAL OF HEAT TRANSFER. Manuscript received by the Heat Transfer Division February 13, 1990; revision received June 27, 1990. Keywords: Conduction, Materials Processing and Manufacturing Processes, Numerical Methods.

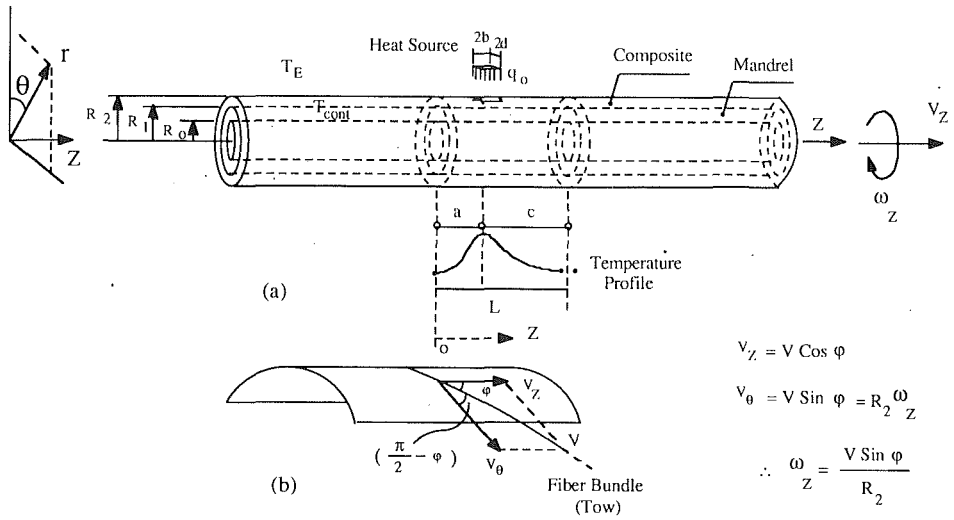

Fig. 2 *(a)* **The geometry and Eulerian Control Volume ("*L*") used in the thermal analysis, *(b)* the winding velocity vector (*V*) and its components (V_θ and V_z) in cylindrical coordinates**

2 Thermal Analysis

Figure 1 shows a schematic view of a typical in-situ filament winding operation. In the present analysis the cylinder is assumed to be relatively long with a localized heat source. Figure 2 depicts the geometry considered in this work. The winding of the tows can be achieved by a combination of the motions between the mandrel and payout eye. Employing a kinematic inversion, it can be modeled with the payout eye and heat source fixed and all existing velocity components assigned to the mandrel (or the mandrel and substrate as a whole).

The problem is transient in a Lagrangian framework; however, in a continuous process where all processing parameters and the geometry remain unchanged, an Eulerian Control Vol-

Nomenclature

α = a constant in the mesh refinement formulae
β = mesh refinement parameter in r and θ directions
$\theta, \bar{\theta}$ = circumferencial coordinate and its transformation
ρ = density, kg/m^3
τ = mesh refinement parameter in z direction
ϕ = winding angle, deg
ω_z = angular velocity about the z axis, rad/s
A_i = area of the interface for the unit cell, m^2
A_q/A = nodal area fraction for the surface exposed to the heat source
a = distance to the left side of the domain from the heat source, m
b = half-width of the heat source, m
c = distance to the right side of the domain from the heat source, m
C = heat capacity, J/kg•°C
C_{ij} = components of the direction cosine matrix
d = half-length of the heat source, m
e = enthalpy, J/kg
h_0, h_2 = convective heat transfer coefficients, W/m^2•°C
h = maximum length/angle in transformations
K = thermal conductivity of a tow, W/m•°C
K_{ij} = components of the conductivity tensor, W/m•°C
l = radial nodal position
$\mathbf{q}$ = heat flux vector
q = heat absorbed by the composite, W/m^2
q_0 = absorbing heat supplied by the heat source, W/m^2
r, R = radial coordinate, m
$\bar{r}_1, \bar{\bar{r}}_1$ = radial transformations in mandrel, m
$\bar{r}_2, \bar{\bar{r}}_2$ = radial transformations in composite, m
T = excess temperature = ($T_{\text{actual}} - T_{\text{environment}}$), °C
U = heat generation, W/kg
$\mathbf{V}$ = winding velocity vector
V_r, V_θ, V_z, V_x = velocity components, m/s
v = volume, m^3
x, y = Cartesian coordinates
x' = x axis shifted to the location of the heat source
$\bar{x}, \bar{y}$ = transformed Cartesian coordinates
Y = symbolic length for r, θ, or z in the transformations
$z, \bar{z}$ = axial coordinate and its transformation, m
z' = z axis shifted to the location of the heat source
z_c = location of the mesh refinement in the z direction, m
Δr = thickness of a tow, m
$\Delta r_1, \Delta r_2$ = radial mesh discretization sizes
$\Delta\theta, \Delta z$ = θ and z mesh discretization sizes

Subscripts

0 = inner surface of mandrel
1 = mandrel/composite interface
2 = outer surface of composite
c, p = composite
deg = degradation
E = environment
g = glass transition
L = longitudinal
m = mandrel
r_1 = radial coordinate for mandrel
r_2 = radial coordinate for composite
t = θ
T = transverse

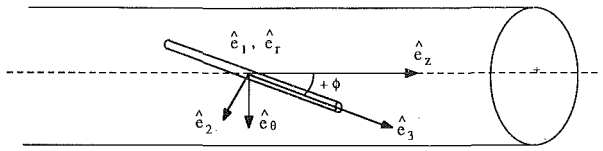

$$\left[K'_{ij}\right]_{\text{Cylinder}} = \left[C_{ij}\right]\left[K_{ij}\right]_{\text{Fiber}}\left[C_{ij}\right]^T$$

$$K_{ij}^{+\phi} = \begin{bmatrix} K_T & 0 & 0 \\ 0 & K_T \cos^2\phi + K_L \sin^2\phi & (K_L - K_T)\sin\phi\cos\phi \\ 0 & (K_L - K_T)\sin\phi\cos\phi & K_T \sin^2\phi + K_L \cos^2\phi \end{bmatrix}$$

Fig. 3 The transformation of the tow conductivity tensor into the mandrel (cylindrical) coordinate system

ume (ECV), which envelops the region influenced by the local heat source (portion "L" of Fig. 2), can be chosen and the problem formulated as steady state. This is possible since at every instant, the temperature distribution would remain unchanged with respect to a fixed coordinate frame (an Eulerian approach). However, the ECV must be chosen large enough to satisfy the boundary conditions at the upstream and downstream ends with respect to the heat source. As shown in Fig. 2, the incoming control temperature (T_{cont}) at the left side of the ECV can be assumed to be the composite/mandrel temperature far away from the local heat source throughout the process. For the right side of the ECV, a gradient type boundary condition becomes applicable, since the primary heat transport at this location is one of medium motion rather than thermal diffusion. Considering the relatively shallow temperature gradient and high rate of motion at this intersection, the preceding assumption can easily be justified (Beyeler and Güçeri, 1988). Moreover, it is assumed that the thickness of the composite substrate at the instant when the analysis is performed is at least an order of magnitude greater than the thickness of the impregnated tow (up to 0.010 in. = 0.025 cm) being wound. Therefore, the effect of the ply-drop is assumed to be negligible. The accuracy of this assumption increases with increasing substrate thickness.

The boundary conditions on the ECV can now be defined in cylindrical coordinates as follows:

In the radial (r) direction:

$$K_{11}\frac{\partial T}{\partial r} = q\left(\frac{A_q}{A}\right) - h_2 T \qquad @r = R_2$$

$$T_c = T_m,\ K_{11}\frac{\partial T}{\partial r} = K\frac{\partial T}{\partial r} \qquad @r = R_1$$

$$K\frac{\partial T}{\partial r} = h_0 T \qquad @r = R_0$$

The requirement of 2π periodicity in the θ direction gives

$$T(r, \theta, z) = T(r, \theta + 2\pi, z) \qquad \text{for } 0 \le \theta \le 2\pi$$

$$\frac{\partial T(r, \theta, z)}{\partial \theta} = \frac{\partial T(r, \theta + 2\pi, z)}{\partial \theta} \qquad \text{for } 0 \le \theta \le 2\pi$$

and in the axial (z) direction:

$$T = T_{\text{cont}} - T_E \qquad @z = 0$$

$$\frac{\partial T}{\partial z} = 0 \qquad @z = a + c$$

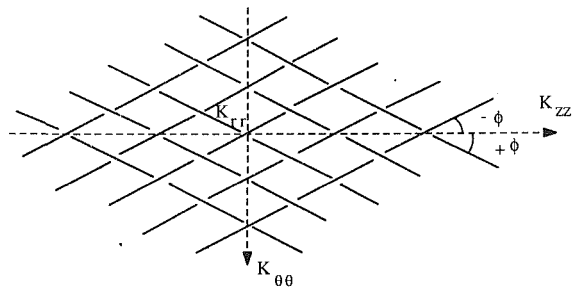

Fig. 4 The modeled orthotropic weave

In these expressions, T represents the excess temperature, and q is the absorbed heat due to the concentrated heat source and equals $q_0\cos\theta$ on the portion of the surface of the composite that is directly below the local heat source and zero at other points on the surface. q_0 is the amount of heat supplied by the heat source and can be absorbed by the composite. A factor of A_q/A is introduced to modify the q term at $r = R_2$ to account for the effective area, on the surface of the composite, which absorbs heat and can be found using a control volume approach. This fraction would be unity for nodes that are within the boundary of the area beneath the local heat source and less than unity for the boundary nodes.

Following the above assumptions, the governing equation for the anisotropic composite domain becomes

$$K_{11}\frac{1}{r}\frac{\partial}{\partial r}\left(r\frac{\partial T}{\partial r}\right) + K_{22}\frac{1}{r^2}\frac{\partial^2 T}{\partial \theta^2} + K_{33}\frac{\partial^2 T}{\partial z^2} + 2K_{12}\frac{1}{r}\frac{\partial^2 T}{\partial r \partial \theta} + 2K_{13}\frac{\partial^2 T}{\partial r \partial z} + K_{13}\frac{1}{r}\frac{\partial T}{\partial z} + 2K_{23}\frac{1}{r}\frac{\partial^2 T}{\partial \theta \partial z} + \rho_c U_{ms} = \rho_c C_p \omega_z \frac{\partial T}{\partial \theta} + \rho_c C_p V_z \frac{\partial T}{\partial z} \qquad (1)$$

and that for the isotropic mandrel is

$$K\frac{1}{r}\frac{\partial}{\partial r}\left(r\frac{\partial T}{\partial r}\right) + K\frac{1}{r^2}\frac{\partial^2 T}{\partial \theta^2} + K\frac{\partial^2 T}{\partial z^2} = \rho_m C_m \omega_z \frac{\partial T}{\partial \theta} + \rho_m C_m V_z \frac{\partial T}{\partial z} \qquad (2)$$

In equation (1), the terms with K_{ij} represent the diffusion in an anisotropic domain. The convective-like terms of the right-hand side account for the motion of the composite/mandrel. The heat generation term, U_{ms}, is included to account for the heat release or absorption effects resulting from the highly irregular and complex melting/solidification that occurs over a range of temperatures. In the present study, the thermal response of the material is modeled by assuming a linear variation of the specific heat of the composite between T_{melt} and T_g. The remaining heat absorption/release is included in the form of a heat generation term. This information can typically be obtained by differentiating the enthalpy–temperature relations, which are provided experimentally. The heat generation term due to crystallization is often small and may be neglected, since the heat capacity of the material is an order of magnitude greater than the enthalpy of crystallization (Velisaris and Seferis, 1988; Seferis and Velisaris, 1986).

2.1 A Model for the Conductivity Tensor in Filament Winding. The composite tow is assumed to be a transversely isotropic (in the plane normal to the fiber direction) material with its conductivity tensor fully defined. K_L and K_T are the tow principal conductivities in the longitudinal and transverse directions, respectively, and all off-diagonal terms are zero. This tensor, defined in the fiber coordinate frame, must be transformed to the mandrel coordinate frame using the tensor

transformations. This is shown in Fig. 3, for $+\phi$ direction. The K_{ij} for the tows in the $-\phi$ direction can be found by inserting $-\phi$ for $+\phi$ in Fig. 3. It is desirable to obtain the conductivity tensor for a typical $+\phi/-\phi$ filament wound layer, which covers the surface of the mandrel fully. In this case the weave pattern can be modeled as an orthotropic material, shown in Fig. 4, where three mutually orthogonal planes of symmetry, namely, normal to z, normal to θ, and normal to r directions can be found. Figure 5 shows a typical unit cell of Fig. 4 where the undulations of the fibers have been neglected. This approach is analogous to the Mosaic Model employed by Ishikawa and Chou (1982, 1983), and Chou and Yang (1986) in the analysis of woven materials and ignores the undulation of the fibers, treating a fabric composite as an assemblage of pieces of angle-ply laminates. Each layer of the unit cell is further assumed to have either $+\phi$ or $-\phi$ tows only (i.e., the top layer $+\phi$ and the bottom layer $-\phi$, uniformly, or vice versa). Finally, the thermal conductivity of the typical unit cell is found using the concept of parallel and series composite walls in heat conduction coupled with Fourier's law for an anisotropic domain (Özışık, 1979; Arpacı, 1966; Kakaç and Yener, 1985) which is

$$\{\mathbf{q}_i\} = -[\mathbf{K}_{ij}]\left\{\frac{\partial \mathbf{T}}{\partial \mathbf{X}_j}\right\} \tag{3}$$

where $i=1, 2, 3=r, \theta, z$ and $j=1, 2, 3=r, \theta, z$. The conductivity tensor of each sublaminate ($+\phi$ or $-\phi$) can be found in Fig. 3.

The analyses for the in-plane properties, those in the θ and z directions, follow those of parallel composite walls. The following equation gives the effective thermal conductivity in the z direction, where an overbar denotes an effective property:

$$\overline{Q}_z = \overline{q}_z \cdot A_z = \int_{\theta-\Delta\theta_1}^{\theta+\Delta\theta_2}\int_{r-\Delta r}^{r+\Delta r} -[K_{31}K_{32}K_{33}]\left\{\frac{\partial T}{\partial X_j}\right\} r\,d\theta\,dr \tag{4}$$

where $\Delta r_1 = \Delta r_2 = \Delta r$ is the thickness of one tow. The left-hand side of equation (4) contains the effective properties to be determined and the right-hand side contains the integrals over the modeled $+\phi/-\phi$ unit cell and is broken into $+\phi$ and $-\phi$ portions in which the corresponding K_{ij} are used. Furthermore, the variation of thermal conductivity with temperature is assumed to be negligible (Blundell and Willmouth, 1986; Beyeler and Güçeri, 1988). The temperature is also assumed to be linear across the unit cell; thus, $\partial T/\partial X_j$ becomes constant, and it follows that

$$\begin{aligned} &-[\overline{K}_{31}\overline{K}_{32}\overline{K}_{33}]\left\{\frac{\partial T}{\partial X_j}\right\}(2)(r\Delta r)(\Delta\theta_1+\Delta\theta_2) = \\ &\quad -[0+K_{32}K_{33}]\left\{\frac{\partial T}{\partial X_j}\right\}(\Delta\theta_1+\Delta\theta_2)\Delta r\left(r-\frac{\Delta r}{2}\right) \\ &\quad -[0-K_{32}K_{33}]\left\{\frac{\partial T}{\partial X_j}\right\}(\Delta\theta_1+\Delta\theta_2)\Delta r\left(r+\frac{\Delta r}{2}\right) \end{aligned} \tag{5}$$

where the first and second terms on the right-hand side are the contributions from the $+\phi$ and $-\phi$ sublaminates, respectively. It should be noted that each unit cell has a thickness twice that of the thickness of a fiber tow, which is normally in the range of 0.125 to 0.250 mm, and the assumption of the linearity of the temperature is justified in the thickness direction. However, the in-plane directions of the unit cell (θ and z) are effectively the sizes of the mesh taken in the numerical analysis, and the temperature linearity assumption within the unit cell becomes reasonable only if the mesh is sufficiently fine in high-temperature gradient zones.

In equation (5) it is assumed that $\Delta r/2 \ll r$, where r is the outer radius of the mandrel (at its minimum). This assumption is justified for all realistic configurations considered in thermoplastic filament winding. In the case of in-plane properties

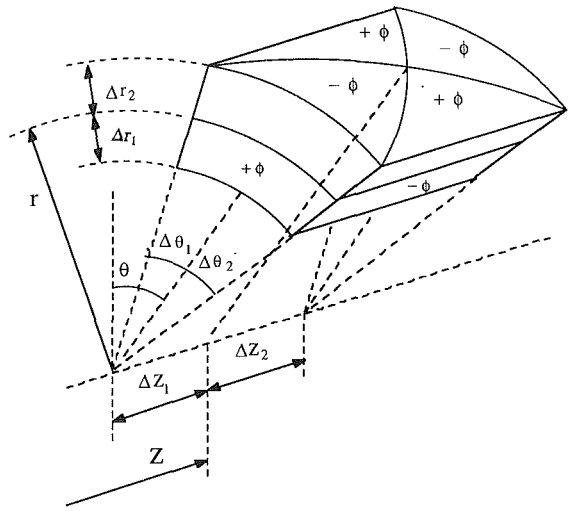

Fig. 5 A typical unit cell of the modeled orthotropic weave using the Mosaic Model

(parallel composite walls), the $\partial T/\partial X_j$ are the same for both $+\phi$ and $-\phi$ portions and can be factored on the right-hand side of equation (5). As a result, equation (5) can be simplified as

$$[\overline{K}_{31}\overline{K}_{32}\overline{K}_{33}] = [0 \;\; 0 \;\; K_{33}] \tag{6}$$

Similarly, for the θ direction, it can be shown that

$$[\overline{K}_{21}\overline{K}_{22}\overline{K}_{23}] = [0 \;\; K_{22} \;\; 0] \tag{7}$$

However, in the r direction, the problem is one of the series composite walls and hence

$$\overline{Q}_r = Q_r^+ = Q_r^- \tag{8}$$

$$\Delta\overline{T} = \Delta T^+ + \Delta T^- \tag{9}$$

Again, the overbar denotes the effective properties, and a plus or minus stands for $+\phi$ or $-\phi$, respectively. Employing Fourier's law and Fig. 3, it follows that

$$q_r^+ = -[K_{11} \;\; 0 \;\; 0]\left\{\frac{\partial T}{\partial X_j}\right\} = -K_{11}^+\frac{\partial T}{\partial r} = -K_{11}^+\frac{\Delta T^+}{\Delta r} \tag{10}$$

$$q_r^- = -[K_{11} \;\; 0 \;\; 0]\left\{\frac{\partial T}{\partial X_j}\right\} = -K_{11}^-\frac{\partial T}{\partial r} = -K_{11}^-\frac{\Delta T^-}{\Delta r} \tag{11}$$

where $K_{11}^+ = K_{11}^- = K_T$. Therefore, it can be written

$$\overline{q}_r = -[\overline{K}_{11}\overline{K}_{12}\overline{K}_{13}]\left\{\frac{\partial T}{\partial X_j}\right\} = -\overline{K}_{11}\frac{\partial T}{\partial r} = -\overline{K}_{11}\frac{\Delta\overline{T}}{2\Delta r} \tag{12}$$

In equations (10)–(12) the ∂'s have been replaced by Δ's using the unit cell temperature linearity assumption. Dividing equation (9) by $2\Delta r$, using equations (10)–(12), and noting that $Q = q \cdot A$, yields

$$\frac{\overline{q}_r}{\overline{K}_{11}}A_i = \frac{1}{2}\frac{q_r^+}{K_{11}^+}A_i + \frac{1}{2}\frac{q_r^-}{K_{11}^-}A_i \tag{13}$$

Again, the assumption of $\Delta r/r \ll 1$ (which implies $r-\Delta r \approx r \approx r+\Delta r$) is used. Therefore, the areas normal to the heat flow in the r direction are assumed to be the same within a unit cell. A_i is the cross-sectional area normal to r at the interface of the cell. Equations (8) and (13) yield

$$\frac{2}{\overline{K}_{11}} = \frac{1}{K_{11}^+} + \frac{1}{K_{11}^-} \tag{14}$$

and since $K_{11}^+ = K_{11}^- = K_T$, it follows that $\overline{K}_{11} = K_{11} = K_T$; thus

$$[\overline{K}_{11}\overline{K}_{12}\overline{K}_{13}] = [K_{11} \;\; 0 \;\; 0] \tag{15}$$

Equations (6), (7), and (15) give the effective thermal conductivity for the modeled layer. Since it is assumed that these

layers are repeated throughout the substrate, the effective orthotropic thermal conductivity model is used throughout the composite domain and is given as

$$\overline{K}_{11} = K_T,$$
$$\overline{K}_{22} = K_T \cos^2\phi + K_L \sin^2\phi,$$
$$\overline{K}_{33} = K_T \sin^2\phi + K_L \cos^2\phi, \text{ and}$$
$$\overline{K}_{ij} = 0 \text{ for } i \neq j$$

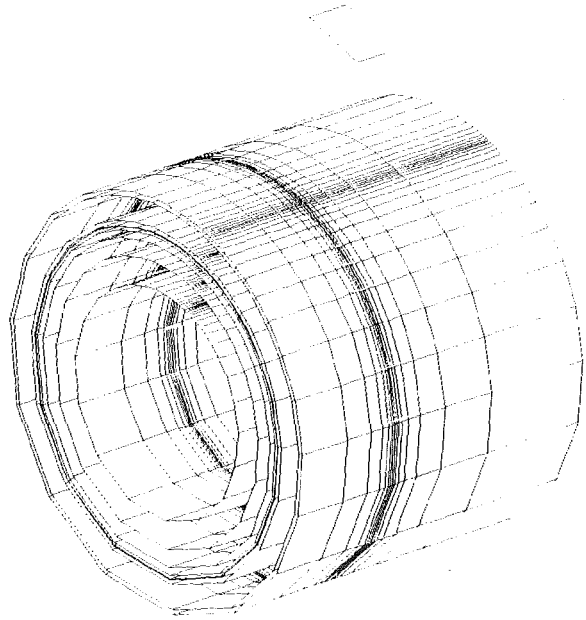

Fig. 6 Mesh concentrations

The governing equation (1), can now be simplified as equation (16) using the effective thermal conductivity, to read

$$K_{11}\frac{1}{r}\frac{\partial}{\partial r}\left(r\frac{\partial T}{\partial r}\right) + K_{22}\frac{1}{r^2}\frac{\partial^2 T}{\partial \theta^2} + K_{33}\frac{\partial^2 T}{\partial z^2} + \rho_c U_{ms} = \rho_c C_p \omega_z \frac{\partial T}{\partial \theta} + \rho_c C_p V_z \frac{\partial T}{\partial z} \quad (16)$$

2.2 Interface Condition. A careful examination of the governing equations for the composite domain, equation (16), and the mandrel, equation (2), reveals that they represent the same partial differential equation with piecewise continuous coefficients (including the source term) with jump discontinuities occurring at the composite/mandrel interface. These discontinuities, if not treated well, would cause severe numerical convergence difficulties. To remedy this, the mesh size should first be refined close to the interface. Next, the general governing equation of the two domains should be integrated over the mesh control volume in the vicinity of the interface (Davis, 1984). Since $V_r = 0$, $\partial V_\theta / \partial \theta = 0$, $V_z = \text{const}$, and $de = CdT$, a general governing equation can be written for the interface as follows:

$$-\nabla \cdot \mathbf{q} - \rho U = \rho \nabla \cdot (e\mathbf{V}) \quad (17)$$

where the boldface letters denote vectors. This equation can be integrated over the mesh volume, neighboring the interface, to give

$$\iiint [\nabla \cdot \mathbf{q} + \rho U + \rho \nabla \cdot (e\mathbf{V})] dv = 0 \quad (18)$$

The Gauss divergence theorem is subsequently applied to the diffusion and convective-like terms to change the volume integrals into the surface integrals employing a nonuniform mesh. This approach yields a discretized equation for the interface. The matching temperature and heat flux boundary conditions at the interface are used in the derivation of the discretized interface equation (Davis, 1984; Varga, 1962).

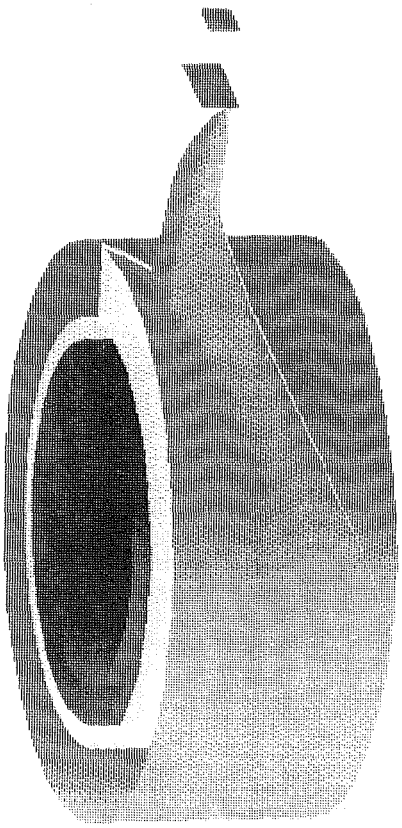

Fig. 7 Temperature distribution (gray) on the surface of the composite ($r = R_2$, bright) with mandrel (dark) in place

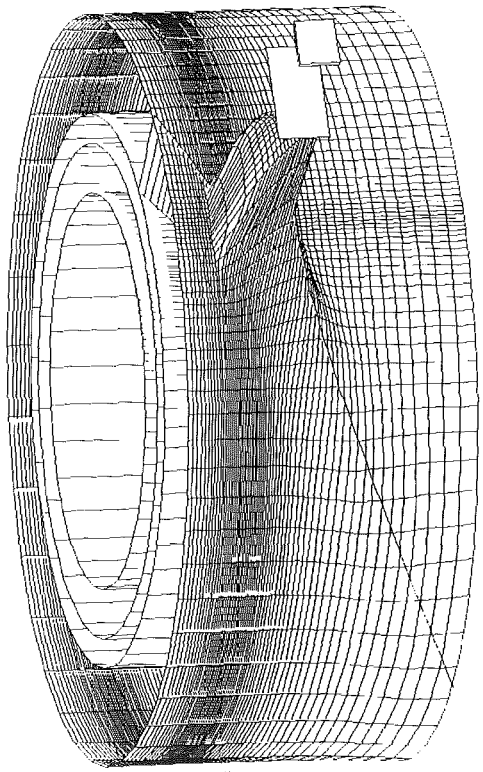

Fig. 8 Temperature distribution at $r = R_2$ with mesh concentrations

2.3 Nonuniform Mesh. Due to the existence of regions with steep temperature gradients, such as the vicinity of the surface exposed to the local heat source, it is advantageous to use a nonuniform mesh over the domain. Furthermore, the temperature is assumed to be linear within each mesh element in the course of modeling the orthotropic conductivity tensor, which becomes more accurate with proper local mesh size. It is also recommended that the mesh structure be refined close to the interface of two different materials for accurate implementation of the interface boundary equations. Appendix A gives the corresponding transformations used for the r, θ, and z directions (Anderson et al., 1984). The transformed governing equation for the composite becomes

$$K_{11}\left(\frac{\partial \bar{r}_2}{\partial r_2}\right)^2 \frac{\partial^2 T}{\partial \bar{r}_2^2} + K_{11}\left[\left(\frac{\partial^2 \bar{r}_2}{\partial r_2^2}\right) + \frac{1}{r}\left(\frac{\partial \bar{r}_2}{\partial r_2}\right)\right]\frac{\partial T}{\partial \bar{r}_2}$$
$$+ K_{22}\frac{1}{r^2}\left(\frac{\partial \bar{\theta}}{\partial \theta}\right)^2 \frac{\partial^2 T}{\partial \bar{\theta}^2} + K_{22}\frac{1}{r^2}\left(\frac{\partial^2 \bar{\theta}}{\partial \theta^2}\right)\frac{\partial T}{\partial \bar{\theta}} + K_{33}\left(\frac{\partial \bar{z}}{\partial z}\right)^2 \frac{\partial^2 T}{\partial \bar{z}^2}$$
$$+ K_{33}\left(\frac{\partial^2 \bar{z}}{\partial z^2}\right)\frac{\partial T}{\partial \bar{z}} + \rho_c U_{ms} = \rho_c C_p \omega_z \left(\frac{\partial \bar{\theta}}{\partial \theta}\right)\frac{\partial T}{\partial \bar{\theta}} + \rho_c C_p V_z \left(\frac{\partial \bar{z}}{\partial z}\right)\frac{\partial T}{\partial \bar{z}} \tag{19}$$

and that for the mandrel is

$$K\left(\frac{\partial \bar{r}_1}{\partial r_1}\right)^2 \frac{\partial^2 T}{\partial \bar{r}_1^2} + K\left[\left(\frac{\partial^2 \bar{r}_1}{\partial r_1^2}\right) + \frac{1}{r}\left(\frac{\partial \bar{r}_1}{\partial r_1}\right)\right]\frac{\partial T}{\partial \bar{r}_1}$$
$$+ K\frac{1}{r^2}\left(\frac{\partial \bar{\theta}}{\partial \theta}\right)^2 \frac{\partial^2 T}{\partial \bar{\theta}^2} + K\frac{1}{r^2}\left(\frac{\partial^2 \bar{\theta}}{\partial \theta^2}\right)\frac{\partial T}{\partial \bar{\theta}} + K\left(\frac{\partial \bar{z}}{\partial z}\right)^2 \frac{\partial^2 T}{\partial \bar{z}^2}$$
$$+ K\left(\frac{\partial^2 \bar{z}}{\partial z^2}\right)\frac{\partial T}{\partial \bar{z}} = \rho_m C_m \omega_z \left(\frac{\partial \bar{\theta}}{\partial \theta}\right)\frac{\partial T}{\partial \bar{\theta}} + \rho_m C_m V_z \left(\frac{\partial \bar{z}}{\partial z}\right)\frac{\partial T}{\partial \bar{z}} \tag{20}$$

The expressions for the different coefficients can be found in Appendix B. The transformations on the boundary conditions were also performed accordingly. For example, the boundary condition at $r = R_2$ transforms as follows:

$$K_{11}\left[\left(\frac{\partial \bar{r}_2}{\partial r_2}\right)\frac{\partial T}{\partial \bar{r}_2}\right] = q\left(\frac{A_q}{A}\right) - h_2 T \tag{21}$$

These expressions are then discretized in the computational domain using central differencing for the diffusion terms. For the heat transfer terms induced by the velocity in the right-hand side of equations (19) and (20) (convective-like terms), a technique inspired from the flow of a fluid particle in a laminar flow whose thermal behavior is dependent on the thermal history of the upstream, i.e., upstream or backward differencing method, is used.

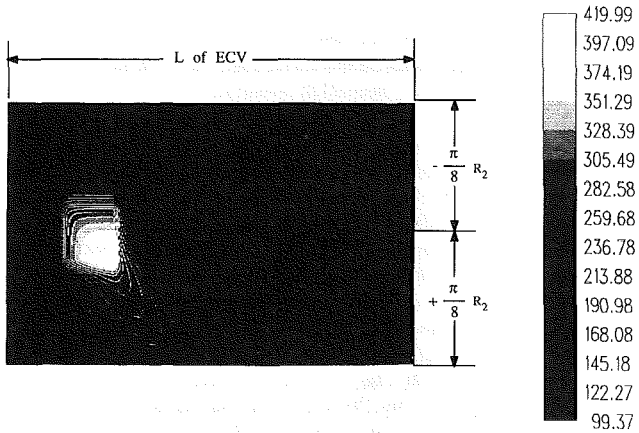

Fig. 9 Temperature contours at $r = R_2$ around the area exposed to the local heat source

3 Numerical Results

In the numerical analysis, the processing and mesh parameters are user input. The mesh parameters are then modified using the Newton–Raphson method to insure that mesh points lie on the boundary of the area exposed to the heat source. The material properties used are those reported by Grove and Short (1984), Cattenach and Cogswell (1985), and Blundell and Willmouth (1986) for APC-2 (see Beyeler and Güçeri, 1988) composite, with 60 percent fiber volume fraction; i.e., $K_L = 6.0$ W/m•°C, $K_T = 0.72$ W/m•°C, $\rho_c = 1.56 \times 10^3$ kg/m^3, $T_g = 140$°C, $T_{\text{melt}} = 340$°C, and $T_{\text{deg}} = 550$°C. The mandrel properties are those for steel; i.e., $K_m = 43.0$ W/m•°C, $\rho_m = 7.8 \times 10^3$ kg/m^3, $C_m = 473.0$ J/kg•°C, and h_2 is taken as 5 W/m^2•°C (Beyeler and Güçeri, 1988). Since the heat loss at the inner surface of the mandrel ($r = R_0$, where the diffusion rate is slow) is negligible, the boundary condition at this location is effectively an insulated one (i.e., $h_0 = 0$). The geometric dimensions are taken as $R_0 = 0.100$ m, $R_1 = 0.125$ m, $R_2 = 0.140$ m, $a = 0.030$ m, $c = 0.120$ m, $b = 0.010$ m, and $d = 0.012$ m. The number of nodes taken in the analysis is $15 \times 72 \times 61$ in the r, θ, and z directions, respectively. The winding angle is taken as $\phi = 57.5$ deg. $T_E = 22$°C, and it is assumed that the overall processing temperature remains at 100°C, and hence $T_{\text{cont}} = 100$°C.

Figure 6 gives the mesh concentrations in the vicinity of the area exposed to the local heat source as well as the composite/mandrel interface. Figure 7 shows the temperature distribution (gray) at the surface of the composite ($r = R_2$). The small and large rectangles are the heat source and the radial projection of the area exposed to it at $r = R_2$, respectively. The coordinates of the center of the area exposed to the heat source are $r = R_2$, $\theta = 0$, and $z = a$. The thin line on the temperature surface shows the temperature profile along the fiber path. The bright and dark rings inside the gray region show the composite and mandrel, respectively. Figure 8 is the wireframe representation of Fig. 7 and gives the actual mesh concentration used in the θ and z directions. Figure 9 shows the temperature contours of the surface of the composite ($r = R_2$) in the vicinity of the local heat source. The length of the figure shows the entire z dimension (of the ECV), and the width gives only the range of

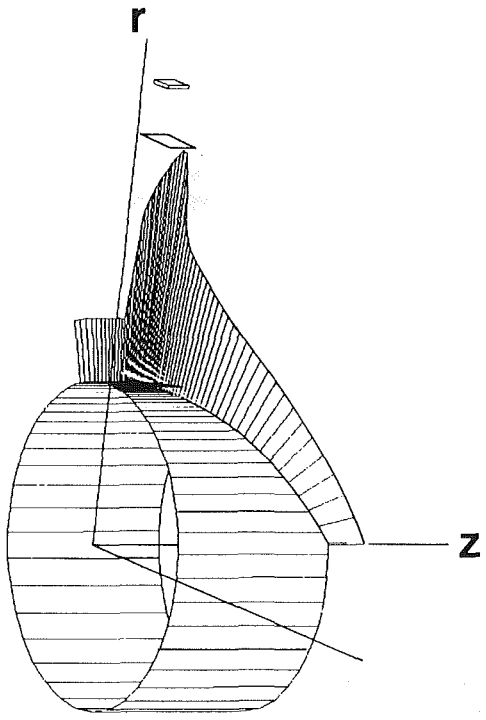

Fig. 10 Temperature profile along the fiber path at $r = R_2$

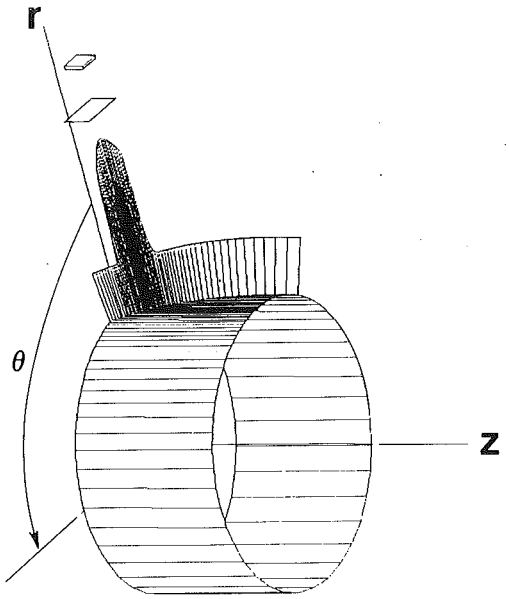

Fig. 11 Temperature profile normal to the fiber path at $r = R_2$

$-\pi/8 \le \theta \le +\pi/8$. Figures 10 and 11 are the temperature profiles along the fiber path and normal to the fiber path, respectively. The cylinders represent the surface of the composite ($r = R_2$).

Figure 12 shows the temperature profile along the fiber path at four radial surfaces, namely, $r = R_0(l_0)$, $r = R_1(l_1)$, $r = R_2(l_2)$, and r at $l_2 - 1$ (which is at $r = 0.1398$ m). The large temperature gradient through the thickness is attributed to the low thermal conductivity in that direction. Moreover, the peak of the temperature is to the right of the center of the heat source, toward the direction of the winding velocity in the analysis (the opposite direction of the motion of the heat source). Figure 13 depicts the effect of the magnitude of the winding velocity (V) on the temperature of the surface of the composite along the fiber path while keeping the heat flux (q_0) constant. This figure shows that as the velocity increases, less time is given for the material to absorb the heat, and hence the temperature decreases. Figure 14 shows the effect of heat flux variation while keeping the winding velocity constant. In this figure $q_0 = 0.75$, 0.60, 0.45, and 0.30 MW/m^2 corresponds to 366.0, 292.8, 219.6, and 146.4 W heat input, respectively, and a decrease in the heat input causes a decrease in the temperature as one would expect. It should be noted that, in Figs. 12–14, the zero position of the z axis is shifted along the z to the position of the local heat source (i.e., $z' = z - a$) to show clearly the location of the center of the heat source by the vertical lines at $z' = 0$.

The total length of the ECV is $a + c$. The values of a and c are obtained by increasing these lengths from some small numbers up to a point where the temperature drops to the control temperature. This was achieved in a shorter distance for the left-hand side of the ECV (i.e., downstream of the motion of the local heat source, a) than for the right-hand side of the ECV (i.e., upstream of the motion of the local heat source, c) as one would expect. The variations between the temperature results presented here and those obtained from an extended right-hand side (from $c = 0.12$ m to $c = 0.15$ m) did not exceed 0.8 percent. Doubling the number of the nodes resulted in variations that did not exceed 2.5 percent. Since the computational model relied on experimental measurements of thermal properties that do not have similar accuracies, the results were considered to be satisfactory. The Gauss–Seidel iteration method is employed in the numerical analysis. The convergence tolerance (i.e., the relative error between the consecutive values

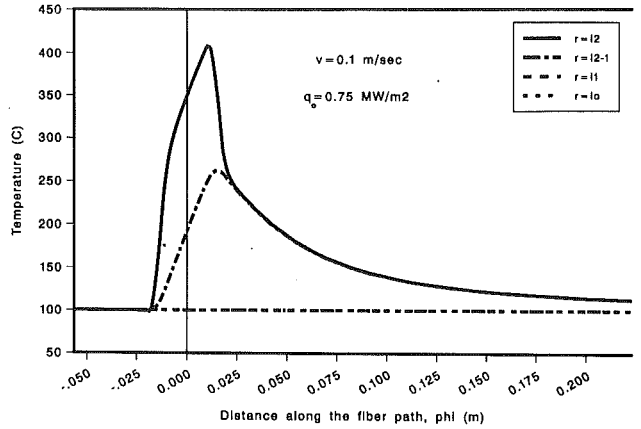

Fig. 12 Temperature profile along the fiber path at four radial surfaces

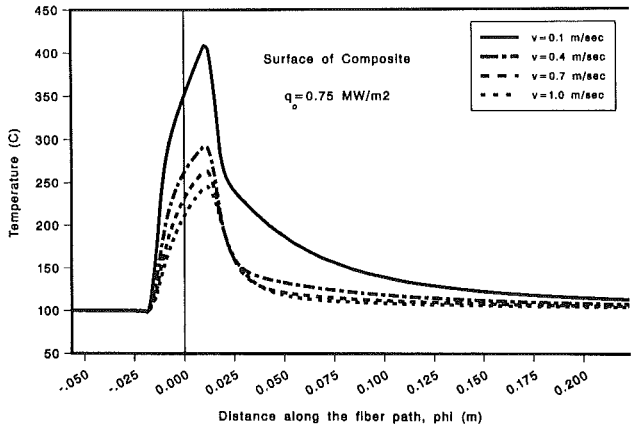

Fig. 13 Effect of the winding speed on the surface temperature along the fiber path

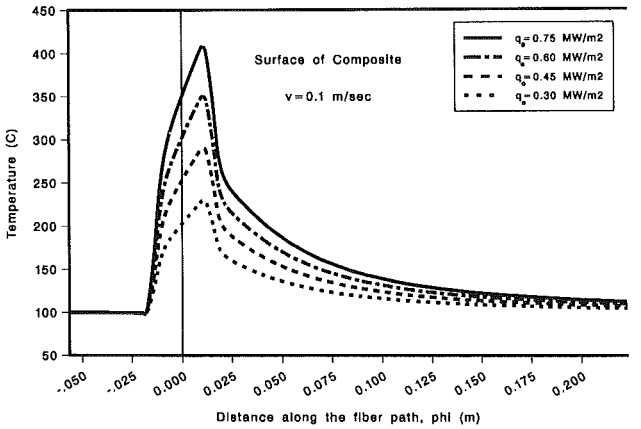

Fig. 14 Effect of heat input on the surface temperature along the fiber path

of the iterations) was taken as 10^{-4}. It should be mentioned that the convergence of the analysis employing a nonuniform mesh was enhanced considerably in comparison with a uniform mesh analysis performed earlier in this study. Successive over/underrelaxation did not enhance the convergence in this study.

This model is also used to generate the effect of ply (tow) thickness on the processing window for the abovementioned material system and geometry. The upper and lower limits of the windows shown in Fig. 15 are defined as follows: If less than or equal to one tow thickness in the transverse direction at the consolidation point is melted ($T_{melt} = 340°C$), then the melting is considered to be insufficient (lower limit, broken

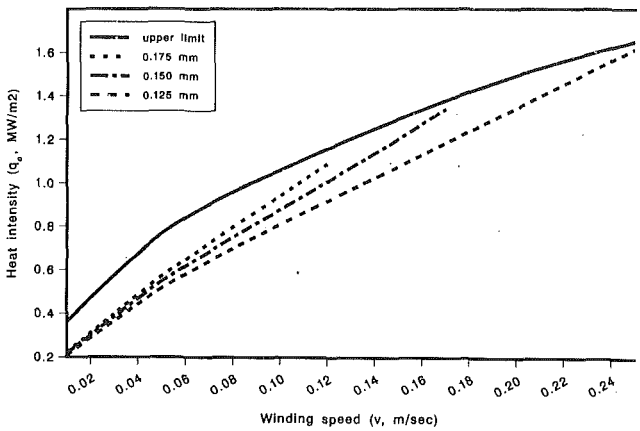

Fig. 15 Numerically generated processing window bound by the polymer degradation (upper limit, solid line) and insufficient melting (lower limits, broken lines) for various winding speeds and three tow thicknesses (0.125 mm, 0.150 mm, and 0.175 mm)

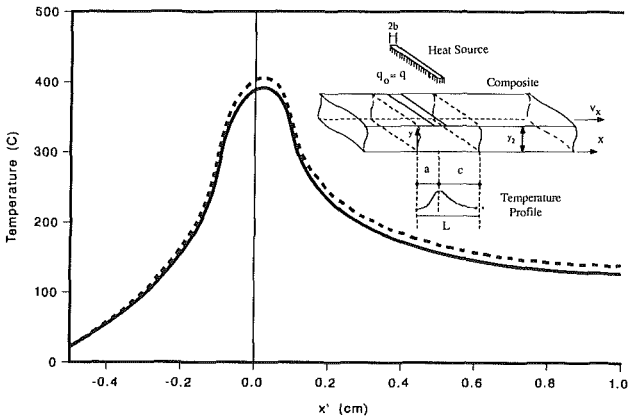

Fig. 16 Comparison between the analytical (dashed line) and numerical (solid line) results for the temperature profile at the top surface of composite (where the error is maximum) for $V_x = 0.05$ m/s and $q_0 = 0.40$ MW/m²; inset shows the geometry and ECV for a tape-laying process

line); i.e., a complete melt-through of the tow being wound is necessary to achieve consolidation. On the other hand, if the maximum temperature, on the surface of the composite, reaches $T_{deg} = 550°C$, significant polymer degradation occurs (upper limit, solid line). The limit at the left-hand side is set at $V =$ 0.01 m/s, since winding speeds below this are considered impractical, and the right-hand side limit is imposed by the nature of the upper and lower limits, which approach each other as the winding speed increases.

While the thickness of the substrate is kept constant (i.e., $r = R_2$) in Fig. 15, the number of the wound tows within the substrate is varied to achieve different tow thicknesses. This is obtained by varying the number of nodes and/or the refinement parameters in the radial direction. Three tow thicknesses of 0.125 mm, 0.150 mm, and 0.175 mm are considered. Figure 13 shows that the temperature decreases with increasing winding speed; however, to achieve a sufficient melting, the heat input should increase (see Fig. 14). It is found that the temperature gradient through the thickness increases with increasing winding speed and heat input. Therefore, the height of the processing window decreases with increasing winding speed for a given tow thickness. Also, since the substrate thickness is taken the same for all three tow thicknesses, the upper limit remains the same while the lower limit increases with increasing tow thickness due to the larger distance of the bottom of the tow from the area exposed to the heat source, thus yielding a smaller processing window for a thicker tow (see Fig. 15).

4 Accuracy Assessment

To check the validity of the numerical results, the numerical method employed for the in-situ thermoplastic filament winding is applied to a tape-laying problem as a test case, and the results are compared with an available analytical solution (Ghasemi Nejhad et al., 1991) where an Eulerian approach is employed. The inset in Fig. 16 shows the geometry of the composite part during a tape-laying process in the presence of a local heat source where the heat transfer inside the incoming tape and the effect of melting/solidification (local heat generation term) are neglected. A detailed numerical analysis of the laser tape-laying process is given by Beyeler and Güçeri (1988) and Grove (1988). All the material properties in the test problem are those used in the filament winding analysis except for the heat capacity, C_p, which is assumed to be a constant 10 J/kg•°C. This value is taken due to difficulties in obtaining an analytical solution using a large C_p value. The dimensions shown in the inset of Fig. 16 are taken as $a = 0.005$ m, $c = 0.01$ m, and $y_2 = 0.005$ m. $h_2 = 5$ and $h_0 = 10^3$ W/m²•°C are the convective heat transfer coefficients for the boundary conditions at the top (environment) and bottom surface (base plate) of the composite, respectively. The boundary conditions for the tape-laying problem are analogous to those for the filament winding one. The width of the heat source is taken as $2b = 0.002$ m, and $T_{cont} = T_E = 22°C$. Also, V_x and q_0 are taken as 0.05 m/s and 0.40 MW/m², respectively. In this case $q = q_0$ for $a - b \le x \le a + b$ and zero, otherwise; and the governing equation is

$$K_{11}\frac{\partial^2 T}{\partial x^2} + K_{22}\frac{\partial^2 T}{\partial y^2} = \rho_c C_p V_x \frac{\partial T}{\partial x} \tag{22}$$

where $K_{11} = K_L$ and $K_{22} = K_T$.

The same numerical considerations used in the filament winding process are applied to the modeled tape-laying problem. Therefore, the same transformations used for $\bar{r}_1$ (mandrel) and z (axis) in filament winding are employed for the y and x directions, respectively, to generate the nonuniform mesh. Equation (22) then becomes

$$K_{11}\left(\frac{\partial \bar{x}}{\partial x}\right)^2 \frac{\partial^2 T}{\partial \bar{x}^2} + K_{11}\left(\frac{\partial^2 \bar{x}}{\partial x^2}\right)\frac{\partial T}{\partial \bar{x}} + K_{22}\left(\frac{\partial \bar{y}}{\partial y}\right)^2 \frac{\partial^2 T}{\partial \bar{y}^2} + K_{22}\left(\frac{\partial^2 \bar{y}}{\partial y^2}\right)\frac{\partial T}{\partial \bar{y}} = \rho_c C_p V_x \left(\frac{\partial \bar{x}}{\partial x}\right)\frac{\partial T}{\partial \bar{x}} \tag{23}$$

where the expressions for the different coefficients can be found in Appendix B by replacing $\bar{r}_1$ and z by y and x, respectively.

The boundary conditions are also transformed accordingly and, for example, can be obtained at $y = y_2$ by replacing $\bar{r}_2$ and K_{11}, in equation (21), by y and K_{22}, respectively. The Newton–Raphson method is used to adjust the size of the mesh to that of the local heat source.

The number of nodes taken in the x and y directions was 61 and 21, respectively. Further increase of the number of nodes had an insignificant effect on the results. The same mesh concentration factors taken in the filament winding analysis in the $\bar{r}_1$ (and/or $\bar{r}_2$) and z directions were taken in the y and x directions, respectively. The convergence tolerance was taken as 10^{-4} (as in filament winding). The effect of the consolidation roller at the outer surface of the composite was taken into account by modifying the outer boundary condition. This effect was found to be insignificant due to the small contact area in comparison with the total outer surface (Ghasemi Nejhad et al., 1991). This relative area is even smaller in the case of filament winding, providing further justification for neglecting the thermal effects of the consolidation roller.

The results obtained from the analytical and numerical methods for the top surface of the composite, where the error is maximum, are shown in Fig. 16. A transformation on the x axis (i.e., $x' = x - a$) is performed to show clearly the location of the heat source at $x' = 0$. The relative error at the maximum temperature is 3 percent, and the maximum relative error over the entire domain is 7 percent, indicating good agreement between the analytical solution and the numerical results.

5 Conclusions

A thermal analysis for in-situ thermoplastic filament winding using a local heat source is described, and an orthotropic model for the effective thermal conductivity of the filament wound parts that incorporates the effect of winding angle is presented. The results show large temperature gradients in the vicinity of the local heat source. The application of the numerical method, used in the filament winding process, to the tape-laying problem as a test case yields temperature profiles that are in a good agreement with the analytical solution. The availability of such an analysis is expected to provide the basis for future studies on heating/cooling rates, resulting microstructures, limits of nongeodesic path, and state of residual stresses, which are strongly coupled in the case of composite materials. It is also expected that the availability of such a bridging between the thermal response of the material system and the various processing parameters will help to optimize the process as well as provide a means for on-line control in thermoplastic filament winding by adjusting the power input and monitoring the linear consolidation speed, which is the subject of the current research.

Acknowledgments

The authors thank Dr. J. W. Gillespie, Jr., and Dr. E. P. Beyeler for useful and enlightening discussions on several aspects of this paper. This work was partially funded by the Center for Composite Materials at the University of Delaware.

References

Anderson, D. A., Tannehill, J. C., and Pletcher, R. H., 1984, *Computational Fluid Mechanics and Heat Transfer*, Hemisphere Publishing Corporation, New York.

Arpacı, V. S., 1966, *Conduction Heat Transfer*, Addison-Wesley Publishing Co., Inc., Reading, MA.

Beyeler, E. P., 1987, "Melting and Solidification in Processing and Applications to Thermoplastic Matrix Composites Manufacturing," Ph.D. Dissertation, University of Delaware, Newark, DE.

Beyeler, E. P., and Güçeri, S. I., 1988, "Thermal Analysis of Laser-Assisted Thermoplastic-Matrix Composite Tape Consolidation," ASME JOURNAL OF HEAT TRANSFER, Vol. 110, pp. 424-430.

Beyeler, E. P., Phillips, W., and Güçeri, S. I., 1988, "Experimental Investigation of Laser-Assisted Thermoplastic Tape Consolidation," *Journal of Thermoplastic Composite Materials*, Vol. 1, pp. 107-121.

Blundell, D. J., Chalmers, J. M., Mackenzie, M. W., and Gaskin, W. F., 1985, "Crystalline Morphology of the Matrix of Peek-Carbon Fiber Aromatic Polymer Composites, I. Assessment of Crystallinity," *SAMPE Quarterly*, Vol. 16, No. 4, pp. 22-30.

Blundell, D. J., and Osborn, B. N., 1985, "Crystalline Morphology of the Matrix of Peek-Carbon Fiber Aromatic Polymer Composites, II. Crystallization Behavior," *SAMPE Quarterly*, Vol. 17, No. 1, pp. 1-6.

Blundell, D. J., and Willmouth, F. M., 1986, "Crystalline Morphology of the Matrix of Peek-Carbon Fiber Aromatic Polymer Composites," *SAMPE Quarterly*, Vol. 17, No. 2, pp. 50-57.

Calius, E. P., and Springer, G. S., 1988, "Filament Winding Process Simulation," *Proceedings, Manufacturing International '88, The Manufacturing Science of Composites*, T. G. Gutowski, ed., Atlanta, GA, Vol. IV, pp. 49-56.

Cattenach, J. B., and Cogswell, F. N., 1985, "Processing With Aromatic Polymer Composites," in: *Developments in Reinforced Plastics*, G. Pritchard, ed., Applied Science Publishers, New York.

Chang, I. Y., and Lees, J. K., 1988, "Recent Development in Thermoplastic Composites: A Review of Matrix Systems and Processing Methods," *Journal of Thermoplastic Composite Materials*, Vol. I, pp. 277-295.

Chou, T-W., and Yang, J-M., 1986, "Structure-Performance Maps of Polymeric, Metal, and Ceramic Matrix Composites," *Metallurgical Transactions A*, Vol. 17 A, pp. 1547-1559.

Davis, M. E., 1984, *Numerical Methods and Modeling for Chemical Engineers*, J. Wiley, New York.

Egerton, M. W., and Gruber, M. B., 1988, "Thermoplastic Filament Winding Demonstrating Economics and Properties Via In-Situ Consolidation," *Proceedings, 33rd International SAMPE Symposium*, Anaheim, CA, Vol. 33, pp. 35-46.

Egerton, M. W., and Gruber, M. B., 1989, "Thermoplastic Filament Wound Parts Demonstrating Properties in Crush Tube and Torque Tube Applications," *Proceedings, 34th International SAMPE Symposium*, Reno, NV, Vol. 34, Book 1, pp. 159-170.

Ghasemi Nejhad, M. N., Cope, R. D., and Güçeri, S. I., 1991, "Thermal Analysis of In-Situ Thermoplastic Composite Tape Laying," *Journal of Thermoplastic Composite Materials*, Vol. 4, No. 1, pp. 20-45.

Griffiths, G. R., Hillier, W. D., and Whiting, J. A. S., 1988, "Thermoplastic Composite Manufacturing Technology for a Flight Standard Tailplane," *Proceedings, 33rd International SAMPE Symposium*, Anaheim, CA, Vol. 33, pp. 308-316.

Grove, S., and Short, D., 1984, "Heat Transfer in APC Fabrication," Final Report for ICI PLC Petrochemicals and Plastics Division, Wilton, DE.

Grove, S. M., 1988, "Thermal Modelling of Tape Laying With Continuous Carbon Fiber-Reinforced Thermoplastic," *Composites*, Vol. 19, No. 5, pp. 367-375.

Hollingsworth, R. D., and Osment, D. R., 1987, "Filament Wound Thermoplastic Matrix Pressure Vessels," *Proceedings, 32nd International SAMPE Symposium*, Anaheim, CA, Vol. 32, pp. 662-669.

Ishikawa, T., and Chou, T-W., 1982, "Stiffness and Strength Behavior of Woven Fabric Composites," *Journal of Materials Science*, Vol. 17, pp. 3211-3220.

Ishikawa, T., and Chou, T-W., 1983, "In-Plane Thermal Expansion and Thermal Bending Coefficients of Fabric Composites," *Journal of Composite Materials*, Vol. 17, pp. 92-104.

Kakaç, S., and Yener, Y., 1985, *Heat Conduction: Second Edition*, Hemisphere Publishing Corporation, New York.

Özışık, M. N., 1979, *Heat Conduction*, Wiley Interscience, New York.

Seferis, J. C., 1984, "Polyetheretherketone (PEEK): A Matrix Semicrystalline Polymer for High Performance Composites," National Academy of Athens, Greece.

Seferis, J. C., and Velisaris, C. N., 1986, "Modeling-Processing-Structure Relationships of Polyetheretherketone (PEEK) Based Composites," *Proceedings, 31st International SAMPE Symposium*, Vol. 31, pp. 1236-1252.

Varga, R. S., 1962, *Matrix Iterative Analysis*, Prentice-Hall, Englewood Cliffs, NJ.

Velisaris, C. N., and Seferis, J. C., 1988, "Heat Transfer Effects on the Processing-Structure Relationships of Polyetheretherketone (PEEK) Based Composites," *Polymer Engineering and Science*, Vol. 28, No. 9, pp. 583-591.

Wells, G. M., and McAnulty, K. F., 1987, "Computer Aided Filament Winding Using Non-geodesic Trajectories," *Proceedings, Sixth International Conference on Composite Materials, Second Europeon Conference on Composite Materials, ICCM & ECCM*, Vol. 1, pp. 1.161-1.173.

Winkel, J. D., and Hurdle, J. R., 1988, "Mechanical Performance of Filament Wound Polyphenylene Sulfide Thermoplastic Composite Tubular Structures," *Proceedings, 33rd International SAMPE Symposium*, Anaheim, CA, Vol. 33, pp. 816-828.

APPENDIX A

Transformations on r for the mandrel (β = refinement parameter, $\alpha = 0$):

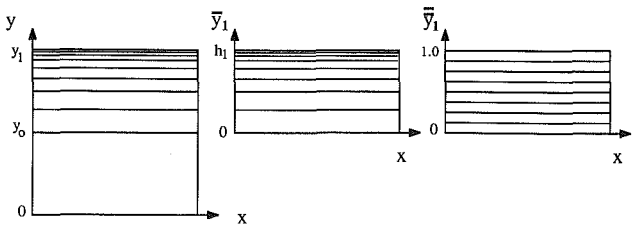

(a) Physical domain **(b) Computational domain**

$$\bar{y}_1 = y - y_0,\quad h_1 = y_1 - y_0$$

$$\bar{y}_1 = \alpha + (1-\alpha)\,\frac{\ln(\{\beta + [\bar{y}_1(2\alpha+1)/h_1] - 2\alpha\}/\{\beta - [\bar{y}_1(2\alpha+1)/h_1] + 2\alpha\})}{\ln[(\beta+1)/(\beta-1)]}$$

Transformations on r for the composite (β = refinement parameter, $\alpha = 1/2$):

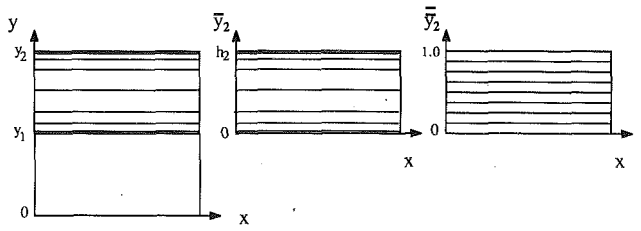

(*a*) Physical domain (*b*) Computational domain

$$\bar{y}_2 = y - y_1,\ h_2 = y_2 - y_1$$

$$\bar{\bar{y}}_2 = \alpha + (1-\alpha)\frac{\ln(\{\beta + [\bar{y}_2(2\alpha+1)/h_2] - 2\alpha\}/\{\beta - [\bar{y}_2(2\alpha+1)/h_2] + 2\alpha\})}{\ln[(\beta+1)/(\beta-1)]}$$

Transformation on θ (β = refinement parameter, $\alpha = 1/2$):

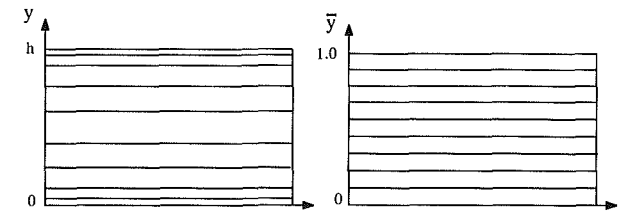

(*a*) Physical domain (*b*) Computational domain

$$\bar{y} = \alpha + (1-\alpha)\frac{\ln(\{\beta + [\bar{y}(2\alpha+1)/h] - 2\alpha\}/\{\beta - [y(2\alpha+1)/h] + 2\alpha\})}{\ln[(\beta+1)/(\beta-1)]}$$

Transformation on Z (τ = refinement parameter):

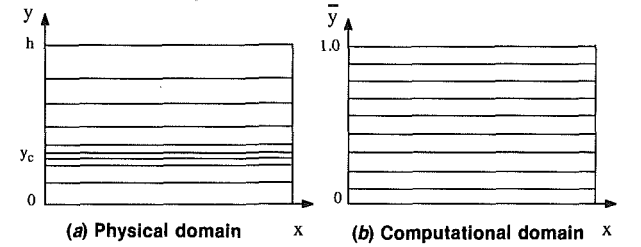

(*a*) Physical domain (*b*) Computational domain

$$\bar{y} = B + (1/\tau)\sinh^{-1}[((y/y_c) - 1)\sinh(\tau B)]$$

$$\text{where } B = (1/2\tau)\ln\left[\frac{1 + (e^{\tau} - 1)(y_c/h)}{1 + (e^{-\tau} - 1)(y_c/h)}\right]$$

APPENDIX B

The coefficients of equations (19) and (20) are:

$$\frac{\partial \bar{\bar{r}}_1}{\partial \bar{r}_1} = \frac{2\beta_{r_1}}{h_{r_1}\{\beta_{r_1}^2 - (\bar{r}_1/h_{r_1})^2\}\ln[(\beta_{r_1}+1)/(\beta_{r_1}-1)]}$$

$$\frac{\partial^2 \bar{\bar{r}}_1}{\partial \bar{r}_1^{\,2}} = \frac{4\beta_{r_1}(\bar{r}_1/h_{r_1})}{h_{r_1}^2\{\beta_{r_1}^2 - (\bar{r}_1/h_{r_1})^2\}^2\ln[(\beta_{r_1}+1)/(\beta_{r_1}-1)]}$$

$$\frac{\partial \bar{\bar{r}}_2}{\partial \bar{r}_2} = \frac{2\beta_{r_2}}{h_{r_2}\{\beta_{r_2}^2 - [(2\bar{r}_2/h_{r_2}) - 1]^2\}\ln[(\beta_{r_2}+1)/(\beta_{r_2}-1)]}$$

$$\frac{\partial^2 \bar{\bar{r}}_2}{\partial \bar{r}_2^{\,2}} = \frac{8\beta_{r_2}[(2\bar{r}_2/h_{r_2}) - 1]}{h_{r_2}^2\{\beta_{r_2}^2 - [(2\bar{r}_2/h_{r_2}) - 1]^2\}^2\ln[(\beta_{r_2}+1)/(\beta_{r_2}-1)]}$$

$$\frac{\partial \bar{\theta}}{\partial \theta} = \frac{2\beta_t}{h_t\{\beta_t^2 - [(2\theta/h_t) - 1]^2\}\ln[(\beta_t+1)/(\beta_t-1)]}$$

$$\frac{\partial^2 \bar{\theta}}{\partial \theta^2} = \frac{8\beta_t[(2\theta/h_t) - 1]}{h_t^2\{\beta_t^2 - [(2\theta/h_t) - 1]^2\}^2\ln[(\beta_t+1)/(\beta_t-1)]}$$

$$\frac{\partial \bar{z}}{\partial z} = \frac{\sinh(\tau B)}{\tau z_c\{1 + [(z/z_c) - 1]^2\sinh^2(\tau B)\}^{1/2}}$$

$$\frac{\partial^2 \bar{z}}{\partial z^2} = \frac{[1 - (z/z_c)]\sinh^3(\tau B)}{\tau z_c^2\{1 + [(z/z_c) - 1]^2\sinh^2(\tau B)\}^{3/2}}$$

Optimization of Cost Subject to Uncertainty Constraints in Experimental Fluid Flow and Heat Transfer

J. Peterson[1]
Graduate Student.
Student Mem. ASME

Y. Bayazitoglu
Professor.
Mem. ASME

Department of Mechanical Engineering and Materials Science,
Rice University,
Houston, TX 77251

Uncertainty analysis in the initial stages of any experimental work is essential in obtaining high-quality data. It insures that the proposed experiment has been thoroughly planned, and that the quantities to be calculated from the experimental measurements will be known with reasonable accuracy and precision. While an uncertainty analysis helps insure reliable results, there is another equally significant aspect in the experimental planning stage: minimization of experimental equipment expenses. A method is presented here in which these two essential experimental elements are combined and viewed as an optimization problem for systematic examination. The analysis allows a systematic search for the least expensive combination of experimental equipment that will give the desired accuracy of results. For the numerical solution the Sequential Gradient Restoration Algorithm (SGRA) is selected. A typical experimental fluid flow and heat transfer problem is given, demonstrating the analysis and numerical solution.

Introduction

An uncertainty analysis in the planning stage of an experiment is necessary to obtain accurate results. Only with such an analysis can the best of a variety of approaches to a problem be determined. Without it there is only the subjective judgment of the experimentalist that the results to be derived from the experimental measurements can be known with sufficient accuracy and precision to be of significance. Of prime significance in the experimental design is selection of equipment, and the inherent uncertainty of differing instruments when applied to the specific problem.

The basic purposes of an uncertainty analysis and procedures for uncertainty estimation have been discussed in previous publications, notably by Kline (1985) and others. In response to a need for a systematic assessment of single-sample experiments, Kline and McClintock (1953) laid the basis of experimental uncertainty determination as determined from a statistical framework. From this beginning, a number of procedures for describing uncertainty have grown. Abernethy et al. (1985) detailed procedures suitable for industrial field, development, and acceptance tests, while Moffat (1988) detailed a method for systematic error reduction, making it most suitable for research applications. Moffat (1982, 1985) has been instrumental in shifting the emphasis from simple calculation of uncertainty for a completed experiment to use of uncertainty analysis in the planning stages. In detailing the various applications of an uncertainty analysis, Moffat defined three different replication levels, which cover most experimental situations. The zeroth-order uncertainty estimate assesses the suitability of instrumentation for the specific application at hand. This analysis is a necessary component of the planning stages of an experiment. Only with such an analysis is it possible to demonstrate the feasibility of a project with proposed instrumentation. The first-order uncertainty interval is an assessment of scatter to be expected in results obtained at different times from the same experimental system. The Nth-order uncertainty interval attempts to consider overall uncertainty from random errors within the measurement system, as well as possible bias errors of each system component (by repetition of the experiment, exchanging instruments for another of the same type). Each order of uncertainty is useful in different stages of the experimental process: the zeroth order for assessment of instrumentation suitability, first order for experimental debugging to determine when an experiment is sufficiently repeatable, and Nth order for comparison of results with those of other experimenters. Regardless of the method of calculation, it has become unacceptable to present experimental results without a corresponding uncertainty analysis; similarly it is inappropriate to propose an experiment without use of an uncertainty analysis to demonstrate its feasibility.

The issue of cost control in experimental work is addressed in a general sense by Smith and Wehofer (1985). They discuss the development of elemental error charts, which assist in identification of dominant error sources. Measurement uncertainty-resource plots, which include cost as a factor, help identify measurement tasks and systems that are cost-efficient. In the current work, the essential nature of an uncertainty analysis is recognized, and is extended to cover the systematic selection of equipment. It is also recognized that in any experimental work the second item of primary importance is the cost of the experimental equipment. These two elements often act in competition with each other, as equipment accuracy can be a costly proposition when state-of-the-art equipment is approached. The method presented here views the allowable uncertainty of the data-reduction equations as constraining equations, and the cost of the experimental equipment as a function of the uncertainty. The cost function is minimized subject to the constraint equations detailing acceptable uncertainty. An optimum uncertainty for each class of measurements is identified and presented with a list of equipment options. The optimization results are not intended to replace subjective judgments based on the experimentalist's experience or personal preference. A large data base of equipment is considered in a systematic manner, allowing equipment selection based on an objective assessment of available equipment. This analysis is then combined with the individual experimentalist's more subjective goals for final equipment selection.

Numerical Method

The numerical method selected for optimization of cost sub-

[1]Present address: University of Florida.

Contributed by the Heat Transfer Division and presented at the ASME Winter Annual Meeting, San Francisco, California, December 10–15, 1989. Manuscript received by the Heat Transfer Division July 13, 1989; revision received March 27, 1990. Keywords: Measurement Techniques, Numerical Methods.

ject to uncertainty constraints is the Sequential Gradient Restoration Algorithm (SGRA) developed by Miele et al. (1972). The SGRA divides the constrained function minimization problem into two sections.

The first section is the gradient phase. The gradient phase begins at a point (δx_j, $j = 1, \ldots, N$), which satisfies all constraint equations ($\Phi_i = 0$, $i = 1, \ldots, q$). For this given nominal point, the total function $f_t(\delta x_j, j = 1, \ldots, N)$, its partial derivatives, and the constraints $\Phi_i(\delta x_j, j = 1, \ldots, N)$ and their partial derivatives are computed. The following linear system of equations is then solved to obtain the vector of Lagrange multipliers, λ_i:

$$\sum_{k=1}^{q}\sum_{j=1}^{N}\frac{\partial\Phi_i}{\partial\delta x_j}\frac{\partial\Phi_k}{\partial\delta x_j}\lambda_k+\sum_{j=1}^{N}\frac{\partial\Phi_i}{\partial\delta x_j}\frac{\partial f_t}{\partial\delta x_j}=0$$

$$i=1, \ldots, q. \tag{1}$$

The augmented function is computed:

$$F=f_t+\sum_{i=1}^{q}\lambda_i\Phi_i \tag{2}$$

and the error index:

$$Q_G=\sum_{j=1}^{N}\left(\frac{\partial F}{\partial\delta x_j}\right)^2 \tag{3}$$

If the error, Q_G, is less than the allowable limit, ϵ_G, the algorithm is terminated. If $Q_G > \epsilon_G$, a single gradient step that reduces the function value must be taken. The step direction and size are computed:

$$p_j=\frac{\partial F}{\partial\delta x_j} \tag{4}$$

$$\Delta(\delta x_j)=-\alpha p_j, \tag{5}$$

$$\delta\tilde{x}_j=\delta x_j+\Delta(\delta x_j) \tag{6}$$

where α is the step size multiplier. The search direction, p_j, from equation (4), is identified using the function gradients; therefore the function value must be reduced if a sufficiently small value of α is selected. Equation (4) also contains the constraint derivatives, insuring that constraint violation will not become excessively large while reducing the function value. The value of α is varied until a set of points $\delta\tilde{x}_j$ is found where $F(\delta\tilde{x}) < F(\delta x)$. The algorithm then proceeds to the restoration phase.

In the restoration phase, only the vector of constraining equations Φ_i is considered. The purpose of the restoration phase is to satisfy the vector of constraint equations: $\Phi_i = 0$ to within the allowable error selected for the restoration phase, ϵ_R. The restoration phase involves several iterations, in each of which the value of the error index, $Q_R = \Sigma\Phi_i^2$, is reduced until the error index is less than or equal to ϵ_R. Given a nominal point (δx_j, $j = 1, \ldots, N$), then Φ_i and the restoration error index Q_R are calculated. If $Q_R < \epsilon_R$ (the allowable restoration error) the restoration phase terminates. If $Q_R > \epsilon_R$, the following linear system of equations is solved to obtain the Lagrange multiplier vector:

$$\sum_{k=1}^{q}\sum_{j=1}^{N}\frac{\partial\Phi_i}{\partial\delta x_j}\frac{\partial\Phi_k}{\partial\delta x_j}\lambda_k-\Phi_i=0, \quad i = 1, \ldots, q \tag{7}$$

Now the search direction for the restoration phase is defined:

$$p_j=\frac{\partial\Phi_i}{\partial\delta x_j}\lambda_i \tag{8}$$

The step is determined as in equations (5) and (6), with the

Nomenclature

a, b, c, d, e, f = constants for use in equation (13)
A_f = rotameter float area
A_r = rotameter flow area
f_i = cost of equipment module i
f_t = total cost function (equation (12))
F = augmented function (equation (2))
l_w = wire length
L_y, L_z = channel dimensions in the y and z direction
$\dot{m}$ = mass flow rate
$\dot{m}_c$ = mass flow rate of rotameter at calibration temperature and pressure
N = total number of variables, δx_i, $N = (n + q)$
Nu = Nusselt number
NY = number of grid points in the y direction
NZ = number of grid points in the z direction
n = number of measurement classes
p_i = step direction (equation (4))
P = pressure
$P_0, P_1, P_2, P_3, P_4, P_5$ = Legendre polynomials (equation (13b))
Q_G = allowable gradient error
Q_R = allowable restoration error
q = number of constraint equations
R = universal gas constant
R_i = data reduction equation i
R_w = wire resistance
Re = Reynolds number
Re_w = Reynolds number based on wire diameter
T = temperature
T_f = film temperature $= (T_g + T_w)/2$
T_g = gas temperature
T_w = hot-wire anemometer temperature
u = velocity
V = voltage
V_f = rotameter float volume
x_j = primary physical measurement
x = axis of channel length
y = axis of channel height
z = axis of channel width
α = step size multiplier
ΔP = difference between stagnation and static pressure (equation (14))
δR_i = uncertainty of R_i
δrot = manufacturer's specification of rotameter uncertainty
δu = uncertainty of velocity measurement
δx_i = uncertainty in measurement of x_i ($i = 1, \ldots, n$); dummy variable ($i = n + 1, \ldots, N$)
ϵ_R, ϵ_G = allowable error in restoration and gradient phases
κ = laser beam intersection angle (equation (16))
κ_g = gas conductivity
λ = Lagrange multipliers (equations (1) and (7)); laser light wavelength (equation (20))
μ = kinematic viscosity
ρ = density
ρ_c = rotameter calibration density
ρ_f = rotameter float density
ρ_g = gas density
Φ_i = constraint function i

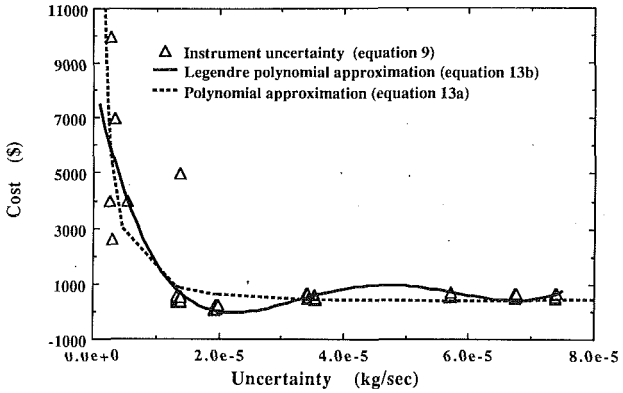

Fig. 1 Cost versus uncertainty in mass flow rate

size, α, varied until a point is found where $Q_R(\delta\tilde{x}) < Q_R(\delta x)$. The SGRA algorithm alternates between the restoration phase, where a number of steps are taken until the constraint equations are satisfied, and the gradient phase, where the function value is reduced while avoiding excessive constraint violation. The algorithm terminates when the gradient error is less than that allowed in the gradient phase ($Q_G < \epsilon_G$) and the restoration error is less than that allowed for the restoration phase ($Q_R < \epsilon_R$).

The constraint equations are developed from the equation defining the uncertainty of functions to be calculated from the experimental data. Using a root-mean-square (rms) summation, the uncertainty, δR_i, of a function, R_i, calculated from a set of input data (x_j, $j = 1, \ldots, n$) is defined:

$$\delta R_i = \left[\left(\frac{\partial R_i}{\partial x_1} \delta x_1 \right)^2 + \ldots + \left(\frac{\partial R_i}{\partial x_n} \delta x_n \right)^2 \right]^{1/2} \tag{9}$$

where x_j denotes the primary physical variables being measured (temperature, pressure, or velocity, for example), and δx_j is the uncertainty of that measurement. The rms summation of contributing experimental uncertainties (equation (9)) results from the assumption that each of the measurement errors is independent of all others. Thus there is a finite probability that all errors will not be simultaneously high or low, but will somewhat cancel each other out. This is indeed the case in most experiments of engineering interest, and equation (9) is the most widely employed definition of uncertainty. If equation (9) is nondimensionalized by dividing each side by R_i, the resulting quantity ($\delta R_i/R_i$) is sometimes called the fractional uncertainty or precision. The fractional uncertainty is the closeness of agreement that can be expected between measurements. It is an approximation of the measurement accuracy: the closeness of agreement between the measured and the true value. In experimental heat transfer the functions, R_i, would typically include such parameters as Reynolds number, Nusselt number, mass and volumetric flow rates, and momentum.

In the experimental planning stage, the calculation of the partial derivatives in the uncertainty function defines the most critical experimental parameters for uncertainty control, and is commonly used as a parameter in equipment selection. However, it is suggested herein that in the planning stage, the uncertainty, δR_i, of a function, R_i, should first be prescribed by the experimenter, and then equipment systematically examined and selected so that the requirements are satisfied.

The first step in detailing the proposed experiment is to select the functions, R_i, to be calculated from experimental data. For each function, R_i, there will be a maximum error, δR_i, which the experimentalist is willing to accept. Thus the second step is selection of this maximum error for each function. This step involves consideration of the relative importance of each function and its intended application. While results with good accuracy are naturally desirable, selection of unnecessarily stringent guidelines will force the selection of expensive state-of-the-art equipment.

The governing equation (equation (9)) can be nondimensionalized and written in a form such that the uncertainty will be less than or equal to the selected maximum:

$$\left(\frac{\delta R_i}{R_i} \right)^2 \geq \frac{1}{R_i^2} \left[\left(\frac{\partial R_i}{\partial x_1} \delta x_1 \right)^2 + \ldots + \left(\frac{\partial R_i}{\partial x_n} \delta x_n \right)^2 \right] \qquad i = 1, \ldots, q \tag{10}$$

Now, assuming it is desired to specify an allowable uncertainty and select equipment that will meet the specification, equation (10) can be written

$$\frac{1}{R_i^2} \left[\left(\frac{\partial R_i}{\partial x_1} \delta x_1 \right)^2 + \ldots + \left(\frac{\partial R_i}{\partial x_n} \delta x_n \right)^2 \right] - \left(\frac{\delta R_i}{R_i} \right)^2 + \delta x_{n+i}^2 = 0, \qquad i = 1, \ldots, q \tag{11}$$

The final term on the left side, δx_{n+i}^2, is a dummy variable. Forcing this dummy variable to be positive forces the actual uncertainty to be less than or equal to the prescribed uncertainty, $(\delta R_i/R_i)^2$. There will be q dummy variables ($\delta x_{n+1}, \ldots, \delta x_{n+q}$), one for each constraint equation. Therefore the total number of variables (δx_i) is N, where $N = n + q$. Equation (11) is now of the form $\Phi_i = 0$, the proper form for the restoration portion of Miele's algorithm. Equation (11) can be written for q constraint equations, $\Phi_1, \ldots, \Phi_q$. In all optimization methods the number of constraint equations must be less than the number of variables. If this condition is not met, there can be no optimization, only a unique solution. Therefore q must be less than n, the number of measurement classes. For use in the restoration algorithm, the derivatives of equation (11) with respect to each uncertainty, δx_i, are readily available. Because SGRA uses the gradient of Φ_i to select step size as well as direction, it is insured that the most accurate equipment will be selected for the measurement of the quantities to which the constraint equations are most sensitive. It is therefore possible to examine the suitability of a library of experimental equipment systematically, and select equipment that will yield results within the user-prescribed uncertainty limits.

Once the constraint equations of equation (11) are satisfied, the algorithm moves to the gradient phase. The uncertainty of each piece of equipment when applied to the specific experimental setup can be determined. The cost of each piece of equipment is viewed as a function of the uncertainty, and a cost versus uncertainty relationship is developed for each class of measurements. Several classes of instruments (rotameter, LDV, hot-wire anemometer) can be used for the same class of measurement (determination of mass flow rate, for example). The function to be minimized is the summation of the individual costs of all applicable measurement classes:

$$f_t = \sum_{j=1}^{n} f_j \tag{12}$$

The cost functions of individual measurement classes are composed of a series of discrete points. Each point represents the uncertainty of an instrument (or combination of instruments) for the specific measurement and experiment in question. Figure 1 shows the uncertainty of the classes of instruments that can be used for measurement of mass flow rate. The more expensive instruments with low uncertainties are the hot-wire anemometer, LDV, and pitot tube with a sensitive micromanometer. The less expensive instruments with higher uncertainties are rotameters, or pitot tubes with less sensitive differential pressure measurement devices. It can be seen that the function of discrete points is discontinuous in slope. As the gradients of the cost function are the driving force in SGRA minimi-

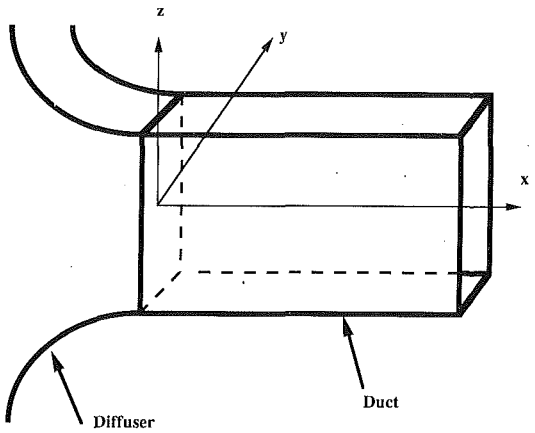

Fig. 2 Test case flow geometry

zation, a detailed curve connecting each point was not found to be useful. It was also found that the cost function is not necessarily a single valued quantity, as different combinations of instruments in a measurement class can yield similar uncertainty results at different expense. Therefore the cost versus uncertainty data for each measurement class (as shown in Fig. 1) were fit with an approximate curve using the method of least squares. Two different profiles were tested. The first profile assumed was a polynomial:

$$f_j = \frac{a_j}{x_j^2} + \frac{b_j}{x_j} + c_j x_j^2 + d_j x_j + e_j \qquad (13a)$$

where a, b, c, d, and e are the constants resulting from the curve fit approximation. The second profile tested was of the form:

$$f_j = a_j P_0 + b_j P_1 + c_j P_2 + d_j P_3 + e_j P_4 + f_j P_5 \qquad (13b)$$

where a, b, c, d, e, and f are again the curve fit constants. P_0, P_1, P_2, P_3, P_4, and P_5 are Legendre polynomials. Either equation 13(a) or 13(b) can be substituted into equation (12) for each of n measurement classes, yielding an analytic expression for the function to be minimized. In both the restoration and gradient phases, the maximum and minimum uncertainty of available equipment is checked for each step, insuring the algorithm is converging to an acceptable solution. Both curve fits of equation (13) are good approximations of the data trends, as seen in Fig. 1. They match the high expense of equipment approaching state-of-the-art, as well as the less expensive and generally less accurate equipment.

Equipment Uncertainty Determination

All data obtained with experimental equipment have an associated uncertainty. The total uncertainty of any measurement, δx_j, is a function of the equipment itself and also the nature of the application. Given the pertinent measurement conditions, the uncertainty of a class of equipment can be assessed by use of the basic equations detailing the basic physical principle exploited by the instrument. A pitot tube, for example, is used for velocity determination by measuring the difference between static and stagnation pressure in a flowing stream. For incompressible flow, the velocity can be determined:

$$u = \left[\frac{2\Delta P R T}{P}\right]^{1/2} \qquad (14)$$

Uncertainties in velocity determination (neglecting yaw of the tube) are due to uncertainty in determination of differential pressure, in pressure measurement, and in temperature measurement. As most experimental research is conducted over a period of time, the uncertainty in temperature and pressure can also be due to ambient variation. The uncertainty of ΔP will depend on the device selected for differential pressure measurement. By taking the appropriate derivatives of equation (14) and combining them as indicated in equation (11), the total uncertainty in velocity determination, δu, can be determined. Each class of experimental equipment will similarly have a governing equation, which can be used to determine the corresponding uncertainty. In this way, the uncertainty of each measurement can be assessed.

A test problem typical in heat transfer applications was used to demonstrate the usefulness of the current method. The problem considered is the determination of Reynolds number of heated air flowing in a rectangular duct, as shown in Fig. 2. To define the Reynolds number, the temperature, pressure, and mass flow rate of the fluid must be known. The first step is to develop a library of equipment to consider for the method. The temperature control equipment is listed in Table 1. Heating a flowing stream of air requires both a heater and a control system. The uncertainties of Table 1 are assumed to be the combined uncertainties of these two elements, and are also assumed to include thermal lag.

The determination of mass flow rate can be accomplished

Table 1 Temperature control equipment

Equipment	Uncertainty °C	Cost $
McMaster-Carr #3309K22	3.0	644.00
McMaster-Carr #3309K24	5.0	644.00
McMaster-Carr #3309K25	6.0	644.00
McMaster-Carr #3309K26	9.0	644.00
Neslab EX-250 Constant Temperature Bath	0.4	3130.00
Laboratory Heater and McMaster-Carr Switch	7.0	29.00

Table 2 Rotameters

Rotameter	Maximum Flow $\frac{m^3}{sec}$	Uncertainty % of full scale	Cost $
Omega FL-1501A	1.5×10^{-3}	2	300.00
Omega FL-1502A	2.8×10^{-3}	2	300.00
Omega FL-1503A	4.9×10^{-3}	2	396.00
Omega FL-1504A	1.2×10^{-2}	2	420.00
Omega FL-121	8.4×10^{-6}	2	305.00
Omega FL-122	5.7×10^{-5}	2	312.00
Omega FL-123	4.1×10^{-5}	2	310.00
Omega FL-124	10.6×10^{-4}	2	409.00
Omega FL-125	2.3×10^{-3}	2	414.00
Omega FL-223	4.1×10^{-4}	2	259.00
Omega FL-224	1.1×10^{-4}	2	384.00
Omega FL-225	2.1×10^{-3}	2	400.00
Omega FL-1408	7.1×10^{-4}	5	468.00
Omega FL-3440C	1.1×10^{-3}	5	111.00
Laboratory Rotameter	6.0×10^{-4}	2	0.0

Table 3 Pressure control equipment

Pressure Meter	Uncertainty Pa.	Cost $
Omega PGT-45L-15	$2.6\text{x}10^2$	240.00
Omega PGT-45L-30	$5.2\text{x}10^2$	240.00
Omega PGT-45L-100	$1.3\text{x}10^3$	240.00
Omega PGT-25L-15	$5.2\text{x}10^2$	87.00
Omega PGT-25L-30	$1.0\text{x}10^3$	99.00
Omega PGH-45L-30	$1.0\text{x}10^3$	115.00
Omega PGS-25L-15	$1.0\text{x}10^3$	51.00
Omega PGS-25L-30	$2.0\text{x}10^3$	51.00

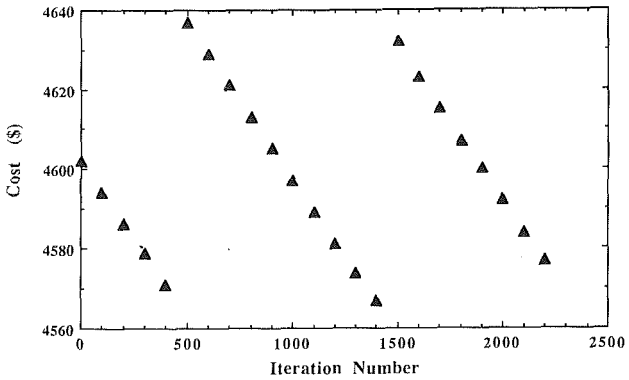

Fig. 3 Gradient convergence monitor showing the solution consistently converging to the same point prior to constraint violation

by a number of different methods, each of which has associated advantages in resultant uncertainties and cost. Each method also has more subjective advantages or disadvantages, such as suitability to the proposed test setup, ease of operation, and in the time and effort required in obtaining results. The first option considered is mass flow rate measurement by use of a rotameter located at the duct entrance. Rotameters are typically rated by the manufacturer at a standard operating temperature and pressure. When operated at the calibration conditions, the uncertainty is generally specified by the manufacturer to be a certain percent of the full scale reading. This uncertainty is generally a result of both the equipment itself and how closely the meter can be read (the least scale division criterion). However, if test conditions include operation of the rotameter at off-calibration conditions, the effect of these variations must also be considered in an uncertainty analysis. Using a force balance, the mass flow rate of the rotameter can be written (Holman, 1978)

$$\dot{m} = \rho_g A_r \left[\frac{1}{C_d} \frac{2gV_f}{A_f} \left(\frac{\rho_f}{\rho_g} - 1 \right) \right]^{1/2} \tag{15}$$

When considering a rotameter operating at conditions other than those for which it was calibrated, equation (15) indicates that variation in fluid density will affect results. The new mass flow rate for operation at differing temperatures and pressures can be determined by ratioing equation (15) to the calibration conditions:

$$\frac{\dot{m}}{\dot{m}_c} = \left[\frac{(\rho_f - \rho_g)}{(\rho_f - \rho_c)} \frac{\rho_g}{\rho_c} \right]^{1/2} \tag{16}$$

where the subscript c indicates the calibration values. As the test problem run was for air at low pressures, the ideal gas equation is used to determine densities as a function of temperature and pressure. The total uncertainty of the rotameter measurement of mass flow rate can then be expressed:

$$\frac{\delta\dot{m}}{\dot{m}_c} = \left[\left(\frac{\delta \text{rot}}{\dot{m}_c} \right)^2 + \left(\frac{\partial}{\partial T} \frac{\dot{m}}{\dot{m}_c} \delta T \right)^2 + \left(\frac{\partial}{\partial P} \frac{\dot{m}}{\dot{m}_c} \delta P \right)^2 \right]^{1/2} \tag{17}$$

where δrot is the specified manufacturer's error (usually calculated using the manufacturer's supplied percent of full scale error multiplied by the rotameter's full scale reading). Given the experimental operating conditions and the anticipated uncertainties, δP and δT, the rotameter uncertainty can be determined. The usefulness of the method currently proposed becomes apparent when it is considered that many pressure control devices are available, each with its own associated cost and uncertainty. Each would result in a different uncertainty in mass flow rate determination. The importance of this equipment can only be assessed in relation to the constraint equations, which detail the derived results of the experimental measurements and the allowable uncertainty of each. The rotameters and gages considered to control rotameter pressure can be seen in Tables 2 and 3.

A second method of measuring mass flow rate of heated air in a duct would be the measurement of fluid velocity at discrete points in the channel and integration of the velocity profile. The channel is divided into discrete sections of dimension dy by dz, and the velocity, u_{ij}, is measured at each grid point. The total mass flow rate is the summation of each section. Therefore the uncertainty in mass flow rate due to velocity can be approximated, again using the ideal gas assumption:

$$\delta\dot{m} = \left[\left(\frac{\partial}{\partial u_{11}} (\rho_g u_{11} dy\, dz) \delta u_{11} \right)^2 + \ldots + \left(\frac{\partial}{\partial u_{NY\,NZ}} (\rho_g u_{NY\,NZ} dy\, dz) \delta u_{NY\,NZ} \right)^2 \right]^{1/2} \tag{18}$$

The uncertainty of each individual velocity measurement, δu_{ij}, can be determined from the derivatives of the governing equation of the piece, equation (14) for a pitot tube, for example. This procedure assumes that velocity is uniform in the control surface, $dy\, dz$. The error in this assumption is a function of the grid resolution, and can be minimized by use of a finer grid.

As the uncertainty in velocity is a function of the velocity being measured, an approximate profile for the velocity distribution in a square duct is assumed (Arpaci, 1984):

$$u(y, z) = \frac{-dp/dx L_y^2}{2\mu} (L_y^2 - y^2) \delta(z) \tag{19a}$$

where

$$\delta(z) = 1 - \frac{\cosh\left(\frac{\sqrt{3}}{L_y} \right) z}{\cosh\left(\frac{\sqrt{3}}{L_y} \right) L_z} \tag{19b}$$

For an experimental design, the desired mass flow rate will be known, and equation (19) is integrated and solved for the pressure term. Once the pressure derivative that will generate the desired mass flow rate is known, the approximate velocity profile is available, and uncertainties of velocity measurements at discrete points within the channel can be found. In most flow situations of engineering interest, an approximate velocity profile will be available from previous work, and can be used for a preliminary uncertainty analysis.

In the present work the pieces of experimental velocity measurement equipment considered for application to mass flow rate determination were the pitot tube, laser-Doppler anemometer, and hot-wire anemometer. The governing equation of the pitot tube at Mach numbers much less than sonic is

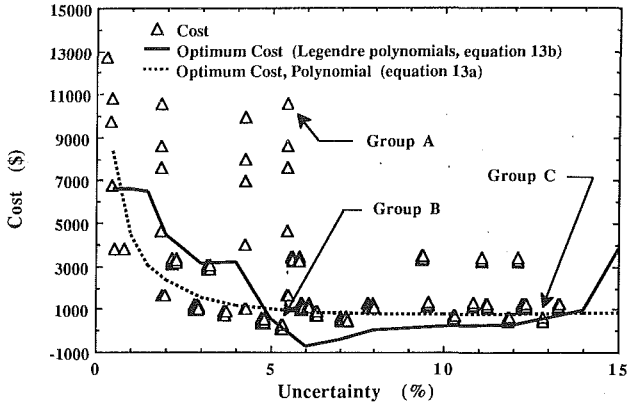

Fig. 4 Optimization results and equipment combinations (Group A: 5 percent uncertainty, $10,594; Group B: 5 percent uncertainty, $80; and Group C: 13 percent uncertainty, $683)

given above (equation (14)). Two instruments for determination of differential pressure ΔP were input to the program: a laboratory micromanometer ($\delta\Delta P = 0.746$ Pa, $100.00 maintenance cost), and a new micromanometer ($\delta\Delta P = 4.7 \times 10^{-3}$ Pa, $2595.00).

The laser-Doppler velocimeter (LDV) is also considered. Velocity as determined by the LDV can be written for node ij in the channel:

$$u_{ij} = \frac{f\lambda}{2 \sin \kappa} \tag{20}$$

The uncertainty in velocity from uncertainties in Doppler frequency, laser wavelength, and beam intersection angle can be determined from this equation. The uncertainty of wavelength is assumed to be negligible. The uncertainty in Doppler frequency is a function of the counter or tracker used, as well as the associated electronic equipment. The uncertainty of the beam intersection angle can be due to such sources as experimental setup and temperature fluctuations within the fluid. The LDV in the equipment listing was a laboratory Argon Ion LDV with $4000 anticipated cleaning and maintenance expense.

The relationship between velocity and voltage output for a constant-temperature hot-wire anemometer is extremely complex due to the various modes of heat transfer that occur from the wire. The heat transfer from the wire with respect to ambient velocity and temperature is extremely nonlinear. As a result, calibration of hot wires is required for each specific application. However, for an uncertainty analysis in the planning stages, a generally applicable relationship is desired. The relationship between Nusselt number and current through the hot wire can be written (Hinze, 1975)

$$\frac{V^2}{R_w} = \pi l_w \kappa_g (T_w - T_g) \mathrm{Nu} \tag{21}$$

where V is the voltage, R_w the wire resistance, l_w the wire length, κ_f the fluid thermal conductivity, and Nu the Nusselt number. For a wide range of flow conditions, Collis and Williams (1959) determined a relationship between Nusselt number and Reynolds number for heat transfer from circular wires normal to a horizontal air stream:

$$\mathrm{Nu}\left(\frac{T_f}{T_g}\right)^{-0.17} = 0.24 + 0.56\mathrm{Re}_w^{0.45} \quad \text{for } 0.02 < \mathrm{Re}_w < 44 \tag{22a}$$

and

$$\mathrm{Nu}\left(\frac{T_f}{T_g}\right)^{-0.17} = \mathrm{Re}_w^{0.51} \quad \text{for } 44 < \mathrm{Re}_w < 140 \tag{22b}$$

where the two correlation equations are divided at a Reynolds number of 44 due to the onset of vortex shedding from the wire. The correlation equations are not applicable below a Reynolds number of 0.02 due to the increasing importance of free convection from the wire at very low velocities. Using equations (21) and (22), an explicit relationship between velocity and voltage, and the pertinent fluid properties and flow parameters, is developed. The uncertainty of the basic hot wire is thus seen to be a function of wire characteristics and geometry, and the ambient fluid properties. The derivatives of the velocity relationship can be taken with respect to each variable, the uncertainty of the variables determined, and the total uncertainty of the velocity measurement by the hot-wire anemometer found from the rms summation as before. The hot-wire anemometer considered was estimated at $4000 for sensor and bridge circuit. Available options for voltage measurement included a free laboratory meter of accuracy 0.002 V, and Hewlett Packard Digital Multimeters of the following accuracy and cost: 8.1×10^{-4} V, $2950; 1.5×10^{-4} V, $5950; and 5.9×10^{-3} V, $995.

In deriving the uncertainties of various pieces of experimental equipment thus far, the emphasis has been placed on examination of the basic physical principles being exploited in the measurement, and how the uncertainty in measurement or control of the underlying quantities will propagate into the experimental results. Clearly, as the proposed experiment becomes progressively complex, other sources of error will enter as well. Each will have an impact on the resulting data, and on the subsequently derived results. Not yet considered are uncertainties in data measurement and signal transmission by electronic equipment, digitization error, traverse location error, and uncertainties from the wide varieties of pressure gages and temperature measurement and control equipment. The variety of experimental equipment available is large but not infinite. The purpose of the current work is systematically to search the wide variety of equipment available for combinations that will achieve the desired accuracy of results, but that will also have a minimum associated cost.

Discussion and Results

The method of cost optimization subject to uncertainty constraints is tested by application to a typical heat transfer problem. The data obtained from the proposed experiment are to be used to determine the Reynolds number of heated air flowing in a duct (Fig. 2). The first step in the analysis is construction of a parametric matrix that defines the proposed operating conditions. The user must input the maximum, minimum, and normal anticipated values of temperature, pressure, and mass flow rate. In this way, the program can examine an equipment library and select only equipment that is suitable for application to the experiment. The user must also input to the program the desired quantity to be calculated (in the test case: Reynolds number), and the percent uncertainty in Reynolds number determination that is allowable. The derivatives of Reynolds number with respect to each of the primary variables (temperature, pressure, and mass flow rate) are input. The work required in developing this information is required in any uncertainty analysis, and therefore would be necessary in any experimental proposal.

The program first performs an uncertainty analysis for all suitable pieces of experimental equipment in each desired measurement class. The operating conditions are obtained from the user-defined parametric matrix; therefore the uncertainty analysis is specific to the proposed experiment. Once the uncertainty of each suitable piece of equipment is known, equipment is sorted by uncertainty from least to most uncertain. The uncertainties of the instruments for each class of measurements are then curve fit to determine the constants of either equation 13(a) or 13(b) and n cost versus uncertainty relationships are constructed as seen in Fig. 1. The SGRA optimization is then performed.

The restoration phase insures that the prescribed uncertainty is met by the equipment selected; the gradient phase insures that the least expensive equipment available is chosen. The algorithm terminates when the restoration phase has satisfied equation (11), and a point is located where the function derivatives are zero. In the current application, the curve fit approximations employed mean that a zero derivative of the function is generally not found. In this case, a typical convergence monitor can be seen in Fig. 3. In this figure, total cost is seen to be reduced in the gradient phase for iterations 1 to 500. At iteration 500, the constraints imposed by equation (11) are found to be violated. The program returns to the restoration phase until the constraint equations are satisfied. The gradient phase is again entered and the function value reduced until the constraint equation is again violated at iteration 1500. The convergence of the algorithm is verified as the gradient phase repeatedly approaches the same minimum before constraint violation occurs. The optimized results for each variable are given, along with a list of suitable experimental equipment, its cost and uncertainty. The user can then select a piece of equipment within the recommended uncertainty from the list of equipment available. Attention can be given to both the uncertainty and such subjective considerations as equipment size, ease of operation, and personal preference of the experimentalist.

Figure 4 shows the cost and percent uncertainty in Reynolds number resulting in possible equipment combinations that were offered to the program. It can be seen that there is a wide possibility of combinations and solutions, even for the simple case considered here. Differing prices can be seen in comparing Groups A and B as indicated in Fig. 4. Group A indicates an equipment combination of the hot-wire anemometer, HP-3458A voltmeter, and McMaster-Carr 3309K22 temperature switch: total cost $10,594. Group B consists of the laboratory rotameter, Omega PGS-25L-15 pressure meter, and the laboratory heater and switch, total cost $80.00. Both Groups A and B yield an uncertainty of approximately 5.5 percent. Group C consists of Omega rotameter FL-125, pressure gauge PGT-45L-30, and the lab heater, $683 total. It can be seen that the increased expense from Group B to C also results in increased uncertainty from 5.5 to 13 percent. The current method is useful as it assesses each equipment combination in relation to the proposed experiment, therefore determining both total equipment cost and suitability.

Optimization results are also shown in Fig. 4. The solid line indicates the summation of cost of all measurement classes (equation (12)), where the cost of each individual measurement class is found from equation 13(a) and 13(b). It can be seen that the optimization method locates a minimum at approximately 6.5 percent when the polynomial approximate curve of equation (13a) is used, and a minimum of 6.0 percent when the Legendre polynomials of equation (13b) are used. These predicted minimums both reflect the least expensive equipment combination (Group B). The fact that both approximate curves of equations (13a) and (13b) yield similar results indicate that as long as the assumed curve is a good approximation of the cost versus uncertainty data, the results are not changed significantly.

When measurement classes are added for more complex problems than the test case considered here, the possibility exists that the optimum solution will be non-unique. This will occur when multiple instrument combinations can all yield acceptable results at differing uncertainties. These differing solutions can be identified by beginning the optimization procedure at a variety of nominal points, δx_j. By starting the algorithm at different assumed initial values, the optimization method will search different regions of the solution space, and locate possible alternative solutions.

The value of the method currently proposed becomes clear in examination of Fig. 4. For the current test case, only a small number of instruments was considered. There is a large variety of possible combinations and corresponding results in even this limited case. The value of the method is its ability to consider unique combinations systematically as more equipment of each class, and more classes of equipment are added. It is then possible to consider a large and comprehensive equipment data base for optimization. The experimentalist is not limited to local catalog availability, or his own prior knowledge and experience. For the novice, valuable information regarding suitable experimental equipment is obtained, which was not previously found in a readily available form. The method also allows consideration by the experienced user of intangible factors such as convenience of use, integration with existing equipment, and personal skills and experience. This is possible as the results indicate an optimum uncertainty for each measurement class, not a specific piece of equipment. The experimentalist is then able to use his expertise in selecting equipment that meets his needs and preferences. In this way, the method offers two distinct advantages: objective assessment of a large data base of experimental equipment, and subsequent subjective choices on the part of the experimentalist.

Conclusions

A method has been demonstrated that views experimental planning as an optimization problem. The method selects appropriate equipment for the proposed experiment and performs an uncertainty analysis for each piece. A cost versus uncertainty function is constructed for each measurement class. It is then possible to minimize total experimental equipment cost for a user-prescribed maximum allowable uncertainty. The method is able systematically and rapidly to consider a wide variety of equipment combinations to obtain the optimum result. Once an optimum uncertainty for each class of equipment has been identified, the experimentalist can select the most appropriate piece from each class, using the information gained from the optimization, the list of available equipment, and his own prior knowledge and experience.

Acknowledgments

The authors wish to express their appreciation to Dr. R. J. Moffat for his valuable discussions.

References

Abernethy, R. B., Benedict, R. P., and Dowdell, R. B., 1985, "ASME Measurement Uncertainty," ASME *Journal of Fluids Engineering*, Vol. 107, pp. 161–164.

Arpaci, V. S., and Larsen, P. S., 1984, *Convection Heat Transfer*, Prentice-Hall, Englewood Cliffs, NJ.

Collis, D. C., and Williams, M. J., 1959, "Two-Dimensional Convection From Heated Wires at Low Reynolds Numbers," *Journal of Fluid Mechanics*, Vol. 6, pp. 357–384.

Hewlett Packard, 1989, *Test & Instrument Catalog*.

Hinze, J. O., 1975, *Turbulence*, McGraw-Hill, New York.

Holman, J. P., 1978, *Experimental Methods for Engineers*, McGraw-Hill, New York.

McMaster-Carr, 1989, *Supply Catalog*.

Kline, S. J., 1985, "The Purposes of Uncertainty Analysis," ASME *Journal of Fluids Engineering*, Vol. 107, pp. 153–160.

Kline, S. J., and McClintock, F. A., 1953, "Describing Uncertainties in Single-Sample Experiments," *Mechanical Engineering*, Vol. 75, pp. 3–8.

Miele, A., Tietze, J. L., and Levy, A. V., 1972, "Comparison of Several Gradient Algorithms for Mathematical Programming Problems," Rice University, Aero-Astronaut. Rep. No. 94.

Moffat, R. J., 1982, "Contributions to the Theory of Single-Sample Uncertainty Analysis," ASME *Journal of Fluids Engineering*, Vol. 104, pp. 250–260.

Moffat, R. J., 1985, "Using Uncertainty Analysis in the Planning of an Experiment," ASME *Journal of Fluids Engineering*, Vol. 107, pp. 173–178.

Moffat, R. J., 1988, "Describing the Uncertainties in Experimental Results," *Experimental Thermal and Fluid Science*, Vol. 1, pp. 3–17.

Omega Engineering, 1988, *Flow and Level Catalog*.

Smith, R. E., and Wehofer, S., 1985, "From Measurement Uncertainty to Measurement Communications, Credibility, and Cost Control in Propulsion Ground Test Facilities," ASME *Journal of Fluids Engineering*, Vol. 107, pp. 165–172.

Second Law Analysis in Assessing Constant Power Input Systems

R. K. Wilcoxon[1]

A. Moutsoglou

Mechanical Engineering Department,
South Dakota State University,
Brookings, SD 57007

A criterion for comparing the relative performance of various heat transfer augmentation methods used in constant power input systems is introduced. The analysis is based on the principle of minimizing the rate of total entropy generation. The heat transfer load (HTL), a parameter determined by the operating requirements of the heat dissipating process that indicates the difficulty of the heat transfer duty to be performed, is defined in the present study. By comparing the irreversibility distribution ratio (ϕ) of various configurations at a given heat transfer load, the most exergy efficient system can be selected. The data for three different types of fin configurations used in two constant power input applications (electronic equipment and internal turbine blade cooling) are utilized in demonstrating the technique. The results indicate which specific fin geometry of the particular configuration type analyzed will transfer the dissipated heat at the specified base surface temperature while requiring the least pumping power. Although the ϕ versus HTL criterion is applied to only fins in this study, the method can be extended to many other applications such as jet impingement cooling or mass transfer.

Introduction

The use of extended surfaces is considered to be one of the most effective methods of enhancing the mechanisms responsible for convective heat transfer. Heat transfer, however, is not the only mechanism increased through the use of fins. The pressure drop of the convecting fluid also increases due to increased surface area and throttling.

Studies of fins abound in the literature and the number of applications is extensive. Typically, in any discussion of fins a description of them includes a list of possible uses, such as in heat exchangers, condensers, regenerators, turbine blades, and electronic equipment. The heat transfer mechanisms involved in all of these applications are generally the same, and the finning methods involved are often similar. However, there are fundamental differences in the purpose of fins used, as encountered for instance in condensers, economizers, and electronic equipment.

In a heat exchanger, such as a condenser, the function of the device is to allow heat to be transferred from one fluid to another. Typically, the inlet and outlet temperatures and the flow rate of at least one fluid are specified by design considerations. The amount of heat to be transferred from the primary fluid is thus fixed. Fins are incorporated to decrease the heat exchanger size and/or the mass flow rate of the secondary fluid. This process shall be herein referred to as heat exchange.

In the process that occurs in a regenerator, such as an economizer, the mass flow rates of both fluid flows are usually fixed. The purpose of the regenerator is to achieve the maximum possible heat transfer to or from a fluid. While the inlet fluid temperatures are fixed, the outlet temperatures are determined by the amount of heat transferred. Fins are incorporated to increase this amount of heat transfer. This type of process shall be referred to as heat regeneration.

In the case of a finned heat sink, which cools electronic equipment, however, the presence of fins does not, in fact, increase the rate of heat transfer to the fluid. Instead, the presence of fins affects the surface temperature from which the heat is dissipated to the convecting fluid. In such devices that dissipate a constant amount of heat, the purpose of fins is to maintain a safe operating temperature. In this respect, an improved fin design is one in which the maximum safe operating temperature is maintained while the required pumping power is reduced. This use of fins for augmenting heat transfer will be referred to as constant power input dissipation.

The recognition of the fundamental differences among the three processes is imperative in selecting criteria for fin optimization in each process. Specifically, these differences determine the appropriate figure of merit to be used when considering total entropy generation due to convective heat transfer, as proposed by Bejan (1979). While the majority of reported work on entropy minimization (see, for instance, Bejan, 1982; Poulikakos and Bejan, 1982; Ouellette and Bejan, 1980) applies to heat exchange and regeneration processes, no study seems to be specifically concerned with constant power input systems. The present study is an adaptation of Bejan's (1979) method, which provides a methodology for the relative effectiveness of various fin configurations to be compared with respect to constant power input dissipation.

Background

Normally, a fin configuration and geometry are optimized with respect to two, or at most three, parameters. An early optimization technique was suggested by Schmidt (1926). This method, which is extensively discussed and expanded upon by Jany and Bejan (1988), determines a fin profile that maximizes total fin heat transfer subject to fixed fin volume. This method is discussed further by Kern and Kraus (1972), as are other fin optimization techniques, where the general approach is to maximize heat transfer from a fin of a specific shape.

A comparison technique relating heat transfer and operating cost (pumping power) was proposed by Mitskevich (1969). In his analysis, the efficiencies of various specimen surfaces were found and compared to each other and to a standard surface, which by definition had an efficiency of 1.

Other performance evaluation criteria that relate heat transfer and pumping power have been proposed. A discussion of various suggested criteria can be found from Shah (1978). Four of these methods (Shah, 1978; London, 1964; London and Ferguson, 1949; Bergles et al., 1974) as recommended by Shah (1978), were used to compare the performance of various fin geometries in a study by Maltson et al. (1989). In that study, the heat transfer and fluid friction characteristics of three heat exchanger configurations were investigated and compared to fins previously studied by Kays and London (1984). The flow

[1]Presently a PhD candidate at University of Minnesota, Minneapolis, MN.

Contributed by the Heat Transfer Division for publication in the JOURNAL OF HEAT TRANSFER. Manuscript received by the Heat Transfer Division June 11, 1990; revision received October 5, 1990. Keywords: Augmentation and Enhancement, Finned Surfaces, Thermodynamics and Second Law.

area goodness factor suggested by London (1964) was also used by Kishimoto et al. (1984) in optimizing a new fin configuration for cooling electronic circuitry. Although the study was concerned with a constant power input system, the conclusions drawn were presented from a heat exchange point of view.

An important optimization technique in forced convection applications was proposed by Bejan (1979) and illustrated by co-workers (Poulikakos and Bejan, 1982; Ouellette and Bejan 1980). In that method, the total entropy generation due to heat transfer and fluid friction was formulated. Since entropy generation is proportional to the destruction of available energy (exergy), an optimum configuration will generate minimum entropy. This concept was applied to numerous situations in addition to heat transfer augmentation, such as energy storage and insulation systems (see Bejan, 1982). Others have expanded on the work to include topics such as mass transfer (San et al., 1987), and manufacturing cost (Aceves-Saborio et al., 1989). Recently, Cheng and Huang (1989) presented local entropy generation rates in laminar flow over transverse fins in the entrance region of a channel.

Applications to Constant Power Input Systems

The preceding discussion of various fin analysis methods indicates a bias toward the design and evaluation of heat exchangers and heat regenerators. If a heat transfer device is to be used for constant power input dissipation, the techniques might not always be appropriate. In the present study, Bejan's (1982) entropy minimization method is extended to heat dissipation applications. Following Bejan's analysis the rate of total entropy generation of an extended surface can be expressed as

$$S_{\text{gen}} = \frac{q(T_s - T_\infty)}{T_\infty^2} + \frac{F_D U_o}{T_\infty} \tag{1}$$

In equation (1) the terms on the right-hand side indicate, respectively, the entropy generation due to heat transfer $S_{\Delta T}$, and the entropy generation due to fluid friction $S_{\Delta p}$.

As previously stated, the purpose of constant power dissipation is to maintain the temperature of a heat-generating device below some critical value. Since the amount of heat generated q, the allowable component temperature T_s, and the ambient fluid (usually air) temperature T_∞ are typically determined by design constraints, the rate of entropy generation due to heat transfer $S_{\Delta T} = q(T_s - T_\infty)/T_\infty^2$ will be fixed. *Thus, the irreversibility of the process is minimized when the entropy generation due to fluid friction, $S_{\Delta p}$, is minimized.*

Equation (1) can be nondimensionalized by dividing through by the constant $S_{\Delta T}$, to get

$$\frac{S_{\text{gen}}}{S_{\Delta T}} = 1 + \phi \tag{2}$$

where ϕ is the irreversibility distribution ratio as defined by Bejan (1982)

$$\phi = \frac{S_{\Delta p}}{S_{\Delta T}} = \frac{F_D U_o T_\infty}{q(T_s - T_\infty)} \tag{3}$$

In heat exchange applications, equation (1) was minimized by expressing the variable base-to-ambient temperature difference $T_s - T_\infty$ and the drag force in terms of a Reynolds number (see Poulikakos and Bejan, 1982). In a constant power input system, where $S_{\Delta T}$ is fixed, the optimization is governed entirely by the magnitude of the irreversibility distribution ratio ϕ. Thus, whereas the irreversibility distribution ratio is a controlling parameter of the entropy minimization of heat exchange systems that "describes the thermodynamic mode in which the passage is meant to function" (Bejan, 1982), in constant power input devices it becomes the optimization criterion in assessing the performance of various fin configurations.

Traditionally, an exergy balance of any system involves an efficiency, defined as the desired output or performance divided by the required input or cost. In applications involving constant power input devices, the desired performance is the transfer of a fixed amount of heat while maintaining a safe operating temperature, and the required cost is the pumping power. With regard to considerations of the second law of thermodynamics, the link between these two factors is that they both generate entropy. Therefore, a viable method of indicating an efficiency of a configuration under any particular operating conditions would be

$$\frac{S_{\Delta T}}{S_{\Delta p}} = \frac{\text{desired performance}}{\text{required cost}} = \frac{1}{\phi} \tag{4}$$

As suggested in the above equation, in constant power input applications the irreversibility distribution ratio ϕ is an inverse indication of efficiency. Systems with low ϕ are thus considered to be better in dissipating a certain amount of heat via a fixed base-to-ambient fluid temperature difference than corresponding configurations with a high ϕ.

In heat exchange applications of the entropy minimization principle, various fin configurations are generally assessed by fixing either the mass flow rate of convecting fluid or required pumping power. In optimizing constant power input systems on the other hand, with the base-to-ambient temperature difference being set by design, neither the mass flow rate nor pumping power can be held fixed. The Reynolds number is not pertinent in the latter case. Instead, for a given heat transfer rate and temperature difference, the mass flow rate and consequently the pressure drop and pumping power are fixed by setting the fin configuration. Thus, the geometry with higher convective heat transfer rates will result at higher exit fluid temperatures and smaller mass flow rates. In effect, the flow rate is dependent on the mechanism of the heat dissipation process. Indeed, the Reynolds number is a function of the heat transfer coefficient, which can be expressed in a nondimensional form such as the Nusselt number or the Stanton number.

The above suggests that although q and $T_s - T_\infty$ are set by design independently, it is the process by which this heat trans-

Nomenclature

A_b = total base area
F_D = drag force
HTL = heat transfer load, equation (5)
k = fluid thermal conductivity
L^* = characteristic length
q = heat transfer rate
S_{gen} = total rate of entropy generation, equation (1)
$S_{\Delta p}$ = rate of entropy generation due to fluid friction
$S_{\Delta T}$ = rate of entropy generation due to heat transfer
T_s = absolute base surface temperature
T_∞ = absolute inlet ambient temperature
U_o = mean characteristic velocity
ϕ = irreversibility distribution ratio, equation (3)

fer over a temperature difference is achieved that affects the irreversibility distribution ratio ϕ. In this study we define a dimensionless heat transfer load (HTL), which quantifies the operating requirements of a constant power input system as

$$\text{HTL} = \frac{L^*/(kA_b)}{(T_s - T_\infty)/q} \tag{5}$$

In equation (5), A_b is the total base area from which heat is transferred, and L^* is a characteristic length fixed by geometric constraints across which heat is being transferred. Thus, L^* is selected as a pertinent length, which is common to all configurations that are being directly compared. The heat transfer load may be interpreted as the ratio of conductive to convective resistances. When there is no fluid motion, the HTL is equal to unity. When fluid motion exists the convective resistance decreases and the HTL has a value greater than 1.

The heat transfer load is determined by operating conditions and is a measure of the "difficulty" of transferring a specific amount of heat via a fixed base-to-ambient temperature difference. For instance, for a given geometry, ambient fluid, and fixed heat dissipating rate q and surface operating temperature T_s, as the inlet ambient fluid temperature increases, $T_s - T_\infty$ decreases, thus requiring higher convective heat transfer rates and normally larger mass flow rates. Consequently, it would be more "difficult" to perform the required task. This difficulty would be indicated by a larger HTL.

The heat transfer load, then, is a common ground on which different geometries can be compared. It indicates the combined effects of heat transfer requirements (q), temperature limitations ($T_s - T_\infty$), fluid properties (k), and geometric constraints (L^*, A_b). Different fin configurations can be compared by determining their relative performance while operating at the same heat transfer load. As stated previously, the relative performance of a configuration shall be indicated by the irreversibility distribution ratio (ϕ). Therefore, in this study the irreversibility distribution ratio will be represented as a function of the heat transfer load. The fin configuration, or geometry, that has the lowest value of ϕ at a particular HTL will be the most efficient—at that HTL. In other words, for a known constant power input application, i.e., a specific HTL, the configuration with the lowest ϕ will require the least pumping power to do the job.

To illustrate the methodology of the ideas set forth above, data presented for three constant power input systems are compiled next in figures of ϕ versus HTL. This enables the assessment of various setups considered in each case from the point of view of minimum entropy generation.

Case I: Analysis of Fins Used to Cool Electronic Equipment

An obvious example of constant power input dissipation occurs in the process of cooling electronic equipment, where it is necessary to remove heat generated in circuitry to avoid temperatures that can damage equipment. Typically, the temperature of semiconductor junctions should remain below 85°C. A comprehensive survey of methods used to cool electronic equipment can be found from Incropera (1988).

An experimental investigation of the heat transfer and pressure drop characteristics was performed by Naik et al. (1987). The fins, which were aligned parallel to the air flow, were typical of those used in cooling electronic packages as shown in Fig. 1. Both the shroud clearance C and the spacing between fins s were varied in the investigation. The results for various configurations were presented in the form of heat transfer coefficient and pressure drop versus the average inlet air velocity.

To apply the results of this study to the irreversibility distribution ratio–heat transfer load analysis, each parameter must be developed in terms of the data given.

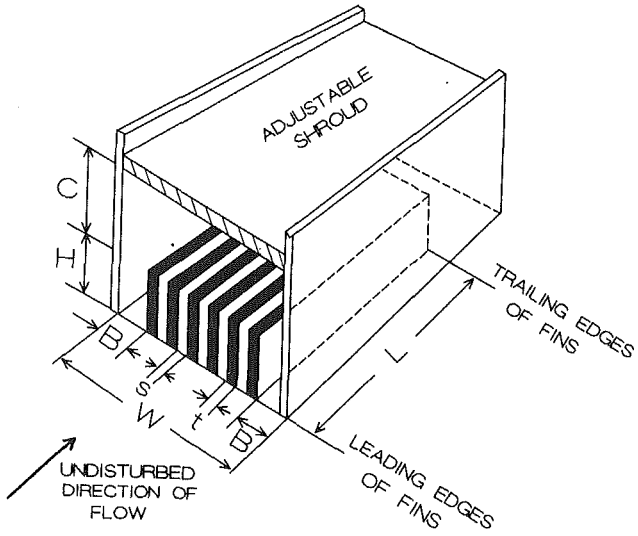

Fig. 1 Definitions of geometric parameters for shrouded fin array configuration (Naik et al., 1987)

After a straightforward manipulation that employs an overall energy balance and the conservation of mass, the heat transfer load as defined by equation (5) can be expressed in terms of parameters prescribed by Naik et al. (1987) as

$$\text{HTL} = \frac{h_{av}L^*}{k}\frac{A}{A_b}\frac{1}{1+\dfrac{h_{av}A}{2A_cU_o\rho C_p}} \tag{6}$$

In the above equation the average heat transfer coefficient h_{av} is presented by Naik et al. (1987) as a function of the mean inlet velocity U_o and the fin configuration, described by the clearance-to-fin height ratio C/H and fin spacing s. The total heat transfer area A is also illustrated in the same reference as a function of the fin spacing s. The total base area from which heat is transferred is given from $A_b = wL$, where $w = 159$ mm is the total channel width and $L = 250$ mm is the streamwise channel length of the fins. The unobstructed cross-sectional area perpendicular to the flow is given from $A_c = wH(1 + C/H)$, where $H = 32$ mm is the fin height. As all the experiments performed by Naik et al. (1987) utilized fins with the same height, it is appropriate to designate the characteristic length L^* to be the constant height of the fins H. In estimating the HTL, the mean properties of air were taken to be $\rho C_p = 1$ kJ/m^{3}K and $k = 0.026$ W/mK. Data are presented by Naik et al. (1987) for fin configurations with clearance-to-fin height ratios of $C/H = 0$, 0.5, and 1 and fin spacings of $s = 3.5$, 5, 10, 12.5, and 19 mm, respectively.

The irreversibility distribution ratio as defined from equation (3) can be expressed in a similar manner as

$$\phi = \frac{\Delta p U_o}{h_{av}}\frac{T_\infty}{(T_s - T_\infty)^2}\frac{A_c}{A}\left[1 + \frac{h_{av}A}{2A_cU_o\rho C_p}\right] \tag{7}$$

where the drag force is expressed as $F_D = \Delta p A_c$, and the characteristic velocity was chosen to be the mean unobstructed inlet velocity U_o. The measured pressure drop Δp is expressed in terms of the mean inlet velocity U_o and fin configuration by Naik et al. (1987).

Results

The irreversibility distribution ratio versus the heat transfer load as calculated from equations (7) and (6) is shown in Figs. 2, 3, and 4 for clearance-to-fin height ratios of $C/H = 0$, 0.5, and 1, respectively. The effects of fin spacing s on the overall performance are illustrated in each figure. These graphs show which configuration will generate the least entropy under given

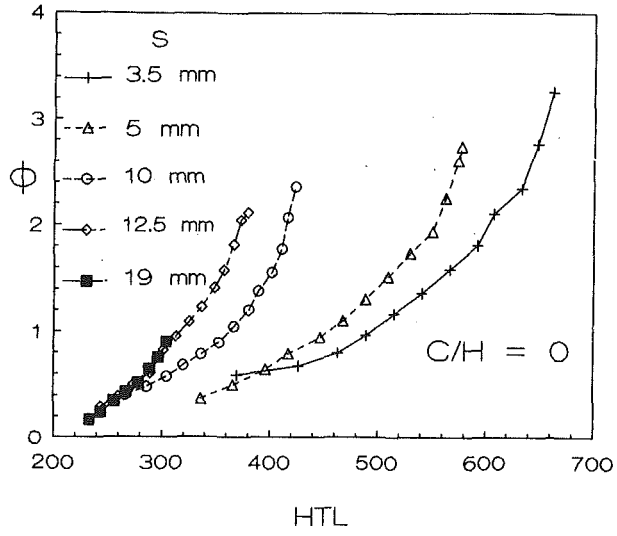

Fig. 2 Irreversibility distribution ratio versus heat transfer load for shrouded plate fins, $C/H = 0$ (Naik et al., 1987)

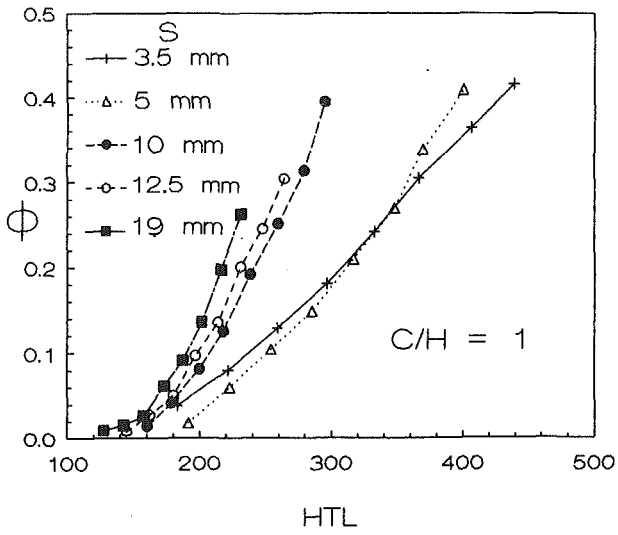

Fig. 4 Irreversibility distribution ratio versus heat transfer load for shrouded plate fins, $C/H = 1$ (Naik et al., 1987)

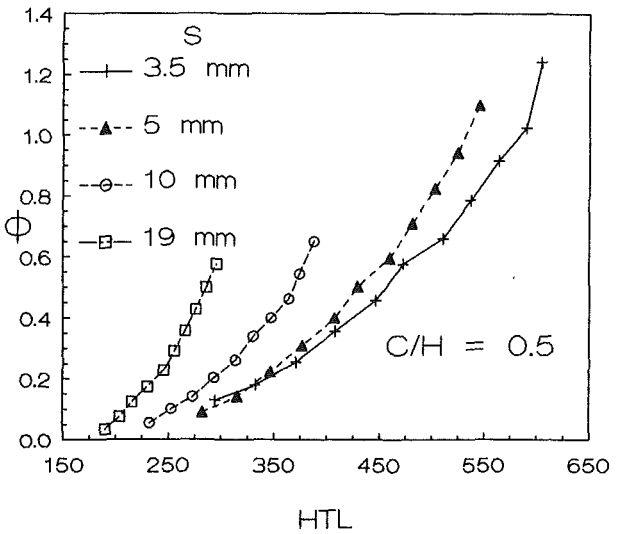

Fig. 3 Irreversibility distribution ratio versus heat transfer load for shrouded plate fins, $C/H = 0.5$ (Naik et al., 1987)

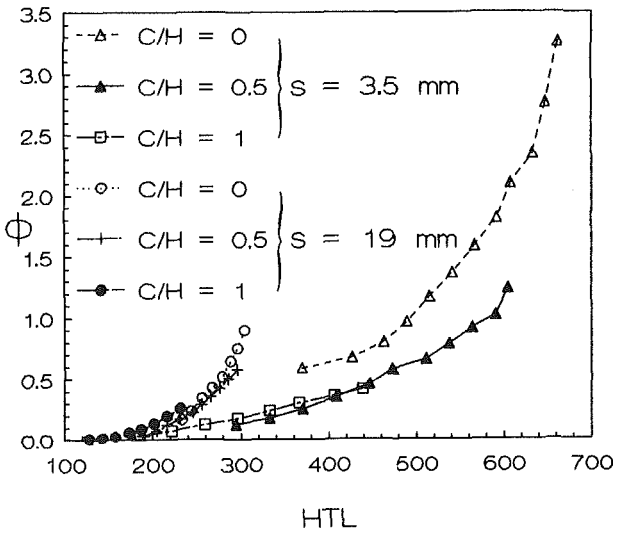

Fig. 5 Irreversibility distribution ratio versus heat transfer load for shrouded plate fins, $s = 3.5$ mm and 19 mm (Naik et al., 1987)

operating conditions. The geometry with the lowest irreversibility distribution ratio for a specific heat transfer load will then be the most efficient configuration—for that particular HTL. In other words, it will dissipate the necessary amount of heat while maintaining the correct base temperature for the minimum cost (pumping power). Generally, in all figures for $s > 5$ mm, the irreversibility distribution ratio ϕ at a given HTL is found to increase as the spacing increases. A statistical analysis that employed an F-test (Milton and Arnold, 1990) for significant differences among the various cases was performed by fitting a quadratic model to the data and using dummy variables. Analysis of the data presented in Figs. 2, 3, and 4 shows that the differences between the HTL-ϕ relationships are statistically significant. The fin configurations with large spacings are shown to be incapable of performing the task reasonably beyond a certain heat transfer load. Thus, at higher HTL's, smaller fin spacings are required. In these instances, the optimum configuration (lower ϕ) is a function of the HTL. For example, in Fig. 4, $C/H = 1$, one can see that when the HTL is greater than 350, the geometry with fin spacing of $s = 3.5$ mm has the lowest ϕ. However, under operating conditions that generate an HTL between 190 and 330, the configuration utilizing fin spacing of $s = 5$ mm will be more efficient.

To highlight the effect of clearance ratio on the irreversibility distribution ratio, Fig. 5 is constructed for two fin spacings of $s = 3.5$ mm and 19 mm. As noted from the figure, at small heat transfer loads for large spacing fins ($s = 19$ mm), lower clearance ratios ($C/H = 0.5$ to 0) seem to be more exergy efficient than larger clearance ratios. For larger heat transfer loads, where small spacing fins need to be employed, larger clearance ratios ($C/H = 0.5$ to 1) are shown to be the better choice. For $s = 3.5$ mm when the HTL is larger than 450, the configuration with the largest clearance ratio, $C/H = 1$, seems to perform the duty with the least pumping power.

In the conclusions presented by Naik et al. (1987), it was stated that the optimal fin separation decreased from 4.8 mm to 4.0 mm as C/H was reduced from unity to zero. This is in general agreement with the results presented in Figs. 2, 3, and 4 in which the fins with $s = 3.5$ mm and 5 mm performed the best in the ranges of flow rates studied. The present second law methodology also reveals a crossover operating point below which the fin configuration with $s = 5$ mm is more exergy efficient and above which the fin configuration with $s = 3.5$ mm is better.

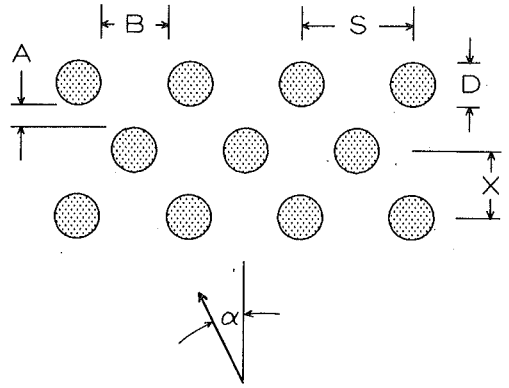

Fig. 6(*a*) Skewed circular pin array geometry (Metzger et al., 1984)

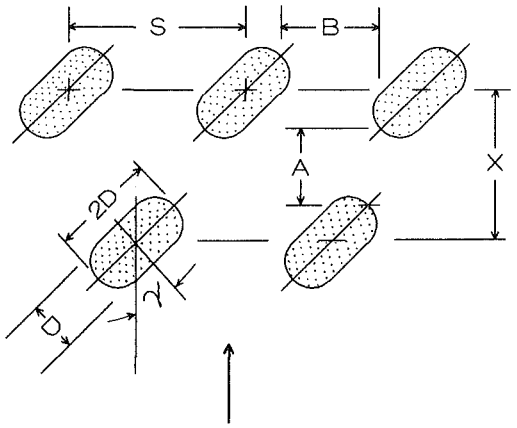

Fig. 6(*b*) Oblong pin array geometry (Metzger et al., 1984)

Case II: Analysis of Fins Used to Cool Turbine Blades Internally: Effect of Various Pin Fin Geometries

The use of pin fins within turbine blades or vanes could be analyzed as another example of constant power input system when all factors external to the blades are constant. In this application, short pins span the cooling passage within the blade, providing structural support in addition to augmenting heat transfer. Typically, the height-to-diameter ratio of these pins ranges from 1/2 to 4. These pins are arranged in a variety of ways, commonly in a staggered array. A number of studies relating to the use of staggered array pin fins for this application have been performed. A comprehensive review of the available literature can be found from Armstrong and Winstanley (1988).

An experimental investigation of the characteristics of these pin fins was performed by Metzger et al. (1984). In that study, two families of pin fin arrays were analyzed. The first family consisted of circular pin fins, which were subjected to flows at various array row orientation angles α (Fig. 6*a*). Experimental data for heat transfer and pressure drop were obtained for $\alpha = 0$, 13, 26, and 40 deg with $S/D = 2.5$, $X/D = 1.5$, $H/D = 1$, $A/D = 0.5$, and $B/D = 1.5$. The diameter of these pins was $D = 0.167$ in.

The other family of pin fin arrays, which was analyzed by Metzger et al. (1984), utilized oblong-shaped pins. In the study, the geometric angle γ (Fig. 6*b*) was varied from $\gamma = 0$, 30, ± 30, 45, ± 45, and 90 deg. The values of the ratios H/D and B/D were the same as for the first family of pin fins while $A/D = 1.5$; however the diameter of the pins was $D = 0.2$ in. A circular pin configuration with the same nominal diameter and H/D, A/D, and B/D ratios was also studied.

Based on the parameters presented by Metzger et al. (1984), after a simple manipulation the heat transfer load and the irreversibility distribution ratio as defined from equations (5) and (3), respectively, can be expressed as

$$\mathrm{HTL} = \mathrm{RePr}(A_{\min}/A_b)\,(H/D)\,(1+e^{q^*}) \tag{8}$$

$$\phi = \frac{2f\mathrm{Re}^2 N_r}{1+e^{q^*}}\frac{\beta}{D^2} \tag{9}$$

where

$$q^* = [\mathrm{Nu}C^*/(2\mathrm{RePr})](A_b/A_{\min}) + \tanh[(\mathrm{Nu}C^*)^{1/2}(H/D)(k/\lambda)^{1/2}](\mathrm{Nu}C^*)^{1/2}(\lambda/k)^{1/2}\Psi \tag{10}$$

and

$$\beta = \frac{\mu^2 T_\infty}{\rho^2 (T_s - T_\infty)^2 C_p} \tag{11}$$

The Nusselt number Nu and the friction coefficient f are presented by Metzger et al. (1984) as a function of the Reynolds number Re and pin orientation angles α or γ. In the equations above the geometric parameter Ψ and the Nusselt number ratio C^* are defined as

$$\Psi = (PaD)^{1/2} N_p/A_{\min},\quad C^* = CA_t/(A_b + CA_p) \tag{12}$$

where C as defined in the same reference is taken to be 2. Also, A_b is the uncovered endwall surface area, A_p is the pin array surface area, A_t is the total surface area $A_b + A_p$, and $A_{\min}$ is the minimum area defined in that study (Metzger, 1990). In addition, N_p is the number of pins in the array, N_r is the number of rows of pins, P is the pin perimeter, a is the pin cross-sectional area, H is the channel height, Pr is the Prandtl number, k is the thermal conductivity of the air, and λ is the thermal conductivity of the fin material. The convection parameter β as defined in equation (11) is fixed by the heat transfer conditions of temperature limitations and convecting fluid type. In the analysis β was assigned the value of $1.4 * 10^{-13}$ m^2, which is characteristic of air and the operating conditions of Metzger et al. (1984). For this case, the characteristic length L^* and characteristic velocity U_o were chosen, respectively, to be the constant channel height H and the velocity at the minimum area $A_{\min}$.

Results

The resulting irreversibility distribution ratios versus the heat transfer loads for the range of data given by Metzger et al. (1984) are shown in Figs. 7 and 8. Figure 7 shows the effect of varying the geometric staggering parameter α in circular pin fins. At small heat transfer loads (HTL < 600) no clear-cut trends can be deduced from the figure. At large heat transfer loads the configuration with $\alpha = 40$ deg (basically an in-line arrangement) is found to be the most exergy efficient. However, it could be inferred from Fig. 7 that at heat transfer loads larger than 1000, the configuration with $\alpha = 0$ deg (staggered configuration) becomes the optimum geometry. Data corresponding to higher heat transfer loads for $\alpha = 0$ deg were not available. The conclusions presented by Metzger et al. (1984) indicated that the $\alpha = 26$ deg configuration performed slightly better than the staggered ($\alpha = 0$ deg) array.

The effect of using oblong pins is shown in Fig. 8. Overall, it appears that the configurations that deflect the flow are not as effective as the circular and $\gamma = 90$ deg oblong pins (longer axis aligned with the flow). Although the oblong pins at $\gamma = 90$ deg did in fact perform slightly better than the circular pins at lower heat transfer loads, statistical analysis employing an F-test (Milton and Arnold, 1990) showed no significant differences between the circular pins and the oblong $\gamma = 90$ deg pins. Overall, the oblong pins cannot be considered an improvement over the circular pins. This observation agrees with the conclusions presented by Metzger et al. (1984), where it was stated that a 20 percent increase in heat transfer for the

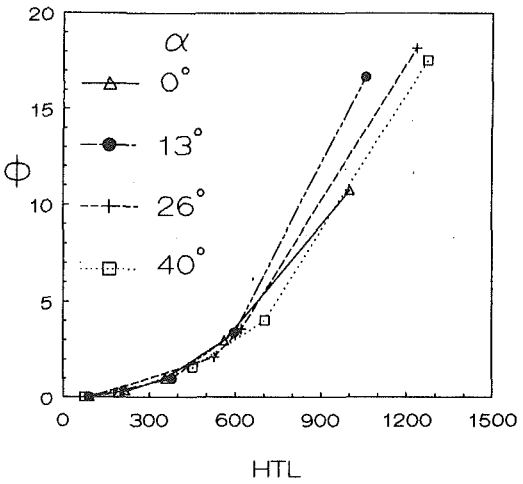

Fig. 7 Irreversibility distribution ratio versus heat transfer load indicating effect of α in circular pin fins (Metzger et al., 1984)

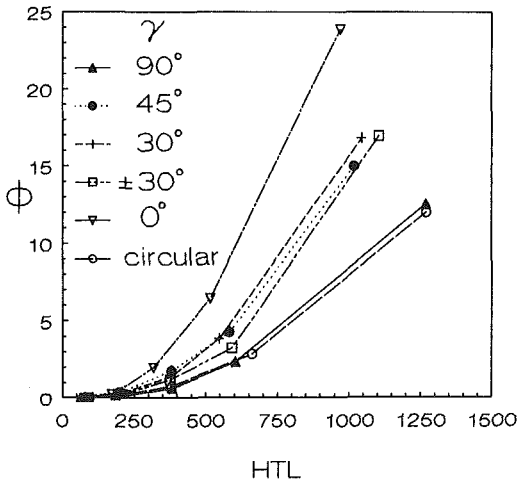

Fig. 8 Irreversibility distribution ratio versus heat transfer load indicating effect of γ in oblong pin fins (Metzger et al., 1984)

case of oblong pins was accompanied by a 100 percent increase in pressure drop.

Case III: Analysis of Fins Used to Cool Turbine Blades Internally: Effect of Various Ejection Hole Configurations

In a typical turbine blade, the cooling air exits the pin fin channel through ejection holes. These ejection holes are located on the trailing edge and at the radial tip of the airfoil. Normally the diameter of these holes is quite small relative to the pin diameter. A study of the effect of these holes on the heat transfer and pressure drop characteristics of the pin fin array was performed by Lau et al. (1989). In that analysis, a fixed pin fin geometry was used in conjunction with various combinations of trailing edge and radial tip ejection holes. The geometry of the test section, along with specific data that provide information with regard to the number and position of the ejection holes for the nine configurations tested by Lau et al. (1989), are depicted in Fig. 9.

The heat transfer load and the irreversibility distribution function as defined from equations (5) and (3), respectively, can be expressed after direct manipulation that employs an overall energy balance as

$$\mathrm{HTL} = \mathrm{RePr}\frac{A_{\min}}{A_b}\frac{L}{D}\left[1 + e^{(\mathrm{St}\ A/A_{\min})}\right] \tag{13}$$

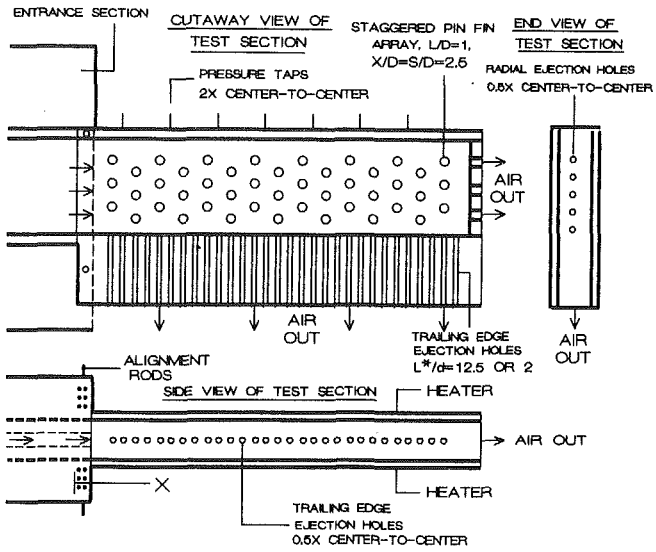

Test Case	L*/d	Exit Hole Configuration: Radial Flow Exit	Exit Hole Configuration: Trailing Edge Ejection Flow Exit
1	2.0	Wide Open	Blocked*
2	2.0	6 Holes	30 Holes
3	2.0	Blocked*	30 Holes
4	2.0	6 Holes	23 Holes**
5	2.0	Blocked*	23 Holes**
6	12.5	6 Holes	30 Holes
7	12.5	Blocked*	30 Holes
8	12.5	6 Holes	23 Holes**
9	12.5	Blocked*	23 Holes**

* Holes were plugged with wooden dowels and sealed with silicone rubber sealant.
** First seven even-numbered holes from the test section entrance were plugged with wooden dowels and sealed with silicone rubber sealant.

Fig. 9 Pin fin array with ejection holes; schematic and test section configurations (Lau et al., 1989)

$$\phi = \frac{f\mathrm{Re}^2}{2N[1 + e^{(\mathrm{St}\ A/A_{\min})}]}\frac{A_c}{A_{\min}}\frac{\beta}{D^2} \tag{14}$$

where $\mathrm{St} = \mathrm{Nu}/(\mathrm{RePr})$ is the Stanton number, and $\beta = \mu^2 T_\infty / [\rho^2 (T_s - T_\infty)^2 C_p]$ is a convection constant. The Nusselt number Nu and friction factor f were correlated from the data of Lau et al. (1989) in terms of the Reynolds number Re for the nine test cases considered (Fig. 9). The Reynolds number defined in terms of the pin diameter D and the air velocity at the minimum flow cross section in the pin fin channel $A_{\min}$ (taken as the characteristic velocity U_o) ranged from 10^3 to $6 * 10^3$. The characteristic length L^* in the HTL expression was taken to be the constant length of the pins L that was equal to the test channel height. In the above equations A_b is the base heat dissipating area (total top and bottom heated surfaces), A_c is the channel cross-sectional area, and A is the total area that includes the exposed surface areas of the top and bottom walls, the pins, the side walls, the radial flow exit blockage and ejection holes. Also, N is the number of pin rows.

The irreversibility distribution ratio versus the heat transfer load as calculated from equations (14) and (13), respectively, for each case is presented in Figs. 10 and 11. A close inspection of the figures reveals that Case 6 and Case 8 are the "best" configurations studied. This is due mainly to the extra heat transfer area corresponding to the long trailing edge ejection holes and the presence of radial edge ejection holes. This is in agreement with the conclusions drawn by Lau et al. (1989). Figure 11 also suggests that Case 6 appears to be better than Case 8 at higher heat transfer loads. In fact, there is a "cross-

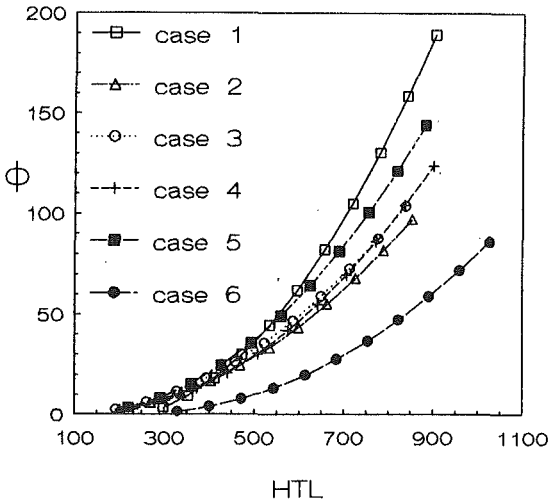

Fig. 10 Irreversibility distribution ratio versus heat transfer load in pin fin channels with ejection holes; test cases 1-6 (Lau et al., 1989)

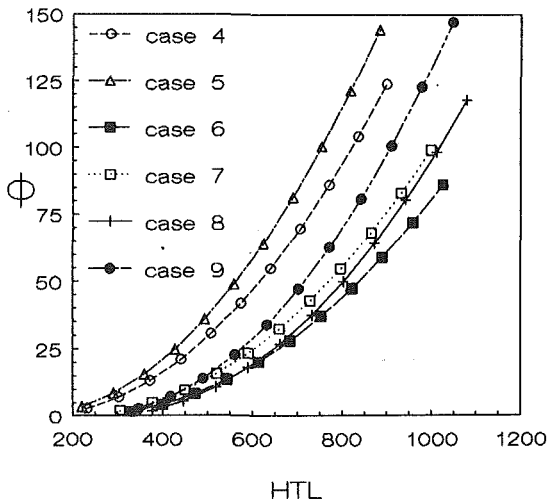

Fig. 11 Irreversibility distribution ratio versus heat transfer load in pin fin channels with ejection holes; test cases 4-9 (Lau et al., 1989)

over" point for each set of configurations with the same radial flow exit and trailing edge ejection hole length but different number of trailing edge ejection holes. In other words, when comparing Case 6 to Case 8, there is a specific HTL, with a value of approximately 600, for which 30 ejection holes (Case 6) is just as exergy efficient as that with 23 ejection holes (Case 8). At any heat load higher than this HTL, Case 6 is better; at lower heat loads Case 8 is more efficient. The same is true for the combinations of Cases 2 and 4, Cases 3 and 5, and Cases 7 and 9. A statistical analysis of the results of the different cases that employed an F-test (Milton and Arnold, 1990) showed that all the relationships are significantly different from each other.

Summary and Conclusions

A criterion for assessing heat transfer augmentation in constant power input systems is introduced. The heat transfer load (HTL) defined as the ratio of conductive to convective thermal resistances provides a common ground for comparison for constant power input systems. For any such system, the heat transfer load is fixed by design constraints of dissipated heat transfer rate, convecting fluid type, inlet fluid temperature, maximum allowable surface temperature, and geometric limitations. It is shown that the irreversibility distribution ratio ϕ, defined as the rate of entropy generation due to fluid friction divided by the rate of entropy generation due to heat transfer, is an inverse indication of efficiency. When two constant power input systems are compared at a given heat transfer load, the one with the lowest ϕ is the most exergy efficient.

Three different studies of heat transfer and pressure drop characteristics of extended surfaces are selected to illustrate the methodology. The first type of configuration analyzed is a geometry consisting of shrouded plate fins used to dissipate heat from electronic equipment. The ϕ versus HTL analysis indicates that, in general, closely spaced fins perform better than the widely spaced ones. The optimum fin spacing, however, is a function of both the shroud clearance and the heat transfer load.

The second application of the ϕ versus HTL criterion involved pin fin arrays used in internal cooling of turbine blades. It is shown that for the data given, an in-line arrangement of pin fins is preferable to a staggered array. It is also found that circular pins basically perform as well or better than oblong pins.

The final application of the criterion is also directed toward pin fins used to cool turbine blades internally. In this case, however, the relative effects of ejection holes are studied. An analysis of the data shows that above a particular heat transfer load, it is desirable to increase the number of trailing edge ejection holes. The results also show that long trailing edge and radial tip ejection holes improve performance.

Although the analyses presented in this study are directed only toward the assessment of extended surface systems, the ϕ versus HTL criterion can be extended to other applications. For example, various jet impingement cooling geometries can be compared to each other and to equivalent extended surface configurations. Also, the methodology can be extended to mass transfer applications. Regardless of the type of system being evaluated, this technique offers the experimentalist a method for presenting results in a format that is very accessible to the designer, and more clearly indicates trends relating to constant power input systems.

References

Aceves-Saborio, S., Ranasinghe, J., and Reistad, G. M., 1989, "An Extension to the Irreversibility Minimization Analysis Applied to Heat Exchangers," ASME JOURNAL OF HEAT TRANSFER, Vol. 111, pp. 29-36.

Armstrong, J., and Winstanley, D., 1988, "A Review of Staggered Array Pin Fin Heat Transfer for Turbine Cooling Applications," ASME *Journal of Turbomachinery*, Vol. 110, pp. 94-103.

Bejan, A., 1979, "A Study of Entropy Generation in Fundamental Convective Heat Transfer," ASME JOURNAL OF HEAT TRANSFER, Vol. 101, pp. 718-725.

Bejan, A., 1982, *Entropy Generation Through Fluid Flow and Heat Transfer*, Wiley, New York.

Bergles, A. E., Blumenkrantz, A. R., and Taborek, J., 1974, "Performance Evaluation Criteria for Enhanced Heat Transfer Surfaces," *Heat Transfer*, Vol. 2, pp. 239-243.

Cheng, C.-H., and Huang, W.-H., 1989, "Entropy Generation and Heat Transfer via Laminar Forced-Convection Channel Flows Over Transverse Fins in Entrance Regions," *Applied Energy*, Vol. 32, pp. 241-267.

Incropera, F. P., 1988, "Convection Heat Transfer in Electronic Equipment Cooling," ASME JOURNAL OF HEAT TRANSFER, Vol. 110, pp. 1097-1111.

Jany, P., and Bejan, A., 1988, "Ernst Schmidt's Approach to Fin Optimization: An Extension to Fins With Variable Conductivity and the Design of Ducts for Fluid Flow," *International Journal of Heat and Mass Transfer*, Vol. 31, No. 8, pp. 1635-1644.

Kays, W. M., and London, A. L., 1984, *Compact Heat Exchangers*, 3rd ed., McGraw-Hill, New York.

Kern, D. Q., and Kraus, A. D., 1972, *Extended Surface Heat Transfer*, McGraw-Hill, New York.

Kishimoto, T., Sasaki, E., and Moriya, K., 1984, "Gas Cooling Enhancement Technology for Integrated Circuit Chips," *IEEE Transactions on Components, Hybrids, and Manufacturing Technology*, Vol. CHMT-7, No. 3, pp. 286-293.

Lau, S. C., Han, J. C., and Batten, T., 1989, "Heat Transfer, Pressure Drop, and Mass Flow Rate in Pin Fin Channels With Long and Short Trailing Edge Ejection Holes," ASME *Journal of Turbomachinery*, Vol. 111, pp. 116-123.

London, A. L., and Ferguson, C. K., 1949, "Test Results of High Performance Heat Exchanger Surfaces Used in Aircraft Intercoolers and Their Significance in Gas-Turbine Regenerator Design," *Transactions of the ASME*, Vol. 71, pp. 17-26.

London, A. L., 1964, "Compact Heat Exchangers, Part 2—Surface Geometry," *Mechanical Engineering*, Vol. 86, pp. 31-34.

Maltson, J. D., Wilcock, D., and Davenport, C. J., 1989, "Comparative Performance of Rippled Fin Plate Fin and Tube Heat Exchangers," ASME JOURNAL OF HEAT TRANSFER, Vol. 111, pp. 21-28.

Metzger, D. E., Fan, C. S., and Haley, S. W., 1984, "Effects of Pin Shape and Array Orientation on Heat Transfer and Pressure Loss in Pin Arrays," ASME *Journal of Engineering for Gas Turbines and Power*, Vol. 106, pp. 252-257.

Metzger, D. E., Feb. 1990, personal communication.

Milton, J. S., and Arnold, J. C., 1990, *Introduction to Probability and Statistics*, 2nd ed., McGraw-Hill, New York.

Mitskevich, A. I., 1969, "Method for Estimating the Efficiency of Convective Heat Transfer," *Heat Transfer—Soviet Research*, Vol. 1, No. 5, pp. 1-21.

Naik, S., Probert, S. D., and Shilston, M. J., 1987, "Forced Convective Steady-State Heat Transfer From Shrouded Vertical Fin Arrays, Aligned Parallel to an Undisturbed Air-Stream," *Applied Energy*, Vol. 26, pp. 137-158.

Ouellette, W. R., and Bejan, A., 1980, "Conservation of Available Work (Exergy) by Using Promoters of Swirl Flow in Forced Convection Heat Transfer," *Energy Int. J.*, Vol. 5, pp. 587-596.

Poulikakos, D., and Bejan, A., 1982, "Fin Geometry for Minimum Entropy Generation in Forced Convection," ASME JOURNAL OF HEAT TRANSFER, Vol. 104, pp. 616-623.

San, J. Y., Worek, W. M., and Lavan, Z., 1987, "Entropy Generation in Convective Heat Transfer and Isothermal Convective Mass Transfer," ASME JOURNAL OF HEAT TRANSFER, Vol. 109, pp. 647-652.

Schmidt, E., 1926, "Die Warmeubertagung durch Rippen," *Z. Ver. Dt. Ing.*, Vol. 70, pp. 885-889, 947-951.

Shah, R. K., 1978, "Compact Heat Exchanger Surface Selection Methods," *Sixth International Heat Transfer Conference*, Vol. 4, pp. 193-199.

Two Principles of Differential Second Law Heat Exchanger Design

R. B. Evans
Georgia Institute of Technology,
The George W. Woodruff School of
Mechanical Engineering,
Atlanta, GA 30332

M. R. von Spakovsky
École Polytechnique Fédérale de Lausanne,
Départment de mécanique,
Laboratoire d'énergétique industrielle,
Lausanne, Switzerland

In this paper, two fundamental principles of differential Second Law analysis are set forth for heat exchanger design. The first principle defines a Second Law temperature, while the second principle defines a Second Law temperature difference. The square of the ratio of the Second Law temperature difference to the Second Law temperature is shown always to be equal to the negative of the partial derivative of the rate of entropy generation (for heat transfer) with respect to the overall conductance of the heat exchanger. For the basic design of elementary heat exchangers, each of these two Second Law quantities is shown to take the form of a simple geometric average. Nonelementary considerations result in corrected geometric averages, which relate directly to the corrected log-mean temperature difference. Both the corrected log-mean temperature difference (nonelementary considerations) and the uncorrected or just log-mean temperature difference (elementary considerations) are widely used in heat exchanger analysis. The importance of these two principles in both exergy and essergy analysis is illustrated by a unified basic treatment of the optimum design of elementary heat exchangers. This results in a single optimization expression for all flow arrangements (i.e., counterflow, parallel flow, and certain crossflow cases).

Introduction

An important concern of differential Second Law analysis (Bejan, 1978, 1987) is the consideration of variations in the rate of entropy generation, $\dot{S}$, which result from differential changes in the parameters upon which $\dot{S}$ depends. In this paper, it is shown that for the design of heat exchangers, the partial derivative with respect to the overall conductance UA (where A is the heat transfer area and U denotes the overall heat transfer coefficient) of the entropy generation due to heat transfer, $\dot{S}_h$, can always be expressed in terms of a Second Law temperature T_{II} and a Second Law temperature difference ΔT_{II} as follows:

$$\frac{\partial \dot{S}_h}{\partial UA} = -\left(\frac{\Delta T_{II}}{T_{II}}\right)^2 \tag{1}$$

Holding the heat transfer rate $\dot{Q}$ constant in $\partial \dot{S}_h/\partial UA$ serves to define what are called *basic* design variations.

For the basic design of *elementary* heat exchangers (where the term "elementary" is defined by equations (14) and (15) below), each of the two Second Law quantities T_{II} and ΔT_{II} is shown to take the form of a simple geometric average. These two principles of differential Second Law analysis are then extended by illustrating that the general definitions of T_{II} and ΔT_{II} each take the form of a *corrected* geometric average, which relates directly to the *corrected* log-mean temperature difference. Both the *corrected* log-mean temperature difference (nonelementary considerations) and the uncorrected or just log-mean temperature difference (elementary considerations) are widely used in heat exchanger analysis (Jacob, 1956; Kays and London, 1958; McAdams, 1954).

In addition, when a comparison of equation (1) with earlier Second Law results (Bejan, 1978, 1987; Evans et al., 1983; Tribus et al., 1956; von Spakovsky and Evans, 1984) is made via an expansion of the right-hand side of equation (1) as a function of the well-known number of transfer units (Jacob, 1956; Kays and London, 1958; McAdams, 1954), a key parameter emerges. This parameter is a heat capacity ratio function b, which serves to delineate the elementary heat exchanger flow forms, i.e., counterflow ($0 \le b \le 1$), parallel flow ($1 \le b \le 2$), and elementary condensers or evaporators ($b = 1$), which admit of crossflow.

Finally, the importance of equation (1) is illustrated by a unified, basic treatment of the optimum design of elementary heat exchangers for both exergy and essergy analysis. However, let us begin our discussions with some basic, differential Second Law analysis of elementary heat exchangers.

Some Basic Differential Second Law Analysis of Elementary Heat Exchangers

From a Second Law standpoint, a key quantity to consider in the design of any component is the rate of entropy generation, $\dot{S}$, in the component. From nonequilibrium thermodynamics (DeGroot and Mazur, 1962; Prigogine, 1955; James and Scalapino, 1963; Callen, 1948), the entropy generation rate $\dot{S}$ can always be expressed in the following form:

$$\dot{S} = \int_0^V \dot{s}\, dV' \tag{2}$$

where

$$\dot{s} = \sum_i \mathbf{J}_i \cdot \nabla F_i \tag{3}$$

Here $\dot{s}$ denotes the entropy generation rate per unit volume with V signifying the volume of the component, V' the integration variable and $\mathbf{J}_i$ and F_i the ith generalized flux (a per-unit-area vector) and potential, respectively. ∇F_i signifies the gradient of the potential F_i. For the case of heat exchangers, we focus upon the entropy generation rate (per unit volume) due to heat transfer and thereby write the first term of equation (3) in the well-known form (DeGroot and Mazur, 1962; Callen, 1948; Hatsopoulos and Keenan, 1960; Tribus, 1961):

$$\dot{s} = \dot{\mathbf{q}} \cdot \nabla\left(\frac{1}{T}\right) + \sum_j \mathbf{J}_j \cdot \nabla F_j \tag{4}$$

Contributed by the Heat Transfer Division and presented at the ASME Winter Annual Meeting, Chicago, Illinois, November 28–December 2, 1988. Manuscript received by the Heat Transfer Division April 26, 1989; revision received August 31, 1990. Keywords: Heat Exchangers, Thermodynamics and Second Law.

where by definition

$$\dot{s}_h \equiv \dot{\mathbf{q}} \cdot \nabla \left(\frac{1}{T}\right) \tag{4a}$$

In equations (4) and (4*a*), $\dot{\mathbf{q}}$ denotes the rate of heat transfer per unit area (a vector), while T is the absolute temperature. Readers unfamiliar with the form $\dot{\mathbf{q}} \cdot \nabla(1/T)$ will find $\dot{S}_h$ presented in a more familiar form in equation (72*a*) of Evans and von Spakovsky (1988), as well as a discussion of the remaining terms $\mathbf{J}_j \cdot \nabla F_j$ in equation (4), especially the ones resulting from the head losses due to the flow of fluid streams through the heat exchanger.

In view of equation (4*a*), the entropy generation rate due to heat transfer, $\dot{S}_h$, is given by

$$\dot{S}_h = \int_0^V \dot{s}_h dV' = \int_0^V \dot{\mathbf{q}} \cdot \nabla \left(\frac{1}{T}\right) dV' \tag{5}$$

For heat exchangers, this integral form of $\dot{S}_h$ must accommodate the following conventional definition for the overall heat transfer coefficient U (Jacob, 1956; Kays and London, 1958; McAdams, 1954):

$$U \equiv \frac{\int_0^A U_l dA'}{\int_0^A dA'} \tag{6}$$

where U_l denotes the local overall heat transfer coefficient defined by

$$U_l \equiv \frac{d\dot{Q}'}{dA'\Delta T} \tag{7}$$

Here A' and $\dot{Q}'$ denote any variable part of the heat transfer area A and the heat transfer rate $\dot{Q}$. The term ΔT signifies

$$\Delta T \equiv T_H - T_L \tag{8}$$

where the subscripts "H" and "L" denote higher and lower values of the absolute temperature T, respectively. The temperatures T_H and T_L represent "bulk" values, which are defined to be consistent with the following expression for $\dot{S}_h$:

$$\dot{S}_h = \int_0^A \left(\frac{1}{T_L} - \frac{1}{T_H}\right) \frac{d\dot{Q}'}{dA'} dA' \tag{9}$$

Here it is understood that the derivative $d\dot{Q}'/dA'$ is actually a partial derivative, which serves to let the terms in equation (4*a*) vary while other quantities such as mass flow rates may be held constant. The difference $[(1/T_L) - (1/T_H)]$ represents the integral of $\nabla(1/T)$ along the path of the gradient between the limits $1/T_L$ and $1/T_H$. The "bulk" temperatures T_L and T_H are (by definition) average temperatures of the masses involved and are defined in such a manner that the evaluation of $\dot{S}_h$ via equations (5) and (9) yields identical values.

Simplifying equation (9) further results in

$$\dot{S}_h = \int_0^{\dot{Q}} \left(\frac{1}{T_L} - \frac{1}{T_H}\right) d\dot{Q}' \tag{10}$$

where the integral over $\dot{Q}$ is understood actually to be an integral over the heat transfer area A.

In order to obtain equation (1), one may form two partial derivatives, $\partial \dot{S}_h/\partial \Delta T_r$ and $\partial UA/\partial \Delta T_r$, with respect to some reference temperature difference ΔT_r [e.g., the pinch temperature difference (Linhoff and Hindmarsh, 1983)] and then take their ratio to obtain $\partial \dot{S}_h/\partial UA$. First we note that

$$\frac{\partial \dot{S}_h}{\partial \Delta T_r} \equiv \left(\frac{\partial \dot{S}_h}{\partial \Delta T_r}\right)_{\underset{\sim}{x},y} \tag{11}$$

where $\underset{\sim}{x}$ and y are the variables that are held constant. The variable y is an extensive rate quantity ($\dot{Q}$ for example), which measures the performance of the exchanger and $\underset{\sim}{x}$ is the set of remaining variables, which are held constant. Via the well-known Leibnitz rule for differentiating integral expressions (Courant and Hilbert, 1962), this partial derivative is written as

$$\left(\frac{\partial \dot{S}_h}{\partial \Delta T_r}\right)_{\underset{\sim}{x},y} = \int_0^{\dot{Q}} \left[\frac{\partial}{\partial \Delta T_r}\left(\frac{1}{T_L} - \frac{1}{T_H}\right)\right]_{\underset{\sim}{x},y,\dot{Q}'} d\dot{Q}' + \left[\frac{1}{T_{L_{\dot{Q}}}} - \frac{1}{T_{H_{\dot{Q}}}}\right] \left(\frac{\partial \dot{Q}}{\partial \Delta T_r}\right)_{\underset{\sim}{x},y} \tag{12}$$

where $T_{L_{\dot{Q}}}$ and $T_{H_{\dot{Q}}}$ denote, respectively, the values of T_L and T_H at the point $\dot{Q}' = \dot{Q}$. If the performance measure y is taken to be the heat rate $\dot{Q}$, then equation (12) reduces to the following basic case:

Nomenclature

A = heat transfer area
b = temperature difference change ratio
$\dot{C}$ = effective heat capacity rate
F_i = ith potential
J_i = ith generalized flux (per unit area)
n_H = higher transfer unit number
n_L = lower transfer unit number
n_{tu} = number of transfer units
$\dot{q}$ = rate of heat transfer per unit area
$\dot{Q}$ = rate of heat transfer
r = heat capacity ratio
r_H = higher reciprocity parameter
r_L = lower reciprocity parameter
$S, \dot{S}$ = entropy creation and rate of entropy creation due to internal irreversibilities
$\dot{s}$ = rate of entropy creation due to internal irreversibilities on a per unit volume basis
T = absolute temperature
U = overall heat transfer coefficient
V = total volume
x = variable
y = variable
α = temperature ratio given by equation (54)
β = temperature ratio given by equation (55)
γ = temperature ratio given by equation (70)
Δ = difference
λ = marginal or unit cost
ν = modified cost parameter
$\sim$ = a set of variables

Subscripts

1 = input
2 = output
I = first average
II = Second Law or second average
c = constant
C = counterflow
gm = geometric mean
h = heat transfer
H = high
L = low
l = local
lm = log mean
P = parallel flow
r = reference
UA = overall conductance
v = variable

Superscripts

$'$ = variable
$+$ = higher effective heat capacity rate

$$\left(\frac{\partial \dot{S}_h}{\partial \Delta T_r}\right)_{\underline{x},\dot{Q}} = \int_0^{\dot{Q}} \left[\frac{\partial}{\partial \Delta T_r}\left(\frac{1}{T_L}-\frac{1}{T_H}\right)\right]_{\underline{x},\dot{Q},\dot{Q}'} d\dot{Q}' \quad (13)$$

This equation simplifies further when applied to *elementary* heat exchangers, which by definition satisfy the following two requirements:

1 The first average temperature difference

$$\Delta T_1 \equiv \frac{\dot{Q}}{UA} \quad (14)$$

is a log-mean temperature difference.

2 The temperature difference change ratio

$$b \equiv \left|\frac{d\Delta T}{dT}\right| \quad (15)$$

is constant throughout the range of the temperature T of the mass with the lower effective heat capacity rate, allowing this rate to be defined by

$$\dot{C} \equiv \left|\frac{d\dot{Q}'}{dT}\right| \quad (16)$$

This definition of elementary heat exchangers is discussed in Appendix A where several relations are derived from these two requirements. For example, $\dot{C}$ is shown to be constant through the range of T so that

$$\dot{Q}' = \dot{C}|T - T_1| \quad (17)$$

with T_1 representing the input temperature of the lower heat capacity stream. In addition, the heat capacity ratio

$$r \equiv \frac{\dot{C}}{\dot{C}^+} \quad (18)$$

where $\dot{C}^+$ denotes the higher effective heat capacity rate, is shown to be related to the temperature difference change ratio, b, as follows:

$r = 1 - b$ counterflow (i.e., $0 \le b \le 1$) (19)

$r = b - 1$ parallel flow (i.e., $1 \le b \le 2$) (20)

$r = 0$ condensers and evaporators that admit of crossflow (i.e., $b = 1$) (21)

The temperature difference change ratio, b, is thus seen to represent a heat capacity ratio function, since $r = |b - 1|$ always. For example, b has the range $0 \le b \le 1$ for counterflow with $b = 0$ or $r = 1$ for balanced counterflow (where $\Delta T_1 = \Delta T = \text{const}$) and $b = 1$ or $r = 0$ for counterflow in a condenser or evaporator.

The quantity b is now used to apply equation (13) to elementary heat exchangers via the following differential relation derived in Appendix A:

$$[\partial \Delta T_r]_{\underline{x},\dot{Q},\dot{Q}'} = [\partial \Delta T]_{\underline{x},\dot{Q},\dot{Q}'} \quad (22)$$

This relation requires that the set of constant variables x must include both $\dot{C}$ and b. Substitution of equation (22) into equation (13) yields

$$\left(\frac{\partial \dot{S}_h}{\partial \Delta T_r}\right)_{\underline{x},\dot{Q}} = \int_0^{\dot{Q}} \left[\frac{\partial}{\partial \Delta T}\left(\frac{1}{T_L}-\frac{1}{T_H}\right)\right]_{\underline{x},\dot{Q},\dot{Q}'} d\dot{Q}' \quad (23)$$

The easiest way to integrate equation (23) is to use the basic method of considering either T_L or T_H as a function $T_c = T_c(\dot{Q}')$, where T_c is a constant w.r.t. ΔT since $\dot{Q}'$ is constant via the Leibnitz rule (as introduced in equation (12)). The input and output values of T_c, denoted respectively by T_{c1} and T_{c2}, are, therefore, constants (i.e., $T_{c1} = T_c(0)$ and $T_{c2} = T_c(\dot{Q})$), so that the sets of constant variables $\underline{x}$, $\dot{Q}$ and $\underline{x}$, $\dot{Q}$, $\dot{Q}'$ in equation (23) may be replaced by T_{c1}, T_{c2}, $\dot{C}$, b and T_{c1}, T_{c2}, $\dot{C}$, b, T_c, respectively. The result is

$$\left(\frac{\partial \dot{S}_h}{\partial \Delta T_r}\right)_{T_{c1},T_{c2},\dot{C},b} = \int_0^{\dot{Q}} \left[\frac{\partial}{\partial \Delta T}\left(\frac{1}{T_L}-\frac{1}{T_H}\right)\right]_{T_{c1},T_{c2},\dot{C},b,T_c} d\dot{Q}' \quad (24)$$

Letting T_v denote the other temperature (which will, of course, be variable), the integrand of equation (24) takes on the following form:

$$\left[\frac{\partial}{\partial \Delta T}\left(\frac{1}{T_L}-\frac{1}{T_H}\right)\right]_{T_{c1},T_{c2},\dot{C},b,T_c} = \left[\frac{d}{d\Delta T}\left|\frac{1}{T_c}-\frac{1}{T_v}\right|\right]_{T_{c1},T_{c2},\dot{C},b,T_c} \quad (25)$$

From equation (8)

$$\Delta T \equiv T_H - T_L = |T_v - T_c| \quad (26)$$

so that equation (25) reduces further to

$$\left[\frac{\partial}{\partial \Delta T}\left(\frac{1}{T_L}-\frac{1}{T_H}\right)\right]_{T_{c1},T_{c2},\dot{C},b,T_c} = \frac{d}{dT_v}\left(-\frac{1}{T_v}\right) = \frac{1}{T_v^2} \quad (27)$$

Substitution of equation (27) into equation (24) yields

$$\left(\frac{\partial \dot{S}_h}{\partial \Delta T_r}\right)_{T_{c1},T_{c2},\dot{C},b} = \int_0^{\dot{Q}} \frac{d\dot{Q}'}{T_v^2} \quad (28)$$

Since

$$d\dot{Q}' = \dot{C}_v |dT_v| \quad (29)$$

for elementary heat exchangers where $\dot{C}_v$ is a constant denoting the effective heat capacity rate for the mass stream with temperature T_v, equation (28) becomes

$$\frac{\partial \dot{S}_h}{\partial \Delta T_r} = \dot{C}_v \int_{T_{v1}}^{T_{v2}} \frac{|dT_v|}{T_v^2} = \dot{C}_v \left|\frac{1}{T_{v1}}-\frac{1}{T_{v2}}\right| = \frac{\dot{C}_v |T_{v2} - T_{v1}|}{T_{v1} T_{v2}} \quad (30)$$

The integrated form of equation (29)

$$\dot{Q} = \dot{C}_v |T_{v2} - T_{v1}| \quad (31)$$

serves to yield

$$\left(\frac{\partial \dot{S}_h}{\partial \Delta T_r}\right)_{T_{c1},T_{c2},\dot{C},b} = \frac{\dot{Q}}{T_{v1} T_{v2}} \quad (32)$$

The theoretical significance of equation (32) may be made clearer via noting the definition of the geometric mean x_{gm} of variables x_1 and x_2, i.e.,

$$x_{gm} = \sqrt{x_1 x_2} \quad (33)$$

This serves to yield the final form of $\partial \dot{S}_h / \partial \Delta T_r$ for the basic treatment of elementary heat exchangers:

$$\frac{\partial \dot{S}_h}{\partial \Delta T_r} = \frac{\dot{Q}}{T_{vgm}^2} \quad (34)$$

In equation (34), it is understood that T_{c1}, T_{c2}, $\dot{C}$, b, and, therefore, $\dot{Q}$ are all constant in the partial derivative.

This expression, thus, serves in the general case (i.e., $\dot{Q} \neq$ constant and nonelementary heat exchangers) to define the Second Law temperature T_{II} via

$$\frac{\partial \dot{S}_h}{\partial \Delta T_r} = \frac{\dot{Q}}{T_{II}^2} \quad (35)$$

where $\partial \dot{S}_h / \partial \Delta T_r$ is found from the right-hand side of equation (12). Methods for determining T_{II} as a corrected value of the geometric mean, T_{vgm}, are discussed later.

Let us now turn our attention to deriving the other term, $\partial UA / \partial \Delta T_r$, needed to obtain $\partial \dot{S}_h / \partial UA$ in equation (1). In the basic case where by definition $\dot{Q}$ is constant, $\partial UA / \partial \Delta T_r$

may be found by differentiating the reciprocal of the first temperature difference, ΔT_{I}, defined by equation (14), i.e.,

$$\frac{\partial UA}{\partial \Delta T_r} = \dot{Q}\,\frac{\partial}{\partial \Delta T_r}\left(\frac{1}{\Delta T_{\mathrm{I}}}\right) \tag{36}$$

For elementary heat exchangers, ΔT_{I} is by definition a log-mean temperature difference, ΔT_{lm}, such that

$$\Delta T_{\mathrm{I}} = \Delta T_{lm} = \frac{\Delta T_H - \Delta T_L}{\ln \dfrac{\Delta T_H}{\Delta T_L}} \tag{37}$$

where ΔT_H and ΔT_L denote, respectively, the highest and lowest values of ΔT. Substitution of equation (37) into equation (36) is carried out in Appendix B, yielding

$$\frac{\partial UA}{\partial \Delta T_r} = -\frac{\dot{Q}}{\Delta T_L \Delta T_H} \tag{38}$$

Use of equation (33) yields the final form of $\partial UA/\Delta T_r$ for the basic treatment of elementary heat exchangers as follows:

$$\frac{\partial UA}{\partial \Delta T_r} = -\frac{\dot{Q}}{(\Delta T_{gm}^2)} \tag{39}$$

As with the development of T_{II}, the Second Law temperature difference, ΔT_{II}, for the general case (i.e., $\dot{Q} \neq$ constant and nonelementary heat exchangers) is defined by

$$\frac{\partial UA}{\partial \Delta T_r} = -\frac{\dot{Q}}{(\Delta T_{\mathrm{II}}^2)} \tag{40}$$

If equation (40) and equation (35) are now substituted into

$$\frac{\partial \dot{S}_h}{\partial UA} = \frac{\partial \dot{S}_h/\partial \Delta T_r}{\partial UA/\partial \Delta T_r} \tag{41}$$

then the expression found in equation (1) is obtained. The quantity ΔT_{II} represents a second average temperature difference (as opposed to the first average, ΔT_{I}). The Second Law character of ΔT_{II} results from the fact that the evaluation of $\partial UA/\partial \Delta T_r$ must be carried out in direct correspondence to the evaluation of $\partial \dot{S}_h/\partial \Delta T_r$. The required expression for doing this (derived in Appendix B and analogous to equation (12)) is

$$\left(\frac{\partial UA}{\partial \Delta T_r}\right)_{\underline{x},y} = \int_0^{\dot{Q}} \left[\frac{\partial}{\partial \Delta T_r}\left(\frac{1}{\Delta T}\right)\right]_{\underline{x},y,\dot{Q}'} d\dot{Q}' + \left(\frac{1}{\Delta T_{\dot{Q}}}\right)\left[\frac{\partial \dot{Q}}{\partial \Delta T_r}\right]_{\underline{x},y} \tag{42}$$

Methods for using equation (42) in equation (40) to obtain ΔT_{II} as a corrected value of the geometric mean, ΔT_{gm}, are discussed below. Before doing this, however, let us carry out an expansion of the right-hand side of equation (1) for elementary heat exchangers in terms of the number of transfer units in order that a comparison with earlier Second Law results can be made.

Expansion of the Second Law Form of $\partial \dot{S}_h/\partial UA$

We begin by first defining some terms such as the well-known number of transfer units

$$n_{tu} \equiv \frac{UA}{\dot{C}_m} \tag{43}$$

$\dot{C}_m$ is the mean value of the lower effective heat capacity rate $\dot{C}$ such that

$$\dot{C}_m \equiv \frac{\dot{Q}}{|T_2 - T_1|} \tag{44}$$

In using the quantity n_{tu}, it is customary to use the effectiveness η, defined by

$$\eta \equiv \frac{\dot{Q}}{\dot{Q}_{\max}} \tag{45}$$

[an approach well known as the effectiveness-n_{tu} method (Kays and London, 1958)]. However, the local number of transfer units,

$$n_{tu,l} \equiv \frac{U_l A_l}{\dot{C}_m} \tag{46}$$

proves to be a more convenient intermediate concept than the effectiveness η for differential Second Law analysis. (For integral expressions for $\dot{S}_h$, the writers find the effectiveness η to be the more convenient parameter; but such considerations are beyond the scope of this paper.) Here U_l is the local overall heat transfer coefficient defined by equation (7), while the local heat transfer area A_l is defined by

$$A_l \equiv \frac{dA'}{d\dot{Q}'}\,\dot{Q} \tag{47}$$

Substitution of equations (7), (44), and (47) into equation (46) yields

$$n_{tu,l} = \frac{|T_2 - T_1|}{\Delta T} \tag{48}$$

For the purposes of comparison, one may observe that substitution of equations (14) and (44) into equation (43) gives

$$n_{tu} = \frac{|T_2 - T_1|}{\Delta T_{\mathrm{I}}} \tag{49}$$

The upper and lower extremes of $n_{tu,l}$ (denoted, respectively, by n_H and n_L) are

$$n_H = \frac{|T_2 - T_1|}{\Delta T_L} \tag{50}$$

$$n_L = \frac{|T_2 - T_1|}{\Delta T_H} \tag{51}$$

where ΔT_H and ΔT_L were defined immediately following equation (37). Both n_H and n_L are particularly useful; and for brevity, we will refer to n_H and n_L, respectively, as the upper and lower n_{tu} while the square root of their product will be called the geometric mean n_{tu}, which denoted by n_{gm} is given by

$$n_{gm} = \frac{|T_2 - T_1|}{\Delta T_{gm}} \tag{52}$$

Turning now to our expression of the Second Law form of $\partial \dot{S}_h/\partial UA$, equation (1) is modified to apply to the basic treatment of elementary heat exchangers by replacing T_{II} and ΔT_{II} by their corresponding geometric averages [as they appear in equations (34) and (39)], i.e.,

$$\left(\frac{\partial \dot{S}_h}{\partial UA}\right)_{T_{c1},T_{c2},\dot{C},b} = -\left(\frac{\Delta T_{gm}}{T_{vgm}}\right)^2 \tag{53}$$

The way to use equation (52) in equation (53) is to use the basic treatment that accompanies equation (34) above. For this purpose, we define the absolute temperature ratios α and β by

$$\alpha \equiv \frac{T_2}{T_1} \tag{54}$$

$$\beta \equiv \frac{T_2^+}{T_1^+} \tag{55}$$

Starting with the α case (where by definition α is constant in $\partial \dot{S}_h/\partial UA$), equation (54) is substituted into equation (53) along with equation (52) so that

$$-\left(\frac{\partial \dot{S}_h}{\partial UA}\right)_{\alpha,b} = \frac{(\alpha-1)^2}{\alpha n_{gm}^2}\left(\frac{T_{gm}}{T_{vgm}}\right)^2 \tag{56}$$

where $T_{gm}^2 = T_1 T_2$. The requirement from equation (53) that the heat capacity, $\dot{C}$, also be held fixed along with α and b when taking the derivative on the left-hand side of equation (56) is found to be unnecessary. The reason is that $\dot{C}$ is an extensive quantity and cannot, therefore, affect the right-hand side of equation (56), since the right-hand side consists exclusively of intensive quantities. In Appendix C of Evans and von Spakovsky (1988), it is shown that the following relation applies to both counterflow and parallel flow:

$$\left(\frac{T_{gm}}{T_{vgm}}\right)^2 = \frac{n_{gm}^2}{\left(n_H + \frac{\alpha-1}{\alpha}\right)(n_L + \alpha - 1)} \tag{57}$$

Substitution of equation (57) into equation (56) yields

$$-\left(\frac{\partial \dot{S}_h}{\partial UA}\right)_{\alpha,b} = \frac{(\alpha-1)^2}{\alpha\left(n_H + \frac{\alpha-1}{\alpha}\right)(n_L + \alpha - 1)} \tag{58}$$

As shown in Appendix C of Evans and von Spakovsky (1988),

$$n_H = \frac{e^{bn_{tu}} - 1}{b} \tag{59}$$

$$n_L = \frac{1 - e^{-bn_{tu}}}{b} \tag{60}$$

Substitution of equations (59) and (60) into equation (58) yields the following expression, which applies to all elementary heat exchangers for the α case:

$$-\left(\frac{\partial \dot{S}_h}{\partial UA}\right)_{\alpha,b} = \frac{(\alpha-1)^2}{\alpha\left[\frac{e^{bn_{tu}} - 1}{b} + \frac{(\alpha-1)}{\alpha}\right]\left[\frac{1 - e^{-bn_{tu}}}{b} + (\alpha - 1)\right]} \tag{61}$$

In equation (61), the quantity b may vary through the range $0 \le b \le 2$. This range includes all possible values of the heat capacity ratio r for both counterflow ($0 \le b \le 1$) and parallel flow ($1 \le b \le 2$). Figure 1 depicts the variations with n_{tu} of the negative change in the rate of entropy creation with respect to UA. These variations are given for b equal to 0, 1, and 2. The n_{tu} represent optimum values taken from Fig. 2.

Equation (61) may also be derived by differentiating separate integral expressions (for all of the various types of elementary heat exchangers) obtained via the effectiveness-n_{tu} method. These separate expressions agree completely with similar ones found by Bejan (1978) and others (Bejan, 1987; Evans et al., 1983; Tribus et al., 1956; von Spakovsky and Evans, 1984), so that equation (61) is in complete agreement with earlier Second Law results.

To illustrate the conformance of equation (61) with earlier results, we examine the α case's most familiar examples of $\partial \dot{S}_h / \partial UA$ for evaporator-condensers ($b = 1$, $\alpha = 1$, $\dot{C} = 0$), balanced counterflow ($b = 0$ or $r = 1$) and condensers or evaporators ($b = 1$ or $r = 0$). For each of these, equation (61) reduces to (using the limits $\alpha \to 1$, $\dot{C} \to \infty$ for equation (62) and $b \to 0$ for equation (63))

$$-\frac{\partial \dot{S}_h}{\partial UA} = \left(\frac{\Delta T}{T_v}\right)^2 \qquad \text{Evaporator-condensers} \tag{62}$$

$$-\left(\frac{\partial \dot{S}_h}{\partial UA}\right)_{\alpha} = \frac{(\alpha-1)^2}{\alpha\left(n_{tu} + \frac{\alpha-1}{\alpha}\right)(n_{tu} + \alpha - 1)} \qquad \text{Balanced counterflow} \tag{63}$$

$$-\left(\frac{\partial \dot{S}_h}{\partial UA}\right)_{\alpha} = \frac{(\alpha-1)^2 e^{n_{tu}}}{(\alpha e^{n_{tu}} - 1)^2} \qquad \text{Condensers, evaporators (admitting of crossflow)} \tag{64}$$

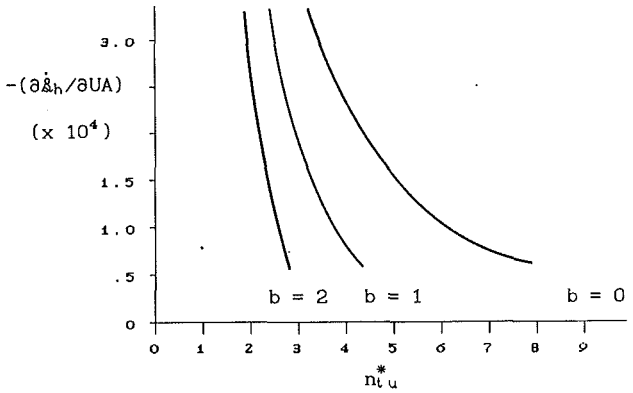

Fig. 1 Plot of $-(\partial \dot{S}_h/\partial UA)_{\alpha,b}$ versus n_{tu}^* for $b = 0, 1, 2$

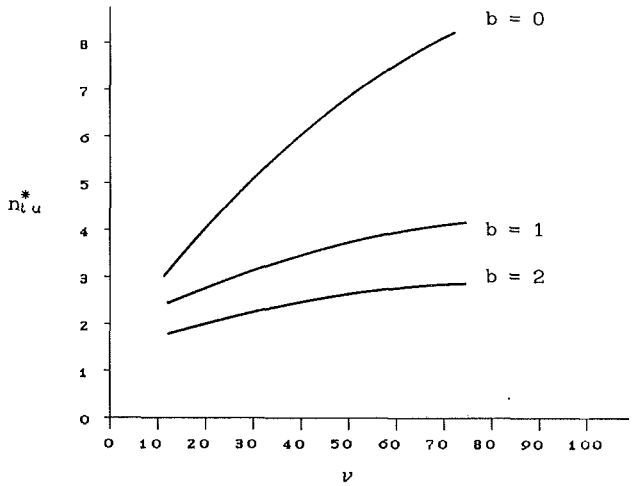

Fig. 2 Optimum number of transfer units, n_{tu}^* versus ν (equation 66)) for $b = 0, 1, 2$

Equation (64) is identical to an earlier effectiveness-n_{tu}, Second Law result (Evans et al., 1983), while equations (62) and (63) agree completely with approximate forms found in 1956 by Tribus (Tribus et al., 1956; Tribus and Evans, 1963). Equation (62) is readily verified via equation (53), since for this special case $T_{vgm} \to T_v$ and $\Delta T_{gm} \to \Delta T$.

The only other basic case is the β case [where the temperature ratio β instead of α is held constant in $(\partial \dot{S}_h/\partial UA)$]. A discussion of this case is not given here but is found from Evans and von Spakovsky (1988).

Some Results of a Preliminary Second Law Optimization for Heat Exchangers

Previous considerations of Second Law heat-exchanger optimization yield the following preliminary optimization criterion (Evans et al., 1983; von Spakovsky and Evans, 1984, 1988):

$$-\frac{\partial \dot{S}_h}{\partial UA} = \frac{\lambda_{UA}}{\lambda_h T_o} \tag{65}$$

Here, λ_h is the unit cost of essergy [or exergy, to a fair approximation (Evans and von Spakovsky, 1987a, 1987b; von Spakovsky and Evans, 1987)], while T_o is the background environment temperature [or "dead state" temperature (Evans and von Spakovsky, 1987a, 1987b)] and λ_{UA} is the marginal cost of the overall conductance UA (Evans et al., 1983; von Spakovsky and Evans, 1984, 1988; Evans and von Spakovsky, 1988). Substitution of equation (58) into equation (65) using a dimensionless modified cost parameter ν

$$\nu \equiv \left(\frac{\lambda_H T_o}{\lambda_{UA}}\right) \frac{(\alpha-1)^2}{\alpha} \tag{66}$$

results in an optimum number of transfer units, n_{tu}^* such that

$$n_{tu}^* = \frac{1}{b} \ln(1 + b n_H^*) \tag{67}$$

where n_H^* is a function of b, α, λ_H, λ_{UA}, and T_o. The details of this function are given on pp. 6 and 7 of Evans and von Spakovsky (1988). We simply repeat the results here as given in Fig. 2 above. This figure depicts the variations with ν of the optimum number of transfer units, n_{tu}^*. As with Fig. 1, b takes on the values of 0, 1, and 2, which include all possible values of the heat capacity ratio r for both counterflow ($0 \leq b \leq 1$) and parallel flow ($1 \leq b \leq 2$).

As before, the β case is not discussed here but is found from Evans and von Spakovsky (1988).

On the Representation of T_{II} and ΔT_{II} as Corrected Geometric Averages

The Second Law temperature T_{II} and temperature difference ΔT_{II} may be evaluated from equations (12) and (42), respectively, providing that there is a known relationship between the reference temperature difference ΔT_r [usually the pinch temperature difference (Linhoff and Hindmarsh, 1983)] and the local temperature difference ΔT. The key parameter in determining such relationships is the temperature difference change ratio b. This ratio is a local parameter (as pointed out in Appendix A) that applies to any point in any heat exchanger. For the basic treatment of elementary heat exchangers, the use of b yields the required relationship in a very simple form, namely equation (22). For more general cases, such as unmixed crossflow (Kays and London, 1958), this relationship is expected to be somewhat more complicated, but nevertheless tractable. Thus, it should always be possible at the very least to evaluate T_{II} and ΔT_{II} numerically if not analytically.

The results found for T_{II} and ΔT_{II} can then be compared to the basic elementary case (where for the α and β cases considered above, T_{II} and ΔT_{II} are geometric means) via the geometric mean correction factors T_{II}/T_{gm} and $\Delta T_{II}/\Delta T_{gm}$. These factors are expected to correlate closely with the familiar log-mean-temperature-difference correction factor $\Delta T_I/\Delta T_{lm}$ (Jacob, 1956; Kays and London, 1958; McAdams, 1954). This is so because for the basic elementary cases (the α and β cases) the relationship between T_{II}, ΔT_{II}, and ΔT_I [as expressed by equations (1), (61) and (49)] is easier to obtain by using the local transfer unit numbers n_H and n_L than by using the effectiveness-n_{tu} method (Jacob, 1956; Kays and London, 1958; McAdams, 1954). If this trend carries over into nonelementary cases as is anticipated, then, in general, a close correlation between the factors T_{II}/T_{gm}, $\Delta T_{II}/\Delta T_{gm}$, and $\Delta T_I/\Delta T_{lm}$ will exist.

Conclusions

Two fundamental principles of differential Second Law analysis have been set forth, namely the existence of a Second Law temperature T_{II} and a Second Law temperature difference ΔT_{II}. Both T_{II} and ΔT_{II} are always related via equation (1) to the change in entropy generation $\dot{S}_h$ caused by a change in overall conductance UA.

Methods for evaluating these two Second Law quantities [using equations (12) and (42) as discussed in the preceding sections] have been suggested. They will take the form of corrected geometric averages, since T_{II} and ΔT_{II} reduce to geometric averages for the basic treatment of elementary heat exchangers. As discussed previously, these corrected averages should correlate closely with the familiar log-mean temperature difference correction factor so widely used in heat exchanger analysis.

The importance of these two principles in both exergy and essergy analysis has also been illustrated by the results presented in Fig. 2 for the preliminary optimum design of elementary heat exchangers. These results give the optimum number of transfer units for all elementary flow arrangements (i.e., counterflow, parallel flow, and elementary crossflow) and for all possible values of the heat capacity rate ratios. The use of geometric mean correction factors is expected to extend this unified optimization treatment to heat exchangers in general.

References

Bejan, A., 1978, "A General Criterion for Rating Heat-Exchanger Performance," *International Journal of Heat and Mass Transfer*, Vol. 21, No. 5, pp. 655–658.

Bejan, A., 1987, "Review: The Thermodynamic Design of Heat and Mass Transfer Processes and Devices," *Journal of Heat and Fluid Flow*, Vol. 8, No. 4.

Callen, H. B., 1948, *Physical Review*, Vol. 73.

Courant, R., and Hilbert, D., 1962, *Methods of Mathematical Physics*, Wiley, New York.

DeGroot, S. R., and Mazur, P., 1962, *Nonequilibrium Thermodynamics*, 1st ed., North Holland Publishing Co., Amsterdam.

Evans, R. B., Hendrix, W. A., and Kadaba, P. V., 1983, "Essergetic Functional Analysis for Process Design and Synthesis," *Efficiency and Costing*, R. A. Gaggioli, ed., American Chemical Society.

Evans, R. B., and von Spakovsky, M. R., 1987a, "Essergy vs. Exergy: Four Critical Postulates Which Separate These Concepts," *Analysis and Design of Advanced Energy Systems: Fundamentals*, ASME AES-Vol. 3-1, New York.

Evans, R. B., and von Spakovsky, M. R., 1987b, "Essergy vs. Exergy: The Differences Between These Concepts," *Proc. of the Copimera XI, Montech 87 Congress*, Canada.

Evans, R. B., and von Spakovsky, M. R., 1988, "Two Principles of Differential Second Law Analysis for Heat Exchanger Design," *Approaches to the Design and Optimization of Thermal Systems*, ASME AES-Vol. 7, New York.

Hatsopoulos, G. N., and Keenan, J. H., 1960, "Thermo-dynamics of Thermoelectric Generators," *Direct Conversion of Heat to Electricity*, J. Kaye and J. A. Welsh, eds., Wiley, New York.

Jacob, M., 1956, *Heat Transfer*, Vol. 2, Wiley, New York.

James, E. T., and Scalapino, D., 1963, "Non-local Transport Theory," A talk given at the first meeting of the Society for Natural Philosophy, Baltimore, MD.

Kays, W. M., and London, F., 1958, *Compact Heat Exchangers*, McGraw-Hill, New York.

Linhoff, B., and Hindmarsh, E., 1983, "The Pinch Design Method for Heat Exchanger Networks," *Chemical Engineering Science*, Vol. 38, pp. 745–763.

McAdams, W. H., 1954, *Heat Transmission*, 3rd ed., McGraw-Hill, New York.

Prigogine, I., 1955, *Introduction to Thermodynamics of Irreversible Processes*, Charles C. Thomas, IL.

Tribus, M., et al., 1956, "Thermodynamic and Economic Considerations in the Preparation of Fresh Water From Sea Water," Report No. 56-16, UCLA.

Tribus, M., 1961, *Thermostatics and Thermodynamics*, Van Nostrand, New Jersey.

Tribus, M., and Evans, R. B., 1963, "The Thermo-Economics of Sea-Water Conversion," University of California, Dept. of Engineering, Los Angeles, Report No. 62-53.

von Spakovsky, M. R., and Evans, R. B., 1984, "Detailed Second Law Design of Components in Complex Thermal Systems," *Second Law Aspects of Thermal Design*, ASME HTD-Vol. 33, New York.

von Spakovsky, M. R., and Evans, R. B., 1987, "The Optimal Design and Performance of Thermal Systems and Their Components," *Analysis and Design of Advanced Energy Systems: Fundamentals*, ASME AES-Vol. 3-1, New York.

von Spakovsky, M. R., and Evans, R. B., 1988, "The Optimal Design and Performance of Components in Thermal System," *Second-Law Analysis in Heat/Mass Transfer and Energy Conversion*, ASME AES-Vol. 6/HTD-Vol. 97, New York.

APPENDIX A

On the Definition of Elementary Heat Exchangers

Heat exchangers, in general, are defined by the requirement that an overall heat transfer coefficient U must be determined in a manner consistent with equations (2)–(10). Heat exchangers, thus defined, are considered "elementary" if Requirements 1 and 2 above are obeyed. Requirement 1 is

$$\Delta T_I = \Delta T_{lm} \tag{A1}$$

where

$$\Delta T_1 \equiv \frac{\dot{Q}}{UA} \tag{A2}$$

$$\Delta T_{lm} \equiv \frac{\Delta T_H - \Delta T_L}{\ln \dfrac{\Delta T_H}{\Delta T_L}} \tag{A3}$$

[equations (14) and (37) in the text]. Since $\dot{Q} = \int d\dot{Q}' = \int (\Delta T) U_l dA'$ from equation (7) while from equation (6) $UA = \int U_l dA'$, one may expand equation (A2) into the following alternate form:

$$\Delta T_1 \equiv \frac{\int (\Delta T) U_l dA' \quad \int d\dot{Q}'}{\int U_l dA' = \int \dfrac{d\dot{Q}'}{\Delta T}} \tag{A4}$$

A similar expansion of the definition of ΔT_{lm} is

$$\Delta T_{lm} \equiv \frac{\int \Delta T d\ln \Delta T \quad \int d\Delta T}{\int d\ln \Delta T = \int \dfrac{d\Delta T}{\Delta T}} \tag{A5}$$

Equation (A1) thereby yields

$$\frac{\int d\dot{Q}' \quad \int d\Delta T}{\int \dfrac{d\dot{Q}'}{\Delta T} = \int \dfrac{d\Delta T}{\Delta T}} \tag{A6}$$

In order for equation (A6) to apply to all limits of the integrals, the following relation must be obeyed:

$$d\dot{Q}' = K d\Delta T \tag{A7}$$

where K is a constant. Equation (A7) is all that can be gleaned from Requirement 1.

Requirement 2 states that the quantity $b \equiv |d\Delta T/dT|$ has a constant value for all temperatures T of the mass with the lower effective heat capacity rate, so that one may write

$$\frac{\int d\Delta T \quad b \int dT \quad \int dT}{\int \dfrac{d\Delta T}{\Delta T} = b \int \dfrac{dT}{\Delta T} = \int \dfrac{dT}{\Delta T}} \tag{A8}$$

Requirement 2 also allows one to define the lower effective heat capacity rate $\dot{C}$ by

$$\dot{C} \equiv \left| \frac{d\dot{Q}'}{dT} \right| \tag{A9}$$

with the understanding that $d\dot{Q}'$ applies to *all* of the mass (of the lower effective heat capacity), which is at temperature T. Equation (A8) becomes

$$\frac{\int d\Delta T \quad \int \dfrac{d\dot{Q}'}{\dot{C}}}{\int \dfrac{d\Delta T}{\Delta T} = \int \dfrac{d\dot{Q}'}{\dot{C}\Delta T}} \tag{A10}$$

Comparison of equations (A10) and (A6) requires that $\dot{C}$, as well as b, be a constant for all temperatures T. Thus, one may integrate either equations (A9) or (A16) below to obtain expressions such as

$$\dot{C}(T_r - T) = \dot{Q}_r' - \dot{Q}' \tag{A11}$$

where the subscript "r" denotes a reference point. It also follows that the constant K in equation (A7) is

$$K = \frac{\dot{C}}{b} \tag{A12}$$

It should be noted in passing that the quantity b is, in general, a local quantity similar to the local overall heat transfer coefficient U_l defined by equation (7). The definition of $\dot{C}$ in equation (A9) is only valid if Requirement 2 holds.

Now we note that for counterflow,

$$|d(\Delta T)| = |dT| - |dT^+| \tag{A13}$$

so that

$$b = 1 - \left| \frac{dT^+}{dT} \right| = 1 - r \tag{A14}$$

where

$$r \equiv \frac{\dot{C}}{\dot{C}^+} \tag{A15}$$

and

$$\dot{C}^+ \equiv \left| \frac{d\dot{Q}'}{dT^+} \right| \tag{A16}$$

For parallel flow

$$|d\Delta T| = |dT| + |dT^+| \tag{A17}$$

whence

$$b = 1 + \left| \frac{dT^+}{dT^-} \right| = 1 + r \tag{A18}$$

It is of interest to observe that the local overall heat transfer coefficient U_l is *not* necessarily constant with respect to the temperature T in the elementary model. This follows from equations (A7) and (A12), which show that the constancy of $\dot{C}$ and b with respect to T is sufficient. This implies the constancy of $\dot{C}^+$ and nothing more. Similarly, the specific heats c_p and c_p^+ need not be constant in the elementary model, since constant c_p does not imply constant $\dot{C}$ because $\dot{m}c_p$ and $\dot{C}$ differ in accordance with the offsetting temperature changes due to both head loss and fluid expansion in compressible flow.

To derive equation (22), one integrates over the key parameter b (equation (15)) as follows:

$$|d\Delta T| = b|dT| \tag{A19}$$

to obtain

$$\Delta T_r - \Delta T = \pm b(T_r - T) \tag{A19a}$$

or in view of equation (A11),

$$\Delta T_r - \Delta T = \pm \frac{b}{\dot{C}} (\dot{Q}_r' - \dot{Q}') \tag{A20}$$

Now for the basic treatment considered in equation (22)—and explained following equation (23)—the quantities b, $\dot{C}$, and $\dot{Q}_r'$ are all taken to be constant with respect to variations in ΔT_r. This constancy of $\dot{Q}_r'$ is consistent with

$$\dot{C}_c(T_{cr} - T_c) = \dot{Q}_r' - \dot{Q}' \tag{A21}$$

where the temperature T_c is discussed following equation (23). Since $\dot{Q}_r'$ is constant via the Liebnitz rule (in equation (23)), the right-hand side of equation (A20) is a constant. Thus, differentiation of equation (A20) yields

$$d(\Delta T_r) = d(\Delta T) \tag{A22}$$

or noting that items such as b, $\dot{C}$, $\dot{Q}$, and $\dot{Q}_r'$ are constant, equation (A22) in partial derivative form is

$$[\partial \Delta T_r]_{\underline{x}, \dot{Q}, \dot{Q}'} = [\partial \Delta T]_{\underline{x}, \dot{Q}, \dot{Q}'} \tag{A23}$$

where $\underline{x}$ denotes the set T_{c1}, T_{c2}, $\dot{C}$, b.

APPENDIX B

Some Details Concerning ΔT_{II}

The Second Law temperature difference ΔT_{II}, given by equation (40), represents a generalization of the elementary case, equation (39). This elementary result depends upon the following relation, which is needed for equation (38) to follow from equation (36):

$$\frac{\partial}{\partial \Delta T_r}\left(\frac{1}{\Delta T_I}\right) = -\frac{1}{\Delta T_L \Delta T_H} \tag{B1}$$

First note from equations (A21) and (A22) that one may write for this case that

$$\partial \Delta T_r = \partial \Delta T = \partial \Delta T_H = \partial \Delta T_L \tag{B2}$$

so that

$$\frac{\partial \Delta T_H}{\partial \Delta T_r} = \frac{\partial \Delta T_L}{\partial \Delta T_r} = 1 \tag{B3}$$

Substituting equation (37) into the left-hand side of equation (B1) yields, therefore,

$$\frac{\partial}{\partial \Delta T_r}\left(\frac{\ln \Delta T_H - \ln \Delta T_L}{\Delta T_H - \Delta T_L}\right) = \frac{\dfrac{1}{\Delta T_H} - \dfrac{1}{\Delta T_L}}{\Delta T_H - \Delta T_L} = -\frac{1}{\Delta T_L \Delta T_H} \tag{B4}$$

which is in agreement with equation (B1).

Generalization of this elementary result requires a general consideration of $\partial UA/\partial \Delta T_r$ as follows:

$$\frac{\partial UA}{\partial \Delta T_r} = \frac{\partial}{\partial \Delta T_r}\int_0^A U_l dA' = \frac{\partial}{\partial \Delta T_r}\int_0^{\dot{Q}} \frac{d\dot{Q}'}{\Delta T} \tag{B5}$$

Now, via the Leibnitz rule (in a manner analogous to equation (12))

$$\frac{\partial UA}{\partial \Delta T_r} = \int_0^{\dot{Q}} \left[\frac{\partial}{\partial \Delta T_r}\left(\frac{1}{\Delta T}\right)\right]_{\dot{Q}'} d\dot{Q}' + \left(\frac{1}{\Delta T_{\dot{Q}}}\right)\frac{\partial \dot{Q}}{\partial \Delta T_r} \tag{B6}$$

Equation (B6) is identical to equation (12) when the notation $\underset{\sim}{x}, y$ is appended to the partial derivatives. It is of interest to observe how equation (B6) reduces for the basic treatment of elementary heat exchangers to the result expressed by equation (B4). First note that if equation (22) is introduced and $\dot{Q}$ held constant, then equation (B6) reduces to

$$\left(\frac{\partial UA}{\partial \Delta T_r}\right)_{\dot{Q}} = \int_0^{\dot{Q}} \frac{d}{d\Delta T}\left(\frac{1}{\Delta T}\right) d\dot{Q}' = -\int_0^{\dot{Q}} \frac{d\dot{Q}'}{\Delta T^2} \tag{B7}$$

Introducing equations (15) and (16) yields

$$\left(\frac{\partial UA}{\partial \Delta T_r}\right)_{\dot{Q}} = -\frac{\dot{C}}{b}\int_{\Delta T_L}^{\Delta T_H} \frac{d\Delta T}{\Delta T^2}$$

$$= \frac{\dot{C}}{b}\left(\frac{1}{\Delta T_H} - \frac{1}{\Delta T_L}\right) = \frac{\dot{C}(\Delta T_L - \Delta T_H)}{b \Delta T_L \Delta T_H} \tag{B8}$$

and since, for elementary heat exchangers,

$$b = \frac{\Delta T_H - \Delta T_L}{|T_2 - T_1|} \tag{B9}$$

one obtains

$$\left(\frac{\partial UA}{\partial \Delta T_r}\right)_{\dot{Q}} = -\frac{\dot{C}|T_2 - T_1|}{\Delta T_L \Delta T_H} = -\frac{\dot{Q}}{\Delta T_L \Delta T_H} \tag{B10}$$

in agreement with equations (38) and (B4).

Maximization of Exergy Gain in High Temperature Solar Thermal Receivers by Choice of Pipe Radius

P. Bannister
Energy Research Centre,
Research School of Physical Sciences,
Australian National University,
Canberra, Australia

The problem of optimizing the radius of boiler tubes in a radiation-dominated environment such as a solar thermal power receiver is examined. The trade-off between heat transfer and pumping power is investigated, resulting in an explicit expression for the radius that maximizes the net exergy gain under turbulent flow conditions. The effect of the pumping power being generated on site is included, thus making the result particularly applicable to the design of stand-alone power systems. Examples using typical design values for small parabolic dish solar thermal collectors using water and steam as the working fluid are given to illustrate the characteristics of the problem.

1 Introduction

One of the major losses in energy quality in Rankine cycle solar thermal power generation systems occurs in the receiver, where high-quality solar radiation is absorbed and converted to lower quality heat in the energy transport fluid. Although this degradation is to a large extent unavoidable, it is possible to improve the performance by careful design. In a receiver for a parabolic dish collector, which normally consists of a cavity formed from a helical winding of fluid-carrying tubing (Kaneff, 1987a, 1987b; Rogers et al., 1988), the general geometry is normally predetermined by thermal and radiation capture constraints, leaving only the details of the tubing to be varied to obtain maximum exergy gain. This paper sets out a method to aid in the choice of tubing by calculating the tube radius that maximizes the net exergy gain in the receiver.

A typical Rankine solar thermal power system consists of high-pressure water/steam loop with the heat being concentrated onto a receiver from a mirror. The heat flux in the receiver cavity, often in the region of 150 kWm^{-2} (Mayer, 1988) causes high exterior tube wall temperatures, increasing re-radiation and lowering heat transfer to the fluid. This effect can be reduced by decreasing the tube radius, thus increasing the Nusselt number of the flow. However, this reduction of radius will also increase the pumping power requirements of the flow, thereby increasing the parasitic power requirements of the plant. Clearly, there must be an optimal radius whereby the total exergy gained by the fluid in the receiver, less the exergy used in pumping, is maximized. In a system where this exergy is converted into work at an approximately constant efficiency this corresponds to a maximization of the net work output of the plant.

This problem was addressed by Bejan (1979, 1982), who derived an expression for the Reynolds number corresponding to the minimum possible entropy generation in internal forced convection problems. However, his analysis makes the assumption that the heat per unit length received by the tube is constant with respect to variation in Re at constant massflow, which limits the applicability of his expression in practical situations. In the analysis that follows, it is the incident heat flux per unit area that is held constant and the radius that is optimized. This is a close representation of the practical problem. Under these conditions Bejan's analysis and results cannot be applied because the heat per unit length is a function of the radius of the tubing through the effects of capture area and of re-radiation.

Contributed by the Heat Transfer Division for publication in the JOURNAL OF HEAT TRANSFER. Manuscript received by the Heat Transfer Division September 18, 1989; revision received July 17, 1990. Keywords: Forced Convection, Solar Energy, Thermodynamics and Second Law.

2 The Optimization Method

The system under examination consists of three major components: the feedwater pump, the receiver and the engine/turbine. The feedwater pump provides the necessary pressure to maintain the desired flow through the receiver and into the engine. This system is investigated here by examining the effect of changing the radius of a small isothermal tube segment (e.g., a single winding in a helically wound receiver) on the overall system performance. The tube in the segment has radius r and is subject to a heat flux Q'' incident on one side only of the tube wall, as is normal in a cavity receiver. In order to simplify the analysis, the second law or exergetic efficiency (i.e., ratio of work output to exergy input) of the feedwater pump and of the combined steam transport system plus engine/turbine are assumed to be approximately constant. The optimization of the net work output of the plant can then be performed by consideration of the receiver output exergy alone. The assumptions are reasonable because of the smallness of the effect of varying the tube size on the major system variables, and the comparatively insensitive nature of the second law efficiencies to such variations.

The exergy gain of the system associated with a small isothermal tube segment is

$$\delta E_{x,\text{useful}} = \delta E_{x,\text{fluid}} + \delta E_{x,\text{diffuse}} - \delta E_{x,\text{pump}} \tag{1}$$

where $\delta E_{x,\text{fluid}}$ is the exergy gain of the fluid in the tube segment, $\delta E_{x,\text{diffuse}}$ is the exergy gain in the rest of the receiver associated with diffuse reflection and emission of radiation from the tube segment, and $\delta E_{x,\text{pump}}$ is the exergy required to provide the pumping power associated with the pressure drop through the segment. These terms are now examined separately.

The energy balance for the exterior surface of the tube is

$$q_f = E_{\text{absorbed}} - E_{\text{emitted}} - E_{\text{convection}} \tag{2}$$

In a high-temperature cavity, the convection term can be ignored as it is small in comparison to the emitted radiation within the cavity. The wall is subject to an incident radiant flux Q'', being the incident radiation per unit cavity wall area, i.e., per unit cross-sectional area of the tube. Allowing for

reflections (assumed to be diffuse), the net heat flux per unit flat cavity wall area is

$$q_f'' = \alpha_1 Q'' - \epsilon_1 \sigma T_w^4 \tag{3}$$

where

$$\alpha_1 = \frac{\alpha}{1-(1-\alpha)F} \tag{4}$$

$$\epsilon_1 = \frac{\pi\epsilon}{2}\frac{1-F}{1-(1-\alpha)F} \tag{5}$$

and F is the radiation exchange factor of the tube segment with itself. These figures assume that the irradiated surface area of the tube is equal to that of a similar length of straight tube. This assumption is justified as long as the cavity radius is significantly larger than the tube radius. The exergy gain of the fluid in the tube segment per unit cavity wall area is therefore

$$\delta E_{x,\text{fluid}}'' = (\alpha_1 Q'' - \epsilon_1 \sigma T_w^4)\left(1-\frac{T_0}{T_f}\right) \tag{6}$$

The precise details of the exergy gain term $\delta E_{x,\text{diffuse}}$ are of course dependent on cavity geometry, but it is desirable to use an approximate value representative of a wide range of cavity shapes. This is achieved by representing the exergy gain in the fluid throughout the cavity resulting from the radiative heat flow q_{diffuse} by ζq_{diffuse}, where

$$\zeta = (1-F_{\text{exit}})\frac{e_x(T_h)-e_x(T_c)}{h(T_h)-h(T_c)} \tag{7}$$

$$= (1-F_{\text{exit}})\varepsilon_{\text{cav}} \tag{8}$$

This is the exergetic efficiency ε_{cav} of heating a body of fluid through the same temperature range (from T_c to T_h) as the cavity, modified by the assumed effective cavity absorptivity $(1-F_{\text{exit}})$ where F_{exit} is the radiation exchange factor of the tube segment with the cavity aperture. Although this is only a coarse approximation to the true exergy gain from diffuse radiation to the cavity, this term is of secondary importance in determining the final value of the optimum radius, as is discussed later.

The terms $\delta E_{x,\text{fluid}}$ and $\delta E_{x,\text{diffuse}}$ can be combined to give a gross fluid gain per unit flat cavity wall area of

$$\delta E_{x,\text{fluid}}'' + \delta E_{x,\text{diffuse}}'' = (\alpha_{\text{eff}} Q'' - \epsilon_{\text{eff}}\sigma T_w^4)\left(1-\frac{T_0}{T_f}\right) \tag{9}$$

where

$$\alpha_{\text{eff}} = \alpha_1 + \zeta\frac{1-\alpha_1}{1-T_0/T_f} \tag{10}$$

$$\epsilon_{\text{eff}} = \epsilon_1\left(1-\frac{\zeta}{1-T_0/T_f}\right) \tag{11}$$

In order to calculate $\delta E_{x,\text{pump}}$, it is useful to introduce a characteristic radius, r_c, and an associated dimensionless radius ρ such that

$$\rho = \frac{r}{r_c} = \frac{1}{\text{Re}} \tag{12}$$

The exergy required by the pump per unit cavity wall area can be calculated for $r = r_c$ from the D'Arcy-Weisbach equation

$$\delta E_{x,\text{pump}}''(r_c) = \frac{f(r_c)}{4}\frac{\dot{m}^3}{\xi\varepsilon_p\varepsilon_g\pi^3\vartheta\vartheta r_c^6} \tag{13}$$

where ε_g and ε_p are the second law efficiencies of the engine/turbine corrected for thermal losses in the transport system, and of the pump, respectively. The corresponding expression for other radii is

$$\delta E_{x,\text{pump}}''(r) = \delta E_{x,\text{pump}}''(r_c)\frac{f(r)}{f(r_c)}\frac{r_c^6}{r^6} \tag{14}$$

The friction factor f can be approximated by expressions of the form $f = A\text{Re}^{-\gamma}$, e.g., $f = 0.184\text{Re}^{-0.2}$ for $\text{Re} > 2 \times 10^4$ or $f = 0.316\text{Re}^{-0.25}$ for $1 \times 10^4 < \text{Re} < 2 \times 10^4$ (Ozisik, 1985). This leads to the following simple expression for the net useful exergy gain per unit flat cavity wall area:

$$\delta E_{x,\text{useful}}'' = (\alpha_{\text{eff}} Q'' - \epsilon_{\text{eff}}\sigma T_w^4)\left(1-\frac{T_0}{T_f}\right) - \delta E_{x,\text{pump}}''(r_c)\rho^{\gamma-6} \tag{15}$$

The optimum radius can now be found through taking the ρ derivative of equation (15). This requires the calculation of the ρ derivative of T_w as a function of ρ, using the ρ derivative of the expression $T_w = T_f + \Delta T$, where, for $t/r < 0.5$

$$\Delta T \approx q_f''\xi\left(\frac{1}{h}+\frac{t}{k_w}\right) \tag{16}$$

The heat transfer coefficient h is calculated from the Dittus-Boelter relation $\text{Nu} = 0.023\text{Re}^{0.8}\text{Pr}^{0.4}$. This allows the derivative $\delta T_w/\delta\rho$ to be found in terms of ρ and the ρ derivative of q_f''. Similarly, this derivative of q_f'' can be found in terms of the ρ derivative of T_w from the derivative of equation (3). These expressions can be solved to give

$$\frac{\delta T_w}{\delta\rho} = 1.8\frac{\alpha_1 Q''\xi\rho^{0.8}}{h_c}\frac{1-\chi}{1+\frac{4\tau}{1+\tau}\frac{\chi}{1-\chi}} \tag{17}$$

where h_c is the heat transfer coefficient obtained by the substitution of $r = r_c$ in the Dittus-Boelter relation, τ is the ratio $\Delta T/T_f$, and χ is the ratio of the emitted power to incident power at the tube segment, calculated from equation (3). The optimum radius can then be shown to be

Nomenclature

E_x = exergetic power, W
e_x = specific exergy, Jkg^{-1}
$f(r)$ = fluid friction factor at internal radius r
F = radiation exchange factor
h = heat transfer coefficient, $\text{Wm}^{-2}\text{K}^{-1}$
$h(T)$ = specific enthalpy, Jkg^{-1}
k = conductivity, W(Km)^{-1}
$\dot{m}$ = mass flow, kgs^{-1}
Nu = Nusselt number
Pr = Prandtl number
q = heat flow, W
Q = incident radiation
r = internal radius of pipe, m
Re = Reynolds number
t = thickness of pipe wall, m
T = temperature, K
W = mechanical power, W
α = absorbtivity of pipe surface
β = ratio $= t/r$
ϵ = emissivity of pipe surface
ε_p = feedwater pump exergetic efficiency
ε_g = exergetic efficiency of steam to work conversion
μ = viscosity, $\text{kgm}^{-1}\text{s}^{-1}$
ξ = area conversion factor $= 2(1+\beta)/\pi$
ρ = dimensionless radius $= r/r_c$
ϑ = density, kgm^{-3}
σ = Stefan-Boltzmann constant
τ = ratio $= \Delta T/T_f$
χ = ratio $= E_{\text{emitted}}/E_{\text{incident}}$

Subscripts and Superscripts

c = characteristic
eff = effective
f = fluid
opt = optimal
w = pipe wall
0 = environment
$''$ = per unit cavity wall area

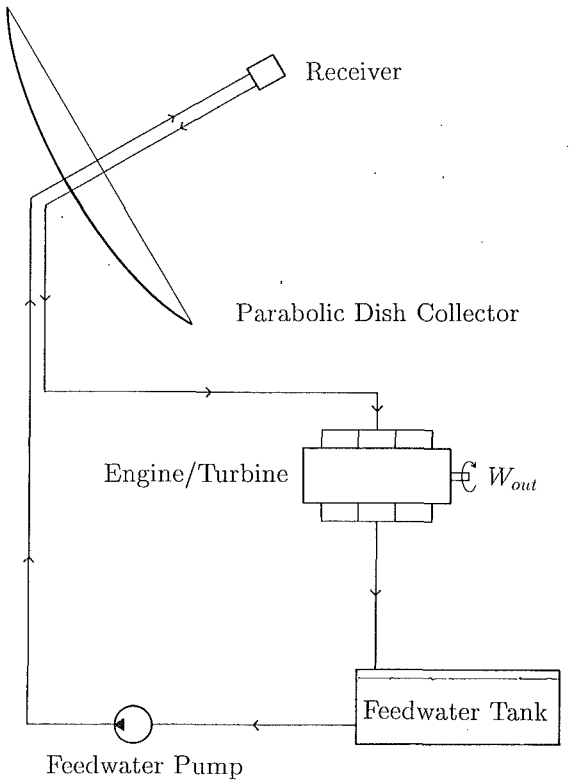

Fig. 1 A Rankine cycle solar thermal power system typical of that considered in this paper; the optimization is performed by considering the effect on the overall system performance of varying the radius of a small isothermal tube segment in the receiver

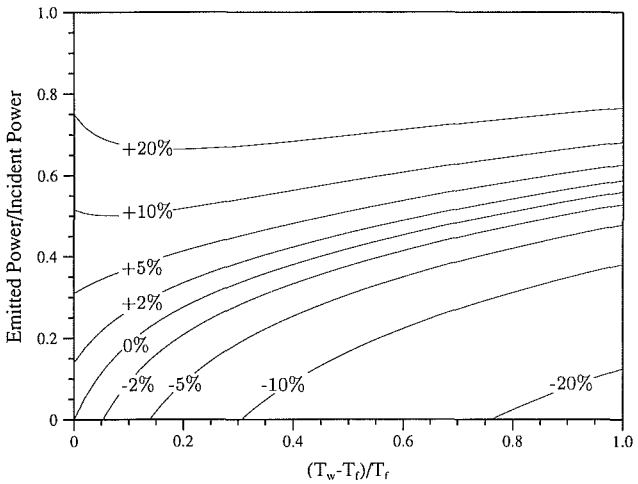

Fig. 2 The effect of the assumption $C_f = 1$ on the accuracy of the optimum radius expression in terms of the ratios τ and χ

$$\rho_{\text{opt}}^{7.8-\gamma} = \frac{(6-\gamma)E''_{x,\text{pump}}(r_c)h_c}{7.2\alpha_1\epsilon_{\text{eff}}\xi C_f Q'' \sigma T_f^3(1-T_0/T_f)} \tag{18}$$

The multiplier C_f is a correction factor, given by

$$C_f = (1+\tau)^3 \frac{1-\chi}{1+\dfrac{4\tau}{1+\tau}\dfrac{\chi}{1-\chi}} \tag{19}$$

As discussed below, the factor C_f can be set to unity in almost all situations, thus making the expressions fully explicit.

3 Discussion

The correction factor C_f appearing in equation (18) contains all the significant mathematical approximations made in the derivation. It can be seen in Fig. 2 that the accuracy of the expression is assured whenever the incident power dominates the emitted power and the tube wall temperature is close to that of the fluid. Normally the choice of tube radii available commercially will mean that values that are accurate to within 10 percent will be quite acceptable. The accuracy of a practical

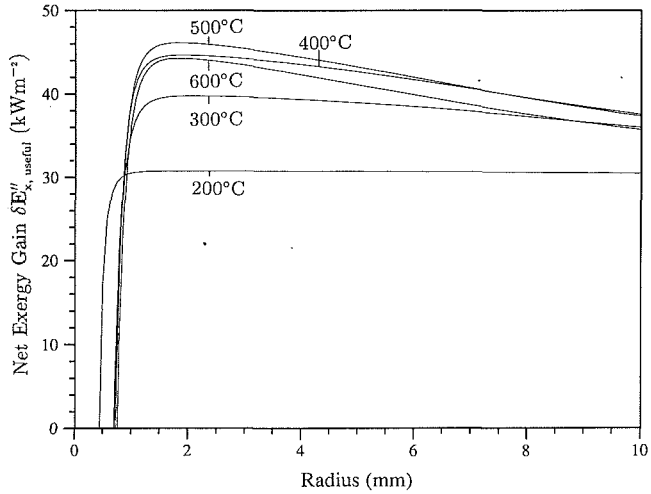

Fig. 3 Net exergy uptake per unit cavity wall area as a function of pipe radius, for different fluid temperatures at a massflow of 5 gs^{-1}

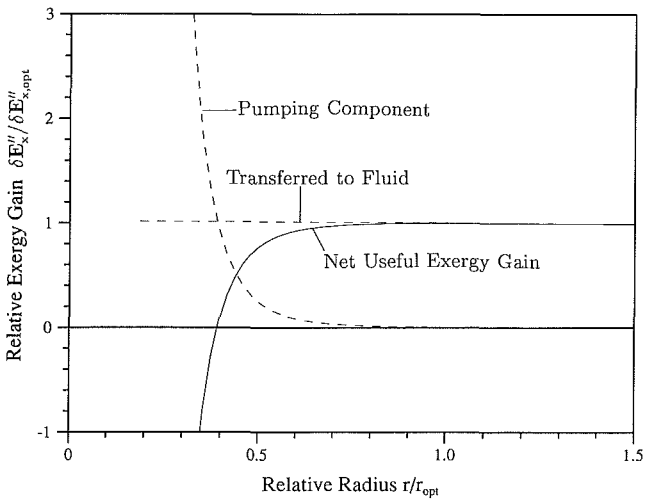

Fig. 4 The breakdown of the net exergy gain function for a massflow of 5 gs^{-1} at 450°C

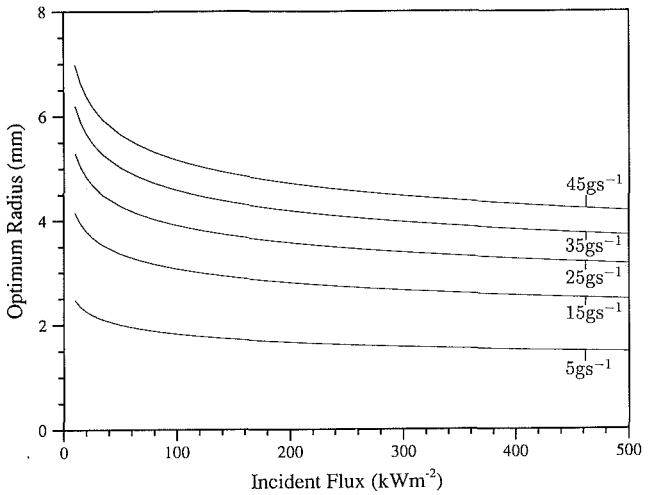

Fig. 5 Values of the optimum radius in a cavity with $T_h = 600$°C under typical conditions

calculation can easily be verified from Fig. 2 by evaluating η and τ for the calculated radius.

The presence of the high-valued exponent $7.8-\gamma$ in equation (18) greatly reduces the effects of the physical approximations made in the analysis. This includes the approximation of the term $\delta E_{x,\text{diffuse}}$ and the assumption of constant second-law efficiencies for the feedwater pump and for the combined engine/turbine and steam transport system. The exclusion of fluid heating through friction is justifiable on this ground as well, but is also shown in Fig. 4 to be insignificant at the calculated optimum radius. As it is the purpose of this paper to produce a formula that can be used as a general guide to choosing the correct size of tubing, such errors as do result from these approximations are unimportant given the comparatively sparse choices of internal tube radii available commercially.

Figures 3, 4, and 5 illustrate the characteristics of the problem, using values typical of those applicable to a small paraboloidal dish solar thermal power plant using water and steam as the working fluid. Unless otherwise indicated the values used are $\alpha=0.9$, $\epsilon=0.9$, $T_h=500°\text{C}$, $T_c=40°\text{C}$, $p=4$ MPa, $\beta=0.2$, $F=0.2$, $F_{ex}=0.2$, $\mathcal{E}=0.8$, $\mathcal{E}_g=0.36$, and $Q''=100$ kWm^{-2}. The general shape of the net exergy gain function is illustrated in Fig. 3. It can be seen that for radii greater than the optimum value the rate of decrease in exergy uptake is always considerably less than that for radii below the optimum, thus indicating that when choosing from commercial stock the radius should be the closest value above that calculated. The figure also highlights the low radiation emission in the case of lower fluid temperatures, leading to unnaturally flat maxima. The inclusion of convection in the calculation would rectify this but would produce little change in the value for optimum radius, as this is primarily determined by the pumping power as shown in Fig. 4. However, there is a possibility of laminar flow occurring in this region, which compromises the accuracy of the formulation. Typical values of the optimum radius for conditions representative of those in parabolic dish receivers are illustrated in Fig. 5.

The methodology for a practical calculation is to calculate the optimum radius using equation (18), evaluate Re to ensure that the flow is indeed turbulent, and finally, to check the accuracy of the radius value by use of Fig. 2. For a full optimization of a receiver design, this process can be repeated for different parts of a receiver, followed by some iteration to adjust for consequent changes in total flux and (in the case of a temperature limited system) mass flow conditions.

4 Conclusion

The performance of the receiver of a solar thermal power generation plant is crucial to the efficiency of the overall system. Normally, the general shape of the receiver is determined by considerations of radiation capture and thermal loss minimization, leaving the tube radius as the only remaining optimizable variable.

In this paper this optimum radius has been derived. The method involved the maximization of the net exergy gain by the fluid in a radiation-dominated environment, taking the exergy requirement of pumping into account. The maximization was performed by considering the effect of varying the tube radius of a small part of the receiver and calculating the resultant change in overall receiver performance. This value has been presented as an explicit function of known parameters, and so is particularly suitable for use in design calculations for receivers of Rankine cycle solar thermal power plants. The function contains an approximation that is valid to engineering accuracy under normal conditions, and that can be checked by use of Fig. 2. Typical results for a small water and steam based system have been presented.

Acknowledgments

The author wishes to thank Professor S. Kaneff, Mr. I. Mayer, and Mr. R. Whelan for their encouragement during the course of this study, and Mr. D. New for his drafting assistance.

References

Bejan, A., 1979, "A Study of Entropy Generation in Fundamental Convective Heat Transfer," ASME JOURNAL OF HEAT TRANSFER, Vol. 101, pp. 718–725.

Bejan, A., 1982, *Entropy Generation Through Heat and Fluid Flow,* Wiley, New York, Chap. 5.

Kaneff, S., 1987a, "The White Cliffs Solar Thermal Electric Power Systems," *Proc. ASME-JSME-JSES Solar Energy Conference,* Honolulu, HI, pp. 815–820.

Kaneff, S., 1987b, "The White Cliffs Project Overview for the Period 1979–87," Department of Engineering Physics Publication EP-RR-47, Research School of Physical Sciences, The Australian National University, Canberra, Australia.

Mayer, I., 1988, "Increasing the Service Life of High Temperature Steam Generating Solar Thermal Receivers," *Proc. Conf. Australian & New Zealand Solar Energy Society (Solar '88),* Melbourne, pp. 14.1–14.10.

Ozisik, M. N., 1985, *Heat Transfer—A Basic Approach,* McGraw-Hill, New York, Chap. 7.

Rogers, W. E., Burton, D. N., Bilodeau, E. A., and Inall, E. K., 1988, "Design of a Solar/Oil Hybrid Plant for the Small Community Solar Experiment (SCSE No. 2) at Molokai, Hawaii," *Proc. Tenth Annual ASME Solar Energy Conf.,* Denver, CO, pp. 265–270.

Optimal Design of Crossflow Heat Exchangers

E. Van den Bulck
Department of Mechanical Engineering,
Katholieke Universiteit Leuven,
Heverlee, Belgium
Mem. ASME

The design of plate-fin and tube-fin crossflow heat exchangers is discussed. The transfer surface area of crossflow heat exchangers is used ineffectively because of the nonuniform distribution of the heat transfer across the volume of the exchanger. The optimal distribution of the transfer surface area for maximum heat exchanger effectiveness and constant total surface area is determined. It is found that a Dirac delta distribution of the transfer surface aligned along the diagonal of the crossflow exchanger gives the best performance; equal to that of a counterflow device. Design guidelines for optimal area allocation within crossflow heat exchangers are established. Compared to conventional designs, designs following these guidelines may lead to either a higher exchanger effectiveness for equal pressure drops and surface area, reduced pressure drops for equal exchanger effectiveness, or reduced weight and a near cubic form of the exchanger core for equal pressure drops and effectiveness.

1 Introduction

Air-to-air heat exchangers are becoming more popular in HVAC applications, in process heat recovery and drying applications in the paper, food, steel and chemical industries, and in regenerative gas turbine systems. These exchangers can be configured as heat-pipe heat exchangers, rotating regenerators, plate recuperators, and plate-fin and tube-fin type heat exchangers (Reay, 1979). Counterflow in rotary heat exchangers and crossflow in recuperators are the most popular duct arrangements because of simplified header designs.

Crossflow heat exchangers show inferior performance when compared to rotary heat exchangers. For equal overall heat transfer conductance and equal capacitance rates of the fluid streams, the effectiveness of the crossflow heat exchanger is consistently lower than the effectiveness of a well-operated rotary heat exchanger. Although the latter type heat exchanger is operated with counterflow of the fluid streams, the modeling equations for both types of exchangers are similar and, for infinite transfer coefficients, the performance of both exchangers is the same, neglecting flow leaks and carry-over effects in the rotary exchanger. This reduced performance of the cross-flow recuperator must result from the fact that the heat transfer surface within the exchanger is not used effectively. This effect thus points towards a nonoptimal design of conventional crossflow heat exchangers.

The design procedures for compact crossflow heat exchangers are well established (Shah, 1978, 1981, 1988). Sizing of a heat exchanger involves computation of the core dimensions to yield a prescribed heat exchanger efficiency and independently prescribed pressure drops for both fluid streams. The dimensions of the heat exchanger are determined by the geometric characteristics of the surfaces selected individually for both fluid sides. Optimization objectives include minimization of the total heat transfer area, minimization of the frontal area, or minimization of the exchanger volume.

These existing rating and sizing procedures use the results obtained from the theoretical and elaborate experimental work on compact heat exchanger surfaces (Kays and London, 1984) to arrive at a design with a uniform distribution of the heat transfer surface area. Optimization theories for crossflow heat exchangers have focused mainly on heat transfer enhancement by using well-designed extended surfaces (Shah et al., 1978; Shah, 1978). Kröger (1983) presents such an optimization procedure for finned-tube crossflow heat exchangers. Variables to be optimized are fin thickness, fin height, and fin pitch. A recent market survey of commercial gas-to-gas heat exchangers (Raimbault et al., 1981) shows that these devices, as well as prototypes of new designs (Shah, 1982; Grehier et al., 1984), follow the same guidelines. The conventional design objectives do not include the use of nonuniformly distributed transfer surface area.

Design procedures for heat exchanger networks generally focus on the optimal area allocation among the different heat exchangers (Ait-Ali and Wilde, 1980). The optimal distribution of the transfer area depends upon the variation of heating duties and operating temperatures with the different devices. However, conditions such as nonuniformly distributed heat transfer and temperature differences can also occur across the volume of single heat exchangers. Thus, the performance of exchangers such as these, for example crossflow heat exchangers, can also be maximized with respect to the optimal area distribution across the volume of these exchangers.

The discussion presented here applies to the design of crossflow heat exchangers, which can be configured with a nonuniform distribution of the transfer surface area across the volume of the exchanger, and in particular to plate-fin and tube-fin type heat exchangers. Wet-plate as well as single phase heat exchangers can be considered.

2 Performance Objective

The effectiveness of heat exchangers depends upon the number of heat transfer units, N_{tu}, which is a nondimensional measure of the transfer capacity of the exchanger. The average $N_{tu,0}$ is generally defined as

$$N_{tu,0} = \frac{1}{C_{\min}} \int_0^A U \, dA = \frac{UA}{C_{\min}} \tag{1}$$

where U is the overall, local thermal conductance per unit transfer area, and A is the total transfer area. For counterflow and parallel flow heat exchangers, the dependence of the effectiveness upon the variation of U with dA can be taken into account by using the average $N_{tu,0}$, based upon the average UA as expressed in equation (1), in the correlation for the heat exchanger effectiveness (Shah, 1983). These types of heat exchangers are usually designed for a constant U in order to minimize the total pressure drop for a given UA. This design

Contributed by the Heat Transfer Division for publication in the JOURNAL OF HEAT TRANSFER. Manuscript received by the Heat Transfer Division December 21, 1989; revision received July 7, 1990. Keywords: Augmentation and Enhancement, Heat Exchangers, Heat Recovery.

constraint follows from the observation that the local pressure drop gradient is quadratic with the local mass velocity, whereas the local U value is at best only proportional with this velocity. The effectiveness of crossflow heat exchangers with a uniform heat transfer surface-area distribution is also generally expressed as a function of the $N_{tu,0}$ as defined in equation (1), although the effectiveness may depend strongly upon the variation of U with dA, as shown in this paper.

Figure 1 illustrates the geometry and flow configuration of a crossflow heat exchanger. The nomenclature of Kays and London (1984) is used. Fluid stream 1 flows in the x direction with a capacity rate C_1. Fluid stream 2 flows in the y direction and has a capacity rate $C_2 \le C_1$. The length of the heat exchanger in both directions is scaled to 1. Contours of constant temperature difference between the two fluid streams for the case $t_{1,in} = 1, t_{2,in} = 0$, and $C_1 = C_2$ are shown in Fig. 2. This figure indicates that for a uniform distribution of UA the majority of the heat transfer takes place along the diagonal of the exchanger while little is transferred in the two opposite corner areas. Thus it makes sense to promote the heat transfer in the zones of high temperature difference while saving on UdA in the areas of low temperature difference.

The performance of a crossflow heat exchanger with both fluids unmixed is described by the following system of conservation and transfer-rate equations:

$$\left.\begin{aligned} \frac{\partial t_1}{\partial x} + C^* \frac{\partial t_2}{\partial y} &= 0 \\ \frac{\partial t_2}{\partial y} &= N_{tu}(t_1 - t_2) \end{aligned}\right\} \quad \text{where } 0 \le x,\ y \le 1 \tag{2}$$

C^* is the minimum to maximum capacity-rate ratio C_2/C_1 and N_{tu} is the *local* number of transfer units, defined such that

$$\int_0^1 \int_0^1 N_{tu}\, dx\, dy = N_{tu,0} \tag{3}$$

where $N_{tu,0}$ is defined as in equation (1) with U a function of dA. The inlet conditions are taken as

$$\begin{aligned} &\text{at } x = 0\text{: } t_1(y) = 1, \text{ for } 0 \le y \le 1 \\ &\text{and at } y = 0\text{: } t_2(x) = 0, \text{ for } 0 \le x \le 1 \end{aligned} \tag{4}$$

It is further assumed that the mass flow distribution is uniform at the inlet faces of the heat exchanger. The effectiveness of the crossflow heat exchanger is then given by

$$\epsilon_{xf} = \int_0^1 t_2(x)\,|_{y=1}\, dx \tag{5}$$

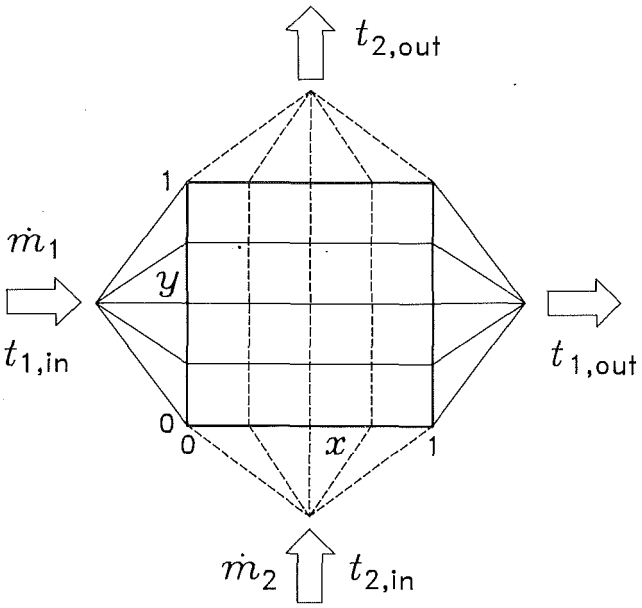

Fig. 1 Crossflow heat exchanger with both fluids unmixed

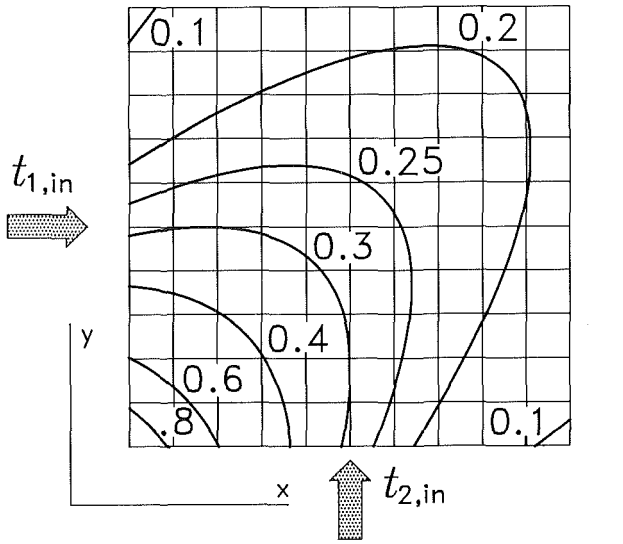

Fig. 2 Temperature difference contours in a crossflow heat exchanger, $t_{1,in} = 1$, $t_{2,in} = 0$, and $C_1 = C_2$

Nomenclature

A = coefficient or total transfer surface area
b = width of transfer zone
c = slope of transfer zone
C = gas stream thermal capacity rate
$C_{\min}$ = minimum capacity rate of gas streams
C^* = minimum-to-maximum capacity-rate ratio
f = mean friction factor
N_{tu} = local number to transfer units
$N_{tu,0}$ = average number of transfer units
p = Laplace variable
St = Stanton number
t = gas stream temperature
$\bar{t}$ = Laplace transform of temperature
U = overall heat transfer coefficient
w = flow coordinate
x = flow coordinate
y = flow coordinate transverse to x
z = flow coordinate transverse to w
β = volumetric heat transfer surface-area density
δ = Dirac delta function
ϵ = heat exchanger effectiveness
ϵ_{cf} = counterflow heat exchanger effectiveness
ϵ_{xf} = crossflow heat exchanger effectiveness
λ = root of characteristic equation
σ = ratio of free-flow area to frontal area

Subscripts

cf = counterflow
corner = outside of the diagonal zone
diag = within the diagonal zone
xf = crossflow

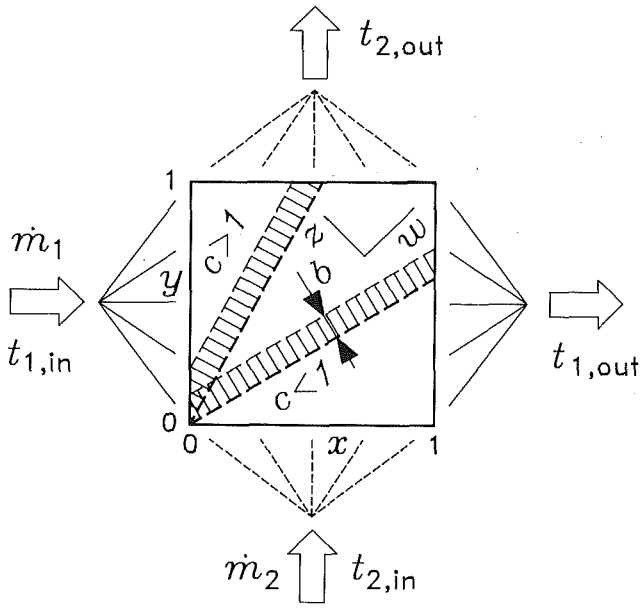

Fig. 3 Crossflow heat exchanger with a rectangular transfer area of width *b* and a base aligned along the line $y = cx$

The *objective* of the design analysis can now be formulated as follows. Find the optimal distribution N_{tu} (x, y) so as to maximize the heat exchanger effectiveness

$$\epsilon = \max_{N_{tu}(x,y)} \epsilon_{xf}(N_{tu}(x, y), C^*) \tag{6}$$

subject to the constraint that $N_{tu,0}$ is constant.

3 Analysis I

The problem formulated above can be theoretically solved using a two-dimensional cubic spline representation for the N_{tu} distribution. The optimization problem is then reduced to maximizing a function with a linear constraint in the unknown nodal parameters that characterize this spline distribution. Using a finite difference solution of the conservation and transfer rate equation in combination with a conjugate gradient optimization method, it can be shown that the optimal N_{tu} distribution tends toward the *Dirac delta* function $N_{tu,0}\delta(x-y)$ along the line $x=y$.

To prove that the effectiveness reaches a maximum for a δ distribution along the diagonal, an analytical solution of equations (2) can be obtained as follows. A coordinate transformation as suggested by the previous optimization analysis is used

$$w = cy + x \text{ and } z = y - cx \tag{7}$$

where c is a parameter. This transformation is illustrated in Fig. 3 for cases where $c<1$ and $c>1$. The heat transfer zone is a rectangular area with its base aligned along the w axis and with width b. The heat transfer coefficient is constant in this zone.

The conservation and transfer rate equation in terms of these coordinates can be written as

$$c\frac{\partial t_1}{\partial z} - C^*\frac{\partial t_2}{\partial z} = \frac{\partial t_1}{\partial w} + C^*c\frac{\partial t_2}{\partial w} \tag{8}$$

$$\frac{\partial t_2}{\partial z} = N_{tu}(t_1 - t_2) - c\frac{\partial t_2}{\partial w} \tag{9}$$

with initial conditions, at $w=0$:

$$\left.\begin{aligned} t_1(z) &= 1 \\ t_2(z) &= 0 \end{aligned}\right\} \quad \text{for } 0 \le z \le b \tag{10}$$

and boundary conditions

$$\left.\begin{aligned} &\text{at } z = b\text{: } t_1(w) = 1 \\ &\text{at } z = 0\text{: } t_2(w) = 0 \end{aligned}\right\} \quad \text{for } 0 \le w \tag{11}$$

Substituting equation (9) into equation (8) and taking the Laplace transform $t(w) \to \bar{t}(p)$ yields

$$\left.\begin{aligned} \frac{d\bar{t}_1}{dz} &= \frac{p + N_{tu}C^*}{c}\bar{t}_1 - \frac{N_{tu}C^*}{c}\bar{t}_2 - \frac{1}{c} \\ \frac{d\bar{t}_2}{dz} &= N_{tu}\bar{t}_1 - (N_{tu} + pc)\bar{t}_2 \end{aligned}\right\} \tag{12}$$

The solution of this system of ordinary differential equations is

$$\left.\begin{aligned} \bar{t}_1(z) &= A_1(N_{tu} + pc + \lambda_1)e^{\lambda_1 z} + A_2(N_{tu} + pc + \lambda_2)e^{\lambda_2 z} \\ &\quad + \frac{N_{tu} + pc}{p(N_{tu} + pc + C^*cN_{tu})} \\ \bar{t}_2(z) &= A_1N_{tu}e^{\lambda_1 z} + A_2N_{tu}e^{\lambda_2 z} + \frac{N_{tu}}{p(N_{tu} + pc + C^*cN_{tu})} \end{aligned}\right\} \tag{13}$$

where λ_1 and λ_2 are the roots of the characteristic equation:

$$\lambda^2 + [N_{tu}(1 - C^*/c) + p(c - 1/c)]\lambda - p(p + N_{tu}/c + N_{tu}C^*) = 0 \tag{14}$$

The coefficients A_1 and A_2 need to be determined from the boundary conditions in equation (11)

$$\left.\begin{aligned} &\text{at } z = b\text{: } \bar{t}_1 = 1/p \\ &\text{at } z = 0\text{: } \bar{t}_2 = 0 \end{aligned}\right\} \quad \text{for } 0 \le w \tag{15}$$

which leads to the system of equations

$$\left.\begin{aligned} A_1N_{tu} + A_2N_{tu} &= -\frac{N_{tu}}{p(N_{tu} + pc + C^*cN_{tu})} \\ A_1(N_{tu} + pc + \lambda_1)e^{\lambda_1 b} &+ A_2(N_{tu} + pc + \lambda_2)e^{\lambda_2 b} = \frac{C^*cN_{tu}}{p(N_{tu} + pc + C^*cN_{tu})} \end{aligned}\right\} \tag{16}$$

The effectiveness is computed from the outlet temperature t_2 at $z=b$. The case of interest here is a *Dirac delta* distribution, which is modeled by taking the limit for $b \to 0$ where $bN_{tu} \to N_{tu,0}$. Taking the limit in equations (14) and (16), solving for the roots λ_1 and λ_2 and coefficients A_1 and A_2, inserting the results in equations (13), and taking the inverse Laplace transform yields a constant outlet temperature for fluid stream 2

$$t_2 = \frac{1 - e^{-N_{tu,0}(1 - C^*/c)}}{1 - (C^*/c)e^{-N_{tu,0}(1 - C^*/c)}} = \epsilon_{cf}(N_{tu,0},\ C^*/c) \tag{17}$$

where ϵ_{cf} is the effectiveness of a counterflow heat exchanger with the number of transfer units equal to $N_{tu,0}$, and with the capacitance-rate ratio equal to C^*/c. The effectiveness of the crossflow heat exchanger with the N_{tu} distributed as $N_{tu,0}\delta(y-cx)$ follows from Fig. 3:

$$\left.\begin{aligned} &\text{for } c \le 1\text{: } \epsilon_{xf,\delta(y-cx)} = t_2 \\ &\text{and for } c \ge 1\text{: } \epsilon_{xf,\delta(y-cx)} = t_2/c \end{aligned}\right\} \tag{18}$$

This effectiveness reaches a maximum for a given $N_{tu,0}$ at $c=1$.

This analysis shows that the effectiveness of a crossflow heat exchanger, with both fluids unmixed, reaches a maximum for a *Dirac delta* distribution of the N_{tu} aligned along the diagonal of the heat exchanger. The effectiveness is then equal to the counterflow heat exchanger effectiveness with the same ca-

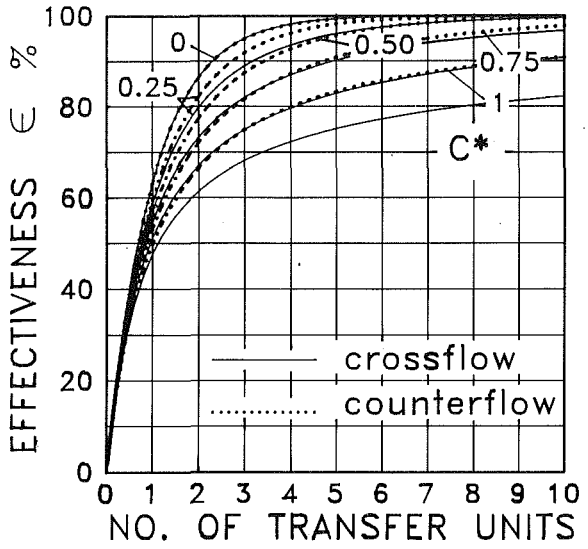

Fig. 4 Heat transfer effectiveness as a function of the number of transfer units and capacitance-rate ratio

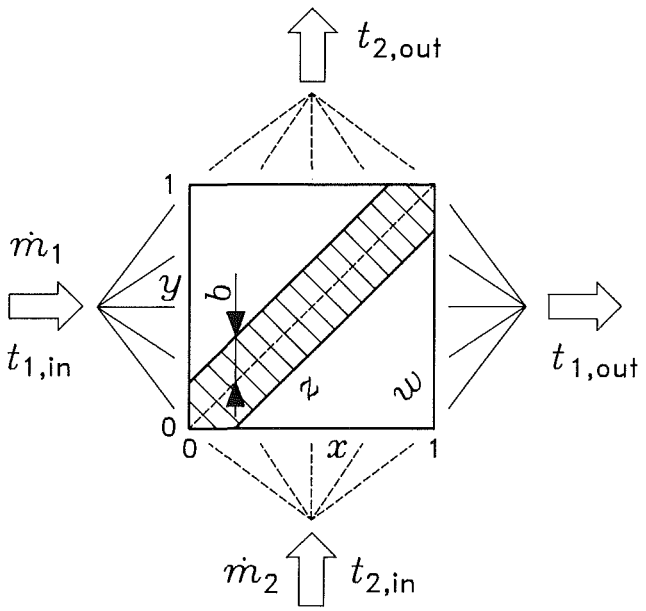

Fig. 5 Crossflow heat exchanger with a rectangular transfer area of half-width b and with the centerline aligned along the diagonal

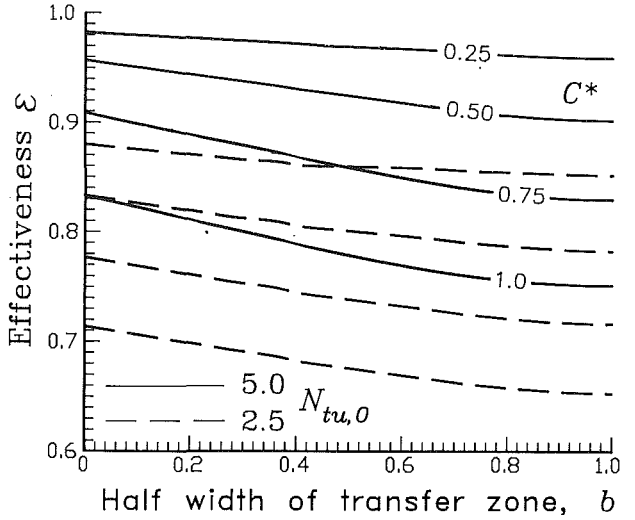

Fig. 6 Crossflow heat exchanger effectiveness as a function of the half-width of the transfer area, with $N_{tu,0}$ and C^* as parameters

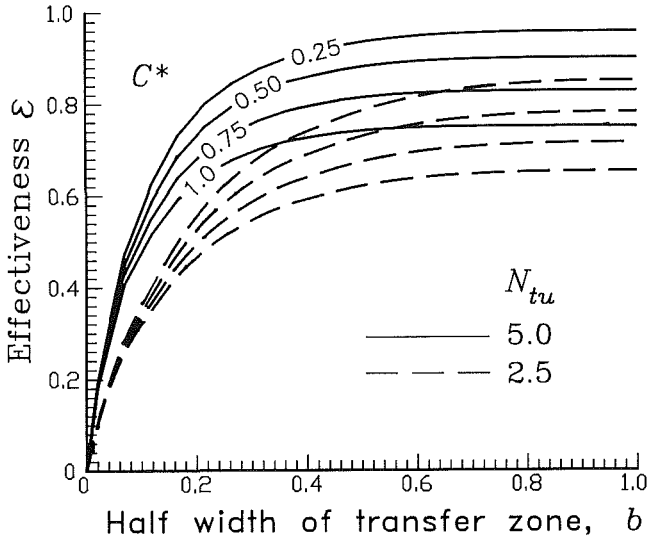

Fig. 7 Crossflow heat exchanger effectiveness as a function of the half-width of the transfer area, with N_{tu} and C^* as parameters

pacitance-rate ratio and the same overall $N_{tu,0}$. Figure 4 shows the effectiveness of a crossflow and counterflow heat exchanger as a function of the N_{tu} with C^* as a parameter. The increase in effectiveness is largest for $C^* = 1$ while for $C^* = 0$, the effectivenesses of both types of heat exchangers, are equal.

4 Analysis II

In practice, the *Dirac delta* function can be approximated with a distribution arranged as a rectangular area aligned along the diagonal of the heat exchanger, as illustrated in Fig. 5. Outside the shaded area in this figure, it is assumed that there is no heat transfer. The half width of the band transfer zone is b. Two cases can be considered for the heat exchanger shown in Fig. 5. As the half-width b varies, the local N_{tu} can remain constant while the average $N_{tu,0}$ varies proportionately with the shaded area, or the average $N_{tu,0}$ remains constant while the local N_{tu} tends toward infinity as $b \to 0$. The results presented in this section are also representative for a gaussian or a triangular distribution of the N_{tu} where b is then proportional with the standard deviation or average width of the distribution.

The effectiveness of the heat exchanger is computed from equation (5) using a numerical solution of the conservation and transfer rate equations (2) with the inlet conditions as specified by equation (4), and the N_{tu} constraint as formulated by equation (3). The numerical method is a central-central explicit finite difference scheme of second order, with Richardson's extrapolation to zero grid size. The trapezium rule is used for the integration of the outlet temperature in equation (5).

Figure 6 shows the effectiveness as a function of b with C^* as a parameter for two different $N_{tu,0}$. The local N_{tu} tends toward infinity as $b \to 0$. This figure shows that the effectiveness increases with the transfer zone shrinking. The effectiveness starts out at the crossflow heat exchanger effectiveness for $b = 1$ and increases to the counterflow effectiveness for $b = 0$. The absolute increase in heat exchanger effectiveness when compressing the transfer zone ranges from 0 to $C^* = 0$ to about 0.07 for $C^* = 1$. The effectiveness of a crossflow heat exchanger with only heat transfer at the diagonal, $\epsilon_{xf,\text{diag}}$, can be approximated as

$$\text{for } b<0.8:\ \epsilon_{xf,\text{diag}}(b)\approx\frac{(0.8-b)\epsilon_{cf}+b\epsilon_{xf}}{0.8}$$
$$\text{for } b>0.8\ \ \epsilon_{xf,\text{diag}}(b)\approx\epsilon_{xf} \tag{19}$$

Figure 7 shows the effectiveness curves for the case where the local N_{tu} remains constant while the average $N_{tu,0}$ varies between 0 for $b=0$ to N_{tu} for $b=1$. As indicated in this figure, major savings in heat transfer area are possible for only minor drops in exchanger performance. For a 0.01 absolute drop in effectiveness, the required heat transfer area decreases by 12 to 25 percent for $N_{tu}=2.5$ and $N_{tu}=5.0$, respectively. These numbers increase up to 20 and 32 percent for a 0.02 effectiveness reduction.

Finally, Fig. 8 shows the relationship between the average $N_{tu,0}$ and the half-width of the transfer zone b for a constant heat exchanger effectiveness. Two sets of curves are shown for $C^*=0.75$ and $C^*=1$, respectively. The range of effectiveness values runs from $\epsilon=0.85$ to $\epsilon=0.70$. These curves indicate the potential savings in UA as more of the heat transfer surface is moved from the corner areas to the middle diagonal of the exchanger matrix, while parts are deleted. The maximum possible savings as b: $1\rightarrow 0$ vary from 60 percent for $\epsilon=0.85$ and $C^*=1$ to 20 percent for $\epsilon=0.70$ and $C^*=0.75$. High-performance, balanced heat exchangers display the highest potential for surface-area savings.

5 Discussion

1 Plate-fin heat exchangers with either plain or interrupted fins are characterized by several design parameters such as the ratio of free flow area to frontal area σ, and the volumetric heat transfer surface-area density β (Kays and London, 1984).

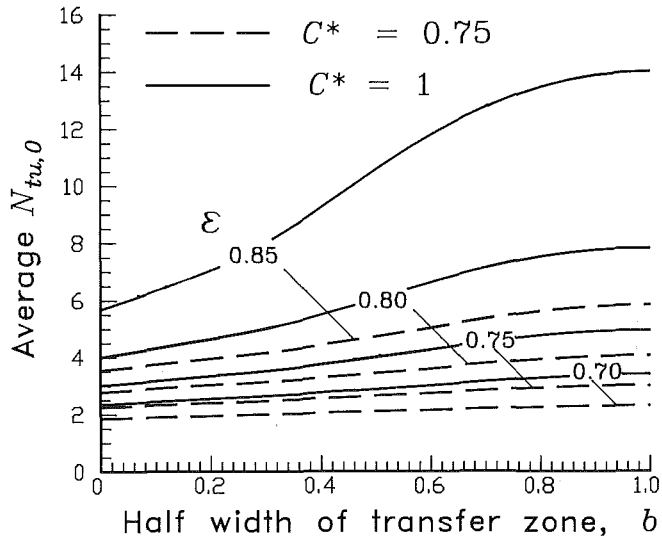

Fig. 8 Average $N_{tu,0}$ of a crossflow heat exchanger as a function of the half-width of the transfer area, with C^* and heat exchanger effectiveness ϵ as parameters

When β is increased by increasing the fin pitch, the fin thickness is usually decreased to compensate for the increase in exchanger weight. Also, the individual fin thickness may be lower when more of these fins are installed. This variation of fin thickness with β results in σ being almost independent from β for a particular type of fin. Thus by compressing some of the transfer surface in a crossflow heat exchanger into a denser diagonal band by varying the fin pitch and fin thickness, the free flow area can remain approximately constant.

Kays and London (1984) have published extensive experimental data on the performance of plate-fin surfaces. This performance can be measured by the St/f ratio, which relates the heat transfer to pressure drop characteristics of the surfaces. For a given class of fin type, their results indicate that the St/f ratio of these surfaces is almost independent of β provided that the flow regime does not switch from laminar to turbulent when the hydraulic diameter of the flow passages is increased.

For the two conditions discussed above where σ and St/f ratio are almost constant with varying β and fin pitch, it can be shown that the pressure drop for flow through plate-fin surfaces is approximately proportional with the average $N_{tu,0}$ for a given mass flow rate. By compressing the heat transfer surface of a plate-fin or tube-fin crossflow heat exchanger, the pressure drop and thus the fan power may be reduced on both sides by the same amount as the transfer area. From Fig. 8 it can be inferred that, for balanced high-performance devices, these savings may add up to 40 percent or more.

2 The use of high-performance surfaces with a high ratio of transfer area to volume generally leads to more compact heat exchangers with a smaller volume. However, the hydraulic diameter of these surfaces is inversely proportional to the surface area density and their use will generally lead to a drastic increase of the pressure drops on both fluid sides. This effect can be compensated by elongating the heat exchanger, i.e., by decreasing the flow length while increasing the flow area, which yields a form like a toothpaste box. Thus, the use of high-performance surfaces in compact heat exchangers for optimizing the exchanger configuration with constraints of limited pressure drops, e.g., minimizing the exchanger volume, may be limited by restrictions on the aspect ratios of the rectangular exchanger core.

The elongating effect associated with the use of compact surfaces as described above can be significantly reduced by optimally distributing the transfer area within the volume of the exchanger. This is illustrated by the following example, which is taken from Shah (1981).

Table 1 Heat exchanger design conditions for sizing example (Shah, 1981)

parameter	units	gas stream	air stream
mass flow rate	kg/s	0.8962	0.8296
inlet temperature	°C	240	4
outlet temperature	°C	61.4	198.2
inlet pressure	kPa	110	110
pressure drop	kPa	0.32	1.67

Table 2 Surface geometry of selected plate-fin surfaces (Kays and London, 1984)

Fin type	Surface designation	Plate spacing mm	Fins/in	Hydraulic diameter mm	Fin thickness mm	Surface area dens. β, m^2/m^3	Fin area/ total area m^2/m^2
plain	11.1	6.35	11.10	3.08	0.152	1204	0.756
plain	19.86	6.35	19.86	1.88	0.152	1841	0.849
strip	$\frac{1}{8}$-15.61	6.35	15.61	2.38	0.102	1548	0.923
strip	$\frac{1}{10}$-27.03	6.35	27.03	1.42	0.102	2466	0.878

Table 3 Core dimensions of heat exchangers with equal effectiveness

exchanger design	gas-side surface type	air-side surface type	gas stream flow length m	air stream flow length m	height m	volume m^3	mass kg
base design							
uniform	19.86	$\frac{1}{8}$-15.61	0.297	0.616	0.896	0.164	66
diagonal b=0.2	19.86	$\frac{1}{8}$-15.61	0.404	0.855	0.513	0.177	64
corners	11.1	11.1					
50 % reduced pressure drop with equal surfaces							
uniform	19.86	$\frac{1}{8}$-15.61	0.226	0.485	1.675	0.184	74
diagonal b=0.2	19.86	$\frac{1}{8}$-15.61 (d)	0.308	0.689	0.949	0.201	72
corners	11.1	11.1					
more compact surfaces with equal pressure drop							
uniform	$\frac{1}{10}$-27.03	$\frac{1}{10}$-27.03	0.085	0.202	2.851	0.049	22
diagonal b=0.2	$\frac{1}{10}$-27.03	$\frac{1}{10}$-27.03	0.151	0.359	1.263	0.069	26
corners	11.1	11.1					
diagonal b=0.1	$\frac{1}{10}$-27.03	$\frac{1}{10}$-27.03	0.228	0.539	0.801	0.099	35
corners	11.1	11.1					

The basic design is that of a gas-to-air single-pass crossflow heat exchanger. Table 1 lists the heat exchanger design conditions. The inlet conditions of both fluid streams and the specifications concerning the gas stream outlet temperature yield a required effectiveness of 0.823. The gas and air side pressure drops are limited to 0.32 and 1.67 kPa, respectively. The plates (parting sheets) and fins are made of aluminum with a thermal conductivity of 190 W/m-K. The plate thickness is of 0.4 mm. The heat transfer surfaces that are used are taken from Kays and London (1984). Table 2 lists the geometric characteristics of some selected surfaces.

The sizing of the heat exchanger core follows the procedures outlined by Shah (1981). The gas is treated as air and correlations for fluid properties are taken from the literature (Touloukian et al., 1970). The heat transfer coefficient and friction factor are evaluated from curve fits of experimental data for each of the surfaces published by Kays and London (1981). The effect of axial heat conduction is neglected. The effectiveness of a crossflow heat exchanger with a high-density surface with half-width b on the diagonal and a low-density surface in the corner areas outside of the diagonal is approximated as the effectiveness of $\epsilon_{xf,\text{diag}}$ (b^*), where $b^* > b$ is a corrected half-width such that

$$(UA)_{xf,\text{diag}} + (UA)_{xf,\text{corner}} = (UA)^*_{xf,\text{diag}} \text{ with } U^* = U_{xf,\text{diag}} \tag{20}$$

Table 3 lists various designs of heat exchangers that meet the specifications. The heat exchanger with a uniform surface area distribution that meets the design specifications in Table 1 is taken as the base design. The second tabulation gives an example of a diagonally distributed surface area with a high-density surface on the diagonal area and a lower-density surface in the corner areas. This example illustrates the primary advantages of the diagonal design, i.e., the lower mass and more cubic form of the exchanger core. The form of the exchanger core is measured in part by the aspect ratio, which is the ratio of the largest-to-smallest dimension of the core.

The advantage of a small aspect ratio becomes more pronounced when the allowable pressure drops on both sides are reduced by 50 percent. The dimensions listed in Table 3 show that the diagonal design has an aspect ratio of 0.949/0.308 = 3.1, which is only half the aspect ratio of the uniform design (1.675/0.226 = 7.4). Although the volume of the uniform design is smaller, the diagonal design has the smaller weight.

Selecting a denser surface for the heat exchanger yields a smaller volume and weight. However, the constraint of maximum permissible pressure drop may reduce the flow lengths of both flows, while increasing the third dimension dramatically, as indicated in Table 3. The dimensions of the uniform design with an aspect ratio of 2.851/0.085 = 33 are unfavorable compared to the dimensions of a design with a diagonally distributed transfer area (aspect ratio = 0.801/0.228 = 3.5 for $b = 0.1$). Notice that this last exchanger fits completely in the uniform base design. The table also shows that as $b \to 0$, the volume and weight tend to increase. The optimal value for b ranges from 0.1–0.2.

Conclusion

A study of the optimal distribution of the UA value across the volume of crossflow heat exchangers is presented. It is shown that the optimal distribution is a band distribution aligned along the diagonal of the exchanger and that the performance of these heat exchangers increases by compacting more of the transfer area. For constant surface area, the exchanger effectiveness may be increased by 0.07 for balanced flow rates. For constant heat exchanger effectiveness, the pressure drop may be reduced by 40 percent through an equal reduction in the required transfer surface area.

From the previous discussions, design guidelines for distributing the transfer area in compact crossflow heat exchangers may be formulated as follows: *Surfaces with a large surface area density should be used along the diagonal of the exchanger and less compact surfaces ought to be used for the remaining parts.* Designs following these principles may lead to either reduced pressure drops for equal exchanger effectiveness, a higher exchanger effectiveness for equal pressure drops, or a heat exchanger with reduced weight and a near square shape of the exchanger core for equal pressure drops and effectiveness.

Although the diagonal design seems promising, there may be concerns about the structural integrity of the exchanger core or performance reductions due to flow maldistribution. These design aspects are not considered here. Whereas the manufacturing cost of devices associated with these design guidelines may increase, the resulting savings in transfer area, the flexibility of the design and especially the substantially reduced pressure drops may result in a lower life cycle cost.

References

Ait-Ali, M. A., and Wilde, D. J., 1980, "Optimal Area Allocation in Multistage Heat Exchanger Systems," ASME JOURNAL OF HEAT TRANSFER, Vol. 102, pp. 199-201.

Grehier, A., Raimbault, C., Rojey, A., Busson, C., Chlique, B., and Dreuihle, J., 1984, "Compact Gas-Gas Heat Exchanger," *Heat Recovery Systems,* Vol. 4, No. 4, pp. 247-256.

Kays, W. M., and London, A. L., 1984, *Compact Heat Exchangers,* McGraw-Hill, New York.

Kröger, D. G., 1983, "Design Optimization of an Air-Oil Heat Exchanger," *Chem. Eng. Sci.,* Vol. 38, No. 2, pp. 329-333.

Raimbault, C., Grehier, A., and Rojey, A., 1981, "Les Échangeurs Gaz-Gaz (types et constructeurs)," I.F.P. Report Nos. 29782 and 29782A, Institut Français du Pétrole, Paris.

Reay, D. A., 1979, *Heat Recovery Systems,* E. and F. N. Spon Ltd., London.

Shah, R. K., 1978, "Compact Heat Exchanger Surface Selection Methods," *Proc. Sixth Int. Heat Transfer Conf.,* Vol. 4, pp. 193-199, Hemisphere Publ. Corp., Washington, DC.

Shah, R. K., Afimiwala, K. A., and Mayne, R. W., 1978, "Heat Exchanger Optimization," *Proc. Sixth Int. Heat Transfer Conf.,* Vol. 4, pp. 185-191, Hemisphere Publ. Corp., Washington, DC.

Shah, R. K., 1981, "Compact Heat Exchanger Design Procedures," in: *Heat*

Exchangers, Thermal-Hydraulic Fundamentals and Design, S. Kakaç, A. E. Bergles, and F. Mayinger, eds., pp. 495–536, Hemisphere Publishing Corp., Washington, DC.

Shah, R. K., 1982, "Advances in Compact Heat Exchanger Technology and Design Theory," *Proc. Sixth Int. Heat Transfer Conf.,* Vol. 4, pp. 193–199, Hemisphere Publ. Corp., Washington, DC.

Shah, R. K., 1983, "Heat Exchanger Basic Design Methods," in: *Low Reynolds Number Flow Heat Exchangers,* S. Kakaç and A. E. Bergles, eds., pp. 21–72, Hemisphere Publishing Corp., New York.

Shah, R. K., 1988, "Plate-Fin and Tube-Fin Heat Exchanger Design Procedures," in: *Heat Transfer Equipment Design,* R. K. Shah, E. C. Subbarao, and R. A. Mashelkar, eds., pp. 255–266, Hemisphere Publ. Corp., Washington, DC.

Touloukian, Y. S., Liley, P. E., and Saxena, S. C., 1970, "Thermal Conductivity," Vol. 3; Touloukian, Y. S., Liley, P. E., Saxena, S. C., and Makita, T., "Specific Heat," Vol. 6; Touloukian, Y. S., Liley, P. E., Saxena, S. C., and Hestermans, P., "Viscosity," Vol. 11; *Thermophysical Properties of Matter,* IFI/Plenum, New York.

Investigation of the Effects of Flow Swirl on Heat Transfer Inside a Cylindrical Cavity

A. Salce
Orval Kent de Linares,
Linares, N.L. 67700 Mexico

T. W. Simon
Mechanical Engineering Department,
University of Minnesota,
Minneapolis, MN 55455

Experiments were conducted to determine local heat transfer coefficients on the inside surfaces of a cylindrical cavity that is cooled by a swirling air flow. Temperature-sensitive liquid crystals were used as temperature sensors. Five blowing (cooling) modes were tested: three with swirl numbers of 0.36, 0.84, and 1.73; a fourth with no swirl (axial flow), and a fifth that was similar to the fourth but had the flow direction reversed. Flow visualization and static pressure measurements were performed to improve understanding of the situation. The smoke-wire technique was successfully used to picture the flow patterns. Plots of local Nusselt number along the cavity surfaces were obtained for the five blowing modes and for three different Reynolds numbers. The swirling cases had similar flow fields with higher heat transfer rates near the cavity top and lower rates near the cavity bottom (the opposite of the nonswirling cases). A tornadolike structure on the cavity bottom was observed in the swirling cases. This structure became stronger and more violent as the degree of swirl and the Reynolds number were increased. The Nusselt number curves for the two nonswirling cases were of similar shape, although the flow direction was reversed.

Introduction

It has been found that heat transfer inside circular ducts can be enhanced by using swirl flow. This method of heat transfer enhancement can be especially useful where high heat transfer rates are needed in the cooling of internal cavities. Applications may be curing of mold linings, carrying of moisture above grain bins, molding of cast metal components, instrumentation inserted into high-temperature regions that must be internally cooled, and "dead-end" heat exchanger tubes. Swirl is also used for augmenting combustion or purging cylinders in internal combustion engines. The results of the following study can be applied anywhere that the internal walls of a closed-end geometry must be cooled and the introduction of swirl is a reasonable option.

There are many entries in the literature on the effects of flow swirl inside pipes or ducts. Khalil (1982) reported increases of local heat transfer coefficients at the inlet of turbulent pipe flow created by using a vane swirler. Enhancements of 40 percent, with respect to axial flow at the same Reynolds number based upon axial velocity, were observed. Free swirling jets were applied in the combustion and plasma fields. The increase of mixing by the use of swirl resulted in more efficient combustion and plasma formation. Beer and Chigier (1972) found the central recirculation bubble generated in a swirling jet flow to be useful for combustion applications in that it plays an important role in flame stabilization by producing a hot flow of recirculated combustion products and a reduced-velocity region where flame speed and flow velocities are matched. Flame lengths and distances from the burner at which the flame is stabilized were shortened significantly. The size and shape of the reverse flow region depended on the degree of swirl.

Present Study

In the present study, air entered and departed from the cavity through concentric openings located at the top of the cavity. Heat transfer measurements were performed on the walls of the cavity as well as on the bottom surface using a liquid crystal technique. The cooling fluid was air. Flow visualization studies using the smoke-wire technique were conducted to improve understanding of the situation.

The cylindrical cavity had a height-to-diameter ratio of 1.70 (diameter, D, was 26 cm; see Fig. 1). The ratio of swirler outer diameter, d, to cylinder cavity diameter, D, was 0.36 and the ratio of exhaust diameter to cylinder cavity diameter was 0.12. The first dimension would influence the separation zone size. It was chosen as representative of the applications cited. The effects of changes in the second dimension were also not tested. The two independent variables of the experimental program were the mass flow rate of cooling air and the degree of swirl of the flow entering the cavity. Three flow rates were used during the experiments: 9.3, 14.0, and 19.5 g/s of air corresponding to Reynolds numbers based upon cylinder diameter of 2540, 3750, and 5270, respectively. Four swirl strengths were tested, each with a different flow angle at the exit of the swirl generator, β. The four angles were $\beta = 0$, 20, 40, and 60 deg, corresponding to swirl numbers, S', of 0.0, 0.36, 0.89, and 1.73, respectively. This swirl number is defined by

$$S' = \frac{W}{U} \tag{1}$$

where U is the axial velocity component and W is the tangential velocity component of the flow, both at the exit plane of the swirl generator (which is the entry plane of the cavity).

In the fifth case, axial (no tangential component) flow entered the cavity through the center (which was the exhaust tube for the cases above). This, then, is the $S' = 0.0$ case but with the flow direction reversed. Herein, this case is called the "Inverted Flow" case.

Figure 1 is a sketch of the basic geometry, which identifies some parameters and variables considered important for this problem. The most important parameters are the fluid properties (ρ, C_p, μ, k) and geometric dimensions (d, L, D). Variables to the problem are the flow characteristics (U, W, $\dot{m}$) and the heat transfer coefficient, h (the dependent variable to the problem).

Contributed by the Heat Transfer Division and presented at the National Heat Transfer Conference, Philadelphia, Pennsylvania, August 6–9, 1989. Manuscript received by the Heat Transfer Division November 9, 1989; revision received October 19, 1990. *Keywords:* Forced Convection, Materials Processing and Manufacturing Processes, Measurement Techniques.

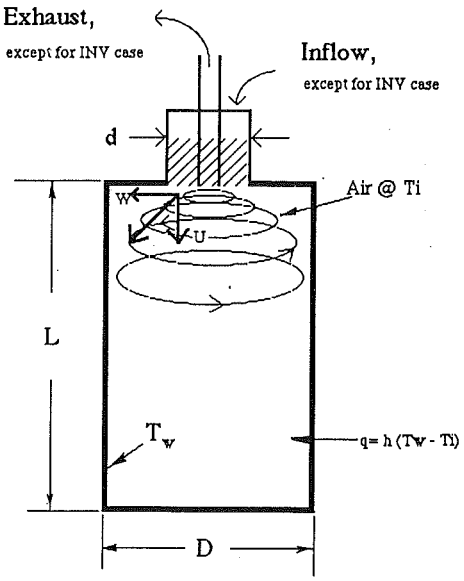

Fig. 1 Test section geometry

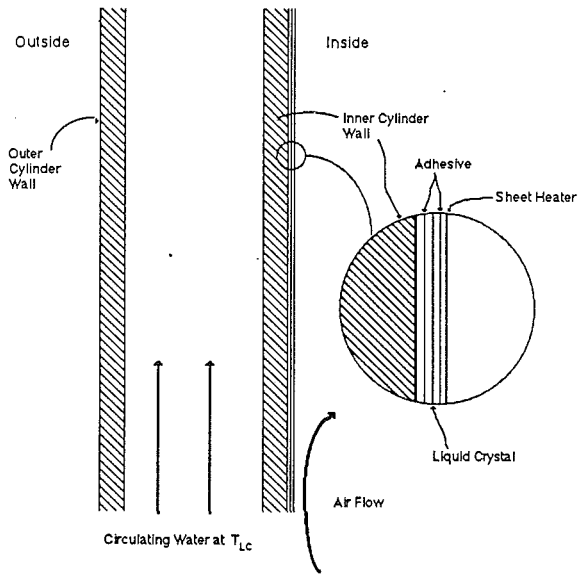

Fig. 2 Heated wall construction

Dimensional analysis was used to find the important dimensionless groups

$$\frac{hD}{k}, \quad \frac{4\dot{m}}{\pi D\mu}, \quad \frac{\mu C_p}{k},$$

which are the Nusselt, Reynolds, and Prandtl numbers, respectively. Dimensionless geometric parameters include the cylinder length, L/D, and entry tube diameter, d/D. The task of the present study is to find the relationships between the Nusselt number distributions and Reynolds number and swirl number for a chosen Prandtl number and geometry, as described by L/D and d/D.

A small cavity model of $D = 0.146$ m was built during the development stage of the experimental program and used to test the similarity parameters of the experiment. Comparison was made with the final model ($D = 0.26$ m) having the same L/D, d/D, and other geometric ratios. Similarity was confirmed by verifying that similar (magnitude and distribution) heat transfer data are obtained on the small and the large models when Reynolds number is matched.

Techniques

Heat Transfer. Local heat transfer coefficients were obtained using the liquid crystal technique. This technique had been successfully used on other convective heat transfer applications (Simonich and Moffat, 1984; Hippensteele et al., 1985). Cholesteric liquid crystals are substances that exhibit different colors at different temperatures by selectively reflecting only certain wavelengths of light when they are illuminated. The liquid crystal film is sandwiched between a transparent wall (acrylic or glass) and an electric heater element, as shown in Fig. 2. On the outside of the test wall, water at a fixed temperature, which is the mapping temperature T_{LC}, is circulated. The mapping temperature is a temperature for which the liquid crystal color is known (the color chosen for doing the temperature mapping). For the present experiment, T_{LC} was 41.8°C and the mapping color was red. In the absence of cooling air inside the cavity, with no power to the heater and with 41.8°C water circulating outside the liquid crystal, the liquid crystal displays the same color, red, over the entire test section.

When power and cooling air are supplied, the liquid crystal displays different colors at different locations across the test section: blues and violets for the higher-temperature areas; red, yellow, and black for the lower-temperature areas. The areas displaying the mapping color, red, are the areas of interest. At these positions, energy balances are easily done to find the heat flux. The areas at which the colors are different from the mapping color are of no interest for this step of the study because there is heat exchange with the circulating water at these positions. For the areas of interest, the temperature outside of the test section wall is the same as the temperature on the inside of the wall, T_w (see Fig. 2). This is because the liquid crystal on the inside and the circulating water on the outside are at the mapping color temperature. Thus, no heat conduction is allowed across the wall and all the heat generated in the heater is removed by the inside cooling air. The heat transfer coefficient is computed from the heat flux, q, and the mapping temperature, T_w, as

$$h = \frac{q}{(T_w - T_i)} \tag{2}$$

Nomenclature

C_p = heat capacity, J/(kg K)
d = swirl generator diameter, m
D = cavity diameter, m
h = heat transfer coefficient = $q/(T_w - T_i)$, W/(m^2 K)
k = thermal conductivity, W/(m K)
L = cavity height, m
$\dot{m}$ = mass flow rate, kg/s
Nu = Nusselt number = hd/k
Pr = Prandtl number = $\mu C_p/k$
q = heat flux, W/m^2
Re_D = Reynolds number = $4\dot{m}/\pi D\mu$
S' = swirling number = W/U
T = temperature, K
U = axial velocity component, m/s
W = tangential velocity component, m/s
β = swirl generator flow angle
μ = viscosity, Ns/m^2
ρ = density, kg/m^3

Subscripts

i = inlet
LC = liquid crystal
w = wall

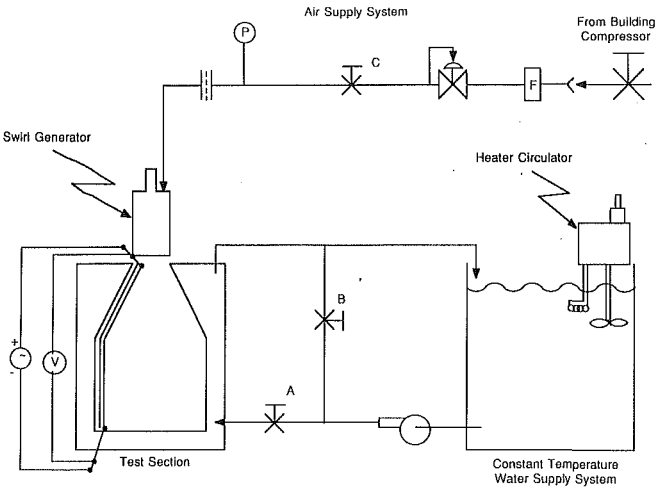

Fig. 3 Schematic of the heat transfer facility

where T_i is the air temperature at the inlet of the swirl generator. Thus, the terms needed to calculate the heat transfer coefficient are known at the positions where the liquid crystal displays the mapping color. Changing the power to the heater moves the mapping color to other locations. In doing so, q is the only term in equation (2) to change. The entire heat transfer coefficient distribution is calculated by continuing until the entire surface has, at one heat flux or another, been at the mapping temperature. One of the main advantages of this technique is that it can be used without destroying the liquid crystal in applications where a large variation in heat transfer coefficient is present.

Flow Visualization. Flow visualization studies were conducted using the smoke-wire technique. Originally developed by Ruspet and Moore (discussed by Mueller, 1983) in the early 1950s, this technique had been successfully used in many flows, especially in wind tunnel studies of bluff bodies. Mueller and Batill (1980) and Nagib (1977) are among several researchers who had used the technique on studies of complex flows.

The smoke-wire technique utilizes evaporation of a thin oil film from a tiny metal wire immersed in the flow. The wire, which extends across the entire diameter of the cylinder, is sufficiently small that the Reynolds number is subcritical. Evaporation is by means of electric heating. Surface tension forms small beads on the wire. When the wire is heated, a smoke filament (streakline) is produced downstream of each oil bead. Precise control over the time of heating and the voltage applied to the wire is essential to generate good smoke for visualization and to prevent the wire from burning out. An electric control box was designed and built to provide the desired synchronization between the smoke generation and the triggering of the recording instruments. This box also provided control over the time of heating and the magnitude of the power applied to the wire.

Pressure Measurements. Static pressure measurements were also taken along the cylinder walls and cavity bottom. The pressure taps were machined through the surface at various places and measurements were taken with respect to a reference point situated at midheight on the cylinder wall.

Apparatus

Heat Transfer Facility. The heat transfer facility consisted of the test section, which is a model of the cavity, and two subsystems: the constant temperature water supply system and the air supply system; see Fig. 3. The water supply system was designed to provide up to 20 liters/min of water at a fixed temperature (nominally 41.8°C) as required by the liquid crystal technique. The air supply system provided cooling air to the inside of the cavity. Thermocouple junctions were used to record the relevant temperatures of the experiment.

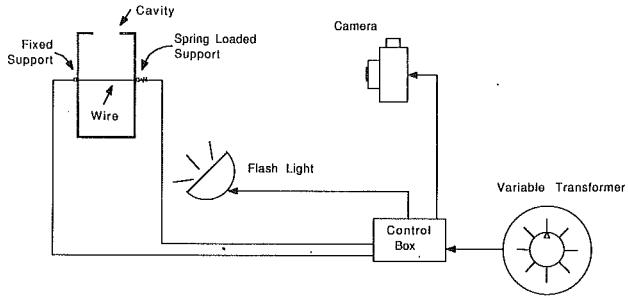

Fig. 4 Flow visualization layout and control schematic

Flow Visualization Facility. The flow visualization facility consisted of a flow visualization model and two subsystems: the same air supply system used in the heat transfer experiments and the smoke-wire electric control box (see Fig. 4). The model was constructed with holes for installing the smoke wire and for use as pressure taps. It was geometrically identical to the heat transfer model. Pressure signals were measured with a variable-reluctance pressure transducer and recorded by a digital voltmeter.

Swirl Generator. Commonly used swirl generator types such as twisted tape, tangential-plus-axial entry, tangential entry, or tangential vane do not provide uniform, well-defined flow distributions. Their use would make it difficult to characterize the exit flow in the present test. In order to avoid this, swirl generators with uniform and known velocity distributions at the exit planes, for all flow rates, were devised. Sketches of these swirl generators are given in Fig. 5. They are each made of two concentric PVC circular tubes, giving an annular region of 9.5 cm (3.75 in.) o.d. and 3.8 cm (1.5 in.) i.d. The space between them contains pieces of Tygon tubing, 4.8 mm (3/16 in.) i.d. and 6.4 mm (1/4 in.) o.d., glued together with RTV silicone rubber forming something similar to a twisted honeycomb. Each piece of Tygon tubing was the same length. By aligning all the Tygon tubing to the same angle, the tangential-to-axial velocity ratio became the same at all positions on the exit plane and the swirl number, S', was well defined. The exit flow was, thus, uniform across the exit plane of the generator in both axial and tangential velocity. Since this flow passes through a series of parallel tubes, it can be characterized as a "disturbed" flow, consisting of merging jets and wakes, as is any flow that has exited a honeycomblike structure. The scales of these disturbances are small and the disturbances would dissipate quickly, however. The precise nature of this particular disturbance is considered to not be important to the problem. A perforated plate (not shown) was placed in the space between the top plane (where the air entered) and the plane of entrance to the Tygon tubing pack. This plate produced a uniform velocity distribution into the tubing. The center tube (3.2 cm, 1.25 in. dia) was the exit path for the air. The swirl generator was mounted on the top of either the heat transfer or the flow visualization facility cavity, as shown in Fig. 1, such that its exit plane was aligned with the cavity top plane. Four swirl generators were built, each for a specific swirl strength. They had different inclination angles, β, of 0, 20, 40, and 60 deg, creating swirl strengths of $S' = 0.0$, 0.36, 0.89, and 1.73, respectively.

Smoke-Wire. Figure 4 shows the smoke-wire arrangement used for flow visualization studies. The system consisted of a variable transformer, a control box, wire supports, wire, camera, and flash. The supports, used to hold the wire in place and serve as electrical contacts, were placed directly opposite

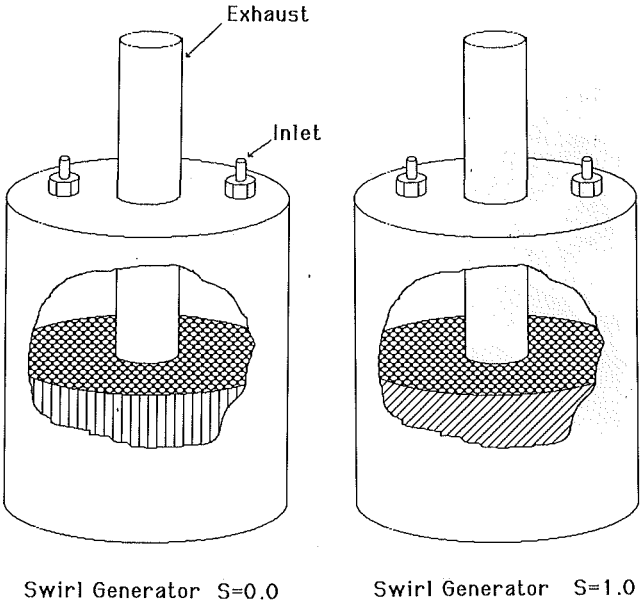

Fig. 5 Swirl generators of $\beta = 0$ and $\beta = 45$ deg

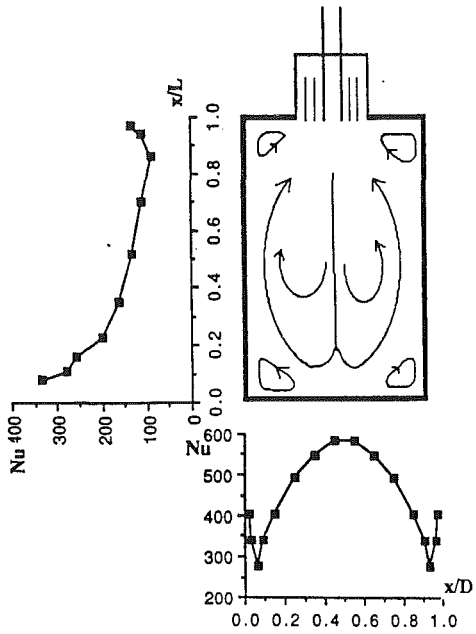

Fig. 6 Nusselt number distributions on the side and bottom of the cavity and the flow pattern for the inverted case, $Re_D = 3750$

one another along a diameter of the cavity. One support was fixed while the other was able to move in the radial direction to remove slack due to elongation of the heated wire.

Experimental Procedure

A heat transfer measurement started with a three-hour warmup of the water in the circulator system. The heater circulator controller was set to a temperature slightly above the mapping temperature, allowing for a temperature drop in the piping system (pump, hoses, etc.). After warmup, all the liquid crystal showed the color red. The appropriate swirl generator was placed on top of the test section and the air flow rate was set to the desired point on the rotameter. The cooling effect of the air turned the liquid crystal areas black. Just enough electric power was then applied to the heater to produce the first appearance of a red area on the liquid crystal. After one or two minutes, the red areas at the mapping temperature were well established. Measurements of the inlet air temperature, the inlet and outlet water temperatures, voltage applied to the heater, and positions of the red isotherms were then recorded. This information was used to record the regions of a single value of convective heat transfer coefficient. Without changing any setting in the air and water supply systems, a slightly higher voltage was applied to the heater and the red areas moved to new positions. Again, sufficient time was allowed for the isotherms to settle to the new positions on the test surface and the temperature, voltage, and position of the isotherms were recorded. The process was repeated, moving the isotherms across the entire test surface, generating plots of Nusselt number versus position on the test surface for the chosen values of Re_D and S'. Different Re_D values were achieved by adjusting the air mass flow rate. Different S' values were obtained by using different swirl generators.

An uncertainty analysis, based on the 95 percent confidence interval, was performed on the Nusselt and Reynolds numbers data. The Nusselt number uncertainty was 3.9 percent and the Reynolds number uncertainty was 3.6 percent. The major sources of Nusselt number uncertainty were: (1) locating the isotherms, (2) liquid crystal calibration, (3) control of water temperature to match the liquid crystal sensitive temperature and calibration of the thermocouples. The major source of Reynolds number uncertainty was calibration of the flowmeters.

Results

The heat transfer data are next presented along with the best estimate of the corresponding flow fields (deduced from the pressure measurements and smoke-wire results). Although the flow had three nonzero velocity components, there was no evidence in the data of a departure from an axisymmetric situation.

Heat Transfer Results. The heat transfer data are presented in terms of a local Nusselt number, Nu, defined as

$$\mathrm{Nu} = \frac{hD}{k}$$

where h is the local heat transfer coefficient, D is the cavity diameter, and k is the thermal conductivity of the air based upon the air entry temperature. The local heat transfer coefficient was calculated as discussed above. Radiation was estimated and determined to be unimportant for this situation due to the large convective heat transfer coefficients. The data are presented as plots of Nusselt number distribution along the surfaces of the cavity. The ordinate is the Nusselt number and the abscissa is either x/L, the position on the sidewall, or x/D, the position on the base.

Inverted Case (No Swirl; Reverse Flow). The air entered the cavity by the exhaust tube; no swirl component was present (see Fig. 6). The high-velocity inlet stream traveled downward through the center of the cavity. The flow impinged upon the bottom surface, then changed direction, returning upward along the outer region near the cylinder wall. Since the inlet and outlet streams were very close to one another and the two streams moved in opposite directions, a region of high shear was established near the cavity top. In this high-shear region, some of the incoming air was drawn out by the exit stream without participating in the cooling of the cavity walls. The Nusselt number was high near the center of the bottom surface because an unheated, high-velocity jet impinged on this region. As the jet spread radially outward, the velocity decreased and the Nusselt number dropped. Separation of the flow occurred and a toroidal recirculation zone was created in the lower corner of the cavity. This recirculation zone is responsible for the high Nusselt numbers in this corner area ($x/D = 0.05$, $x/D = 0.95$, and $x/L = 0.05$). The air continued its upward

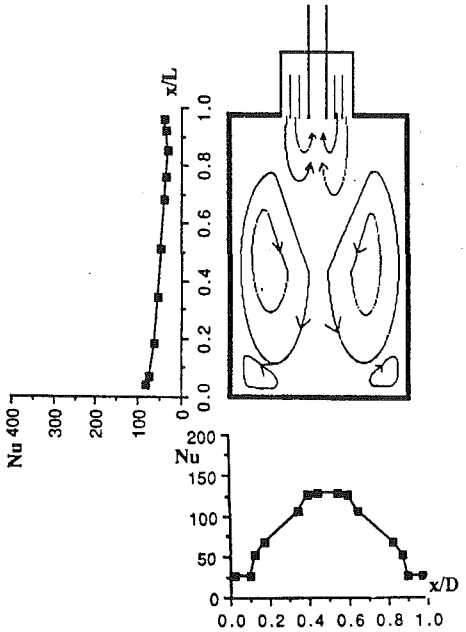

Fig. 7 Nusselt number distributions on the side and bottom of the cavity and the flow pattern for the $S' = 0.0$ case, $Re_D = 3750$

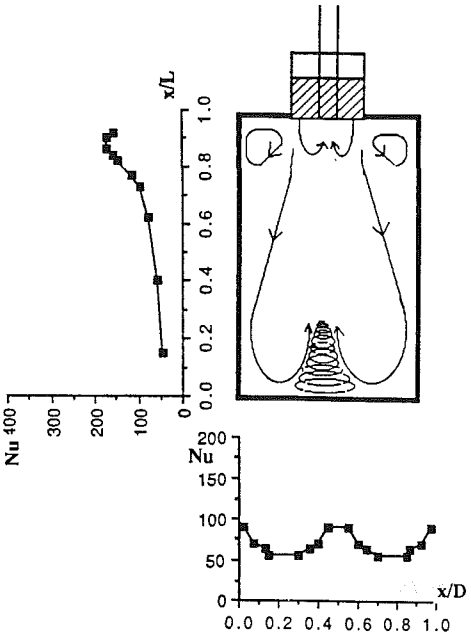

Fig. 8 Nusselt number distributions on the side and bottom of the cavity and the flow pattern for the $S' = 0.36$ case, $Re_D = 3750$

movement, washing the cylindrical walls. But, as the fluid remained in contact with the wall, its temperature rose, creating a decreasing Nusselt number as x/L increased. As the flow approached the top surface, it separated again from the wall creating another toroidal recirculation zone in the top corner. This top recirculation zone is responsible for the slight increase in the Nusselt number in that region.

The $S' = 0.0$ Case (No Swirl; Forward Flow). Again, there was no swirl component in this case. The air entered the cavity through an annular region and exited by the central exhaust tube (Fig. 7). The inlet and outlet streams were close to one another, and, since they had flows of opposite direction, a strong shear region was formed. This shear region was again responsible for forcing a large portion of the incoming air to

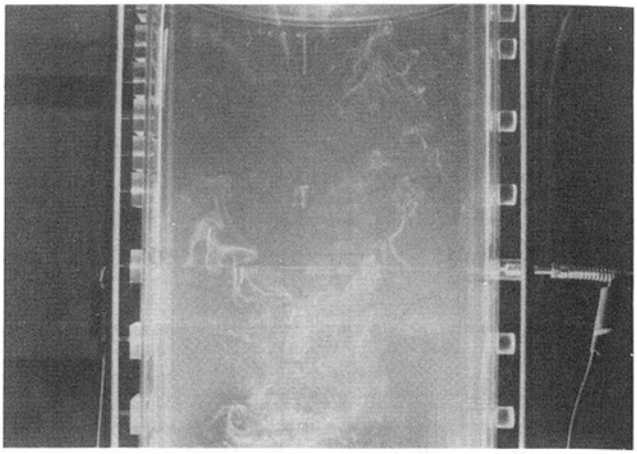

Fig. 9 Smoke-wire photography, $S' = 0.0$

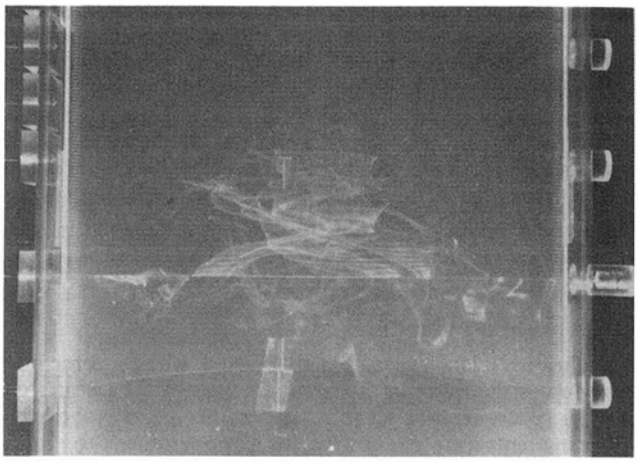

Fig. 10 Smoke-wire photography, $S' = 0.36$

reverse and leave the cavity without cooling the heated surfaces. The result of this was that much of the potential cooling effect of the fresh air was lost and the Nusselt numbers were low throughout. The cavity was cooled by a very large recirculating flow similar to that of the inverted flow case (see Figs. 6, 7, and 9). As a result of this, the Nusselt number distributions were nearly the same in shape, although the inverted flow case had much larger values.

The $S' = 0.36$ Case (Mild Swirl). In this case, the tangential component of the velocity imposed on the flow by the swirl generator caused the inlet stream to spread radially outward upon entering the cavity (Fig. 8). This outward movement allowed more cool air to wash the cavity walls. As a result, the Nusselt numbers in the upper portions of the cavity were significantly higher than those for the $S' = 0.0$ case. The flow traveled down near the wall and returned along the cavity centerline. Flow approached the bottom surface of the cavity by traveling near the cylinder wall. It then turned and traveled radially inward, turning upward as it approached the center. In approaching the center, it accelerated to satisfy continuity and its vorticity increased to conserve angular momentum. A tornadolike structure of high tangential velocity was thus formed in the lower cavity near the centerline (see Figs. 8 and 10). The highest Nusselt number values were on the cavity sidewalls near the top of the cavity ($x/L = 0.9$). The attachment of the flow and the formation of an upper toroidal recirculation zone, both containing cool fluid, were responsible for this.

The $S' = 0.84$ Case (Moderate Swirl). The flow field in this case was very similar to that of the mild swirl case, but with

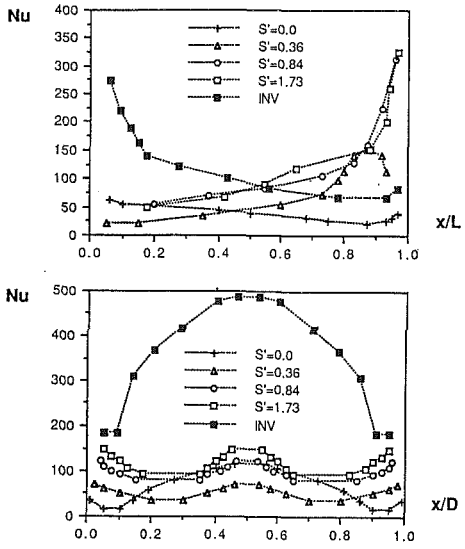

Fig. 11 Nusselt number distributions for various entry conditions at Re_D = 2540

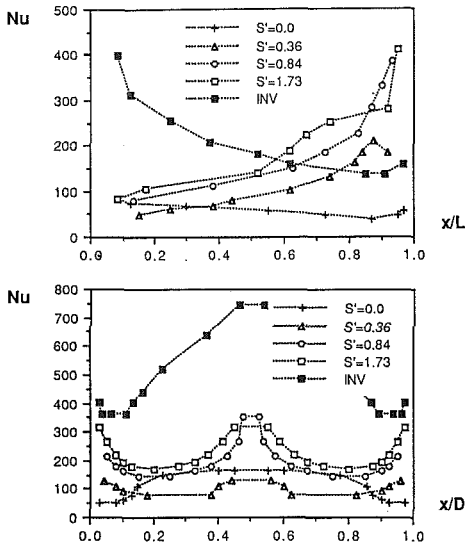

Fig. 13 Nusselt number distributions for various entry conditions at Re_D = 5270

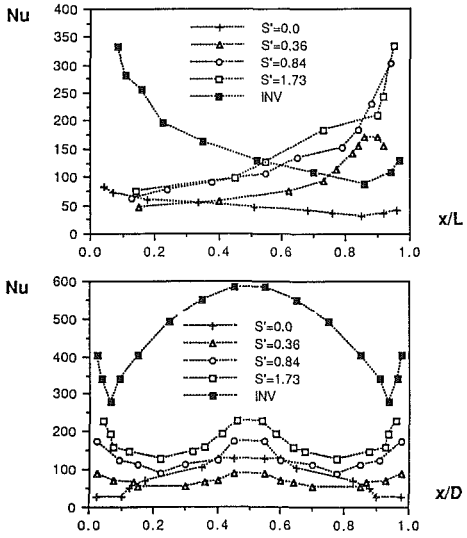

Fig. 12 Nusselt number distributions for various entry conditions at Re_D = 3750

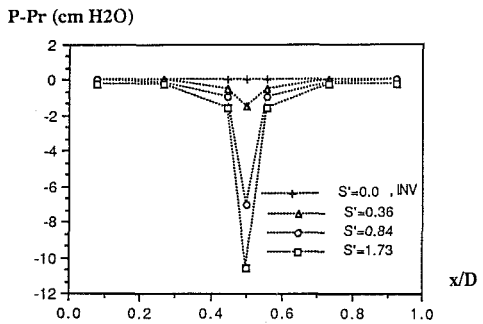

Fig. 14 Pressure distribution on the cavity bottom

all the swirling effects augmented. The higher angular velocity caused the flow to attach to the cylindrical wall nearer the cavity top than for the $S' = 0.36$ case, compressing the upper recirculation zone. In general, the Nusselt number profiles are also like those of the previous case; they are shifted upward because of the higher near-wall velocity gradients produced by the higher swirl number, however. Also, since the incoming flow spread at a wider angle, there was less cool inlet flow entrained into the exiting stream. The tornado structure formed on the bottom surface was stronger and larger than in the $S' = 0.36$ case. Figures 11–13 compare the various cases at selected Reynolds numbers.

The $S' = 1.73$ Case (Strong Swirl). Flow field and Nusselt number profiles for this case are very similar to those for the moderate swirl case (Figs. 11–13). The curves are skewed a bit toward the top of the cavity, however. The tornado structure was stronger, more violent, and visible along the entire axis of the cavity. In the vicinity of $x/L = 0.9$, the Nusselt number is higher for the $S' = 0.84$ case than for the $S' = 1.73$ case. The reason for this is unknown.

Flow Visualization. Figure 9 shows the large-scale recirculation zone that was created on the $S' = 0.0$ case. Note that the flow in the center was traveling downward and the flow near the walls was traveling upward. Figure 10 shows the tornadolike structure that was formed in the swirling cases $S' = 0.36$, $S' = 0.84$, and $S' = 1.73$. The tornado shape was similar for these three cases except that the tangential velocity increased as S' increased.

Pressure Measurements. Static pressure measurements were taken along the cylinder wall and bottom surfaces. All pressures were referenced to the static pressure on the side-wall at midheight, P_r. An example is shown on Fig. 14 for pressures on the bottom wall at $Re_D = 3750$. It was found that no significant pressure differences ($P - P_r$) existed on the cylinder walls for any of the five blowing modes at any Re_D number, though the absolute values of P and P_r increased as Re_D increased. This result was not expected, especially in the recirculation zones and near the reattachment points near the top of the cavity.

On the bottom surface, negative values of pressure (relative to the cylinder wall pressure) were detected near the centerline of the cavity (Fig. 14). It is presumed that the high velocities of the tornado structure were responsible for this. The magnitude of the negative pressure is a measure of the local velocity, and thus, the swirl strength. Two opposing factors affected the swirl strength in this area: the flow rate, as characterized by Re_D in this study, and the length of the cavity. As Re_D increased, the swirl became stronger and more influential on the bottom wall. When the cavity was longer (auxiliary cases not discussed) the swirl strength was dissipated, somewhat, and the vortex was less influential.

Conclusions and Comments

The liquid crystal technique used in this study is well suited for the present problem and is capable of measuring over a wide range of Nusselt numbers (18 to 1800).

Experiments performed at the same Reynolds number on two geometrically similar (same L/D and d/D) cavities, but of different size (D = 0.146 m and D = 0.260 m) and with different mass flow rates, demonstrated that Reynolds number, Re_D, is an appropriate parameter for characterizing the flow.

Flow visualization results and pressure measurements are qualitatively consistent with the heat transfer data and are shown to be useful in understanding the flow.

Although the flow had three nonzero velocity components, there was no evidence in the data of a departure from an axisymmetric situation.

From the data collected, the following conclusions can be drawn:

1 The Nusselt number distribution is a function of Re_D number, the degree of swirl, and the flow direction; in this test, compressibility, buoyancy, and roughness effects were not investigated.

2 For the geometry and the Re_D range of this experiment, the flow pattern was a function only of the blowing mode. The flow pattern did not change with Re_D.

3 The two nonswirling cases, one with central exhaust (S' = 0.0) and the other with central entry (the inverted case), produced Nusselt number distributions of similar shape, though they had different flow directions. The S' = 0.0 case had much lower values of Nusselt number because the cavity was washed by a recirculation zone driven by the entry flow. In the inverted flow case, the cavity was directly washed by the entry flow.

4 The swirling cases (S' of 0.36, 0.84, and 1.73) had similar flow fields. Higher heat transfer rates were found near the cavity top due to swirl and lower rates were found near the cavity bottom. This is opposite to results from the nonswirling cases. A tornadolike structure on the cavity bottom increased in strength as S' or Re_D was increased.

If one is looking for uniformity in cooling, the nonswirling (S' = 0.0) case may be better. However, if the intention is to enhance transport from the wall in the region near the cavity top, swirl is clearly beneficial. If the intention is to have effective transport at the bottom, the inverted flow case is the best.

Because of the complexity of the flow/geometry, no correlations can be presented between Nu, Re_D, and S'. The important conclusions to be drawn from this study are the changes in distributions with these parameters, as shown in the figures.

Acknowledgments

The authors would like to thank the AMOCO Foundation for partial support and AT&T for an equipment grant in support of this project.

References

Beer, J. M., and Chigier, N. A., 1972, *Combustion Aerodynamics*, Applied Science Publishers Ltd.

Hippensteele, S. A., Russell, L. M., and Torres, F. J., 1985, "Local Heat-Transfer Measurements on a Large Scale-Model Turbine Blade Airfoil Using a Composite of a Heater Element and Liquid Crystals," ASME *Journal of Engineering for Gas Turbines and Power*, Vol. 107, pp. 953–960.

Khalil, E. E., 1982, "Heat Transfer to Turbulent Pipe Flows With Swirl and Following a Sudden Enlargement," *Proc. of the Seventh Int. Heat Transfer Conf.*, FC10.

Mueller, T. J., and Batill, S. M., 1980, "Experimental Studies of the Laminar Separation Bubble on a Two-Dimensional Airfoil at Low Reynolds Numbers," AIAA Paper No. 80-1440.

Mueller, T. J., 1983, "Flow Visualization by Direct Injection," in: *Fluid Mechanics Measurements*, R. J. Goldstein, ed., Hemisphere Publishing Corp., New York.

Nagib, H. M., 1977, "Visualization of Turbulent and Complex Flows Using Controlled Sheets of Smoke Streaklines," *Proc. of the Int. Symp. on Flow Visualization*, Tokyo, pp. 181–186.

Simonich, J. C., and Moffat, R. J., 1984, "Liquid Crystal Visualization of Surface Heat Transfer on a Concavely Curved Turbulent Boundary Layer," ASME *Journal of Engineering for Gas Turbines and Power*, Vol. 106, pp. 619–627.

Heat Transfer Through a Pressure-Driven Three-Dimensional Boundary Layer

S. D. Abrahamson
Department of Aerospace Engineering and Mechanics,
University of Minnesota,
Minneapolis, MN 55455

J. K. Eaton
Thermosciences Division,
Department of Mechanical Engineering,
Stanford University,
Stanford, CA 94305

An experimental investigation of heat transfer through a three-dimensional boundary layer has been performed. An initially two-dimensional boundary layer was made three dimensional by a transverse pressure gradient caused by a wedge obstruction, which turned the boundary layer within the plane of the main flow. Two cases, with similar streamwise pressure gradients and different lateral gradients, were studied so that the effect of the lateral gradient on heat transfer could be deduced. The velocity flowfield agreed with previous hydrodynamic investigations of this flow. The outer parts of the mean velocity profiles were shown to agree with the Squire–Winter theorem for rapidly turned flows. Heat transfer data were collected using a constant heat flux surface with embedded thermocouples for measuring surface temperatures. Mean fluid temperatures were obtained using a thermocouple probe. The temperature profiles, when plotted in outer scalings, showed logarithmic behavior consistent with two-dimensional flows. An integral analysis of the boundary layer equations was used to obtain a vector formulation for the enthalpy thickness, **H**

$$\mathbf{H} \triangleq \left[\frac{\int_0^\infty \rho u i_s \, dy}{\rho_\infty i_{i,o} (u_\infty^2 + w_\infty^2)^{1/2}},\ 0,\ \frac{\int_0^\infty \rho w i_s \, dy}{\rho_\infty i_{s,o} (u_\infty^2 + w_\infty^2)^{1/2}} \right]$$

(where i_s is the stagnation enthalpy), which is consistent with the scalar formulation used for two-dimensional flows. Using the vector formulation, the heat transfer data agreed with standard two-dimensional correlations of the Stanton number and enthalpy thickness Reynolds number. It was concluded that although the heat transfer coefficient decreased faster than its two-dimensional counterpart, it was similar to the two-dimensional case. The vector form of the enthalpy thickness captured the rotation of the mean thermal energy flux away from the free-stream direction. Boundary layer three dimensionality increased with the strength of the transverse pressure gradient and the heat transfer coefficients were smaller for the stronger transverse gradient.

1 Introduction

The evolution of energy conversion systems is critically dependent upon understanding the mechanisms of convective heat transfer. Lack of understanding impedes evolution because it necessitates the use of conservative designs, thus leading to lower system performance and higher cost, weight, and complexity. Most heat transfer design involving turbulent flow situations is done using empirical correlations developed in geometries that are either quite application specific or very simple in nature. It is difficult to unravel the information obtained from experiments in detailed geometries due to the complicated, three-dimensional nature of the flowfields. The alternative to investigations of accurate geometries is to achieve understanding through the study of building block flows; the addition of a single new parameter to a well-studied flow geometry.

The current experiment adds the complexity of heat transfer from a constant heat flux surface to a simple, three-dimensional turbulent boundary layer experiment. The earlier experiment (Anderson and Eaton, 1989) was a study of the effect of transverse pressure gradients on an initially two-dimensional turbulent boundary layer. In that experiment the transverse pressure gradient was created by a wedge obstruction as described below. The lateral pressure gradient caused the development of a crossflow, giving the boundary layer a skewed profile as illustrated in Fig. 1.

Generally, the results of Anderson and Eaton (1989) were similar to several previous experiments on simple three-dimensional boundary layers such as the infinite swept wing experiments of Van den Berg and Elsenaar (1972) and Bradshaw and Pontikos (1985) or the obstacle flow of Dechow and Felsch (1977).[1] In summary, comparing three-dimensional results to two-dimensional boundary layers, it has been observed that the ratio between the shear stress and turbulent kinetic energy (the so-called α_1 parameter $= [\overline{u'v'} + \overline{v'w'}]/q^2$) decreased near the wall. The decrease is significant because it indicates a decrease in the ability of the layer to mix momentum by turbulent means. This is emphasized by the fact that the decrease in α_1 was due to both a decrease in the primary shear stresses, $\overline{u'v'} + \overline{v'w'}$, and an increase in the turbulent kinetic energy q^2. So while the flow became more turbulent, its ability to affect the mean flow decreased. As a consequence, the skin friction under the layer decreased. The results of these experiments indicated the need for turbulence models more complex than eddy viscosity models because the shear stress vector was not aligned with the velocity gradient vector. In most cases, the shear stress vector lagged behind the gradient vector, except

Contributed by the Heat Transfer Division for publication in the JOURNAL OF HEAT TRANSFER. Manuscript received by the Heat Transfer Division December 15, 1989; revision received September 25, 1990. Keywords: Forced Convection, Turbulence.

[1] See Anderson and Eaton (1989, 1987) for a complete review of three-dimensional boundary layer experiments.

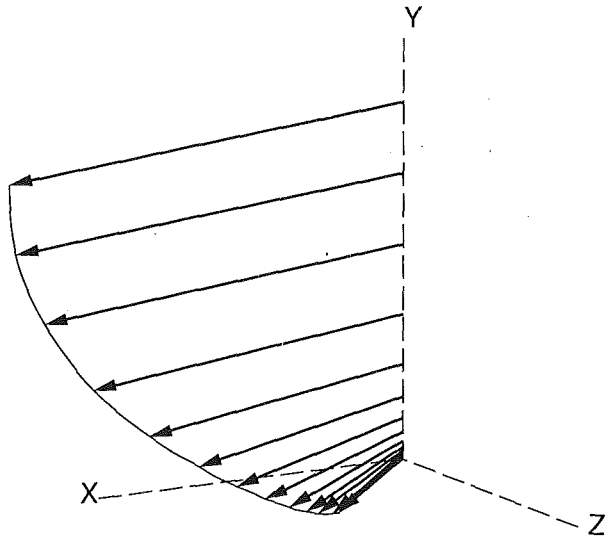

Fig. 1 Three-dimensional boundary layer profile

in flows approaching three-dimensional separation, where the stresses lead the gradient vector (cf. Fernholz and Vagt, 1981). Another common feature of pressure-driven three-dimensional boundary layers is the strong turning that occurs near the wall. This may affect the near-wall turbulence structure, and thus, the heat transfer.

For all the investigations into the fluid mechanics of three-dimensional boundary layers, there are very few data on the heat transfer through them. The data that exist are primarily due to two types of experiments: flows around obstructions and rotating disk flows. Numerous experiments such as those of Eibeck and Eaton (1987), Fisher and Eibeck (1987), Pauley and Eaton (1988), McEwan (1961), and Fiebig et al. (1986) investigated the effects of boundary layer three dimensionality due to the presence of longitudinal vortices on heat transfer. The vortices caused distortion of the boundary layer, including significant skewing of the velocity profiles. They reported enhancement of heat transfer in the downwash regions of the vortices and decreases in the upwash regions. Eibeck and Eaton (1987) concluded that the changes in the heat transfer were due primarily to distortions of the boundary layer by the vortex rather than to the three dimensionality. For example, in the downwash region of the vortices, the boundary layer was significantly thinned compared to undisturbed regions, and it was the thinning with its nonzero mean v component that resulted in heat transfer enhancement. Pauley and Eaton (1988) examined stronger vortices and showed that temperature profiles in regions beneath the longitudinal vortices deviated from the two-dimensional law of the wall while retaining a logarithmic shape. The Stanton numbers were also shown to deviate from two-dimensional correlations. Obstacle flow studies such as those of Fisher and Eibeck (1987), Goldstein et al. (1985), and Blair (1984) have been primarily concerned with downstream effects such as horseshoe vortices and wakes or with the region upstream of the obstacle where the horseshoe vortex forms. The three-dimensional region due to the pressure gradient upstream of the obstacle has generally not been studied. Indeed, the upstream region contains significant spanwise gradients that further complicate the interpretation of results. There have been numerous studies of the heat transfer from the endwall in a turbine blade cascade; Pauley and Eaton (1988) present an extensive review. The results of Graziani et al. (1980) are representative of the general features observed in all the studies. The flow on the endwall is a complex three-dimensional one containing both the complications due to vortices (such as the passage vortex) and the skewed-type three dimensionality near the pressure surface downstream of the passage vortex. In the skewed region they report that Stanton numbers decreased relative to the upstream boundary layer, and lower than the passage vortex region.

The heat transfer from a rotating disk has been studied extensively (Cobb and Saunders, 1956; Young, 1956; Kreith et al., 1959; Richardson and Saunder, 1963; Metzger, 1970; Popiel and Boguslawski, 1975; McComas and Hartnett, 1970; Hartnett 1959). The disk flow is different from the current study because the boundary layer begins, undergoes transition to turbulent, and develops fully in a three-dimensional state, rather than developing as a two-dimensional layer and being driven into its three-dimensional state. The majority of the rotating disk experiments summarize their results in a functional relationship between the Nusselt number and disk Reynolds number. In the turbulent flow regime, Popiel and Boguslawski (1975) showed the Nusselt number to be dependent upon the 0.8 power of the Reynolds number. Using the local disk speed as a velocity scale, Popiel and Bogus-

Nomenclature

a_1 = ratio of turbulent stresses and kinetic energy
C_f = skin friction coefficient
$\dot{E}_{\text{conv}}$ = convective energy flow rate
h = heat transfer coefficient
$\mathbf{H}$ = enthalpy thickness vector
i = enthalpy
i_s = stagnation enthalpy
Pr = Prandtl number
q^2 = turbulent kinetic energy
$\dot{q}_o''$ = wall heat flux
$\dot{q}_{\text{rad}}$ = radiation heat flux
$\dot{q}_{\text{cond}}$ = conduction heat flux (back loss)
r = local radius
Re = Reynolds number
s = streamline coordinate
St = Stanton number
T, t = temperature
$\mathbf{U}$ = velocity vector
u, v, w = velocity components in x, y, z
u', v', w' = fluctuating velocity components in x, y, z
$\overline{u't'}$, $\overline{v't'}$, $\overline{w't'}$ = correlations of fluctuating velocities and t
$\overline{u'v'}$, $\overline{v'w'}$ = correlations of fluctuating velocities
x, y, z = initial mean flow, normal, transverse directions
α = free-stream flow angle (relative to x)
γ = mean flow angle (relative to x)
Δ = scalar enthalpy thickness
ϵ = surface emissivity
ϵ = a small value (defined in context)
Θ = dimensionless temperature
κ_T = von Kármán constant = 0.41
ν = kinematic viscosity
ρ = density
σ = Stefan–Boltzmann constant
ω = disk rotation rate
$( )_o$ = quantity evaluated at the wall
$( )_\infty$ = quantity evaluated in the free-stream
$( )_Y$ = quantity evaluated at y location Y
$( )_+$ = quantity scaled in wall units
$\| \|$ = vector magnitude

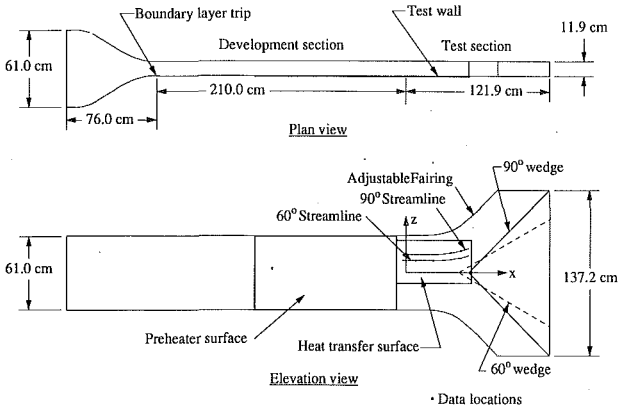

Fig. 2 Experimental facility

lawski's Nusselt number can be converted to a Stanton number

$$\mathrm{St} = 0.0264\ \mathrm{Re}^{-0.2} \text{ where } \mathrm{Re} = \frac{r^2\omega}{\nu}$$

This correlation differs from the standard two-dimensional boundary layer correlation only by the value of the constant, which Kays and Crawford (1980) give as 0.0329. None of the studies about the heat transfer from a rotating disk contain turbulence measurements.

2 Experimental Facility

2.1 Wind Tunnel Description. The wind tunnel used in this experiment was the same facility used by Anderson and Eaton (1989). The tunnel is sketched in Fig. 2. Briefly, the tunnel is blower driven with a 4.8:1 contraction ratio. The boundary layer was grown on the wind tunnel wall after being tripped at the inlet of 12.7 cm × 61 cm × 210 cm long development section. The nominal free-stream velocity was 16.3 m/s with a free-stream turbulence intensity of 0.2 percent. At the inlet to the test section the two-dimensional boundary layer was approximately 3 cm thick, with the shape factor of 1.35 and a momentum thickness Reynolds number of 3570. In the test section, a transverse pressure gradient was created by a wedge whose vertex was on the tunnel centerline and whose axis was normal to the test wall. The pressure gradient turned the mean flow in planes parallel to the test wall. Two wedges were used (one with a 90 deg included angle and the other with a 60 deg included angle) in order to create two different sets of transverse pressure gradients. The fairings in the test section were adjusted to match the experimental configurations of Anderson and Eaton (1989).

The wind-tunnel operations were controlled by a Masscomp MCP-5400 laboratory computer. Velocity measurements were also obtained using the 5400 and a three-hole pressure probe mounted in a computer-controlled two-axis traverse. The probe was calibrated over a range of ±30 deg and was referenced to a static pressure map of the test section. Mean velocities were determined from the measured pressure differences through two fourth-order polynomials fit to calibration data. For further details on the calibration and data reduction for the probe see Anderson and Eaton (1987). Data were collected at four streamwise locations (x = 7.6, 22.9, 38.1, and 45.7 cm, with reference to the beginning of the test section), along the two streamlines used by Anderson and Eaton (1989). These were selected to have similar streamwise pressure gradients with different transverse gradients in order to investigate the onset of boundary layer three dimensionality and the effect of cross-stream pressure gradient. The x locations appropriate to each of the streamlines are shown in Table 1.

Table 1 Streamline coordinates

x(cm)	7.6	22.9	38.1	45.7
$z_{90°}$(cm)	15.00	15.39	16.71	18.39
$z_{60°}$(cm)	10.00	10.11	10.59	11.71

2.2 Heat Transfer Surfaces. Energy for the thermal boundary layer was provided by two heat transfer surfaces, which used resistance heating to provide a uniform heat flux into the flowfield. The first of these surfaces, 120 cm long × 61 cm wide, was placed in the development section of the wind tunnel 80 cm downstream of the trip. At the trailing end of this preheater surface, effects due to the unheated starting length were absent from the thermal boundary layer profile, which agreed with the thermal law of the wall as presented by Kays and Crawford (1980). The preheater surface is described by Eibeck and Eaton (1987). Briefly it consists of a 0.01-cm-thick stainless steel foil bonded to a thin phenolic sheet and mounted on a 1.3-cm balsa backing, which was then further insulated. Type K thermocouples were mounted against the back of the foil to measure surface temperature. AC power was supplied to the narrow sides of the surface through copper bus bars and controlled using a variable transformer.

The design of the heat transfer surface in the test section was slightly different from the preheater. It was 36 cm × 61 cm and the foil was mounted onto a 0.16-cm-thick sheet of epoxy board, which was attached to a laminate of 1.3-cm balsa and 1.3-cm plexiglass. A 3.8-cm-thick insulation-filled cavity was sandwiched between the assembly and a 1.3-cm-thick backing plate of plexiglass. Low voltage AC power was supplied to the surface through two copper bus bars (1.3 cm × 1.3 cm in cross section) attached to each of the short sides of the surface. Because of their size, each bus bar was assumed to be at uniform potential. To measure the foil surface temperature, 25 type K thermocouples are mounted through the first assembly next to the foil. The thermocouples were arranged along five spanwise (z) rows of five. One thermocouple from each row was on the tunnel centerline, one along a streamline selected for the 60 deg configuration, and the other three were mounted around a streamline for the 90 deg case with one on the streamline and the others 1 cm on either side of it. The thermocouples were wired directly to an ice bath reference and the resulting voltages measured by a Fluke model 8520 digital voltmeter through a Fluke scanner, which was controlled by an IBM PC-AT computer through an IEEE-488 bus. Temperature profiles were measured using a 0.003 in. diameter butt-welded thermocouple probe mounted on a hot-wire-type stem.

2.3 Determination of Surface Heat Flux. The convective heat flux was deduced from the difference between the power input to the surface and the losses. The input power was obtained by measuring both the voltage and current. The heating foil was assumed to have uniform thickness so that the local resistance heating matched the average. Thus for the case of the 90 deg configuration the local electrical power input was the product of the voltage and current divided by the surface area. In the case of the 60 deg configuration, the tip of the plexiglass wedge extended over part of the test surface. Since the plexiglass would insulate the constant heat flux surface, it would cause a large local increase in the surface temperature and thus contaminate the measurements, so it was decided to short circuit electrically those portions of the foil covered by the tip of the wedge to the bus bar. The local electrical power input was then deduced from a numerical solution to Laplace's equation on the rectangular domain with the wedge cut out of one end. The solution was obtained using successive overrelaxation and the resulting calculated surface voltages compared well to measured surface voltages. The local power input was computed from the gradient of the surface potential and an

average resistivity deduced from the measured voltage and current input.

There were three loss terms to consider: radiation losses, conduction losses (or back losses), and side losses. The last of these was assumed to have little effect on the measurements because the in-plane temperature gradients were found to be small. The local radiation losses were computed (assuming the plexiglass wind tunnel walls to be essentially a black body for the infrared wavelengths) from

$$\dot{q}_{\text{rad}} = \epsilon\sigma(T_o^4 - T_\infty^4) \tag{2.1}$$

where ϵ is the surface emissivity, σ is the Stefan-Boltzmann constant, T_o is the surface temperature, and T_∞ the temperature of the plexiglass walls, assumed to be the same as free-stream temperature. A surface emissivity of 0.15 was measured using a Devices and Services model AE Emissometer. The conduction losses were determined by calibration in a two-dimensional flow. The wedge was removed from the tunnel and the fairings adjusted to match the slightly favorable pressure gradient (due to the displacement effect) in the development section. Several velocity profiles were measured at different spanwise locations in each of the x-station instrumentation slots to verify flow two dimensionality. The velocity profiles were fit to the law of the wall to deduce the skin friction coefficient. The Stanton number was deduced from temperature profiles measured at the locations of the thermocouples on the two test streamlines and the skin friction coefficient. The profiles were fit to the thermal law of the wall as presented by Kays and Crawford (1980) yielding the Stanton number. The convective heat flux was then determined from the known temperature difference and the Stanton number. The resulting back losses were deduced from the electrical input, radiation losses, and wall heat flux. In order to assure a match in the wall heat flux between the preheater and the test surfaces, the electrical input was modified and the procedure repeated until the fluxes agreed. A back loss heat transfer coefficient was then determined using the computed losses and the difference between the surface and laboratory temperatures so that back losses for each case were computed separately from

$$\dot{q}_{\text{cond}} = h_{\text{local}}(T_o - T_{lab}) \tag{2.2}$$

Once the surface was calibrated, it was then possible to compute the convective heat flux $\dot{q}_o''$ and the Stanton number

$$\text{St} = \frac{\dot{q}_o''}{\rho c \|\mathbf{U}_\infty\| (T_o - T_\infty)} \tag{2.3}$$

2.4 An Enthalpy Thickness Vector. A vector formulation consistent with the two-dimensional scalar formulation of the enthalpy thickness is developed by performing an integral energy analysis on the three-dimensional boundary layer. Consider the steady flow over a smooth flat surface with nonzero mean velocities u_∞ and w_∞. In the general case a surface mass transfer velocity v_o may be applied along with a surface heat flux rate $\dot{q}_o''$. For this analysis we use the control volume sketched in Fig. 3. It has infinitesimal extent in x and z and sufficient extent Y in the y direction to enclose the boundary layer. Applying conservation of energy to the control volume in Fig. 3, where the convective energy fluxes are obtained from Taylor series expansions about the center of the volume, e.g.,

$$\dot{E}_{\text{conv}_2} = \delta z \int_0^Y \rho u i_s \, dy + \delta z \frac{\partial}{\partial x} \int_0^Y \rho u i_s \, dy \frac{\partial z}{2} \tag{2.4}$$

we obtain

$$\frac{\partial}{\partial x} \int_0^Y \rho u i_s \, dy + \frac{\partial}{\partial z} \int_0^Y \rho w i_s \, dy - \rho_o v_o i_{s,o} - \dot{q}_o'' = 0$$

where i_s is the stagnation enthalpy, defined relative to the free-stream stagnation enthalpy

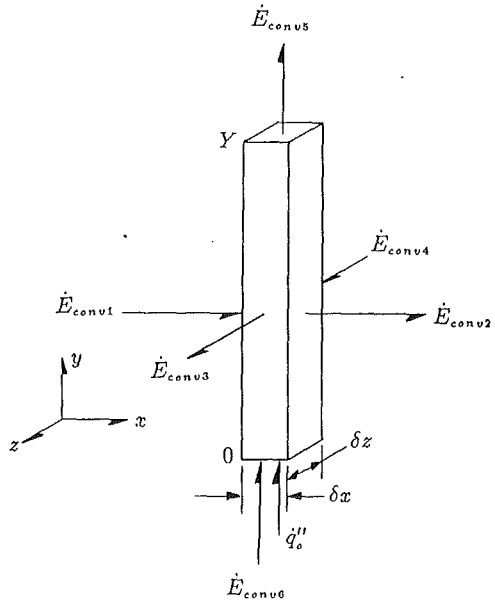

Fig. 3 Control volume for integral analysis

$$i_s = \left(i + \frac{u^2 + w^2}{2}\right) + \left(i_\infty + \frac{u_\infty^2 + w_\infty^2}{2}\right) \tag{2.5}$$

where i is the internal energy. Rearranging,

$$\dot{q}_o'' + \rho_o v_o i_{s,o} = \frac{\partial}{\partial x} \int_0^Y \rho u i_s \, dy + \frac{\partial}{\partial z} \int_0^Y \rho w i_s \, dy \tag{2.6}$$

Now this equation is analogous to the two-dimensional formulation of Kays and Crawford (1980), from which the enthalpy thickness is defined as $\Delta = \int_0^\infty \rho u i_s \, dy$. Here we define an analogous enthalpy thickness vector $\mathbf{H}$

$$\mathbf{H} \triangleq \left[\frac{\int_0^\infty \rho u i_s \, dy}{\rho_\infty i_{s,o} (u_\infty^2 + w_\infty^2)^{1/2}}, 0, \frac{\int_0^\infty \rho w i_s \, dy}{\rho_\infty i_{s,o} (u_\infty^2 + w_\infty^2)^{1/2}} \right] \tag{2.7}$$

Here we note that

$$\frac{\partial}{\partial x} \int_0^\infty \rho u i_s \, dy + \frac{\partial}{\partial z} \int_0^\infty \rho w i_s \, dy = \nabla \cdot (\rho_\infty i_{s,o} \|\mathbf{U}_\infty\| \mathbf{H}) \tag{2.8}$$

so that by substitution into equation (2.6) and normalizing, we obtain

$$\frac{\dot{q}_o''}{\rho_\infty i_{s,o} \|\mathbf{U}_\infty\|} + \frac{\rho_o v_o}{\rho_\infty v_\infty} = \nabla \cdot \mathbf{H} + \mathbf{H} \cdot \nabla (\ln \{\rho_\infty i_{s,o} \|\mathbf{U}_\infty\|\}) \tag{2.9}$$

This formulation reduces to the two-dimensional scalar enthalpy thickness formulation

$$\frac{\dot{q}_o''}{\rho_\infty i_{s,o} u_\infty} + \frac{\rho_o v_o}{\rho_\infty v_\infty} = \frac{d\Delta}{dx} + \Delta \frac{d}{dx} \ln(\rho_\infty i_{s,o} u_\infty) \tag{2.10}$$

when $w(y) = 0$. In the current experiment, $v_o = 0$, so equation (2.9) reduces to

$$\frac{\dot{q}_o''}{\rho_\infty i_{s,o} \|\mathbf{U}_\infty\|} = \nabla \cdot \mathbf{H} + \mathbf{H} \cdot \nabla (\ln \{\rho_\infty i_{s,o} \|\mathbf{U}_\infty\|\}) \tag{2.11}$$

The significance of this vector $\mathbf{H}$ may be determined by examining the definition (2.7). The scalar enthalpy thickness Δ is taken to be a scale of the two-dimensional convective thermal boundary layer, and so should the magnitude of $\mathbf{H}$ be the scale of the three-dimensional boundary layer. The direction of the enthalpy thickness vector is the direction of mean thermal energy flux in the layer.

To calculate the components of $\mathbf{H}$, the u and w components of the velocity profile and the temperature profile were sep-

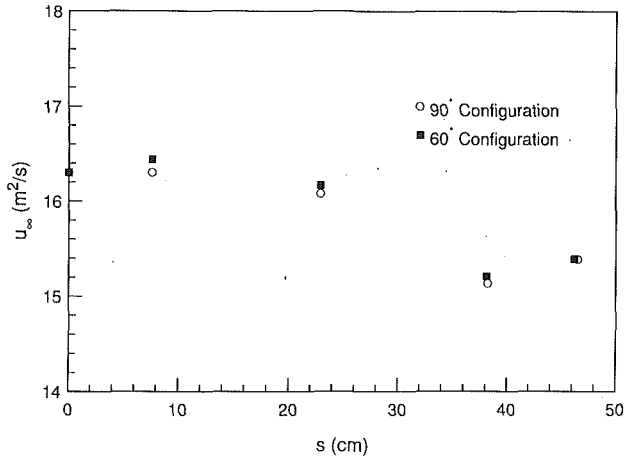

Fig. 4 Free-stream velocity evolution

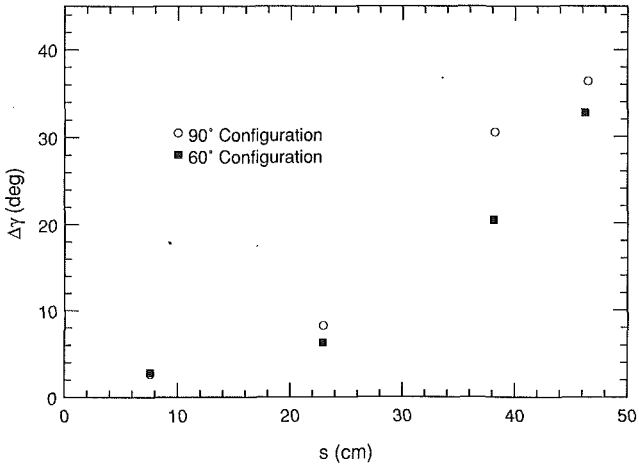

Fig. 7 Skew angle development

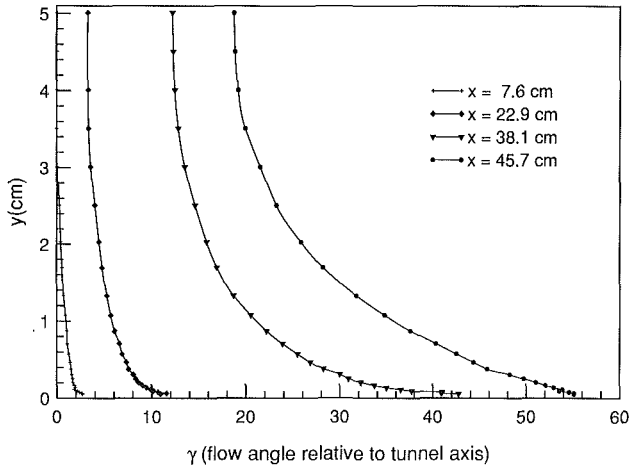

Fig. 5 Mean flow angles: 90 deg case

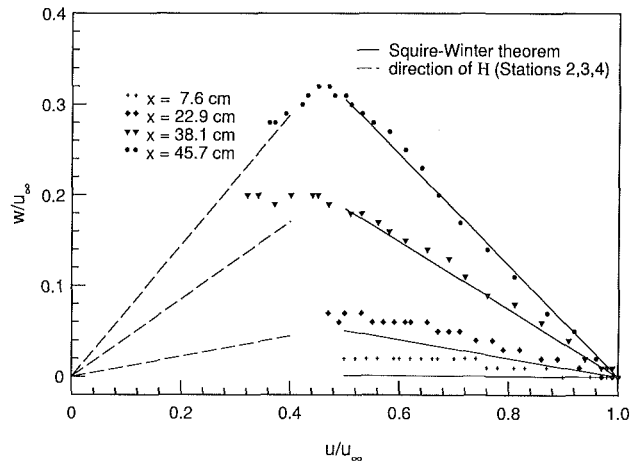

Fig. 8 Local mean velocities: 90 deg case

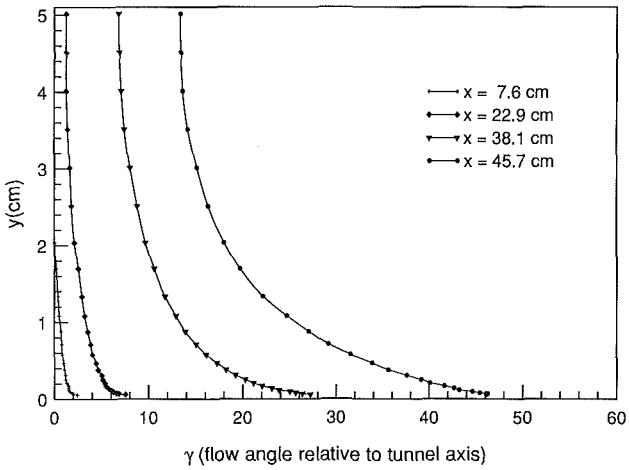

Fig. 6 Mean flow angles: 60 deg case

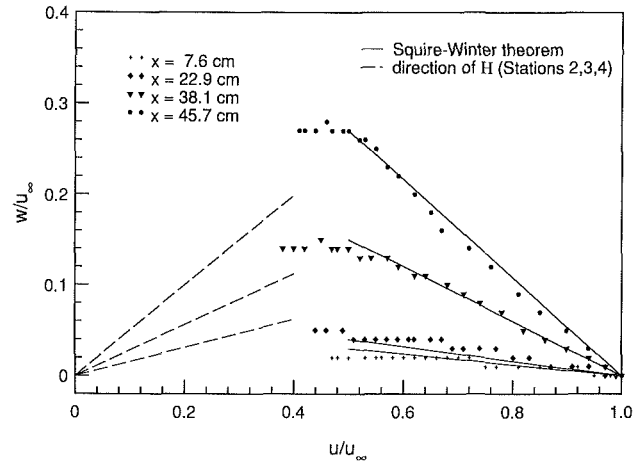

Fig. 9 Local mean velocities: 60 deg case

arately fit to piecewise cubic splines and interpolated onto a dense, logarithmically spaced data set. The interpolated data were then combined according to equation (2.7), integrated, and normalized to form the components of **H**.

2.5 Uncertainty Analysis. Since the data reduction for the enthalpy thickness was computerized from the raw data values, the uncertainty in the enthalpy thickness was most easily determined using the method of Moffat (1988), whereby the uncertainties in each of the raw data values were used directly in the reduction routine to compute the uncertainty due to each measurand in the final result. The primary measurands were pressures and temperatures. The uncertainty in the pressure measurements ranged from 8 percent near the wall to 2 percent in the free stream. The temperature uncertainty was estimated at 0.1°C with typical boundary layer temperature differences on the order of 20°C. The method computed the uncertainties of the enthalpy thickness between 5.6 and 7.9

percent for the different measurement stations, with the free-stream temperatures being the largest contributors to the overall uncertainty.

The uncertainty in the Stanton number was computed using the method outlined by Kline and McClintock (1953) and was found to be 4 percent. The greatest contributor to the Stanton number uncertainty was the estimate of the back losses.

3 Results and Discussion

The presentation of the results is divided into three sections. The first discussion concerns the velocity fields, followed by the temperature fields and then the heat transfer results.

3.1 Velocity Fields Figure 4 is a plot of the development of the free-stream velocity along the streamlines selected for the 90 and 60 deg cases. It shows that the behavior of the free-stream velocity (magnitude) is nearly identical for both cases so the streamwise pressure gradients are similar. Thus comparing the two cases will give a good indication of the effects due to the different transverse pressure gradients. It should be noted that the velocity profiles presented here agree well with those of Anderson and Eaton (1989) and that the current measurements have a slightly better agreement between the free-stream velocities between the two cases. Figures 5 and 6 are plots of the flow angles for the 90 and 60 deg cases, respectively. Comparing the two figures we see several differences: The free-stream flow angles for the 60 deg case were smaller than those of the 90 deg case, indicating that its cross-stream pressure gradient was smaller. As a consequence, the overall skewing in the 60 deg boundary layer was less than in the 90 deg case and it developed more slowly as shown in Fig. 7. The maximum angular differences between the smallest and largest y values were 32.8 and 36.4 deg, respectively.

Figures 8 and 9 show a comparison between velocity fields plotted in the hodograph plane and the theorem of Squire and Winter (1951)

$$\frac{w}{u_\infty} = 2\alpha\left(1 - \frac{u}{u_\infty}\right) \tag{3.1}$$

The Squire–Winter theorem is an inviscid theorem that predicts the modification of mean velocity profiles for rapidly turned flows. In the theorem, the changes in the mean velocity profiles are due to the rotation of the mean vorticity. The plot shows that the behavior of the outer portions of the boundary layer profiles is well predicted by the theorem, indicating that the outer layer behaves in an inviscid manner. However, the skin friction changes direction, creating a disturbance that grows outward with downstream distance. Anderson and Eaton (1989) report that the turbulence in the near-wall regions of these profiles was strongly modified. They noted that primary turbulent shear stresses ($\overline{u'v'}$, $\overline{v'w'}$) were strongly suppressed near the wall and even though there was a slight increase in $\overline{v'w'}$ it was small compared to the drop in $\overline{u'v'}$. They also reported that the region of reduced shear stress grew as the flow moved downstream. Thus the ability of the turbulence field to redistribute momentum was reduced. By analogy, one would expect the near-wall region to have a reduced ability to mix thermal energy by turbulent means. It should be noted that there was a rather pronounced increase in the turbulence kinetic energy as the flow proceeds downstream primarily due to the increases in the $\overline{w'^2}$ component. However, the turbulent transport of thermal energy should be of the form

$$\frac{\partial}{\partial x}(\overline{u't'}) + \frac{\partial}{\partial y}(\overline{v't'}) + \frac{\partial}{\partial z}(\overline{w't'})$$

and since Anderson and Eaton reported that the spanwise gradients were relatively weak, the increase in w activity should have little effect upon the thermal energy transport.

3.2 Temperature Profiles. Figure 10 is a plot of the dimensionless temperature versus the Reynolds number based on u_∞. If this were a two-dimensional layer, we would plot these in wall coordinates (t^+, u^+). However, in this case, the value of the wall velocity scale is not known, but we can still scale the profiles in a similar fashion. Note that in the two-dimensional case

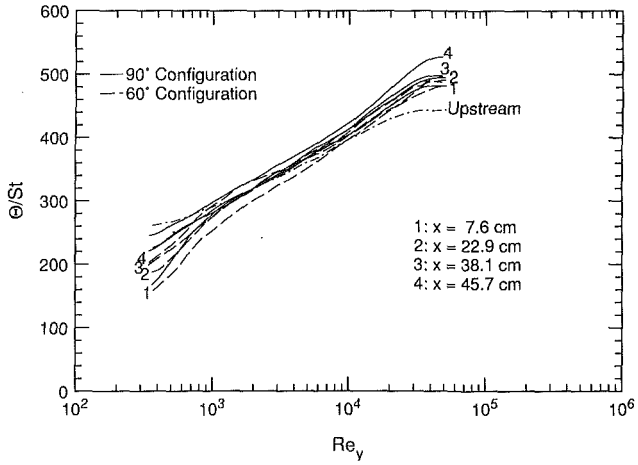

Fig. 10 Temperature profiles

$$t^+ = \frac{\Theta\sqrt{\frac{C_f}{2}}}{\mathrm{St}}; \quad \Theta = \frac{t_o - t(y)}{t_o - t_\infty}$$

and

$$y^+ = \frac{yU_\infty}{\nu}\sqrt{\frac{C_f}{2}} = \mathrm{Re}_y\sqrt{\frac{C_f}{2}}$$

we plot the profiles in outer variables by omitting the skin friction component. In the two-dimensional case, changes in the skin friction result in slight modifications to the slope of the Θ/St versus Re_y curve. Anderson and Eaton (1989) measured the magnitude of the skin friction along the 90 deg streamline and reported $|C_f| = 0.0029 \pm 0.0002$. Using this result in the standard log-law form

$$\frac{\Theta}{\mathrm{St}} = \frac{1}{\kappa_T\sqrt{\frac{C_f}{2}}}\log(\mathrm{Re}_y) + B \tag{3.2}$$

we can estimate the effects to a two-dimensional layer due to small variations in C_f. We expand the first term on the right-hand side using $C_f = 0.0029\,[1 \pm \epsilon]$

$$\frac{\Theta}{\mathrm{St}} = \frac{26.3}{\kappa_T[1\pm\epsilon]^{-1/2}}\log(\mathrm{Re}_y) + \ldots$$

$$= \frac{26.3}{\kappa_T}\left[1 \pm \frac{1}{2}\epsilon - \frac{1}{16}\epsilon^2 + \text{h.o.t.}\right]\log(\mathrm{Re}_y) + \ldots$$

$$= \frac{26.3}{\kappa_T}[1 \pm 0.04 - 0.004 + \text{h.o.t.}]\log(\mathrm{Re}_y) + \ldots$$

So in a two-dimensional layer we would expect to see only about a 4 percent chance in the slopes due to variations in the skin friction. This does not, however, address the issue of the appropriateness of two-dimensional scalings in a three-dimensional boundary layer. In Fig. 10 we see that all of the curves, including the upstream (two-dimensional) profile, have similar slopes in the logarithmic region except for the first x station in the 60 deg case. From a least-squares fit of the log regions of all but this one curve to the relation

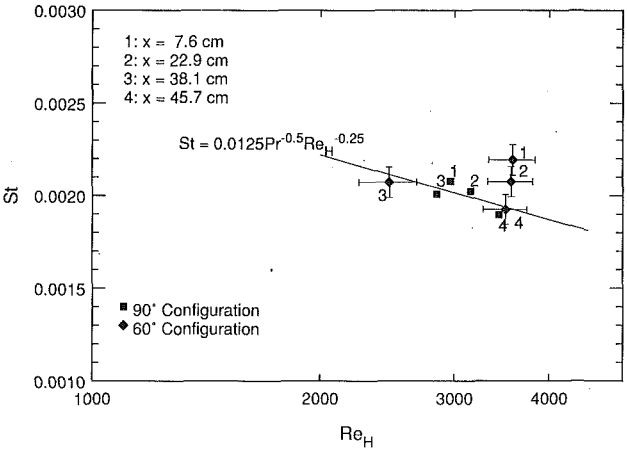

Fig. 11 Stanton number development

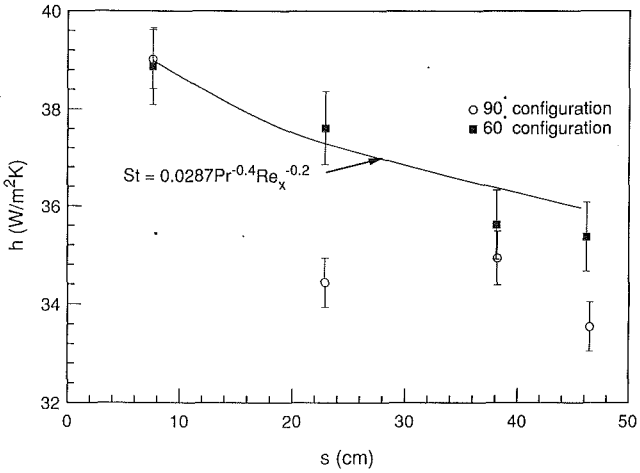

Fig. 12 Heat transfer coefficient

$$\frac{\Theta}{\mathrm{St}}=\frac{1}{k}\log(\mathrm{Re}_y)+B' \tag{3.3}$$

we find $k = 0.0191$ and $B' = -79.61$. So it appears that the temperature profiles in the three-dimensional boundary layer obey the two-dimensional scalings quite well (with the exception of the first station in the 60 deg case).

3.3 Stanton Number and Enthalpy Thickness. Figure 11 is a plot of the Stanton number versus the Reynolds number based on the magnitude of the enthalpy thickness and free-stream velocity vectors ($\|\mathbf{U}_\infty\|\,\|\mathbf{H}\|/\nu$) for both the 60 and 90 deg cases. Uncertainty bands are shown for the 60 deg case only. For comparison, the two-dimensional correlation given by Kays and Crawford (1980) is also plotted. With the exception of the first two x stations in the 60 deg case the three-dimensional cases lie very close to the two-dimensional correlation, within the range of certainty of the results. (Because the three dimensionality is minimal at the first two x stations one would expect them to have best agreement with the two-dimensional correlation. However, the distortion of the test surface potential field by the 60 deg wedge caused a step increase in the wall heat flux of 8 percent, leading to larger Stanton numbers of ~12.5 percent 2.1 boundary layer thicknesses downstream of the step increase and ~7.8 percent 6.4 thicknesses downstream. Note that the third x station is ~11 thickness downstream.) Johnston (1960) hypothesized that the very near-wall region of a three-dimensional boundary layer contained collateral flow. Others, such as Klinksiek and Pierce (1970), later showed that although the flow is not exactly collateral, it is close. Thus the near-wall flow is essentially two dimensional. The outer portions of the boundary layer agree well with the Squire–Winter (1951) theorem; therefore we conclude that in the outer regions, the turbulent structure, and therefore the transport mechanisms, were not substantially modified, but rather rotated. Since the heat transfer is strongly controlled by the turbulent mechanisms close to the wall, Johnston's hypothesis indicates that the heat transfer should be similar to the two-dimensional case, but not aligned with the free-stream flow direction. In the formulation of the enthalpy thickness above, it was concluded that the orientation of the enthalpy thickness vector should be aligned with the principal direction of the energy flux. If this conclusion is correct, then the orientation of the vector should be in line with the near wall flow. We can test this idea by comparing the profiles in the polar plots (Figs. 8 and 9). In both of these plots at the last two x stations, the behavior of the near-wall flow could be interpreted as tending toward the origin, indicating collateral flow. The direction of the enthalpy thickness vector has been added to the plot. The line for the fourth station in the 90 deg case agrees well with the data, and the others are close but low. In the determination of the enthalpy thickness, the major contribution to the result is from close to the wall, but the effect of the outer portion of the boundary layer is significant still. The outer region effect would skew the orientation of the enthalpy thickness vector away from the collateral region toward the free stream as shown in the figure.

Figure 11 also shows that the relationship between St and Re_H does not follow the development of St in either x or s. For both cases, Re_H and $x = 38.1$ cm is less than Re_H at the other measurement stations. This effect is primarily due to the adverse streamwise pressure gradient, which results in a reduced streamwise velocity $\|\mathbf{U}_\infty\|$ and, because of the form of $\mathbf{H}$ (equation (2.7)) results in similarly reduced enthalpy thickness magnitude. Figure 12 is a plot of the development of the heat transfer coefficient. The values have been plotted dimensionally in order to remove the u effects on St from the h effects. Also plotted in the figure is the heat transfer coefficient obtained from

$$\mathrm{St}=0.0287\mathrm{Pr}^{-0.4}\mathrm{Re}_x^{-0.2} \tag{3.4}$$

(Kays and Crawford, 1980). In order to fit equation (3.4), a value for x at the exit of the development section ($s = 0$) was obtained by matching the measured Stanton number to equation (3.4). The curve was obtained using a constant free-stream velocity instead of the variation shown in Fig. 4. The figure shows that the effect of the transverse pressure gradient was to decrease the heat transfer coefficient dramatically. The behavior in the 60 deg configuration was close to the two-dimensional correlation with a drop as flow three dimensionality developed downstream, whereas the behavior of the 90 deg case showed an immediate drop due to the stronger lateral pressure gradient. Thus while the formulation of the enthalpy thickness captures the changes in the orientation of the near-wall region and indicates that the heat transfer mechanisms in the three-dimensional case are not too far distant from the two-dimensional one, it does not illustrate the decreased ability of the three-dimensional boundary layer to transfer thermal energy.

4 Conclusions

In the case of a two-dimensional boundary layer driven to three dimensionality, a vector formulation for the enthalpy thickness is necessary to capture the rotation of the thermal energy flux away from the free-stream. When the data are reduced using the vector form, the heat transfer was shown to lie near the standard two-dimensional correlation between the enthalpy thickness and the Stanton number. It was hypothesized that this agreement was due to the fact that the near-wall region, which controls the heat transfer, was dominated

by two-dimensional transport mechanisms. The effect of the lateral pressure gradient was seen to be a decrease in the heat transfer coefficient with increased pressure gradient. The decrease in the heat transfer coefficient is consistent with the results from hydrodynamic investigations of three-dimensional boundary layers, which showed increased near-wall turbulence energy with decreased near-wall momentum transport.

Acknowledgments

The authors gratefully acknowledge the support of the Department of Energy Basic Energy Sciences Program (Contract # DEFG0386ER-13608). In addition we would like to thank Mr. Howard Littell for his computation of the surface potential field used to determine the electrical input in the 60 deg case.

References

Anderson, S., and Eaton, J., 1987, "An Experimental Investigation of Pressure Driven Three-Dimensional Turbulent Boundary Layers," Thermosciences Division Report MD-49, Dept. of Mechanical Engineering, Stanford University, Stanford, CA.

Anderson, S., and Eaton, J., 1989, "Reynolds Stress Development in Pressure-Driven Three Dimensional Turbulent Boundary Layers," *J. Fluid Mech.*, Vol. 202, pp. 263–294.

Blair, M., 1984, "Heat Transfer in the Vicinity of a Large-Scale Obstruction in a Turbulent Boundary Layer," Paper No. AIAA-84-1723.

Bradshaw, P., and Pontikos, N., 1985, "Measurements in the Turbulent Boundary Layer on an 'Infinite' Swept Wing," *J. Fluid Mech.*, Vol. 159, pp. 105–130.

Cobb, E., and Saunders, O., 1956, "Heat Transfer From a Rotating Disk," *Proc. R. Soc. London*, Ser. A, pp. 343–351.

Dechow, R., and Felsch, K., 1977, "Measurements of the Mean Velocity and of the Reynolds Stress Tensor in a Three-Dimensional Turbulent Boundary Layer Induced by a Cylinder Standing on a Wall," *Proc. Symposium on Turbulent Shear Flows*, Vol. I, Apr., University Park, PA.

Eibeck, P., and Eaton, J., 1987, "Heat-Transfer Effects of a Longitudinal Vortex Embedded in a Turbulent Boundary Layer," ASME JOURNAL OF HEAT TRANSFER, Vol. 109, No. 1, pp. 16–24.

Fernholz, H., and Vagt, J., 1981, "Turbulence Measurements in an Adverse Pressure Gradient Three Dimensional Turbulent Boundary Layer Along a Circular Cylinder," *J. Fluid Mech.*, Vol. 111, pp. 233–269.

Fiebig, M., Kallweit, P., and Mitra, N., 1986, "Wing Type Vortex Generators for Heat Transfer Enhancement," *Proc. Eighth International Heat Transfer Conference*, Vol. 6, San Francisco, CA.

Fisher, E., and Eibeck, P., 1987, "The Influence of a Horseshoe Vortex on Local Convective Heat Transfer Rates," *Proc. ASME Winter Annual Meeting*, Boston, MA.

Goldstein, R. J., Chyu, M. K., and Hain, R. C., 1985, "Measurement of Local Mass Transfer on a Surface in the Region of the Base of a Protruding Cylinder With a Computer-Controlled Data Acquisition System," *Int. J. Heat Mass Transfer*, Vol. 28, pp. 977–985.

Graziani, R., Blair, M., Taylor, J., and Mayle, R., 1980, "An Experimental Study of Endwall and Airfoil Surface Heat Transfer in a Large Scale Turbine Blade Cascade," ASME *Journal of Engineering for Power*, Vol. 102.

Hartnett, J., 1959, "Heat Transfer From a Non-isothermal Disk Rotating in Still Air," ASME *Journal of Applied Mechanics.*, Vol. 26, pp. 672–673.

Johnston, J., 1960, "On the Three-Dimensional Turbulent Boundary Layer Generated by Secondary Flow," ASME *Journal of Basic Engineering.*, Vol. 82.

Kays, W., and Crawford, M., 1980 *Convective Heat and Mass Transfer*, 2nd ed., McGraw-Hill, New York.

Kline, S., and McClintock, F., 1953, "Describing Uncertainties in Single-Sample Experiments," *Mech. Engr.*, Jan., pp. 3–8.

Klinksiek, W., and Pierce, F., 1970, "Simultaneous Lateral Skewing in a Three Dimensional Turbulent Boundary-Layer Flow," ASME *Journal of Basic Engineering*, Vol. 92, pp. 83–92.

Kreith, F., Taylor, J., and Chong, J., 1959, "Heat and Mass Transfer From a Rotating Disk," ASME JOURNAL OF HEAT TRANSFER, Vol. 81, pp. 95–105.

McComas, S., and Hartnett, J., 1970, "Temperature Profiles and Heat Transfer Associated With a Single Disk Rotating in Still Air," *Proc. 4th Ann. Int'l. Heat Transfer Conf.*

McEwen, A., 1961, "Turbulent Convective Heat Transfer From a Flat Plate and Its Improvement Using Vortex Generators," Masters Thesis, Dept. of Mechanical Engineering, University of Melbourne, Australia.

Metzger, D., 1970, "Heat Transfer and Pumping on a Rotating Disk With Freely Induced and Forced Cooling," ASME *Journal of Engineering for Power*, Vol. 92, pp. 342–348.

Moffat, R., 1988, "Describing the Uncertanties in Experimental Results," *Experimental Thermal and Fluid Science*, Vol. 1.

Pauley, W., and Eaton, J., 1988, "The Fluid Dynamics and Heat Transfer Effects of Streamwise Vortices Embedded in a Turbulent Boundary Layer," Thermosciences Division Report MD-51, Dept. Mechanical Engineering, Stanford University, Stanford, CA.

Popiel, CzO., and Boguslawski, L., 1975, "Local Heat Transfer Coefficients on a Rotating Disk in Still Air," *Int. J. Heat Mass Transfer*, Vol. 18, pp. 167–170.

Richardson, P., and Saunders, O., 1963, "Studies of Flow and Heat Transfer Associated With a Rotating Disc," *J. of Mech. Eng. Sci.*, Vol. 5, pp. 336–342.

Squire, H., and Winter, K., 1951, "The Secondary Flow in a Cascade of Airfoils in a Non-uniform Stream," *J. Aero. Sciences*, Vol. 18, pp. 271–277.

Van den Berg, B., and Elsenaar, A., 1972, "Measurements in a Three Dimensional Incompressible Turbulent Boundary Layer in an Adverse Pressure Gradient Under Infinite Swept Wing Conditions," NLR TR 72092 U.

Young, R., 1956, "Heat Transfer From a Rotating Plate," *Trans. ASME*, Vol. 78, pp. 1163–1168.

Transient Analysis on the Onset of Thermal Instability in the Thermal Entrance Region of a Horizontal Parallel Plate Channel

F. S. Lee
Ph. D. Candidate.

G. J. Hwang
Professor.
Mem. ASME

Department of Power Mechanical Engineering,
National Tsing Hua University,
Hsinchu, Taiwan 30043

A transient analysis on the onset of thermal instability in the thermal entrance region of a horizontal parallel plate channel, where the lower plate is heated isothermally, is presented. A novel time-dependent approach based on a three-dimensional linear stability theory is developed to determine the neutral stability position, where a disturbance neither grows nor decays with time. The range of parameters Pe = 30, 40, 60, 80, and 100, and Pr = 0.2, 0.7, 1.0, and 7.0 are covered in the study. One finds that increasing Prandtl number has a destabilizing effect on the flow for a fixed Peclet number along the streamwise direction. On the other hand, increasing Peclet number or Reynolds number tends to stabilize the flow. As the onset of thermal instability moves upstream, the critical Rayleigh number and the critical wave number are increased. The result shows a good agreement with the previous experimental investigations.

Introduction

The mixed convection phenomenon occurs when the effect of the buoyancy force in forced convection or the effect of forced flow in free convection becomes significant. Buoyancy-driven secondary flow can enhance the forced convection heat transfer in compact heat exchangers and flat plate solar collectors, and in the cooling of electronic components. Since thermal instability will occur in the development region, the mixed convection effect is also important in a horizontal chemical vapor deposition (CVD) reactor. The buoyancy force on the laminar internal flow induces a secondary flow, which can reduce the thermal entry length, enhance the heat transfer, and promote an early transition to turbulence. The thermal instability of mixed convection in horizontal parallel-plate channel or rectangular ducts has been studied theoretically and experimentally by many investigators.

Mori and Uchida (1966) applied a linear stability analysis to determine the onset of an infinitesimally small disturbance in the form of longitudinal vortex rolls for fully developed laminar flow between parallel plates, with the bottom and top surfaces heated and cooled, respectively. The critical Rayleigh numbers corresponding to the onset of the first and the second type rolls were determined. Nakayama et al. (1970) studied the conditions marking the onset of longitudinal vortices for fully developed laminar flow between horizontal parallel plates with nonlinear basic temeperature profile.

Using a linear stability theory, Hwang and Cheng (1973) determined the conditions marking the onset of longitudinal vortex rolls in the thermal entrance region of a horizontal parallel plate channel heated from below. They found that for $Pr \geq 0.7$ the flow is more stable in the thermal entrance region than that in the fully developed region, but the situation is just the opposite for small Prandtl numbers, say $Pr \leq 0.2$. Cheng and Wu (1976) studied the effect of axial heat conduction on the onset of instability of a channel flow. They found that the transverse vortex disturbances are preferred over the longitudinal vortex disturbances for $Pe \leq 1$ and $Pr \geq 1$ (low Re) in the developing region upstream and downstream of the thermal entrance.

Incropera and Schutt (1985) used a laminar three-dimensional, steady-state model to determine the nature and effect of thermally driven secondary flows in a horizontal channel. Incropera et al. (1986) performed a theoretical prediction and experimental investigation for water flow of a duct. The results showed that the onset of thermal instability is approximately independent of Reynolds number, Prandtl number, aspect ratio, and whether a uniform temperature or heat flux is maintained at the bottom surface, while weakly dependent on the velocity profile development only. Mahaney et al. (1987) employed a vectorized finite difference marching technique and calculations were performed for water in the combined entry region. They found that as Gr^* increases, the onset of instability is advanced and heat transfer enhancement relative to the forced convection limit is increased. The number of vortices increases with increasing Grashof number and aspect ratio.

Akiyama et al. (1971) studied experimentally the onset of longitudinal vortex rolls for the fully developed laminar flow of air between two horizontal flat plates subjected to a uniform axial wall temperature gradient. Ostrach and Kamotani (1975) measured the heat transfer rate for a fully developed forced convection flow between two horizontal plates. Hwang and Liu (1976) studied the onset of longitudinal vortices due to buoyant force in the thermal entrance region of a horizontal parallel-plate channel heated from below to verify the theoretical prediction of Hwang and Cheng (1973). They observed that the critical Rayleigh number from flow visualization was 1.4 to 10 times higher than the theoretical results. Kamotani and Ostrach (1976) and Kamotani et al. (1979) performed experiments for air flow in the thermal entrance region of a horizontal parallel-plate channel. They determined the onset of thermal instability from visualization of the secondary flow. Measurements of Nusselt numbers and temperature distributions indicated that the critical Rayleigh numbers agree reasonably with those of Hwang and Liu (1976).

Osborne and Incropera (1985) performed an experiment to determine hydrodynamic and thermal conditions in laminar water flow between horizontal parallel plates with a uniform asymmetric heat flux. Flow visualization and temperature

Contributed by the Heat Transfer Division for publication in the JOURNAL OF HEAT TRANSFER. Manuscript received by the Heat Transfer Division December 21, 1989; revision received June 18, 1990. Keywords: Flow Instability, Forced Convection, Numerical Methods.

measurements revealed the existence of a bouyancy-driven flow that strongly influenced bottom plate conditions, but had a weak influence on top plate conditions. Heat transfer at the top plate was dominated by forced convection, while heat transfer at the bottom plate was characterized by mixed convection. Incropera et al. (1987) detected the secondary flow by flow visualization and heat transfer measurement for water flow. They found that the wavelength of vortex decreases continuously with increasing Gr_D^*. Maughan and Incropera (1987) studied the effect of surface heat flux and channel orientation on the local Nusselt number. The onset of instability was delayed by decreasing the Grashof number and/or by increasing the Reynolds number and the inclination angle. Chiu and Rosenberger (1987) measured the onset point positions of instability from velocity profile by laser-Doppler anemometry. They also observed unsteady longitudinal convection rolls. Ouazzani et al. (1989) found that in the range $2000 < Ra < 12{,}000$, $1 < Re < 9$, and $Pr = 0.7$, there are transverse rolls for low Reynolds number and longitudinal vortices for higher Reynolds number.

In this paper a transient three-dimensional linear stability theory is developed to determine the onset of thermal instability in the thermal entrance region of a horizontal parallel plate channel, where the lower plate is heated isothermally. In this study, the time-dependent approach is a mechanism for obtaining the desired result. The perturbation mode is expressed as time dependent and a function of space variables X, Y, and Z. Therefore normalized transient perturbation equations in the normal and streamwise directions are derived, and then solved to determine the neutral stability condition.

Theoretical Analysis

Consider a fully-developed laminar flow of an incompressible viscous fluid in the thermal entrance region between horizontal parallel plates with gap h, where the lower plate is heated isothermally for $X \geq 0$. The inlet fluid temperature is constant and equals the upper wall temperature T_0. The thermodynamic properties of fluid are assumed constant and the Boussinesq approximation is used. The physical configuration and coordinate system are shown in Fig. 1.

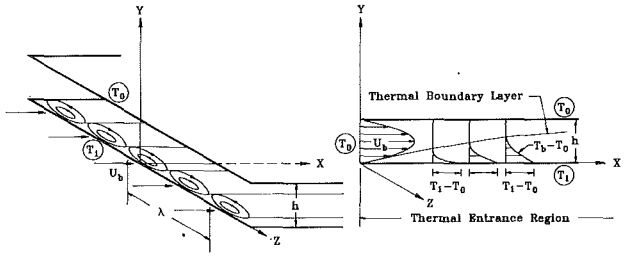

Fig. 1 Physical configuration and coordinate system

The governing equations for the basic flow are

$$U_b \frac{\partial T_b}{\partial X} = \alpha \left(\frac{\partial^2 T_b}{\partial X^2} + \frac{\partial^2 T_b}{\partial Y^2} \right) \tag{1}$$

$$U_b = 6U_m \left[\left(\frac{Y}{h} \right) - \left(\frac{Y}{h} \right)^2 \right] = U_m \phi_u \tag{2}$$

where U_m is the mean velocity and ϕ_u is a dimensionless basic velocity function. By introducing dimensionless variables $x = X/\mathrm{Pe}h$, $y = Y/h$, $z = Z/h$, $\phi_\theta = (T_b - T_0)/(T_1 - T_0)$ and the parameter $\mathrm{Pe} = U_m h/\alpha$, the following normalized equation results:

$$\phi_u \frac{\partial \phi_\theta}{\partial x} = \frac{1}{\mathrm{Pe}^2} \frac{\partial^2 \phi_\theta}{\partial x^2} + \frac{\partial^2 \phi_\theta}{\partial y^2} \tag{3}$$

The boundary conditions are

$$\phi_\theta(0, y) = \phi_\theta(\infty, y) - (1 - y) = \phi_\theta(x, 0) - 1 = \phi_\theta(x, 1) = 0 \tag{4}$$

for $x \geq 0$ and $0 \leq y \leq 1$.

Perturbation Equations

For forced convection flow in the thermal entrance region, there is a nonlinear basic temperature distribution $T_b - T_0$ in

Nomenclature

a = wave number of longitudinal vortex $= 2\pi h/\lambda$
D = dimensionless continuity variable
g = gravitational acceleration
Gr = Grashof number based on $h = \beta g (T_1 - T_0) h^3/\nu^2$
h = distance between two parallel plates
n = number of time step
NI, NJ = number of grids in streamwise and normal directions
p', P, P_b = perturbation, resultant, and basic pressures
Pe = Peclet number $= U_m h/\alpha$
Pr = Prandtl number $= \nu/\alpha$
Ra = Rayleigh number $= \beta g (T_1 - T_0) h^3/\nu\alpha$
Re = Reynolds number $= U_m h/\nu$
t = dimensionless time
t', T, T_b = perturbation, resultant, and basic temperatures
u, v, w = dimensionless amplitude functions of perturbation velocity in x, y, and z directions
u', v', w' = streamwise, normal, and spanwise perturbation velocities
$\hat{u}, \hat{v}, \hat{w}$ = dimensionless streamwise, normal, and spanwise perturbation velocities
U, V, W = resultant streamwise, normal, and spanwise velocities
U_b, U_m = streamwise basic and mean velocities
x, y, z = dimensionless streamwise, normal, and spanwise coordinates $= X/\mathrm{Pe}h$, Y/h, and Z/h
X, Y, Z = streamwise, normal, and spanwise coordinates
α = thermal diffusivity of fluid
β = volumetric coefficient of thermal expansion
Δ = difference
θ = dimensionless perturbation temperature
λ = wavelength
ν = kinematic viscosity of fluid
ρ = density of fluid
τ = time
ϕ_u = dimensionless basic streamwise velocity
ϕ_θ = dimensionless basic temperature

Superscripts

$'$ = perturbation quantity
$\hat{}$ = dimensionless perturbation quantity
$*$ = critical condition
$\underline{0}$ = initial state
$\bar{}$ = root mean square value

Subscripts

b = basic flow quantity
c = characteristic quantity
m = mean flow
w = condition at wall
x = quantity based on streamwise distance
0 = entrance
1 = lower plate

Table 1 Comparison of perturbation modes on longitudinal vortex instability in developing flow

	Configuration	Pr	Perturbation modes
Hwang and Cheng (1973)	Horizontal channel	$0.1 \sim \infty$	$\hat{f}(y, z) = f(y) \cdot e^{iaz}$
Cheng and Wu (1976)	Horizontal channel	$0.1 \sim 100$	$\hat{f}(y, z) = f(y) \cdot e^{iaz}$
Moutsoglou et al. (1981)	Horizontal plate	0.7, 7	$\hat{f}(y, z) = f(y) \cdot e^{iaz}$
Chen et al. (1982)	Inclined plate	0.7	$\hat{f}(y, z) = f(y) \cdot e^{iaz}$
Yoo et al. (1987)	Horizontal plate	∞	$\hat{f}(x, y, z) = f(x, y) \cdot e^{iaz}$
Present analysis	Horizontal channel	$0.2 \sim 7$	$\hat{f}(x, y, z, t) = f(x, y, t) \cdot e^{iaz}$

the normal direction near the lower plate. The distribution becomes linear in the thermally fully developed region. When the buoyant flow is superimposed on the forced convection flow, the temperature distribution will be changed; even in the fully developed region the linear temperature profile no longer exists. The perturbation quantities are superimposed on the basic flow quantities as

$$\begin{aligned} U &= U_b(Y) + u'(X, Y, Z, \tau) \\ V &= v'(X, Y, Z, \tau) \\ W &= w'(X, Y, Z, \tau) \\ P &= P_b(X, Y) + p'(X, Y, Z, \tau) \\ T &= T_b(X, Y) + t'(X, Y, Z, \tau) \end{aligned} \tag{5}$$

The above perturbation quantities are considered as functions of space variables X, Y, and Z and time variable τ. By substituting the resultant velocity, pressure, and temperature (equation (5)) into the conservation equations for mass, momentum, and energy, and subtracting the basic flow equation, we have the following linearized perturbation equations:

$$\frac{\partial u'}{\partial X} + \frac{\partial v'}{\partial Y} + \frac{\partial w'}{\partial Z} = 0 \tag{6}$$

$$\frac{\partial u'}{\partial \tau} + U_b \frac{\partial u'}{\partial X} + v' \frac{\partial U_b}{\partial Y} = -\frac{1}{\rho} \frac{\partial p'}{\partial X} + \nu \nabla_1^2 u' \tag{7}$$

$$\frac{\partial v'}{\partial \tau} + U_b \frac{\partial v'}{\partial X} = -\frac{1}{\rho} \frac{\partial p'}{\partial Y} + \nu \nabla_1^2 v' + \beta g t' \tag{8}$$

$$\frac{\partial w'}{\partial \tau} + U_b \frac{\partial w'}{\partial X} = -\frac{1}{\rho} \frac{\partial p'}{\partial Z} + \nu \nabla_1^2 w' \tag{9}$$

$$\frac{\partial t'}{\partial \tau} + U_b \frac{\partial t'}{\partial X} + u' \frac{\partial T_b}{\partial X} + v' \frac{\partial T_b}{\partial Y} = \alpha \nabla_1^2 t' \tag{10}$$

where $\nabla_1^2 = \dfrac{\partial^2}{\partial X^2} + \dfrac{\partial^2}{\partial Y^2} + \dfrac{\partial^2}{\partial Z^2}$.

After introducing the following dimensionless variables and parameters: $X = [\mathrm{Pe}h]x$, $Y = [h]y$, $Z = [h]z$, $u' = [U_m]\hat{u}$, $v' = [U_m]\hat{v}$, $w' = [U_m]\hat{w}$, $U_b = [U_m]\phi_u$, $T_b - T_0 = [\Delta T]\phi_\theta$, $t' = [\Delta T]\hat{\theta}$, $\tau = [t_c]t$, $p' = [p_c]\hat{p}$

where $\Delta T = T_1 - T_0$, $t_c = h^2/\nu$, $p_c = \rho\nu U_m/h$, and $\mathrm{Ra} = \beta g \Delta T h^3/\alpha\nu$, the dimensionless perturbation equations become

$$\frac{1}{\mathrm{Pe}} \frac{\partial \hat{u}}{\partial x} + \frac{\partial \hat{v}}{\partial y} + \frac{\partial \hat{w}}{\partial z} = 0 \tag{11}$$

$$\frac{\partial \hat{u}}{\partial t} + \frac{1}{\mathrm{Pr}} \phi_u \frac{\partial \hat{u}}{\partial x} + \mathrm{Re}\ \hat{v} \frac{\partial \phi_u}{\partial y} = -\frac{1}{\mathrm{Pe}} \frac{\partial \hat{p}}{\partial x} + \nabla_2^2 \hat{u} \tag{12}$$

$$\frac{\partial \hat{v}}{\partial t} + \frac{1}{\mathrm{Pr}} \phi_u \frac{\partial \hat{v}}{\partial x} = -\frac{\partial \hat{p}}{\partial y} + \nabla_2^2 \hat{v} + \frac{\mathrm{Ra}}{\mathrm{Pe}} \hat{\theta} \tag{13}$$

$$\frac{\partial \hat{w}}{\partial t} + \frac{1}{\mathrm{Pr}} \phi_u \frac{\partial \hat{w}}{\partial x} = -\frac{\partial \hat{p}}{\partial z} + \nabla_2^2 \hat{w} \tag{14}$$

$$\mathrm{Pr} \frac{\partial \hat{\theta}}{\partial t} + \phi_u \frac{\partial \hat{\theta}}{\partial x} + \hat{u} \frac{\partial \phi_\theta}{\partial x} + \mathrm{Pe}\ \hat{v} \frac{\partial \phi_\theta}{\partial y} = \nabla_2^2 \hat{\theta} \tag{15}$$

where $\nabla_2^2 = \dfrac{1}{\mathrm{Pe}^2} \dfrac{\partial^2}{\partial x^2} + \dfrac{\partial^2}{\partial y^2} + \dfrac{\partial^2}{\partial z^2}$.

Since a transient three-dimensional perturbation mode is used in this study, one may choose the following disturbance form for longitudinal vortex rolls:

$$\begin{aligned} \hat{u}(x, y, z, t) &= u(x, y, t) \cdot \exp(iaz) \\ \hat{v}(x, y, z, t) &= v(x, y, t) \cdot \exp(iaz) \\ \hat{w}(x, y, z, t) &= w(x, y, t) \cdot i \cdot \exp(iaz) \\ \hat{p}(x, y, z, t) &= p(x, y, t) \cdot \exp(iaz) \\ \hat{\theta}(x, y, z, t) &= \theta(x, y, t) \cdot \exp(iaz) \end{aligned} \tag{16}$$

where $a = 2\pi h/\lambda$ is the wave number of the disturbances. By consideration of the vortex-type perturbation quantities and the continuity equation, a different expression for $\hat{w}$ is used in the above equations (16). It should be noted that these roll-type disturbances are taken to be periodic in the z direction, with u, v, w, p, and θ as the amplitude functions depending on x, y, and t. In Table 1, a comparison is made of perturbation modes on longitudinal vortex instability in developing flow in the existing literature (Hwang and Cheng, 1973; Cheng and Wu, 1976; Moutsoglou et al., 1981; Chen et al., 1982; Yoo et al., 1987). It is seen that the steady two-dimensional disturbance $\hat{f}(y, z) = f(y) \cdot \exp(iaz)$ assumes the damping of disturbances in the streamwise direction upstream of the onset point, and the amplification of disturbances downstream of the onset point. The neutrally stable condition at the onset point is indicated by $\partial\hat{f}/\partial x = 0$. The steady three-dimensional perturbation $\hat{f}(x, y, z) = \hat{f}(x, y) \cdot \exp(iaz)$ with the assumption of large Prandtl number is used by Yoo et al. (1987) for mixed convection on an isothermal horizontal plate. In the present study, the perturbation amplitude functions are presumed as functions of x, y, and t. The onset of vortex instability is characterized by $\partial\hat{f}/\partial t = 0$, which is different from $\partial\hat{f}/\partial x = 0$ for two-dimensional disturbances.

After substituting the disturbance form (16) into equation (11)–(15), one obtains the following equations in the x–y plane for the time-dependent amplitude functions:

$$\frac{1}{\mathrm{Pe}} \frac{\partial u}{\partial x} + \frac{\partial v}{\partial y} - aw = 0 \tag{17}$$

$$\frac{\partial u}{\partial t} + \frac{1}{\mathrm{Pr}} \phi_u \frac{\partial u}{\partial x} + \mathrm{Re}\ v \frac{\partial \phi_u}{\partial y} = -\frac{1}{\mathrm{Pe}} \frac{\partial p}{\partial x} + \nabla^2 u \tag{18}$$

$$\frac{\partial v}{\partial t} + \frac{1}{\mathrm{Pr}} \phi_u \frac{\partial v}{\partial x} = -\frac{\partial p}{\partial y} + \nabla^2 v + \frac{\mathrm{Ra}}{\mathrm{Pe}} \theta \tag{19}$$

$$\frac{\partial w}{\partial t} + \frac{1}{\mathrm{Pr}} \phi_u \frac{\partial w}{\partial x} = -ap + \nabla^2 w \tag{20}$$

$$\mathrm{Pr} \frac{\partial \theta}{\partial t} + \phi_u \frac{\partial \theta}{\partial x} + u \frac{\partial \phi_\theta}{\partial x} + \mathrm{Pe}\ v \frac{\partial \phi_\theta}{\partial y} = \nabla^2 \theta \tag{21}$$

where $\nabla^2 = \dfrac{1}{\mathrm{Pe}^2} \dfrac{\partial^2}{\partial x^2} + \dfrac{\partial^2}{\partial y^2} - a^2$. The equation for the pressure amplitude function is obtained after some manipulations and incorporation of the dimensionless equations (17)–(20).

$$\nabla^2 p = -\frac{\partial D}{\partial t} + \nabla^2 D - \frac{1}{\mathrm{Pr}} \phi_u \frac{\partial D}{\partial x} - \frac{2}{\mathrm{Pr}} \frac{\partial v}{\partial x} \frac{\partial \phi_u}{\partial y} + \frac{\mathrm{Ra}}{\mathrm{Pe}} \frac{\partial \theta}{\partial y} \tag{22}$$

Table 2 Numerical experiments for Pe = 100

	Ra*		
Onset position (x^*)	0.01	0.05	0.10
Typical calculation†	63,032	8181	3513
$\Delta t = 0.15 \times 10^{-3}$	64,033	8276	3536
$Ra^0 = 8.0 \times 10^4$	62,941	8078	3506
$Ra^0 = 3.0 \times 10^5$	61,518	8256	3515
$\theta^0 = 1.0 \times 10^{-11}$	63,032	8181	3513
$\theta^0 = 1.0 \times 10^{-9}$	63,032	8181	3513
$NI \times NJ = 125 \times 28$	64,370	7971	3446
$NI \times NJ = 90 \times 36$	64,686	8312	3548

†$\Delta t = 0.20 \times 10^{-3}$, $Ra^0 = 1.6 \times 10^5$, $\theta^0 = 1.0 \times 10^{-10}$, $NI \times NJ = 90 \times 28$.

where $D = \frac{1}{Pe}\frac{\partial u}{\partial x} + \frac{\partial v}{\partial y} - aw$. It is noted that the present study utilizes the reduced two-dimensional equations (18)–(22) instead of the three-dimensional ones (11)–(15), and solves the unabridged pressure equation (22) in comparing with the simplified equations used for the determination of p in the SIMPLE and SIMPLER methods (Patankar, 1980).

The appropriate boundary conditions of the perturbation quantities are

$$u = v = w = \theta = 0 \qquad \text{at } y = 0 \text{ and } 1$$
$$u = v = w = \theta = 0 \qquad \text{at } x = 0 \tag{23}$$
$$\frac{\partial u}{\partial x} = \frac{\partial v}{\partial x} = \frac{\partial w}{\partial x} = \frac{\partial \theta}{\partial x} = \frac{\partial p}{\partial x} = 0 \qquad \text{at } x = 1$$

and the initial conditions of the perturbation quantities are

$$u = v = w = \theta - \theta^0 = p = 0 \qquad \text{at } t = 0 \tag{24}$$

where θ^0 is set to 1×10^{-10} in the present computation. It is noted that the pressures at walls and inlet are not listed above. Following the procedure of Harlow and Welch (1965), the boundary conditions for the pressure equation (22) can be derived directly from the momentum equations (18) and (19), which must be consistent with the vanishing of the perturbation velocities u and v at walls and inlet.

It may be interesting to see the effect of Pe on the thermal instability. Therefore, the streamwise convection and diffusion terms of the governing equations are not neglected in this study. The convection terms with coefficient 1/Pr also show that the Prandtl number plays an important role on the onset of thermal instability.

Solution Procedure

The numerical solution of the governing equations is based on the Mark and Cell (MAC) scheme (Harlow and Welch, 1965) with a staggered grid system. The velocity amplitude functions u, v are calculated at the points on the surface of a control volume, while the velocity, pressure, and temperature amplitude functions are solved at the grid point in the control volume. Since the streamwise convection terms in the governing equations are first-order derivatives with a factor of 1/Pr, equations (18)–(20) will become stiff when the Prandtl number is small, and the power law scheme (Patankar 1980) is employed for the conduction-convection terms. Equation (22) is a Poisson equation which can be solved by a successive overrelaxation iteration method. The explicit forward time marching is utilized to treat the time-dependent form.

It is seen in equation (19) that the buoyancy term is a driving force, which supplies the energy to increase the perturbation velocity, and then the perturbation temperature in equation (21) is promoted by the normal convection but suppressed by the streamwise convection. In computation one can modify the Rayleigh number at each time step by a linear extrapolation according to the perturbation temperature amplitudes at the two previous time steps on a specified streamwise position. This process is repeated until a minimum value of the Rayleigh number is obtained.

The basic concept of this approach is that the unstable region is located downstream of the onset position of instability, and the perturbation quantities appearing in the unsteady linear perturbation equations can grow endlessly as time increases. The stable region is located upstream, and the initial perturbations will decrease continuously. The numerical procedure for solving equations (18)–(22) for a given wave number and unknowns u, v, w, θ, and p with the associated boundary conditions (23) is stated as follows:

1 Assign values for Prandtl number and Peclet number, and solve equation (3) for the basic flow temperature distribution with the boundary conditions (4).

2 Assign initial values for variables u, v, w, θ, and p and an initial value for Rayleigh number. In the present study, zero values for u, v, w, and p, $\theta^0 = 1.0 \times 10^{-10}$ and $Ra^0 = 1.6 \times 10^5$ are used for computation.

3 Solve equation (22) for pressure distribution.

4 With the obtained p, solve equations (18)–(20) for u, v, and w at a new time step.

5 With the obtained u and v, solve equation (21) for θ at the new time step.

6 Adjust the value of Rayleigh number for the next computation by the ratio of the root mean square values of new θ and old θ at a given axial position.

7 Repeat steps 3–6, until the perturbation temperature amplitude and the values of minimum Rayleigh number meet the convergence criterion for a specified dimensionless streamwise position

$$\left|\frac{\bar{T}_{x,t} - \bar{T}_{x,t-\Delta t}}{\bar{T}_{x,t}}\right| \le \epsilon \tag{25}$$

for perturbation temperature amplitude, where $\epsilon = 10^{-3} \sim 5 \times 10^{-5}$ in the study, and

$$Ra_{t-\Delta t} + Ra_{t+\Delta t} - 2 \cdot Ra_t > 0$$
$$\text{and } Ra_{t-\Delta t} > Ra_t < Ra_{t+\Delta t} \tag{26}$$

for the determination of minimum Rayleigh number, where $\bar{T}_{x,t}$ is the root mean square value of the temperature amplitude at time t on a specified dimensionless streamwise position x.

8 For various values of wave number, one can determine the corresponding minimum Rayleigh number for each wave number. The minimum value of those Rayleigh numbers is the critical Rayleigh number Ra* and the corresponding wave number is the critical wave number a^*. The specified streamwise position is the onset position of the thermal instability.

The main objective of this study is to determine the critical condition of the onset of thermal instability for a specified streamwise position. The grid is uniform in the normal direction and nonuniform in the streamwise direction to save computation time. A finer mesh near the inlet region is employed to get better accuracy in the solution. Table 2 shows a typical result of numerical experiments for Pe = 100. Time steps of 0.20×10^{-3} and 0.15×10^{-3}, initial Rayleigh numbers of 8.0×10^4, 1.6×10^5, and 3.0×10^5, initial disturbances of 1.0×10^{-9}, 1.0×10^{-10}, and 1.0×10^{-11} and grid sizes of 90×28, 90×36, and 125×28 are used to perform the numerical calculation. One finds that the difference in numerical results decreases as the onset streamwise position moves downstream. For example, the result at $x = 0.01$ has a largest difference of 2.6 percent but the difference at $x \ge 0.10$ is less than 1 percent. Numerical experiments for the other Peclet numbers are also performed, and a similar trend is observed.

Results and Discussion

Figures 2(*a*) and 2(*b*) show the solution procedure in this study. In Fig. 2(*a*) these curves present the variation of Rayleigh

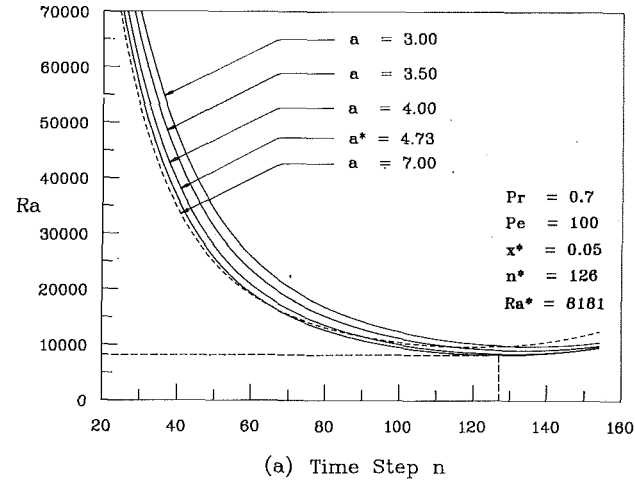

(a) Time Step n

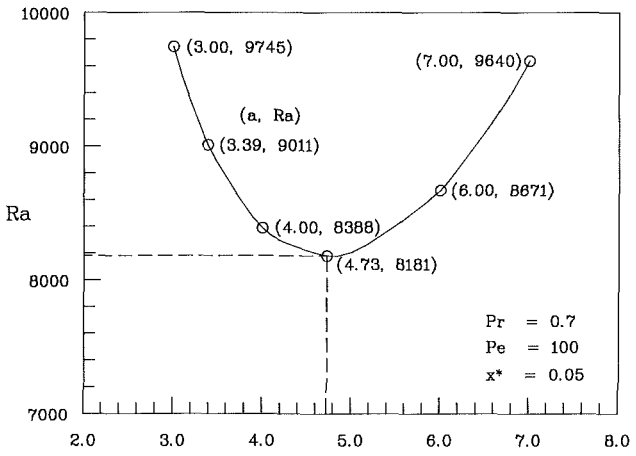

(b) Wave Number a

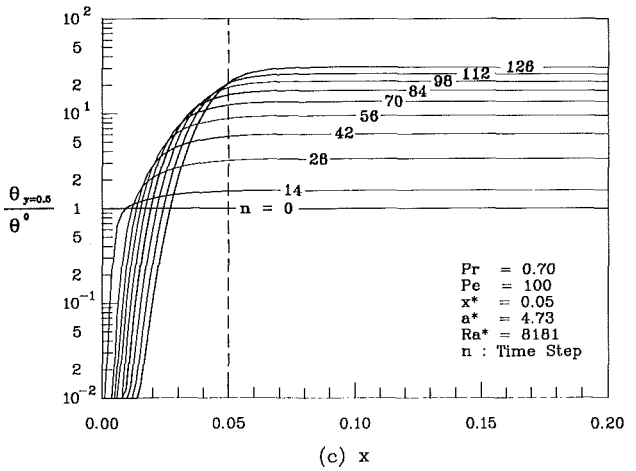

(c) x

Fig. 2 Solution procedure: (*a*) Ra versus *n*, (*b*) Ra versus *a*, (*c*) $\theta_{y=0.5}/\theta^0$ versus *x*

number for various wave numbers during the marching procedure. The Rayleigh number decreases from the initial value $Ra^0 = 1.6 \times 10^5$ as time increases, then it reaches a minimum value and then increases gradually. If the computation is continued after a minimum Rayleigh number is obtained, the perturbation quantities in the downstream will be increased. Therefore, the corresponding new Rayleigh number will be higher than the minimum critical value. It is believed that a steady finite amplitude vortex-type secondary flow will be generated only when the products of the perturbation quantities

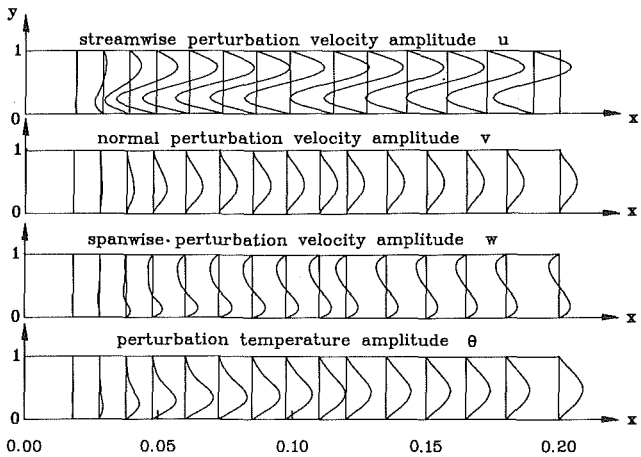

Fig. 3 Developing of the perturbation amplitude functions along the streamwise direction

are kept in the governing equations. For each wave number one can obtain the corresponding minimum Rayleigh number. As shown in Fig. 2(*b*) the minimum of this curve is the critical Rayleigh number Ra* and the corresponding critical wave number a^*. Figure 2(*c*) shows the streamwise variation of perturbation temperature θ along $y = 0.5$ during the time marching procedure, in which the onset position of thermal instability is located at $x = 0.05$ for the time step $n = 126$. In this study an initial uniform disturbance $\theta^0 = 1 \times 10^{-10}$ is applied throughout the flow field. As time increases, the perturbation temperature amplitude near the inlet decreases gradually. But in the region downstream of the onset position, the perturbation temperature increases continuously. One can say that in the unstable region of the flow field the strong buoyancy force supports the perturbation growth in the downstream of the onset position. On the other hand, in the stable region the disturbance is damped by the viscous force.

The profiles of perturbation amplitude quantities *u*, *v*, *w*, and θ on the *x*–*y* plane are shown in Fig. 3. These data are obtained at the final time step for the onset of instability at $x = 0.05$. It is seen that the perturbation amplitude quantities are very small near the inlet region and increase gradually along the streamwise direction, then become fully developed after a certain streamwise distance. The streamwise and spanwise perturbation velocity amplitudes *u* and *w* behave like a sine function in the *y* direction. Since the channel is heated from below, the normal perturbation velocity *v* and the perturbation temperature θ are positive. The maximum perturbation temperature θ is close to the lower wall in the inlet region, and moves to the central region gradually along the streamwise direction. This figure also presents the streamwise dependence of the perturbation amplitude quantities. The shapes of the *v* and *w* profiles may be explained via the circulation pattern shown in Fig. 1, while the *u* profile may be explained in light of the *v* profile, which drives low-momentum fluid away from the bottom wall and high-momentum fluid toward the top wall. It should be noted that these results correspond to the perturbation amplitude only, while the actual perturbation value as a function of *z* is derived from equation (16).

Figure 4 shows the critical Rayleigh number Ra* marking the onset of instability along the streamwise direction for various Peclet numbers $Pe = 30 \sim 100$ with $Pr = 0.7$. The previous theoretical and experimental data are also plotted for comparison. The theoretical prediction of Hwang and Cheng (1973) is the first investigation of the onset of thermal instability in the thermal entrance region between horizontal plates heated from below. The difference between the previous prediction and the experimental data is more than one order of magnitude near the inlet region. The linear stability theory predicts the

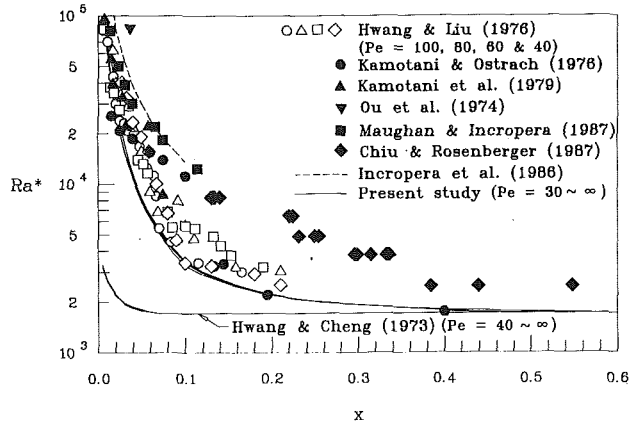

Fig. 4 Ra* versus x

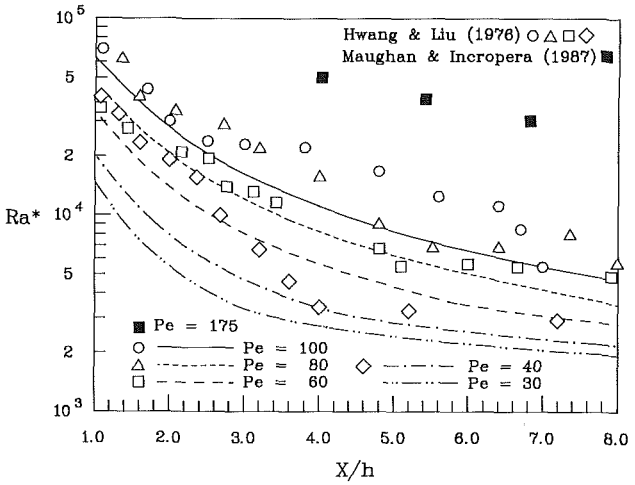

Fig. 5 Effect of Peclet number on the onset of instability for Pr = 0.7

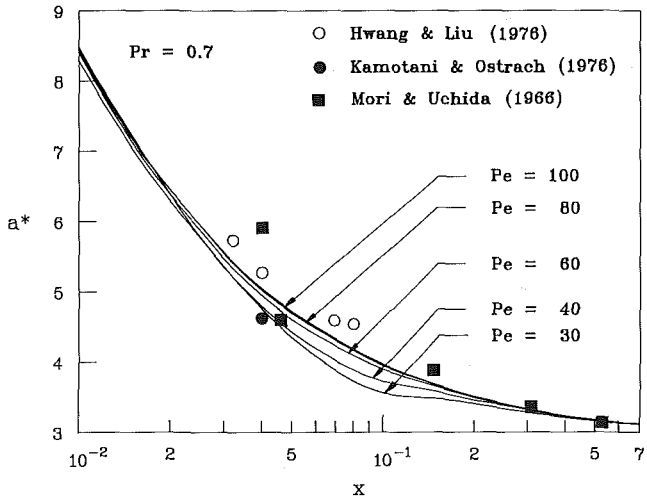

Fig. 6 The critical wave number a^* versus the streamwise coordinate for Pr = 0.7

onset of infinitesimal disturbances. Of course only finite amplitude disturbances can be observed experimentally. In Fig. 4 one can find that the present curves lie below but not too far from the existing experimental results. At the same time, the present curves show that the critical Rayleigh number decreases monotonically with the increasing streamwise distance and finally approaches a limiting value of 1708. This implies that the flow in the upstream is more stable than that in the downstream. It is seen that the streamwise dependence of perturbation quantities is considered in the governing equations.

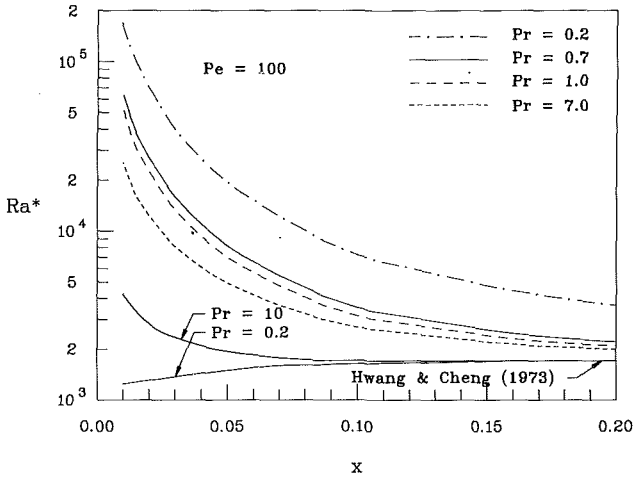

Fig. 7 Effect of the Prandtl number on the critical Rayleigh numbers for Pe = 100

The streamwise inertia and convection terms suppress the thermal instability, and therefore larger critical Rayleigh numbers than those found by Hwang and Cheng (1973) are predicted.

Figure 5 presents the variation of the critical Rayleigh number along the dimensionless streamwise distance X/h for various Peclet numbers with Pr = 0.7. The experimental data of Hwang and Liu (1976) are also plotted for comparison. A qualitative agreement between the theoretical and experimental results is observed. This figure also shows that the values of Ra* increase with an increase in Pe or Re. The flow is stabilized by the streamwise velocity. This confirms the results of the previous investigations (Incropera and Schutt, 1985; Maughan and Incropera, 1987; Chiu and Rosenberger, 1987).

Figure 6 shows the critical wave number a^* versus the dimensionless streamwise coordinate. In this figure the critical wave number decreases monotonically along the streamwise distance, and all the curves approach the limiting value of $a^* = 3.12$ for the limiting critical Rayleigh number of 1708 in the thermally fully developed region. One can conclude that as the critical Rayleigh number increases, the onset of instability moves upstream and the corresponding critical wave number increases due to a thinner thermal boundary layer near the inlet. The critical wave numbers obtained from the experiments by Hwang and Liu (1976), Kamotani and Ostrach (1971), and Mori and Uchida (1966) are also plotted for comparison. It is seen that most experimental data lie on the theoretical curve within a few percent of deviation.

Figure 7 presents the variation of the critical Rayleigh number along the dimensionless streamwise distance for Pe = 100 with the Prandtl number as a parameter. The critical Rayleigh number decreases with an increase in the Prandtl number. This trend is opposite to the prediction of Hwang and Cheng (1973), but consistent with the experimental investigation (Incropera and Schutt, 1985), which concludes that air is more stable than water. Referring to equations (17)–(22), the streamwise convection terms with the coefficient 1/Pr, which is excluded in the previous study (Hwang and Cheng, 1973), have an important effect on the onset of instability and cannot be neglected here. It is seen in equations (18)–(20) that for fixed Pe and x, the streamwise inertia force, which suppresses the thermal instability, will be increased with the decrease in the Prandtl number; therefore, the increased stability of low Prandtl number flows is observed. Due to the neglect of the streamwise inertia force, the opposite trend is predicted by Hwang and Cheng (1973).

Figure 8 shows the variation of the critical wave number along the dimensionless streamwise distance for Pe = 100 and

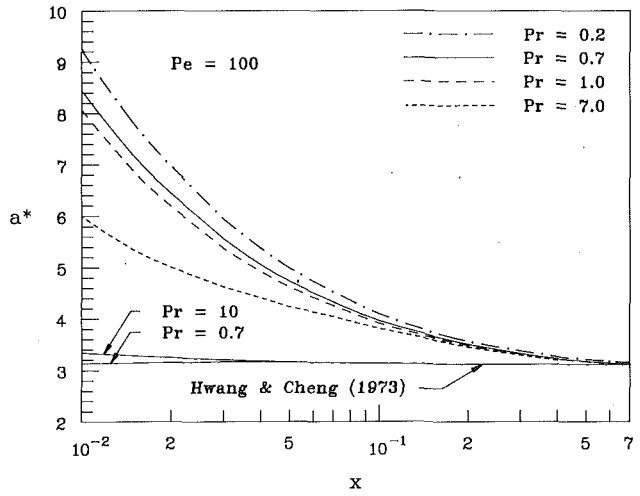

Fig. 8 Effect of the Prandtl number on the critical wave numbers for Pe = 100

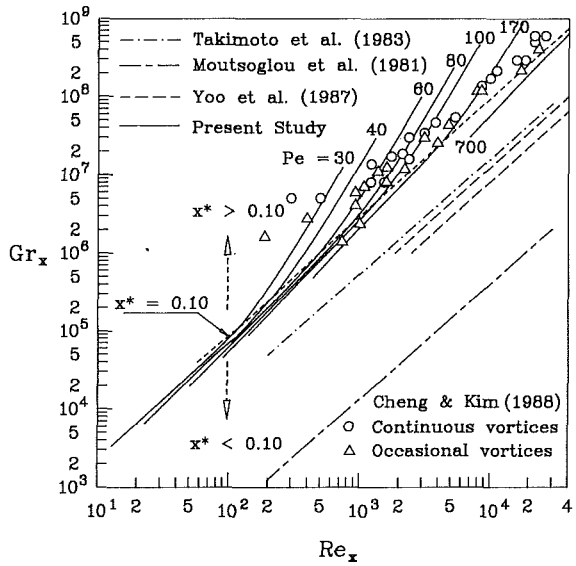

Fig. 9 Comparison of results on an isothermal horizontal plate

different Prandtl numbers. It is seen that the critical wave number decreases with an increase in the Prandtl number and the dimensionless coordinate. The values eventually approach the limiting value of $a^* = 3.12$ for large x.

In the region near the inlet of a parallel plate channel, the thermal boundary layer is thin and the temperature and flow fields in this region may not be far from those of a single plate. It is interesting to compare the results for these two physical configurations. Figure 9 shows the results of previous works for the onset of flow instability in the thermal boundary layer over an isothermal horizontal plate. It is seen that there is a significant difference of more than two orders of magnitude between the previous experimental investigation (Cheng and Kim, 1988) and theoretical prediction (Moutsoglou et al., 1981). This discrepancy is similar to that of the horizontal parallel-plate channel in the present study. The results of Yoo et al. (1987) present an improvement of the discrepancy based on a large Pr assumption. For comparison, the values of Ra*, Pe, and x^* in this study are transformed into Gr_x and Re_x by the following transformations:

$$\mathrm{Re}_x = \left(\frac{\mathrm{Pe}}{\mathrm{Pr}}\right) \cdot \left(\frac{X^*}{h}\right)$$
$$\mathrm{Gr}_x = \left(\frac{\mathrm{Ra}^*}{\mathrm{Pr}}\right) \cdot \left(\frac{X^*}{h}\right)^3 \qquad (27)$$
$$X^* = \mathrm{Pe} \cdot h \cdot x^*$$

A dashed line for $x^* = 0.10$ is also plotted to indicate the onset point located at $x = 0.10$, which presents the thermal entrance length. It is seen from this figure that the onset of the instability in the thermal entrance region of a horizontal parallel-plate channel at $x^* < 0.10$ agrees well with the experimental results of Cheng and Kim (1988) in the thermal boundary layer over a single horizontal plate. The results in the thermally fully developed region $x^* > 0.10$ provide higher values of Gr_x than those for a single plate. This is due to the existence of the upper plate, which stabilizes the flow.

Concluding Remarks

1 The onset of longitudinal vortices in the thermal entrance region of a horizontal parallel-plate channel flow heated from below is solved by a new approach to bridge the discrepancy between the previous theoretical and experimental investigations. Based on a transient three-dimensional linear stability theory, this approach predicts the critical Rayleigh number corresponding to each onset position along the streamwise direction.

2 In this paper the streamwise convection and diffusion terms are included in the governing equations. The streamwise convection terms not only improve significantly the accuracy of the theoretical prediction but also show the important effect of Prandtl number. The Prandtl number has a destablizing effect on the flow for a fixed Peclet number along the streamwise direction, and the critical Rayleigh number decreases with an increase in the Prandtl number.

3 The critical Rayleigh number decreases monotonically along the streamwise direction from the entrance region and eventually approaches the limiting value of $Ra^* = 1708$ in the fully developed region. When the dimensionless streamwise distance is defined as X/h, it is important to see that the flow is more stable with a larger value of Peclet number or Reynolds number with a fixed value of Prandtl number. In other words, the forced convection tends to suppress the onset of longitudinal vortices.

4 For the variation of wave number along the streamwise direction, one finds that as the onset of instability moves toward the inlet, the critical Rayleigh number and the corresponding critical wave number are increased. This implies that the corresponding wavelength is decreased at the same time.

5 The results of the onset of thermal instability near the inlet region of a parallel-plate channel, $x^* < 0.10$, may be used to predict the onset of the thermal instability on a heated single plate. The results in the thermally fully developed region, $x^* > 0.10$, provide higher values of Gr_x than those for a single plate. This is due to the existence of the upper plate, which stabilize the flow.

Acknowledgments

The authors would like to acknowledge the National Science Council, ROC for its support of the present work through project NSC 79-0404-E007-07. One of the authors (F. S. Lee) wishes to express his sincere thanks to Mr. W. L. Peng of the Ministry of Education Computer Center for his assistance in the computer system.

References

Akiyama, M., Hwang, G. J., and Cheng, K. C., 1971, "Experiments on the Onset of Longitudinal Vortices in Laminar Forced Convection Between Horizontal Plates," ASME JOURNAL OF HEAT TRANSFER, Vol. 93, pp. 335-341.

Chen, T. S., Moutsoglou, A., and Armaly, B. F., 1982, "Thermal Instability of Mixed Convection Flow Over Inclined Surfaces," *Numerical Heat Transfer*, Vol. 5, pp. 343-352.

Cheng, K. C., and Wu, R. S., 1976, "Axial Heat Conduction Effects on Thermal Instability of Horizontal Plane Poiseuille Flows Heated From Below," ASME JOURNAL OF HEAT TRANSFER, Vol. 98, pp. 564–569.

Cheng, K. C., and Kim, Y. W., 1988, "Vortex Instability Phenomena Relating to the Cooling of a Horizontal Isothermal Flat-Plate by Natural and Forced Laminar Convection Flows," *Cooling Technology for Electronic Equipment,* W. Aung, ed., Hemisphere, Washington, DC, pp. 169–182.

Chiu, K. C., and Rosenberger, F., 1987, "Mixed Convection Between Horizontal Plates—I. Entrance Effects," *Int. J. Heat Mass Transfer,* Vol. 30, pp. 1645–1654.

Harlow, F. H., and Welch, J. E., 1965, "Numerical Calculation of Time-Dependent Viscous Incompressible Flow of Fluid With Free Surface," *The Physics of Fluids,* Vol. 8, pp. 2182–2189.

Hwang, G. J., and Cheng, K. C., 1873, "Convective Instability in the Thermal Entrance Region of a Horizontal Parallel-Plate Channel Heated From Below," ASME JOURNAL OF HEAT TRANSFER, Vol. 95, pp. 72–77.

Hwang, G. J., and Liu, C. L., 1976, "An Experimental Study of Convective Instability in the Thermal Entrance Region of a Horizontal Parallel-Plate Channel Heated From Below," *Can. J. Chem. Eng.,* Vol. 54, pp. 521–525.

Incropera, F. P., and Schutt, J. A., 1985, "Numerical Simulation of Laminar Mixed Convection in the Entrance Region of Horizontal Rectangular Ducts," *Numerical Heat Transfer,* Vol. 8, pp. 707–729.

Incropera, F. P., Knox, A. L., and Schutt, J. A., 1986, "Onset of Thermal Driven Secondary Flow in Horizontal Rectangular Ducts," *Proc. Eighth International Heat Transfer Conference,* Vol. 3, Hemisphere, Washington, DC, pp. 1395–1400.

Incropera, F. P., Knox, A. L., and Maughan, J. R., 1987, "Mixed-Convection Flow and Heat Transfer in the Entry Region of a Horizontal Rectangular Duct," ASME JOURNAL OF HEAT TRANSFER, Vol. 109, pp. 434–439.

Kamotani, Y., and Ostrach, S., 1976, "Effect of Thermal Instability on Thermally Developing Laminar Channel Flow," ASME JOURNAL OF HEAT TRANSFER, Vol. 98, pp. 62–66.

Kamotani, Y., Ostrach, S., and Miao, H., 1979, "Convective Heat Transfer Augmentation in Thermal Entrance Regions by Means of Thermal Instability," ASME JOURNAL OF HEAT TRANSFER, Vol. 101, pp. 222–226.

Mahaney, H. V., Incropera, F. P., and Ramadhyani, S., 1987, "Development of Laminar Mixed Convection Flow in a Horizontal Rectangular Duct With Uniform Bottom Heating," *Numerical Heat Transfer,* Vol. 12, pp. 137–155.

Maughan, J. R., and Incropera, F. P., 1987, "Experiments on Mixed Convection Heat Transfer for Airflow in a Horizontal and Inclined Channel," *Int. J. Heat Mass Transfer,* Vol. 30, pp. 1307–1318.

Mori, Y., and Uchida, Y., 1966, "Forced Convective Heat Transfer Between Horizontal Plates," *Int. J. Heat Mass Transfer,* Vol. 9, pp. 803–816.

Montsoglou, A., Chen, T. S., and Cheng, K. C., 1981, "Vortex Instability of Mixed Convection Flow Over a Horizontal Flat Plate," ASME JOURNAL OF HEAT TRANSFER, Vol. 103, pp. 257–261.

Nakayama, W., Hwang, G. J., and Cheng, K. C., 1970, "Thermal Instability in Plane Poiseuille Flow," ASME JOURNAL OF HEAT TRANSFER, Vol. 92, pp. 61–68.

Osborne, D. G., and Incropera, F. P., 1985, "Laminar Mixed Convection Heat Transfer for Flow Between Horizontal Parallel Plates With Asymmetric Heating," *Int. J. Heat Mass Transfer,* Vol. 28. pp. 207–217.

Ostrach, S., and Kamotani, Y., 1975, "Heat Transfer Augmentation in Laminar Fully Developed Channel Flow by Means of Heating From Below," ASME JOURNAL OF HEAT TRANSFER, Vol. 97, pp. 220–225.

Ou, J. W., Cheng, K. C., and Lin, R. C., 1974, "Natural Convection Effects on Graetz Problem in Horizontal Rectangular Channels With Uniform Wall Temperature for Large Pr," *Int. J. Heat Mass Transfer,* Vol. 17, pp. 835–843.

Ouazzani, M. T., Caltagirone, J. P., Meyer, G., and Mojtabi, A., 1989, "Numerical and Experimental Study of Mixed Convection Between Two Horizontal Plates at Different Temperatures" [in French], *Int. J. Heat Mass Transfer,* Vol. 32, pp. 261–269.

Patankar, S. V., 1980, *Numerical Heat Transfer and Fluid Flow,* Hemisphere, Washington, DC.

Takimoto, A., Hayashi, Y., and Matsuda, O., 1983, "Thermal Instability of Blasius Flow Over a Horizontal Flat Plate," *Heat Transfer—Japanese Research,* Vol. 12, pp. 19–33.

Yoo, J. Y., Park, P., Choi, C. K., and Ro, S. T., 1987, "An Analysis on the Thermal Instability of Forced Convection Flow Over Isothermal Horizontal Flat Plate," *Int. J. Heat Mass Transfer,* Vol. 30, pp. 927–935.

Buoyancy-Driven Heat Transfer and Flow Between a Wetted Heat Source and an Isothermal Cube

D. J. Close

M. K. Peck

R. F. White

K. J. Mahoney

Commonwealth Scientific and Industrial Research Organisation, Division of Building, Construction, and Engineering, Highett, Victoria 3190, Australia

This paper describes flow visualization and heat transfer experiments conducted with a heat source inside an isothermal cube filled with a saturated or near-saturated gas/vapor mixture. The mixture was formed by vaporizing liquid from the surface of the heat source, and allowing it to condense on the surfaces of the cube, which was initially filled with a noncondensing gas. Visualization studies showed that for air and ethanol below 35°C, and for air and water, the flow patterns were similar with the hot plume rising from the source. For air and ethanol above 35°C the flow pattern reversed with the hot plume flowing downward. For temperatures spanning 35°C, which is the zero buoyancy temperature for the ethanol/water azeotrope and air, no distinct pattern was observed. Using water, liquid droplets fell like rain throughout the cube. Using ethanol, a fog of droplets moved with the fluid flow. Heat transfer experiments were made with water and air, and conductances between plate and cube of around 580 $W \cdot m^{-2} \cdot K^{-1}$ measured. Agreement between the similarity theory developed for saturated gas/vapor mixtures, and correlations for single component fluids only, was very good. Together with qualitative support from the visualization experiments, the theory developed in a earlier paper deriving a similarity relationship between single fluids and gas/vapor mixtures has been validated.

1 Introduction

This paper deals with natural convection in open cavities where the heat source is covered with a liquid film, and the addition of a noncondensing gas results in a gas/vapor mixture being present in the cavity. A diagram of the experimental equipment is shown in Fig. 1.

The reason for interest in this topic is the problem of cooling electronic components in sealed boxes. The use of a vaporizing liquid at the heat source and its condensation on the cavity walls provides a heat-pipe-like effect, and the addition of the noncondensing gas allows the pressure within the cavity to be maintained at 1 atm. From work on packed beds (Close, 1983; Close and Peck, 1986; Sheridan and Close, 1987), it can be inferred that natural convection, considerably modified by the coupling between the heat and vapor transfer, occurs in the cavity.

Natural convection with concentration effects has been studied previously. For example, coupled boundary layers in an infinite medium have been examined by Adams and Lowell (1986), and cavity problems, both open and containing a porous medium but with the heat and mass transfer uncoupled, have been studied by a number of workers, for example Gill et al. (1965), Gebhart and Pera (1971), Lee et al. (1982), Trevisan and Bejan (1985, 1987), and Zhang and Bejan (1987). This case differs in that coupling will play a major role in cavity transfer and, as will be shown, the mixture is likely to be at or near saturation. A theory has already been developed (Close and Sheridan, 1989), and in this paper, experimental evidence of its validity and data on the very high heat transfer rates that can be achieved are shown.

2 Theoretical Summary

In a cavity as shown in Fig. 1, filled with a single component fluid, the governing equations can be manipulated to produce the dimensionless groups Gr, Pr, and a geometric descriptor. Hence a heat transfer index such is as Nu given by

$$\mathrm{Nu} = f(\mathrm{Gr}, \mathrm{Pr}, \text{geometry}) \tag{1}$$

The theory by Close and Sheridan (1989) shows that with certain assumptions, the governing equations for gas/vapor mixtures can be manipulated to

$$\mathrm{Nu}_s = f(\mathrm{Gr}_s, \mathrm{Pr}_s, \text{geometry}) \tag{2}$$

with the function the same as in equation (1).

The most important assumptions are that:

(*a*) the mixture is saturated everywhere, and

(*b*) the temperature difference between the heat source and the sink is not large, around 5°C being reasonable for air and water vapor. At larger temperature differences, $(\partial T/\partial x)^2$ and $(\partial T/\partial y)^2$ terms become important and these are not usually considered in single fluid convection. These terms arise because the effective thermal conductivity k_s varies considerably over relatively small temperature differences. For air and water vapor at 1 atm, the change is from 0.056 to 9.06 $\mathrm{W \cdot m^{-1} \cdot K^{-1}}$

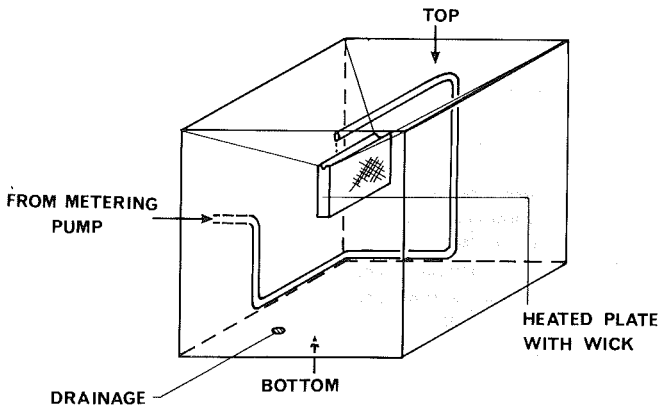

Fig. 1 Diagram of isothermal cube with internal wetted heat source

Contributed by the Heat Transfer Division for publication in the JOURNAL OF HEAT TRANSFER. Manuscript received by the Heat Transfer Division October 3, 1989; revision received June 18, 1990. Keywords: Heat Pipes and Thermosyphons, Mass Transfer, Natural Convection.

as the temperature increases from 10 to 95°C. For air only, the change is from 0.025 to 0.031 $W \cdot m^{-1} \cdot K^{-1}$.

Since the mixture will be saturated at the source and sink, it is reasonable to suppose that the mixture is saturated everywhere. However, to maintain saturation throughout the field, a liquid supply must be present so that vapor can be generated when the mixture temperature rises. Close and Sheridan postulated that a fog moved with the fluid.

The Nusselt, Grashof, and Prandtl numbers for the gas/vapor mixture are defined as

$$\mathrm{Nu}_s = \frac{h_{cs} l}{k_s} \tag{3}$$

$$\mathrm{Gr}_s = \frac{g \beta_s \Delta T l^3}{\nu_m^2} \tag{4}$$

and

$$\mathrm{Pr}_s = \frac{\rho_d C_s \nu_m}{k_s} \tag{5}$$

and an examination of the properties used in each parameter show them to be strongly influenced by vapor concentration and hence temperature.

Of most interest are the buoyancy β_s, the effective specific heat C_s, and the effective thermal conductivity k_s. Previous work (Close, 1983; Close and Peck, 1986) has discussed these in relation to natural convection in packed beds, and only a brief summary will be given here.

For perfect gases and employing the Clausius-Clapeyron equation

$$\beta_s = \beta \left[1 - \left(\frac{m}{1+m} \right) (M_c - M_d) \frac{h_{fg}}{RT} \right] \tag{6}$$

Hence if $M_d > M_c$, for example for water vapor/air, β_s is always positive, varying from close to β at temperatures near the vapor freezing point to very large values near the boiling point.

If $M_d < M_c$, a neutral buoyancy temperature exists where $\beta_s = 0$. For temperatures below this, β_s is positive, tending to β near the vapor freezing point. For temperatures above this, β_s is negative, with very large values for temperatures approaching the boiling point. For ethanol vapor/air, the neutral buoyancy temperature is around 31°C, but for the ethanol/water azeotrope it is around 35°C.

The reasons for considering the ethanol/water azeotrope and air were that for confirmatory experiments:

(*a*) a mixture was required where the vapor molecular weight was higher than that of the gas;

(*b*) it was desirable that the components be readily available and nontoxic, and using air removed the need for a completely sealed cube;

(*c*) a neutral buoyancy temperature between 0 and 100°C at atmospheric pressure was required for experiments in an apparatus where the cube temperature was controlled by heated water; and

(*d*) the component properties needed to be such that the neutral buoyancy temperature differed by a reasonable amount from either the vapor freezing or boiling points. This allowed both negative and positive buoyancies to be observed.

The ethanol/water azeotrope and air mixture satisfied these criteria.

The enthalpy of a saturated gas/vapor mixture is

$$h = \int_{T_0}^{T} C_d \, dT + m \left[\int_{T0}^{T} C_l dT + h_{fg} \right] \tag{7}$$

Hence

$$C_s = \frac{dh}{dT} - h_l \frac{dm}{dT} = Cd + m \left[C_l + \frac{dh_{fg}}{dT} \right]$$

$$+ \frac{dm}{dT} \left[\int_{T_0}^{T} C_l \, dT + h_{fg} \right] - h_l \frac{dm}{dT} \tag{8}$$

which is much greater than C_d.

The effective thermal conductivity is given by

$$k_s = k_m + \frac{\rho_m^2}{\rho_d} D \, h_{fg} \frac{d}{dT} \left(\frac{m}{1+m} \right) \tag{9}$$

As for β_s and C_s, this value is close to k_m at temperatures near

Nomenclature

A = surface area of heat source, m^2
C_d = specific heat of noncondensing component, $J \cdot kg^{-1} \cdot K^{-1}$
C_l = specific heat of liquid, $J \cdot kg^{-1} \cdot K^{-1}$
C_s = $(\partial h/\partial T) - h_l(dm/dT)$ = effective specific heat of saturated mixture, $J \cdot kg^{-1} \cdot K^{-1}$
D = diffusivity of gas/vapor mixture, $m^2 \cdot s^{-1}$
Gr = Grashof number of single component fluid
Gr_s = Grashof number of saturated mixture
g = gravitational acceleration, $m \cdot s^{-2}$
h_c = heat transfer coefficient for single component fluid, $W \cdot m^{-2} \cdot K^{-1}$
h_{cs} = heat transfer coefficient for saturated mixture, $W \cdot m^{-2} \cdot K^{-1}$
h_{fg} = latent heat of vaporization of vapor component, $J \cdot kg^{-1}$
h_l = enthalpy of liquid, $J \cdot kg^{-1}$
h = enthalpy of saturated mixture per unit mass of noncondensing component, $J \cdot kg^{-1}$
k = thermal conductivity of single component fluid, $W \cdot m^{-1} \cdot K^{-1}$
k_m = thermal conductivity of saturated mixture excluding mass diffusion, $W \cdot m^{-1} \cdot K^{-1}$
k_s = thermal conductivity of saturated mixture including mass diffusion, $W \cdot m^{-1} \cdot K^{-1}$
l = characteristic dimension, m
M_c = molecular weight of vapor, kg/kg mole
M_d = molecular weight of noncondensing component, kg/kg mole
m = mass ratio of vapor to noncondensing component
Nu = Nusselt number for single component fluid
Nu_s = Nusselt number for saturated mixture
P = pressure, Pa
Pr = Prandtl number for single component fluid
Pr_s = Prandtl number for saturated mixture
R = universal gas constant, $J \cdot kg\,mole^{-1} \cdot K^{-1}$
Ra = Rayleigh number for single component fluid
Ra_s = Rayleigh number for saturated mixture
T = temperature of fluid, K
T_s = liquid surface temperature at heat source, K
T_c = isothermal cube temperature, K
$\bar{T}$ = mean of T_s and T_c, K
T_o = reference temperature, K
β = buoyancy of single component fluid, K^{-1}
β_s = buoyancy of saturated mixture, K^{-1}
ΔT = reference temperature difference, K
ν_m = kinematic velocity of saturated mixture, $m^2 \cdot s^{-1}$
ρ_d = density of noncondensing component, $kg \cdot m^{-3}$ mixture
ρ_m = density of gas/vapor mixture, $kg \cdot m^{-3}$ mixture

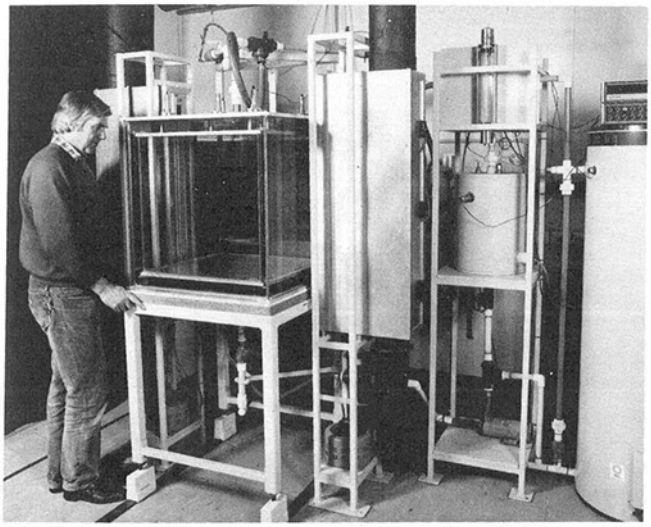

Fig. 2 Photograph of glass tanks used for flow visualization; air-cooled light boxes are located either side of the tanks

the vapor freezing point but reaches very large values near the boiling point.

The predicted heat transfer coefficients can be very high compared to those for a gas only. This is due to the heat-pipe-like effect of evaporation at the heat source and condensation at the heat sink, and the large buoyancy forces, which can be generated by concentration gradients.

The experimental program reported in the remainder of this paper is aimed at verifying the critical assumptions in the theory, illustrating the effects of mixture properties on flow structure, and showing the enhancement in heat transfer rates obtainable.

3 Flow Visualization Experiments

The flow visualization apparatus is shown in Fig. 2. As it is fully described by Salt and White (1985), only a brief description will be given here.

Since results were sought to compare flow structures with those obtained for parallel plate heat sources in an air filled isothermal cube by Symons et al. (1987), the same geometry was used here. The isothermal cube comprises two glass-sided boxes with aluminum tops and bottoms, the inner having a side length of 600 mm. The space between them is filled with water pumped from a temperature-controlled tank. An illuminated zone, 5 mm wide, is provided by collimated light sources at each side of the box, and photographs and video recordings are taken at right angles to the illuminated plane. Cigar smoke can be introduced through a tube in the base of the boxes.

The two $150 \times 150 \times 10$ mm electrically heated plates were mounted in the inner box with a gap of 28 mm between them and then covered with black fabric material about 0.5 mm thick. The fabric was draped from plastic troughs mounted on the top of each plate.

For the experiments, the boxes were initially air filled, and then the appropriate liquid was fed to the troughs on top of the heated plates. Cigar smoke was admitted to the base of the inner box, and the stabilized flow pattern photographed.

In the photographs presented, the plates were mounted vertically in the center of the cube with their edges facing the camera. Photographs were taken of the illuminated center plane.

Figure 3(*a*) shows the flow pattern when the plates were wet with water. The heated plume rose from the plates, flowed along the top of the box and down the walls, and resembled that for air only. A complete cell was not observed, presumably because of the progressive spreading of the flow across the box and hence lower velocities in the lower half of the box. While only one pair of plate and cube surface temperatures is shown, the same general structure was seen for all temperatures tried.

Not seen in the photograph is the carriage of water droplets. These rose from the plates, were carried along the top of the box, progressively falling like rain through the box interior.

Figures 3(*b*), 3(*c*), and 3(*d*) show the flow patterns observed when ethanol was used. As noted in Section 2, a neutral buoyancy temperature exists for those saturated mixtures where the vapor molecular weight is larger than that of the gas. For pure ethanol and air, this temperature is calculated to be about 31.5°C, but it is around 35°C for the ethanol/water azeotrope with air. The three photographs correspond to source and cube temperatures below 35°C, above 35°C, and spanning 35°C.

In Fig. 3(*b*), the flow pattern resembles that in Fig. 3(*a*). In Fig. 3(*c*), the flow pattern reverses, with the heated plume flowing downwards, along the bottom of the box and up the walls. It should be noted that as the smoke was admitted at the base of the cube, it was not readily carried into the upper section. This mirrors the pattern in Figs. 3(*a*) and 3(*b*), where most flow activity was observed above the lower edge of the heated plate.

In Fig. 3(*d*), no coherent flow pattern could be observed, and no distinct heated plume was present, corresponding to the source and box temperatures spanning the neutral buoyancy temperature. The tracer in Figs. 3(*b*), 3(*c*), and 3(*d*) was almost all liquid droplets, which moved with the flow. Only a small amount of smoke was admitted to the box, and this appeared to cause nucleation of the alcohol from a super saturated mixture. The difference between this phenomenon and the "falling rain" seen with water is attributed to the higher surface tension of water in contact with air compared to ethanol in contact with air, leading to larger droplets of water than alcohol.

The main conclusions to be drawn from these experiments are:

(*a*) the predictions relating to the effects of mixture properties on buoyancy have been verified; and

(*b*) saturating mechanisms for water and ethanol have been identified, and the evidence from the ethanol experiments is that a fog moved with the gas/vapor mixture.

4 Heat Transfer Experiments

A diagram of the experimental equipment is shown in Fig. 1. It consists of a heated plate located inside an isothermal cube whose wall temperatures were determined by water circulated from a temperature-controlled tank. The electric power dissipated in the heated plate is provided by a d-c power supply, and the liquid supply to the wick by a metering pump. The pressure inside the cube is kept constant using an inflatable bladder.

The cube with internal dimensions of $440 \times 440 \times 440$ mm is formed by screwing together six aluminum plates, which are fabricated from two pieces of aluminum, machined flat on the faces, and then grooved on two mating faces to take 12.5-mm-dia copper tube. The tube forms a serpentine coil through which water is circulated. The thickness of the aluminum and the tube spacing ensured a uniform wall temperature.

The heated plate, $150 \times 150 \times 10$ mm, was fabricated from two copper plates, with an electrical resistance wire sandwiched between them. In experiments reported in an earlier paper (Close et al., 1988), a cloth wick 0.5 mm thick was draped over the plate. However, significant problems were encountered with it, and very thin (0.05 mm) paper wicks were used in the experiments reported here.

The water pumped to the cube is in two circuits, each in-

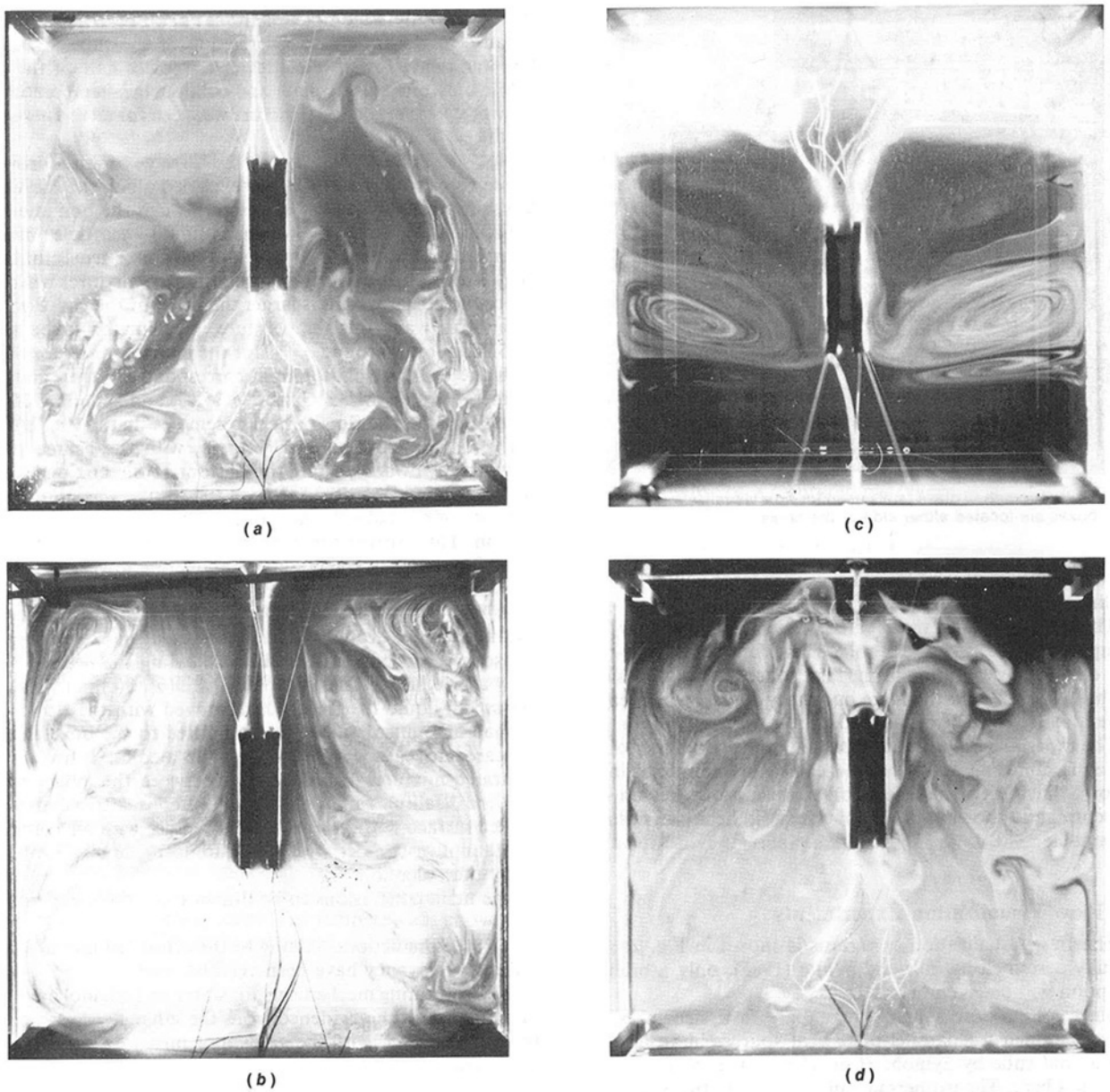

Fig. 3 Photographs of flow patterns in an isothermal cube with heat source: (*a*) air and water; heat source 49°C, cube 40°C; (*b*) air and ethanol/water azeotrope; heat source 35°C, cube 25°C; (*c*) air and ethanol/water azeotrope; heat source 50°C, cube 40°C; (*d*) air and ethanol/water azeotrope; heat source 40°, cube 30°C

cluding three walls of the cube, but with a common water tank, whose temperature is controlled by a circulator.

A known and constant liquid supply rate to the heat source is achieved using a metering pump. The liquid is drawn from a supply tank and preheated in a copper tube in contact with the cube walls, then delivered to the reservoir on the top of the heated plate.

Temperatures are measured using copper constantan thermocouple wire. Each wall of the cube contains four thermocouples, which are glued using silicone rubber, into holes drilled in the aluminum plate. The temperature of the heated plate is measured using a thermopile of three thermocouples in parallel, and one thermocouple is located on the liquid line discharging into the wick reservoir.

The temperatures and heated plate current and voltage are logged automatically. The thermocouple output referenced to an ice bath and the voltage to the heated plate are logged directly, but the current is measured indirectly using a current shunt.

The temperature and power measurement systems were calibrated prior to any experimental runs, and the output and stability of the metering pump checked. The uncertainty estimate on any measurement and the manner in which this propagates through subsequent calculated values has been obtained using the method of Kline and McClintock (1953), with odds of 20 to 1. The overall uncertainty in the measurement of temperature is estimated to be better than ± 0.2 K, while the uncertainty in the power measurement is estimated to be ± 0.5 percent.

Experiments were performed either at constant power to the heated plate while changing the isothermal cube temperature, or adjusting the power to give approximately constant temperature difference over a range of cube temperatures. The liquid flow rate to the plate was adjusted to the required value

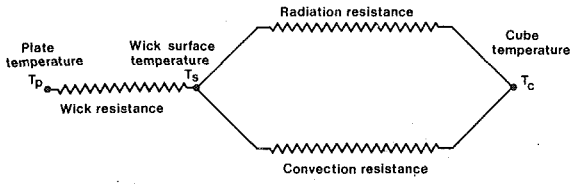

Fig. 4 Energy transfer paths between plate and cube

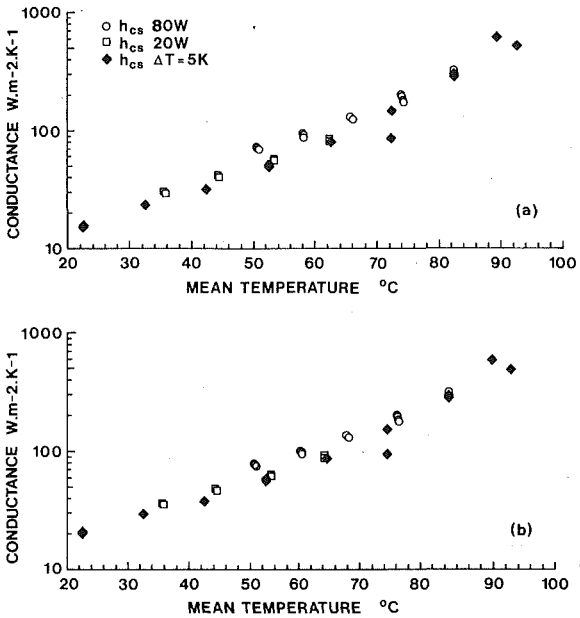

Fig. 5 Thermal conductances between heat source and cube: (*a*) overall conductances based on plate and cube temperatures; (*b*) gas/vapor mixture only

of 1.5 times the flow rate needed if all the power supplied to the plate resulted in evaporation of the liquid. Measurements were made when the system reached steady state, usually after several hours. The cube temperature was varied by changing the temperature of the water bath, the range of cube wall temperatures used being 20 to 90°C.

5 Analysis of Results

The energy transfer paths associated with the heated plate are shown in Fig. 4. To calculate the convective conductance between the liquid surface adjacent to the plate and the isothermal cube, the wick surface temperature was required. This was calculated assuming a liquid layer 0.1 mm thick and had little influence on the results, as the temperature difference through a layer this thick, for a power input of 80 W, is less than 0.3°C. The error made in incorrectly assessing the wick thickness is much less than this.

Radiation transfer may be significant at relatively low mean system temperatures, being calculated to be 25 percent of the total heat transfer. However, at mean temperatures near 90°C, the radiation transfer proportion drops to near 2 percent. The radiation contribution was calculated assuming the emittances of the water layers on the heated plate and cube surfaces were 0.96, and no allowance was made for absorption by liquid droplets. Their presence reduces the amounts quoted above.

Some data were taken at mean temperatures around 90°C with very small temperature differences between plate and cube. Owing to the uncertainties mentioned above, only data where the temperature differences were larger than 3.5°C are reported.

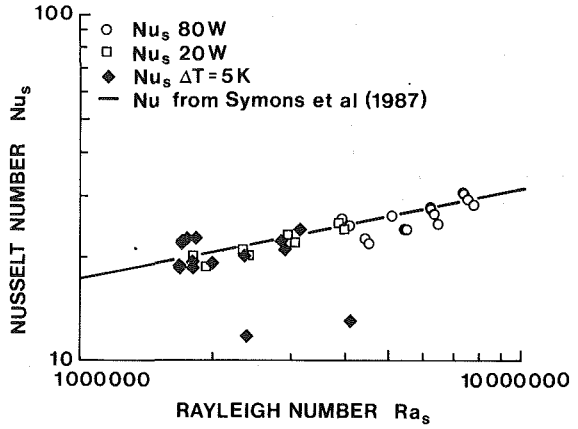

Fig. 6 Nu_s as a function of Ra_s compared with correlation for Nu versus Ra from Symons et al. (1987)

6 Results

To calculate the Nusselt and Rayleigh numbers, the characteristic dimension used was the side length of the heated plate. This followed the procedure used by Symons et al. (1987) in their studies of heated sources in air-filled cubes.

The uncertainties in temperature and power measurements given in Section 4 lead to the following uncertainties in calculated parameters. For Nusselt number Nu_s the uncertainty ranges from about 1.4 to 11.4 percent, the maximum values occurring at the lowest mean temperature. The uncertainty in Rayleigh number Ra_s ranges from about 1.8 to 9.2 percent, the maximum occurring at the highest mean temperature. The uncertainty in heat transfer coefficient h_{cs}, ranges from about 1.4 to 11.4 percent with the maximum corresponding to the lowest mean temperature.

Thermal conductances as functions of mean temperature of plate and cube are shown in Fig. 5. The conductances in 5(*a*) are based on plate temperature only, while those in Fig. 5(*b*) include liquid layer and radiation corrections. The differences range from about 33 percent at the lower temperatures to less than 4 at the higher, due mainly to the much higher convective as compared to radiative conductances at the higher temperatures. Mean temperature was chosen as the independent variable in the presentation of these results, primarily to show the way in which conductances increase as the mean temperature approaches the vapor boiling point.

The data generally show excellent repeatability for temperatures below 90°C. At temperatures higher than this conductances above 580 $W \cdot m^{-2} \cdot K^{-1}$ were measured, and they may be pessimistic due to wick dryout and vapor bubble formation beneath the wick. Both these effects were observed at these temperatures.

Nu_s versus Ra_s points are shown in Fig. 6 compared with the correlation due to Symons et al. for Nu versus Ra using air only. The relation derived by them is $Nu = 0.545\ Ra^{1/4}$. Symons et al. used a cube with side length 600 mm and heated plates of 150 mm side length. Subsequent experiments by J. G. Symons, CSIRO (personal communication), show that even with heated plates of 300 mm side length in a 600 mm cube, the correlation still applies. Consequently, it is appropriate to use this correlation for a heated plate of side length 150 mm in a cube of side length 440 mm. The mean difference and standard deviation between the data and the correlation are −3.3 and 12.3 percent, respectively. If two points, which as seen in Fig. 6 do not fall close to the correlation, are deleted, then the values are −1 and 6.7 percent, respectively. While the range covered by the the gas/vapor mixture experiments is relatively small, the agreement is most encouraging in supporting the similarity proposition in equations (1) and (2).

Periodically the cube was cooled down and the wick changed. The two points on Fig. 6 that depart from the air-only correlation were repeated after a wick change. The repeated points are included in Fig. 6 and are close to the correlation. While no obvious problems were observed with the wick, the most likely explanations for this phenomenon are dry-out of the wick and/or vapor bubble formation beneath it. Because of the construction and operation of the apparatus, the wick could not be observed during the heat transfer experiments.

7 Conclusions and Discussion

The objectives of this study have been to demonstrate the validity of the similarity theory relating natural convection of single component fluids in cavities to gas/vapor mixtures, and to show that very high heat transfer conductances can be achieved.

The visualization experiments confirm the predictions from the theory of the effect of mixture properties on the buoyancy and hence flow directions. Of importance is the observation of liquid droplet formation, as the theory required some liquid presence throughout the cavity to ensure mixture saturation. In the case of the ethanol/air mixture, the droplets were small enough to be carried with fluid flow, but with water this was not so. Fluid saturation with different mixtures, particularly for those liquids with high surface tension and where the hot plume flows downward, requires investigation.

The heat transfer experiments show very high thermal conductances of above 580 $W \cdot m^{-2} \cdot K^{-1}$ at mean plate and cube temperatures of 90°C or more. These may be compared with conductances of 15 $W \cdot m^{-2} \cdot K^{-1}$ at comparable temperature differences achievable in air only with radiation included. These show that gas/vapor mixtures can provide a worthwhile cooling method for heat sources in enclosures, for example electronic equipment.

The agreement between the data plotted as Nu_s versus Ra_s and the Symons et al. (1987) correlation provides quantitative support to the theory presented by Close and Sheridan (1989), as well as the qualitative support from the visualization experiments.

From experience with porous beds (Close and Peck, 1986), it is to be expected that other mixtures, for example water and Freon 12, will give even larger conductances, and will allow the Ra_s range to be increased.

References

Adams, J. A., and Lowell, R. L., Jr., 1968, "Free Convection Organic Sublimation," *International Journal of Heat and Mass Transfer*, Vol. 11, pp. 1215–1224.

Close, D. J., 1983, "Natural Convection With Coupled Mass Transfer in Porous Media," *International Communications in Heat and Mass Transfer*, Vol. 10, pp. 465–476.

Close, D. J., and Peck, M. K., 1986, "Experimental Determination of the Behaviour of Wet Porous Beds in Which Natural Convection Occurs," *International Journal of Heat and Mass Transfer*, Vol. 29, pp. 1531–1541.

Close, D. J., Peck, M. K., White, R. F., and Park Hing Wong, 1988, "Natural Convection Heat Transfer Rates and Flow Patterns in a Cavity Filled With a Gas/Vapor Mixture," in: *Natural Convection in Enclosures 1988*, R. S. Figliola and P. G. Simpkins, eds., ASME HTD-Vol. 99, pp. 23–28.

Close, D. J., and Sheridan, J., 1989, "Natural Convection in Enclosures Filled With a Vapor and a Non-condensing Gas," *International Journal of Heat and Mass Transfer*, Vol. 32, No. 5, pp. 855–862.

Gebhart, B., and Pera, L., 1971, "The Nature of Vertical Natural Convection Flows Resulting From the Combined Buoyancy Effects of Thermal and Mass Diffusion," *International Journal of Heat and Mass Transfer*, Vol. 14, pp. 2025–2050.

Gill, N., Del Casal, E., and Zeh, D. W., 1965, "Binary Diffusion and Heat Transfer From a Vertical Plate," *International Journal of Heat and Mass Transfer*, Vol. 8, pp. 1135–1151.

Kline, S. J., and McClintock, F. A., 1953, "Describing Uncertainties in Single-Sample Experiments," *Mechanical Engineering*, Jan., pp. 3–8.

Lee, T. S., Parikh, P. G., Acrivos, A., and Bershader, D., 1982, "Natural Convection in a Vertical Channel With Opposing Buoyancy Forces," *International Journal of Heat and Mass Transfer*, Vol. 25, pp. 499–511.

Salt, H., and White, R. F., 1985, "Flow Visualization of Mixed Convection," *Proc. Third Australasian Conference on Heat and Mass Transfer*, May, pp. 9–16.

Sheridan, J., and Close, D. J., 1987, "Transfer Mechanisms Governing Natural Convection in Porous Media With Coupled Mass Transfer," *Proc. 1987 ASME-JSME Thermal Engineering Joint Conference*, Honolulu, HI, March 22–27, P. J. Marto and I. Tanasawa, eds., New York, Vol. 2, pp. 421–426.

Symons, J. G., Mahoney, K. J., and Bostock, T. C., 1987, "Natural Convection in Enclosures With Through Flow Heat Sources," *Proc. 1987 ASME-JSME Thermal Engineering Joint Conference*, Honolulu, HI, March 22–27, P. J. Marto and I. Tanasawa, eds., ASME, New York, Vol. 2, pp. 215–220.

Trevisan, O. V., and Bejan, A., 1985, "Natural Convection With Combined Heat and Mass Transfer Buoyancy Effects in a Porous Medium," *International Journal of Heat and Mass Transfer*, Vol. 28, pp. 1597–1611.

Trevisan, O. V., and Bejan, A., 1987, "Mass and Heat Transfer by High Rayleigh Number Convection in a Porous Medium Heated From Below," *International Journal of Heat and Mass Transfer*, Vol. 30, pp. 2341–2356.

Zhang, Z., and Bejan, A., 1987, "The Horizontal Spreading of Thermal and Chemical Deposits in a Porous Medium," *International Journal of Heat and Mass Transfer*, Vol. 30, pp. 2289–2303.

Z. Zhang

A. Bejan
J. A. Jones Professor
of Mechanical Engineering.
Fellow ASME.

J. L. Lage

Department of Mechanical Engineering
and Materials Science,
Duke University,
Durham, NC 27706

Natural Convection in a Vertical Enclosure With Internal Permeable Screen

This paper documents the thermal insulation effect of a screen installed inside a vertical rectangular enclosure (e.g., double-glazed window). The screen is a venetian blind system made out of horizontal strips that can be rotated. The focus is on the "closed" position, where the strips almost touch. The effect of this permeable screen on the temperature field, the flow field, and the overall heat transfer rate is determined numerically. The study shows that there exists a ceiling (critical) conductance for the air leakage through the screen, above which the screen does not cause a significant drop in the overall heat transfer rate. A numerical example shows how this critical conductance can be used to calculate the critical spacing that can be tolerated between two consecutive strips in the screen.

1 Introduction

Cavities filled with trapped air have long been recognized for their thermal insulation potential in the design of buildings. One primary example is the double-glazing window, in which a layer of air is held between two vertical sheets of glass and sealed at the top and bottom ends. In a more advanced design (Fig. 1), the air space also contains a screen made out of a large number of thin strips oriented horizontally, i.e., in the direction perpendicular to the plane of Fig. 1. The strips can be tilted, remaining parallel to one another regardless of the tilt angle (Shurcliff, 1980).

One function of the tilting-blade screen is to modulate the radiation heat transfer through the window, for example, by blocking out the sunlight in daytime. Another function is to interfere with the buoyancy-induced air calculation, and to increase the insulation capability of the trapped air. This second effect is most pronounced when the blades are oriented close to the vertical (Fig. 1, right), creating a permeable partition along the vertical midplane of the air cavity.

The objective of the present study is to determine the thermal insulation effect that is due to the midplane screen when the blades are almost vertical. The focus of the analysis is on the natural convection heat transfer mechanism, i.e., on the partial suppression of this mechanism by the midplane partition. As an alignment of partially overlaying strips, the partition will be modeled as a solid vertical wall that is permeable to the flow of air in the horizontal direction. Indeed, the engineering objective of this study is to determine how tight the strip-to-strip spacing must be in order to effectively interfere with the natural circulation in the vertical enclosure.

The present geometry is related to several configurations that have been studied previously. If some of the blades were missing from the present vertical screen then the flow would have features similar to that found in a partially divided enclosure (e.g., Zimmerman and Acharya, 1987). Or, if the blades of the screen were oriented horizontally, their effect on each of the two vertical boundary layers would be similar to that found when roughness elements and fins are mounted on the vertical walls (Shakerin et al., 1988; Hasnaoui et al., 1990).

2 Mathematical Formulation

Consider the two-dimensional rectangular enclosure shown in Fig. 1, and assume that the enclosed fluid (air) is Newtonian and with constant transport properties. Assuming further that the fluid is Boussinesq-incompressible, we can write the following statements for the conservation of mass, momentum, and energy in the fluid:

$$\frac{\partial U}{\partial X}+\frac{\partial V}{\partial Y}=0 \tag{1}$$

$$U\frac{\partial U}{\partial X}+V\frac{\partial U}{\partial Y}=-\frac{\partial P}{\partial X}+\left(\frac{\mathrm{Pr}}{\mathrm{Ra}}\right)^{1/2}\left(\frac{\partial^2 U}{\partial X^2}+\frac{\partial^2 U}{\partial Y^2}\right) \tag{2}$$

$$U\frac{\partial V}{\partial X}+V\frac{\partial V}{\partial Y}=-\frac{\partial P}{\partial Y}+\left(\frac{\mathrm{Pr}}{\mathrm{Ra}}\right)^{1/2}\left(\frac{\partial^2 V}{\partial X^2}+\frac{\partial^2 V}{\partial Y^2}\right)+\theta \tag{3}$$

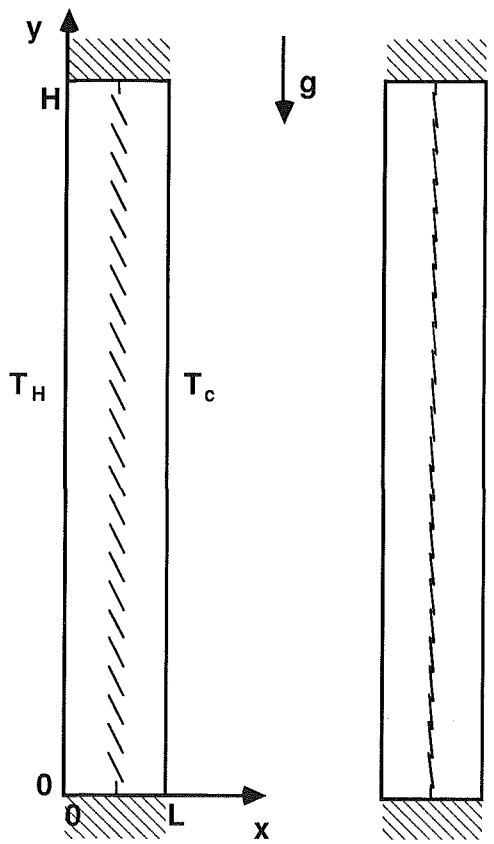

Fig. 1 Two-dimensional air cavity with a vertical midplane screen of tilting strips

Contributed by the Heat Transfer Division for publication in the JOURNAL OF HEAT TRANSFER. Manuscript received by the Heat Transfer Division June 21, 1990; revision received October 1, 1990. Keywords: Building Heat Transfer, Enclosure Flows, Natural Convection.

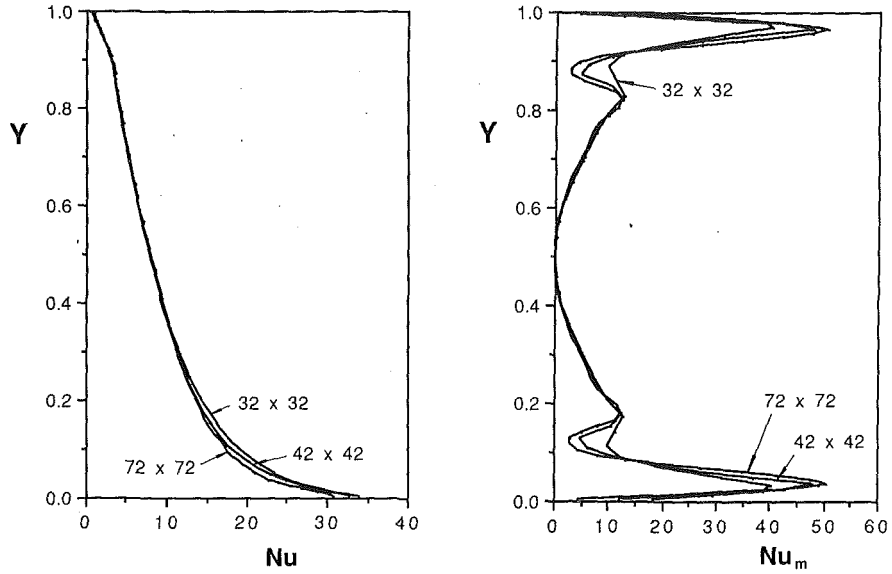

Fig. 2 The effect of grid size on numerical accuracy (Pr = 0.72, Ra = 10^6, $L/H = 0.3$, $C = 1.6 \times 10^{-3}$, $R_t = 10^{-3}$)

$$U\frac{\partial\theta}{\partial X}+V\frac{\partial\theta}{\partial Y}=(\mathrm{Ra\,Pr})^{-1/2}\left(\frac{\partial^2\theta}{\partial X^2}+\frac{\partial^2\theta}{\partial Y^2}\right) \tag{4}$$

These dimensionless equations are based on the following set of definitions, in which the lower-case symbols represent the physical (dimensional) quantities:

$$(X,Y)=\frac{(x,y)}{H},\quad (U,V)=\frac{(u,v)}{(\alpha/H)(\mathrm{Ra\,Pr})^{1/2}} \tag{5}$$

$$P=\frac{H^2(p+\rho gy)}{\rho\alpha^2\mathrm{Ra\,Pr}},\quad \theta=\frac{T-(T_H+T_C)/2}{T_H-T_C} \tag{6}$$

$$\tau=\frac{\alpha t}{H^2}(\mathrm{Ra\,Pr})^{1/2},\quad \mathrm{Pr}=\frac{\nu}{\alpha},\quad \mathrm{Ra}=\frac{g\beta H^3(T_H-T_C)}{\alpha\nu} \tag{7}$$

The conditions imposed along the rectangular perimeter of the enclosure cross section state that the top and bottom walls are impermeable, no-slip, and adiabatic, while the side walls are impermeable, no-slip, and at different temperatures:

$$U=0,\ V=0,\ \theta=\frac{1}{2}\ \text{at}\ X=0 \tag{8}$$

$$U=0,\ V=0,\ \theta=-\frac{1}{2}\ \text{at}\ X=\frac{L}{H} \tag{9}$$

$$U=0,\ V=0,\ \frac{\partial\theta}{\partial Y}=0\ \text{at}\ Y=0\ \text{and}\ 1 \tag{10}$$

Along the permeable partition that occupies the vertical midplane of the enclosure ($X = L/2H$), we recognize first the condition of no slip,

$$V_-=0\ \text{and}\ V_+=0 \tag{11}$$

in which the − and + subscripts indicate the left and right

Nomenclature

C = flow conductance, equations (18) and (29)
C_e = end effects parameter, equation (32)
g = gravitational acceleration, m/s^2
H = height, m
k = fluid thermal conductivity, W/m·K
k_p = partition thermal conductivity, W/m·K
K = permeability, m^2
L = enclosure horizontal dimension, m
Nu = local Nusselt number, equation (21)
Nu_m = local midplane Nusselt number, equation (22)
$\overline{\mathrm{Nu}}$ = overall Nusselt number, equation (24)
p = pressure, N/m^2
P = dimensionless pressure, equation (6)
Pr = Prandtl number, equation (7)
q'' = local heat flux, W/m^2
R_t = partition thermal resistance, equation (15)
Ra = Rayleigh number, equation (7)
t = time
t_p = partition thickness, m
T = temperature, K
T_C = cold wall temperature, K
T_H = hot wall temperature, K
u = horizontal velocity, m/s
U = dimensionless horizontal velocity, equation (5)
$\bar{u}$ = gap-averaged velocity, equation (26)
v = vertical velocity, m/s
V = dimensionless vertical velocity, equation (5)
W_o = width of overlapping regions, m
W_s = strip width, m
x = horizontal position, m
X = dimensionless horizontal position, equation (5)
y = vertical position, m
Y = dimensionless vertical position, equation (5)
α = thermal diffusivity, m^2/s
β = coefficient of volumetric thermal expansion, K^{-1}
$\beta_{x,y}$ = grid stretching parameters
δ = gap width, m, Fig. 10
η = vertical coordinate, equation (20)
θ = dimensionless temperature, equation (6)
μ = viscosity, kg/s·m
ν = kinematic viscosity, m^2/s
ξ = horizontal coordinate, equation (19)
ρ = density, kg/m^3
τ = dimensionless time, equation (7)
Ψ = dimensionless stream function, equation (23)

Subscripts

( )$_-$ = left side of partition
( )$_+$ = right side of partition

sides, respectively, of the partition. Another condition is the conservation of energy across the vertical midplane,

$$(\mathrm{Ra\,Pr})^{1/2}U(\theta_+ - \theta_-) = \left(\frac{\partial\theta}{\partial X}\right)_+ - \left(\frac{\partial\theta}{\partial X}\right)_- \tag{12}$$

The left side of this equation represents the net convection heat flux through the partition, while the right side accounts for the difference between the conduction heat fluxes found on the two sides of the partition. The conduction heat flux through the partition itself can be approximated as the average of the conduction heat fluxes that pass through the two faces of the partition,

$$k_p\frac{T_- - T_+}{t_p} = \frac{1}{2}\left[-k\left(\frac{\partial T}{\partial x}\right)_- - k\left(\frac{\partial T}{\partial x}\right)_+\right] \tag{13}$$

In this equation, k_p, t_p, and k are the thermal conductivity of the partition material, the partition thickness, and the thermal conductivity of the fluid. The dimensionless version of equation (13) is

$$\theta_+ - \theta_- = \frac{1}{2}R_t\left[\left(\frac{\partial\theta}{\partial X}\right)_- + \left(\frac{\partial\theta}{\partial X}\right)_+\right] \tag{14}$$

in which R_t is the partition "thermal resistance" parameter

$$R_t = \frac{t_p}{k_p}\frac{k}{H} \tag{15}$$

The final partition condition concerns the slow flow of air through the narrow parallel-plate passages formed between the blades of the folded screen (Fig. 1). Assuming that this flow is sufficiently slow, we recognize the Darcy flow model

$$u = \frac{K}{\mu}\frac{p_- - p_+}{t_p} \tag{16}$$

in which u is the horizontal velocity (volume averaged) through the porous partition, and p_- and p_+ are the local pressures on the two faces of the partition. To the physical relation between the permeability constant K and the geometry of each parallel-plate channel we return in section 5, where we also relax the Darcy flow assumption. Here we record only the dimensionless counterpart of equation (16),

$$U = \left(\frac{\mathrm{Ra}}{\mathrm{Pr}}\right)^{1/2} C(P_- - P_+) \tag{17}$$

by defining the horizontal flow "conductance" parameter

$$C = \frac{K}{Ht_p} \tag{18}$$

Finite-difference approximations of equations (1)–(4) were solved numerically in conjunction with the boundary conditions (8)–(10) and the partition conditions (11), (12), (14), and (17). The numerical scheme was based on the control-volume formulation (Patankar, 1980), the SIMPLEC algorithm (Van Doormaal and Raithby, 1984), the power-law method of evaluating the convection terms, and the ADI method for solving the system of discretized equations. The local criterion for numerical convergence (the maximum relative difference between two consecutive iterations for any local variable) was 10^{-3}.

The rectangular domain X, Y was covered with an orthogonal nonuniform grid,

$$\xi = \frac{1}{4}\left\{1 + \frac{\tan[(4X-1)\beta_x]}{\tan\beta_x}\right\} \tag{19}$$

$$\eta = \frac{1}{2}\left\{1 + \frac{\tan[(2Y-1)\beta_y]}{\tan\beta_y}\right\} \tag{20}$$

so that the (ξ, η) domain is covered by a uniform grid. Equation (19) refers only to the left half of the cavity. The grid for the entire cavity consisted of 42×42 lines, with $\beta_x = 3.927$ and $\beta_y = 1.134$. This was chosen based on accuracy tests of the type exhibited in Fig. 2. The graph on the left shows that the grid fineness has only a weak influence on the local Nusselt number (or local heat flux, q'') on the left side of the enclosure

$$\mathrm{Nu} = \frac{q''}{k(T_H - T_C)/L} = -\frac{L}{H}\left(\frac{\partial\theta}{\partial X}\right)_{X=0} \tag{21}$$

Therefore, it was necessary to examine the effect of grid fineness on quantities in the enclosure interior. The graph on the right side of Fig. 2 shows the behavior of the local midplane Nusselt number (conduction plus convection)

$$\mathrm{Nu}_m = \frac{L}{H}\left[(\mathrm{Ra\,Pr})^{1/2}U\theta - \frac{\partial\theta}{\partial X}\right]_{x=\frac{L/2}{H}} \tag{22}$$

The difference between the height-averaged midplane Nusselt

Table 1 Overall Nusselt number for a square cavity: comparison between the present calculations and other experimental, numerical, and analytical results [the numbers in the table represent the values of $\overline{\mathrm{Nu}}$ defined in equation (24)]

Ra	10^5	10^6	10^7	10^8	10^9
Present work, Pr = 1	4.9	9.2	17.9	31.8	62.7
Berkovsky and Polevikov (Catton, 1979), Pr = 1	4.81	9.38	18.3	35.7	69.6
Henkes (1990), Pr = 0.71		8.82		30.2	
Bejan (1984), Pr > O (1)				36.4	64.7

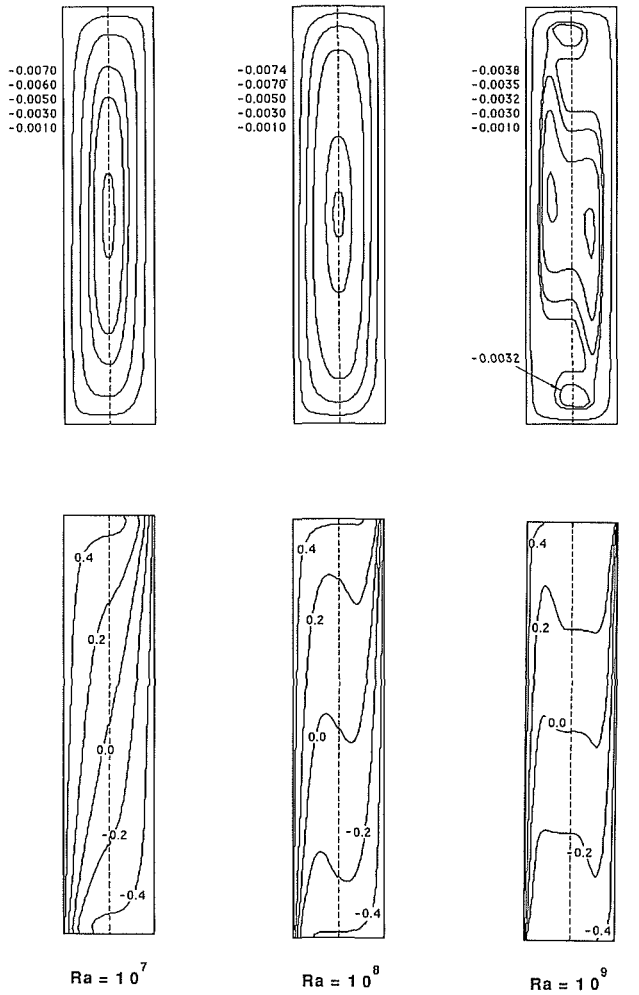

Fig. 3 The Ra effect on the flow and temperature fields (Pr = 0.72, $L/H = 0.1$, $C = 1.6\times10^{-3}$, $R_t = 10^{-4}$)

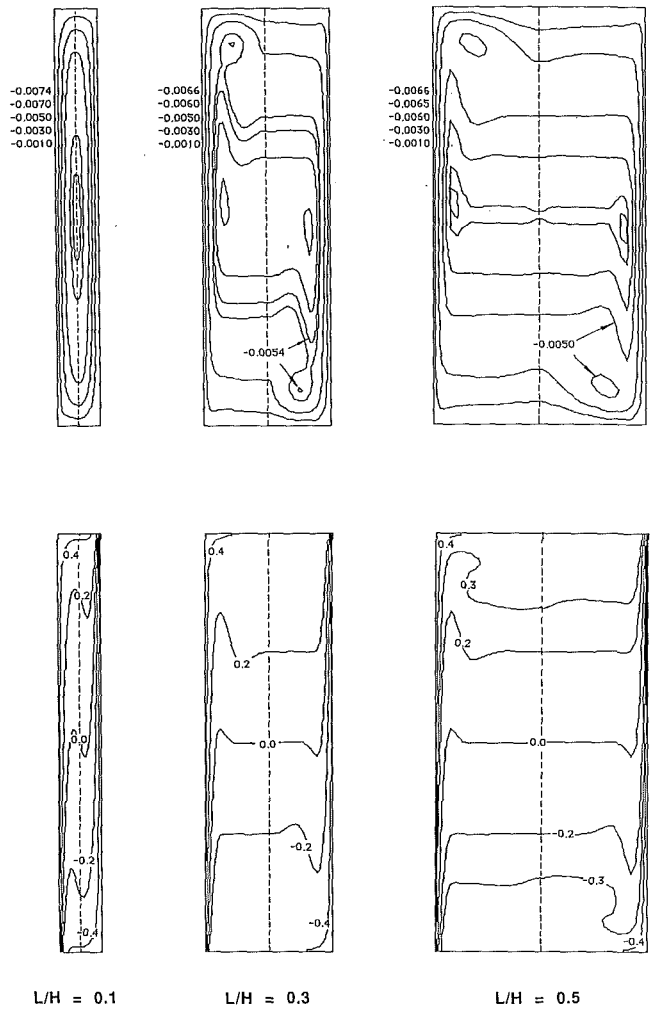

Fig. 4 The L/H effect on the flow and temperature fields ($Pr = 0.72$, $Ra = 10^8$, $C = 1.6 \times 10^{-3}$, $R_f = 10^{-4}$)

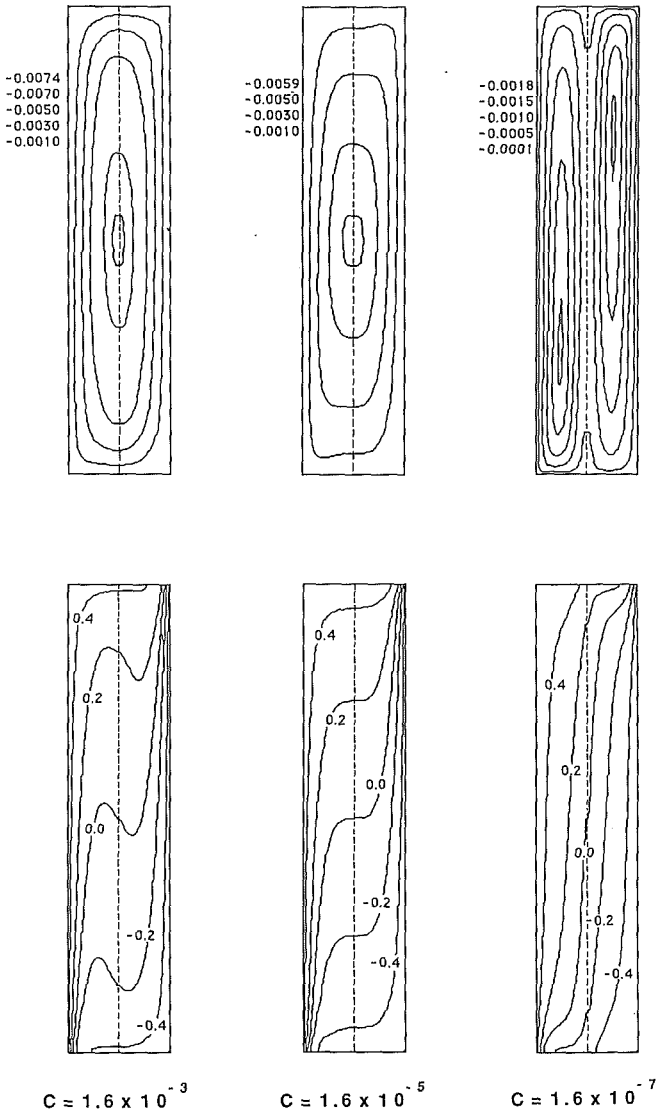

Fig. 5 The partition permeability effect on the flow and temperature fields ($Pr = 0.72$, $Ra = 10^8$, $L/H = 0.1$, $R_f = 10^{-4}$)

numbers ($\overline{Nu}_m$) calculated with the 42×42 and 72×72 grids is less than 2 percent. The corresponding difference between the height-averaged Nusselt numbers for the side wall ($\overline{Nu}$) is less than 0.5 percent.

The numerical code was tested further by simulating the convection in a square enclosure without vertical partition, and by calculating the overall Nusselt number defined in equation (24). The calculated $\overline{Nu}$ values are shown in Table 1, next to older experimental, numerical, and analytical results. The present $\overline{Nu}$ results agree very well with Berkovsky-Polevikov correlation recommended by Catton (1979), and with Henkes' (1990) recent numerical calculations. Bejan (1984, p. 184) showed that the theoretical formula $\overline{Nu} = 0.364\,(L/H)Ra^{1/4}$ is very good for $Pr > O$ (1) fluids in square enclosures, especially in the Ra range 10^8–10^9. Table 1 shows that the present results agree fairly well even with this formula, despite the different Prandtl number ranges.

3 Flow and Temperature Distribution

The flow and temperature fields inside the partitioned cavity depend on five dimensionless groups, Ra, Pr, L/H, R_f, and C. The Prandtl number was fixed at $Pr = 0.72$, which is the room-temperature value for air. The effects of the remaining parameters were examined systematically, with particular emphasis on the manner in which the partition characteristics (R_f, C) affect the overall heat transfer rate across the cavity.

Figure 3 illustrates the changes that occur in the flow and temperature fields as the Rayleigh number increases from 10^7 to 10^9. The width of each rectangular frame in Fig. 3 was magnified by a factor of 2.5 in order to facilitate the viewing of the streamlines and the isotherms. The actual value of the cavity aspect ratio was $L/H = 0.1$. Listed to the left of each set of streamlines are the corresponding streamfunction values,

$$U = \frac{\partial \Psi}{\partial Y}, \quad V = -\frac{\partial \Psi}{\partial X} \tag{23}$$

so that the largest absolute value of Ψ corresponds to the innermost streamline.

The air circulation is oriented clockwise. It consists of a single roll centered in the geometric center of the enclosure (i.e., at the partition midheight) when Ra does not exceed 10^8. The third frame in Fig. 3 shows that when $Ra = 10^9$ the streamfunction minimum occurs near the middle of each half of the enclosure. There are also two additional cells (near the top and bottom walls), which carry fluid in "two-way" fashion through the permeable partition. This change in the flow pattern is associated with the development of distinct boundary layers along the four walls of the cavity. The gradual development of boundary layers is more visible in the patterns of isotherms exhibited in the lower half of the figure.

The streamlines in the $Ra = 10^9$ frame of Fig. 3 may give the (wrong) impression that regions of high fluid shear exist near

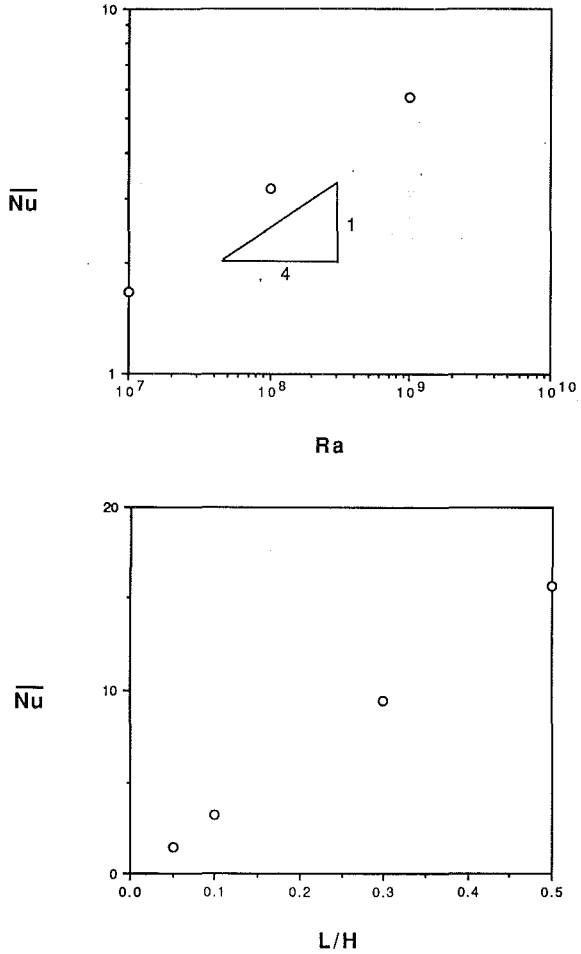

Fig. 6 The effects of Ra and L/H on the overall Nusselt number (Pr = 0.72, $C = 1.6\times10^{-3}$, $R_t = 10^{-4}$); top: $L/H = 0.1$, bottom: Ra = 10^8

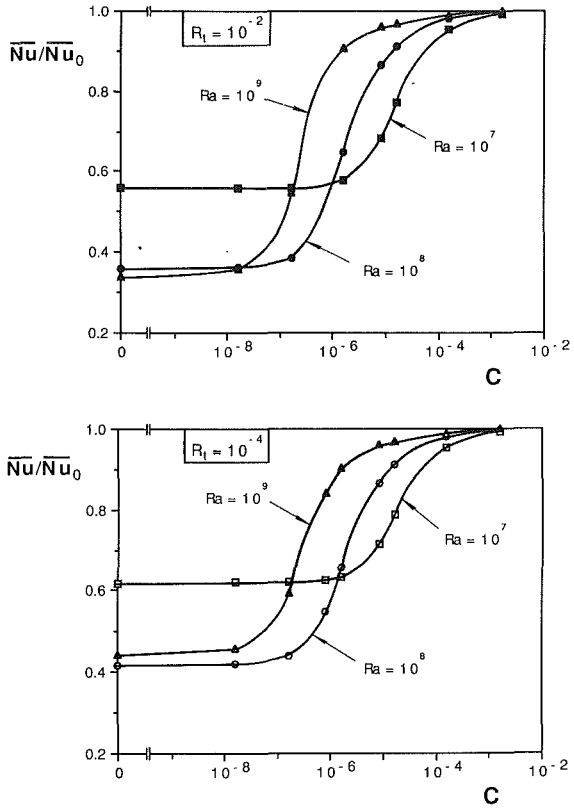

Fig. 7 The effect of the partition (C, R_t) on the overall Nusselt number (Pr = 0.72, Ra = 10^8, $L/H = 0.1$)

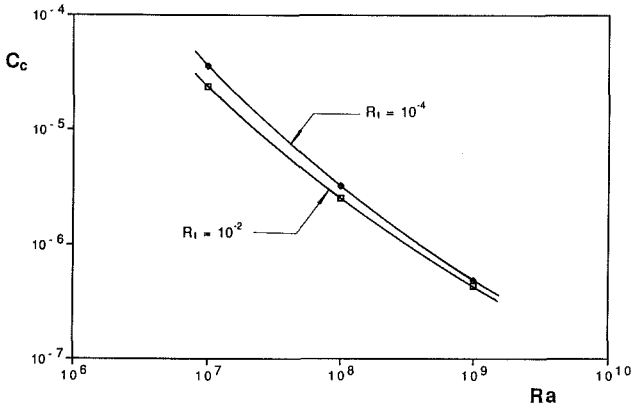

Fig. 8 The critical flow conductance C_c, and the effects of Ra and R_t

the midplane of each of the two halves of the cavity. The clustering of these streamlines is due to the narrow range covered by the numerical Ψ values chosen for illustration. These values were favored in order to emphasize the features of the cells near the top and bottom of the cavity.

The formation of boundary layers and the multiplication of cells are also visible in Fig. 4, which shows the effect of increasing the width of the enclosure. When L/H is large, the top and bottom cells reside in the top-left and bottom-right corners, i.e., in the corners where the vertical boundary layers arrive. These cells no longer penetrate the permeable partition; therefore the flows through the top and bottom sections of the partition are locally "one-way."

The effect of the partition flow conductance is illustrated in Fig. 5. The conductance parameter C decreases from 1.6×10^{-3} in the first frame, to 1.6×10^{-7} in the third frame of the figure. As the partition becomes less permeable, the circulation is gradually severed into two half-width cells of the type seen earlier on the left side of Fig. 4. The temperature field shows the gradual disappearance of the vertical boundary layers, and the establishment of a regime characterized by nearly vertical isotherms (close to pure conduction). The center of each half-width cell is not located in the geometric center of the half-width enclosure.

4 Heat Transfer

The behavior of the total heat transfer rate through the enclosure is illustrated in Figs. 6 and 7. The overall Nusselt number $\overline{\mathrm{Nu}}$ is defined in accordance with equation (21),

$$\overline{\mathrm{Nu}} = \frac{\overline{q''}}{k(T_H - T_C)/L} \tag{24}$$

by writing $\overline{q''}$ for the height-averaged heat flux on the side wall. Note that the denominator in this definition is the heat flux for pure conduction across the cavity. This means that in the laminar boundary layer regime, where $\overline{q''} \sim k(T_H - T_C)/(H\mathrm{Ra}^{-1/4})$, the overall Nusselt number can be expected to vary approximately as (Bejan, 1984)

$$\overline{\mathrm{Nu}} \sim \frac{L}{H}\mathrm{Ra}^{1/4} \tag{25}$$

This trend is confirmed by the $\overline{\mathrm{Nu}}$ data displayed in Fig. 6. The upper graph shows that $\overline{\mathrm{Nu}}$ is proportional to $\mathrm{Ra}^{1/4}$, while the lower graph shows a linear relation between $\overline{\mathrm{Nu}}$ and L/H.

More complicated is the relationship between the overall Nusselt number and the partition parameters R_t and C. In order to isolate the effect of the partition on the overall heat transfer rate, in Fig. 7 we plotted the ratio $\overline{\mathrm{Nu}}/\overline{\mathrm{Nu}}_0$ in which

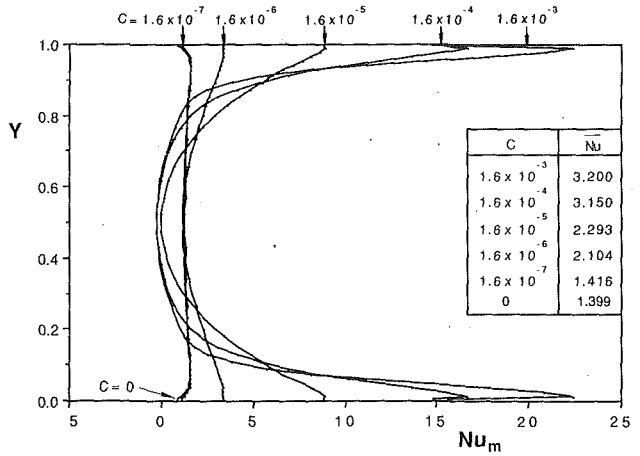

Fig. 9 The effect of the partition flow permeability on the local midplane Nusselt number (Pr = 0.72, Ra = 10^8, $L/H = 0.1$, $R_t = 10^{-4}$)

$\overline{Nu}_0$ is the overall Nusselt number when the partition is absent. Reliable correlations for $\overline{Nu}_0$ can be found in the literature, for example in the Berkovsky–Polevikov formulas recommended by Catton (1979).

Figure 7 shows that when the flow conductance C is sufficiently small, the overall Nusselt number drops to approximately half of the value calculated by assuming that the partition is absent. The most abrupt decrease in the $\overline{Nu}/\overline{Nu}_0$ ratio occurs in a "characteristic" band of C values, which has a width of approximately two orders of magnitude. When $Ra = 10^8$, this band is centered around $C = 10^{-6}$, which can be regarded as a threshold value for the design in which the impermeability of the partition begins to show its effect on the overall heat transfer rate. The C threshold migrates to the left (toward lower C values) as Ra increases, which means that at higher Rayleigh numbers the partition has to be less permeable to cause a significant drop in $\overline{Nu}$.

This trend can be illustrated quantitatively by defining the "critical" value of the parameter C for which the overall Nusselt number experiences only half of the total decrease from the "no partition" limit ($\overline{Nu}_0$) to the impermeable partition limit ($C = 0$). This critical value has been labeled C_c in Fig. 8, which shows that in the (Ra, R_t) domain investigated numerically, the R_t effect is minor. The critical flow conductance C_c decreases almost as 1/Ra as Ra increases.

The effect of the partition permeability is illustrated further in Fig. 9. When the partition is permeable (large C values) the local midplane Nusselt number peaks in the vicinity of the top and bottom walls, where the heat transfer mechanism is dominated by horizontal jets. As C decreases, these jets and the Nu_m maxima disappear. At C values below 10^{-6}, the local midplane Nusselt number is nearly independent of Y, suggesting a heat transfer process dominated by conduction on both sides of the partition.

The partition thermal resistance effect can be seen by comparing the top graph of Fig. 7 ($R_t = 10^{-2}$) with the bottom graph ($R_t = 10^{-4}$). The overall Nusselt number decreases as R_t increases. In the range $10^{-4} < R_t < 10^{-2}$ this effect is minor compared with the effect of the flow permeability parameter C.

5 Application: The Critical Spacing Between Partially Overlaying Strips

The critical flow conductance information of Fig. 8 can be used in order to determine the proper position of the partially overlaying strips, so that the permeable screen of Fig. 1 is effective in inhibiting the natural convection heat transfer. Figure 10 shows an enlarged view of the screen, in which the strip width, angle of inclination and strip-to-strip spacing are exaggerated for better clarity. The geometry is determined by the strip-to-strip spacing δ, the strip width W_s, and the width of the area of overlap W_o.

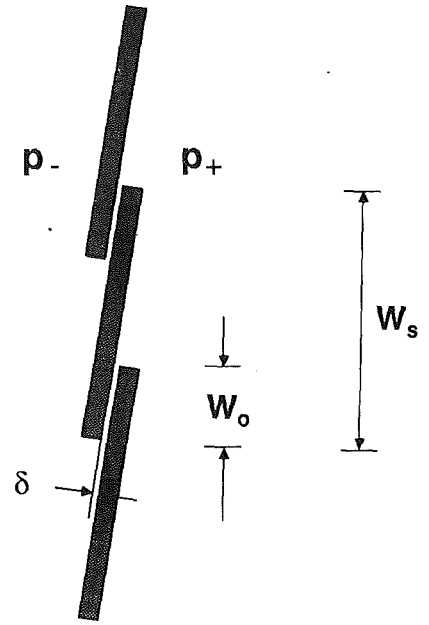

Fig. 10 Geometric details of the partially overlaying strips

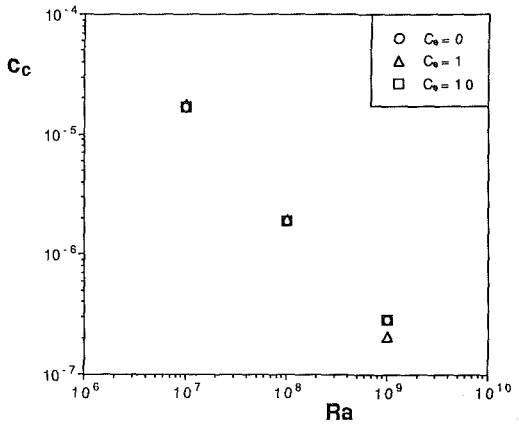

Fig. 11 The effect of the "ends" parameter C_e on the critical flow conductance C_c

Consistent with the assumption that the fluid leakage through the screen obeys Darcy's law, equation (16), is the assumption that the flow through the δ-wide gap is slow enough to behave as Hagen-Poiseuille flow between two parallel plates (e.g., Bejan, 1984, p. 73)

$$u = \frac{\delta^2}{12\mu W_o}(p_- - p_+) \tag{26}$$

In this equation, $\bar{u}$ is the velocity averaged over the δ-wide cross section. The proportionality between $\bar{u}$ and the volume-averaged horizontal velocity through the permeable screen [u of equation (16)] is

$$\bar{u} = \frac{W_s - W_o}{\delta} u \tag{27}$$

Combining equations (16), (26), and (27) we obtain the relationship between the permeability K and the geometry of the screen,

$$K = \frac{\delta^3 t_p}{12 W_o (W_s - W_o)} \tag{28}$$

The corresponding expression for the flow conductance parameter is

$$C=\frac{\delta^3}{12W_oH(W_s-W_o)} \tag{29}$$

As a numerical example, consider the design implications of Fig. 8, in which $\mathrm{Ra}\sim 10^8$ is the representative order of magnitude of the window Rayleigh number. The same figure shows that $C_c\sim 10^{-6}$ is the order of magnitude of the critical flow conductance. If 1 m is the scale of the window height H, 0.5 cm the scale of the overlap W_o, and 2 cm the scale of the strip width W_s, then equation (29) indicates that the "critical" strip-to-strip spacing that corresponds to $C_c\sim 10^{-6}$ is $\delta\sim 0.1$ cm.

A spacing much smaller than 0.1 cm moves the design toward lower C values, i.e., toward the impermeable screen limit. In the critical design case, $\delta\sim 0.1$ cm and $W_o\sim 0.5$ cm indicate a parallel plate channel with a length/spacing ratio of order 5. This ratio may not be large enough to justify fully the assumption that the entire pressure drop across the $\delta\times W_o$ channel is due to the Hagen–Poiseuille flow resistance expressed by equation (26).

A more general expression for the pressure drop across the channel is

$$p_- - p_+ = 0.9\,\rho|\bar{u}|\bar{u}+12\frac{\mu W_o}{\delta^2}\bar{u} \tag{30}$$

in which the new term—the first on the right side—accounts for the contraction and expansion of the flow as it enters and exits the channel. The 0.9 coefficient results from using Kays' chart (Kays and London, 1964), which shows $K_c\sim 0.8$ for the entrance pressure drop coefficient, and $K_e=1$ for the exit pressure drop coefficient.

The dimensionless counterpart of equation (30) is

$$U=\left(\frac{\mathrm{Ra}}{\mathrm{Pr}}\right)^{1/2}\frac{C}{1+C_e|U|}(P_- - P_+) \tag{31}$$

where C_e is the new dimensionless group accounting for the ends of the $\delta\times W_o$ parallel-plate channel,

$$C_e=0.9\frac{W_s-W_o}{W_o}\frac{\delta}{12H}\left(\frac{\mathrm{Ra}}{\mathrm{Pr}}\right)^{1/2} \tag{32}$$

All the numerical work that was described in the preceding sections was repeated by using equation (31) in place of the Darcy-limit equation (17). The end-effect parameter C_e was assigned the values 1 and, later, 10, while noting that the preceding results (Figs. 2–9) correspond to $C_e=0$.

Of special interest is the effect that the new parameter C_e might have on the critical flow conductance C_c. Figure 11 shows that this effect is insignificant in the C_e range 0–10. Note also that Fig. 11 was drawn only for $R_t=10^{-2}$; a nearly identical graph was obtained for $R_t=10^{-4}$, and is not shown here.

Returning to the numerical example that opened this section, we use equation (32) and find that the C_e value that corresponds to that example is 2.25. This C_e value belongs to the range covered by the latest numerical runs (Fig. 11); therefore, the conclusions reached in the numerical example are valid.

6 Conclusions

The chief conclusion of this study is that the use of a vertical screen can reduce significantly the overall heat transfer rate by natural convection through a tall enclosure (Fig. 7). The numerical results showed that there exists a critical screen flow conductance (air leakage) above which the screen does not have a significant effect on the heat transfer rate (Figs. 8, 11). It has been shown how this critical flow conductance can be used to calculate the spacing (air gap δ) that can be tolerated between two consecutive strips in the screen.

Experimental results on the effect of a solid vertical baffle on the overall heat transfer rate have been reported by Emery (1969). Those results cannot be compared with the present calculations, because in Emery's experiments the baffle was solid, and its height varied from 25 to 90 percent of the enclosure height H. In other words, in the experiments the air circulation was completed through two relatively wide "gates" (wide relative to the present δ-size openings), which were left between the ends of the solid partition and the top and bottom walls of the enclosure. The size (height) of each gate varied from 38 to 5 percent of the enclosure height H. This is why in Emery's study the effect of the baffle on heat transfer was minor: The decrease in the overall heat transfer rate was less than 8 percent, at Rayleigh numbers (Ra) in the range 10^9–10^{10}.

A final observation concerns the pressure drop formula (30), in which the effect of the entrance to the δ-wide channel has been neglected. That the entrance effect is indeed negligible can be seen by estimating the channel Reynolds number.

To begin with, the vertical boundary layer has the vertical velocity scale $(\alpha/H)\mathrm{Ra}^{1/2}$ and the thickness scale $H\,\mathrm{Ra}^{-1/4}$ (Bejan, 1984, p. 120). The flow rate is therefore of order $\alpha\,\mathrm{Ra}^{1/4}$, and, as seen in Figs. 3–5, this flow rate returns (i.e., completes the circuit) through the core of height H. It follows that the horizontal velocity scale u is $\alpha\,\mathrm{Ra}^{1/4}/H$.

The channel velocity scale that corresponds to this u scale is [see equation (27)]

$$\bar{u}\sim\frac{W_s-W_o}{\delta}\frac{\alpha}{H}\mathrm{Ra}^{1/4} \tag{33}$$

The corresponding channel Reynolds number is

$$\frac{\bar{u}\delta}{\nu}\sim\frac{W_s-W_o}{H}\mathrm{Ra}^{1/4} \tag{34}$$

in which we used the fact that $\mathrm{Pr}\sim 1$. In the numerical example that preceded equation (30) we had $W_s\sim 2$ cm, $W_o\sim 0.5$ cm, and $\mathrm{Ra}\sim 10^8$. According to equation (34) then, the channel Reynolds number is of order 1. This means that the "entrance" length of the channel is of order δ (i.e., there are no "thin" boundary layers in the entrance), and that the flow resistance associated with the developing flow is negligible when, as in the numerical example, $\delta < W_o$.

The channel Reynolds number of order 1 is in fact the reason why the use of the Darcy model (17) yields nearly the same conclusion as the more general model (30).

References

Bejan, A., 1984, *Convection Heat Transfer,* Wiley, New York, Chap. 5.

Catton, I., 1979, "Natural Convection in Enclosures," *6th Int. Heat Transfer Conference 1978,* Vol. 6, pp. 13–43.

Emery, A. F., 1969, "Exploratory Studies of Free-Convection Heat Transfer Through an Enclosed Vertical Liquid Layer With a Vertical Baffle," ASME JOURNAL OF HEAT TRANSFER, Vol. 91, pp. 163–165.

Hasnaoui, M., Vasseur, P., and Bilgen, E., 1990, "Natural Convection in Rectangular Enclosures With Fins Attached to One of the Isothermal Walls," presented at the 1990 Int. ASME Solar Energy Conference, Miami, FL, Apr. 1–4.

Henkes, R. A. W. M., 1990, "Natural-Convection Boundary Layers," Ph.D. Thesis, Technical University of Delft, The Netherlands.

Kays, W. M., and London, A. L., 1964, *Compact Heat Exchangers,* 2nd ed., McGraw-Hill, New York, p. 94.

Shakerin, S., Bohn, M., and Loehrke, R. I., 1988, "Natural Convection in an Enclosure With Discrete Roughness Elements on a Vertical Heated Wall," *Int. J. Heat Mass Transfer,* Vol. 31, pp. 1423–1430.

Shurcliff, W. A., 1980, *Thermal Shutters and Shades,* Brick House Publishing Co., Andover, MA, pp. 100–101.

Van Doormaal, J. P., and Raithby, G. D., 1984, "Enhancement of the Simple Method for Predicting Incompressible Fluid Flows," *Numerical Heat Transfer,* Vol. 7, pp. 147–163.

Zimmerman, E., and Acharya, S., 1987, "Free Convection Heat Transfer in a Partially Divided, Vertical Enclosure With Conducting Walls," *Int. J. Heat Mass Transfer,* Vol. 30, pp. 319–331.

T. F. Lin
Professor.
Assoc. Mem. ASME

C. P. Yin
Graduate Student.

W. M. Yan
Graduate Student.

Department of Mechanical Engineering,
National Chiao Tung University,
Hsinchu, Taiwan

Transient Laminar Mixed Convective Heat Transfer in a Vertical Flat Duct

Unsteady laminar aiding and opposing mixed convection heat transfer in a vertical flat duct is numerically investigated for an initially fully developed flow. Results indicate that unsteady heat transfer characteristics in the flow are principally determined by wall-to-fluid heat capacity ratios. Effects of the buoyancy and degree of asymmetric heating or cooling are rather insignificant. Correlation equations for the time variations of local Nusselt numbers with wall-to-fluid heat capacity ratios are proposed.

Introduction

Mixed convection heat transfer is of considerable interest to the technical field due to its frequent occurrences in industrial, technological, and natural surroundings. Buoyancy effects on heat transfer in flow through a parallel-plate channel are relevant to solar energy collection, as in conventional flat plate collectors, and the cooling of modern electronic equipment. In the latter application, electronic components are normally mounted on parallel circuit boards, which are positioned vertically in a cabinet, forming vertical flat channels through which coolant passes. The coolant may be driven by natural convection, forced convection, or mixed convection depending on the power density of the circuit boards. Unsteady heat transfer plays an important role during the power-on and power-off periods and any off-normal surges during system operation. The present study investigates transient heat transfer characteristics in laminar mixed convection through a parallel-plate channel. Comprehensive reviews of internal flow mixed convection were recently presented by Incropera (1986), Aung (1987), and Gebhart et al. (1988). In the following the literature on mixed convection in vertical ducts is briefly reviewed.

Steady laminar mixed convection in a vertical plane channel has been extensively studied in the past. An analytic method was proposed by Tao (1960) to study fully developed mixed convection in a vertical plane channel. Developing mixed convection was approximately treated by Quintiere and Mueller (1973). The predicted Nusselt number was contrasted with the limiting cases of pure free and forced convection. Various axial length scales to distinguish regions of different convective mechanisms from the developing state to the fully developed state were presented by Yao (1983). Flow reversal in forced convection flow influenced by an opposing buoyancy force was numerically investigated by Cebeci et al. (1982) for Gr/Re^2 ranging from 0.001 to 1.0. Steady buoyancy aiding laminar mixed convection for air in a vertical channel with symmetric or asymmetric wall temperatures was numerically investigated by Habchi and Acharya (1986). Their results show that air temperature increases with Gr/Re^2; the velocity profile peaks near the hot plate and exhibits a concavity, which, in the symmetric heating case, occurs around the centerline, and Nusselt number decreases monotonically from the channel entrance. A similar study was carried out by Aung and Worku (1986a), showing that buoyancy force can cause a severe distortion in the velocity profiles, especially under an asymmetric wall heating condition. In the symmetric heating case the distortion eventually disappears and the velocity profile becomes fully developed with a parabolic shape at a large distance from the channel entrance. Quantitative results for the Nusselt number and bulk temperature indicate that buoyancy force and asymmetric heating exhibit profound influences on the heat transfer process. Finally, the hydrodynamic entrance length is found to increase dramatically with buoyancy, which has an opposite influence on the thermal entrance length. In a companion paper (Aung and Worku, 1986b), they obtained an exact solution for velocity and temperature in the fully developed region. Based on this solution, flow reversal will occur if $Gr/Re > 72/(1-\gamma_T)$ for $\gamma_T < 1$, where $\gamma_T = (T_1 - T_e)/(T_2 - T_e)$. A similar investigation for flow with unequal wall heat fluxes (Aung and Worku, 1987) shows that for the symmetric wall heating condition, buoyancy introduces a lesser degree of skewness in the velocity distribution and flow reversal is more prone to occur in the uniform wall temperature situation. In particular, no flow reversal is predicted for Gr/Re up to 500. Recently, Ingham et al. (1988a, 1988b) developed a numerical method to treat the flow reversal in buoyancy aiding and opposing flows. They noted poor heat transfer results for flow retarded by an opposing buoyancy force, but for a large and negative Gr/Re, heat transfer is rather effective. In fact, heat transfer is greatly improved over the section containing reversed flow. An exact solution was obtained by Lavine (1988) for laminar fully developed opposing mixed convection between inclined parallel plates with a uniform wall heat flux boundary condition. Four different flow reversal regimes have been observed, namely, no reversal, top reversal, bottom reversal, and top and bottom reversal, depending on the magnitudes of the parameters $Gr \cdot \sin\phi/Re$ and $Gr \cdot \cos\phi/Re^2 \cdot Pr$ (where ϕ is the tilt angle measured counterclockwise from the horizontal). Steady laminar mixed convection in a short channel at low Peclet numbers including axial heat conduction in the flow was investigated by Chow et al. (1984) by solving the full Navier-Stokes equations.

Heat transfer in steady mixed convection in a vertical tube was numerically and experimentally investigated by Scheele et al. (1960), Scheele and Hanratty (1963), and Lawrence and Chato (1966) for buoyancy aiding and opposing flows. Flow reversal was noted at high Gr/Re. The effect of natural convection on instability and transition of the forced flow was experimentally examined. A similar study was performed by Zeldin and Schmidt (1972). Through a detailed numerical simulation of unsteady mixed convection, Shadday (1986) predicted the flow reversal at $Re = 100$ and $Gr = 10^5$ and unstable

Contributed by the Heat Transfer Division for publication in the JOURNAL OF HEAT TRANSFER. Manuscript received by the Heat Transfer Division September 26, 1989; revision received July 14, 1990. Keywords: Mixed Convection, Transient and Unsteady Heat Transfer.

flow at Gr = 10^6 and Re = 100. Unsteady vortex shedding from the boundary layer on the channel wall to the central core of the flow was found to enhance the heat transfer significantly. However, no detail information on the formation of recirculating flow was given. Additionally, in the analysis, heat capacity of the wall was not included. This is inappropriate especially during the transient stage, as evident from the studies of transient pure natural convection (Joshi, 1988) and forced convection (Sucec and Sawant, 1984; Sucec, 1987; Lin and Kuo, 1988) in channels. Visualization of the recirculating flow in aiding and opposing mixed convection flows was recently conducted by Morton et al. (1989) and Lavine et al. (1989).

Despite the extensive studies on steady mixed convection in vertical channels that have been carried out in the past, relatively little attention has been paid to investigating transient thermal characteristics of internal mixed convection flow. The purpose of this study is to explore unsteady laminar mixed convection in a vertical plane channel under buoyancy aiding and opposing conditions.

The physical model under consideration and the coordinates chosen are depicted in Fig. 1. As shown in the figure, a parallel plane channel is oriented along the gravitational direction. Flow entering the channel from the upstream region approaches the inlet of the heated section ($x=0$) with a uniform temperature ($T=T_e$) and corresponding fully developed velocity profile. The two vertical plates are relatively large in both the x and z directions with plate thickness δ_1 and δ_2, respectively, and the whole system is at a uniform temperature T_e. At $t=0$, uniform heat fluxes q_1'' and q_2'' are suddenly applied at the outer surfaces of the left and right plates from $x \geq 0$, respectively. Attention is focused on the temporal development of the hydrodynamic and thermal characteristics in the flow after the sudden heat input to the channel.

Analysis

Flow and thermal characteristics in a vertical flat duct can be considered as two dimensional when the plate depth w is at least ten times the interplate spacing b, that is, $w > 10b$. To facilitate the analysis, the Boussinesq approximation is invoked. Besides, only high Peclet number flow is treated here so that the longitudinal conduction in the flow is negligibly small. Also the plates are rather thin so that heat conduction in them can be neglected. In an initial attempt to investigate transient mixed convection, only boundary layer flow is examined.

Under the above assumptions, the basic equations in dimensionless form describing the conservation of mass, momentum, and energy for unsteady mixed convection in a vertical plane channel are (Aung, 1987)

$$\frac{\partial U}{\partial X}+\frac{\partial U}{\partial Y}=0 \tag{1}$$

$$\frac{\partial U}{\partial \tau}+U\frac{\partial U}{\partial X}+V\frac{\partial U}{\partial Y}=-\frac{dP}{dX}+\frac{\partial^2 U}{\partial Y^2}+\frac{\mathrm{Gr}}{\mathrm{Re}}\theta \tag{2}$$

$$\frac{\partial \theta}{\partial \tau}+U\frac{\partial \theta}{\partial X}+V\frac{\partial \theta}{\partial Y}=\frac{1}{\mathrm{Pr}}\frac{\partial^2 \theta}{\partial Y^2} \tag{3}$$

and

Nomenclature

A_1 = wall-to-fluid heat capacity ratio for plate $1=\frac{\rho_w c_w \delta_1}{\rho c_p\, b}$
A_2 = wall-to-fluid heat capacity ratio for plate $2=\frac{\rho_w c_w \delta_2}{\rho c_p\, b}$
b = duct spacing
c_p = specific heat at constant pressure
g = gravitational acceleration
h_x = local heat transfer coefficient $= q''/(T_x - T_e)$
Gr = Grashof number $= g\beta q_1'' b^4/k\nu^2$
i = grid position in longitudinal direction
j = grid position in transverse direction
k = thermal conductivity
l = values for the lth time step
m = a dimensionless group $= (2\mathrm{Gr}/\mathrm{Re})^{1/4}$
n = values for the nth iteration
NI = total number of nodes in longitudinal direction
NJ = total number of nodes in transverse direction
NK = total number of time steps
Nu_x = local Nusselt number $= h_x \cdot b/k$
p_m = dynamic pressure
P = dimensionless pressure $= p_m/\rho \tilde{u}_e^{-2}$
Pe = Peclet number = Re•Pr
Pr = Prandtl number = $\mu c_p/k$
Q = dimensionless interfacial heat flux $= q_{I1}''/q_1''$ or q_{2i}''/q_1''
q'' = heat flux
Re = Reynolds number $= \tilde{u}_e \cdot b/\nu$
t = time
T = temperature
T_x = plate temperature
u = axial velocity
U = dimensionless axial velocity $= u/\tilde{u}_e$
v = transverse velocity
V = dimensionless transverse velocity $= vb/\nu$
$\tilde{u}_e$ = mean velocity at entrance
x = axial coordinate
X = dimensionless axial coordinate $= x/b \cdot \mathrm{Re}$
y = transverse coordinate
Y = dimensionless transverse coordinate $= y/b$
z = spanwise coordinate
α = thermal diffusivity $= k/\rho c_p$
β = thermal expansion coefficient
γ = enlarged factor for time step
γ_H = heat flux ratio $= q_1''/q_2''$
$\Delta X, \Delta Y, \Delta \tau$ = grid intervals in X, Y, and τ
ϵ = enlarged factor for grid interval in longitudinal direction
θ = dimensionless temperature $= (T - T_e)/(q_1'' b/k)$
ν = kinematic viscosity
ξ = dimensionless axial coordinate $= x/2 \cdot b \cdot \mathrm{Pe}$
ρ = density
τ = dimensionless time $= t/(b^2/\nu)$
ω = enlarged factor for grid interval in transverse direction

Subscripts

e = condition at entrance of duct
o = pure forced convection
ss = condition at steady state
w = condition at wall
1 = pertaining to left wall
2 = pertaining to right wall

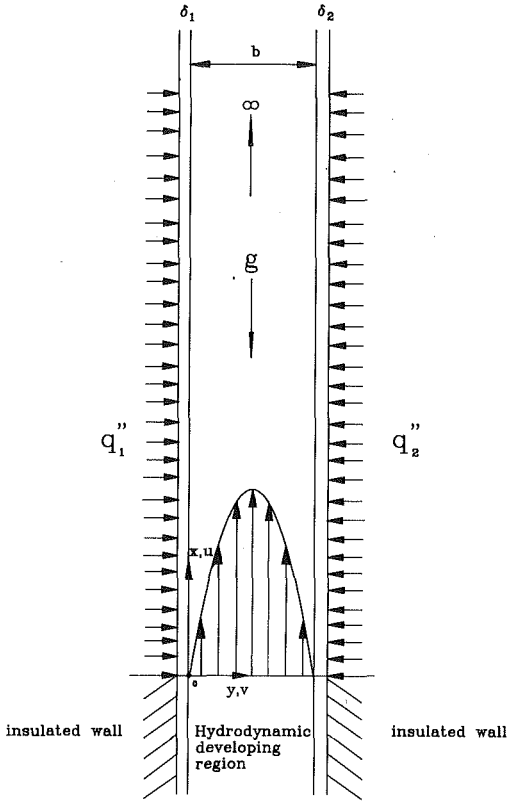

Fig. 1 Schematic diagram of the physical system

$$\int_0^1 U dy = 1 \tag{4}$$

These equations are subject to the following initial and boundary conditions

$$\tau = 0, \quad U = 6(Y - Y^2), \quad \theta = 0 \tag{5}$$

$$\tau > 0, \quad x = 0, \quad U = 6(Y - Y^2), \quad \theta = 0 \tag{6a}$$

$$Y = 0, \quad U = 0, \quad A_1 \mathrm{Pr} \frac{\partial \theta}{\partial \tau} - \frac{\partial \theta}{\partial Y} = 1 \tag{6b}$$

$$Y = 1, \quad U = 0, \quad A_2 \mathrm{Pr} \frac{\partial \theta}{\partial \tau} + \frac{\partial \theta}{\partial Y} = \gamma_H \tag{6c}$$

In writing the above equations, the following nondimensional variables were used:

$$X = \frac{x}{b \cdot \mathrm{Re}}, \quad Y = \frac{y}{b}, \quad U = \frac{u}{u_e}, \quad V = \frac{vb}{\nu},$$

$$\theta = \frac{T - T_e}{q_1'' (b/k)}, \quad P = \frac{p_m}{\rho \bar{u}_e^2}, \quad \mathrm{Pr} = \frac{\nu}{\alpha}, \quad \mathrm{Re} = \frac{\bar{u}_e b}{\nu},$$

$$\mathrm{Gr} = \frac{g\beta q_1'' b^4}{k\nu^2}, \quad \gamma_H = \frac{q_2''}{q_1''}, \quad \tau = \frac{t}{(b^2/\nu)},$$

$$A_1 = \frac{\rho_w c_{pw} \delta_1}{\rho c_p \, b}, \; A_2 = \frac{\rho_w c_{pw} \delta_2}{\rho c_p \, b} \tag{7}$$

Note that thermal energy storage in the channel walls due to finite wall heat capacity, which is rather important in the transient heat transfer process (Sucec, 1987; Lin and Kuo, 1988), is accounted for in equations (6*b*) and (6*c*).

Due to transient interactions between the convection heat transfer in the flow and the energy storage in the channel walls through the fluid–wall interfaces as described by the governing equations, solution for the problem can be better sought by finite-difference procedures. The governing equations are parabolic in X and τ. Hence the solution can be marched in time and in the downstream direction. Equations (2) and (3) are expressed in terms of finite difference approximations by employing the upstream difference in the convection terms and central difference in the diffusion terms. The unsteady terms are treated by the backward difference so that the scheme is fully implicit. The resulting system of algebraic equations can be cast into a tridiagonal matrix equation, which can be efficiently solved by the Thomas Algorithm (Anderson et al., 1984). The solution procedures are briefly outlined as follows:

For a given time instant and axial location

(1) Guess $(-dP/dX)$ and θ;
(2) Solve the finite difference form of equation (2) for U;
(3) Numerically integrate the continuity equation for V by $V = -\int_0^1 \frac{\partial U}{\partial X} dY$;
(4) Solve the finite difference form of equation (3) for θ;
(5) Check if $\left| \int_0^1 U dY - 1 \right| < 10^{-6}$ and $\frac{\mathrm{Max}\left| {}^{l}\theta_{i,j}^{n} - {}^{l}\theta_{i,j}^{n-1} \right|}{\mathrm{Max}\left| {}^{l}\theta_{i,j}^{n} \right|} < 10^{-6}$.

If yes, repeat procedures (1)–(5) for the next axial location. If not, repeat procedures (1)–(5) for the current axial location. Apply the above procedures from the entrance to the desired downstream location. Then march the solution from the onset of the transient to the final steady state.

To obtain enhanced accuracy, the gridlines were positioned nonuniformly. In the transverse direction the highest grid density is near the walls due to the steep velocity and temperature gradients there. In the longitudinal direction, the highest grid density is near the entrance, $X = 0$. The grid intervals and time steps were determined by a geometric series in which the enlargement factors are all taken as $\epsilon = \omega = \gamma = 1.03$. Specifically, ΔX_i, ΔY_j, and $\Delta \tau_l$ are computed by

$$\Delta X_1 = 0.2 \times \frac{1 - \epsilon}{1 - \epsilon^{(NI-1)}} \tag{8}$$

$$\Delta X_i = X_{i+1} - X_i = \epsilon \Delta X^{i-1} \tag{9}$$

$$\Delta Y_1 = 0.5 \times \frac{1 - \omega}{1 - \omega^{(NJ-1)}} \tag{10}$$

$$\Delta Y_j = Y_{j+1} - Y_j = \omega \Delta Y_{j-1} \tag{11}$$

$$\Delta \tau_1 = 10 \times \frac{1 - \gamma}{1 - \gamma^{(NK-1)}} \tag{12}$$

$$\Delta \tau_l = \tau_{l+1} - \tau_l = \gamma \Delta \tau_{l-1} \tag{13}$$

In the X direction 101 gridlines were used, while 61 grid points were placed in the Y direction. NK varies from 200 to 300 depending on the governing nondimensional parameters.

During the program tests, solution for a typical case with $\mathrm{Pr} = 5.0$, $\mathrm{Gr/Re} = 1000.0$, $A_1 = A_2 = 10.0$, and $\gamma_H = 0.5$ were obtained using different space and time intervals to ensure that the solution is grid-independent. The results from the computation for various grids are given in Table 1 for a transient state. It is noted that the differences in the wall temperature are always less than 1 percent. In the separate computations, a reduction in the time interval to one-half of the original one results in less than 2 percent difference in the wall temperature. To reduce the cost of computation, the 101×61 grid is chosen

Table 1 Comparison of transient hot wall temperature for various grid arrangements for Pr = 5.0, Gr/Re = 1000.0, $A_1 = A_2 = 10.0$, $\gamma_H = 0.5$, and $\tau = 8.271$

X	131 × 61	101 × 61	101 × 81
0.000550	0.039390	0.037409	0.036815
0.012187	0.086385	0.086211	0.086222
0.040882	0.104591	0.104534	0.104508
0.130739	0.120377	0.120358	0.120359
0.200000	0.125844	0.125834	0.125816

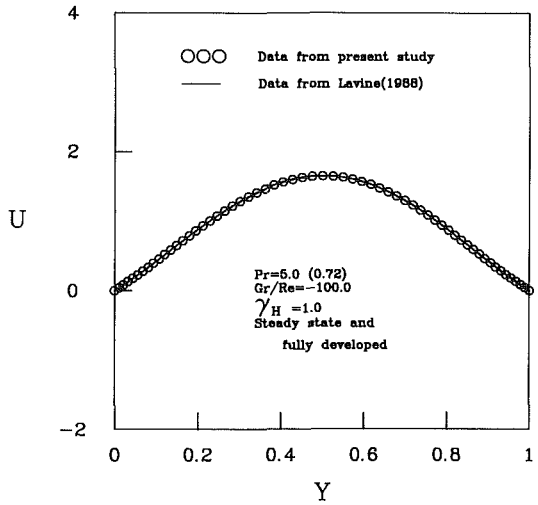

Fig. 2 Comparison of the predicted velocity profile with the analytic solution of Lavine (1988)

for the subsequent computation. In addition, our predictions are compared with the results of Aung and Worku (1987) for a case with Pr = 0.72, Gr/Re = 250, $\gamma_H = 1.0$, $A_1 = A_2 = 1$ at steady state. The agreement is good. Furthermore, the predicted fully developed velocity profile under buoyancy opposing condition is contrasted with the closed-form solution of Lavine (1988) in Fig. 2. The analytic solution is

$$U = c_1[\sinh(mY) + \sin(mY)] + c_2[\cosh(mY) - \cos(mY)] + \frac{m}{2}\sin(mY) \quad (14)$$

Here c_1 and c_2 are determined from the solution of the equations

$$c_1[\sinh(m) + \sin(m)] + c_2[\cosh(m) - \cos(m)] = -\frac{m}{2}\sin(m) \quad (15)$$

and

$$c_1[\cosh(m) - \cos(m)] + c_2[\sinh(m) - \sin(m)] = \frac{m}{2}[1 + \cos(m)] \quad (16)$$

In the above equations, $m = (2\mathrm{Gr/Re})^{1/2}$. Excellent agreement is noted in Fig. 2. Through these program tests, the proposed numerical algorithm is considered to be suitable for the problem.

Results and Discussion

The foregoing analysis indicates that heat transfer characteristics in the flow depend on the Prandtl number Pr, ratio of the Grashof number to Reynolds number Gr/Re, degree of asymmetric heating γ_H, and wall-to-fluid heat capacity ratios A_1 and A_2. While computations can be performed for any combination of these parameters, the objective here is to present a sample of results that would illustrate the effects of these parameters on the transient heat transfer characteristics. In particular, we deal with transient mixed convection in water with Pr = 5.0. The wall heat capacity ratios A_1 and A_2 are considered to be equal and vary from 0 to 10. In aiding flow, Gr/Re varies from 0 to 1000, while in opposing flow it varies from 0 to −100.

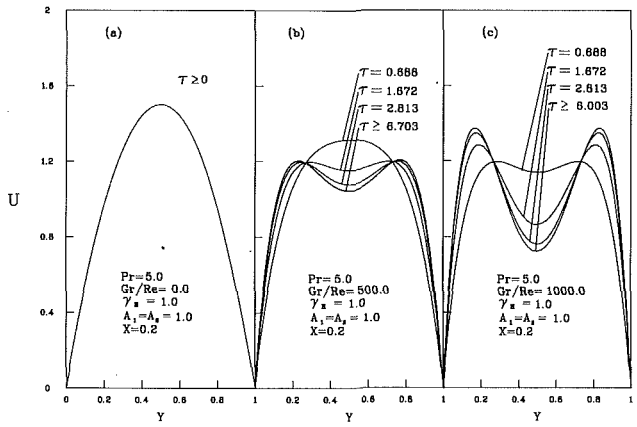

Fig. 3 Buoyancy effect on the velocity profile during transient process in aiding flow at $X = 0.2$

Local Nusselt numbers are of interest to thermal system design. They can be evaluated as:

for the left wall

$$\mathrm{Nu}_{x,1} = \frac{h_{x,1} \cdot b}{k} = \frac{q_1'' b}{(T_{x,1} - T_e) \cdot k} = \frac{1}{\theta_{x,1}} \quad (17)$$

while for the right wall

$$\mathrm{Nu}_{x,2} = \frac{h_{x,2} \cdot b}{k} = \frac{q_2'' \cdot b}{(T_{x,2} - T_e) \cdot k} = \frac{\gamma_H}{\theta_{x,2}} \quad (18)$$

Here $T_{x,1}$ and $T_{x,2}$ are, respectively, the left and right wall temperatures at x.

Another informative parameter for conjugate heat transfer, used to describe the energy transfer into the fluid through the wall-fluid interface, is the dimensionless interfacial heat flux, defined as:

for plate 1

$$Q_1 = \frac{q_{1i}''}{q_1''} \frac{-k(\partial T/\partial Y)_{y=0}}{q_1''} = -\left(\frac{\partial \theta}{\partial Y}\right) Y = 0 \quad (19)$$

for plate 2

$$Q_2 = \frac{q_{2i}''}{q_1''} = \frac{k(\partial T/\partial y)_{y=b}}{q_1''} = \left(\frac{\partial \theta}{\partial Y}\right) Y = 1 \quad (20)$$

where q_{1i} and q_{2i} are the heat fluxes through the wall-fluid interfaces at the left and right walls, respectively.

Effect of Gr/Re. The temporal development of the velocity profiles for various Gr/Re is exemplified in Fig. 3 for a typical case with $\gamma_H = 1.0$, $A_1 = A_2 = 1.0$ at $X = 0.2$ for aiding flow. For pure forced convection, U remains unchanged with time (Fig. 3). In the presence of the buoyancy force, flow near the channel walls is continuously accelerated by the aiding buoyancy after the initiation of the transient by imposing heat fluxes to the flow. To maintain the over mass conservation, equation (4), flow in the central portion of the channel is slowed down. After a certain τ, concavity in the velocity profile appears in the central portion and becomes more pronounced at a higher Gr/Re (Fig. 3c). Near the channel inlet, the time rate of change in U is small since the flow is only accelerated by the aiding buoyancy over a short distance. Careful inspection of the figure reveals that steady state occurs earlier for a larger Gr/Re, but the effect is very slight.

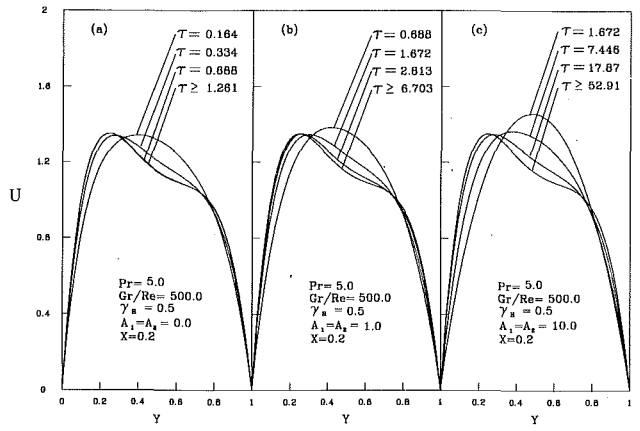

Fig. 4 Wall heat capacity effect on the transient velocity development during asymmetric heating

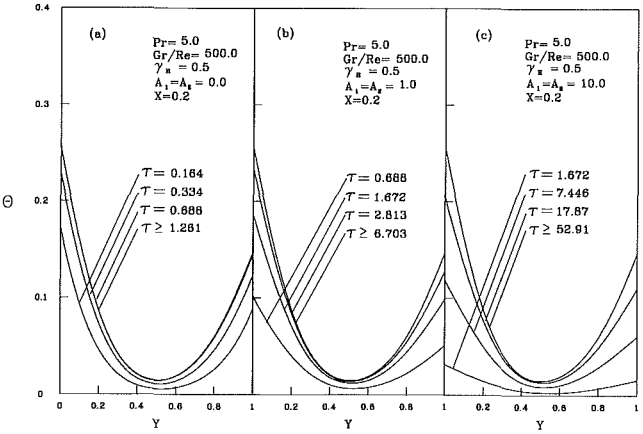

Fig. 5 Wall heat capacity effect on the transient temperature development under asymmetric heating

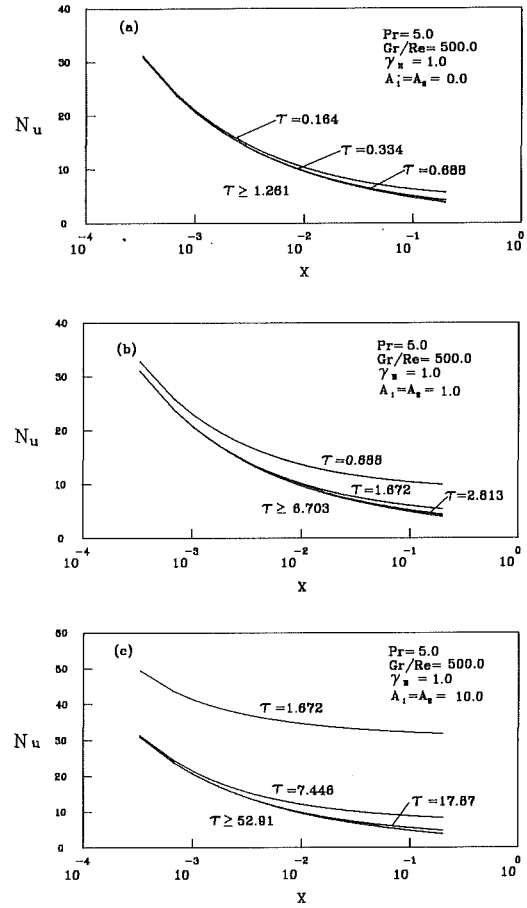

Fig. 6 Wall capacity effect on the unsteady local Nusselt number during symmetric heating

When the buoyancy opposes the forced flow (negative Gr/Re), flow near the wall decelerates with time under the action of the opposing buoyancy, while the flow in the core region speeds up to maintain mass conservation. Unlike the buoyancy aiding flow, the increase in the opposing buoyancy results in a slightly longer transient period.

For asymmetric heating with $\gamma_H = 0.5$, flow near the hotter plate is speeded up to a larger degree under the larger aiding buoyancy near this plate with the accompanying flow slowdown in the core region. Maximum flow velocity appears near the hotter plate. At a higher Gr/Re (= 1000) concavity in the velocity profile is also noted.

The influences of Gr/Re on the time variation of the temperature profiles are less significant. However, it can still be observed that for aiding flow, temperature in the near-wall region is lower for a larger Gr/Re, resulting from the higher velocity in this region. The reverse is true for opposing flow.

Effect of A_1 and A_2. The influences of the wall-to-fluid heat capacity ratios on the transient velocity and temperature development are illustrated in Figs. 4 and 5 for different values of A_1 and A_2 with Gr/Re = 500, $\gamma_H = 0.5$ at $X = 0.2$. The results indicate that the evolution of the flow and thermal fields becomes slower for larger A_1 and A_2. Specifically, the flow reaches steady state at $\tau = 6.7$ for $A_1 = A_2 = 1$, while for $A_1 = A_2 = 10$ the flow is still in its early transient. Apparently, a significant increase in thermal lag results as A_1 and A_2 are raised from 1 to 10.

When A_1 and A_2 are raised from 0 to 10, a substantial change in the transient variation of the local Nusselt number is noted in Fig. 6 for a typical case with Gr/Re = 500 and $\gamma_H = 1.0$. This can be more clearly illustrated by plotting Nu/Nu_{ss} versus X at various τ, as given in Fig. 7. For $A_1 = A_2 = 10$, Nu/Nu_{ss} can be as high as eight at $\tau = 1.672$ and $X = 0.2$. This great increase in Nu apparently results from the large wall heat capacity, which makes the interface temperature T_x still very low at this time instant, and according to the definition of the Nusselt numbers, equations (17) and (18), $Nu_{x,1}$ and $Nu_{x,2}$ are very high. Thermal lag in the system due to finite wall heat capacity can be distinctly exhibited by examining the nondimensional interfacial heat flux. If the wall heat capacity is ignored ($A_1 = A_2 = 0$) in the analysis, Q is equal to unity for all τ. No thermal lag exists in the system. The unsteady distributions of Q for different values of A_1 and A_2, as shown in Fig. 8, indicate that Q gradually increases from 0 at $\tau = 0$ to unity at steady state. Clearly, it takes much longer for the heat input to the channel to transfer completely to the fluid inside it for $A = A_2 = 10$.

To provide quantitative information on the effects of A_1 and A_2 for the design of thermal systems during transient operation, correlation equations for Nu/Nu_{ss} are given here.

For buoyancy aiding flow

$$Nu/Nu_{ss} = \left[e^{-X} + a \cdot (1 + dA_1^b) \cdot X \cdot \tau^{(c+fA_1)} \right]^{1/3} \qquad (21)$$

where $a = 1.0012$, $b = 4.1781$, $c = -1.454$, $d = 35.452$, $f = -0.869$. Equation (21) can also be used for buoyancy opposing flow with $a = 1.2526$, $b = 4.0398$, $c = -1.593$, $d = 26.930$, $f = -0.689$. The above equation is good for both symmetric and asymmetric thermal boundary conditions. Com-

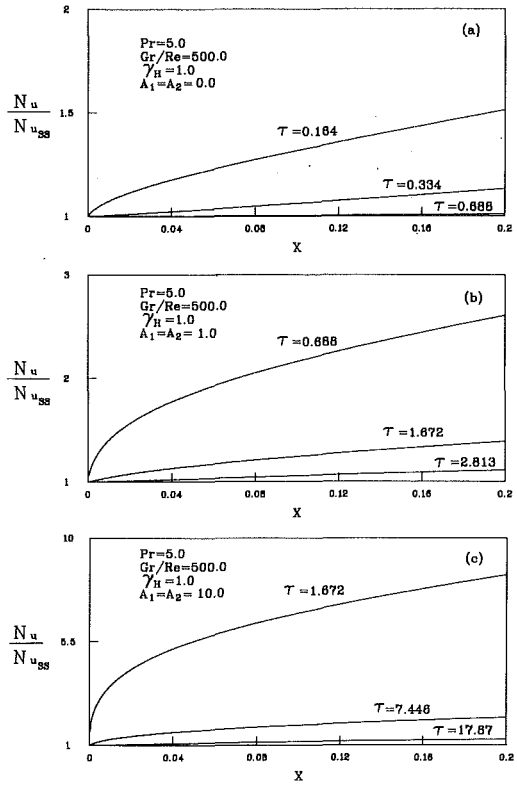

Fig. 7 Distributions of the transient local Nusselt number normalized by the steady local Nusselt number for various wall heat capacities

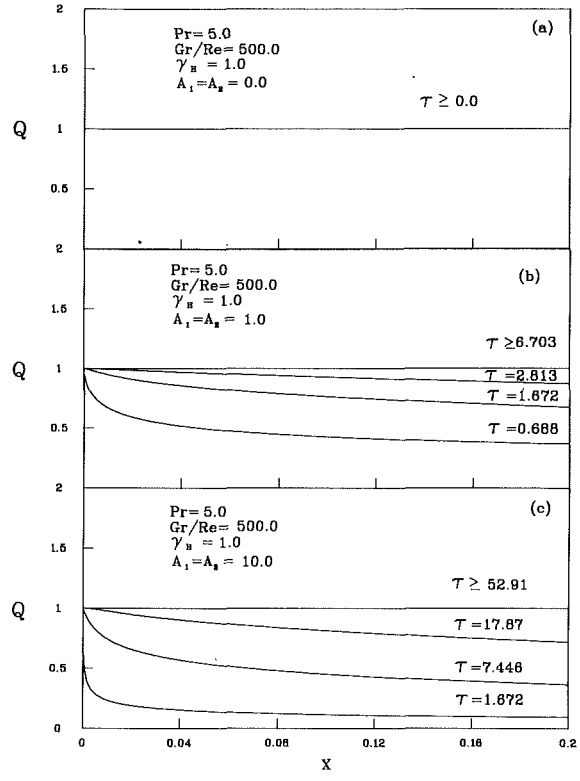

Fig. 8 Unsteady variations of the dimensionless interfacial heat flux for various wall heat capacities

pared with our predictions, these equations have a maximum deviation of 15 percent.

To facilitate the application of the above results, correlating equations for the steady-state Nusselt numbers for both buoyancy aiding and opposing flows are also given here.

For buoyancy aiding flow

$$\mathrm{Nu}_{ss}/\mathrm{Nu}_0 = [e^{-2X} + 0.0184(\mathrm{Gr/Re})^{0.7463} \cdot X^{0.5} \cdot \gamma_H^{-0.165}]^{1/3} \tag{22}$$

For buoyancy opposing flow

$$\mathrm{Nu}_{ss}/\mathrm{Nu}_0 = [1 - 0.0012(\mathrm{Gr/Re})^{1.2272} \cdot X^{0.5} \cdot \gamma_H^{-0.6126}]^{1/3} \tag{23}$$

In the above equations Nu_0 is the steady local Nusselt number for pure forced convection flow, which can be readily calculated from the empirical equations proposed by Shah and London (1978). For completeness, these correlating equations are given here.

$$\mathrm{Nu}_0 = \begin{cases} 0.745\xi^{-1/3} & \text{for } \xi \leq 0.0002 \\ 0.745\xi^{-1/3} - 0.2 & \text{for } 0.0002 < \xi \leq 0.001 \\ 4.118 + 4.34(10^3 \cdot \xi)^{-0.506} \cdot e^{-164\xi} & \text{for } \xi > 0.001 \end{cases}$$

where $\xi = x/2 \cdot b \cdot \mathrm{Pe}$.

Conclusion and Remarks

The major results obtained in the present study can be summarized as follows:

1 Raising the buoyancy force in aiding flow increases the Nusselt number both in the transient process and at steady state. But for opposing flow the increase in the magnitude of Gr/Re reduces the Nusselt number.

2 The dominant factor to determine the time rate of energy transfer into fluid is the wall-to-fluid heat capacity ratio. The effects of Gr/Re and γ_H are not so important.

It has been known for many years that when the buoyancy is strong enough, irrespective of the aiding or opposing flow, reverse flow will appear in the channel. Unsteady flow and heat transfer characteristics under this situation are much more complicated. Further research is needed in this area.

Finally, it should be pointed out that the distorted velocity profiles in mixed convection flow (Figs. 3 and 4) have inflection points at a high Gr/Re. Flow is prone to instability and may become transitional. For an unstable or transitional flow the results presented above for laminar mixed convection are then invalid.

Acknowledgment

The financial support of this study by the engineering division of National Council of Taiwan, R.O.C., through contract No. NSC78-0401-E0009-11 is greatly appreciated.

References

Anderson, D. A., Tannehill, J. C., and Pletcher, R. H., 1984, *Computational Fluid Mechanics and Heat Transfer*, Hemisphere, Washington, DC, Chap. 4.

Aung, W., 1987, "Mixed Convection in Internal Flow," in: *Handbook of Single-Phase Convective Heat Transfer*, S. Kakac, R. K. Shah, and W. Aung, eds., Wiley, New York, Chap. 15.

Aung, W., and Worku, G., 1986a, "Developing Flow and Flow Reversal in a Vertical Channel With Asymmetric Wall Temperatures," ASME JOURNAL OF HEAT TRANSFER, Vol. 108, pp. 299–304.

Aung, W., and Worku, G., 1986b, "Theory of Fully Developed Combined Convection Including Flow Reversal," ASME JOURNAL OF HEAT TRANSFER, Vol. 108, pp. 485–488.

Aung, W., and Worku, G., 1987, "Mixed Convection in Ducts With Asymmetric Wall Heat Flux," ASME JOURNAL OF HEAT TRANSFER, Vol. 109, pp. 947–951.

Cebeci, T., Khattab, A. A., and LaMont, R., 1982, "Combined Natural and Forced Convection in Vertical Ducts," *Proc. 7th Int. Heat Transfer Conference*, U. Grigull, E. Hahne, K. Stephan, and J. Straub, eds., Vol. 3, pp. 419–424.

Chow, L. C., Husain, S. R., and Campo, A., 1984, "Effects of Free Convection and Axial Conduction on Forced Convection Heat Transfer Inside a Vertical Channel at Low Peclet Numbers," ASME JOURNAL OF HEAT TRANSFER, Vol. 106, pp. 297–303.

Gebhart, B., Jaluria, Y., Mahajan, R. L., and Sammakia, 1988, *Buoyancy-Induced Flows and Transport*, Hemisphere, Washington, DC, Chap. 10.

Habchi, S., and Acharya, S., 1986, "Laminar Mixed Convection in a Symmetrically or Asymmetrically Heated Vertical Channel," *Numerical Heat Transfer*, Vol. 9, pp. 605–618.

Incropera, F. P., 1986, "Buoyancy Effects in Double-Diffusive and Mixed Convection Flows," *Proc. 8th Int. Heat Transfer Conference*, C. L. Tien, V. P. Carey, and J. K. Ferrel, eds., Vol. 1, pp. 121–130.

Ingham, D. B., Keen, D. J., and Heggs, P. J., 1988a, "Two Dimensional Combined Convection in Vertical Parallel Plate Ducts, Including Situations of Flow Reversal," *International Journal for Numerical Methods in Engineering*, Vol. 26, pp. 1645–1664.

Ingham, D. B., Keen D. J., and Heggs, P. J., 1988b, "Flows in Vertical Channels With Asymmetric Wall Temperatures and Including Situations Where Reversal Flows Occur," ASME JOURNAL OF HEAT TRANSFER, Vol. 110, pp. 910–917.

Joshi, H. M., 1988, "Transient Effect in Natural Convection Cooling of Vertical Parallel Channels," *International Communications in Heat and Mass Transfer*, Vol. 15, pp. 227–238.

Lavine, A. S., 1988, "Analysis of Fully Developed Opposing Mixed Convection Between Inclined Parallel Plates," *Warme- und Stoffubertragung*, Vol. 23, pp. 249–257.

Lavine, A. S., Kim, M. Y., and Shores, C. N., 1989, "Flow Reversal in Opposing Mixed Convection Flow in Inclined Pipes," ASME JOURNAL OF HEAT TRANSFER, Vol. 111, pp. 114–120.

Lawrence, W. T., and Chato, J. C., 1966, "Heat Transfer Effects on the Developing Laminar Flow Inside Vertical Tubes," ASME JOURNAL OF HEAT TRANSFER, Vol. 88, pp. 214–222.

Lin, T. F., and Kuo, J. C., 1988, "Transient Conjugated Heat Transfer in Fully Developed Laminar Pipe Flows," *International Journal of Heat and Mass Transfer*, Vol. 31, pp. 1093–1102.

Morton, B. R., Ingham, D. B., Keen, D. J., and Heggs, P. J., 1989, "Recirculating Combined Convection in Laminar Pipe Flow," ASME JOURNAL OF HEAT TRANSFER, Vol. 111, pp. 106–113.

Quintiere, J., and Muller, W. K., 1973, "An Analysis of Laminar Free and Forced Convection Between Finite Vertical Parallel Plates," ASME JOURNAL OF HEAT TRANSFER, Vol. 95, pp. 53–59.

Scheele, G. F., Rosen, E. M., and Hanratty, T. J., 1960, "Effect of Natural Convection on Transition to Turbulence in Vertical Pipes," *The Canadian Journal of Chemical Engineering*, Vol. 38, pp. 67–73.

Scheele, G. F., and Hanratty, T. J., 1963, "Effect of Natural Convection Instabilities on Rates of Heat Transfer at Low Reynolds Numbers," AIChE *Journal*, Vol. 9, pp. 183–185.

Shadday, M. A., Jr., 1986, "Combined Forced/Free Convection Through Vertical Tubes at High Grashof Numbers," *Proc. 8th International Heat Transfer Conference*, C. L. Tien, V. P. Carey, and J. K. Ferrel, eds., Vol. 3, pp. 1433–1437.

Sucec, J., 1987, "Unsteady Conjugated Forced Convection Heat Transfer in a Duct With Convection From the Ambient," *International Journal of Heat and Mass Transfer*, Vol. 30, pp. 1963–1970.

Sucec, J., and Sawant, A., 1984, "Unsteady, Conjugated, Forced Convection Heat Transfer in a Parallel Plate Duct," *International Journal of Heat and Mass Transfer*, Vol. 27, pp. 95–101.

Tao, L. N., 1960, "On Combined Free and Forced Convection in Channels," ASME JOURNAL OF HEAT TRANSFER, Vol. 82, pp. 233–238.

Yao, L. S., 1983, "Free and Forced Convection in the Entry Region of a Heated Vertical Channel," *International Journal of Heat and Mass Transfer*, Vol. 26, pp. 65–72.

Zeldin, B., and Schmidt, F. W., 1972, "Developing Flow With Combined Forced-Free Convection in an Isothermal Vertical Tube," ASME JOURNAL OF HEAT TRANSFER, Vol. 94, pp. 211–233.

A Numerical Solution of Variable Porosity Effects on Natural Convection in a Packed-Sphere Cavity

E. David

G. Lauriat

Laboratoire de Thermique,
CNAM,
75141 Paris, France

P. Cheng

Department of Thermal Engineering,
University of Hawaii at Manoa,
Honolulu, HI 96822

The problem of natural convection in differentially heated vertical cavities filled with spherical particles saturated with Newtonian fluids is investigated numerically. The Brinkman–Darcy–Ergun equation is used as the momentum equation, and the wall effect on porosity variation is approximated by an exponential function. The effect of variable stagnant thermal conductivities is taken into consideration in the energy equation. The formulation of the problem shows that the flow and heat transfer characteristics depend on six dimensionless parameters, namely, the Rayleigh and Prandtl numbers of the fluid phase, the dimensionless particle diameter, the conductivity ratio of the two phases, the bulk porosity, and the aspect ratio of the cavity. The influences of these parameters on the heat transfer rate are thoroughly investigated. The predicted Nusselt numbers are compared with existing experimental results. It is found that the computed Nusselt numbers based on the present model compare the best with experimental data.

1 Introduction

The problem of natural convection in a rectangular porous cavity has attracted considerable attention in the past three decades [see Cheng (1978) for a review of early literature]. Most of the early analyses were based on Darcy's law with the assumption of a constant porosity medium. Results of these analyses show that the Nusselt number of the problem depends only on the Rayleigh number and the aspect ratio. Recent experimental results (Seki et al., 1978; Prasad et al., 1985) on natural convection in porous cavities show that, under certain conditions, the Nusselt number depends not only on the Rayleigh number and the aspect ratio, but also on the Prandtl number, the Darcy number (which is related to the dimensionless particle diameter), and the thermal conductivity ratio of the fluid phase to the solid phase.

The disparity of theoretical and experimental results has prompted researchers to study a number of effects that have been neglected in the early analyses. Owing to the limitations of the Darcy law, additional terms have been included in the governing equations to account for boundary and inertial effects. These effects were analyzed theoretically by Vafai and Tien (1981) for forced flow over a flat plate buried in a porous medium and experimentally for transient mass transfer through uniform porosity media (Vafai and Tien, 1982). Georgiadis and Catton (1986) and Prasad and Tuntomo (1987) have attributed the Prandtl number dependence of the Nusselt number to the inertial effects, while Tong and Subramanian (1985) and Lauriat and Prasad (1987) have attributed the Darcy number dependence of the Nusselt number to the boundary effects.

Results relevant to flow channeling caused by spatial variation of porosity near solid walls for forced convection in porous media have been presented by Vafai (1984), Vafai et al. (1985), Cheng (1986, 1987), Cheng et al. (1988a), and Poulikakos and Renken (1987), who showed that the porosity variation has important effects on heat transfer if the dimensionless particle diameter is high. As far as the authors are aware, the only analysis pertinent to natural convection in nonuniform porosity media was presented by Hong et al. (1987), who also showed that the flow channeling effect significantly increases the heat transfer rate.

In this paper, the effect of variable porosity on natural convection in a rectangular cavity heated differentially on the vertical sides is studied numerically. The Brinkman–Darcy–Ergun (BDE) equation is used as the momentum equation. The porosity of the medium is assumed to vary exponentially with distance from the walls. The variable stagnant thermal conductivity effect is taken into consideration in the energy equation. The present study complements a preliminary work presented recently by David et al. (1988). In this paper, the effects of the dimensionless particle diameter, Rayleigh and Prandtl numbers, aspect ratio, conductivity ratio, and bulk porosity of the bed on the heat transfer characteristics in a rectangular porous cavity are investigated. In addition, computations were carried out corresponding to the experiments conducted by Seki et al. (1978) for natural convection of water, ethyl alcohol, and transformer oil in rectangular cavities filled with glass beads. Predictions of the Nusselt number were obtained based on three flow models, i.e., the Darcy model and the Brinkman–Forchheimer–extended Darcy model with variable and constant porosity. It is found that the calculated Nusselt numbers for free convection in a porous cavity based on the present model agree the best with experimental data with water/glass-beads and ethyl-alcohol/glass-beads systems. For the transformer-oil/glass-beads system, the predicted Nusselt numbers are lower than those of experiments.

2 Formulation of the Problem

We consider a two-dimensional, rectangular enclosure of height H and width D, filled with a fluid-saturated porous medium. The vertical walls are maintained at uniform but different temperatures, while the top and bottom walls are insulated. The dimensional coordinate along the bottom wall is denoted by x' and that along the vertical hot wall is denoted by y'.

The governing equations for natural convection in a variable porosity medium based on the Brinkman–Darcy–Ergun model with the Boussinesq approximation are

$$\nabla \cdot \mathbf{V}_D = 0 \tag{1}$$

Contributed by the Heat Transfer Division for publication in the JOURNAL OF HEAT TRANSFER. Manuscript received by the Heat Transfer Division January 26, 1989; revision received May 18, 1990. Keywords: Enclosure Flows, Natural Convection, Porous Media.

$$\frac{\epsilon\mu \mathbf{V}_D}{K}+\frac{\epsilon\rho F|\mathbf{V}_D|\mathbf{V}_D}{\sqrt{K}}=\nabla P_D+\mu\nabla^2\mathbf{V}_D-\beta\rho_o(T-T_o)\epsilon g \quad (2)$$

$$(\rho c)_f \mathbf{V}_D\cdot\nabla T=\nabla\cdot(k_m\nabla T) \quad (3)$$

where $\mathbf{V}_D$ is the Darcian velocity vector and P_D is the volumetric average pressure related to the fluid phase average pressure by $P_D=\epsilon\langle P\rangle^f$. K and F are the permeability and the inertial coefficient of the porous medium, which are given by the following correlations for a packed-sphere bed:

$$K=\frac{\epsilon^3 d_p^2}{a(1-\epsilon)^2} \quad (4)$$

$$F=\frac{b}{\sqrt{a}\epsilon^{3/2}} \quad (5)$$

where a and b are empirical constants, d_p is the particle diameter, and ϵ is the porosity, which is assumed to vary exponentially with distance from the walls (Chandrasekhara and Vortmeyer, 1979). For example, for the porous medium near a wall at $y'=0$, the porosity variation is given by

$$\epsilon=\epsilon_\infty[1+C_1\exp(-N_1 y'/d_p)] \quad (6)$$

where y' is the distance from the wall, $C_1=1.4$, $N_1=5$ (Cheng et al., 1988a; Hsu and Cheng, 1988) and ϵ_∞ is the porosity at the core.

The quantity k_m in equation (3) is the stagnant thermal conductivity of the saturated porous medium, which is given by (Zehner and Schlünder, 1970; Cheng, 1986)

$$\frac{k_m}{k_f}=\left[1-\sqrt{1-\epsilon}\right]+\frac{2\sqrt{1-\epsilon}}{1-\sigma B}\times\left[\frac{(1-\sigma)B}{(1-\sigma B)^2}\ln\left(\frac{1}{\sigma B}\right)-\frac{B+1}{2}-\frac{B-1}{1-\sigma B}\right] \quad (7a)$$

where k_f is the thermal conductivity of the fluid phase, $\sigma=k_f/k_s$ is the thermal conductivity ratio of the fluid phase to that of the solid phase, and

$$B=1.25\left(\frac{1-\epsilon}{\epsilon}\right)^{10/9} \text{ for a packed-sphere bed} \quad (7b)$$

In the above formulation, the thermal dispersion effect is neglected. Thus, the present model is applicable only for flow with small Péclet number.

The boundary conditions for natural convection in a rectangular cavity with width D and height H are

$$u_D=v_D=0 \quad \text{on the walls} \quad (8)$$

$$T(0, y')=T_c \quad (9)$$

$$T(D, y')=T_h \quad (10)$$

$$\left.\frac{\partial T}{\partial y'}\right|_{y'=0}=\left.\frac{\partial T}{\partial y'}\right|_{y'=H}=0 \quad (11)$$

Equations (1)–(3) can be combined and expressed in terms of dimensionless stream function ψ, vorticity Ω, and temperature θ to give

$$\nabla^2\psi=-\Omega \quad (12)$$

$$\left[\frac{a}{\gamma^2}\left(1-\frac{1}{\epsilon}\right)^2+\frac{b(1-\epsilon)}{\gamma \mathrm{Pr}\epsilon^2}\left(\sqrt{\left(\frac{\partial\psi}{\partial x}\right)^2+\left(\frac{\partial\psi}{\partial y}\right)^2}\right)\right]\Omega=\nabla^2\Omega+\mathrm{Ra}\frac{\partial(\epsilon\theta)}{\partial x}+\frac{\partial\psi}{\partial x}\frac{\partial}{\partial x}\left[\frac{a}{\gamma^2}\left(1-\frac{1}{\epsilon}\right)^2+\frac{b(1-\epsilon)}{\gamma \mathrm{Pr}\epsilon^2}\left(\sqrt{\left(\frac{\partial\psi}{\partial x}\right)^2+\left(\frac{\partial\psi}{\partial y}\right)^2}\right)\right]+\frac{\partial\psi}{\partial y}\frac{\partial}{\partial y}\left[\frac{a}{\gamma^2}\left(1-\frac{1}{\epsilon}\right)^2+\frac{b(1-\epsilon)}{\gamma \mathrm{Pr}\epsilon^2}\left(\sqrt{\left(\frac{\partial\psi}{\partial x}\right)^2+\left(\frac{\partial\psi}{\partial y}\right)^2}\right)\right] \quad (13)$$

Nomenclature

A = aspect ratio of the cavity
a = Ergun's constant
B = constant defined in equation (7b)
b = Ergun's constant
C_1 = empirical constant in equation for porosity variation
c_p = specific heat of the fluid at constant pressure
D = width of the cavity
Da_∞ = bulk Darcy number
d_p = particle diameter
F = inertial coefficient
g = gravitational acceleration
h = heat transfer coefficient
H = height of the rectangular cavity
k_d = thermal dispersive conductivity
k_f, k_s = thermal conductivities of the fluid and solid phases
k_m = stagnant thermal conductivity of the saturated porous medium
$k_{m,\infty}$ = bulk stagnant thermal conductivity of the saturated porous medium
K = permeability of the porous medium
Nu = Nusselt number $=hD/k_f$
Nu_m = modified Nusselt number $=hD/k_m$
N_1 = empirical constant in equation for porosity variation
P_D = volume average pressure
Pr = Prandtl number of the fluid
Pr_m = modified Prandtl number $=\nu/\alpha_m$
q_w = local wall heat flux
Ra = Rayleigh number of the fluid
Ra_m = modified Rayleigh number $=g\beta KD\Delta T/\nu\alpha_m$
T = dimensional temperature
T_h, T_c = temperature of the hot and cold wall
T_o = reference temperature $=(T_c+T_h)/2$
u, v = dimensionless velocity components
$\mathbf{V}_D$ = Darcian velocity vector
x, y = dimensionless coordinates
x', y' = dimensional coordinates
α = thermal diffusivity of fluid
α_m = thermal diffusivity of the porous medium
β = thermal expansion coefficient of fluid
γ = dimensionless particle diameter $=d_p/D$
ϵ = porosity
θ = dimensionless temperature $=(T-T_o)/(T_h-T_c)$
λ = dimensionless stagnant thermal conductivity $=k_m/k_f$
λ_∞ = dimensionless bulk stagnant thermal conductivity $=k_{m,\infty}/k_f$
μ = dynamic viscosity of fluid
ν = kinematic viscosity of fluid
ρ = density of fluid
σ = stagnant thermal conductivity ratio $=k_f/k_s$
ψ = dimensionless stream function
Ω = dimensionless vorticity

$$\frac{\partial\psi}{\partial y}\frac{\partial\theta}{\partial x}-\frac{\partial\psi}{\partial x}\frac{\partial\theta}{\partial y}=\frac{\partial}{\partial x}\left(\lambda\frac{\partial\theta}{\partial x}\right)+\frac{\partial}{\partial y}\left(\lambda\frac{\partial\theta}{\partial y}\right) \tag{14}$$

where the dimensionless variables are defined in the Nomenclature. In equation (13), Pr and Ra denote the Prandtl number and Rayleigh number of the fluid, respectively, which are defined as $\mathrm{Pr}=\nu/\alpha_f$, $\mathrm{Ra}=g\beta(T_h-T_c)D^3/\nu\alpha_f$. In terms of the dimensionless coordinates y, equation (6) becomes

$$\epsilon=\epsilon_\infty[1+C_1\exp(-N_1 y/\gamma)] \tag{15}$$

where $\gamma=d_p/D$ is the dimensionless particle diameter.

The boundary conditions (8)-(11) in terms of the dimensionless variables are

$$\theta(0,y)=0.5,\quad \psi=\frac{\partial\psi}{\partial x}=0,\quad 0\le y\le A \tag{16}$$

$$\theta(1,y)=-0.5,\quad \psi=\frac{\partial\psi}{\partial x}=0,\quad 0\le y\le A \tag{17}$$

$$\left.\frac{\partial\theta}{\partial x}\right|_{y=0}=\left.\frac{\partial\theta}{\partial x}\right|_{y=A}=0,\quad \psi=\frac{\partial\psi}{\partial x}=0,\quad 0\le x\le 1 \tag{18}$$

where $A=H/D$ is the aspect ratio. With this formulation, the dimensionless governing equations and boundary conditions for the problem of natural convection in a nonuniform porosity cavity contain six dimensionless parameters, namely, the aspect ratio A, the Prandtl number Pr, the Rayleigh number Ra, the thermal conductivity ratio σ, the dimensionless particle diameter γ, and the bulk porosity ϵ_∞. For a packed-sphere bed, γ is related to the bulk Darcy number (Da_∞) by

$$\mathrm{Da}_\infty=K_\infty/\mathrm{D}^2=\frac{\epsilon_\infty^3 d_p^2}{a(1-\epsilon_\infty)^2D^2}=5.18\times10^{-4}\gamma^2 \tag{19}$$

if $a=220$ and $\epsilon_\infty=0.36$. It is relevant to note that for a constant porosity medium where $C_1=0$ in equation (15), the dimensionless governing equations and boundary conditions for this problem also contain the six dimensionless parameters mentioned above, if the thermal inertia is taken into consideration.

3 Numerical Solution

The governing equations (12)-(15) subject to the boundary conditions (16)-(18) were solved numerically by a modified version of the procedure documented in earlier papers (Lauriat and Prasad, 1987, 1989). The modifications included the use of a linearization technique for handling the Forchheimer term, which was split into two parts. The first part was combined with the Darcy term while the other part involving derivatives of the velocity modulus was treated as a source term. Because of the nonslip boundary conditions and the nonuniform porosity effects, steep velocity gradients exist adjacent to the walls. Therefore, variable sized grids must be used to resolve the flow field adequately in the viscous sublayers adjacent to the walls. Transformation of coordinates similar to those used previously has been introduced to map the nonuniform grid in the physical domain onto a uniform grid in the computational domain. This method is generally more accurate than geometric changes of mesh size. The applicability of the method and its accuracy for Darcy-Brinkman-Forchheimer flow are discussed elsewhere (Lauriat and Prasad, 1987, 1989).

After the values of θ have been computed, the local Nusselt number along the hot wall can be computed according to

$$\mathrm{Nu}(y)=\frac{q_w(y')\,D}{k_f(T_h-T_c)}=\lambda(0,y)\left.\frac{\partial\theta}{\partial x}\right|_{x=0} \tag{20}$$

and the average Nusselt number is given by

$$\mathrm{Nu}=-\frac{1}{A}\int_0^A\lambda(0,y)\frac{\partial\theta}{\partial x}dy \tag{21}$$

where $q_w(y')$ is the surface heat flux along the hot wall at $x'=0$. It follows from equation (20) and (21) that the effect

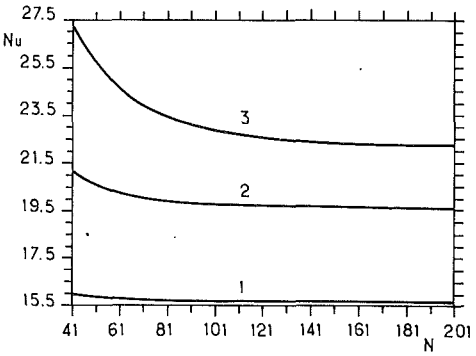

Fig. 1 Variation of the average Nusselt number as a function of the number of grid points ($\sigma=1$, $\epsilon_\infty=0.36$, $A=1$, $\mathrm{Pr}=5$): (1) $\gamma=0.2$, $\mathrm{Ra}=10^7$; (2) $\gamma=0.1$, $\mathrm{Ra}=10^8$; (3) $\gamma=0.05$, $\mathrm{Ra}=5\times10^8$

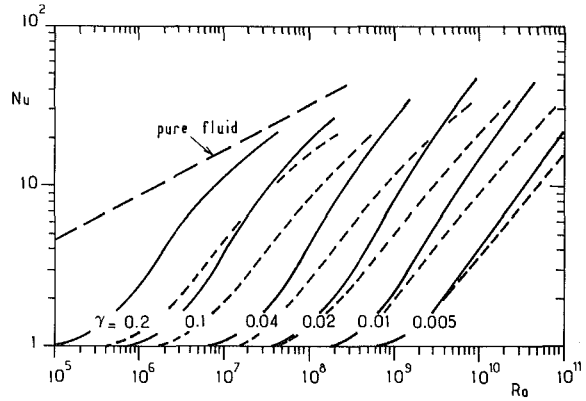

Fig. 2 Effects of γ on the average Nusselt number of a square cavity with a uniform porosity (dashed lines) or a nonuniform porosity (solid lines) medium with $\mathrm{Pr}=5$, $\sigma=1$, and $\epsilon_\infty=0.36$

of σ plays a role on the heat transfer rate not only through the temperature gradient at the wall but also through $\lambda(0,y)$.

Comparisons with numerical results based on the pure Darcy formulation and the Brinkman-Forchheimer-extended Darcy formulation were shown in previous papers. For nonuniform porosity media, much finer grid systems should be used in order to have sufficient resolution near the walls.

The coarsest meshes used in the present study involved 61 nodes in each direction while the finest one had 201 nodes. Most of the runs were repeated by increasing the number of nodes until the computed values of the mean Nusselt number do not change by more than 2 percent. The Nusselt number was chosen as the test quantity because it is one of the most sensitive quantities to mesh size. Figure 1 shows the effect of mesh changes on the average Nusselt number for $A=1$ and various γ and Ra values. As can be seen, an 81×81 grid could be considered as a good compromise between accuracy and computational costs for $\gamma=0.2$ and $\mathrm{Ra}=10^7$, while a 141×141 grid should be used for $\gamma=0.05$ and $\mathrm{Ra}=10^8$. For the few computations carried out for $\gamma\le0.02$ (see Fig. 2), a grid as fine as 201×201 was used. All the present computations were performed on a Siemens VP200 supercomputer after vectorization of the algorithm.

4 Parametric Study

In this section, the effects of particle diameter, Prandtl number, aspect ratio of the cavity, thermal conductivity ratio, and bulk porosity on natural convection in a rectangular cavity, filled with a porous medium, are considered.

Effect of Dimensionless Particle Diameter. To investigate the effect of dimensionless particle diameter on heat transfer, computations were first carried out with $A=1$, $\mathrm{Pr}=5$, $\epsilon_\infty=0.36$,

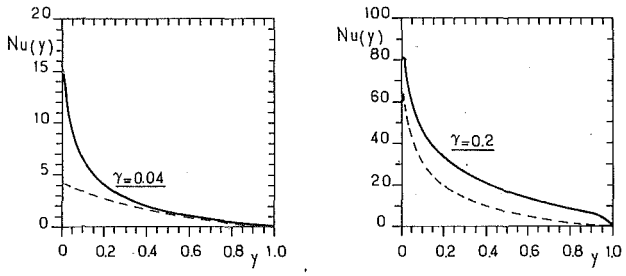

Fig. 3 Effects of γ on the local Nusselt number along the hot wall in square cavity filled with a uniform porosity (dashed lines) or a nonuniform porosity (solid lines) medium with $Ra = 5.10^7$, $Pr = 5$, $\sigma = 1$, and $\epsilon_\infty = 0.36$

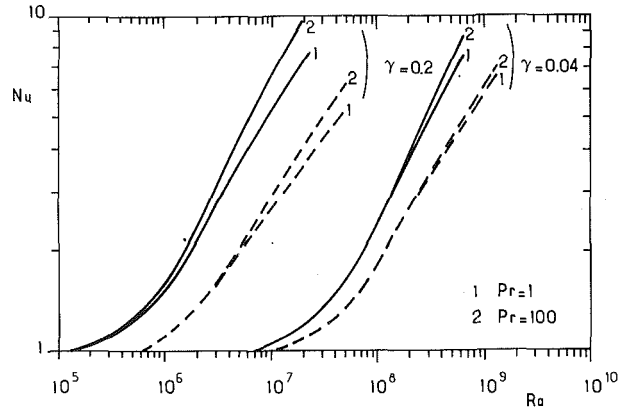

Fig. 4 Effects of Prandtl number on the average Nusselt number of a rectangular cavity ($A = 5$) filled with a uniform porosity (dashed lines) or a nonuniform porosity (solid lines) medium with $\sigma = 1$ and $\epsilon_\infty = 0.36$

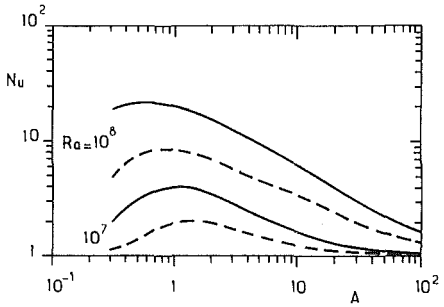

Fig. 5 Effects of aspect ratio on the average Nusselt number of a cavity filled with a uniform porosity (dashed lines) or a nonuniform porosity (solid lines) medium with $Pr = 5$, $\sigma = 1$, $\epsilon_\infty = 0.36$

and $\sigma = 1$ (i.e., thermal conductivity of the fluid phase equal to that of the solid phase) at different values of γ. Results of the computations for the average and local Nusselt numbers are presented in Figs. 2 and 3, where the dashed lines represent the results for a uniform porosity medium while the solid lines represent those for a nonuniform porosity medium.

Figure 2 shows the average Nusselt number in a uniform and a nonuniform porosity square cavity with different values of γ. It is shown that at $\gamma = 0.005$, Darcy's law with uniform porosity can be used to predict the average Nusselt number without much error at a Rayleigh number as high as 5×10^{10}. This is because the bulk Darcy number and the inertial coefficient are small, of the order of 10^{-8} and 10^{-4}, respectively. At higher values of γ, the porosity variations must be taken into account at much lower Rayleigh numbers. Of particular interest is the case of $\gamma = 0.2$, where the value of the average Nusselt number at $Ra > 10^8$ approached that of a fluid-filled cavity. This finding was reported also for uniform porosity media in several earlier studies (Beckermann et al., 1986; Prasad et al., 1985, 1988; Kladias and Prasad, 1988).

Figure 2 shows that in a variable porosity medium, the slopes of the curves start decreasing at lower Ra numbers as the value of γ is increased. This is due to wall channeling, which enhances the viscous and inertial effects. For example, the critical Rayleigh number that characterizes the end of the Darcian regime is reduced from $Ra \simeq 10^7$ to $Ra \simeq 3 \times 10^6$ at $\gamma = 0.2$ and from $Ra \simeq 10^9$ to $Ra \simeq 2 \times 10^8$ at $\gamma = 0.04$ when including variable porosity effects. For higher Rayleigh numbers, an asymptotic convection regime could be reached and the exponent of Ra should be close to the one obtained for a fluid filled cavity (of the order of 0.3 for a square cavity). On the other hand, it can be seen from Fig. 2 that the slopes of the Nu curves are higher in the Darcian convection regime for nonuniform porosity medium. Indeed the slopes of the dashed lines are close to 0.62 for all γ values considered in the present work and at Ra values for which the viscous and inertial effects have a negligible influence (note that the slope decreases to 0.5 in a tall cavity at high Ra). The slopes of the Nu curves for nonuniform porosity increase up to 0.82. Moreover, the Nu curves are almost parallel, indicating that wall channeling results in Ra dependence with an exponent nearly independent of γ. Therefore, concerning the overall heat transfer rate, the general trends based on the Darcy model are similar to those with variable porosity media.

Figure 3 shows the effect of γ on the local Nusselt number along the hot wall at $Ra = 5 \times 10^7$ for a uniform and a variable porosity medium. At low values of γ the local Nusselt numbers in a variable porosity cavity are higher than those of a uniform porosity cavity only near the bottom adiabatic wall at $y = 0$, while at high values of γ, the local Nusselt number in a variable porosity cavity is higher everywhere along the hot wall. The variation of the local Nusselt number in a variable porosity cavity with $\gamma = 0.2$ is similar to those in a fluid-filled cavity.

Effect of Prandtl Number. The effects of the Prandtl number on the average Nusselt number for a uniform porosity cavity (represented by dashed lines) and a variable porosity cavity (represented by solid lines) are illustrated in Fig. 4. Since the inertial effect decreases as the Prandtl number is increased, the effect of Pr is significant only at the Rayleigh numbers for which the inertial effect is important. It is shown from this figure that the smaller the value of γ, the larger is the value of Ra at which the Prandtl number effect becomes significant. The Prandtl number effect is more pronounced for a nonuniform porosity medium than for a uniform porosity medium.

As in cavities filled with pure fluids, the Prandtl number has a small influence on the Nusselt number for fluids with $Pr > 1$ (Le Peutrec and Lauriat, 1987). The present computations for $1 < Pr < 100$ reveal Prandtl number dependence of the forms $Pr^{0.02}$ and $Pr^{0.04}$ for uniform and nonuniform porosity media, respectively. The Pr exponent for uniform porosity agrees with the one obtained by Beckermann et al. (1986) from computations for the Brinkman-Darcy-Ergun model.

Effect of Aspect Ratio. Figure 5 shows the average Nusselt number as a function of the aspect ratio at $Ra = 10^7$ and $Ra = 10^8$ for $Pr = 5$, $\sigma = 1$, and $\gamma = 0.1$ in uniform and nonuniform porosity cavities. For a given value of Ra, it is shown that there is a critical aspect ratio for which the Nusselt number is maximum. With further increase in the Rayleigh number ($Ra > 10^8$, for example), this critical aspect ratio is reduced below unity, which is consistent with the analytical solution of Bejan and Tien (1983). As the cavity becomes longer or taller, the heat transfer rate at constant Ra decreases. However, for tall enough cavities, it should be noted that if a correlation $Nu = c \cdot A^{-n}$ can be obtained, the exponent n would depend upon the Rayleigh number unless the heat transfer rate is clearly dominated by convective effects. The present results for uniform porosity yield $n = 0.46$ at $Ra = 10^8$ and $5 \leq A \leq 10$. It is in good agreement with the prediction of Weber's theory (1975) since the non-Darcian effects are weak for $\gamma = 0.1$ and $Ra = 10^8$ (Lauriat and Prasad, 1989).

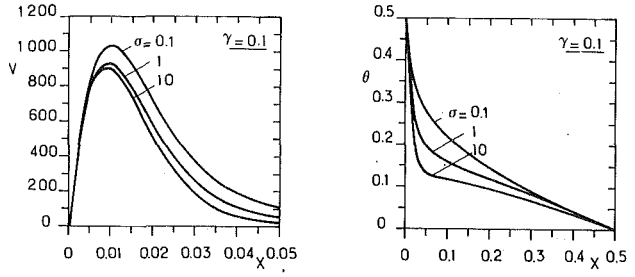

Fig. 6 Effects of conductivity ratio σ on the vertical velocity profiles and temperature distributions along the horizontal midplane in a nonuniform porosity cavity with Ra = 10^8, Pr = 5, $\gamma = 0.1$, and $\epsilon_\infty = 0.36$

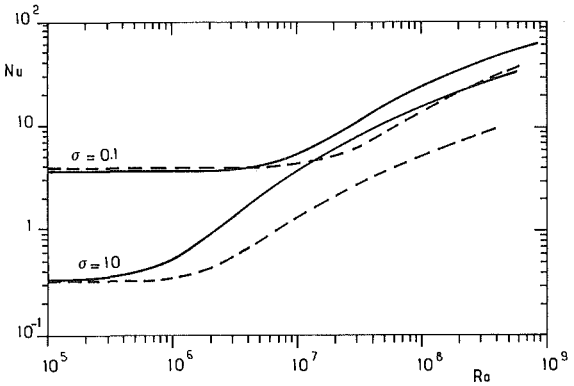

Fig. 7 Effects of conductivity ratio σ on the average Nusselt number of a square cavity filled with a uniform porosity (dashed lines) or a nonuniform porosity (solid lines) medium with $\gamma = 0.1$, Pr = 5, and $\epsilon_\infty = 0.36$

From the computations performed for nonuniform porosity media, it can seen in Fig. 5 that the general trends previously described are still obtained. However, the critical aspect ratio is reduced and falls between values found for a fluid-filled cavity and a fluid-saturated porous cavity. Also, the slope of the Nu curves versus A is higher for $A \gg 1$ since the wall channeling would have a negligible influence on the heat transfer rate only in the conduction regime and for $\sigma = 1$. In the convection-dominated regime in tall enough cavities ($A \geq 5$), the curves attain a slope of $n = 0.59$ instead of 0.46 for uniform porosity medium.

Effect of Thermal Conductivity Ratio. The effects of σ on fluid flow and heat transfer characteristics in a uniform or a nonuniform porosity square cavity with Pr = 5, $\gamma = 0.1$, and $\epsilon_\infty = 0.36$ are presented in Figs. 6 and 7. Figure 6 shows the effect of σ on the vertical velocity profile and temperature distribution on the horizontal midplane in a porous cavity at Ra = 10^8. When σ is reduced, the wall channeling is enhanced and the temperature gradients near the wall become flatter, which is in agreement with previous findings by Cheng (1986).

The effects of σ on the average Nusselt number of a square cavity filled with a uniform porosity medium (dashed lines) and a nonuniform porosity medium (solid lines) are shown in Fig. 7. At the heat conduction regime where the Nusselt number is independent of Ra, it is shown that the high conductivity of the solid phase (i.e., small value of σ) greatly increases the conduction heat flux. At the convection regime, the value of Nu is higher for a lower value of σ. This can be explained based on equation (21), which shows that the value of Nu depends not only on $\partial\theta/\partial x$ (0, y) but also on λ (0, y). At lower values of σ, the decrease in $\partial\theta/\partial x$ (0, y) is smaller relative to the increase in λ (0, y) leading to a net increase in Nu. Since the deviation of the horizontal line marks the onset of free convection, it can also be seen from this figure that decreasing the value of σ would increase the critical Rayleigh number and enhance the onset of free convection, which confirms recent results based on a linear stability analysis (Cheng et al., 1988b).

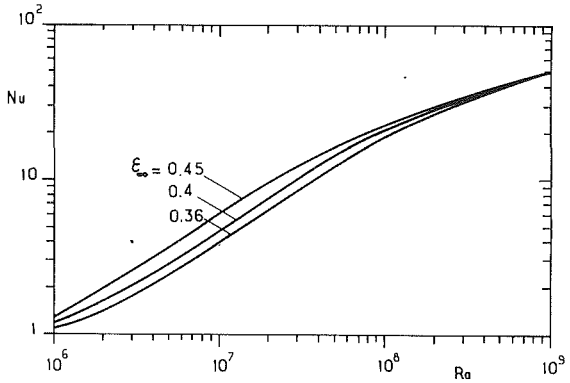

Fig. 8 Effect of bulk porosity on the average Nusselt number for a square cavity filled with a nonuniform porosity medium with $\gamma = 0.1$, Pr = 5, and $\sigma = 1$

For $\sigma < 1$, the average Nusselt number of a variable porosity medium in the conduction regime is smaller than those for a uniform porosity medium while the relative magnitude is reversed in the convection regime owing to the channeling effect. For $\sigma > 1$, the average Nusselt number of a variable porosity cavity is always higher than that of uniform porosity cavity regardless of the Rayleigh number. These results are supported, at least qualitatively, by the data of Seki et al. (1978) and Prasad et al. (1985) once their experimental results for fixed γ are presented in terms of Ra and σ.

If one writes $\mathrm{Nu} \simeq a\sigma^{-m}$, it is observed that for $0.1 < \sigma < 10$ an m value close to 0.1 could be obtained in the Darcian convection regime for a variable porosity medium (i.e., $\mathrm{Ra} > 10^7$ at $\gamma = 0.1$) while $m \simeq 0.24$ for uniform porosity. Such a reduction of the exponent for σ dependency of Nu suggests increasing influence of wall channeling effect in the convection regime. Also, the above σ dependency of Nu can be restated in term of $\lambda_\infty = k_{m,\infty}/k_f$. Then, the exponent of λ_∞ is found to be close to 0.18 for variable porosity media, as will be discussed in section 5.

Effect of Bulk Porosity. All of the previous calculations were performed based on $\epsilon_\infty = 0.36$. However, experimentally measured average porosities were found in the range of $0.35 \leq \epsilon_\infty \leq 0.45$ [see Seki et al. (1978), Prasad (1983), or Vafai (1984)].

For a uniform porosity medium, the influence of ϵ_∞ on the temperature distribution may be scaled by a modified Rayleigh number based on k_m, while its influence on the flow field may be determined through the Darcy number, which is approximately proportional to ϵ_∞ for $\epsilon_\infty \simeq 0.4$. Therefore, a 10 percent variation in ϵ_∞ has no influence on the modified Nusselt number in the conduction regime and its effect becomes more pronounced as Ra increases. For nonuniform porosity media, however, the effect of ϵ_∞ is not straightforward. For $\sigma = 1$, the bulk porosity has no influence in the conduction regime. At intermediate Ra numbers, Fig. 8 shows that ϵ_∞ has a maximum effect. The bulk porosity does not modify the Nusselt numbers for Ra greater than 5×10^8 for $\gamma = 0.1$ (or $\mathrm{Ra}_{m,\infty} \cong 2500$). This can be explained by the fact that the heat transfer at the walls occurs mostly in a thin layer with thicknesses being of the order of one sphere diameter at sufficiently high Ra numbers.

5 Comparisons with Experiments

In this section, we shall compare the predicted Nusselt numbers with the experimental results reported by Seki et al. (1978) for natural convection in rectangular cavities filled with glass balls and saturated with water ($k_f = 0.593$ W/mK, Pr = 7.1), ethyl alcohol ($k_f = 0.182$, Pr = 15.4), or transformer oil ($k_f = 0.124$, Pr = 480). Seki et al. (1978) have obtained the following correlation equation:

Table 1 Comparison between experimental data from Seki et al. (1978) and numerical predictions (the symbols W1, TD, W2, and EA are used in Figs. 9 and 10)

Fluid	d_p	ϵ_∞	γ	A	k_f	k_m	σ	Pr	Ra	Nu (Seki)	Nu (Darcy)	Nu (DBF)	Nu (VPM)
Water (W1)	16.4	0.46	0.141	5	0.593	0.675	0.786	7.1	6.432×10^7	15.88	10.30	8.776	14.60
									9.262×10^7	17.19	12.31	10.30	16.85
									1.183×10^8	20.72	13.90	11.38	18.51
									1.852×10^8	28.91	17.24	13.75	21.82
Transformer oil (TO)	16.4	0.46	0.141	5	0.124	0.320	0.164	480	6.416×10^6	12.58	4.624	4.501	5.827
									1.866×10^7	20.76	8.173	7.845	10.63
									6.416×10^7	32.98	15.49	14.38	19.06
									9.333×10^7	40.65	18.72	17.14	22.19
Water (W2)	5.7	0.39	0.088	10	0.593	0.687	0.786	7.1	1.830×10^7	2.595	1.727	1.705	2.405
									3.519×10^7	3.707	2.299	2.273	3.496
									7.038×10^7	4.901	3.302	3.230	5.305
Ethyl alcohol (EA)	5.7	0.39	0.088	10	0.182	0.425	0.240	15.4	2.270×10^8	12.56	8.509	8.337	13.08
									3.121×10^8	15.13	10.02	9.775	15.57
									4.256×10^8	18.03	11.72	11.37	18.29

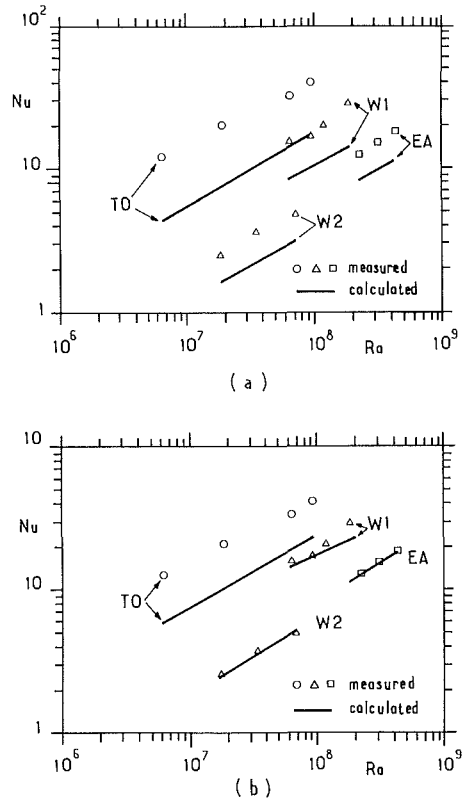

Fig. 9 Comparisons between experimental data of Seki et al. (1978) and numerical predictions (the symbols EA, TO, W1 and W2 refer to data reported in Table 1): (*a*) DBF solutions; (*b*) VPM solutions

$$\mathrm{Nu}_m = 0.627\ \mathrm{Ra}_m^{0.463}\ \mathrm{Pr}_m^{-0.13}\ A^{-0.527} \tag{22}$$

which is valid for $1<\mathrm{Pr}_m<200$, $5<A<20$, and $10^2<\mathrm{Ra}_m<10^4$, where Pr_m and Ra_m are modified Prandtl number and Darcy-Rayleigh number based on measured porosities and thermal conductivities, which should be close to the bulk porosities and conductivities for small enough diameters of the glass balls.

Computations corresponding to the experiments of Seki et al. were performed for glass balls ($k_s=0.754$ W/mK) whose diameters were chosen not too small in order to have possible significant effects of porosity variations. The two sizes of ball selected were $d_p=5$ mm and 16.4 mm for which the bulk porosity was $\epsilon_\infty=0.39$ and $\epsilon_\infty=0.46$, respectively (Seki et al., 1978). The height of the test cells was maintained at $H=571$ mm and the aspect ratio was $A=10$ for the small ball diameter ($\gamma=0.088$) and $A=5$ for the largest ($\gamma=0.141$). On account of the relatively large aspect ratios considered, the conduction heat losses through the top and bottom horizontal walls in the experimental setup are expected to play a small influence on the heat transfer rate between the isothermal walls. Thus, it was assumed in the numerical model that boundary conditions along the horizontal walls are adiabatic.

The results of computations carried out for 14 experimental runs are reported in Table 1. The stagnant thermal conductivity of the porous medium was evaluated using equation 7. When taking $\epsilon\simeq\epsilon_\infty$, the computed values of k_m reported in Table 1 were found to be very close to the measured values. Calculations for the Nusselt number were made using the Darcy model and the Brinkman-Forchheimer-Darcy model (DBF) with uniform porosity, as well as using the present formulation for a variable porosity medium (VPM).

A comparison of the Nu values predicted by Darcy model with those for the extended model (DBF) in Table 1 shows noticeable viscous and inertia effects for most of the cases considered. The largest reductions in heat transfer rates are obtained for a water/glass beads system with $\gamma=0.141$. Indeed, these cases have the highest Darcy number ($\mathrm{Da}_\infty=3.016\times10^{-5}$) and lowest Prandtl number ($\mathrm{Pr}=7.1$), and thus, maximum viscous and inertia effects are observed. It should be noted that the results based on the DBF model were found in good agreement with the Nusselt numbers calculated using the correlation reported by Beckermann et al. (1986), which is valid for an intermediate range of Darcy number (i.e., $10^{-6}<\mathrm{Da}<10^{-4}$).

Figure 9(*a*) exemplifies the discrepancies between the numerical values for uniform porosity (DBF) and the experimental data of Seki et al. (1978). As can be seen, the numerical predictions are always lower than the measurements for both 5 mm and 16.4 mm-dia. glass balls with the largest discrepancies being for transformer oil/glass beads (TO). However, it is worth noting that the curves of the experimental and numerical values of Nu are almost parallel to each other. Hence, the percentage differences between the numerical and experimental values are almost independent of Ra.

Taking into account the effects of porosity and conductivity variations yields large heat transfer enhancements for all the cases investigated, as seen in Table 1. As can be expected, the larger the particle diameter and the Rayleigh number, the larger are the increases in Nu. By comparing the numerical predictions with experimental data as shown in Fig. 9(*b*), it appears clearly that the present model reduces the discrepancies significantly, except for transformer oil/glass beads. The large discrepancies between theory and experiments for the transformer oil/glass beads system could be attributed to the thermal dispersion effect, which has been neglected in the present model. This point will be examined in the next section. The improvements achieved for the other cases are illustrated in Fig. 9(*b*) and it can be seen that the predicted Nusselt numbers for 5-mm glass

beads fall very close to the measurements for both water and ethyl alcohol.

One of the interesting results shown in Fig. 9(*b*) is that the slope of the Nu versus Ra curve for 16.4-mm dia. glass beads/water (W1) starts decreasing at $Ra > 10^8$. The slope of the curves for uniform porosity, however, are almost constant for $10^7 < Ra < 2 \times 10^8$. Except for the numerical values obtained with large balls and water, Fig. 9(*b*) shows that only one exponent could be found for the Rayleigh number in a Nusselt number correlation. Therefore, an attempt was made to correlate the Nusselt number results reported in Table 1 in terms of the six parameters Ra, Pr, A, γ, ϵ_∞, and σ or λ_∞.

In order to separate the influences of ϵ_∞ both on temperature distribution and flow field, the bulk Darcy number, $Da_\infty = \gamma^2 \epsilon_\infty^3 / a\ (1-\epsilon_\infty)^2$, and the dimensionless stagnant bulk conductivity, $\lambda_\infty = k_{m,\infty}/k_f$, were chosen as independent parameters instead of γ, ϵ_∞, and $\sigma = k_f/k_s$. A correlation valid only for limited ranges of parameters corresponding within the boundary layer regime ($Ra > 10^7$) was obtained. This correlation was expressed as products of powers of the aforementioned parameters as follows:

$$\overline{Nu} = C\ Ra^n\ Pr^{0.04} \lambda_\infty^{0.18} Da_\infty^{0.36} A^{-0.59} \tag{23}$$

It should be emphasized that the values of the exponents of Pr, λ_∞, Da_∞, and A are deduced from the parametric study. A plot of the computed and measured Nusselt numbers normalized by the product of powers of the above four parameters is shown in Fig. 10. The equation for the dashed line was obtained from least-squares fit to the 14 numerical values reported in Table 1 (VPM) and it was found that $n = 0.55$ and $c = 0.07$. It should be pointed out that the present numerical results have been correlated over a narrow range of Rayleigh number. Such an exercise shows only that the numerical predictions can be correlated in terms of the five governing parameters. As can be seen in Fig. 10, equation (23) also predicts experimental data fairly well, with the exception of transformer oil. It is worth mentioning that similar agreement cannot be found when assuming uniform porosity media (DBF values in Table 1). Figures 9 and 10 suggest that the present model is quite effective in reducing the gap between experimental data and theoretical predictions of Nu values reported in the literature for porous media saturated with fluids having moderate or low Prandtl number.

Effects of Thermal Dispersion. Thermal dispersion effects in natural convection have been investigated by Hong and Tien (1987) for a vertical plate embedded in a porous medium and by Neischloss and Dagan (1975) and Georgiadis and Catton (1988a) for porous layers heated from below. All these studies show that hydrodynamic mixing of the interstitial fluid at the pore scale enhances the heat transfer. Similar effects were also found in forced convection by Hsu and Cheng (1988), Hunt and Tien (1988), and Georgiadis and Catton (1988b). In this section, we shall investigate whether the discrepancies between numerical results and experimental data for the case of the

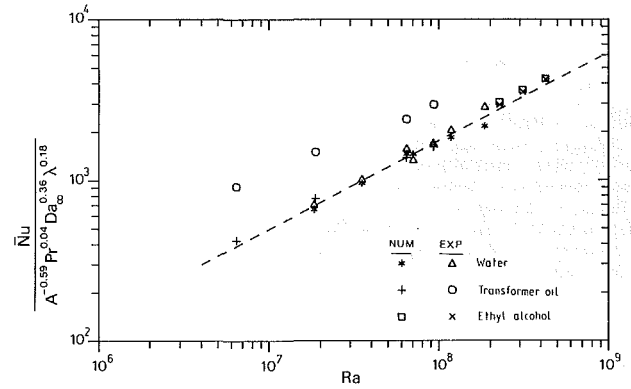

Fig. 10 Comparisons of the average Nusselt numbers from experimental data and numerical predictions for variable porosity media

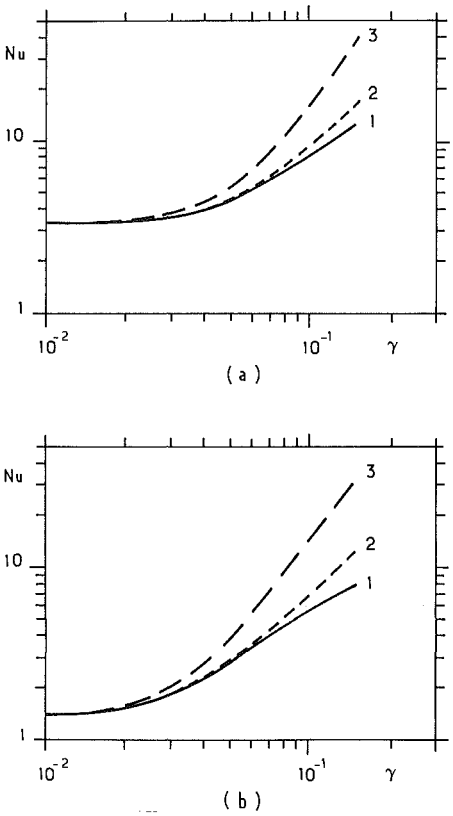

Fig. 11 Effect of thermal dispersion as a function of the dimensionless sphere diameter for uniform porosity media ($Ra = 10^8$, $A = 5$, $\epsilon_\infty = 0.36$): (1) thermal dispersion neglected; (2) equation (28); (3) equation (27); (*a*) transformer oil/glass beads ($\sigma = 0.136$); (*b*) water/glass beads ($\sigma = 0.586$)

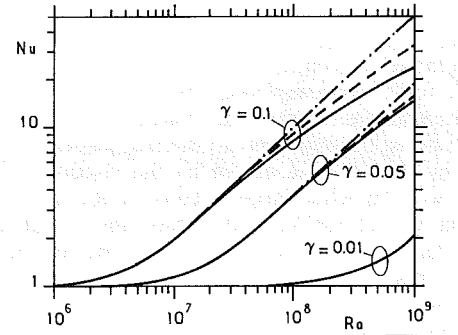

Fig. 12 Variations of Nu as a function of fluid Rayleigh number for uniform porosity ($\sigma = 1$, $\epsilon_\infty = 0.36$, $Pr = 5$, $A = 1$): - - - - Darcy's model; ——— DBF model without thermal dispersion; - · - · - DBF model with thermal dispersion (equation (28))

Table 2 Effect of dispersive conductivity on Nusselt number ($\sigma = 1$, $\gamma = 0.1$, $\epsilon_\infty = 0.36$, $Pr = 5$, $A = 1$)

	Uniform ϵ			Nonuniform ϵ		
	DBF	DBF + (27)	DBF + (28)	DBF	DBF + (27)	DBF + (28)
$Ra = 10^7$	1.985	2.022	2.479	3.990	4.177	4.910
$Ra = 2 \times 10^8$	12.03	16.76	32.86	27.23	50.19	66.96

transformer oil/glass beads system is owing to the omission of the thermal dispersion effect. To this end, the thermal dispersion models derived by Georgiadis and Catton (1988b) and by Hsu and Cheng (1988) will now be used.

The effective thermal conductivity of the saturated porous medium can be written as

$$k^* = k_m + k_d \tag{24}$$

where k_m is the stagnant thermal conductivity and k_d is the dispersive conductivity. According to the stochastic phenomenological model of Georgiadis and Catton, k_d can be expressed as

$$k_d = D_i(\rho c)_f d_p |\mathbf{V}_D|/(1-\epsilon) \tag{25}$$

where the coefficient D_i in equation (25) depends on the type of packing of the bed. The value of $D_i = 0.36$ has been shown by Georgiadis and Catton (1988b) to give the best fit of experimental data.

Another model proposed by Hsu and Cheng (1988) for k_d is

$$k_d = 0.02(\rho c)_f d_p |\mathbf{V}_D|(1-\epsilon)/\epsilon \tag{26}$$

Equations (25) and (26) in dimensionless form are given by

$$\lambda^* = \lambda\ (1 + 0.36\gamma|\mathbf{V}|/(1-\epsilon)) \tag{27}$$

$$\lambda^* = \lambda\ (1 + 0.02\gamma|\mathbf{V}|/(1-\epsilon)/\epsilon) \tag{28}$$

In order to separate the effects of nonuniform porosity and thermal dispersion, computations were first performed for a constant porosity medium. The results of these computations for the Nusselt number as a function of γ at $\mathrm{Ra} = 10^8$ for transformer oil/glass beads and water/glass beads systems are presented in Fig. 11. It can be concluded from this figure that: (1) the thermal dispersion effect tends to increase the heat transfer rate; (2) thermal dispersion effects increase with the dimensionless particle diameter γ; (3) the thermal dispersion effect based on Hsu and Cheng's model; and (4) the effect of Prandtl number on thermal dispersion enters indirectly through the inertia term and Rayleigh number dependency.

The thermal dispersion effect on the Nusselt number, based on Hsu and Cheng's model and the DBF formulation, as a function of the Rayleigh number at different dimensionless particle diameters for a constant porosity medium is presented in Fig. 12. For comparison purposes, numerical results based on the Darcy formulation are also presented in the same graph. As expected, the results based on Darcy model are higher than those based on the DBF model without thermal dispersion and the Darcy model is accurate for $\gamma = 0.01$ at Rayleigh numbers up to 10^9. With increasing value of γ, viscous, inertial, and thermal dispersion effects become increasingly important. The increase in Nusselt number due to thermal dispersion is almost balanced by the decrease of Nu by the viscous and inertial effects at $\gamma = 0.05$ while larger effects of thermal dispersion are seen at $\gamma = 0.1$ for $\mathrm{Ra} > 10^8$. Thus, the results based on Darcy model lie between those based on DBF model with and without thermal dispersion for the case of a constant porosity medium. Similar results can be observed for the case of a nonuniform porosity medium (see Table 2).

From the above discussion it is clear that including thermal dispersion effect for the cases having a high value of γ would increase the discrepancies for water/glass beads systems while the agreement would be better for the transformer oil/glass beads system. Therefore, it can be concluded that the origin of the discrepancies between numerical predictions and experimental data cannot be reduced through the inclusion of the thermal dispersion effect.

6 Conclusion

The effect of variable porosity on natural convection in a packed-sphere cavity has been investigated numerically. The major conclusions obtained are summarized as follows:

1 The nonuniform porosity effects depend greatly on the value of the dimensionless sphere diameter, γ. A high value of γ leads to wall channeling, which results in an increase in heat transfer rate. At $\gamma = 0.2$ (or $\mathrm{Da}_\infty = 2.5 \times 10^{-5}$), $\sigma = 1$, and $\mathrm{Ra} > 10^8$, the Nusselt number in a square porous cavity approaches that of a fluid-filled cavity.

2 In the conduction regime, variation of porosity leads to nonlinear temperature distributions, resulting in the reduction of the critical Rayleigh number and in the enhancement of the onset of free convection.

3 The effect of the thermal conductivity of the solid phase on the Nusselt number is more pronounced at low Rayleigh numbers where the conduction heat transfer is predominant. The larger γ and Ra, the smaller is the influence of σ, especially in a variable porosity medium because of the strong wall channeling effect.

4 The general effects of Prandtl number and cavity aspect ratio in a variable porosity medium were similar to those in a uniform porosity medium.

5 For a fluid with a moderate Prandtl number (such as water or ethyl alcohol), the predicted Nusselt numbers are found in agreement with experimental results. The introduction of additional terms to account for nonuniform porosity has been shown quantitatively necessary.

6 The Nusselt number data for the transformer oil are substantially higher than those predicted by the theory. This cannot be attributed to the fact that thermal dispersion effect has been neglected in the present model.

References

Beckermann, C., Viskanta, R., and Ramadhyani, S., 1986, "A Numerical Study of Non-Darcian Natural Convection in a Vertical Enclosure Filled With a Porous Medium," *Numerical Heat Transfer,* Vol. 10, pp. 557–570.

Bejan, A., and Tien, C. L., 1983, "Natural Convection in a Horizontal Porous Medium Subjected to an End-to-End Temperature Difference," ASME JOURNAL OF HEAT TRANSFER, Vol. 105, pp. 683–684.

Chandrasekhara, B. C., and Vortmeyer, D., 1979, "Flow Model for Velocity Distribution in Fixed Beds Under Isothermal Conditions," *Wärme- und Stoffübertragung,* Vol. 12, pp. 105–111.

Cheng, P., 1978, *Heat Transfer in Geothermal Systems,* Advances in Heat Transfer, Vol. 14, pp. 1–105.

Cheng, P., and Hsu, C. T., 1986, "Fully Developed, Forced Convective Flow Through an Annular Packed-Sphere Bed With Wall Effects," *International Journal of Heat and Mass Transfer,* Vol. 29, pp. 1843–1853.

Cheng, P., 1987, "Recent Studies of Wall Effects on Fluid Flow and Heat Transfer in Packed-Sphere Beds," presented at 32nd Indian Congress of Theoretical and Applied Mechanics, Bombay, India.

Cheng, P., Hsu, C. T., and Chowdhury, A., 1988a, "Forced Convection in the Entrance Region of a Packed Channel With Asymmetric Heating," ASME JOURNAL OF HEAT TRANSFER, Vol. 110, pp. 946–954.

Cheng, P., Pang, K., and Vortmeyer, D., 1988b, "Effects of Nonuniform Porosity on the Onset of Free Convection in a Porous Medium Between Parallel Plates Heated From Below," submitted for publication.

David, E., Lauriat, G., and Cheng, P., 1988, "Natural Convection in Rectangular Cavity Filled With Variable Porosity Media," *Proceedings of the 1988 National Heat Transfer Conference,* Houston, Vol. 1, pp. 605–612.

Georgiadis, J. G., and Catton, I., 1986, "Prandtl Number Effect on Bénard Convection in Porous Media," ASME JOURNAL OF HEAT TRANSFER, Vol. 108, pp. 284–290.

Georgiadis, J. G., and Catton, I., 1988a, "Dispersion in Cellular Thermal Convection in Porous Layers," *International Journal of Heat and Mass Transfer,* Vol. 31, pp. 1081–1091.

Georgiadis, J. G., and Catton, I., 1988b, "An Effective Equation Governing Convective Transport in Porous Media," ASME JOURNAL OF HEAT TRANSFER, Vol. 110, pp. 635–641.

Hong, J. T., and Tien, C. L., 1987, "Analysis of Thermal Dispersion Effect on Vertical-Plate Natural Convection in Porous Media," *International Journal of Heat and Mass Transfer,* Vol. 30, pp. 143–150.

Hong, J. T., Yamada, Y., and Tien, C. L., 1987, "Effects of Non-Darcian and Non-uniform Porosity on Vertical Plate Natural Convection in Porous Media," ASME JOURNAL OF HEAT TRANSFER, Vol. 109, pp. 356–362.

Hunt, M. L., and Tien, C. L., 1988, "Non-Darcian Convection in Cylindrical Packed Beds," ASME JOURNAL OF HEAT TRANSFER, Vol. 110, pp. 374–384.

Hsu, C. T., and Cheng, P., 1988, "Closure Schemes of the Macroscopic Energy Equation for Convective Heat Transfer in Porous Media," *Int. Comm. Heat and Mass Transfer,* Vol. 15, pp. 689–703.

Kladias, N., and Prasad, V., 1988, "Bénard Convection in Porous Media: Effects of Darcy and Prandtl Numbers," *Proceedings of the 1988 National Heat Transfer Conference,* Houston, Vol. 1, pp. 593–603.

Lauriat, G., and Prasad, V., 1987, "Natural Convection in a Vertical Porous Cavity—A Numerical Study for Brinkman-Extended Darcy Formulation," ASME JOURNAL OF HEAT TRANSFER, Vol. 109, pp. 688–696.

Lauriat, G., and Pradad, V., 1989, "Significance of Forchheimer and Brinkman's Extensions to Darcy's Law: A Numerical Study for Natural Convection in a Vertical Porous Cavity," *International Journal of Heat and Mass Transfer,* Vol. 32, pp. 2135–2148.

Le Peutrec, Y., and Lauriat, G., 1987, "Three-Dimensional Natural Convection Flows of Air and Water in Vertical Differentially Heated Cavities," ASME HTD-Vol. 92, pp. 351–360.

Neischloss, H., and Dagan, G., 1975, "Convective Currents in a Porous Layer Heated From Below: The Influence of Thermal Dispersion," *Physics of Fluids,* Vol. 18, pp. 757–761.

Poulikakos, D., and Renken, K., 1987, "Analysis of Forced Convection in a Duct Filled With Porous Media," ASME JOURNAL OF HEAT TRANSFER, Vol. 109, pp. 880–888.

Prasad, V., 1983, "Natural Convection in Porous Media-An Experimental and Numerical Study for Vertical Annular and Rectangular Enclosures," Ph. D. Dissertation, University of Delaware, Newark, DE.

Prasad, V., Kulacki, F. A., and Keyhani, M., 1985, "Natural Convection in Porous Media," *J. of Fluid Mechanics,* Vol. 150, pp. 89–119.

Prasad, V., and Tuntomo, A., 1987, "Inertia Effects on Natural Convection in a Vertical Porous Cavity," *Numerical Heat Transfer,* Vol. 11, pp. 89–119.

Prasad, V., Lauriat, G., and Kladias, N., 1988, "Reexamination of Darcy-Brinkman Solutions for Free Convection in Porous Media," *Proceedings of the 1988 National Heat Transfer Conference,* Houston, TX, Vol. 1, pp. 569–579.

Seki, N., Fukusako, S., and Inaba, H., 1978, "Heat Transfer in a Confined Rectangular Cavity Packed With Porous Media," *International Journal of Heat and Mass Transfer,* Vol. 21, pp. 985–989.

Tong, T. W., and Subramanian, E., 1985, "A Boundary Layer Analysis for Natural Convection in Porous Enclosure: Use of the Brinkman-Extended Darcy Model," *International Journal of Heat and Mass Transfer,* Vol. 28, pp. 563–571.

Vafai, K., and Tien, C. L., 1981, "Boundary and Inertia Effects on Flow and Heat Transfer in Porous Media," *International Journal of Heat and Mass Transfer,* Vol. 24, pp. 195–203.

Vafai, K., and Tien, C. L., 1982, "Boundary and Inertia Effects on Convective Mass Transfer in Porous Media," *International Journal of Heat and Mass Transfer,* Vol. 25, pp. 1183–1190.

Vafai, K., 1984, "Convection Flow and Heat Transfer in Variable Porosity Media," *J. Fluid Mechanics,* Vol. 147, pp. 233–259.

Vafai, K., Alkire, R. L., and Tien, C. L., 1985, "An Experimental Investigation of Heat Transfer in Variable Porosity Media," *J. Fluid Mechanics,* Vol. 147, pp. 233–259.

Weber, J. E., 1975, "The Boundary Layer Regime for Convection in a Vertical Porous Layer," *International Journal of Heat and Mass Transfer,* Vol. 87, pp. 449–474.

Zehner, P., and Schlünder, E. U., 1970, "Waermeleitfahigkeit von Schuettungen bei Massigen Temperaturen," *Chem. Ingr. Tech.,* Vol. 42, pp. 993–941.

A Three-Dimensional Analysis of the Flow and Heat Transfer for the Modified Chemical Vapor Deposition Process Including Buoyancy, Variable Properties, and Tube Rotation

Y. T. Lin

M. Choi[1]

R. Greif

Department of Mechanical Engineering,
University of California at Berkeley,
Berkeley, CA 94720

A study has been made of the heat transfer, flow, and particle deposition relative to the modified chemical vapor deposition (MCVD) process. The effects of variable properties, buoyancy, and tube rotation have been included in the study. The resulting three-dimensional temperature and velocity fields have been obtained for a range of conditions. The effects of buoyancy result in asymmetric temperature and axial velocity profiles with respect to the tube axis. Variable properties cause significant variations in the axial velocity along the tube and in the secondary flow in the region near the torch. Particle trajectories are shown to be strongly dependent on the tube rotation and are helices for large rotational speeds. The component of secondary flow in the radial direction is compared to the thermophoretic velocity, which is the primary cause of particle deposition in the MCVD process. Over the central portion of the tube the radial component of the secondary flow is most important in determining the motion of the particles.

Introduction

The Modified Chemical Vapor Deposition (MCVD) process is widely used for the manufacture of optical fiber preforms (MacChesney et al., 1974a, 1974b; Nagel et al., 1982). In this process reactant gases flow through a rotating silica tube, which is heated by a traversing exterior torch. As the reactant gases pass by the torch a chemical reaction occurs, which results in the formation of submicron particles. Downstream of the reaction zone particles are deposited on the surface of the tube and the particulate deposit is consolidated into a thin layer as the torch traverses. In the MCVD process particle deposition results from thermophoresis; that is, from the net force that a suspended particle experiences in the direction of decreasing temperature in a nonisothermal medium (Simpkins et al., 1979; Walker et al., 1979). After 40–60 layers are deposited the tube is collapsed into a solid preform rod and then drawn into a long thin fiber.

In analyses of the MCVD process the effects of variable properties, buoyancy, and tube rotation have generally been neglected and most studies have been two dimensional. However, in view of the large temperature differences and rotational rates that are present in MCVD, these effects may be important in the three-dimensional particle deposition process.

In studies of laser-enhanced MCVD, buoyancy effects have been included in a nonrotating vertical cylinder (Wang et al., 1985; DiGiovanni et al., 1985) and a strong buoyant soot plume has been observed (Morse et al., 1986). Thermophoretic particle deposition has been studied in variable property flow (Walker et al., 1980) and a study of chemical kinetics and silica aerosol dynamics has been carried out (Kim and Pratsinis, 1988). Three-dimensional variations of the temperature profiles resulting from the rotation of the tube and the circumferential variation of the wall temperature have been studied utilizing a parabolic velocity profile (Choi et al., 1989). The effects of buoyancy and tube rotation have also been studied using a perturbation analysis to the basic three-dimensional flow with buoyancy present (but small compared to the forced flow; Choi et al., 1990). An earlier work studied the effects of variable properties with tube rotation for a fast moving torch (Choi et al., 1987).

In the present work, the effects of tube rotation, buoyancy, and variable properties are numerically studied in a three-dimensional flow field relative to the MCVD process. Of particular interest is the quantitative comparison of the effects of the buoyant secondary flow with respect to thermophoresis and the determination of the interaction between buoyancy and tube rotation. It is noted that an accurate determination of the particle trajectories requires that the effects of buoyancy and variable properties be included in the analysis.

Analysis

The gas is flowing inside a horizontal circular tube of radius a, which is rotating about its axis with an angular velocity Ω (see Fig. 1). The introduction of a coordinate ξ, defined by $\xi = x - V_o t$, V_o being the torch speed, together with the polar coordinates r, θ results in the steady-state reference coordinate system (ξ, r, θ).

The flow is considered to be three dimensional and laminar. The governing equations in the cylindrical coordinate system (ξ, r, θ) are (Burmeister, 1982):

Continuity

$$\frac{1}{r}\frac{\partial(\rho r v)}{\partial r}+\frac{1}{r}\frac{\partial(\rho u)}{\partial \theta}+\frac{\partial(\rho w)}{\partial \xi}=0 \qquad (1)$$

[1]Present address: Seoul National University, Seoul, Korea.

Contributed by the Heat Transfer Division for publication in the JOURNAL OF HEAT TRANSFER. Manuscript received by the Heat Transfer Division January 23, 1990; revision received October 12, 1990. Keywords: Forced Convection, Materials Processing and Manufacturing Processes, Mixed Convection.

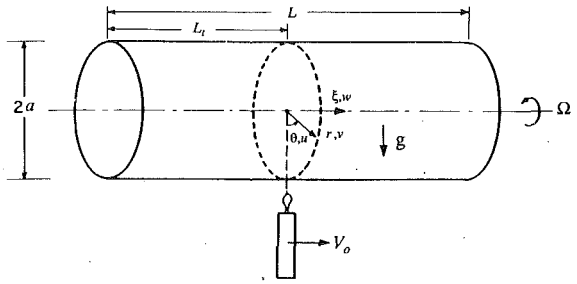

Fig. 1 Sketch of the system

Momentum

$$\rho\left(v\frac{\partial w}{\partial r}+\frac{u}{r}\frac{\partial w}{\partial \theta}+w\frac{\partial w}{\partial \xi}\right) = -\frac{\partial p}{\partial \xi}+\left(\frac{1}{r}\frac{\partial (r\tau_{r\xi})}{\partial r}+\frac{1}{r}\frac{\partial \tau_{\theta\xi}}{\partial \theta}+\frac{\partial \tau_{\xi\xi}}{\partial \xi}\right) \quad (2)$$

$$\rho\left(v\frac{\partial v}{\partial r}+\frac{u}{r}\frac{\partial v}{\partial \theta}+w\frac{\partial v}{\partial \xi}-\frac{u^2}{r}\right) = -\frac{\partial p}{\partial r}+\rho g\cos\theta + \left(\frac{1}{r}\frac{\partial (r\tau_{rr})}{\partial r}+\frac{1}{r}\frac{\partial \tau_{r\theta}}{\partial \theta}+\frac{\partial \tau_{r\xi}}{\partial \xi}-\frac{\tau_{\theta\theta}}{r}\right) \quad (3)$$

$$\rho\left(v\frac{\partial u}{\partial r}+\frac{u}{r}\frac{\partial u}{\partial \theta}+w\frac{\partial u}{\partial \xi}+\frac{vu}{r}\right) = -\frac{1}{r}\frac{\partial p}{\partial \theta} -\rho g\sin\theta+\left(\frac{1}{r^2}\frac{\partial (r^2\tau_{r\theta})}{\partial r}+\frac{1}{r}\frac{\partial \tau_{\theta\theta}}{\partial \theta}+\frac{\partial \tau_{\theta\xi}}{\partial \xi}\right) \quad (4)$$

Energy

$$\rho C_p\left(v\frac{\partial T}{\partial r}+\frac{u}{r}\frac{\partial T}{\partial \theta}+w\frac{\partial T}{\partial \xi}\right) = -\left(\frac{1}{r}\frac{\partial (rq_r)}{\partial r}+\frac{1}{r}\frac{\partial q_\theta}{\partial \theta}+\frac{\partial q_\xi}{\partial \xi}\right) \quad (5)$$

The viscous dissipation and pressure work terms in the energy equation are assumed to be negligible. The effects of buoyancy and variable properties are included with the density, thermal conductivity, and viscosity being functions of the temperature. The density ρ is obtained from the ideal gas law. The variation of the conductivity and viscosity are obtained from *CRC Handbook of Chemistry and Physics* (Weast and Astle, 1981) and from *Steam and Gas Tables With Computer Equations* (Irvine and Liley, 1984). In the region behind the torch, chemical reactions do not occur and the gas is comprised of $SiCl_4$, O_2, etc. In the region ahead of the torch, particles have been formed. In this region it is assumed that the particle mass loading does not strongly influence the flow field. A study of the effects of particle loading is given by Rosner and Park (1988).

The boundary conditions are:

at $r=a$, $u=a\,\Omega$, $v=0$, $w=-V_0$,

$$T_w=(T_M-T_i)\frac{(L_t+\xi)}{L_t}+T_i \quad \text{for } -L_t\le\xi\le 0$$

$$T_w=(T_M-T_i)\exp\left[-\left(\lambda\frac{\xi}{a}\right)^2\right]+T_i \quad \text{for } \xi>0$$

at $r=0$, u, v, w, T are finite;

at $\xi=-L_t$, $u=r\,\Omega$, $v=0$, $w=2V_{av}\left(1-\frac{r^2}{a^2}\right)-V_o$, $T=T_i$ (6)

Note that the wall temperatures in the above equations are based on the measurements of Walker et al. (1980). The circumferential variation of the wall temperature has also been studied and is discussed later. The torch is located at $\xi = 0$. At the entrance, $\xi = -L_t$, the temperature is equal to a constant value, T_i, the axial component of velocity is given by the fully developed Poiseuille velocity profile, the angular component of velocity varies linearly with respect to the radius corresponding to rigid body rotation, and there is no radial component of velocity. At the outlet plane the first derivative in the axial direction of the dependent variables is set equal to a nonzero value. This value is obtained by extrapolating the values of the upstream quantities and is equivalent to setting the second derivative to zero at the exit. (Calculations were carried out for two different boundary conditions; i.e., the first derivatives or the second derivatives set equal to zero. The results for the two conditions are virtually identical.)

The governing partial differential equations are nonlinear and coupled. The numerical procedure employed to solve for the velocity and temperature fields utilizes the primitive variables, u, v, w, p, and T. The computer code contains a basic structure that is similar to the TEACH code (Gosman and Ideriah, 1976; revised by Arnal, 1983) with a staggered grid arrangement (Harlow and Welsh, 1965; Patankar, 1980). The discrete equations of continuity, momentum, and energy on the three-dimensional grid are obtained by integrating the governing equations (1)–(5) over appropriate control volumes. In order to improve accuracy (and convergence), a central difference representation is used for the diffusion terms and a second-order upwind differencing scheme is used for the con-

Nomenclature

a = tube radius
C_p = specific heat
g = gravitational acceleration
K = thermophoretic coefficient
L = length of the tube
L_t = distance between the torch and the specified inlet
p = pressure
q = heat flux
r = radial coordinate
T = temperature
T_i = temperature at the inlet plane
T_M = maximum temperature on the tube wall
T_{rxn} = reaction temperature
T_w = wall temperature
t = time
u = circumferential velocity
V_o = torch speed
V_{av} = average velocity of gas in the axial direction
v = radial velocity
V = thermophoretic velocity
V_r = thermophoretic velocity in the radial direction
w = axial velocity relative to the torch speed
x = axial coordinate
θ = angle
λ = parameter in torch heating distribution
ν = kinematic viscosity
ξ = moving coordinate = $x - V_o t$
ρ = density
τ = viscous stress
Ω = angular velocity of tube

Subscripts

i = original particle locations for particle trajectories
d = positions of particle deposition
r = radial coordinate
θ = angle
ξ = moving coordinate = $x - V_o t$

vective terms (Leonard, 1979; Pollard and Siu, 1982; Freitas, 1985; Goering, 1989). The resulting discretized transport difference equations are solved by the SIMPLER algorithm ("Semi-Implicit Method for Pressure-Linked Equations Revised," Patankar, 1980). A bulk pressure correction technique (Lavine, 1984; Freitas, 1985; Goering, 1989) is applied in the axial direction. At each cross-section plane, an average pressure correction is calculated in order to ensure that the flow through the cross section satisfies global continuity. It is stressed that the implementation of the bulk pressure correction has been extremely important in the present study and substantially enhances the convergence rate. Calculations were carried out for constant properties and small buoyancy effects and the results were in good agreement with a perturbation solution (cf. Choi et al., 1990). Grid sensitivity tests were made for several uniform and nonuniform grids. The results for a 22 × 11 × 100 uniform node grid are found to differ by less than 1 percent from 32 × 22 × 100 and 22 × 11 × 150 grids at several points near and far downstream from the torch and the 22 × 11 × 100 grid was used in the calculations. It is noted that the SIMPLER iteration procedure has a slower convergence rate for nonuniform grids. The typical CPU time needed to obtain convergent solutions is about 60 min on a CRAY X-MP. A total axial length, L, of 0.6 m was used with L_t equal to 0.275 m for the distance between the torch and the location where the velocity and temperature are specified. A total axial length of 0.9 m was also used to determine the effects of the exit condition. The results were virtually the same as for the $L = 0.6$ m case.

The thermophoretic velocity may be written in the following form (Talbot et al., 1980):

$$V = -\frac{K\nu}{T}\nabla T \tag{7}$$

where K is the thermophoretic coefficient. A value of 0.9 for K is used in the present work (Walker et al., 1980). The motion of the particles is determined from the combined effects resulting from thermophoresis and the forced and secondary flow. It is noted that for the MCVD process the effects of particle Brownian diffusion are negligible in comparison to the effects of thermophoresis (Walker et al., 1979; Simpkins et al., 1979). The emphasis here is on the effects of buoyancy, rotation, variable properties, etc., on the particle trajectories. Note that to obtain the wall deposition rates, including inertial and Brownian diffusion effects, the particle concentration field is also required (Fernandez de la Mora and Rosner, 1981). Using a Lagrangian description for the particle motion, the following differential equations are obtained for the velocity of the particle:

$$\frac{d\xi}{dt} = w - \frac{K\nu}{T}\frac{\partial T}{\partial \xi}$$

$$\frac{dr}{dt} = v - \frac{K\nu}{T}\frac{\partial T}{\partial r}$$

$$r\frac{d\theta}{dt} = u - \frac{K\nu}{T}\frac{1}{r}\frac{\partial T}{\partial \theta} \tag{8}$$

where $\frac{d\xi}{dt}$, $\frac{dr}{dt}$, $r\frac{d\theta}{dt}$ are the axial, radial, and angular velocities of the particles, respectively. To determine the particle trajectories, equations (8) were solved by using the second-order Runge-Kutta method after u, v, w, and T had been obtained from equations (1)–(5).

Results and Discussion

Figure 2 shows the axial variation of the wall temperature

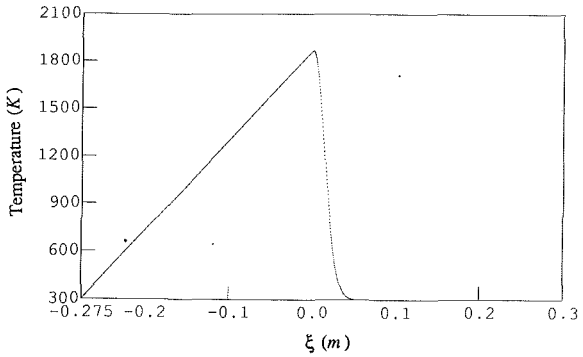

Fig. 2 Distribution of the wall temperature; T_M = 1873 K, T_i = 300 K, λ = 0.5, L_t = 0.275 m, a = 0.01 m

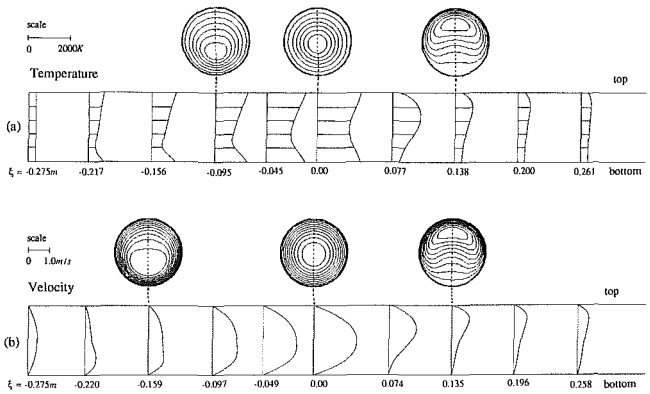

Fig. 3 *(a)* Temperature distribution along the vertical diameter and constant temperature contours; *(b)* axial velocity distribution along the vertical diameter and constant axial velocity contours; Ω = 0, a = 0.01 m, V_{av} = 0.1665 m/s, V_o = 0.003 m/s (20.0 cm/min)

distribution given in equation (6) (cf. Walker et al., 1980). Conditions are specified at the entrance at $\xi = -L_t$; that is, the temperature is equal to 300 K, the axial component of velocity is given by the fully developed Poiseuille velocity profile, and the angular component of velocity varies linearly with respect to the radius corresponding to rigid body rotation. At this location there is no radial component of velocity. The torch is located at $\xi = 0$.

Figures 3(*a*) and 3(*b*) show the calculated temperature and axial velocity distributions along the vertical diameter at different axial locations for the nonrotating case, Ω = 0. Also shown are constant temperature and constant axial velocity contours at several axial locations. In the region behind the torch, $\xi < 0$, the gas temperature is lower than the (surrounding) wall temperature, as shown in Fig. 3(*a*). The decreased density of the gas near the wall in conjunction with the effect of gravity results in a secondary flow pattern (deviation from rigid body rotation) as shown in Fig. 4(*a*). The gas flows symmetrically upward around the hot wall and then downward in the cold central region. There is symmetry about the vertical diameter for this nonrotating case (cf. contours in Figs. 3*a* and 3*b*). The cooler gas in the interior flowing downward in the core results in colder temperatures over the bottom half of the tube (cf. Fig. 3*a*). This downward flow pattern also results in larger axial velocities over the bottom half (cf. Fig. 3*b*).

In the region ahead of the torch, $\xi > 0$, the wall temperature decreases rapidly to 300 K. The heated gas flows ahead of the torch and thus may be at a higher temperature than the surrounding cold wall surface (cf. Fig. 3*a*). It is repeated that in the absence of tube rotation the secondary flow pattern is symmetric about the vertical diameter. As the gas continues

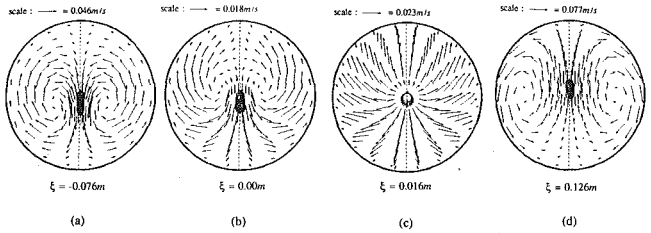

Fig. 4 Secondary flow pattern for Ω = 0: *(a)* at ξ = −0.076 m; *(b)* at ξ = 0.0 m; *(c)* at ξ = 0.016 m; *(d)* at ξ = 0.126 m

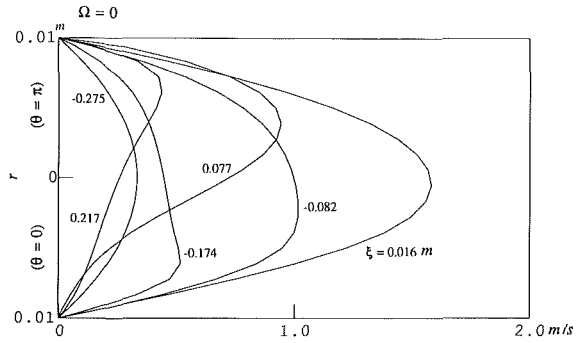

Fig. 5 Axial velocity component distribution along the vertical diameter at different axial locations; Ω = 0, *a* = 0.01 m, V_{av} = 0.1665 m/s, V_o = 0.003 m/s (20.0 cm/min)

downstream, its temperature continues to decrease and becomes more uniform as shown in Fig. 3(*a*). In this region the peak temperature occurs in the gas (rather than on the wall); the resulting secondary flow pattern here is upward in the hot gas core and downward around the cold tube wall (cf. Fig. 4*d*). (This flow pattern is opposite to that in the region behind the torch.) Since the gas, which is hot, flows upward in the core region, the gas temperature is higher over the upper half of the cross section (cf. Fig. 3*a*) and the axial component of velocity is larger in the upper half (cf. Fig. 3*b*).

Near the torch the gas temperatures are very high and there is a large flow in the radial direction over the entire cross section (cf. Fig. 4*c*). The strong radial flows occur for variable properties but are not present for constant properties (discussed later). For variable properties, this outward radial flow is a consequence of the volume expansion resulting from the decrease of the density (increase of the gas temperature) near the center of the tube and the volume contraction resulting from the increase of the density (decrease of the gas temperature) near the tube wall. In this region the strong outward radial flow would aid the thermophoretic velocity in causing particle deposition. Note that in regions away from the torch, the radial component of the secondary flow may be inward and therefore hinder deposition. Upward buoyant flow in the core ahead of the torch aids thermophoresis over the upper half of the tube but opposes thermophoresis over the lower half. These effects would result in nonuniform particle deposition over the tube surface.

The increasing gas temperature (decreasing density) in the axial direction also causes the gas to accelerate from the entrance to the region near the torch and then decelerate ahead of the torch as the temperature decreases (cf. Figs. 3*b* and 5). Note that at ξ = 0.016 m the maximum value of the axial component of velocity is about five times the value at the entrance plane.

When there is tube rotation, the interaction of angular convection with buoyancy and axial convection results in complex velocity fields. The effect of angular convection is essentially to tilt the nonrotating symmetric fields in the direction of the rotation. A more detailed discussion follows.

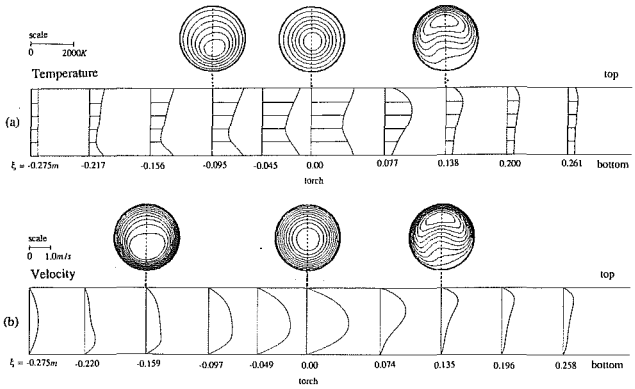

Fig. 6 *(a)* Temperature distribution along the vertical diameter and constant temperature contours; *(b)* axial velocity distribution along the vertical diameter and constant axial velocity contours; Ω = 60 rpm, *a* = 0.01 m, V_{av} = 0.1665 m/s, V_o = 0.003 m/s (20.0 cm/min)

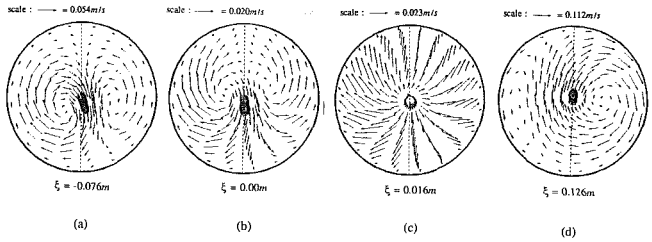

Fig. 7 Secondary flow pattern for Ω = 60 rpm: *(a)* at ξ = −0.076 m; *(b)* at ξ = 0.0 m; *(c)* at ξ = 0.016 m; *(d)* at ξ = 0.126 m

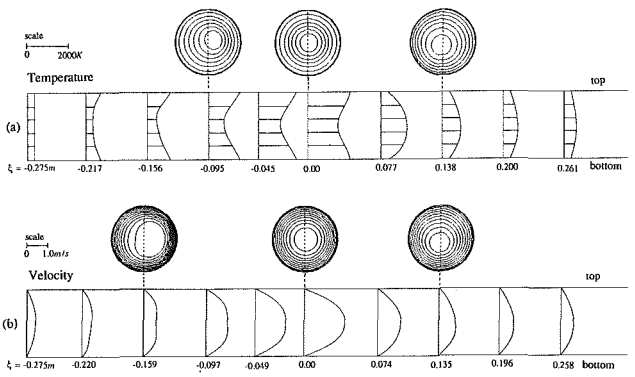

Fig. 8 *(a)* Temperature distribution along the vertical diameter and constant temperature contours; *(b)* axial velocity distribution along the vertical diameter and constant axial velocity contours; Ω = 300 rpm, *a* = 0.01 m, V_{av} = 0.1665 m/s, V_o = 0.003 m/s (20.0 cm/min)

For moderate rotational speeds, e.g., Ω = 60 rpm (counterclockwise) (cf. Simpkins et al., 1979), the temperature and the axial velocity distributions along the vertical diameter differ only slightly from the nonrotating case (cf. Figs. 3*a*, 6*a* and 3*b*, 6*b*). It is seen that the constant temperature and axial velocity contours in the cross sections (at different axial locations) are no longer symmetric about the vertical diameter but are tilted slightly. The secondary flow patterns are also tilted as shown in Figs. 7(*a*, *b*, *c*, and *d*). Behind the torch the gas still flows upward around the hot wall and then downward in the cold central region, while ahead of the torch the gas flows downward around the cold wall and upward in the hot core. In the region near the torch, the strong secondary radial flow pattern that was present for the nonrotating case and results from variable property effects (cf. Fig. 7*c*) is also present with rotation.

At larger rotational speeds, e.g., Ω = 300 rpm, the stronger

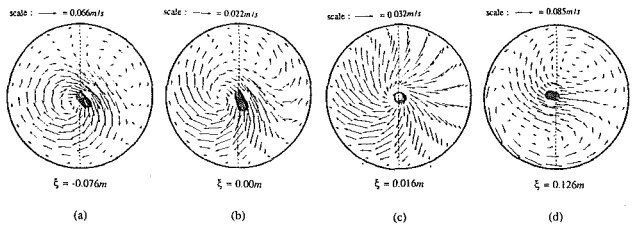

Fig. 9 Secondary flow pattern for Ω = 300 rpm: *(a)* at $\xi = -0.076$ m; *(b)* at ξ = 0.0 m; *(c)* at ξ = 0.016 m; *(d)* at ξ = 0.126 m

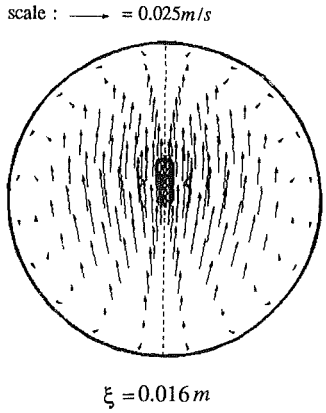

Fig. 10 Secondary flow pattern for constant properties at ξ = 0.016 m; Ω = 0, a = 0.01 m, V_{av} = 0.1665 m/s, V_o = 0.003 m/s (20.0 cm/min)

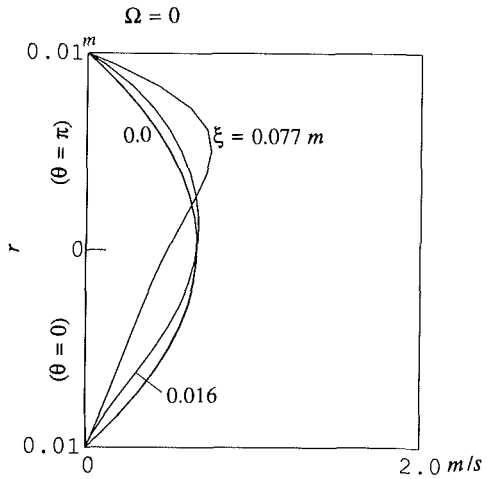

Fig. 11 Axial velocity component distribution along the vertical diameter at different axial locations for constant properties, Ω = 0 rpm

angular convection results in more uniform temperature and axial velocity profiles about the tube axis (cf. Figs. 8*a* and 8*b*); the secondary flow patterns exhibit a larger tilt (cf. Figs. 9*a*, *b*, *c*, and *d*). Again, in the high-temperature region near the torch a strong secondary radial flow is present due to the effects of variable properties (cf. Fig. 9*c*).

Figure 10 shows, for nonrotation, the secondary flow pattern in the region near the torch that results for constant properties (except for the buoyancy terms in the momentum equations). The density in these buoyancy terms is obtained from the ideal gas law. Note that the strong secondary radial flow pattern, which is present for variable property flow (cf. Figs. 4*c*, 7*c*, and 9*c*), is not present here (for constant properties). In the region far from the torch (either behind or ahead) the secondary flow patterns (not shown) are essentially the same as for variable property flow (cf. Figs. 4*a*, *d*). It is also seen that there

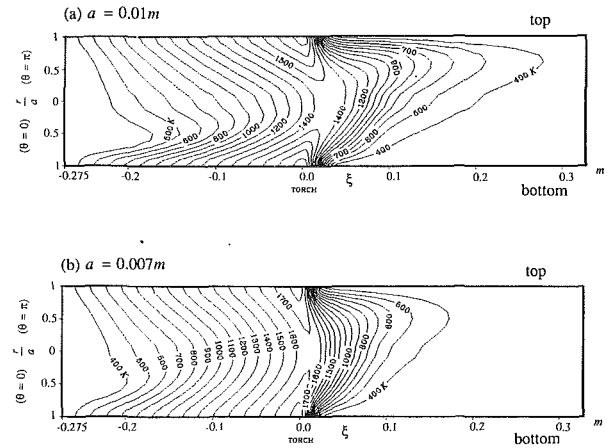

Fig. 12 Isothermal contours in the central vertical plane: *(a)* a = 0.01 m, *(b)* a = 0.007 m; Ω = 60 rpm, V_{av} = 0.1665 m/s, V_o = 0.003 m/s (20.0 cm/min)

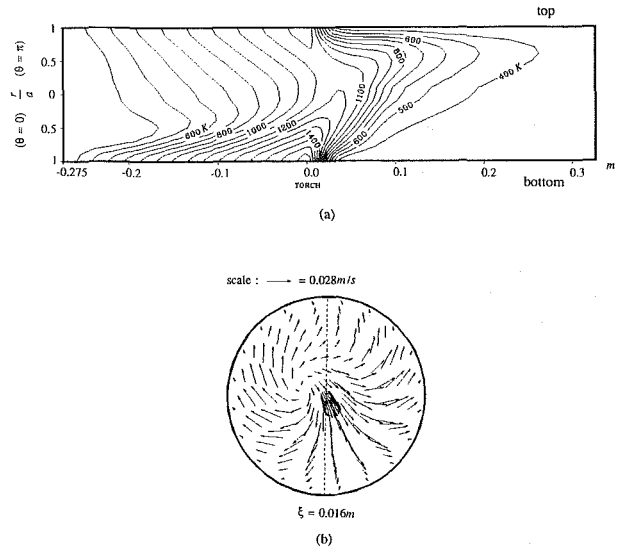

Fig. 13 *(a)* Isothermal contours in the central vertical plane; *(b)* secondary flow pattern at ξ = 0.016 m with circumferential wall temperature variation; Ω = 60 rpm, a = 0.01 m, V_{av} = 0.1665 m/s, V_o = 0.003 m/s (20.0 cm/min), $T(\xi = 0, \theta = 0)$ = 1873 K, $T(\xi = 0, \theta = \pi)$ = 1273 K

is no significant change in the axial component of velocity along the tube as was obtained for variable properties (cf. Fig. 11).

Figure 12(*a*) shows the isothermal contours in the vertical plane for Ω = 60 rpm. The gas temperature does not exceed the reaction temperature ($T_{rxn} \approx$ 1573 K) (cf. Walker et al., 1980) in the central region of the tube and thus no chemical reaction occurs there (even in the region above the torch). Therefore particles will not form in the central region. However, for a smaller tube radius or smaller flow rate (with the same wall temperature distribution), the gas temperature does exceed the reaction temperature in the central region at some locations near the torch (cf. Fig. 12*b*).

To study the effect of the variation of the wall temperature in the circumferential direction, a symmetric cosine variation about the vertical diameter has been assumed (Choi et al., 1987); i.e., highest temperature at the bottom, θ = 0, and lowest temperature at the top, $\theta = \pi$. The axial variation of the temperature is the same as was previously specified in equations (6). Calculations were performed for two cases; at ξ = 0 temperature differences between θ = 0 and π equal to 300 K and 600 K, respectively, for Ω = 60 rpm. Both cases have the same temperature at the bottom at ξ = 0, $T(\xi$ = 0,

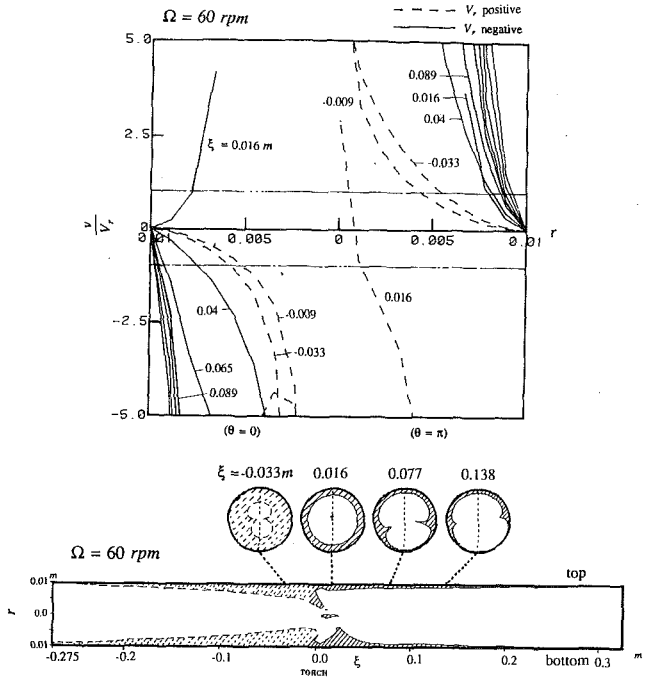

Fig. 14 *(a)* **Ratio of radial velocity v to radial thermophoretic velocity V_r, Ω = 60 rpm;** *(b)* **curve of $|v/V_r| = 1$ in the central vertical plane and $|v/V_r| = 1$ contours at different axial locations**

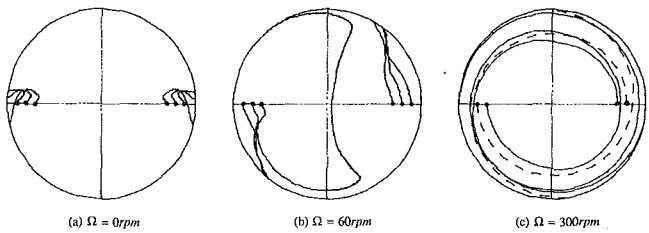

Fig. 15 Particle trajectories with $\xi_i = -0.025$ m: *(a)* **Ω = 0 rpm, r_i = 0.009, 0.008, and 0.007 m; $\theta_i = \pi/2$ and $3\pi/2$;** *(b)* **Ω = 60 rpm, r_i = 0.009, 0.008, and 0.007 m; $\theta_i = \pi/2$ and $3\pi/2$;** *(c)* **Ω = 300 rpm, r_i = 0.008 and 0.007 m; $\theta_i = \pi/2$ and $3\pi/2$**

Table 1 Locations of particle deposition (ξ_d, θ_d) with $\xi_i = -0.025$ m, r_i = 0.009, 0.008, and 0.007 m, $\theta_i = \pi/2$ and $3\pi/2$

$\xi_i = -0.025m$	(ξ_d, θ_d)		
(r_i, θ_i)	$\Omega = 0rpm$	$\Omega = 60rpm$	$\Omega = 300rpm$
$(0.009m, \pi/2)$	$(0.029m, 1.700)$	$(0.029m, 2.628)$	$(0.03m, 0.295)$
$(0.009m, 3\pi/2)$	$(0.029m, 4.583)$	$(0.028m, 5.557)$	$(0.028m, 3.230)$
$(0.008m, \pi/2)$	$(0.040m, 1.628)$	$(0.039m, 2.524)$	$(0.041m, 0.192)$
$(0.008m, 3\pi/2)$	$(0.040m, 4.655)$	$(0.040m, 5.618)$	$(0.043m, 3.157)$
$(0.007m, \pi/2)$	$(0.060m, 1.355)$	$(0.057m, 2.503)$	$(0.058m, 1.370)$
$(0.007m, 3\pi/2)$	$(0.060m, 4.928)$	$(0.257m, 3.852)$	$(0.118m, 4.875)$

$\theta = 0) = 1873$ K. The gas temperature distribution for both cases (cf. Fig. 13*a* for the 600 K temperature difference, not shown for the 300 K temperature difference) differs from the results for the constant circumferential wall temperature (cf. Fig. 12*a*). For the 600 K temperature difference (colder top surface, $T(\xi = 0, \theta = \pi) = 1273$ K) the strong radial flow pattern (previously obtained near the torch) is now not pronounced (cf. Fig. 13*b*). This is because the cooler gas temperatures at the top result in a smaller volume expansion effect (at the top). Note, however, that there is still a significant radial flow pattern present over the bottom half because the volume contraction effect is more significant over the bottom surface where the temperature decreases from 1873 K at the torch to 300 K in front of the torch, while over the top surface the corresponding temperature decrease is from 1273 K to 300 K. For the 300 K temperature difference the secondary flow patterns are essentially the same as were obtained for the case of constant circumferential wall temperature and a strong secondary radial flow pattern is present near the torch. Thus, the surrounding wall temperature variation for both cases affects the temperature distribution and the corresponding thermophoresis, i.e., temperature gradient. However, the secondary flow pattern is affected only by large temperature differences.

Figure 14(*a*) shows, for $\Omega = 60$ rpm, the ratio of the secondary radial velocity component, v, to the radial component of the thermophoretic velocity $V_r = -\frac{K\nu}{T}\frac{\partial T}{\partial r}$. Thermophoresis is the primary cause for particle deposition in the MCVD process. The solid curves correspond to positive values of V_r, i.e., the thermophoretic velocity is toward the wall and positive values of the ratio, v/V_r, mean that the secondary flow aids deposition. When $|v/V_r|$ is greater than unity the secondary flow is the dominant effect for particle motion in the radial direction and this is true in the core region of the tube. This result was also obtained in a perturbation study (Choi et al.,1990). Note that in the region near the tube wall the ratio $|v/V_r|$ is always less than one; i.e., thermophoresis is more important in this region. This is because the secondary flow must vanish on the wall but the thermophoretic velocities, which depend on the local temperatures and radial temperature gradients, may have nonzero values. Figure 14(*b*) shows the influence of the secondary flow over the central vertical plane. The curves correspond to $|v/V_r| = 1$. In the shaded area $|v/V_r|$ is less than 1 and here thermophoresis is more important than the secondary flow. Only the solid curves are important because in the region behind the torch the gas temperature is less than the reaction temperature and no particles are formed (thermophoresis is meaningless without particles). In the region ahead of the torch the gas temperature decreases and becomes more uniform (cf. Fig. 6*a*) and thus the secondary flow effect resulting from the density differences (temperature differences) within the plane in conjunction with gravity decreases. The decrease in the temperature gradient causes a decrease in thermophoresis in this region. Thus, both the thermophoretic velocity, V_r, and the radial velocity, v, induced by the secondary flow are small in this region with the latter contribution prevailing. Curves for $|v/V_r| = 1$ are also shown for several cross sections in Fig. 14(*b*). In the region near the torch the curve is nearly circular because of the uniformly strong radial flow pattern. Ahead of the torch the magnitude of the radial velocity of the gas is larger along the vertical diameter and smaller along the horizontal diameter (cf. Fig. 4*d*). Thus the $|v/V_r| = 1$ curve penetrates further into the core near the horizontal diameter (cf. Fig. 14*b* contours at $\xi = 0.077$ m and $\xi = 0.138$ m showing the increased region of influence of thermophoresis away from the wall).

Figures 15(*a–c*) show particle trajectories for different values of the rotational speed, Ω. Particles have been initiated at the same locations for all of the cases corresponding to temperatures greater than the reaction temperature, T_{rxn}. Particles formed in the region near the wall deposit on the wall surface; however, particles formed in the central region may be carried out of the tube. The axial locations for the particle deposition depend only slightly on the tube rotation but the circumferential locations of deposition are strongly affected by the tube rotation (cf. Table 1). The axial deposition locations are mostly in the range from $\xi = 0.025$ m to 0.125 m. The particle trajectories are affected by the tube rotation as shown in Figs. 15(*a–c*). When there is strong tube rotation, e.g., $\Omega = 300$ rpm, the particle trajectories are helices (cf. Fig. 15*c*); for the

nonrotating case particle trajectories in the cross-stream plane are essentially due to the secondary flow effects and symmetric with respect to the vertical diameter.

Summary and Conclusions

A study has been made of the heat transfer and flow relative to the modified chemical vapor deposition (MCVD) process. Numerical solutions for the three-dimensional velocity and temperature fields have been obtained including the effects of variable properties, tube rotation and buoyancy. The following conclusions are made:

1 In the absence of rotation, secondary flows are downward in the cold core behind the torch and upward in the hot core ahead of the torch. The effect of tube rotation essentially tilts the temperature and velocity fields in the direction of rotation; this effect is significant only for large rotational speeds.

2 The effects of variable properties (primarily due to the density changes) result in a significant change in the variation of the magnitude of the axial velocity along the tube. They also result in a strong secondary radial flow pattern in the region near the torch, which aids thermophoresis for particle deposition.

3 With respect to the secondary flow, thermophoresis is dominant in determining particle trajectories near the wall but less important in the larger central region of the tube.

4 The variation of the circumferential wall temperature has a significant effect on the secondary flow when there is a large temperature difference between the bottom and top of the tube.

5 The particle trajectories and the deposition locations are dependent on the tube rotation and the initial locations of the particles.

Acknowledgments

The authors thank D. J. Goering, University of Alaska, for the use of his numerical code and helpful discussions concerning the code. The interest of U. C. Paek, AT&T Engineering Research Center, in this research is also greatly appreciated. Support from the National Science Foundation, the San Diego Supercomputer Center, and the Computing Center of the University of California at Berkeley is gratefully acknowledged.

References

Arnal, M. P., 1983, "Revision to TEACH-2E: A General Computer Program for Two-Dimensional, Turbulent, Recirculating Flows" (by A. D. Gosman and J. F. K. Ideriah), Dept. of Mechanical Engineering Report No. FM-83-2, University of California at Berkeley.

Burmeister, L. C., 1983, *Convective Heat Transfer*, Wiley, New York.

Choi, M., Baum, H. R., and Greif, R., 1987, "The Heat Transfer Problem During the Modified Chemical Vapor Deposition Process," ASME JOURNAL OF HEAT TRANSFER, Vol. 109, pp. 642-646.

Choi, M., Greif, R., and Baum, H. R., 1989, "A Study of Heat Transfer and Particle Motion Relative to the Modified Chemical Vapor Deposition Process," ASME JOURNAL OF HEAT TRANSFER, Vol. 111, pp. 1031-1037.

Choi, M., Lin, Y. T., and Greif, R., 1990, "Analysis of Buoyancy and Tube Rotation Relative to the Modified Chemical Vapor Deposition Process," ASME JOURNAL OF HEAT TRANSFER, Vol. 112, pp. 1063-1069.

DiGiovanni, D., Wang, C. Y., Morse, T. F., and Cipolla, J. W., Jr., 1985, "Laser Induced Buoyancy and Forced Convection in Vertical Tubes," *Natural Convection: Fundamentals and Applications*, S. Kakac, W. Aung, and R. Viskanta, eds., Hemisphere, New York, pp. 1118-1139.

Fernandez de la Mora, J., and Rosner, D. E., 1981, "Inertial Deposition of Particles Revisited and Extended: Eulerian Approach to a Traditionally Lagrangian Problem," *PhysicoChemical Hydrodynamics*, Vol. 2, No. 1, pp. 1-21.

Freitas, C. J., 1985, "Numerical Simulation of Three-Dimensional Flow in a Cavity," Ph.D. Thesis, Stanford University, Stanford, CA.

Goering, D. J., 1989, "The Influence of Curvature and Buoyancy in Three-Dimensional Pipe Flows," Ph.D. Thesis, University of California, Berkeley, CA.

Gosman, A. D., and Ideriah, J. F. K., 1976, "TEACH-2E: A General Computer Program for Two-Dimensional, Turbulent, Recirculating Flows," Imperial College, London, United Kingdom.

Harlow, F. H., and Welsh, J. E., 1965, "Numerical Calculation of Time Dependent Viscous Incompressible Flow of Fluid With a Free Surface," *Phys. of Fluids*, Vol. 8, pp. 2182-2189.

Irvine, T. F., and Liley, P. E., Jr., 1984, *Steam and Gas Tables With Computer Equations*, Academic Press, New York, pp. 161-165.

Kim, K. S., and Pratsinis, S. E., 1988, "Manufacture of Optical Waveguide Preforms by Modified Chemical Vapor Deposition," *AIChE J.*, Vol. 34, No. 6, pp. 912-920.

Lavine, A. G., 1984, "A Three-Dimensional Analysis of Natural Convection in a Toroidal Loop," Ph.D. Thesis, University of California, Berkeley, CA.

Leonard, B. P., 1979, "A Stable and Accurate Convective Modeling Procedure Based on Quadratic Upstream Interpolation," *Comp. Meths. Appl. Mech. Eng.*, Vol. 19, pp. 59-98.

MacChesney, J. B., O'Connor, P. B., DiMarcello, F. V., Simpson, J. R., and Lazay, P. D., 1974a, "Preparational Low-Loss Optical Fibers Using Simultaneous Vapor Phase Deposition and Fusion," *Proc. 10th Int. Congr. Glass*, Kyoto, Japan, pp. 6-40-6-44.

MacChesney, J. B., O'Connor, P. B., and Presby, H. M., 1974b, "A New Technique for Preparation of Low-Loss and Graded Index Optical Fibers," *Proc. IEEE*, Vol. 62, pp. 1278-1279.

Morse, T. F., DiGiovanni, D., Chen, Y. W., and Cipolla, J. W., Jr., 1986, "Laser Enhancement of Thermophoretic Deposition Process," *J. of Lightwave Technology*, LT-4, No. 2, pp. 151-155.

Nagel, S. R., MacChesney, J. B., and Walker, K. L., 1982, "An Overview of the Modified Chemical Vapor Deposition (MCVD) Process and Performance," *IEEE J. Quantum Electronics*, Vol. QE-18, No. 4, pp. 459-476.

Patankar, S. V., 1980, *Numerical Heat Transfer and Fluid Flows*, Hemisphere Publishing Co., New York.

Pollard, A., and Siu, A. L.-W., 1982, "The Calculation of Some Laminar Flows Using Various Discretisation Schemes," *Computer Methods in Applied Mechanics and Engineering*, Vol. 35, pp. 293-313.

Rosner, D. E., and Park, H. M., 1988, "Thermophoretically Augmented Mass-, Momentum- and Energy-Transfer Rates in High Particle Mass Loaded Laminar Forced Convection Systems," *Chem. Eng. Sci.*, Vol. 43, No. 10, pp. 2689-2704.

Simpkins, P. G., Kosinski, S. G., and MacChesney, J. B., 1979, "Thermophoresis: The Mass Transfer Mechanism in Modified Chemical Vapor Deposition," *J. Appl. Physics*, Vol. 50, pp. 5676-5681.

Talbot, L., Cheng, R. K., Schefer, R. W., and Willis, D. R., 1980, "Thermophoresis of Particles in a Heated Boundary Layer," *J. Fluid Mech.*, Vol. 101, Part 4, pp. 737-758.

Walker, K. L., Homsy, G. M., and Geyling, F. T., 1979, "Thermophoretic Deposition of Small Particles in Laminar Tube Flow," *J. Colloid Interface Sci.*, Vol. 69, pp. 138-147.

Walker, K. L., Geyling, F. T., and Nagel, S. R., 1980, "Thermophoretic Deposition of Small Particles in the Modified Chemical Vapor Deposition (MCVD) Process," *J. Am. Ceram. Sci.*, Vol. 63, pp. 552-558.

Wang, C. Y., Morse, T. F., and Cipolla, J. W., Jr., 1985, "Laser Induced Natural Convection and Thermophoresis," ASME JOURNAL OF HEAT TRANSFER, Vol. 107, pp. 161-167.

Weast, R. C., and Astle, M. J., 1981, *CRC Handbook of Chemistry and Physics*, 61th ed., CRC Press Inc., Boca Raton, FL.

A. Tuntomo[1]

C. L. Tien
UCI Distinguished Professor.

Department of Mechanical Engineering,
University of California,
Irvine, CA 92717

S. H. Park
Korea Institute of Energy and Resources,
71-2 Jang-dong, Jung-gu,
Daejon, Korea

Internal Distribution of Radiant Absorption in a Spherical Particle

This paper applies electromagnetic wave theory for the study of the internal radiant absorption field of a small spherical particle, particularly to determine the optimum combination of size-to-wavelength parameter and complex refractive index for maximum local peak absorption. A map is devised to illustrate the general pattern of the internal field, which can be divided into three main regimes: uniform, front-concentrated, and back-concentrated absorption. In addition, the current study employs geometrical optics to investigate the internal field of radiant absorption. A comparison between the results from the geometrical optics approach to those from electromagnetic wave theory shows that the error involved in the geometrical optics approach increases sharply with the real part of the complex refractive index. A criterion is established to define the region of the applicability of geometrical optics.

Introduction

Thermal radiation absorption is known to be an important mechanism of energy transfer in particulate systems and has been studied extensively. Up to this time, however, radiation interaction with a particle has been analyzed mostly from an *external*-field viewpoint, which accounts for energy absorption indirectly from the external scattered radiant. The particles in such systems have often been considered to behave like bulk materials, and consequently the absorption process has been treated strictly as a *surface* interaction (Tien, 1988). The *internal* radiant absorption field has received relatively little attention. Nevertheless, there are certain applications, such as spray combustion and medical irradiation therapy, for which the internal spatial distribution of radiative energy absorption can be of critical importance.

Knowledge of the local distribution of absorbed radiant energy within a fuel droplet is essential for the improvement of the performance of a spray combustion system. The medical irradiation treatment of cancerous cells in the human body requires a precise determination of the location and magnitude of the peak radiative energy absorption in the tissues. In addition, the phenomenon of micro-explosion, which occurs during the combustion of a fuel droplet, may be attributed to the extreme concentration of absorbed radiant energy at a spot inside the droplet. Furthermore, it has been suggested that the photophoretic effect may contribute significantly to particulate transport and deposition in combustion systems (Akhtaruzzaman and Lin, 1977; Arnold and Lewittes, 1982; Mackowski, 1989). In order to analyze photophoretic force, the detailed structure of the internal radiative energy absorption field must be clearly described. These examples demonstrate the need for an investigation of the internal field of particulate radiation absorption.

The objective of the present work is to study the local volumetric interaction of thermal irradiation with an absorbing particle. In order to simplify the analysis, a homogeneous spherical particle, irradiated by a monochromatic plane wave, is considered. The classical electromagnetic wave theory is employed to investigate the nonuniformity of the local spatial absorption within the spherical particle. Although the nonuniformity of the absorption distribution has been investigated previously (Dusel et al., 1979; Greene et al., 1985, Dobson and Lewis, 1989), detailed information for practical engineering applications has not been available. Therefore, in the present work, a thorough analysis of the effect of both size parameter and complex refractive index on the location of the highest concentration of absorbed radiative energy in a spherical particle is carried out, particularly, to devise a regime map that indicates the region of the peak radiant absorption. Moreover, a diagram that defines the optimum combination of size parameter and complex refractive index for maximum local peak absorption is constructed for engineering system design.

In addition to electromagnetic wave theory, the present study also applies the geometrical optics approach, which is an approximate method that is valid only under certain conditions. Previous studies utilizing this technique have again been concerned with only the bulk phenomenon of radiative absorption (Kamiuto, 1988). Some of them have considered the radial dependence of absorption (Harpole, 1980); however, none of them have evaluated both the radial and angular dependences of radiative absorption in a spherical particle. Here, the Monte Carlo ray tracing method is employed to determine the two-dimensional spatial dependence of radiative absorption.

Although the geometrical optics approach is frequently adopted for simple engineering calculations of thermal radiation interactions, restrictions on the applicability of this method are still not clearly defined. The current effort, therefore, focuses on the evaluation of the accuracy of geometrical optics. An error analysis based on a comparison with the results obtained from electromagnetic wave theory is conducted for various size parameters and complex refractive indices. Consequently, a criterion is established to describe the applicability of the geometrical optics approach as an approximating method for radiation absorption problems.

Analysis

The internal distribution of radiant absorption in a spherical particle irradiated by an unpolarized monochromatic plane wave is determined by applying two different methods: the classical electromagnetic (EM) theory and the geometrical optics approach. The physical geometry of the system is shown in Fig. 1. The particle, which is assumed to be a linear, isotropic, and homogeneous medium, is illuminated along the x

[1]Also, Research Assistant in the Department of Mechanical Engineering, University of California, Berkeley, CA 94720.

Contributed by the Heat Transfer Division and presented at the Joint AIAA/ASME Thermophysics and Heat Transfer Conference, Seattle, Washington, June 18–20, 1990. Manuscript received by the Heat Transfer Division March 6, 1990; revision received August 8, 1990. Keywords: Radiation Interactions.

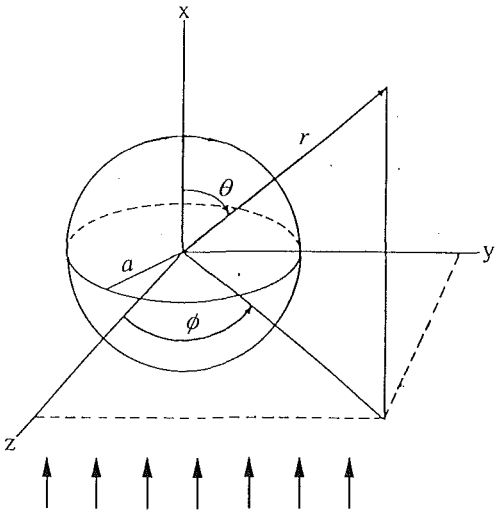

Fig. 1 Schematic diagram of an irradiated spherical particle

axis. The internal distributions of absorbed radiant energy obtained from both methods are further utilized to compute the dimensionless absorption cross section.

EM Theory. In order to obtain the local spatial distribution of absorbed radiative energy in a sphere, the internal electric field must first be determined. For every point in space where the physical properties are continuous in the immediate neighborhood, the electromagnetic field is governed by Maxwell's equations (Kerker, 1969). As a result, the internal electromagnetic field can be obtained by solving Maxwell's equations both inside and outside the sphere, which involves matching the internal field with the external one at the boundary. The solution to the internal electromagnetic field of a sphere has already been established by Mie. For a monochromatic plane incident wave, the spherical components of the internal electric field vector of a linear, isotropic, and homogeneous spherical particle can be expressed as (Bohren and Huffman, 1983)

$$E_r=\frac{E_o\cos\phi}{m^2\rho^2}\sum_{n=1}^{\infty} i^{n+1}(2n+1)a_n\psi_n(m\rho)P_n^1(\cos\theta) \tag{1}$$

$$E_\theta=\frac{E_o\cos\phi}{m\rho}\sum_{n=1}^{\infty}\frac{i^{n+1}(2n+1)}{n(n+1)} \times\left[a_n\psi_n'(m\rho)\frac{dP_n^1(\cos\theta)}{d\theta}+ib_n\psi_n(m\rho)\frac{P_n^1(\cos\theta)}{\sin\theta}\right] \tag{2}$$

$$E_\phi=-\frac{E_o\sin\phi}{m\rho}\sum_{n=1}^{\infty}\frac{i^{n+1}(2n+1)}{n(n+1)} \times\left[a_n\psi_n'(m\rho)\frac{P_n^1(\cos\theta)}{\sin\theta}+ib_n\psi_n(m\rho)\frac{dP_n^1(\cos\theta)}{d\theta}\right] \tag{3}$$

where E_o is the incident electric field amplitude, m is the complex refractive index, and ρ is the dimensionless radial coordinate given by

$$\rho=\frac{2\pi r}{\lambda}. \tag{4}$$

The function ψ_n is the Riccati-Bessel function of order n and the prime denotes differentiation with respect to the argument; $P_n^1(\cos\theta)$ is the associated Legendre polynomial; and a_n and b_n are the expansion coefficients. The Ricatti-Bessel function and its derivative are computed from the Miev0 code (Wiscombe, 1979). The expansion coefficients, a_n and b_n, can be written as

$$a_n=\frac{m\psi_n'(x)\xi_n(x)-m\psi_n(x)\xi_n'(x)}{m\psi_n(mx)\xi_n'(x)-\psi_n'(mx)\xi_n(x)} \tag{5}$$

$$b_n=\frac{m\psi_n'(x)\xi_n(x)-m\psi_n(x)\xi_n'(x)}{\psi_n(mx)\xi_n'(x)-m\psi_n'(mx)\xi_n(x)} \tag{6}$$

where x is the size parameter and ξ_n is the Ricatti-Bessel function of the third kind (Abramowitz and Stegun, 1970). For the case of unpolarized incident radiation, the internal electric field is axisymmetric, and thus is independent of the azimuthal angle ϕ (Fig. 1). The spherical components of the internal field induced by unpolarized incident wave are obtained by setting $\phi=\pi/4$ (Mackowski, 1989).

The local distribution of radiant absorption, Q, can then be determined from the internal electric field by employing the relation

$$Q(r,\theta)=\frac{1}{2}\sigma|E_o|^2S(r,\theta) \tag{7}$$

where σ is the electrical conductivity of the particle. The spatial

Nomenclature

a = sphere radius
a_n, b_n = internal electric field coefficients
C_a = absorption cross section
$\mathbf{E}$ = internal electric field vector
E_o = incident electric field amplitude
F = modified Snell's law coefficient
i = $\sqrt{-1}$
I_o = intensity of incidence radiation
k = imaginary part of complex refractive index
L_{ij} = length of ray path in region ij
m = complex refractive index = $n+ki$
n = real part of complex refractive index
P_n = Legendre polynomial
q_{ray} = energy carried by each ray
Q = internal distribution of radiant absorption
r = radial coordinate
S = normalized source function
u, v = reflectance coefficients
V = sphere volume
x = size parameter = $2\pi a/\lambda$
α_{ij} = fraction of radiant energy absorbed by region ij
ϵ_o = electrical permitivity of free space
θ = polar coordinate
θ_o = incidence angle
θ_r = refracted angle
λ = wavelength
μ_o = magnetic permeability of free space
ξ_n = Ricatti-Bessel function of the third kind
ρ = dimensionless radial coordinate
ρ_T = total reflectance
$\rho_\perp$ = perpendicular reflectance
$\rho_\parallel$ = parallel reflectance
σ = electrical conductivity
τ_{ij} = transmitted radiant energy to region ij
ϕ = azimuthal coordinate
ψ_n = Ricatti-Bessel function

Subscripts

r, θ, ϕ = spherical coordinate system components

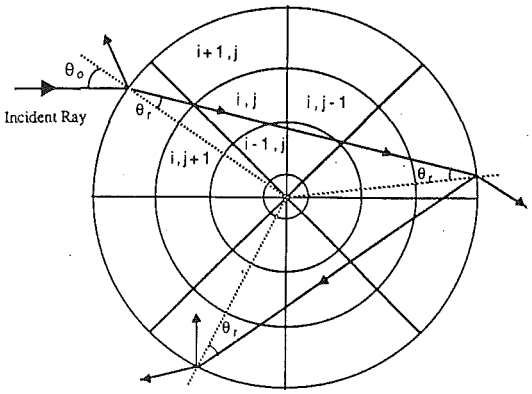

Fig. 2 Schematic diagram of geometrical optics ray tracing

function, S, denotes the normalized source function and is given by

$$S(r, \theta) = \left| \frac{\mathbf{E}}{E_o} \right|^2 \tag{8}$$

where $\mathbf{E}$ is the internal electric field vector. The electrical conductivity is related to the real and imaginary parts of the complex refractive index, n and k, by the expression

$$\sigma = \frac{4\pi nk}{\lambda} \left[\frac{\epsilon_o}{\mu_o} \right]^{1/2} \tag{9}$$

where ϵ_o and μ_o are the electrical permittivity and magnetic permeability of free space. It should be noted from equation (9) that the magnetic permeability of the particle is assumed to be the same as that of free space. Moreover, the incident electric field strength, E_o, may also be expressed in terms of the intensity of the incident radiation, I_o, as

$$|E_o|^2 = 2I_o \left[\frac{\mu_o}{\epsilon_o} \right]^{1/2} \tag{10}$$

By substituting equations (9) and (10) into equation (7), the internal distribution of radiant absorption, Q, becomes

$$Q(r, \theta) = \frac{4\pi nkI_o}{\lambda} S(r, \theta) \tag{11}$$

Given the size parameter and the complex refractive index of the particle, the spatial distribution of absorbed radiative energy inside the particle can be readily obtained from equation (11).

Geometrical Optics Approach. For the geometrical optics approach, the Monte Carlo ray tracing technique is employed to determine the internal spatial distribution of absorbed radiant energy of a spherical particle. Since radiant energy absorption varies both radially and azimuthally, a spherical particle is discretized into radial and angular regions, as shown in Fig. 2.

In tracing a single ray through a particle, the Monte Carlo method starts by randomly assigning a point on the cross-sectional plane surface of the sphere for the ray to enter. Each of the rays carries an equal amount of energy, q_{ray}, which is computed from the relation

$$q_{\text{ray}} = \frac{I_o A_{cr}}{N_{\text{ray}}} \tag{12}$$

where A_{cr} is the cross-sectional area of the particle and N_{ray} is the total number of rays selected for tracing. Since the Monte Carlo technique is a method of statistical sampling of events to determine the average behavior of a system, the accuracy of the result obtained from this method increases with increasing N_{ray} (Siegel and Howell, 1981). Depending on the incidence angle, the ray loses part of its energy by reflection upon encountering the surface. The total reflectance, ρ_T, is determined from

$$\rho_T = \frac{1}{2}(\rho_\perp + \rho_\parallel) \tag{13}$$

where $\rho_\perp$ and $\rho_\parallel$ are the perpendicular and parallel reflectances, respectively, relative to the plane of incidence. For an ambient refractive index of one (i.e., vacuum or air), the perpendicular and parallel reflectances can be expressed as (Born and Wolf, 1970)

$$\rho_\perp = \frac{(n \cos \theta_o - u)^2 + v^2}{(n \cos \theta_o + u)^2 + v^2} \tag{14}$$

$$\rho_\parallel = \frac{[n^2(1-k^2)\cos \theta_o - u]^2 + (2n^2k \cos \theta_o - v)^2}{[n^2(1-k^2)\cos \theta_o + u]^2 + (2n^2k \cos \theta_o + v)^2} \tag{15}$$

where θ_o is the incidence angle, and u and v are the analytical coefficients, which are calculated from

$$2u^2 = [n^2(1-k^2) - \sin^2\theta_o] + \sqrt{[n^2(1-k^2) - \sin^2\theta_o]^2 + 4n^4k^2} \tag{16}$$

$$2v^2 = -[n^2(1-k^2) - \sin^2\theta_o] + \sqrt{[n^2(1-k^2) - \sin^2\theta_o]^2 + 4n^4k^2} \tag{17}$$

The modified Snell's law is applied to account for the refraction of the ray occurring at the surface (Bell et al., 1969; Harpole, 1980). The angle of refraction, θ_r, is thus obtained from the relation

$$\sin \theta_r = \frac{1}{n} \sin \theta_o \, F \tag{18}$$

where

$$F = \left[\frac{-(n^2 - k^2 + \sin^2 \theta_o) + \{(n^2 - k^2 + \sin^2\theta_o)^2 + 4[n^2k^2 - (n^2 - k^2)\sin^2 \theta_o]\}^{1/2}}{2\left[k^2 - \left(1 - \frac{k^2}{n^2}\right)\sin^2 \theta_o\right]} \right]^{1/2} \tag{19}$$

The fraction of energy absorbed from a single ray, α_{ij}, by the region ij is determined from Beer's law, which can be expressed as

$$\alpha_{ij}(r, \theta) = 1 - \exp\left(-\frac{4\pi k}{\lambda} L_{ij}\right) \tag{20}$$

where L_{ij} is the length of the ray path through the region. Hence, the volumetric radiant absorption in the region, Q_{ij}, from a single ray is

$$Q_{ij}(r, \theta) = \frac{\tau_{ij}(r, \theta)\alpha_{ij}(r, \theta)}{2\pi r_i^2 \sin \theta_j \, \delta\theta_j \delta r_i} \tag{21}$$

where τ_{ij} is transmitted energy of the ray just before entering the region ij.

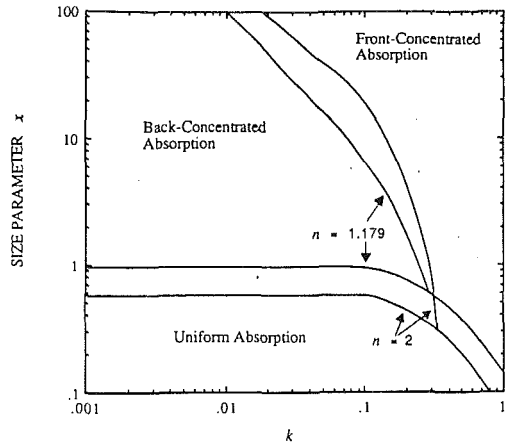

Fig. 3 Regime map for the internal distribution of radiant absorption

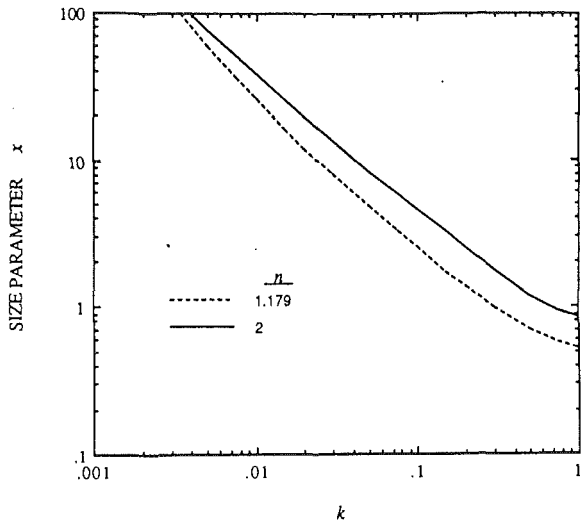

Fig. 4 Diagram for maximum local peak absorption as a function of size parameter and complex refractive index

It should be noted that the reflectance determined from equations (13)–(17) can also be used for internal reflection. By symmetry arguments, the incident angle for all the internal reflections in tracing a single ray is equal to its initial refracted angle θ_r. Each ray is traced until 99 percent of its energy is lost.

Dimensionless Absorption Cross Section. The absorption cross section, C_a, is a parameter that indicates the amount of energy absorbed by a particle per unit irradiation intensity. This dimensionless parameter directly depends on the physical size, a, and the irradiation wavelength, λ. The direct dependences of C_a upon a and λ are removed here by nondimensionalizing the absorption cross section with particle volume and incident wavelength. The dimensionless absorption cross section is expressed as

$$\frac{\lambda C_a}{V}=\frac{6\pi nk}{a^3}\int_0^a\int_0^\pi S(r,\theta)r^2\sin\theta d\theta dr \qquad (22)$$

where V is the total volume of a particle. Unlike the dimensional one, the dimensionless absorption cross section depends only on the size parameter and the complex refractive index, but not directly on a and λ. There are, however, indirect physical size and wavelength dependences through x and m. It is, therefore, a more general parameter for describing the absorption capability of an irradiated particle than the previous dimensional absorption cross section. The results determined from both EM theory and the geometrical optics approach are evaluated by comparing the dimensionless absorption cross section obtained from equation (22) to that from Mie scattering theory. The difference between Mie scattering theory and the current analysis is that the scattering theory accounts for radiation absorption indirectly from the *external scattered* field, whereas the current analysis does it directly from the *internal absorption* field.

Results and Discussion

The regime map presented in Fig. 3 gives the general pattern of the local distribution of radiant absorption within an irradiated particle as a function of size parameter and complex refractive index. The pattern of the internal field can be divided into three main regimes: uniform, front-concentrated, and back-concentrated absorption. Uniform absorption is distinguished here when the difference between maximum and minimum absorptions is not more than 10 percent. If more energy is absorbed by the front hemisphere of an irradiated particle, then front-concentrated absorption is obtained. Otherwise, the distribution is termed as back-concentrated absorption. The map is devised by analyzing an abundance of results obtained from equation (11). Since the primary interest of the present work is the internal field of radiant absorption of a fuel droplet in spray combustion systems and that of a cancerous tumor in medical irradiation therapy, the scope of the investigation is limited to the range of 0.1 to 100 for x, 1.179 to 2 for n, and 0.001 to 1 for k.

In spray combustion systems, the radiant feedback from the flame is absorbed by the fuel droplets. Under such circumstances, it is preferable to have front-concentrated absorption so that most of the fuel droplet evaporation will take place at the illuminated side, which will in turn enhance the ignition process. For medical irradiation therapy, it is better to deliver the radiant energy uniformly within a cancerous tumor. Figure 3 can be used to determine the conditions for achieving the desired pattern of internal radiant absorption field. In addition, Fig. 4 presents the maximum local absorption as a function of size parameter and complex refractive index. Given the complex refractive index of an irradiated particle, the optimum size parameter for maximum local peak absorption can readily be determined.

The internal field of absorbed radiative energy is presented in three dimensions to illustrate its spatial variation vividly. The effect of size parameter on this spatial variation, which is determined from EM theory, is shown in Fig. 5(*a*). Lying on the x–y plane is the cross section of a spherical particle, where the irradiation traverses from left to right in the positive x direction. The magnitude of the dimensionless local absorbed radiative energy, $4\pi nkS$, is illustrated by the scale along the vertical axis. The complex refractive index, m, is fixed at $1.5+0.1i$, while the size parameter, x, varies from 0.5 to 100. It is shown that the internal distribution is fairly uniform for x less than one. Highly nonuniform distribution, however, occurs when the size parameter becomes larger. The absorption of radiative energy is intensively concentrated at the back side, as depicted for the cases of $x=10$. This precipitous increase in energy absorption at the back of the particle is due to the focusing effect, where the curved surface of the particle acts like a convex lens and concentrates the electromagnetic waves at the focal point. The wavelike structure of the internal absorption field can also be seen clearly for this range of size parameter. This phenomenon is attributed to electromagnetic wave interference. As the size parameter increases further, the radiant energy is largely absorbed at the illuminated side. For large size parameters (i.e., $x=50$), the irradiative surface ab-

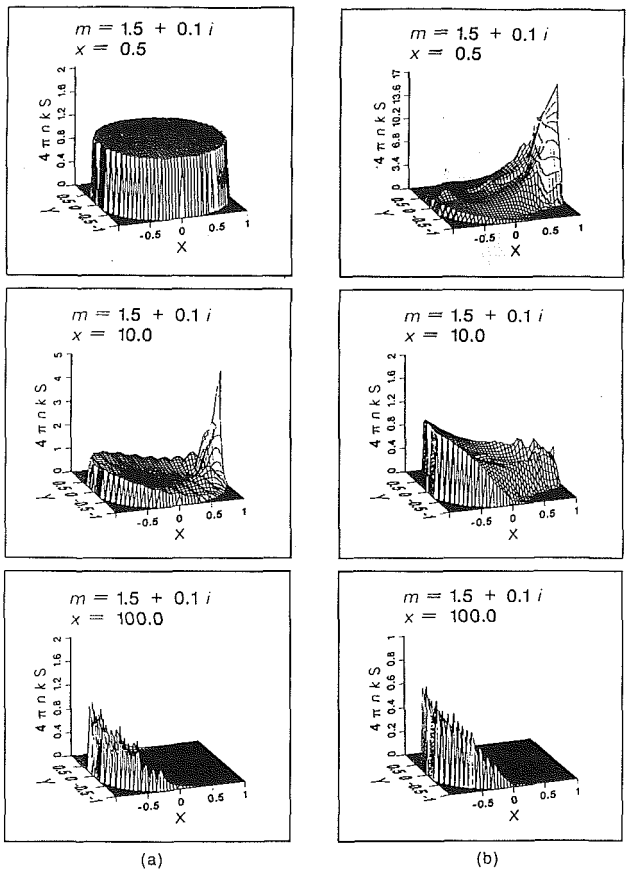

Fig. 5 Comparison of internal radiant absorption distribution obtained from: (*a*) EM theory, and (*b*) geometrical optics for various size parameters

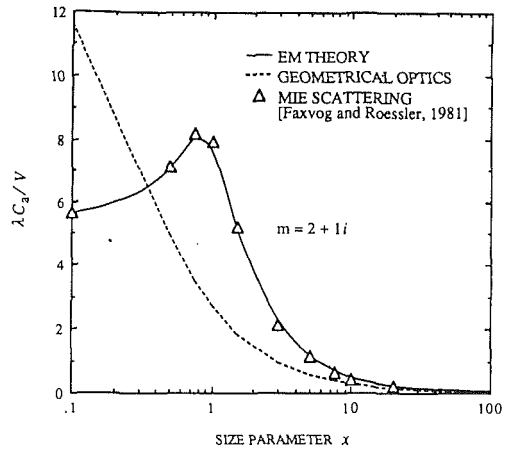

Fig. 6 The dimensionless absorption cross section obtained from different analyses where "EM THEORY" and "GEOMETRICAL OPTICS" refer to the volumetric integration over the internal radiant absorption distribution

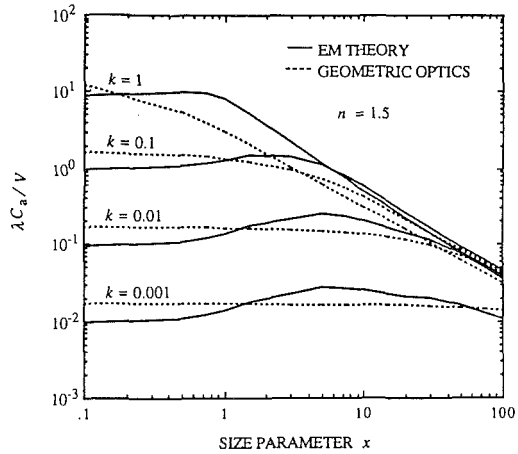

Fig. 7 The dimensionless absorption cross section obtained from EM theory and geometrical optics approach for various *k*

sorption is predominant. There is neither any wavelike structure nor any appreciable internal absorption observed for such large size parameters.

A comparison of the internal distribution of radiant absorption obtained from EM theory with that from geometrical optics is also carried out for various size parameters in Figs. 5(*a*) and 5(*b*). As shown in the cases of $x=0.5$, EM theory depicts a uniform distribution, whereas geometrical optics predicts a back-concentrated distribution. The absorption patterns appear completely different from each other at such small size parameters. The disagreement can be explained by the well-known diffraction effect, which causes the bending of incident electromagnetic wave. This effect is especially significant for small x. Since the geometrical optics approach, unlike EM theory, does not consider diffraction at all, the large discrepancy shown in the figure must be engendered mostly by this effect. On the contrary, the focusing effect plays a dominant role in geometrical optics at small x, and thus the radiative energy absorption is intensively concentrated in the back. As the size parameter increases, the local peak absorption at the back diminishes much faster in the geometrical optics results than in the EM results. Moreover, the wavelike structure of the internal field observed from the EM results at $x=10$ cannot be seen from those of geometrical optics. These phenomena are attributed to the inaccuracy of the geometrical optics approach in accounting for radiant absorption along the ray path, since wave interference is not taken into consideration in the ray tracing. However, the agreement between geometrical optics and EM theory improves as the size parameter is increased. Such agreement is expected since most of the absorption takes place at the illuminated front at large x, and the penetration depth of the irradiation becomes extremely short relative to the physical diameter of the particle. It can be concluded that only for large size parameters, at which surface absorption is predominant, does geometrical optics agree closely with EM theory.

The local distribution of radiant absorption obtained from both EM theory and geometrical optics has been integrated over the particle volume to obtain the dimensionless absorption cross section $\gamma C_a/V$, which is presented in Fig. 6 as a function of size parameter, and is compared with that determined from Mie scattering theory (Faxvog and Roessler, 1981). It can be discerned from the figure that the dimensionless absorption cross section obtained from EM theory agrees well with the computed from Mie scattering theory, whereas that determined from geometrical optics does not. Figure 6 further demonstrates the fact that, even at fairly large size parameters (i.e., $x=10$), the geometrical optics ray tracing technique is not an accurate scheme for bulk absorption calculations.

Figure 7 compares the dimensionless absorption cross section determined from EM theory with that from geometrical optics for various k. It is shown that the disagreement between EM theory and geometrical optics in the bulk absorption calculations does not lessen as k increases. In fact, the largest discrepancy between the two schemes occurs for $k=1$. There is no general trend concerning k to judge the accuracy of the

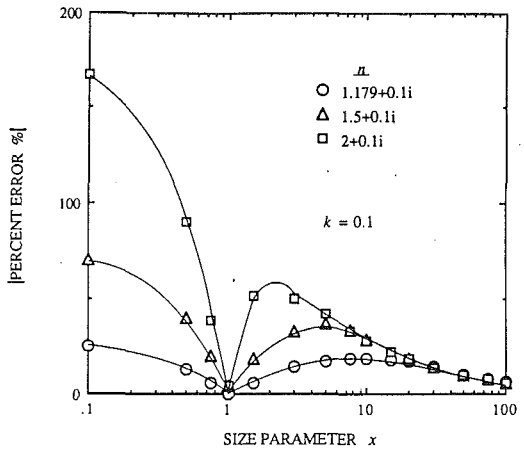

Fig. 8 The percent error of dimensionless absorption cross section obtained from geometrical optics approach compared with that from EM theory

geometrical optics approach. As shown in Fig. 7, the error of the geometrical optics approach is less than 20 percent for *all* k only when the size parameter is larger than 50.

The dimensionless absorption cross section obtained from EM theory reaches its maximum value at a certain size parameter, as is observed in Fig. 7. The value of $\lambda C_a/V$ declines as x decreases further from that size parameter. The decrease in the dimensionless absorption cross section is attributed to the diffraction effect, which becomes predominant at small size parameters. However, the dimensionless absorption cross section obtained from the geometrical optics does not decrease at all with the size parameter. The reason is that, as mentioned previously, the diffraction effect is neglected in the geometrical optics approach. Therefore, the dimensionless absorption cross section at small size parameters is always overpredicted by geometrical optics.

The absolute percent error of the dimensionless absorption cross section obtained from geometrical optics, which is based on the EM results, is presented in Fig. 8 for various n. The figure clearly illustrates that the error of the geometrical optics approach increases with n. It is discovered that both the internal absorption field and the volumetric total absorption determined from the geometrical optics agree with those from EM theory with a maximum tolerance of 20 percent only when the condition

$$\frac{x}{n^3} \geq 20 \text{ for } \begin{matrix} 1 < n \leq 2 \\ 0.001 \leq k \leq 1 \end{matrix} \tag{23}$$

is satisfied. This criterion, which is established through empirical correlation, defines the region of the applicability of geometrical optics.

Conclusions

The present work has thoroughly investigated the effects of size parameter and complex refractive index on the internal radiant absorption field of a small spherical particle. The scope of the investigation is limited to the range of 0.1 to 100 for size parameter, 1.179 to 2 for the real part of complex refractive index, and 0.001 to 1 for the imaginary part. A devised regime map indicates the general pattern of the internal field and the approximate location of the peak absorption. The pattern of the local absorption can be categorized by three main regimes: uniform, front-concentrated, and back-concentrated absorption. The optimum combination of size parameter and complex refractive index for achieving maximum local peak absorption has also been determined. These organized results provide information for practical engineering applications in determining the desired distribution of radiant absorption within a particle.

In addition, the current study has employed the geometrical optics approach to determine the internal field of radiant absorption. The focus has been particularly on the evaluation of the accuracy of the geometrical optics approach as an approximating method. The significance of the diffraction and interference effects on the internal absorption field has been illustrated by comparing the results obtained from the geometrical optics approach to those from electromagnetic wave theory. The comparison has further revealed that the error involved in the geometrical optics approach strongly depends on the real part of the complex refractive index, n. The error rises sharply as n increases. Moreover, a criterion has been established to describe the applicability of geometrical optics for radiative absorption problems.

Acknowledgments

The authors wish to express their appreciation to Professor D. K. Edwards for his helpful discussions, to Mr. C. C. Dobson for providing the Miev0 code, and to Mr. P. E. Phelan to reviewing the manuscript.

References

Abramowitz, M., and Stegun, I. A., 1970, *Handbook of Mathematical Functions,* Dover, New York, pp. 437–445.

Akhtaruzzaman, A. F. M., and Lin, S. P., 1977, "Photophoresis of Absorbing Particles," *Journal of Colloid and Interface Science,* Vol. 61, pp. 170–182.

Arnold, S., and Lewittes, M., 1982, "Size Dependence of the Photophoretic Force," *Journal of Applied Physics,* Vol. 53, pp. 5314–5319.

Bell, R. J., Armstrong, K. R., and Nichols, C. S., 1969, "Generalized Laws of Refraction and Reflection," *Journal of Optical Society of America,* Vol. 67, pp. 187–189.

Bohren, C. F., and Huffman, D. R., 1983, *Absorption and Scattering of Light by Small Particles,* Wiley, New York, pp. 82–100.

Born, M., and Wolf, E., 1970, *Principles of Optics,* Pergamon, New York, pp. 627–629.

Dobson, C. C, and Lewis, J. W. L., 1989, "Survey of the Mie Problems Source Function," *Journal of Optical Society America A,* Vol. 6, pp. 463–466.

Dusel, P. W., Kerker, M., and Cooke, D. D., 1979, "Distribution of Absorption Centers Within Irradiated Spheres," *Journal of Optical Society America,* Vol. 69, pp. 55–69.

Faxvog, F. R., and Roessler, D. M., 1981, "Optical Absorption in Thin Slabs and Spherical Particles," *Applied Optics,* Vol. 20, pp. 729–731.

Greene, W. M., Spjut, R. E., Bar-Ziv, E., Sarofim, A. F., and Longwell, J. P., 1985, "Photophoresis of Irradiated Spheres: Absorption Centers," *Journal of Optical Society America B,* Vol. 2, pp. 998–1004.

Harpole, G. M., 1980, "Radiative Absorption by Evaporating Droplets," *International Journal of Heat and Mass Transfer,* Vol. 23, pp. 17–26.

Kamiuto, K., 1988, "The Geometrical Optics Approximation to the Radiative Properties of a Large Absorbing Sphere," *Journal of Quantitative Spectroscopy and Radiative Transfer,* Vol. 39, pp. 435–440.

Kerker, M., 1969, *The Scattering of Light and Other Electromagnetic Radiation,* Academic Press, New York, pp. 8–82.

Mackowski, D. W., 1989, "Photophoresis of Aerosol Particles in the Free Molecular and Slip-Flow Regimes," *International Journal of Heat and Mass Transfer,* Vol. 32, pp. 843–854.

Siegel, R., and Howell, J. R., 1981, *Thermal Radiation Heat Transfer,* Hemisphere, New York, pp. 751–766.

Tien, C. L., 1988, "Thermal Radiation in Packed and Fluidized Beds," ASME JOURNAL OF HEAT TRANSFER, Vol. 110, pp. 1230–1242.

Wiscombe, W. J., 1979, "Mie Scattering Calculations: Advances in Technique and Fast, Vector-Speed Computer Codes," NCAR/TN-140+STR.

A. F. Emery

O. Johansson

M. Lobo

A. Abrous

Department of Mechanical Engineering,
University of Washington,
Seattle, WA 98195

A Comparative Study of Methods for Computing the Diffuse Radiation Viewfactors for Complex Structures

Several different numerical methods for calculating diffuse radiation viewfactors are described. Each is applied to a range of surface configurations, from almost completely unobstructed to a dense set of intersecting surfaces. The speed, accuracy, and unique characteristics are discussed in order to define optimal methods for different surface geometries.

1 Introduction

In the absence of an absorbing medium, radiative heat exchange between surfaces is a function of the surface conditions and the optical view that each surface has of the others. The net radiant heat transferred in the wavelength range, λ to $\lambda + d\lambda$, between two diffuse surfaces that form an enclosure and whose respective emissive powers are constant over the surface, is given by

$$Q_{IJ} = \frac{(e_I^{b\lambda} - e_J^{b\lambda})d\lambda}{\frac{1-\epsilon_I}{\epsilon_I A_I} + \frac{1}{A_I F_{IJ}} + \frac{1-\epsilon_j}{\epsilon_j A_j}} \tag{1}$$

where ϵ is the surface emissivity and $e^{b\lambda}$ is the emissive power in a given spectral range. If the surfaces are isothermal and gray, $e^{b\lambda}$ can be replaced by σT^4, to determine the net total radiant heat transfer. The term F_{IJ}, commonly referred to as the viewfactor, shapefactor, or configuration factor, is defined as

$$A_I F_{IJ} = \int_{A_I}\int_{A_J} \frac{\cos\theta_I \cos\theta_J}{\pi r_{IJ}^2}\, dA_I\, dA_J \tag{2}$$

and represents the fraction of radiant energy leaving surface I that is intercepted by surface J (Fig.1).

Note that the view I has of J, represented by F_{IJ}, depends only upon surface I being diffuse and having a spatially constant emissive power. It does not depend upon the characteristics of surface J, which may be arbitrary. Although F_{IJ} satisfies the reciprocity relationship

$$A_I F_{IJ} = A_J F_{JI} \tag{3}$$

irrespective of the thermal conditions of the surfaces, to use F_{IJ} in equation (1) in computing the net radiation exchange, surface J must also be diffuse and have a spatially constant emissive power.

Analytical, tabular, or graphic values of F_{IJ} have been given for only a few, relatively simple geometries (Hamilton and Morgan, 1952; Howell, 1982; Gross et al., 1981). In real structures, for which the surface geometries are complex, or portions of I may not see J, or surfaces intervene between I and J, analytical expressions are not available. In such cases, different approximate techniques must be used (Kadaba, 1982).

In the following sections of this paper, we describe several numerical methods. A brief description of each method, its unique characteristics and the type of problems it is best applied to, and limitations of the method are given. Finally, each method is used to compute the values of F_{IJ} for a set of test cases, ranging from simple but practical geometries to extremely complex configurations.

2 Accuracy and Reciprocity

Before describing the methods, it is worthwhile to comment on typical values of F_{IJ}. The viewfactor from one inside surface of a cube to any of the others is approximately 0.2. Values of F_{IJ} for unit squares, separated by distances of 1, 2, 5, and 10, are approximately 0.2, 0.05, 0.01, and 0.005. Since separations of the order of 5 times a characteristic side dimension are more the rule than the exception in real structures, most values of F_{IJ} will be between 0.01 and 0.1. For many surface pairs, values on the order of 0.001 will be found. Thus any computational method must be capable of an accuracy on the order of four digits for surfaces whose dimensions and separations are measured in units of 10 or more. That is, a minimum overall resolution of at least six digits will be required in evaluating F_{IJ}.

It should also be noted that there are no inherent ways of determining the accuracy of the computed values of F_{IJ}. Some methods, such as the Monte Carlo, provide approximate estimates of accuracy. Most methods rely upon computing the sum of F_{IJ} or comparing values of F_{IJ} and F_{JI} with the results from the reciprocity relationship. Although the sum of F_{IJ} is unity for a surface that is completely enclosed, the accuracy with which this sum approaches unity is no measure of the accuracy of the individual values. The accuracy with which the reciprocity relationship is satisfied is a better measure, but its use requires that both F_{IJ} and F_{JI} be calculated; this doubles

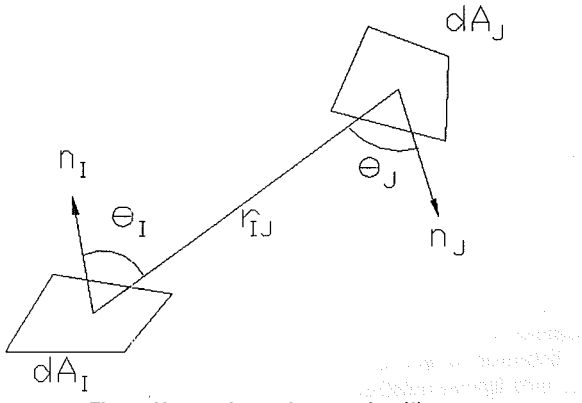

Fig. 1 Nomenclature for equation (1)

Contributed by the Heat Transfer Division for publication in the JOURNAL OF HEAT TRANSFER. Manuscript received by the Heat Transfer Division January 4, 1990; revision received July 16, 1990. Keywords: Computer Codes, Numerical Methods, Radiation.

Table 1 Classification of methods

Method	a_i	a_j
Analytical	infinite number, uniformly distributed	infinite number uniformly distributed
Monte Carlo	a very large number randomly located	ranging from moderate to a very large number proportional to F_{ij}
Projected Contour	a finite small number at specified points	infinite number, uniformly distributed
Projection Methods	a finite small number at specified points	ranging from small to large number at specified points
Double Area	a finite small number at specified points	a finite small number at specified points

the computational cost and is usually an unacceptable choice. Almost all thermal analyzers utilize the reciprocity relationship directly to avoid having to determine the N^2 values of F_{IJ}, evaluating only those for which $J>I$, which number only $N(N-1)/2$.

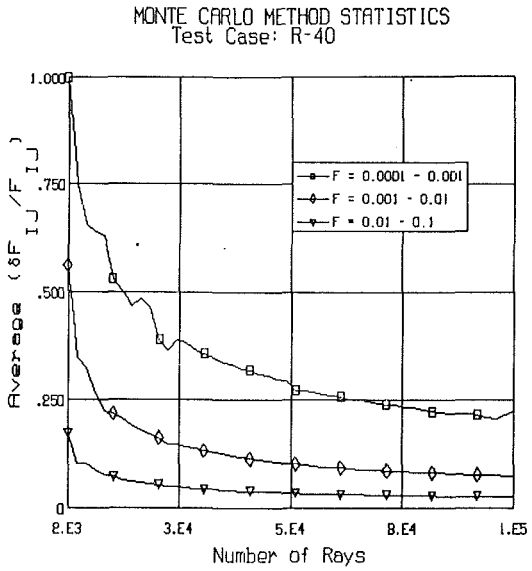

Fig. 2 Average error as a function of the number of Monte Carlo rays

3 Methods

The viewfactor, F_{IJ}, as given by equation (2), is the integration over both surfaces, I and J. The most convenient way to classify the different methods is by the way in which the intergration is carried out. Let us imagine that surface I is subdivided into a number of small subelements, a_i and surface J is subdivided into a_j. Table 1 lists the different methods in terms of the number and location of a_i and a_j. The characteristics and accuracy of each method can be most easily visualized if this classification is kept in mind.

3.1 Analytical. For a very limited number of configurations, F_{IJ} may be evaluated analytically. Although of little practical value, such situations are normally used to check the accuracy of the approximate methods. Evaluation of F_{IJ} involves taking the difference of a function at upper and lower limits of integration and may lead to errors. However, the function is usually expressed in terms of ratios of distances and normally is in the range of 10 to 100. Thus little accuracy is lost, even if the integration is accomplished numerically.

3.2 Monte Carlo Ray Tracing. In this method, rays are emitted in random directions from random points on surface I. Each ray is checked to see which surface it strikes (Siegel and Howell, 1981). Those rays that are intercepted by surface J then contribute to the value of F_{IJ}. The choice of the emitting location and the direction are made using distributions based upon random numbers. These distributions may be tailored to represent emissivities, which depend upon angle, or any other desired variation. Typically, ten to hundreds of thousands of rays are used, with the accuracy increasing as the number increases. Although high accuracy in the sum of F_{IJ} may be achieved, if the density of rays striking surface J is not high enough to accurately describe the shape of J, the value of F_{IJ} may be in error. Since the relative accuracy is inversely proportional to the square root of the number of rays striking the surface, the total number of rays needed is given by

$$M = \text{Number of Rays} \sim \frac{1}{F_{IJ}}\left(\frac{F_{IJ}}{\delta F_{IJ}}\right)^2 \tag{4}$$

Figure 2 shows this inverse $\sqrt{M}$ approach to the final value of F_{IJ}. Even after the average relative error is acceptable, local deviations make it difficult to know when to cease computing.

Nomenclature

A = area
a = subelement of A
b = base subelement for the unit sphere
c = centroid location of subelement
d = obstruction flag for double area method
E = emissive power
F = viewfactor between surfaces
f = viewfactor from subelement to surface or from subelement to subelement
l = contour
M = number of Monte Carlo rays
N = total number of surfaces
N_s = number of subelements
N_s^0 = nominal number of subelements
Q = radiant energy exchange
r = distance
s = subelement of unit sphere
T = temperature, K
x, y, z = Cartesian coordinate system
x', y', z' = transformed coordinate system
α = absorptivity
ϵ = emissivity
λ = wavelength
σ = Stefan-Boltzmann constant

Subscripts

ave = average
b = unit sphere base pixel
e = hemi-cube pixel
I = surface I
i = subelement i
J = surface J
j = subelement j
max = maximum
min = minimum
p = ADAP surface pixel
s = unit sphere pixel

Superscripts

b = blackbody
λ = spectral

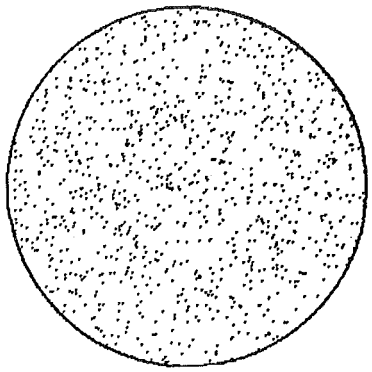

Fig. 3 Distribution of interception points

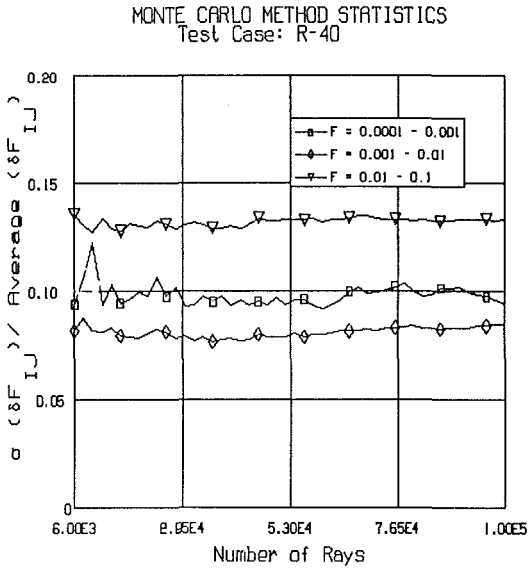

Fig. 4 Normalized standard deviation of the error as a function number of Monte Carlo rays

Because the number of rays is usually very large, care must be taken in choosing a random number generator to ensure that a reasonably valid set of ray directions is generated. Figure 3 shows a typical distribution of interception points on a circle, and areas where the rays have been inadequately directed are easily visible. Figure 4 shows the normalized standard deviation of the estimated error. The standard deviation, as expected, is essentially constant with respect to the number of rays and the value of the viewfactor.

There are a number of standard modifications of the basic Monte Carlo method. One is to preselect the emitting points, and use the random distribution to specify only the direction of the rays. Another, which is of value when a single surface pair is being considered, is to restrict the ray directions to the cone that encloses the two surfaces. Such an adaptive method is difficult to use for a general structure and often increases execution times substantially. A third approach is to select the emitting and receiving point locations randomly and then to check each ray for interception. Although Monte Carlo methods are expensive, and inherently depend for accuracy upon the total number of rays, they do not suffer from the inaccuracy associated with the difference of large numbers since the contribution of each ray is strictly additive and they ensure a sum of F_{IJ} of unity if I is enclosed.

3.3 Projection Methods. All projection methods are based upon a variation of the original Nusselt projection method (Siegel and Howell, 1981) (Fig. 5). Surface I is subdivided into a number of subelements, a_i. Surface J is then

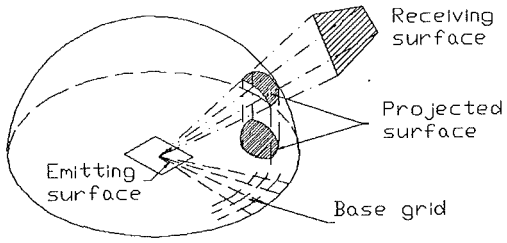

Fig. 5 Nusselt projection method

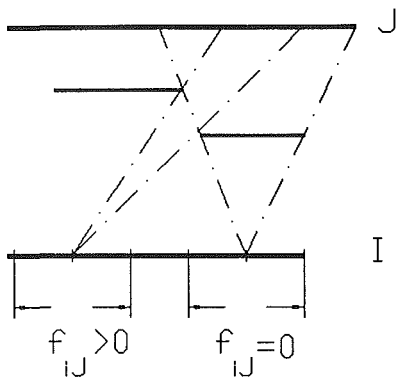

Fig. 6 Effect of using centroidal view to represent finite subelements

viewed from the centroid, c_i, of each of these subelements. It is then assumed that the view of J from c_i represents the view from any portion of the subelement a_i. The viewfactor, f_{iJ}, is computed either from an infinitesimal area centered at c_i if a_i is small enough, or from the entire subelement, a_i. The sum of f_{iJ} over the set of subelements is F_{IJ}. The accuracy of all of the projection methods depends upon how well the view centered at c_i represents the view from each portion of a_i. If the view from J changes discontinuously over the range of subelements a_i (Fig. 6), the resulting f_{iJ} may be seriously in error. As the number of subelements increases, the projection methods approach the Monte Carlo method in nature and result.

Because of the inherent geometric complexities of the projection method, the first step is to construct a new coordinate system centered at the point c_i, and whose z' axis is normal to a_i. Each of the other surfaces is then clipped so that only that portion above the $z' = 0$ plane is treated. Surfaces that are entirely below the $z' = 0$ plane have a zero value of f_{iJ}. Projection methods are capable of considering surfaces that intersect each other, although the accuracy may be reduced unless special provisions are made. Although surface I can be curved, it is most common to represent it by a set of one or more flat planes to simplify the computations.

3.3.1 Projected Contour. This method is based upon using a contour integral to evaluate f_{iJ} (Siegel and Howell, 1981). From each of the centroids of the subelements, surface J is viewed and the contours surrounding the visible portions of J are defined. The value of f_{iJ} is then determined by contour integration around each of these visible contours. The accuracy of the method depends not only upon the number and position of the subelements, but also the accuracy with which the viewfactor to the visible portion of J is evaluated. In contrast to Monte Carlo, in which each ray contributes a positive component of f_{iJ}, or to the analytical method in which the terms to be subtracted are reasonable in value, the contour method frequently requires double precision. For surfaces bounded by straight lines, Mitalas and Stephenson (1966) showed that the contribution to the contour integral from any point on the

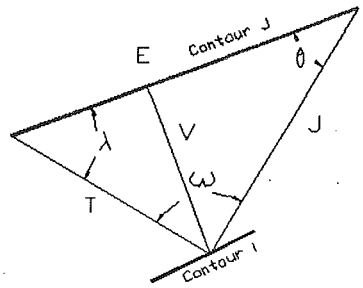

Fig. 7 Nomenclature for equation (5)

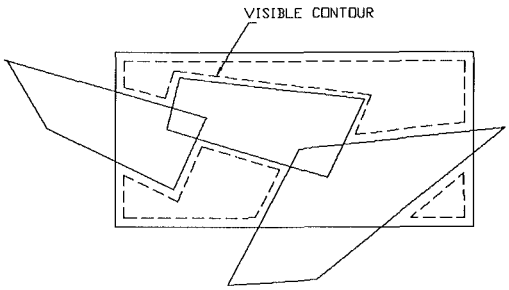

Fig. 8 Contours of visible area

contour l_i of subelement i to the line l_J on the contour of surface J could be given by

$$(T \ln T \cos \gamma + J \ln J \cos \theta + L\omega - E)\ (\mathbf{l}_i \cdot \mathbf{l}_J)dl \qquad (5)$$

where $\mathbf{l}_i \cdot \mathbf{l}_J$ is the dot product of the direction cosines of l_i and l_J and where the terms are shown in Fig.7. For many contours, this term when integrated over a side has a relatively large numerical value. Yet because of the changing sign of the direction cosine product, the contributions generally alternately add and subtract. Consider a rectangle whose center is located directly above the element l_i and whose sides are parallel or at right angles to l_i. Each term given by equation (5) will be equal in magnitude, but opposite in sign. Thus the integral over all four sides of J will be zero. To avoid errors in f_{iJ}, the computations should be carried out with at least 10 or more significant digits of accuracy.

A major expense in the projected contour method is the determination of the visible portions of J as seen from each c_i. Figure 8 illustrates a typical view in which there are three visible portions, two of which are concave polygons. Since it cannot be specified in advance how many sides the visible contour may have, and since the computation is sensitive to both the number of sides and the accuracy with which the sides are defined, a straightforward application of the contour method is not used. Rather, the following process is employed (Walton, 1986). An obstructor, O_1, is projected onto surface J and clipped so that only the portion that actually obstructs J is retained. The viewfactor to this portion, f_{iO_1} is then subtracted from f_{iJ}. The next obstructor, O_2, is then clipped to J and projected. That portion that is distinct from all preceding obstructor projections is retained and its value of f_{iO_2} determined. The process continues until all obstructors have been considered or surface J is completely covered (Fig. 9). The process is not straightforward, since that portion of O_2 that is distinct from O_1 may be concave and have a large number of sides. Walton (1968) observed that by appropriately subdividing O_2 into smaller areas o_2, it is possible to limit the number of edges of the projection of each o_2 and to ensure that these projections are convex. Depending upon the nature of the obstructors, this procedure may result in a very large number of projected surfaces whose viewfactors must be calculated, with a consequent increase in computation time. Because the final value of f_{iJ} is found by subtraction, care must be taken to achieve the desired accuracy. Generally, obstructors or their subdivisions are ignored if the projected areas are small enough (less than A_{min}) and the computation ceases when f_{iJ} reaches some specified minimum value, f_{min}, or the area covered reaches some fraction, A_{max}, of A_J.

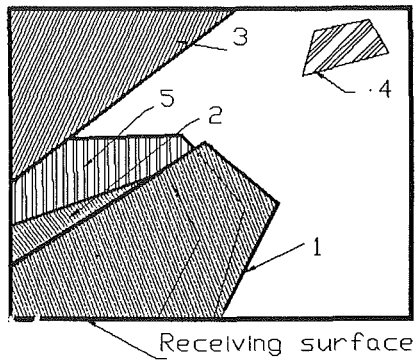

Fig. 9 Obstructors projected onto surface J

3.3.2 Graphic Projection. A. Unit Sphere. A simpler way, although less accurate, is to project surface J and each of the obstructors onto the unit sphere and then to the base of the sphere (Fig. 5). The unit sphere is subdivided into a large number of subelements, s_i, henceforth called *pixels*, which are projected onto small areas, on the base, b_i. As each surface is projected onto the base, we determine which base element, b_i, is covered. A surface, K, may cover a pixel that has already been covered by J. In this case, the ray that projects to the centroid of s_i is extended from the sphere to surface K and to surface J and the distance from the coordinate origin, r_i, determined. The surface nearest to I is then credited as covering the pixel. After all surfaces have been considered, the viewfactor from a_i to each of the pixels s_i, is then attributed to the nearest surface that covered b_i.

This method has three fundamental problems: (1) The projection of the edges of a surface onto the unit sphere, and thus to its base, is generally bounded by curved lines. An accurate description of such curves using straight line segments (the only kind practical in computer geometry) requires a very large number of such segments. The determination of which base element is intercepted by such a large number of line segments is expensive. (2) Aliasing is common; i.e., the determination of which pixel is covered when the edge only partially intrudes into the element is inaccurate (Fig. 10). Since the pixel is assigned uniquely to a surface, and not partially, errors in f_{iJ} may exist. This difficulty may be minimized by choosing a statistical approach to assigning partial coverage (Ames et al., 1987). (3) Finally, from each surface I it is necessary to consider all surfaces, not just those for which $J>I$, since a surface numbered less than I may obstruct the view of J.

The projection methods have one immediate advantage: The sum of f_{iJ} is automatically unity for an enclosed surface since all pixels must be covered.

B. Hemi-Cube. Cohen et al. (1986) developed the hemicube method to avoid the curved lines of the unit sphere approach. Instead of a sphere, the subelement a_i is surrounded by a one half of a cube (Fig.11). The surfaces are projected onto the faces of the cube. After processing, each pixel, e, of each face is associated with a given surface, J, and the value of f_{ie} is assigned to f_{iJ}. The method requires some preclipping of the surfaces to determine just what portion of J projects to each face. Such preclipping is not needed for the unit sphere. Disadvantages 2 and 3 listed for the unit sphere method apply to this method. Automatic satisfaction of the sum ensured.

C. Adaptive Projection. Emery et al. (1987) developed the

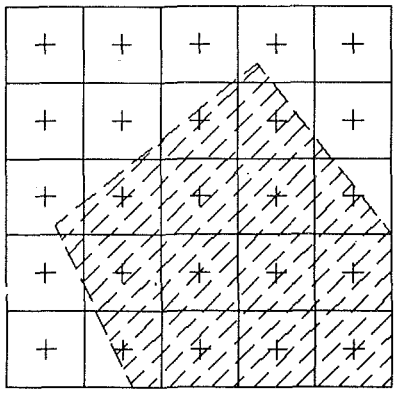

Fig. 10 Effect of edges only partially intruding into the element

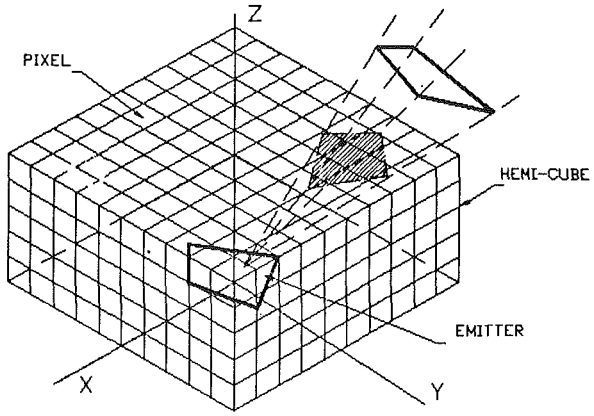

Fig. 11 The hemi-cube method

adaptive projection method to eliminate the need to consider all surfaces and to provide better accuracy. When projecting to the sphere or to the hemi-cube, the accuracy of the computation depends upon the number of pixels used. The more pixels, the smaller the values of f_{ie} and the more accurate the result. In the ADAP method, surface J is surrounded by a cone and all obstructors that do not intrude into this cone or are behind J are ignored. J is projected onto a surface P, which is subdivided into a sufficient number of pixels, p, to ensure the desired accuracy in evaluating f_{iJ}. Then each obstructor is projected onto P and those pixels covered by J are used to evaluate f_{iJ}. The method has two disadvantages: (*a*) Since the number of pixels depends upon the value of f_{iJ}, precomputed values of f_{ip} cannot be used. However, by restricting the method to a small set of possibilities (e.g. 40×40, 80×80 pixels of P), this problem can be avoided. (*b*) Each surface must be considered multiple times. For example surface O may be a candidate obstructor for surfaces 1, 2, and 3. Then O would be considered a total of four times, instead of the single time as in the unit sphere or hemi-cube methods.

However, if the number of obstructors is few, and the conical clipping is effective, then each obstructor will be considered only a limited number of times. Since the method permits the evaluation of F_{IJ} for only those surfaces J, $J>I$, which can see I, there is an inherent savings of a factor 2/frac where frac is the fraction of surfaces that can see I. The actual savings depends upon the complexity of the scene and the efficiency of projection and clipping.

D. Scan Line. A variant of the projection methods is to scan the projection of surface J, projected either to the faces of the hemi-cube or the ADAP surface P, in the same manner as a TV screen is scanned, using a method similar to Watkin's (Newman and Sproull, 1981). In this approach, surface J is described by a series of raster lines and the length of each visible portion of a raster line is determined. The accuracy of the representation of J is controlled only by the number of scan lines used since the endpoints of the scan lines are determined exactly. In effect, this method is equivalent to using an infinite number of pixels in the horizontal direction and a finite number in the vertical. Although contour integration can be used to determine the viewfactors associated with the area between each pair of horizontal scan lines, the cost is exorbitant. It is more efficient to define the scan line as passing through the centroids of pixels.

E. Precomputing f_{is}, f_{ie}, or f_{ip}. The number, size, and position of each pixel are predefined. For the unit sphere method, the viewfactor is simply the area of the base that surface b_i covers; a trivial computation. For the hemi-cube or adaptive projection methods, the viewfactors form point c_i to each pixel are computed in advance, usually using contour integration unless the pixels are extremely small, and then stored. After the projection of all surfaces is complete, the contribution from each pixel is read from a table and summed to compute f_{iJ}.

3.4 Double Area Integration. Although this method is usually termed "Double Area Integration," it is a misnomer. The method, a primitive form of projection, consists of subdividing surfaces I and J into subelements a_i and a_j. A ray is drawn from the centroid of a_i to that of a_j. If the ray is obstructed, it is assumed that all of a_i can see all of a_j. The viewfactor is then computed either simply by

$$f_{ij} = d_{ij}\, a_i \cos\theta_i \cos\theta_j / r_{ij}^2 \tag{6}$$

where r_{ij} is the distance between the centroids, or by contour integration between the subelements a_j and a_i. d_{ij} is zero for obstructed rays and unity for unobstructed rays. The number of rays is either constant or determined by the unobstructed value of F_{IJ}. Additionally, it is common not to calculate obstructed viewfactors if the unobstructed value is less than a specified value, F_{min}. If the simple method is used, significant errors will occur when the surfaces are too close to each other, if they intersect each other, or if other surfaces intersect them. A variation is to use isoparametric finite elements to integrate equation (2) (Chung and Kim, 1982). The method is usually faster than the other methods, usually two to four times faster, and normally has acceptable accuracy for practical surface configurations if the surfaces are of approximately equal size and reasonably distant. Because of the errors associated either with the evaluation of f_{ij} or the discrete number of a_j subelements, the values of F_{IJ} may not sum to unity. On the other hand, because of its speed it is possible to use many more subelements in defining surface I than do the other methods for the same execution speed.

4 Overall Performance of Projection Methods

In general, the methods described above have a number of common problems: (*a*) the determination of the pixel viewfactors with reasonable accuracy; (*b*) efficient clipping of possible obstructors to reduce the number of operations, especially by choosing the most probable obstructors to check first; (c) a satisfactory representation of the visible portions of J with a reasonable number of pixels. Above all, all the methods rely critically upon the representation of the view from surface I by the view from a discrete number of points. Too few, and critical differences in the actual and modeled view will exist; too many and the computational speed will be too slow. In all of the methods, the cost is directly proportional to the number of subelements of I and the complexity of the view that I has of J. The projected contour, scan line, adaptive projection, and double area methods reduce the scene complexity by limiting the view to that from I to J. The speed of these methods

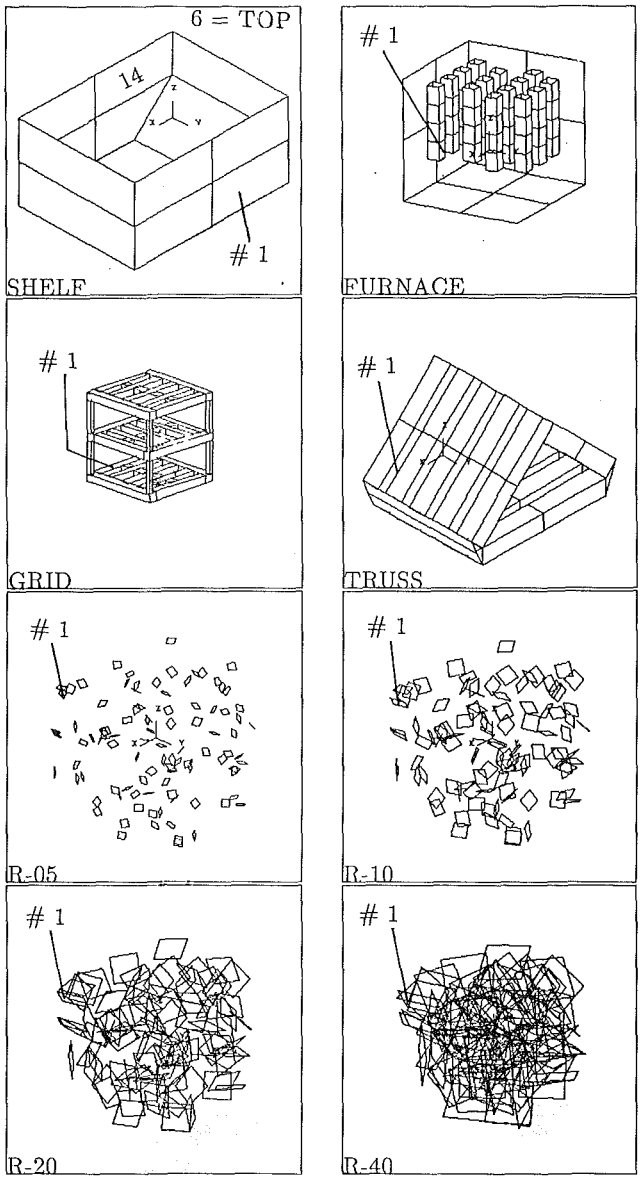

Fig. 12 Illustration of test cases

depends critically upon the effectiveness of the clipping operations. The unit sphere and hemi-cube methods must treat the entire view, and thus it is the complexity of the entire scene that controls their execution times.

The Test Problems. The different test cases are illustrated in Fig. 12. These configurations were chosen because of their differing characteristics.

Case 1: Shelf. A simple geometry with only one obstructor. Most views will be obstructed by a simple overlapping of two rectangles, with relatively large effects on the viewfactors. However, there is a small opening due to the diagonal shelf edge, which changes nearly discontinuously as the viewing point moves about on surface 1.

Case 2: Furnace. This case typifies the one-dimensional obstructions found in a furnace. Because the views are obstructed only as the line of sight moves horizontally, the obstruction calculation is at most two dimensional and should be fast.

Case 3: Grid. This is a generalization of the furnace. Obstructions now occur in three dimensions and will be a more severe test of the algorithm, particularly of that part that eliminates nonobstructors.

Table 2 Parameters used for base case calculations

FACET	16 subelements
VIEWC	16 subelements, $F_{min} = .0$
HEMI	80x80 pixels
VIEWP	$A_{min} = 0.001$, $F_{min} = 0$, $A_{max} = 0.999$
MONTE CARLO	100000 rays

Case 4: Truss. This case was chosen to represent a typical space structure. In practice, the triangular legs would be more widely separated (Thornton and Mahaney, 1984). Because of the triangular shape of the opening and the open spaces that intervene between the legs, the view of space changes as one moves from front to back.

Cases 5–8: Random Surfaces. 100 squares, all of equal size, were randomly located in a $100 \times 100 \times 100$ cube. The squares are 5, 10, 20, and 40 units on a side for the four cases. For R-05 the separation distance is large compared to the surface size, there are few obstructors, and the viewfactors are small, typical of space structures. In R-40, the surfaces are so large and so densely packed that almost every surface is penetrated by several others. Although the configuration is not physically realizable, it serves two important purposes:

(*a*) It is an extreme test of the algorithms and robustly exercises the clipping routines.

(*b*) It represents a convenient way to represent real structures. Rather than dividing the exterior surfaces of a complex structure into many small surfaces, one can form the structure from the intersection of a few larger surfaces. For example, a wheel on an axle is modeled by the intersection of two cylinders. Modern B-rep surface representation programs (Foley and Van Dam, 1984) can thus be used to define complex structures without the need for subsequent subdivision.

Programs Used. The test calculations were made using the following programs:

1 Monte Carlo. The RADSIM program (Corlett, 1988). This is a generic Monte Carlo program with no special enhancements or accelerators, although we did modify the random number generator following the suggestions of Press et al. (1986).

2 Projected Contour. Module VIEWP of version 6.0 of the VIEWC family was used. The algorithm drew substantially from the work of Walton (1986).

3 Hemi Cube. Module VIEWH of version 6.0 of the VIEWC family was used.

4 ADAP. A special program, referred to as ART (Emery et al., 1987), was used.

5 Double Area. Version 5.6.5 of VIEWC (Emery, 1988) and FACET (Shapiro, 1983) was used. VIEWC contains a number of accelerated clipping and accuracy algorithms. It also contains a provision for improved self-obstruction cases and for intersecting surfaces (VIEWC-PC, Section 5.3). FACET appears to be a relatively simple combination of double area and contour integration methods. Documentation for FACET suggests that this code has been optimized for speed and accuracy.

All programs were compiled using Digital Fortan 77 and run on a VAX 8700 with 32 MByte of memory and a floating point accelerator and operating under VMS 4.5. Speed compared to a standard VAX 780 is rated at 6 MIPS. The test cases were run on an unloaded machine, inasmuch as possible, to provide minimum times. Base case calculations were made using the parameters listed in Table 2.

5 Results

5.1 Base Values. Since no analytical values were avail-

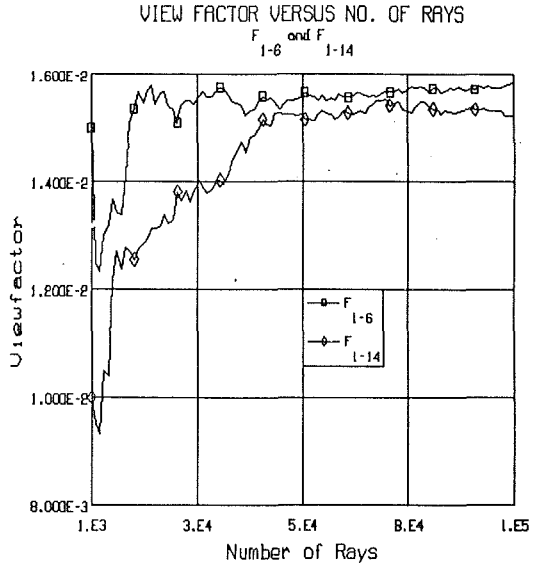

Fig. 13 Convergence patterns for the Monte Carlo method

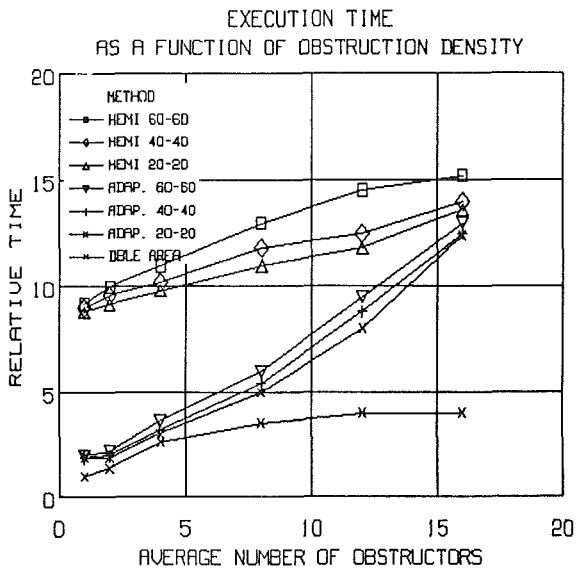

Fig. 14 Comparison of execution times for double area, ADAP, and hemi-cube

able, we chose to compare the results of all methods with those of the Monte Carlo. Monte Carlo computations were carried out for 10^5 rays, which should give an accuracy better than 90 percent for viewfactors greater than 0.001, equation (4). Figure 13 illustrates the performance of this method for Case 1 in which surface 1 has a nearly discontinuous view of surface 14. While the average error diminishes quickly, the approach to the limit is slow. Table 3 lists the rms error as a function of the number of rays. Although the average error is small for 50,000 to 100,000 rays, the rms error reduces only slightly over this range.

5.2 Execution Times. Tables 4 and 5 list the times for radiation from surface 1 only and for the entire structure. For single surface emission, the time depends upon the number of surfaces and the average number of obstructors, shown in rows 1 and 2. The projected contour method is very sensitive to the nature of the obstructions, particularly if it results in the subdivision of many of the projected obstructors. In cases 2, 3 and 4, as many as 400 surfaces were created for some specific surface J, by the projected contour process, leading to lengthy

Table 3 Effect of number of rays: Monte Carlo method

	Shelf	Shelf	Shelf	R-40	R-40	R-40
Ray Number	Sum	rms	Time	Sum	rms	Time
20,000	0.9997	0.0676	18.38	0.077	0.5809	47.65
40,000	0.9997	0.0477	37.37	0.0784	0.4070	95.21
60,000	0.9997	0.0389	56.66	0.0787	0.3317	142.43
80,000	0.9996	0.0337	75.31	0.0783	0.2880	189.74
100,000	0.9996	0.0301	94.62	0.0774	0.2704	236.86

Table 4 Execution times for emitting from surface 1 (s)

Case	Shelf	Furnace	Grid	Truss	R-05	R-10	R-20	R-40
Number of Surfaces	16	248	226	148	100	100	100	100
Obstruction Density	2	14.04	18.43	14.25	0.83	2.06	6.69	26.09
FACET	0.59	23.2	52.1	11.7	0.86	1.38	2.54	8.03
VIEWC	0.62	18.2	21.4	17.6	2.22	3.52	5.60	4.08
VIEWC-PC					2.62	4.49	8.75	7.81
HEMI	8.9	34.3	28.9	25.7	5.37	7.50	10.6	16.6
VIEWP	0.82	96.2	72.4	83.4	1.64	4.28	15.7	41.2
MONTE CARLO	93.0	645	663	368	280	295	301	274

Obstruction density = average number of obstructors between surface 1 and all other surfaces

Table 5 Execution times for emitting from all surfaces

Case	Shelf	Furnace	Grid	Truss	R-05	R-10	R-20	R-40
VIEWC	4.37	1358	1470	66.5	134.6	223.2	289.7	228.6
HEMI	132	7085	5328	2902	630.7	758.6	1046	1950
VIEWP	4.94	9904	5020	4662	139.8	411.4	974.3	2514

Table 6 Sum of viewfactors from surface 1

Case	Shelf	Furnace	Grid	Truss	R-05	R-10	R-20	R-40
FACET	1.0215	1.1473	1.3610	1.5901	0.0034	0.0140	0.0623	0.1307
VIEWC	1.0005	0.9764	1.0000	1.0015	0.0034	0.0135	0.0441	0.0562
VIEWC-PC	0.9998				0.0034	0.0135	0.0494	0.0710
HEMI	1.0000	1.0000	0.9983	0.9188	0.0032	0.0133	0.0484	0.0666
VIEWP	1.0000	1.0012	0.9800	1.0206	0.0035	0.0136	0.0492	0.0715
MONTE CARLO	0.9996	1.0000	0.9386	0.9984	0.0034	0.0152	0.0541	0.0774

execution times. Generally speaking, for a view from a single surface to a complex scene, the speed of the hemi-cube method was similar to that of the projected contour method. For unobstructed views the hemi-cube method was significantly slower. The projected contour method was as fast as double area for simple geometries but about 2 to 4 times slower for complex geometries. Figure 14 compares the double area, ADAP, and hemi-cube methods for the random surface cases. For a low obstruction density (defined to be the average of the actual number of obstructors between all pairs of surfaces), ADAP is equivalent to the double area. As the surface size increases, the need to consider a surface a multiple number of times causes this method to become slower than hemi-cube.

When the entire structure is considered, the speed of the projection methods degrades because of the need to examine all surfaces for each emitter, i.e., N^2 instead of $N(N-1)/2$ computations.

5.3 Accuracy. We chose to measure accuracy by the sum of the viewfactors and by the rms difference from those Monte Carlo values whose accuracy was estimated to be greater than 90 percent. The sums are listed in Table 6. As expected, the hemi-cube method sums exactly to unity, except for the Grid. Since the viewfactor to a face pixel is credited to the closest surface covering the centroid of the pixel, a problem arises when an edge falls exactly on the centroid, but because of numerical imprecision is represented as being on one side or the other. In this case, when the common edge between two surfaces is projected, it is seen as not being covered by either surface and the pixel may not be assigned to any surface. For case R-40, this occurred for about 50 pixels, out of the 19,200

Table 7 The rms error of A_1F_{1J}, when compared to Monte Carlo values whose accuracy is better than 90 percent; entries are normalized by $(A_1F_{1J})_{ave}$

Case	Shelf	Furnace	Grid	Truss	R-10	R-20	R-40
FACET	0.0342	0.1862	0.5332	2.2285	0.037	0.1511	0.5246
	0.000	0.0764	0.0011	0.000	0.0001	0.0018	0.0069
	0.1157	1.3943	3.248	19.128	0.2795	1.0705	4.4987
VIEWC	0.0136	0.1083	0.1112	0.0384	0.0370	0.1284	0.1684
	0.000	0.000	0.000	0.000	0.0001	0.0003	0.0001
	0.0455	1.4836	1.1831	0.2772	0.2796	1.0712	1.0954
HEMI	0.0161	0.0418	0.0768	0.3572	0.0357	0.0449	0.1597
	0.000	0.000	0.000	0.000	0.0001	0.0002	0.0001
	0.0486	0.5814	0.654	4.0435	0.2485	0.3061	0.9676
VIEWP	0.0161	0.0388	0.0828	0.1804	0.0352	0.1058	0.0559
	0.000	0.0008	0.0014	0.000	0.0002	0.0045	0.0022
	0.0477	0.4899	0.7882	2.1148	0.2796	0.7311	0.3813
M CARLO	0.0301	0.1735	0.1878	0.2266	0.1594	0.1278	0.1265
$(A_1F_{1J})_{ave}$	17.167	0.311	0.695	1.043	0.196	2.182	10.794
$(A_1F_{1J})_{max}$	108.07	5.113	4.286	14.333	0.397	6.756	51.152

The 3 entries for the different methods are indicative of the following:
1st rms error for which Monte Carlo predicts non-zero viewfactors
2nd rms error for which Monte Carlo predicts zero viewfactors
3rd Maximum error

The entry for the Monte Carlo method represents the error estimate in the sum of the viewfactors times area.

used. This effect can be reduced by statistically treating such occurrences. The Monte Carlo method also had difficulties with this configuration. Apparently the very regular spacing of the surfaces, and the fact that many edges would line up exactly, led to rays not being credited to any surface, which is commonly referred to as "leaking" of rays. For most surface configurations, these effects will be statistically averaged out. For the Grid, with its unusually high degree of repeatable surface location, the effect does not.

VIEWC incorporates a test for such grazing incidence and assigns fractional values of d_{ij}, equation (6). This accounts for its relatively good performance. For the furnace case, the enclosing surface areas were large compared to that of surface 1 or of the other obstructors. Consequently the view that surface 1 had of the enclosure was inaccurate, leading to an erroneous sum. Similar errors will occur unless all of the surfaces are of approximately equal size.

If the projection of surface I intersects surface J, the use of predefined subelements in VIEWC leads to significant errors but high execution speeds. Much of the speed of VIEWC is due to the very efficient clipping to reduce the number of candidate obstructors. When this occurs, those rays whose endpoints are below the intersection line (Fig. 15) will be assigned a value, $d_{ij}=0$, and there is no need to check the ray for being obstructed by other surfaces. If the visible portion of J is small, then the computed viewfactor will be too small. This accounts for the poor performance of VIEWC for case R-40. VIEWC-PC (PC = pairing clipping) is a modification of VIEWC in which J is replaced by the visible portion of J' (Fig. 15), and the original number of ray endpoints are distributed over this visible section. While the accuracy increases, the execution times also increase because every ray from I can now reach J and must be checked against all candidate surfaces for obstruction.

Because of its use in equation (1), the accuracy of F_{IJ} is best expressed in terms of the product A_IF_{IJ} as compared to either the average or maximum values of A_IF_{IJ}. Table 7 lists the rms values of the errors in A_1F_{1J}. The errors are normalized by the average value of A_IF_{1J}. Table 7 also lists the average value, $(A_1F_{1J})_{ave}$, and maximum value $(A_1F_{1J})_{max}$. The first row applies to the incorrect computation of nonzero viewfactors; the second row represents the error caused by computing a nonzero value when Monte Carlo predicts zero; the third row is the maximum error detected. Since it is not possible for the projection methods to compute a nonzero value when it is truly zero, the second row is a measure of the performance of the random number generator used in the Monte Carlo method. Often system-supplied random number generators fail to give a uniform distribution, particularly near $\theta=90°$ and it is prudent to test the distribution. Initial tests with RADSIM showed poor coverage of the angular region $\theta>88°$ and produced errors of the order of 0.07 (row 2 of VIEWP). Use of the modification suggested by Press et al. (1986) reduced the error to that shown in Table 7, row 2.

Table 8 Effect of number of emitting subelements on the sum of viewfactors from surface 1 (R-40 case)

	VIEWC	VIEWC	VIEWC-PC	VIEWC-PC	VIEWP	VIEWP
	Sum	Time	Sum	Time	Sum	Time
1	0	0.44	0.0065	0.65	0.0020	3.63
4	0.0422	0.84	0.0958	1.22	0.0738	11.2
9	0.0600	1.73	0.0800	3.05	0.0758	25.4
16	0.0563	4.08	0.0710	7.81	0.0715	41.2
25	0.0737	9.15	0.0753	18.62	0.0713	58.7
Auto(25)	0.0738	7.29	0.0774	9.77		

The documentation for FACET suggests that the code is optimized for speed and accuracy. As indicated in Table 4, when it is fast it is very fast, but when slow it is quite slow. It also appears to be very inaccurate when there are many obstructors, both from the point of view of the sum and of the rms errors, particularly in computing nonzero values when no other methods do (row 2). Because of this, testing of this code was not continued.

5.4 Number of Emitting Subelements. Table 8 compares the effect of increasing the number of emitting points. As expected, both the accuracy and the cost increase proportionately. For small viewfactors, it would appear reasonable to reduce the number of emitting points. The line entitled Autoray (25) lists the performance when a nominal 25 subelements, 5×5, were used, but the number reduced for smaller values of the unobstructed viewfactor according to

$$N_S = N_S^0 - \log_{10}\left(\frac{F_{IJ}}{F_{IJ}^0}\right) \tag{7}$$

where F_{IJ}^0 was chosen as 0.01. Significant reductions in time were noted, but the effect on accuracy was erratic.

What is clear is that a reasonable number of subelements must be used: at least 4 for the projected contour and 16 for the double area methods. It is unfortunately common that too few are used. While the TMG analyzer (Anon, 1983) permits a user-specified number, the ANSYS thermal analyzer (Smith and Ketelarr, 1987) uses only one under the assumption that the surfaces are small and far apart and thus often produces substantial errors; larger surfaces should be subdivided into smaller ones. While this can be done in principle, if the surfaces are intended to represent the faces of finite elements for structural and thermal analyses, one cannot afford the cost of so many small elements unless a sophisticated subdivision and subsequent merging routine must be incorporated.

5.5 Size of Projected Obstructors and Number of Gaussian Points. Since as many as 400 projected areas were created for some views in the space truss, there is concern that discarding small obstructors with small projected areas or inaccurately computing f_{iJ} may lead to errors. Table 9 illustrates the effect of ignoring small projected obstructors. Any projected area less than $A_{min}\times A_J$ is ignored. Values of A_{min} greater than 1 percent lead to increasing errors, both in the sum and in the rms values, but to increasing speed. Table 10

Table 9 Effect of A_{min}; VIEWP

A_{min}	Sum	Time
0.001	1.0012	96.2
0.002	1.0020	76.9
0.005	1.0036	57.2
0.010	1.0120	40.3
0.020	1.0280	31.8

Table 10 Effect of number of gaussian integration points; VIEWP

	R-40 $A_{min} = 0.001$	R-40 $A_{min} = 0.001$	TRUSS $A_{min} = 0.005$	TRUSS $A_{min} = 0.005$
Number	Sum	Time	Sum	Time
1	0.0692	16.6	1.024	24.8
2	0.0711	22.6	1.024	29.1
3	0.0713	29.3	1.024	33.7
4	0.0715	35.4	1.024	37.6
5	0.0715	42.6	1.024	42.5

Table 11 Effect of number of subelements and pixel size; HEMI for case R-40

Subelement	Sum	Time	Pixels	Sum	Time
			10x10	0.0646	8.1
1	0.07078	1.39	20x20	0.0675	8.7
5	0.05738	4.73	40x40	0.0702	10.6
9	0.06276	7.89	60x60	0.0708	12.8
16	0.06660	12.80	80x80	0.0671	16.6
			100x100	0.0674	20.5

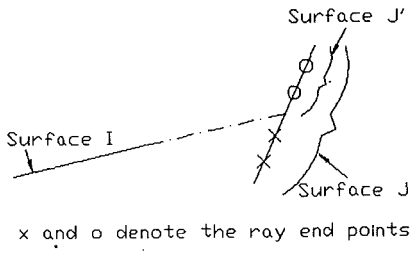

Fig. 15 Illustration of pair clipping

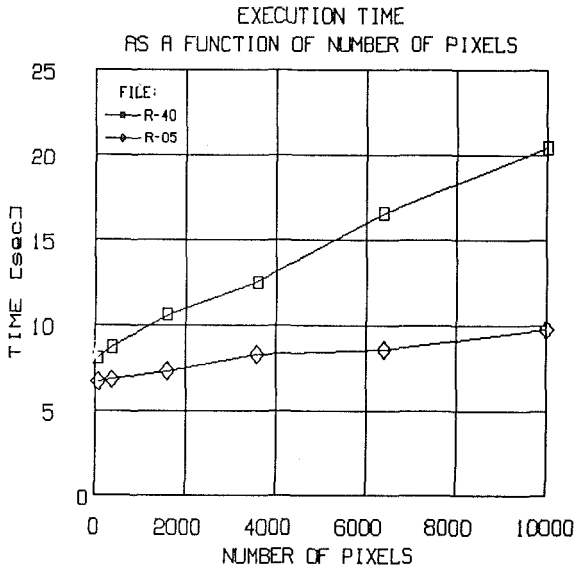

Fig. 16 Execution time as a function of the number of pixels in the hemi-cube method

shows the effect of the accuracy of contour integration over the obstructor. Even though the final viewfactor is obtained by subtracting the sum of a large number of individual viewfactors, use of relatively few gaussian points does not appear to degrade the result significantly. A choice of 3 gaussian points yields acceptable accuracy and speed.

Choosing different numbers of pixels for describing the hemi-cube faces is comparable in effect to altering the value of A_{min}. Table 11 shows the effect of choosing different pixel sizes and number of emitting points. Using a large number of small pixels gives a fine resolution to the surface projection and a small pixel viewfactor, f_{ie}, thus leading to improved accuracy as shown. Although the use of increased number of pixels eventually guarantees improved accuracy, as illustrated, the progress is not always monotonic.

It is important to realize that specifying the number of emitting subelements has a different effect in the hemi-cube and sphere methods than in the others. Because these methods must consider all surfaces, not a specified pair, it is not possible to clip surfaces I and J such that only the visible portions are studied. Thus, the positions of the emitting points of surface I remain constant throughout the computation. If the projection of surface J intercepts I, leaving only a small visible area, and if no emitting points are located therein (Fig. 15), the value of f_{ij} will be in error, although the sum will still be precise (assuming that I is truly enclosed). Fig. 16 compares the execution times for a sparse and dense structure, R-05 and R-40. The difference in slopes and intercept are the result of the larger area of the R-40 surfaces, which project to more than one face, adding to the number of operations.

5.6 Extensions of the Method. Real engineering surfaces are curved, not flat, are partially specular, and have surface radiation properties that are dependent upon angle. Of the methods surveyed, those involving contour integration cannot be used unless the surfaces are diffuse and spatially constant in emissive power. The remaining methods can be extended. Clearly the Monte Carlo methods can be used to treat any type of surface, although the cost may be high.

When using the projection methods, variation of surface emissivity or absorptivity can be easily accommodated by multiplying the values of f_{ib} or f_{ie} by the appropriate values of ϵ or α. Curved surfaces pose no problems for diffuse radiation when they are the receiving surface other than that it may be difficult to determine the projection of the curved surface onto the unit sphere, the faces of the hemi-cube, or the adaptive surface P. If the emitting surface is curved, then it can be modeled by a set of small planes either with little loss in accuracy. Likewise, an angular dependence of the emissivity or absorptivity can be easily treated. Spatial variation of emissive power can be treated, but it must be realized that the resulting value of F_{IJ} is no longer a general value, but specific to the problem solved and does not satisfy a sum of unity nor possess reciprocity.

Modeling of curved surfaces by flat surfaces will not cause any problems if a sufficient number is used. The use of straight-sided flat surfaces is not theoretically necessary but is a practical necessity because of the difficulties of projecting curved edges, or of integrating along curved contours.

On the other hand, if specular reflections are important, then flat surfaces cannot be used without incurring significant errors in individual values of F_{IJ}, although the total radiation will still be accurately computed. If accuracy is needed, then only a ray tracing technique can be used. However, if flat surfaces will suffice, then any of the projection methods can be used. Based upon the direction of the reflected radiation from surface I, one simply defines an imaginary surface, IM, of a shape equal to the projected shape of I. Only surfaces that intrude upon the cylinder enclosing I and IM can receive

reflected radiation. Each surface is projected onto *IM* in the same way as done in the projected contour method for diffuse radiation, except that only the surface closest to *I* is retained. Because this feature of retention significantly complicates the projected contour method, if accuracy permits, it is better to use a projection onto the ADAP P surface, which has been subdivided into a sufficient number of pixels. The energy intercepted by each receiver is computed and stored along with the angle of incidence. Each one of these surfaces then is treated in the same way as surface *I*. Unfortunately a surface may receive reflected radiation from a large number of other surfaces, and thus reflect in a number of directions. Since the computation must be performed for each angle of reflection, it may be very expensive. If there is only one source of radiation, such as the sun, then the approach is fairly straightforward.

6 Conclusions

Although the Monte Carlo method converges slowly and sometimes erratically, it probably represents the best numerical method for computing F_{IJ} and gaining some idea of the sensitivity of any specified F_{IJ} to the level of computational effort required.

In contrast to the double area and projected contour methods in which maximal speed is achieved by eliminating all nonobstructors from the candidate list, optimal Monte Carlo speed will be achieved by improvements in defining the smallest list of surfaces that may intercept a ray. We believe that this can be effected by implementing Hedgeley's Grid Block method. Results reported for hidden surface computations (Hedgeley, 1982) suggest that speed increases of a factor of 10 are easily achieved. This would make Monte Carlo nearly competitive with the hemi-cube, but with the advantage of generating the estimated error in addition to the viewfactor values.

In addition, if adaptive subdivision of pixels as described by Wyvill et al. (1986) or an octree representation is used, the overall speed may approach that of the faster methods. However, unless this method can be accelerated by factors of 100, its need to compute all N^2 values and its dependence upon the square root of the number of walkers will tell against it.

F realistic engineering structures, in which surfaces do not intersect, and yet for which there is a fair number of obstructors, the double area/contour method with pair clipping is adequate in accuracy and speed. Its main advantage is its efficient method for determining whether a ray is obstructed and its need to evaluate F_{IJ} only for $J>I$. If the scene is not too complex, the projected contour method is preferred. If it is important to specify the maximum error in any F_{IJ}, ADAP should be used, unless the scene is very complex when the hemi-cube approach is preferred.

Acknowledgments

We would like to thank R. C. Corlett and G. Walton for supplying us with copies of their source codes RADSIM and VIEW3D. The projected contour module of VIEWC was based, in part, on ideas proposed by G. Walton. We would also like to thank Mr. J. Robinson, technical monitor of NASA Grant, for his assistance and suggestions.

References

Ames, F., et al., 1987, "Vertically Integrated Computer Aided Engineering System for Thermal Analysis/Design," TSS Annual Rept., Lockheed MSC.

Anon, 1983, "TMG, Thermal Model Generator Users Manual," MAYA Heat Transfer Technologies Ltd., Montreal, Quebec, Canada.

Chung, T. J., and Kim, J. Y., 1982, "Radiation Viewfactors by Finite Elements," ASME JOURNAL OF HEAT TRANSFER, Vol. 104, pp. 792-795.

Cohen, M. F., Greenberg, D. P., Brock, P. J., and Immel, D. S., 1986, "An Efficient Radiosity Approach for Realistic Image Synthesis," *IEEE CG&A*, Vol. 6, No. 3, pp. 26-35.

Corlett, R. C., 1988, "Draft: A User's Manual for RADSIM-PC," Univ. of Washington, Seattle, WA.

Emery, A. F., Johansson, O., and Abrous, A., 1987, "Radiation Heat Transfer Calculations for Space Structures," Paper No. AIAA-87-1522, 22nd AIAA Thermophysics Conference, June 8-10, Honolulu, HI.

Emery, A. F., 1988, "VIEWC Users Manual," Univ. of Washington, Seattle, WA.

Foley, J. D., and Van Dam, A., 1984, *Fundamentals of Interactive Computer Graphics*, Addison-Wesley, Reading, MA.

Gross, U., Spindler, K., and Hahne, E., 1981, "Shapefactor Equations for Radiation Heat Transfer Between Plane Rectangular Surfaces of Arbitrary Position and Size With Parallel Boundaries," *Letters in Heat and Mass Transfer*, Vol. 8, pp. 219-227.

Hamilton, D. C., and Morgan, W. R., 1952, "Radiant Interchange Configuration Factors," NACA TN-2836.

Howell, J. R., 1982, *A Catalog of Radiation Configuration Factors*, McGraw-Hill, New York.

Hedgeley, D. R., Jr., 1982, "A General Solution to the Hidden Line Problem," NASA Reference Publ. 1085.

Kadaba, P. V., 1982, "Thermal Radiation Viewfactor Methods, Accuracy and Computer Aided Procedures," NASA/MSFC Report, Contract NGT-01-002-099.

Mitalas, G. P., and Stephenson, D. G., 1966, "Fortran IV Programs to Calculate Radiant Interchange Factors." NRC of Canada, Ottawa, Canada, DBR-25.

Newman, W. M., and Sproull, R. F., 1981, *Principles of Interactive Computer Graphics*, McGraw-Hill, New York.

Press, W. H., Flannery, B. P., Teukolsky, S. A., and Vetterling, W. T., 1986, *Numerical Recipes*, Cambridge University Press, Cambridgeshire-New York.

Shapiro, A., 1983, "FACET—A Radiation Viewfactor Computer Code for Axisymmetric 2D Planar and 3D Geometries With Shadowing," Univ. of California, Lawrence Livermore National Lab, UCID-19887.

Siegel, R., and Howell, J. R., 1981, *Thermal Radiation Heat Transfer*, Hemisphere Publ. Corp., New York.

Smith, R. W., and Ketelaar, D. D., 1987, "Radiation Matrix Generation Utility," ANSYS Tutorial, Re 4.3, DN-T004.

Thornton, E. A., and Mahaney, J., 1984, "Self-Shadowing Effects on the Thermal Structural Response of Orbiting Trusses," Paper No. AIAA-84-1765, AIAA 19th Thermo-physics Conference, June 25-28, Snowmass, CO.

Walton, G. N., 1986 "Algorithms for Calculating Radiation Viewfactors Between Plane Convex Polygons With Obstructions, " NBSIR 86-3463.

Wyvill, G., Kunii, T. L., and Shirai, Y., 1986, "Space Division for Ray Tracing in CSG," *IEEE CG&A*, Vol. 6, No. 4, pp. 28-34.

Heat Transfer Characteristics of Porous Radiant Burners

T. W. Tong
Professor.

S. B. Sathe
Research Assistant.

Department of Mechanical and Aerospace Engineering,
Arizona State University,
Tempe, AZ 85287

This paper reports a numerical study of the heat transfer characteristics of porous radiant burners, which have significant advantages over conventional burners. The heat transfer characteristics are investigated using a one-dimensional conduction, convection, and radiation model. The combustion phenomenon is modeled as spatially dependent heat generation. Nonlocal thermal equilibrium between the gas and solid phases is accounted for by using separate energy equations for the two phases. The solid matrix is assumed to emit, absorb, and scatter radiant energy. The spherical harmonics approximation is used to solve the radiative transfer equation. The coupled energy equations and the radiative transfer equations are solved using a numerical iterative procedure. The effects of the various factors on the performance of porous radiant burners are determined. It is revealed that for a given rate of heat generation, large optical thicknesses and high heat transfer coefficients between the solid and gas phases are desirable for maximizing radiant output. Also, low solid thermal conductivities, scattering albedos and flow velocities, and high inlet environment reflectivities produced high radiant output.

Introduction

Based on field test data available (*Gas Research Institute Digest*, 1984), porous radiant burners (PRBs) have many advantages over conventional burners. Demonstrated advantages include higher thermal efficiency due to reduced enthalpy loss through the flue gas, elimination of hot spots in heat transfer devices because of more uniform heating, and lower emission of toxic nitrogen oxides as a result of lower flame temperatures. If PRBs gain wide acceptance in industrial, commercial, and residential heating applications, the benefits from the standpoint of reduced energy consumption, increased lifetime of heat transfer equipment, and improved air quality will be tremendous. One factor that directly impacts on the acceptability of PRBs is their radiant output. Because the PRB technology is still in its infant stage, the understanding on how the various parameters affect the radiative output of PRBs is limited. This has provided the impetus for carrying out the present analysis. The purpose is to provide a better understanding of the heat transfer characteristics of PRBs and to establish ways for increasing their radiant output, making them desirable for adoption in as many heating applications as possible.

In PRBs, a gaseous fuel–air mixture is passed through a noncombustible porous medium. Combustion is stabilized inside the porous medium by adjusting the mass flow rate of the fuel–air mixture so that flashback or blowoff is prevented. The heat of combustion released in the gas phase heats up the solid matrix of the porous medium, which in turn emits energy in the form of thermal radiation to a heat load.

Since the PRB technology is rather new, very little literature exists on the subject. In a somewhat related topic, Echigo (1982) studied the problem of recovering energy from hot exhaust gases by placing a porous segment in exhaust ducts. His analysis revealed that a substantial amount of the exhaust gas energy might be recovered by converting it to radiative energy traveling upstream from the porous segment. The solid was assumed not to scatter radiant energy. Wang and Tien (1984) extended Echigo's analysis by including the effect of radiation scattering in the analysis. They demonstrated the importance radiation scattering had on the effectiveness of the energy conversion. By considering a heat generation zone inside a porous medium, Echigo et al. (1986) extended their earlier work (Echigo, 1982) to investigate the use of porous media for combustion augmentation. It was found that energy recirculation by radiation preheated the combustion mixture, resulting in significant combustion augmentation. Chen et al. (1987) investigated the effect of radiation on the structure of methane premixed flames in porous media by using a detailed multistep chemistry model for the combustion process. However, Chen et al. (1987) neglected radiation scattering and nonlocal thermal equilibrium between the gas and solid phases in their heat transfer model. Recently, Tong et al. (1987) studied the effects of the position of the combustion zone location, the optical thickness, and the type of scattering on the radiant output of PRBs. Their heat transfer model was a purely radiative model with no convective effects, but it accounted for scattering of radiation.

The present work investigates the combined effects of convection, conduction, and radiation on the radiant output of PRBs. The analysis is based on one-dimensional fluid flow through a thin porous segment in which combustion takes place. Nonlocal thermal equilibrium between the gas and solid phases is accounted for. Conduction through the solid phase and scattering of radiation are incorporated into the model. Combustion is modeled as a constant heat generation zone inside the porous segment. The inlet boundary condition for the gas is specified far upstream from the porous segment so that the effect of preheating the combustion mixture before it enters the porous segment is allowed for.

Mathematical Analysis

The situation considered is shown schematically in Fig. 1. A gaseous fuel–air mixture enters an adiabatic duct that may be either cylindrical or rectangular. The heat generation zone, representing the flame, is situated in the porous region. The duct hydraulic diameter is assumed to be much larger than the heat generation zone thickness. All thermophysical properties are constant. Slug flow is assumed, and it is steady and laminar. The solid is assumed to be gray and to emit, absorb, and scatter radiant energy isotropically. Radiant energy emitted is assumed to be primarily due to continuum emission by the solid matrix of the porous medium. Comparatively, gaseous radiation is not as important as solid radiation and is neglected. Since the solid and gas are not in local thermal equilibrium, separate

Contributed by the Heat Transfer Division for publication in the JOURNAL OF HEAT TRANSFER. Manuscript received by the Heat Transfer Division May 19, 1989; revision received August 20, 1990. Keywords: Combustion, Porous Media, Radiation.

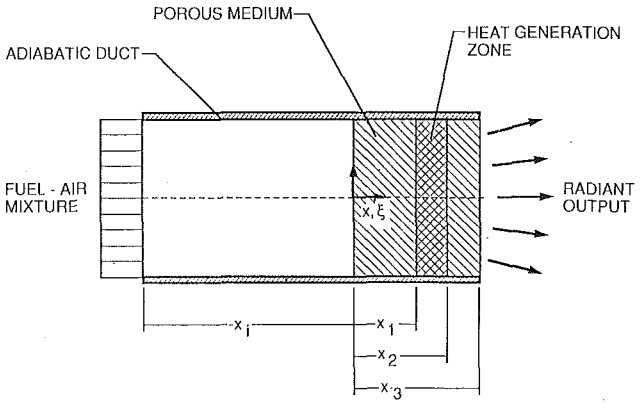

Fig. 1 Schematic diagram of the porous radiant burner

Table 1 Summary of dimensionless parameters

Parameter	Physical Significance	Typical Value†	Range Studied
$P_1 = \rho u c_g T_i / Q x_3$	flow enthalpy	0.014	0.01–0.05
$P_2 = h a T_i / Q$	convective energy coupling between gas and solid	4 (100 μm fiber) 400 (10 μm fiber)	1–500
$P_3 = k_g T_i / Q x_3^2$	gas conduction	2.5×10^{-4}	10^{-5}–10^{-3}
$P_4 = k_s T_i / Q x_3^2$	solid conduction	0.02 (non-metals) 0.20 (metals)	0.002–0.2
$P_5 = h x_3 / k_s$	Biot number	5	0.05–500

† Based on $\rho = 0.19$ kg/m^3, $u = 2.8$ m/s, $c_g = 1.28$ kJ/kg K, $T_i = 298$ K, $Q = 1.5 \times 10^9$ W/m^3, $x_3 = 0.01$ m, $ha = 2 \times 10^9$ and 2×10^7 W/m^3 K for 10 and 100 μm fibers, respectively, $k_g = 0.125$ W/m K, $k_s = 10$ and 100 W/m K for non-metals and metals, respectively.

energy equations are needed to describe energy transfer in these two phases. To save space, only the dimensionless form of the governing equations are presented here. Interested readers can find the dimensional form of the equations in the conference version of the paper (Tong and Sathe, 1988). Hence, the energy equation for the gas is

$$P_1 \frac{d\theta_g}{d\xi} + (1-\phi)P_2(\theta_g - \theta_s) = \phi\delta(\xi) + P_3 \frac{d^2\theta_g}{d\xi^2} \tag{1}$$

where θ_g and θ_s are the dimensionless gas and solid temperatures defined as $(T_g - T_i)/T_i$ and $(T_s - T_i)/T_i$, respectively, $\xi = x/x_3$, ϕ is the porosity defined such that $\phi = 1$ for $\xi < 0$ and $0 \le \phi \le 1$ for $0 \le \xi \le \xi_3$, and $\delta(\xi)$ is a delta function defined as unity for $\xi_1 \le \xi \le \xi_2$ and zero elsewhere. The term $\phi\delta(\xi)$ represents unit heat generation in the heat generation zone. Table 1 gives the definitions and physical significance of P_1, P_2, P_3, as well as P_4 and P_5, which will appear later. The definitions of all dimensional variables are provided in the Nomenclature.

A known temperature at the inlet and an adiabatic condition at the outlet constitute the gas phase boundary conditions. Adiabatic conditions at the outflow position are justified if local one-way behavior exists (Patankar, 1980), which is the case in the present work. Thus, we have

$$\theta_g = 0 \text{ at } \xi = -\xi_i \tag{2a}$$

$$\frac{d\theta_g}{d\xi} = 0 \text{ at } \xi = \xi_3 \tag{2b}$$

The energy equation of the solid phase in the porous segment is

$$(1-\phi)P_4 \frac{d^2\theta_s}{d\xi^2} + (1-\phi)P_2(\theta_g - \theta_s) = \frac{dQ^r}{d\xi} \tag{3}$$

where Q^r, defined as q^r/Qx_3, is the net radiative heat flux in the ξ direction. The boundary conditions for equation (3) are formulated based on the following consideration. An integration of equation (3) for an infinitesimal thickness across an interface results in an energy balance of the total energy flux (sum of conductive, convective, and radiative fluxes). As a limit is taken from both sides of the interface toward the interface, the convective fluxes drop out because the solid surface area is disappearing. Further, the radiative heat fluxes on both sides must balance each other as there is no solid within a radiation mean free path to alter the radiative flux. Thus, one ends up with the conductive flux on one side balancing the conductive flux on the other side of the interface. For the situation under consideration, Newton's law of cooling is used to represent the conductive flux on the gas side at both $\xi = 0$ and $\xi = \xi_3$. Therefore, we have

$$-\frac{d\theta_s}{d\xi} = P_5(\theta_g - \theta_s) \text{ at } \xi = 0 \tag{4a}$$

$$\frac{d\theta_s}{d\xi} = P_5(\theta_g - \theta_s) \text{ at } \xi = \xi_3 \tag{4b}$$

Radiative heat transfer in the porous segment is modeled using the equation of transfer. In one-dimensional form the equation of transfer can be written as (Ozisik, 1973)

$$\frac{\mu}{\tau}\frac{\partial I(\xi,\mu)}{\partial \xi} + I(\xi,\mu) = (1-\omega)I_b(T_s) + \frac{\omega}{2}\int_{-1}^{1} I(\xi,\mu')d\mu' \tag{5}$$

Nomenclature

- a = solid surface area per unit volume of solid, 1/m
- c = specific heat, J/kg K
- G = dimensionless emissive power $= \sigma T^4/Qx_3$
- h = heat transfer coefficient, W/m^2 K
- i = radiant intensity, W/m^2 sr
- I = dimensionless radiant intensity $= i/Qx_3$
- k = thermal conductivity, W/m K
- P_1–P_5 = dimensionless parameters as defined in Table 1
- q^r = net radiative heat flux, W/m^2
- Q = heat generation rate per unit volume, W/m^3
- Q^r = dimensionless net radiative heat flux $= q^r/Qx_3$
- Q_o^r = dimensionless radiant output $= Q^r(\xi_3)$
- r = reflectivity
- T = temperature K
- u = velocity, m/s
- x = coordinate, m
- x_1–x_3 = lengths defined in Fig. 1, m
- δ = unit step function
- ϵ = emissivity
- θ = dimensionless temperature $= (T - T_i)/T_i$
- μ = direction cosine
- ξ = dimensionless coordinate $= x/x_3$
- ξ_{fl} = dimensionless flame zone location $= (\xi_1 + \xi_2)/2$
- ρ = density, kg/m^3
- σ = Stefan–Boltzmann constant, W/m^2 K^4
- σ_a, σ_s = absorption and scattering coefficients, 1/m
- τ = optical thickness $= (\sigma_a + \sigma_s)x_3$
- ϕ = porosity
- ω = scattering albedo $= \sigma_s/(\sigma_a + \sigma_s)$

Subscripts

- b = blackbody
- d = diffuse
- e = outlet environment
- g = gas
- i = inlet
- s = solid

where I, defined as i/Qx_3, is the dimensionless radiant intensity, μ is the cosine of the angle between the direction of the intensity and the ξ direction, $\tau=(\sigma_a+\sigma_s)x_3$ is the optical thickness of the porous segment, $\omega=\sigma_s/(\sigma_a+\sigma_s)$ is the scattering albedo, and I_b is the dimensionless blackbody radiant intensity defined as i_b/Qx_3.

The upstream boundary condition for the intensity is written by assuming the upstream condition can be characterized by a gray and diffusely emitting and reflecting surface at T_i. Therefore,

$$I^+(0)=\epsilon\frac{G_i(T_i)}{\pi}+2\,r_d\int_{-1}^{1}I^-(0,\,-\mu')\mu'd\mu' \qquad (6a)$$

where I^+ and I^- are the radiant intensities in the positive and negative ξ directions, respectively, $G_i=\sigma T_i^4/Qx_3$, ϵ and r_d are the emissivity and diffuse reflectivity of the upstream boundary, respectively. The burner is assumed to be seeing a black environment at T_e. Thus, the boundary condition for the intensity at ξ_3 can be expressed as

$$I^-(\xi_3)=\frac{G_e(T_e)}{\pi} \qquad (6b)$$

with $G_e=\sigma T_e^4/Qx_3$.

The net radiative heat flux Q' appearing in equation (3) is obtained by integrating the first moment of the radiant intensity over all directions. That is

$$Q'=2\pi\int_{-1}^{1}I(\xi,\,\mu')d\mu' \qquad (7)$$

Method of Solution

Equation (5) is transformed to a set of twelve first-order ordinary differential equations in terms of the moments of the radiant intensity using the P-11 spherical harmonics approximation (Swathi et al., 1987; Tong et al., 1987). Equations (6*a*) and (6*b*) are replaced by the Marshak's boundary conditions, which require the intensity moments to be conserved. The spherical harmonics method and the Marshak boundary conditions for solving the equation of transfer have been well documented elsewhere (Davison and Sykes, 1957; Ozisik, 1973; Menguc and Viskanta, 1985; Swathi et al., 1987; Tong et al., 1987). The readers are referred to these references for the mathematical details.

The twelve equations governing the moments of radiant intensity and equations (1) and (3) are solved according to the following procedure:

1 Guess $\partial\theta_g/\partial\xi$ at $\xi=0$;
2 Solve equation (1) analytically for the region $-\xi_i\le\xi\le0$ using equation (2*a*) and the boundary condition from step 1;
3 Determine θ_g at $\xi=0$ using the solution from step 2;
4 Numerically solve equations (1) and (3) and the twelve equations resulting from the P-11 spherical harmonics approximation for the region $0\le\xi\le\xi_3$ using equations (2*b*), (4*a*), and (4*b*), the boundary condition from step 3, and the Marshak boundary conditions;
5 Determine $\partial\theta_g/\partial\xi$ at $\xi=0$ using the solution from step 4; and
6 Repeat steps 2–5 until convergence is achieved.

Subroutine DVCPR from the IMSL library was used to perform the computation in step 4. The subroutine was a two-point boundary value problem solver with adaptive meshing capability. The mesh was chosen in such a manner that the local errors were approximately of the same size at all grid points. The magnitude of the error could be controlled by specifying a relative error tolerance. As will be explained in the next section, a relative error tolerance of 1×10^{-4} was chosen to yield accurate results and yet efficient computations. Discretization of the governing equations was done using the trapezoidal rule. The resulting algebraic system of equations was solved by Newton's method. Convergence for step 6 was assumed only when all the following conditions were met:

1 Fractional change in $\partial\theta_g/\partial\xi$ at $\xi=0$ in consecutive iterations was less than 1×10^{-4};
2 Fractional change in θ_g at $\xi=0$ in consecutive iterations was less than 1×10^{-4}; and
3 An overall energy balance of less than 0.1 percent was achieved.

Computations and Test Cases

Computations for a wide range of conditions, including those typical for operating PRBs, were performed. The following values were used as a guide to set the parameters P_1–P_5: $u=2.8$ m/s, $T_i=298$ K, $Q=1.5\times10^9$ W/m^3, $\rho=0.19$ kg/m^3, $c_g=1.28$ kJ/kg K, $k_g=0.125$ W/m K, $k_s=10$ and 100 W/m K, $ha=2\times10^9$ and 2×10^7 W/m^3 K. The values of P_1–P_5 resulting from these properties are summarized in Table 1. The heat generation rate (Q) used was based upon the lower heating value for stoichiometric methane–air combustion. The gas properties were for air at 1800 K. The lower and higher values for k_s were intended to be representative of nonmetallic and metallic fibers, respectively. The values of ha were estimated from the experimental data for h for cylinders in crossflow (Incropera and DeWitt, 1985) and a for infinitely long fibers that were either 10 or 100 μm in diameter. In addition, the porous segment was assumed to be composed of monodispersed cylindrical fibers with a thickness (x_3) of 0.01 m and a porosity (ϕ) of 0.95. The heat generation zone was assumed to be one-tenth of x_3 (i.e., $x_2-x_1=0.001$ m). The length x_i was considered to be large (1 m) so that the gas temperature at $x=0$ was not affected by preheating. Only the results for $P_3=2.5\times10^{-4}$ and $P_5=5$ are presented since varying these parameters over the ranges indicated in Table 1 resulted in negligible changes in the radiant output.

All calculations were performed on an IBM 3090 computer. To determine the effect of the relative error tolerance in DVCPR, test calculations were conducted for $P_1=0.01$, $P_2=100$, $P_3=2.5\times10^{-4}$, $P_4=0.02$, $P_5=5$, $\omega=0.5$, $r_d=0$, $\xi_{fl}=0.5$, $\tau=2$, and $G_i=G_e=2.98\times10^{-5}$. It was found that for a relative error tolerance of 1×10^{-4}, the calculation took 240 cpu seconds and required 350 grid points. An overall energy balance of 0.022 percent for the porous layer was achieved. When the relative error tolerance was 1×10^{-5}, the computation took 515 cpu seconds and 520 grid points, with an energy balance of 0.014 percent. The corresponding change in radiant output was less than 0.1 percent. For all subsequent calculations, 1×10^{-4} was chosen as the relative error tolerance so as to achieve accurate results without incurring prohibitively high computation times.

Results and Discussion

Effect of τ. Figure 2 shows the effect of the optical thickness (τ) on the temperature distribution inside the porous medium. The heat generation zone position represented by ξ_{fl} [$=(\xi_1+\xi_2)/2$] is 0.5. That is, the flame was regarded as situated in the middle of the porous segment. Because P_2 is large for the results presented in this figure, meaning there is strong convective heat transfer between the gas and solid, the temperatures for the two phases are almost identical. When the temperature distributions are plotted as shown, they exhibit no observable differences. The curve for $\tau=0$ corresponds to the situation when there is no heat transfer by radiation. In comparison to the other curves for $\tau>0$, it is seen that the peak temperature is highest when there is no radiation. This indicates that radiation serves as a mechanism for heat removal from the heat generation zone. The temperature at $\xi=0$ is

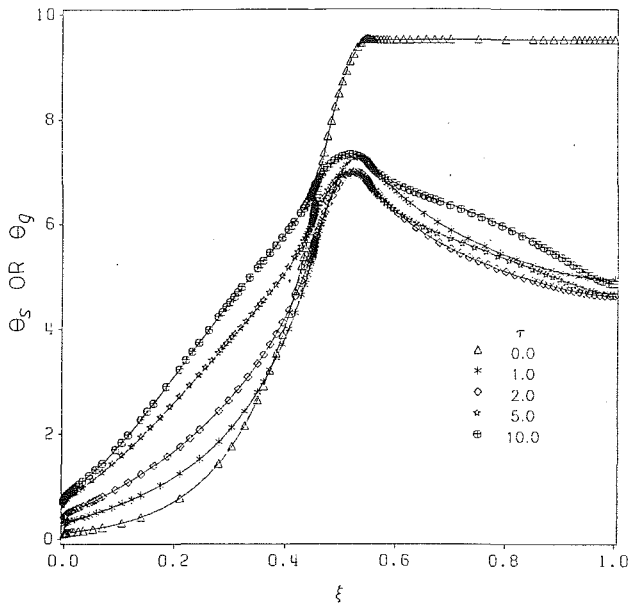

Fig. 2 Effect of the optical thickness on the temperature distribution; $P_1 = 0.01$, $P_2 = 500$, $P_3 = 2.5 \times 10^{-4}$, $P_4 = 0.02$, $P_5 = 5$, $\omega = 0.5$, $r_d = 0$, $\xi_{fl} = 0.5$, $G_i = G_e = 2.98 \times 10^{-5}$

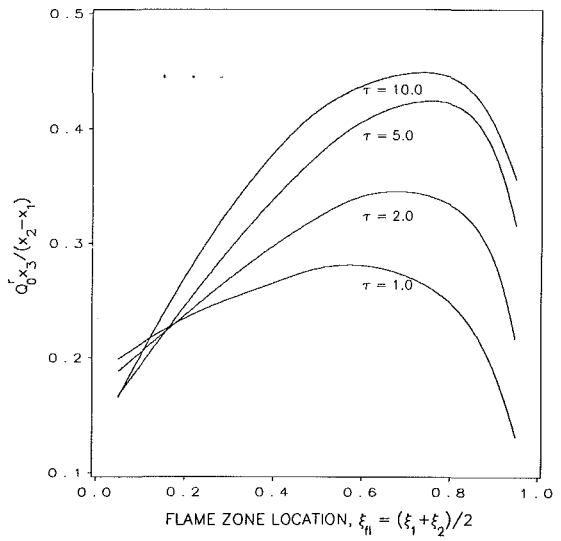

Fig. 3 Effect of the optical thickness on the radiative output; $P_1 = 0.01$, $P_2 = 500$, $P_3 = 2.5 \times 10^{-4}$, $P_4 = 0.02$, $P_5 = 5$, $\omega = 0.5$, $r_d = 0$, $G_i = G_e = 2.98 \times 10^{-5}$

higher for larger τ due to preheating by radiation. However, the peak temperature and the postflame ($\xi > \xi_2$) temperature at first decrease with increasing τ; but when $\tau > 2$ they increase as τ is increased further. This is because the postflame region is optically thick enough when τ reaches 2 and it begins to prevent radiative heat loss from the heat generation zone.

Figure 3 shows the effect of τ on the radiant output ($Q^r_0 = Q^r$ at ξ_3) for different locations of the heat generation zone. The abscissa represents the fraction of heat generation that is emitted as radiant energy. When ξ_{fl} is closer to 0, the postflame region acts like a shield and results in lower radiant output. On the other hand, if ξ_{fl} is close to ξ_3, there is only a small region for the gas to transfer heat to the solid before the gas leaves the porous region. Thus, only a small region of the solid is at a high temperature and the radiant output tends to be low. As a result of these counteracting phenomena, there exists an optimal position of ξ_{fl} for which the radiant output is

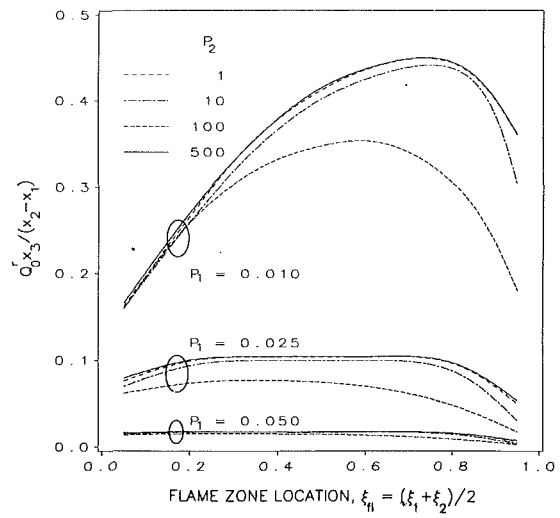

Fig. 4 Effects of P_1 and P_2 on the radiative output; $P_3 = 2.5 \times 10^{-4}$, $P_4 = 0.02$, $P_5 = 5$, $\omega = 0.5$, $r_d = 0$, $\tau = 10$, $G_i = G_e = 2.98 \times 10^{-5}$

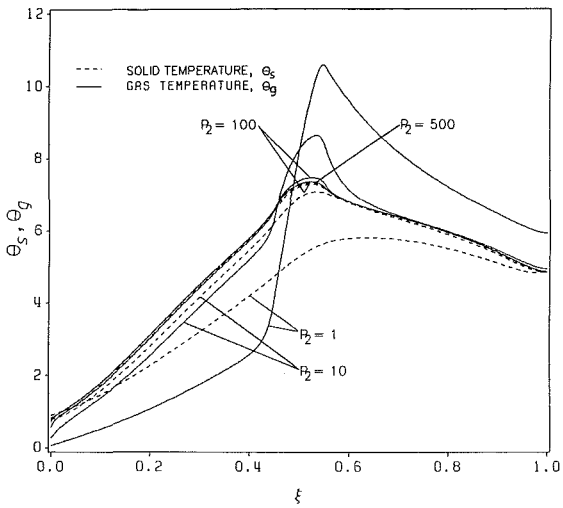

Fig. 5 Temperature distributions for different P_2; $P_1 = 0.01$, $P_3 = 2.5 \times 10^{-4}$, $P_4 = 0.02$, $P_5 = 5$, $\omega = 0.5$, $r_d = 0$, $\xi_{fl} = 0.5$, $\tau = 10$, $G_i = G_e = 2.98 \times 10^{-5}$

maximized. When ξ_{fl} is not close to 0 the radiant output increases substantially with an increase in τ. Because of the shielding effect, the converse is true when ξ_{fl} is close to 0.

Effect of P_1. The results in Fig. 4 show that radiant output can be increased by decreasing P_1. Smaller P_1 can be obtained by slowing the gas flow. It takes longer for the gas to travel through the porous segment and more energy can be transferred from the gas to the solid, resulting in higher radiant output. Based on the results, one would attempt to continue to decrease P_1 to enhance the radiant output. In reality there is a lower limit for P_1. When the gas flow is too low flashback will occur and the burner will cease to function. However, such a limit cannot be established through a purely heat transfer analysis. The optimal ξ_{fl} for which the radiant output is maximized depends on the gas flow. In general, the optimal position is more toward the downstream direction when the gas flow is lower. This trend is consistent with the findings of Tong et al. (1987). They illustrated that when there was no convection, the flame should be positioned right at the front surface to maximize radiant output.

Effect of P_2. Depicted in Fig. 5 are the temperature dis-

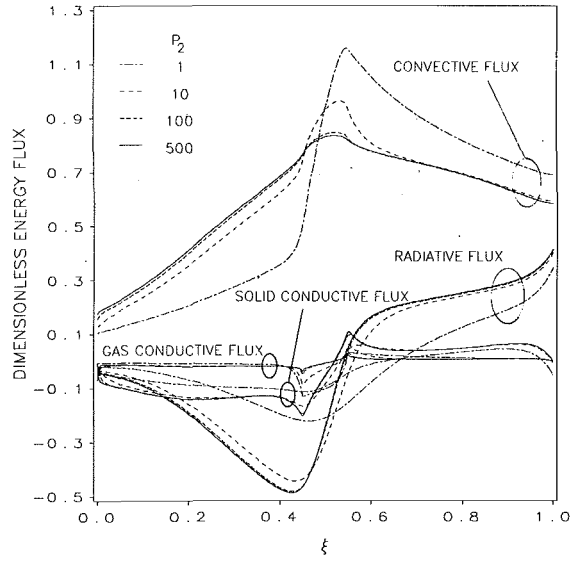

Fig. 6 Comparison of the convective, radiative, and conductive energy fluxes for different P_2; $P_1 = 0.01$, $P_3 = 2.5 \times 10^{-4}$, $P_4 = 0.02$, $P_5 = 5$, $\omega = 0.5$, $r_d = 0$, $\xi_{fl} = 0.5$, $\tau = 10$, $G_i = G_e = 2.98 \times 10^{-5}$

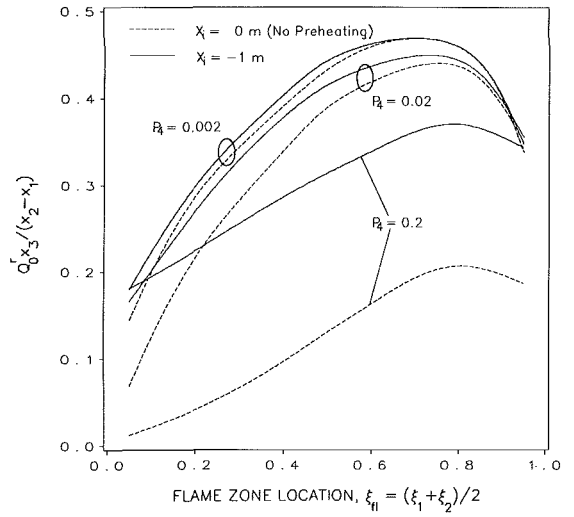

Fig. 7 Effect of P_4 on the radiative output; $P_1 = 0.01$, $P_2 = 500$, $P_3 = 2.5 \times 10^{-4}$, $P_5 = 5$, $\omega = 0.5$, $r_d = 0$, $\tau = 10$, $G_i = G_e = 2.98 \times 10^{-5}$

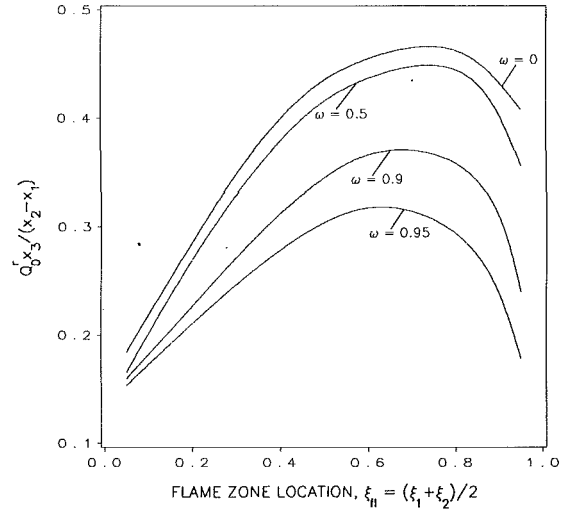

Fig. 8 Effect of the scattering albedo on the radiative output; $P_1 = 0.01$, $P_2 = 500$, $P_3 = 2.5 \times 10^{-4}$, $P_4 = 0.02$, $P_5 = 5$, $r_d = 0$, $\tau = 10$, $G_i = G_e = 2.98 \times 10^{-5}$

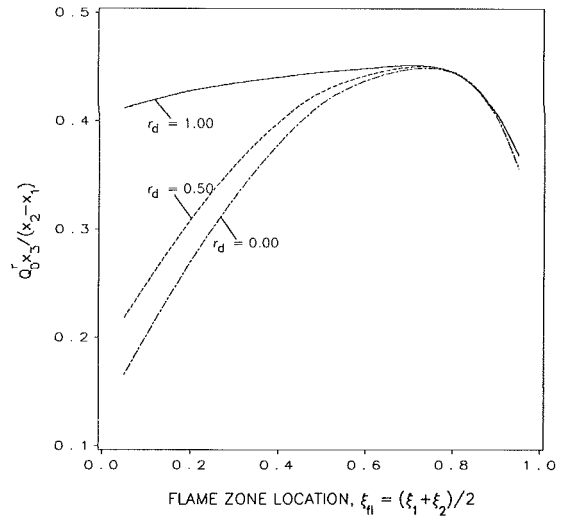

Fig. 9 Radiative output for different r_d; $P_1 = 0.01$, $P_2 = 500$, $P_3 = 2.5 \times 10^{-4}$, $P_4 = 0.02$, $P_5 = 5$, $\omega = 0.5$, $\tau = 10$, $G_i = G_e = 2.98 \times 10^{-5}$

tributions for different values of P_2. For large fibers, P_2 is small. Heat transfer between the gas phase and the solid phase is poor, resulting in gas temperatures significantly higher than the solid temperatures. This is undesirable from the standpoint of maximizing the radiant output and minimizing NO_x production. It is seen that when $P_2 \geq 100$ the two phases are quite close to local thermal equilibrium.

Figure 6 shows the distributions of the convective, conductive, and radiative heat fluxes. Gas conduction is almost negligible compared to the other modes of heat transfer. This supports the use of an adiabatic outflow boundary condition as discussed earlier. The results also reveal that the solid conductive flux is comparable in magnitude to the radiative flux. Since the value of P_4 (0.02) is representative of nonmetallic fibers, the results indicate that solid conduction should not be neglected in such an analysis. The convective flux is most predominant. This indicates that there is high potential for significant increase of the radiant output by converting more of the convective energy to radiative energy. This can be achieved by increasing P_2. For instance, the ratio of the radiative heat flux to the convective heat flux at $\xi = 1$ is seen to increase with an increase in P_2. However, the increase appears to be miminal once P_2 has reached 100. Therefore, further increase in the radiant output must be achieved by adjusting other parameters.

Combined Effect of P_4 and Preheating the Gas Before It Enters the Porous Segment. The effect of P_4 or solid conduction is shown in Fig. 7. Smaller P_4 results in higher radiant output because less energy is removed from the heat generation zone via solid conduction. It should be pointed out, however, that if actual combustion is considered, higher solid conduction may promote more effective preheating of the incoming gas, increasing the rate of combustion and hence, the radiant output. This remains to be determined. The dashed curves correspond to the case when $\xi_i = 0$. That is, the effect of preheating the incoming gas before it enters the porous segment is not taken into account. The radiant output is grossly underpredicted in many instances. The underprediction is greater for higher solid conduction and when the heat generation zone is closer to $\xi = 0$.

Effect of ω. Figure 8 shows the radiation scattering effects. A lower albedo results in a higher radiant output due to stronger emission by the solid. Thus a strong emitting-absorbing me-

dium is preferred for obtaining high radiant output. The results indicate that scattering of radiation is an important effect.

Effect of r_d. Reflection of radiant energy from the inlet environment has negligible effects if the heat generation zone is located in the downstream half of the porous segment, as seen in Fig. 9. However, if the heat generation zone is located in the upstream half of the porous segment, reflection affects the radiant output significantly. A higher reflectivity increases the radiant output from the burner since less radiative energy is lost in the upstream direction.

Conclusions

The heat transfer characteristics of PRBs have been studied using a multimode heat transfer model. The model accounted for nonlocal thermal equilibrium between the gas and solid phases of the porous layer, and radiation scattering by the solid. Preheating of the gas before it entered the porous layer was also allowed for. Heat generation was treated as a specified quantity. The spherical harmonics method was used to transform the equation of radiative transfer to a set of ordinary differential equations, which were numerically solved simultaneously with the energy equations.

It was found that gas conduction had a negligible effect on the radiant output of PRB. On the other hand, solid conduction and radiation scattering both exhibited considerable influence. Low solid conduction and low radiation scattering resulted in higher radiant output. The effect of preheating the gas before it entered the porous segment was significant for solids that had a high thermal conductivity. To maximize the output: P_1 (flow enthalpy) should be as small as possible without causing flashback to occur; P_2 (convection between the gas and solid) should be at least 100; the values of τ should be large enough for the porous segment to be optically thick.

Acknowledgments

The authors greatly appreciate the support of this work by the U.S. Department of Energy under contract number DE-FG02-87ER13697.

References

Chen, Y.-K., Matthews, R. D., and Howell, J. R., 1987, "The Effect of Radiation on the Structure of Premixed Flame Within a Highly Porous Inert Medium," *Radiation, Phase Change Heat Transfer, and Thermal Systems*, Y. Jaluria, V. P. Carey, W. A. Fiveland, and W. Yuen, eds., ASME HTD-Vol. 81, pp. 35–42.

Davison, B., and Sykes, J., 1957, *Neutron Transport Theory*, Oxford University Press, United Kingdom.

Echigo, R., 1982, "Effective Energy Conversion Method Between Gas Enthalpy and Thermal Radiation and Application to Industrial Furnaces," *Proceedings, 7th International Heat Transfer Conference*, Vol. 6, pp. 361–366.

Echigo, R., Yoshizawa, Y., Hanamura, K., and Tomimura, T., 1986, "Analytical and Experimental Studies on Radiative Propagation in Porous Media With Internal Heat Generation," *Proceedings, 8th International Heat Transfer Conference*, Vol. 2, pp. 827–832.

Gas Research Institute Digest, 1984, "Pyrocore-Radiant Burner With a Bright Future," Vol. 7, No. 4, pp. 4–9.

Incropera, F. P., and DeWitt, D. P., 1985, *Fundamentals of Heat and Mass Transfer*, Wiley, New York.

Menguc, M. P., and Viskanta, R., 1985, "Radiative Transfer in Three-Dimensional Rectangular Enclosures Containing Inhomogeneous, Anisotropically Scattering Media," *Journal of Quantitative Spectroscopy and Radiative Transfer*, Vol. 33, No. 6, pp. 533–549.

Ozisik, M. N., 1973, *Radiative Heat Transfer and Interactions With Conduction and Convection*, Wiley Interscience, New York.

Patankar, S. V., 1980, *Numerical Heat Transfer and Fluid Flow*, McGraw-Hill, New York.

Swathi, P. S., Tong, T. W., and Cunnington, G. R., Jr., 1987, "Reflectance of Two-Layer Composite Porous Media With Linear-Anisotropic Scattering," *Journal of Quantitative Spectroscopy and Radiative Transfer*, Vol. 38, No. 4, pp. 273–279.

Tong, T. W., Lin, W. Q., and Peck, R. E., 1987, "Radiative Heat Transfer in Porous Media With Spatially Dependent Heat Generation," *International Communications in Heat and Mass Transfer*, Vol. 14, No. 6, pp. 627–638.

Tong, T. W., and Sathe, S. B., 1988, "Heat Transfer Characteristics of Porous Radiant Burners," *Collected Papers in Heat Transfer*, K. T. Yang, ed., ASME HTD-Vol. 104, Vol. 3, pp. 147–155.

Wang, K. Y., and Tien, C. L., 1984, "Thermal Insulation in Flow Systems: Combined Radiation and Convection Through a Porous Segment," ASME JOURNAL OF HEAT TRANSFER, Vol. 106, pp. 453–459.

R. L. Billings

J. W. Barnes

J. R. Howell

O. E. Slotboom

Department of Mechanical Engineering,
The University of Texas,
Austin, TX 78712

Markov Analysis of Radiative Transfer in Specular Enclosures

This paper is directed at the use of Markov chains in the modeling of radiative heat transfer in specular enclosures containing nonparticipating gases. Following a brief review of previous literature in that area of investigation, a two-parameter state definition is given. The analysis of general infinitely long enclosures using that definition is then discussed, and the paper concludes with a report of selected implementation results.

Introduction

This paper presents a new method of analyzing radiative heat transfer using Markov chains, which have a two-parameter state definition. In the discussion below, this general method is specialized to the application of enclosures with specular surfaces and nonparticipating media. Because the concepts are so important to the following presentation, a brief summary of the fundamental properties associated with Markov chains is given below.

A variable whose numerical value is determined by the outcome of a random experiment is called a *random variable* and can be continuous or discrete in nature. A *stochastic process* describes a random phenomenon changing with respect to time and may be characterized as a set of random variables, $\mathbf{x}_t$, depending on the time parameter t, which may be continuous or discrete. For example, $\mathbf{x}_t$ may be the position of a fluid particle in a flow field or the reflecting point for the radiating energy bundle on an enclosure surface. Each observed point of time, t, is an *epoch*, and the possible values of $\mathbf{x}_t$ are called *states*. A record of observed $\mathbf{x}_t$'s over time is a *realization* of the process and each change of the state is called a state *transition*.

An ordinary *Markov chain* is a discrete time stochastic process, where

$$\text{Prob}\{\mathbf{x}_{n+1}|\mathbf{x}_n, \mathbf{x}_{n-1}, \mathbf{x}_{n-2},\ldots,\mathbf{x}_0\} = \text{Prob}\{\mathbf{x}_{n+1}|\mathbf{x}_n\} \quad (1)$$

In other words, the probability of each event in the chain is dependent only on the immediately preceding event and not on any other previous events. The term "chain" suggests this linking of the random variables only to their immediately adjacent neighbors in the sequence. An order-l multiple Markov chain (or l-dependent Markov chain) is a similar stochastic process in which the probability of each state depends on the outcome of its l immediate predecessors, or

$$\text{Prob}\{\mathbf{x}_{n+1}|\mathbf{x}_n, \mathbf{x}_{n-1}, \mathbf{x}_{n-2},\ldots,\mathbf{x}_0\} = \text{Prob}\{\mathbf{x}_{n+1}|\mathbf{x}_n, \mathbf{x}_{n-1}, \mathbf{x}_{n-2},\ldots,\mathbf{x}_{n-l}\} \quad (2)$$

The probability $\text{Prob}\{\mathbf{x}_{n+1}|\mathbf{x}_n\}$ is called the single step transition probability. For a time-homogeneous Markov Chain, these probabilities are time invariant and may be formed into a square *transition probability matrix*, $\mathbf{P}$, where $\mathbf{P} = \{P_{jk}\}$ and

$$P_{jk} = \text{Prob}\{\mathbf{x}_{n+1} = k | \mathbf{x}_n = j\} \quad (3)$$

The elements of each row of $\mathbf{P}$ sum to one and the state corresponding to each row is identical to the state corresponding to the same numbered column.

Brief Literature Review

This section gives a brief review of the published research, which focuses specifically on the analysis of radiative transfer in enclosures, especially those composed of specular surfaces. For a more comprehensive and in-depth discussion of the literature that touches on this subject, see the more extensive research report (Billings et al., 1990) from which this paper is drawn.

Eckert and Sparrow (1961) pioneered the angle factor method using mirror images for analyzing specular reflections. Sparrow et al. (1962) and Bobco (1964) extended those methods to enclosures made of specular and diffuse surfaces. Bevans and Edwards (1965) developed three approximation methods for directional wall properties. Sparrow and Lin (1965) and Sarofim and Hottel (1966) introduced enclosures made of surfaces each having specular and diffuse reflectance components. Schornhorst and Viskanta (1968) and Hering and Smith (1970) experimentally verified the accuracy of the purely diffuse model for most common surfaces. Rabl (1977) modeled radiative heat transfer through specular passages.

Another important method for analyzing radiative heat transfer in enclosures was the use of Monte Carlo simulation. Pioneered by Howell and Perlmutter (1964) and others, Monte Carlo simulation proved to be a very powerful tool. However, the comparatively large amount of computation time required for numerical accuracy made this method unattractive except for enclosures too complex to analyze by other methods and for validating the results of other methods.

Naraghi and Chung (1984) were the first to use Markov chains to analyze radiative transfer between surfaces in enclosures containing thermally transparent media. Surfaces were assumed to reflect diffusely and/or specularly and *multiple* Markov chains were used to model specular reflections. The objective in that paper was to determine the absorption factors matrix $\mathbf{B} = \{B_{ij}\}$ where B_{ij} is the fraction of emission of surface i that is eventually absorbed by surface j.

Naraghi and Chung first consider only diffuse reflectivities where the transition probability matrix may be obtained from the matrix of configuration factors, $\mathbf{F} = \{F_{ij}\}$, and two diagonal matrices that contain the absorptivities, $\mathbf{A} = \{\alpha_i\delta_{ij}\}$, and reflectivities, $\mathbf{R} = \{\rho_i\delta_{ij}\}$. F_{ij} is the fraction of energy leaving surface i that travels toward surface j and is *assumed* to be known. $B_{ij}^{(k)}$ denotes the probability that radiation emitted from surface i is absorbed by surface j in exactly k transitions. It may be shown that $\mathbf{B}^{(k)} = \{B_{ij}^{(k)}\} = (\mathbf{FR})^{k-1}\mathbf{FA}$. The absorption factors matrix, $\mathbf{B}$, is the sum of all $\mathbf{B}^{(k)}$ terms; therefore

$$\mathbf{B} = \sum_{k=1}^{\infty} \mathbf{B}^{(k)} = (\mathbf{I} - \mathbf{FR})^{-1}\mathbf{FA}.$$

After the consideration of diffuse surfaces, Naraghi and Chung allow some surfaces to reflect specularly. Since specular reflection is not independent of the incident angle with which energy reaches the surface, the Markovian property that is valid for diffuse surfaces is lost. However, a multiple Markov chain can approximate this case by considering h past reflec-

Contributed by the Heat Transfer Division for publication in the JOURNAL OF HEAT TRANSFER. Manuscript received by the Heat Transfer Division March 12, 1990; revision received August 13, 1990. Keywords: Enclosure Flows, Numerical Methods, Radiation.

tions. Let $\mathbf{B}$ be defined as the sum of h terms: $\mathbf{B}=\mathbf{B}^{(1)}+\mathbf{B}^{(2)}+\ldots+\mathbf{B}^{(h-1)}+\mathbf{B}^{(h+)}$ where $\mathbf{B}^{(k)}$ retains its earlier definition but is computed as follows (for $k<h$):

$$B_{ij}^{(k)}=\sum_{i_1,i_2,\ldots,i_{k-1}}\rho_{i_1}\rho_{i_2}\ldots\rho_{k-1}\alpha_j\text{Prob}\{x_0=i,\ x_1=i_1,\ x_2=i_2,\ldots,x_{k-1}=i_{k-1},\ x_k=j\} \quad (4)$$

This is a sum over all possible paths from i to j through $k-1$ intermediate points of reflection of the product of the reflectivities of the intermediate points, the absorptivity of the point of absorption, and the probability that the path is taken.

$\mathbf{B}^{(h+)}$ is the term that contributes the exchange due to h or more energy bundle movements (including specular reflections) and is what introduces the concept of multiple Markov chains. In order to compute the term $\mathbf{B}^{(h+)}$, the multiple Markov chain transition probability matrix, $\mathbf{P}=\{P_{(i_1,i_2,\ldots,i_h),(j_1,j_2,\ldots,j_h)}\}$, is defined. $\mathbf{P}$ is analogous to the single Markov chain transition probability matrix, $\mathbf{F}$. The size of the $\mathbf{P}$ matrix is on the order of the number of surface elements to the *power* of the number of reflection lags, and manipulating it can be quite demanding of computation time. The h-step reflection configuration factor $P_{(i_1,i_2,\ldots,i_h),(j_1,j_2,\ldots,j_h)}$ is only nonzero if $i_2,\ i_3,\ldots,i_h$ equal $j_1,j_2,\ldots,j_{h-1}$ and is generally very difficult to compute (as will be discussed later in the computational results). Absorptivity and reflectivity matrices are also defined in a similar way: $\mathbf{A}=\{\alpha_{jh}\,\delta_{(i_1,i_2,\ldots,i_h),(j_1,j_2,\ldots,j_h)}\}$ and $\mathbf{R}=\{\rho_{jh}\,\delta_{(i_1,i_2,\ldots,i_h),(j_1,j_2,\ldots,j_h)}\}$.

A diagonal matrix, $\mathbf{Q}=\{q_{(i_1,i_2,\ldots,i_h)}\,\delta_{(i_1,i_2,\ldots,i_h),(j_1,j_2,\ldots,j_h)}\}$, is used where $q_{(i_1,i_2,\ldots,i_h)}=\text{Prob}\{x_0=1,x_1=i_2,x_2=i_3,\ldots,x_h\}$ is the probability that a radiated energy bundle is not absorbed in states $x_0=i,\ x_1=i_2,\ x_2=i_3,\ldots,x_{h-1}=i_h$. The multiple Markov chain absorption factors matrix, $\mathbf{C}=\{C_{(i_1,i_2,\ldots,i_h),(j_1,j_2,\ldots,j_h)}\}=\mathbf{Q}(\mathbf{I}-\mathbf{PR})^{-1}\mathbf{PA}$ is analogous to the single Markov chain absorption factors matrix, $\mathbf{B}$. $\mathbf{C}$ can be collapsed into $\mathbf{B}^{(h+)}$ as follows:

$$B_{ij}^{(h+)}=\sum_{\substack{i_2,i_3,\ldots,i_h\\ \text{all}\ j_1,j_2,\ldots,j_{h-1}}}C_{(i,i_1,i_2,\ldots,i_h),(j_1,j_2,\ldots,j_h,j)} \quad (5)$$

Finally Naraghi and Chung address the case where each surface has a combination of diffuse and specular reflectivity, $\rho=\rho_d+\rho_s$, where ρ_d is the diffuse component of reflectivity and ρ_s is the specular component. This expands the state space and requires slightly different definitions for $\mathbf{B}^{(k)}$, $\mathbf{Q}$, and $\mathbf{P}$. Computational results of this hybrid diffuse-specular analysis as applied to an infinitely long triangular enclosure and to two infinitely long parallel strips are reported in the paper.

Naraghi and Chung found that $h=2$ gave results as good as or better than previously published approximations and very close to the exact solution. This should come as no surprise since two consecutive positions completely determine all future reflections in a specular enclosure. The only reason that the results improved for $h>2$ is that, since each side was treated as a whole, the only way to increase the "resolution" of energy transfer was to increase the number of reflections. Another reason that $h=2$ gave such good results is that the enclosures modeled had at most two or three nondiffuse surfaces.

Naraghi and Chung (1986) extended the analytical methods from the previous paper to enclosures with surfaces having directional emissivities, directional absorptivities, and bidirectional reflectivities. However, the bidirectional reflectivities modeled were only those that had a diffuse component and a deterministic bidirectional component. This analysis was applied to an infinitely long triangular enclosure and to two infinitely long parallel strips.

This paper extends Markov analysis of radiative transfer in enclosures in a different direction by using a two-parameter state definition consisting of energy bundle position and direction of travel. Immel et al. (1986) presented a radiosity method for producing computer-generated images that involved discretizing surfaces and directions to define matrix elements. However, that method was not probabilistic in its approach and was too computationally demanding to be of practical use.

Markov Chain Analysis Using a Two-Parameter State Definition

In an enclosure of diffuse surfaces containing a nonparticipating medium, the point at which an energy bundle impacts an enclosure surface is dependent only on the point from which it was last emitted or reflected and not on any other history. This simple dependency structure allows the radiative heat transfer in the enclosure to be easily modeled using the well-

Nomenclature

0 = matrix of zeros
$\mathbf{A}$ = diagonal absorptivity matrix
$\mathbf{B}$ = absorption factors matrix
$\mathbf{B}^{(k)}$ = k-step absorption factors matrix
$\mathbf{B}^{(l+)}$ = extended absorption factors matrix
$\mathbf{C}$ = multiple absorption factors matrix
$\mathbf{D}$ = emission distribution matrix
$\mathbf{E}$ = diagonal emissivity matrix
$\mathbf{F}$ = configuration factors matrix
h = number of energy bundle jumps
$\mathbf{I}$ = identity matrix
i = side index
j = discrete index corresponding to x
k = discrete index corresponding to ϕ
l = number of sides in enclosure
m = number of elements per side
n = number of angle ranges per element
$\mathbf{N}$ = fundamental matrix
$\mathbf{P}$ = Markov transition probability matrix
$\mathbf{Q}$ = path probability matrix
$\mathbf{q}$ = vector of net heat fluxes, W/m^2
$\mathbf{R}$ = diagonal reflectivity matrix
$\mathbf{S}$ = transition submatrix from emitting or reflecting states to absorbing states
$\mathbf{T}$ = transition submatrix for remaining in the class of emitting or reflecting states
$\mathbf{t}$ = vector of absolute fourth-power temperatures, K^4
$\mathbf{u}$ = vector of initial energy bundle distribution
$\mathbf{x}$ = random vector
x = distance counterclockwise along side, m
α = surface absorptivity
δ_{ij} = Kronecker delta (=1 if $i=j$ and 0 otherwise)
ρ = surface reflectivity
σ = Stefan–Boltzmann constant, W/m^{2}K^4
ϕ = angle measured counterclockwise from direction perpendicular to surface

Subscripts

d = diffuse
D = departure
I = incidence
n = Markov event sequence index
R = reflection
s = specular
t = time

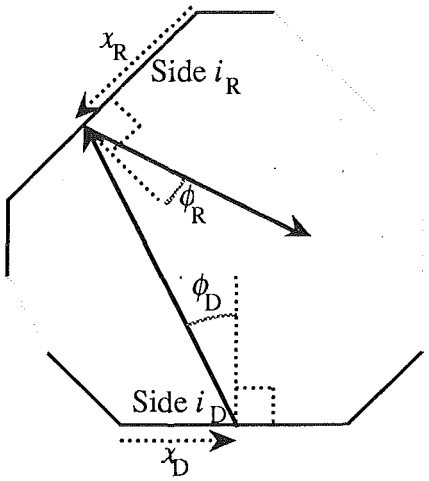

Fig. 1 General infinitely long enclosure

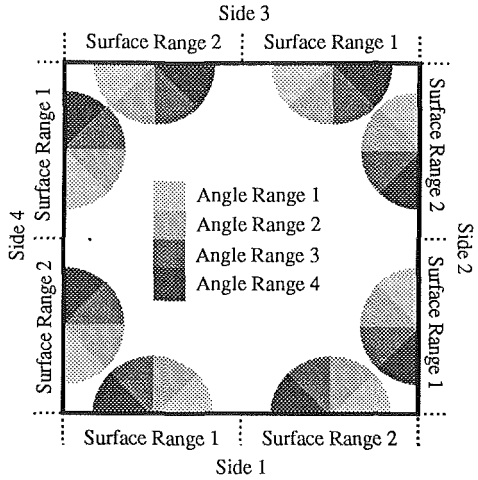

Fig. 2 Surface and angle discretization in the square cylinder

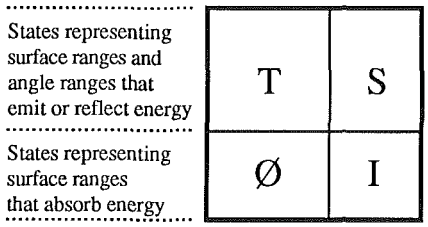

Fig. 3 The two-parameter transition probability matrix

known theory of Markov chains by defining a transition to be the movement of an energy bundle from one point of emission or reflection to the next point of reflection or absorption. For specular surfaces, however, that simple Markovian property no longer holds: The direction in which an energy bundle will travel is very much a function of its prior travels.

Naraghi and Chung (1984) attacked this problem by modeling the radiative transfer using a multiple Markov chain that considered h past reflections. However, except for special cases, that solution is only an approximation for h less than *infinity*. A better alternative is to redefine the states of the Markov chain to include not only the energy bundle's current position around the enclosure but also its direction of departure from that position. This two-parameter state definition completely recaptures the Markovian property, since a knowledge of a bundle's present location and angle of departure gives as complete a description of its future travel as does a knowledge of its possibly infinite number of past reflections.

As examples of Markov chain analysis using the two-parameter state definition, we have modeled an infinitely long enclosure, which has a cross section that is a regular convex polygon with an arbitrary number of sides. Such an enclosure allows all modeling to be done in two dimensions. We have specifically implemented a square cylinder and a triangular cylinder. In every case, all sides are of unit width, the enclosures do not contain participating media, the interior surfaces reflect specularly, and the initial distribution of energy bundle generation is uniformly diffuse emission along the bottom side. As illustrated in Fig. 1, the present state of the energy bundle is defined by the side i_D from which it is departing, its distance x_D across that side in a counterclockwise direction around the enclosure, and the angle ϕ_D at which it is departing. ϕ_D is in the plane of the cross section perpendicular to the axis of the enclosure and is measured counterclockwise from the direction perpendicular to surface i_D. Similarly, the next state of the energy bundle is defined by the side i_R that receives it next, the distance x_R of the point of impact across that side in a counterclockwise direction, and, if it is not absorbed, the angle ϕ_R at which it is reflected, measured in the same way as ϕ_D. Note that the coordinate system is not static; the absolute directions of x_D and x_R depend on which sides the energy bundle is leaving and approaching.

Although, in theory, this two-parameter description completely captures all pertinent knowledge of an energy bundle's past travels, in practice we must approximate that information by discretizing both parameters. To discretize the position of departure or impact in a *general* enclosure, we divide all of its surfaces into discrete planar elements. To discretize the direction of travel, we divide the unit hemisphere (which contains all possible angles of departure from a differential surface element) into discrete solid angle ranges. Specifically, for the kind of infinitely long enclosure modeled here with l sides, each side is divided into m surface range strips of equal width and at each surface range the unit semicircle is divided into n angle ranges. Figure 2 shows this discretization for a square cylinder in which each side has been divided into two surface ranges and the unit semicircle has been divided into four equal angle ranges. The discrete indices corresponding to the discrete surface and angle ranges associated with x_D, ϕ_D, x_R, and ϕ_R are j_D, k_D, j_R, and k_R, respectively.

The process for generating the transition probability matrix is discussed in detail in Appendix 1. In overview, the major steps of the process are as follows. Find every surface range j_R on every side i_R that can be seen from each surface range j_D on each side i_D when viewed through each angle range k_D. Compute the reflected angle range k_R. Compute the fraction of angle range k_D that impacts surface range j_R, multiply that fraction times ρ or α, and put the products into the appropriate elements of the transition probability matrix.

Shown in Fig. 3 is the canonical form (Ravindran et al., 1980) of the two-parameter state definition transition probability matrix. Here, the transition probability matrix is divided into four submatrices that define transitions between and among the two classes of states: absorbing and emitting/reflecting (or *transient* in Markov nomenclature). The transition submatrix for staying in the absorbing states is an identity matrix, and the transition submatrix for going from absorbing states to emitting/reflecting states is a matrix of zeros. The two remaining submatrices are **S**, the transition submatrix for going from emitting/reflecting states to absorbing states, and **T**, the transition submatrix for remaining in the class of emitting/reflecting states.

Let B_{ij} be the probability that an energy bundle that was emitted from emitting/reflecting state i finally ends up at absorbing state j. It is easily shown that $\mathbf{B} = \{B_{ij}\} = \mathbf{S} + \mathbf{TB} = (\mathbf{I} - \mathbf{T})^{-1}\mathbf{S}$. If the vector $\mathbf{u}$ contains the initial distribution of energy bundles in the emitting/reflecting states

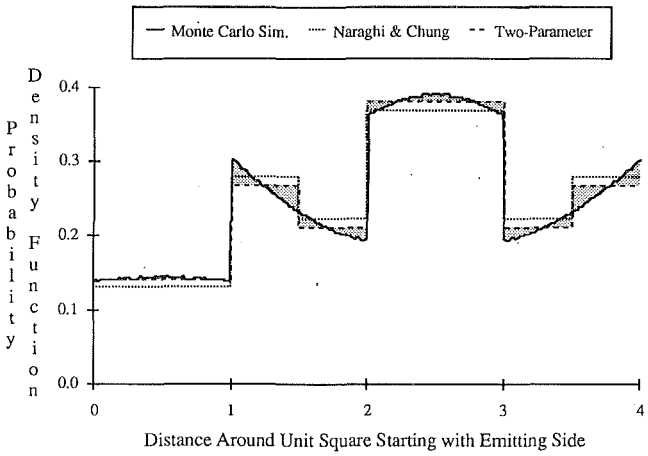

Fig. 4 Final absorption probability density for square cylinder

of the transition matrix, then the matrix product **uB** gives their ultimate distribution in the absorbing states. Note that **u** may contain any arbitrary initial emission distribution and need not be uniform over any side. **B** may also be used to relate the heat fluxes and temperatures by use of the equation $\mathbf{q} = \sigma \mathbf{t}\,\mathbf{E}(\mathbf{I} - \mathbf{D}\,\mathbf{B})$ where **q** is the vector of net heat fluxes at each surface range, **t** is the vector of surface range absolute temperatures to the fourth power, **E** is a diagonal matrix of emissivities at each surface range, and **D** is a matrix with the opposite dimensions as **B** such that when **D** is multiplied by **B** the resulting product is a square matrix of the order of the total number of surface ranges. **D** is a block-diagonal matrix where each block has only one row, and the elements of each block sum to one and represent the initial distribution of emission into all of the angle ranges at each surface range, similar to the vector **u**. Note that the heat fluxes, temperatures, or initial emission distributions do not need to be specified until after **B** has been computed. This ability to reuse the **B** matrix makes the Markov analysis superior to Monte Carlo since a new Monte Carlo simulation must be run for each change in heat fluxes, temperatures, or initial emission distributions. This benefit of Markov analysis could be quite useful for modeling heat flux and temperature transients.

Computational Results

The theory presented in the previous two sections has been implemented using VaxFORTRAN 4.0 on a DEC VaxStation 3200. The program models infinitely long enclosures where the number of enclosure sides, the reflectivity of each side, the number of surface ranges per side, the number of angle ranges, and the initial distribution of energy bundles are input parameters. Additional parameters govern the angle range spacing, the distribution of outgoing radiation within each angle range, and the distribution of outgoing radiation across each surface range. Two programs were also written to validate the results of the two-parameter Markov analysis. The first program models the square cylinder or the triangular cylinder using direct Monte Carlo simulation. As detailed in Appendix 2, the second program models the specular reflections in only the square cylinder using a large analytical summation of reflection terms. For comparison with the two-parameter model, the method of Naraghi and Chung (1984) was also implemented for $h = 2$ and $h = 3$ and was *extended* to use more than one surface range per side.

The output of each of these programs is a distribution of the final resting place of energy bundles around the enclosure in the form of discrete probabilities of final absorption at each surface range. In order to compare results for different numbers of surface ranges per side, these discrete probabilities are converted to a piecewise-uniform probability density function. Figure 4 shows three such probability density functions generated by three different methods of analysis for a square cylinder enclosure when the reflectivity of all sides was 0.5, and diffuse bundle generation was uniformly distributed across the bottom side only. The output of the two-parameter state definition method is given for the case where ten equal angle ranges were used per surface range. In addition, the significantly less accurate results for the method of Naraghi and Chung (1984) are given for the case where $h = 2$. For both of these methods, two surface ranges were used per side. Also shown is the nearly continuous probability density function output by the Monte Carlo simulation. Note that if the analytical summation results were presented here, they would be virtually indistinguishable from those of the Monte Carlo simulation.

As is indicated by the simulation results in Fig. 4, the "true" theoretical distribution of energy bundle absorption is continuous. The simulation results given in Fig. 4 are a close approximation to that theoretical distribution and were achieved by simulating ten million energy bundles and using 2520 surface ranges per side, but aggregated into 60 data points per side for the figure. A more accurate and more efficient approximation to the continuous distribution around the square cylinder was achieved by using the analytical summation method discussed in Appendix 2, also with 2520 surface ranges per side.

A method was needed to measure how accurately the results from the two-parameter Markov analysis compared with the theoretical distribution. For simplicity, the accuracy measure needed to be expressed in a single number and needed to allow direct comparisons between analyses using different numbers of surface and angle ranges. One method that satisfies these criteria is the Integrated Absolute Density Difference (IADD). The IADD error is one-half of the integral of the absolute difference between the probability density function generated by any method of analysis and an approximation to the theoretical density function. The results of the analytical summation method were used for this approximation for rectangular enclosures. For nonrectangular enclosures, the Monte Carlo simulation results were used and were assumed to be correct and accurate. The IADD error ranges between zero and one. For example, the IADD error of the two-parameter method results given in Fig. 4 is one-half of the area shown in gray. For any given number of surface ranges per side, there is an inherent IADD error due to the discretization of the surfaces. Also, the experimental error due to the variability of the Monte Carlo simulation output can slightly increase the IADD error. For that reason, the more accurate approximation to the continuous distribution produced by the analytical summation method (as discussed in Appendix 2) was used in the results that follow.

Figures 5–8 show the IADD error versus CPU time for the specular square cylinder where all sides have a reflectivity of 0.5, 0.7, 0.9, and 0.95, respectively, and diffuse energy bundle generation was uniformly distributed across the bottom side only. Shown in each figure is a curve for the two-parameter method when one through six surface ranges were used per side. For these results, energy bundles were assumed to leave from points distributed uniformly across the surface range and radiation within each angle range was assumed to be diffuse. These assumptions are discussed in detail in Appendix 1. In addition, each figure shows only the results for a constant setting of ten equal angle ranges for each surface range.

Below this curve in each figure is another curve showing the inherent error for that number of surface ranges per side. Note that for higher reflectivities, these two curves appear flat for increasing numbers of surface ranges. The reason for this is that as the reflectivity approaches unity, the absorption probability density function approaches a constant over each side, as shown in Fig. 9. Thus, using more surface ranges per side

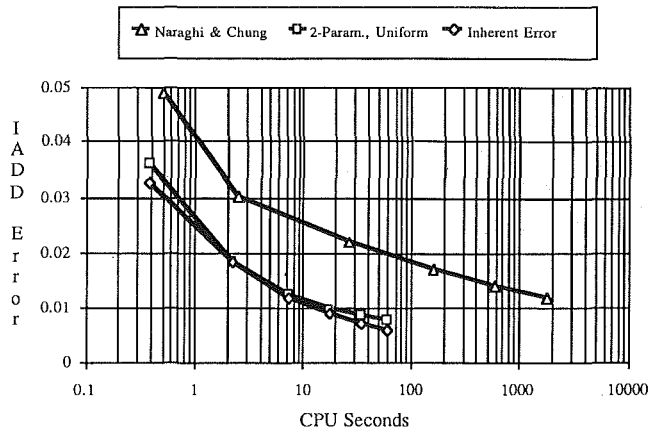

Fig. 5 Error versus CPU time for square cylinder with 0.5 reflectivity

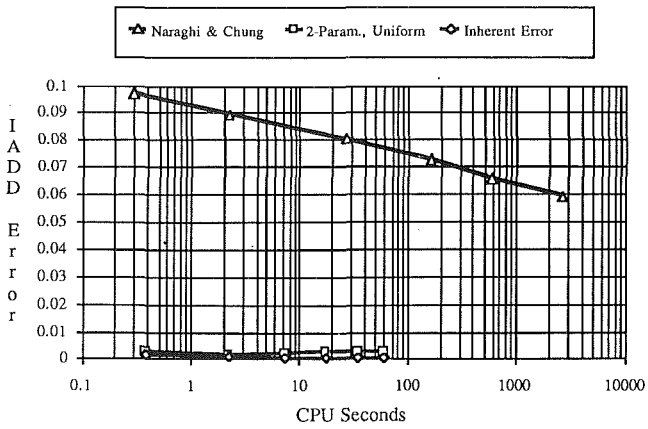

Fig. 7 Error versus CPU time for square cylinder with 0.9 reflectivity

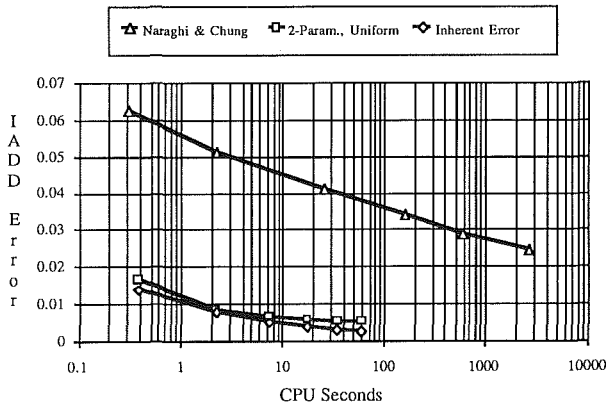

Fig. 6 Error versus CPU time for square cylinder with 0.7 reflectivity

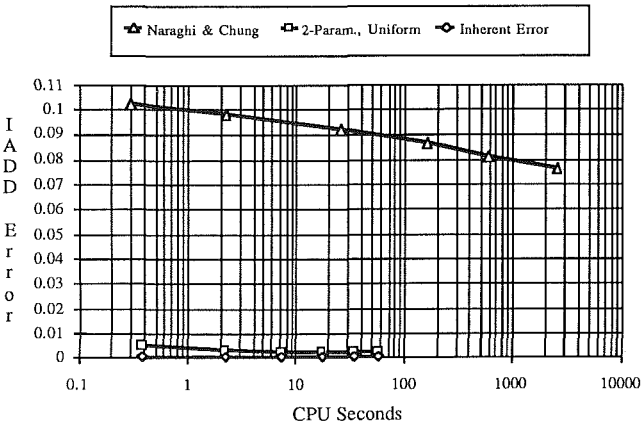

Fig. 8 Error versus CPU time for square cylinder with 0.95 reflectivity

produces only marginally better accuracy. Note that for $\rho \to 1$, the probability density in Fig. 9 was derived from the angular distribution of diffuse emission from the bottom side, which remains constant as the angular distribution of energy bundle paths in a perfectly reflecting rectangular specular enclosure. For $\rho = 0$, the probability density is just a continuous set of the configuration factors between the diffusely emitting side and differential strip elements on the other surfaces. The curves for the other reflectivities were given by the analytical summation method.

Also shown in Figs. 5–8 are the results of the method of Naraghi and Chung (1984) for the $h = 2$ case when one through six surface ranges were used per side. Note that the time axis is logarithmic. Although the method of Naraghi and Chung gives increasingly better results as more surface ranges are used, it does so at a tremendous cost of computation time. This is because the size of the associated **P** matrix that must be inverted is on the order of the number of surface elements to the *power* of the number of reflection lags. In the two-parameter method, the size of the **I**–**T** matrix that must be inverted is on the order of the number of surface elements *times* the number of angle ranges. The vast majority of the CPU time required by either method is devoted to inverting the respective matrices. Note that although Figs. 5–8 show the results of the two-parameter method for the fixed number of ten angle ranges, the CPU time and accuracy increased when either the number of surface ranges or the number of angle ranges increased.

For higher reflectivities, the method of Naraghi and Chung with $h = 2$ gives increasingly worse results because the fraction of energy bundles that is absorbed in zero or one reflections becomes smaller and smaller, and the approximation becomes less and less valid. Increasing h to account for more reflections is not practical because of the inherent difficulty of computing

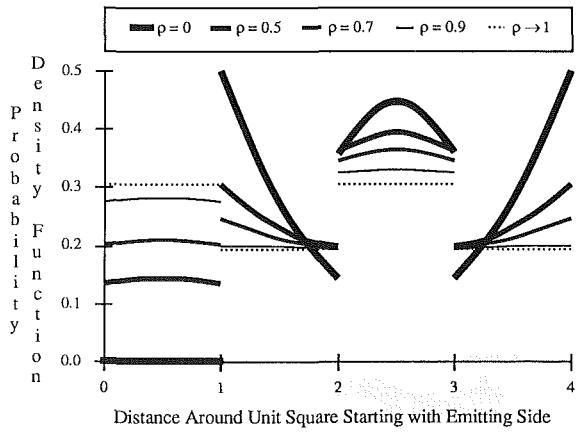

Fig. 9 PDFs for different reflectivities

the elements of the multiple Markov chain transition probability matrix **P**. Even for $h = 2$, these reflection configuration factor expressions were so complicated that each one was computed by hand. For that reason, the effort required to perform these computations is *not* reflected in Figs. 5–8. If it were, the curves for Naraghi and Chung would be shifted to the right. The $h = 3$ case was attempted for only one surface range per side because of the combinatorial explosion of the number of values that had to be computed. Part of the difficulty of computing these configuration factor elements is due to the fact that the states of the **P** matrix are an ordered set of surface ranges. The probability computations required by the analytical sum method discussed in Appendix 2 are much simpler because they only require a knowledge of which sides were used for reflections, not the order in which the reflections

occurred (as required by the method of Naraghi and Chung).

When the two-parameter method was applied to an infinitely long triangular enclosure, the results were very similar to those for the square cylinder.

Conclusion

The computational results presented here demonstrate that the two-state Markov chain method is a superior technique for modeling specular reflection in enclosures. Even for small numbers of angle ranges and surface ranges, the method gave good results. The best results were given when equal angle ranges were used, radiation within each angle range was assumed to be diffuse, and energy was assumed to radiate from points distributed uniformly across each surface range (as discussed in Appendix 1), although the alternatives to each of these choices did not give markedly worse results. Much more information about the physical heat transfer process can also be provided from the transition probability matrix using the wealth of existing Markov theory results. For example, the mean and variance of the number of times an energy bundle passes through any given state before being absorbed can be calculated (Kemeny and Snell, 1960). Also, the ability to reuse one computed **B** matrix for any number of combinations of heat fluxes, temperatures, and initial emission distributions makes the Markov analysis method superior to Monte Carlo and quite useful for modeling heat flux and temperature transients.

Current investigations indicate that small extensions of the methods presented in this paper show great promise in the analysis of enclosures with sides having general bidirectional reflectivities. The transition probability matrices would have the same states as for specular enclosures and computing the probabilities that form that matrix is straightforward if the bidirectional reflectivity function is tractable.

Future research will also be directed at extending and broadening the application of Markov chains with a two-parameter state definition to the analysis of radiative transfer in enclosures. Specifically, finite three-dimensional enclosures will be modeled. It is our expectation that three dimensions will increase the complexity of the analysis. This added complexity will present larger but not insurmountable obstacles in such considerations as the calculation of fractions of emission, the subdivision of solid angles, and the manipulation of significantly larger matrix sizes. More general conditions will also be studied such as probabilistic anisotropically scattering media, thermal nonequilibrium, and transient temperature profiles.

Acknowledgments

The research reported in this paper was funded by the Texas Higher Education Coordinating Board Advanced Research Program.

References

Bevans, J. T., and Edwards, D. K., 1965, "Radiation Exchange in an Enclosure With Directional Wall Properties," ASME JOURNAL OF HEAT TRANSFER, Vol. 87, No. 3, pp. 388–396.

Billings, R. L., Barnes, J. W., Howell, J. R., and Singh, S. K., 1989, "Using Markov Chains to Analyze Thermal Radiation Heat Transfer in Participating Media," presented at the Joint National Meeting of the Canadian Operations Research Society, the Institute for Management Science and the Operations Research Society of America, May.

Billings, R. L., Barnes, J. W., Howell, J. R., Singh, S. K., and Slotboom, O. E., 1990, "Using Markov Chains to Analyze Thermal Radiation Heat Transfer in Enclosures," *Working Papers in Operations Research*, ORP90-03, University of Texas.

Bobco, R. P., 1964, "Radiative Heat Transfer in Semigray Enclosures With Specularly and Diffusely Reflecting Surfaces," ASME JOURNAL OF HEAT TRANSFER, Vol. 86, No. 1, pp. 123–130.

Deissler, R. G., 1984, "Diffusion Approximation for Thermal Radiation in Gases With Jump Boundary Condition," ASME JOURNAL OF HEAT TRANSFER, Vol. 86, pp. 240–246.

Eckert, E. R. G., and Sparrow, E. M., 1961, "Radiative Heat Exchange Between Surfaces With Specular Reflection," *International Journal of Heat and Mass Transfer*, Vol. 3, No. 1, pp. 42–54.

Hering, R. G., and Smith, T. F., 1970, "Surface Roughness Effects on Radiant Transfer Between Surfaces," *International Journal of Heat and Mass Transfer*, Vol. 13, No. 4, pp. 725–739.

Hottel, H. C., and Sarofim, A., 1967, *Radiative Transfer*, McGraw-Hill, New York.

Howell, J. R., and Perlmutter, M., 1964, "Monte Carlo Solution of Thermal Transfer Through Radiant Media Between Gray Walls," ASME JOURNAL OF HEAT TRANSFER, Vol. 86, pp. 116–122.

Immel, D. S., Cohen, M. F., and Greenberg, D. P., 1962, "A Radiosity Method for Non-diffuse Environments," *Computer Graphics*, Proceedings of SIGGRAPH '86, Dallas, TX, Aug. 18–22, pp. 133–142.

Kemeny, J. G., and Snell, J. L., 1960, *Finite Markov Chains*, Van Nostrand, New York, 1960.

Naraghi, M. H. N., 1984, "A Stochastic Approach for Radiative Exchange in Enclosures," Ph.D. Dissertation, Department of Mechanical Engineering, University of Akron, Akron, OH, May.

Naraghi, M. H. N., and Chung, B. T. F., 1984, "A Stochastic Approach for Radiative Exchange in Enclosures With Nonparticipating Medium," ASME JOURNAL OF HEAT TRANSFER, Vol. 106, pp. 690–698.

Naraghi, M. H. N., Chung, B. T. F., 1986, "A Stochastic Approach for Radiative Exchange in Enclosures With Directional-Bidirectional Properties," ASME JOURNAL OF HEAT TRANSFER, Vol. 108, pp. 264–270.

Rabl, A., 1977, "Radiation Transfer Through Specular Passages—A Simple Approximation," *International Journal of Heat and Mass Transfer*, Vol. 20, No. 4, pp. 323–330.

Ravindran, A., Phillips, D. T., and Solberg, J. J., 1980, *Operations Research: Principles and Practice*, 2nd ed., Wiley, New York.

Sarofim, A. F., and Hottel, H. C., 1966, "Radiative Exchange Among Non-Lambert Surfaces," ASME JOURNAL OF HEAT TRANSFER, Vol. 88, No. 1, pp. 37–44.

Schornhorst, J. R., and Viskanta, R., 1968, "An Experimental Examination of the Validity of the Commonly Used Methods of Radiant Heat Transfer Analysis," ASME JOURNAL OF HEAT TRANSFER, Vol. 90, No. 4, pp. 429–436.

Siegel, R. and Howell, J. R., 1981, *Thermal Radiation Heat Transfer*, 2nd ed., Hemisphere Publishing Corp., New York.

Sparrow, E. M., Eckert, E. R. G., and Jonsson, V. K., 1962, "An Enclosure Theory for Radiative Exchange Between Specularly and Diffusely Reflecting Surfaces," ASME JOURNAL OF HEAT TRANSFER, Vol. 84, No. 4, pp. 294–300.

Sparrow, E. M., and Lin, S. L., 1965, "Radiative Heat Transfer at a Surface Having Both Specular and Diffusive Reflectance Components," *International Journal of Heat and Mass Transfer*, Vol. 8, No. 5, pp. 769–779.

APPENDIX 1

Methods for Computing Transition Probability Matrix

This appendix describes the methods used to compute the nonzero transition probability matrix elements. Readers desiring more detail on these methods are referred to Billings et al. (1990) who give a step-by-step description including thoroughly annotated source code.

In general, matrix elements are generated as follows. For each sending surface range j_D and angle range k_D on side i_D, there is at least one receiving surface range, j_R on side i_R, which can be viewed by j_D through k_D. Because the surfaces are specular, the reflected angle range, k_R can be easily determined from the sending angle range and side. In fact, there is a one-to-one mapping between k_D and k_R when all angle ranges are of equal size and the number of angle ranges is an even number for the square cylinder or is a multiple of three for the equilateral triangular cylinder. For this reason, results were slightly less accurate when unequal angle ranges based on equal increments of diffuse emission were used. For other numbers of angle ranges, k_R can be found by the following process. Find the angle ϕ_D that points from reflected angle $\phi_R = \pi[2(i_R - i_D/l \pm 1] - \phi_D$. Find the angle range k_R that contains ϕ_R.

The element of the transition probability submatrix **T** corresponding to present state (i_D, j_D, k_D) and next reflecting state (i_R, j_R, k_R) is the fraction of angle range k_D that impacts surface range j_R multiplied by the reflectivity ρ_{i_R}. Similarly, the element of the transition probability submatrix **S** corresponding to present state (i_D, j_D, k_D) and next absorbing state (i_R, j_R) is the fraction of angle range k_D that impacts surface range j_R multiplied by the absorptivity α_{i_R}.

One difficulty in computing the fraction of angle range k_D at surface range j_D that impacts surface range j_R is that the origin and direction of radiation incident on surface range j_D is unknown. Thus, the distribution of the points of reflection of energy bundles from surface range j_D and the distribution of the angles of departure are also unknown. However, assumptions about both distributions may be made with good results.

Two alternative distributions have been assumed for the direction of departure of energy bundles within each angle range, and both are based on the uniform distributions as the distribution of ignorance. The first simplistically assumes that the *angles* of departure are distributed uniformly across each angle range. The second and better assumption is that the *sources* of radiation incident on surface range j_D are distributed continuously and uniformly around the unit semicircle. The result is that the angles have the same distribution as diffuse emission within each angle range.

Two alternative distributions have also been assumed for the points of departure of energy bundles from surface range j_D. The first assumes that all energy bundles emitted or reflected from surface range j_D leave from points distributed uniformly across that surface range. The second assumes that all energy bundles leave from the centroid of the surface range. Computing the fraction in the second method is a simple process of subtracting angles. While the first method is theoretically more correct, it is more complex because integrals must be taken across surface range j_D and angle range k_D to find the fraction of angle range k_D that impacts surface range j_R. The limits on the integral over angle range k_D are not constant since the viewing angle to the boundaries of surface range j_R changes as one sweeps across surface range j_D, so the viewing angle may move in or out of angle range k_D. There are closed-form solutions to all the integrals, but they are not simple. This first method gives slightly more accurate results than the second, but it may not be as computationally attractive for modeling participating media or other enclosure geometries.

For example, consider again a square cylinder in which each side has been divided into two surface ranges the unit semicircle has been divided into four equal angle ranges, and radiation within each angle range is diffuse. Since there is an even number of equal angle ranges, the reflected angle range on a given side after a given number of reflections is completely predicted by the emitting angle range. Figure 10 shows the fraction of surface range 2 on side 2 that is seen by surface range 1 on side 1 when viewed through angle range 2. As shown in Fig. 10(*a*), from the left end of surface range 1, none of the other surface ranges can be seen. Figure 10(*c*) shows that from the right end of surface range 1, all of the other surface ranges can be seen. Reflection from surface range 2 on side 2 will be in angle range 1.

If all energy bundles leave from the centroid of surface range 1, as in Fig. 10(*b*), and radiation within the angle range is diffuse, then the nonzero element of the transition probability submatrix $\mathbf{T}$, $T_{(i_D,j_D,k_D),(i_R,j_R,k_R)}$, is

$$T_{(1,1,2),(2,2,1)} = \frac{\sin\left[\arctan\left(-\frac{3}{4}\right)\right] - \sin\left(-\frac{\pi}{4}\right)}{\sin(0) - \sin\left(-\frac{\pi}{4}\right)} \rho_2 \tag{6a}$$

$$= \left[1 - \frac{3\sqrt{2}}{5}\right]\rho_2 = 0.1515\rho_2 \tag{6b}$$

If the point of departure of the energy bundles is distributed uniformly across surface range 1, and radiation within the angle range is diffuse, then the fraction must be computed with the following integral:

$$T_{(1,1,2),(2,2,1)} = \frac{2\rho_2 \int_0^{0.5} \int_{-\pi/4}^{\arctan(x-1)} \frac{\cos(\phi_D)}{2}\, d\phi_D\, dx_D}{\frac{1}{2}\left[\sin(0) - \sin\left(-\frac{\pi}{4}\right)\right]} \tag{7a}$$

$$= [\sqrt{10} - 3]\rho_2 = 0.1623\rho_2 \tag{7b}$$

APPENDIX 2

Analytical Summation Method

Specular reflections in the square cylinder were modeled directly using a large analytical summation of reflection terms. A side can see a surface range in any number of reflections (three are shown in Fig. 11). If one sums up the view factors to each of these reflections, multiplied by the absorptivity of

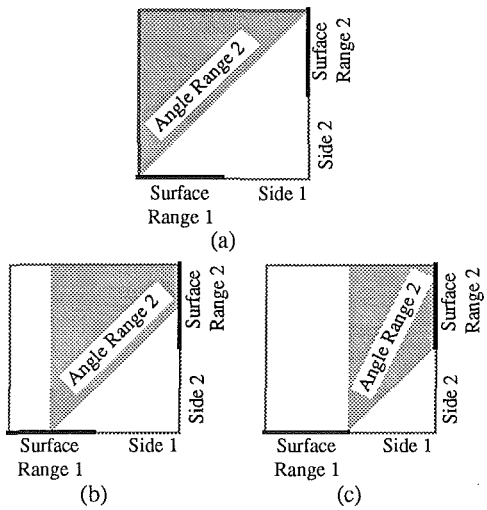

Fig. 10 Transition probability matrix computation

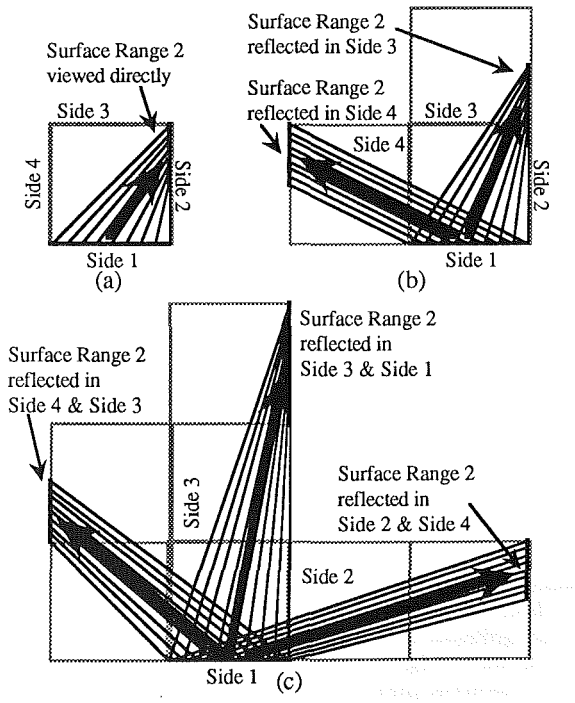

Fig. 11 Analytical sum reflections

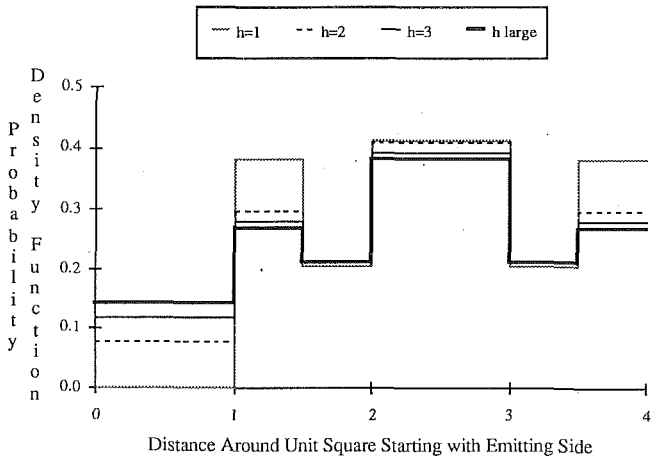

Fig. 12 Analytical sum PDF convergence

that receiving surface and the reflectivity of any surfaces in which that receiving surface is reflected, the final distribution would result. This is an infinite sum, but only a few reflections need to be considered for a relatively accurate result. Such analytical summations have been used before, but not with sides divided into surface ranges. From a practical point of view, this method is applicable only to infinitely long enclosures of rectangular cross section. Fortunately, it provides a useful validation tool for our current purpose.

Figure 11 shows an example of the configuration factors needed by the first three summation terms for the probability that diffuse emission from side 1 is absorbed in the second of two surface ranges on side 2. Figure 11(*a*) shows the real surface range viewed in the first term ($h=1$, i.e., no reflections). Fig. 11(*b*) shows the two reflected images viewed in the second term ($h=2$, i.e., one reflection), and Fig. 11(*c*) shows the three reflected images viewed in the third term ($h=3$, i.e., two reflections).

The actual summation for this case is

$$\text{Prob}\left\{\begin{array}{c|c}\text{Absorbed in surface range 2 on side 2} & \text{Diffusely emitted from side 1}\end{array}\right\}$$

$$=\sum_{h=1}^{\infty}\sum_{j=1}^{h}\left\{\rho_2^{\left[\frac{h-j}{2}\right]}\rho_4^{\left[\frac{h+1-j}{2}\right]}\rho_1^{\left[\frac{j-1}{2}\right]}\rho_3^{\left[\frac{j}{2}\right]}\right. \tag{8a}$$

$$\left.\cdot(1-\rho_2)\,F[h+1-j,\,j,\quad 1+\text{Mod}(j,\,2)]\right\} \tag{8b}$$

where Mod(a, b) is the modulo of a over b, [x] is the greatest integer less than or equal to x, and

$$F[i,\,j,\,k]=\frac{1}{2}\left\{\sqrt{\left(j-1+\frac{k-1}{2}\right)^2+i^2}\right.$$

$$\left.+\sqrt{\left(j-1+\frac{k}{2}\right)^2+(i-1)^2}\right. \tag{9a}$$

$$\left.-\sqrt{\left(j-1+\frac{k}{2}\right)^2+i^2}-\sqrt{\left(j-1+\frac{k-1}{2}\right)^2+(i-1)^2}\right\} \tag{9b}$$

Figure 12 shows the resulting probability density functions when h equals one through three and for h sufficiently large to show the convergence value. The enclosure was a square cylinder with two surface ranges used per side and the reflectivity of all sides equal to 0.5. The results for "h large" have been previously presented in Fig. 4.

Infrared Radiation Statistics of Nonluminous Turbulent Diffusion Flames

M. E. Kounalakis
Research Assistant.

Y. R. Sivathanu[1]
Research Assistant.

G. M. Faeth
A. B. Modine Professor.
Fellow ASME

Department of Aerospace Engineering,
The University of Michigan,
Ann Arbor, MI 48109-2140

Mixture fraction and radiation statistics were studied for radiation paths through turbulent carbon monoxide/hydrogen diffusion flames burning in still air. Measurements included Mie scattering for mixture fraction statistics and fast-response infrared spectroscopy for radiation statistics. Measured mixture fraction statistics also were used to predict radiation statistics based on stochastic time series methods, the laminar flamelet approximation, and a narrow-band radiation model. Measured intensities of radiation fluctuations were in the range 10–40 percent, which causes mean radiation levels to be 1.1–4.2 times larger than estimates based on mean scalar properties in the flames. In contrast, stochastic predictions of mean and fluctuating radiation properties were generally in excellent agreement with measurements. An exception was the temporal integral scales of radiation fluctuations, where differential diffusion errors of the Mie scattering measurements were identified as the source of the discrepancies.

Introduction

Turbulence/radiation interactions within diffusion flames cause mean radiation levels to be biased upward (often by factors of 2–3) from levels based on mean scalar property distributions within the flames, and also cause flame radiation to fluctuate similar to other properties of turbulent flames. During the present study, these phenomena were studied both theoretically and experimentally for infrared gas band radiation from nonluminous turbulent jet diffusion flames. The objective was to determine whether stochastic simulations of mixture fraction distributions along radiation paths through the flame—combined with use of the laminar flamelet approximation to relate all scalar properties to mixture fraction and a narrow-band radiation model—could treat biasing of mean radiation levels and provide a means of finding other statistical properties of nonluminous flame radiation.

Markstein (1981) and Porscht (1974) report early observations of radiation fluctuations from turbulent diffusion flames. Subsequent studies established that biasing of mean radiation levels by turbulence/radiation interactions can be avoided by finding the radiation properties of realizations of the scalar field first, and then averaging them (see Fischer et al., 1987, Gore et al., 1987, Grosshandler and Joulain, 1986, Kounalakis et al., 1988, 1989, Sivathanu et al., 1990, and references cited therein). This procedure is particularly tractable when the laminar flamelet approximation of turbulent diffusion flames can be adopted, since only realizations of the mixture fraction field must be simulated because all other scalar properties are solely functions of mixture fraction and can be found from their state relationships (Bilger, 1977: Faeth and Samuelsen, 1986). Past studies have generally either prescribed scalar properties or used turbulence models to simulate scalar properties in this way (see Gore et al., 1987, Grosshandler and Joulain, 1986, Kounalakis et al., 1988, 1989, and references cited therein).

While earlier work suggests the feasibility of stochastic simulations of mixture fraction distributions to treat flame radiation properties, assessments of the methodology involve uncertainties of turbulence models to find scalar properties and ad hoc features of the simulations needed to estimate probability density functions (PDF's) and correlations of mixture fractions. Thus, the objectives of the present investigation were to measure mixture fraction statistics directly, to use the measured mixture fraction statistics to compute radiation statistics employing statistical time-series methods, to measure radiation statistics, and to compare predictions and measurements. The study was limited to turbulent round jet diffusion flames of carbon monoxide/hydrogen mixtures burning in still air, because these reactants have fast chemistry and generally satisfy the laminar flamelet approximation (Faeth and Samuelsen, 1986; Gore et al., 1987). Radiation measurements involved the 2700 and 4300 nm gas bands of carbon dioxide and water vapor, to provide optically thin and thick conditions, respectively.

The paper begins with discussions of experimental and theoretical methods. Measured mixture fraction statistics are then discussed, including moments, PDFs, and spatial and temporal correlations. The paper concludes with examination of predicted and measured radiant emission properties, considering moments, PDFs, and temporal power spectral densities of spectral radiation intensities for horizontal paths through the axes of the test flames. The following discussion is brief; additional details and a complete tabulation of data can be found from Kounalakis (1990).

Experimental Methods

Apparatus. The test apparatus involved turbulent round jet diffusion flames injected vertically upward from a water-cooled burner in still air. The burner consisted of a 7-mm-dia passage, 40 passage diameter long, to yield nearly fully developed turbulent pipe flow at the exit. The fuel gas was primarily carbon monoxide, but hydrogen (roughly 2 and 20 percent on mass and molal bases, respectively) was added to the carbon monoxide so that the flames attached naturally at the burner exit.

The burner operated within a screened enclosure to reduce effects of room disturbances. Instrumentation was mounted rigidly; therefore, the entire enclosure could be traversed horizontally (5 μm positioning accuracy) with a stepping-motor-driven linear positioner, and the burner height within the enclosure could be varied (0.6 mm positioning accuracy) using a manual linear positioner, in order to access various points

[1]Current address: Research Fellow, Department of Mechanical Engineering, University of Maryland, Baltimore County, MD.

Contributed by the Heat Transfer Division and presented at the Joint ASME/JSME Thermal Engineering Conference, Reno, Nevada, March 1990. Manuscript received by the Heat Transfer Division June 21, 1990; revision received October 29, 1990. Keywords: Combustion, Radiation Interactions, Turbulence.

within the flames. Exhaust products were removed through a metal hood at the top of the enclosure, with a blower and bypass system adjusting the exhaust flow rate to minimize disturbances of the test flames.

Mixture Fraction Measurements. Measurements of mixture fraction statistics employed Mie scattering, along the lines of Becker et al. (1967), Ebrahimi and Kleine (1977), Kennedy and Kent (1981) and Stårner and Bilger (1981, 1983). This involves seeding the fuel stream with small particles and collecting light scattered from a laser beam by the particles. Aluminum oxide particles having a nominal diameter of 400 nm were used to seed the fuel stream. The particles were added to the fuel gas using a reverse cyclone seeder similar to that of Glass and Kennedy (1977). The gas jet into the seeder had a velocity of 70 m/s, which provided initial particle densities of roughly 1750 particles per mm^3.

The particle scattering signal was provided by the beam from an unfocused cw argon-ion laser operating with 500 mW of optical power at 488 nm (Coherent Innova 90-4 with a 1.5 mm beam diameter to the e^{-2} points). The laser beam passed horizontally through the flame axis along the same paths as the radiation measurements. The scattered light was measured by two detectors: one mounted rigidly and the other traversable along the laser beam with a 0.1 mm positioning accuracy. Combined with burner traversing, this arrangement allowed two-point measurements throughout the flames. The scattering signals were observed at right angles to the laser beam with collecting lens systems having diameters of 80 mm and focal lengths of 165 mm. The apertures of the detectors were selected to give measuring volume diameters and lengths of 1.0 and 1.5 mm. The detectors were photomultipliers (Hamamatsu, Model R268) with laser line filters (10 nm bandwidth) over their apertures to minimize effects of background and flame radiation. Measurements were made in a darkened room to minimize background radiation as well.

The operation of the laser system was monitored with laser power meters (Newport, Model 820): one measuring laser power before crossing the flame to detect laser power variations, the other measuring laser power after passing through the flame to account for laser extinction by scattering from the particles. The operation of the seeding system was monitored using a Mie scattering system similar to the primary two-channel instrument, but centered at the burner exit and based on a 15 mW HeNe laser. The outputs of all detectors were amplified and then low-pass filtered to control alias signals (Ithaco, Model 4213 with 12.5 kHz break frequencies). The signals were then sampled at 25 kHz using an a/d converter and buffer storage system (LeCroy, Models 8800, 8212A18, 8901A). The digital output was transferred to an IBM 9000 computer for processing to correct for argon-ion laser power and seeding level fluctuations and to find mixture fraction statistics.

After correction for radiative heat losses, both carbon monoxide/air and hydrogen/air diffusion flames have state relationships that agree with estimates based on local thermodynamic equilibrium for stretch rates comparable to the present flames (Faeth and Samuelson, 1986). This still leaves potential problems of differential diffusion of CO and H_2; however, since most of the reacting mass, energy release, and radiation signal were associated with CO oxidation, this effect is not very significant. Therefore, the scattering signals were related to mixture fractions using equilibrium predictions based on the Gordon and McBride (1971) algorithm. The results of these computations are plotted in Fig. 1 as a function of mixture fraction for the present flames. Findings for radiative heat losses of 0 and 10 percent are shown, the latter being representative of the test flames; however, radiative heat losses in this range have little effect on the Mie scattering measurements. The scattering signal is proportional to $\rho f/\rho_f$: Given the value of this parameter, the state relationship yields f. Using this relationship, the data processing system generated a time series of 260,000 elements, which was then reduced in the usual manner to find moments, PDFs (with f bins of 0.01), and spatial and temporal correlations of f (Kounalakis, 1990).

Major error sources for the Mie scattering technique involve marker shot noise, gradient broadening, initial particle density variations, and effects of differential diffusion. Since particle densities at the burner exit were large, and the measuring volume was roughly 1 mm^3, effects of marker shot noise were small (less than 3 percent for $\bar{f}'$). Similarly, radial flow widths were large (greater than 80 mm) in comparison to the measuring volume diameter (1 mm) so that gradient broadening errors were small as well. Particle density fluctuations at the burner exit were in the range 4–7 percent even after extensive development, which is typical of systems of this type (Glass and Kennedy, 1977; Stårner and Bilger, 1981, 1983). Low-fre-

Nomenclature

a = acceleration of gravity
d = burner exit diameter
$E(n)$ = power spectral density of i_λ
f = mixture fraction
i_λ = spectral radiation intensity
n = frequency
$P(\phi)$ = probability density function of ϕ
r = radial distance
Re = burner exit Reynolds number
$R_i(\Delta t)$ = temporal correlation at point i
s_i = uncorrelated Gaussian random shock at point i, equation (2)
t = time
T = temperature
u = streamwise velocity
u_m = average velocity at burner exit
x = streamwise distance
x_o = virtual origin
X_i = mole fraction of species i
z = transformed mixture fraction variable, equation (1)
Γ_r = integral length scale
Δr = radial distance increment
Δt = time interval between realizations
λ = wavelength
μ = viscosity
ν = kinematic viscosity
ρ = density
τ = time delay
τ_I = integral time scale of mixture fraction fluctuations
τ_{Ir} = integral time scale of radiation fluctuations
ϕ_{ij} = weighting functions in stochastic simulation

Subscripts

c = property along axis
f = fuel gas property at burner exit
m = average property at burner exit
0 = standard or reference condition

Superscripts

$( )'$ = instantaneous fluctuation from time-averaged mean value
$\bar{( )}$, $\bar{( )}'$ = time-averaged mean and rms fluctuating quantities

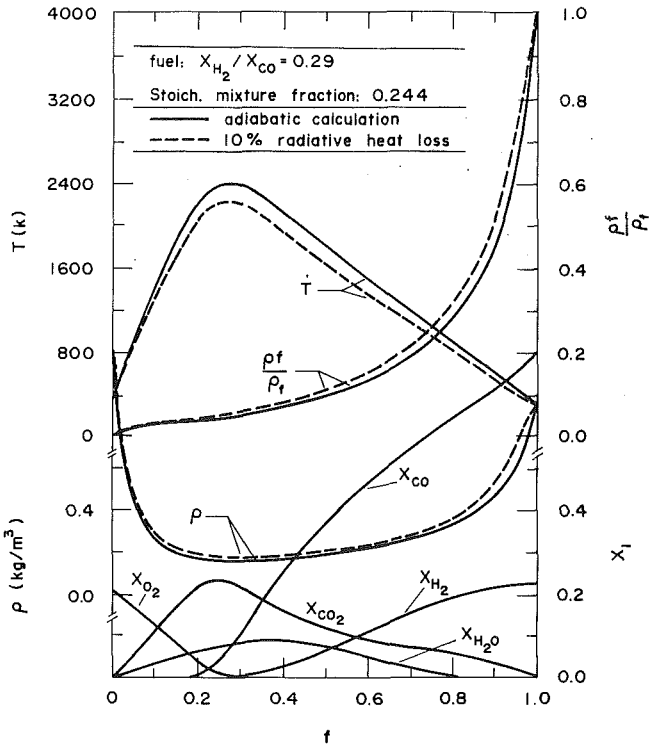

Fig. 1 State relationships for the test flames

quency particle density fluctuations, less than the reciprocal of the particle residence time, were corrected following Stårner and Bilger (1983): This involved passing the particle density monitoring signal through a low pass filter and taking the ratio of signals to a standard measurement where all channels observed the burner exit.

Differential diffusion is the most problematical source of errors when Mie scattering is used in flames because particles have negligible mass diffusivities due to their large size while gases can have rather high molecular diffusivities at flame temperatures. Potential errors due to differential diffusion were evaluated following Stårner and Bilger (1981), yielding estimated errors less than 6 percent for mean mixture fractions and less than 16 percent for mixture fraction fluctuations and correlations (Kounalakis, 1990). Present measurements, however, suggest that these estimates of errors are probably too low; this subject will be taken up later.

Experimental uncertainties were dominated by effects of differential diffusion and finite sampling times with seeding level fluctuations and state relationship uncertainties being contributing factors. Accepting the differential diffusion error estimates just discussed, estimates of experimental uncertainties (95 percent confidence) of mixture fraction measurements are less than 10 percent for $\bar{f}$ and less than 25 percent for $\bar{f}'$ and its correlations.

Radiation Measurements. Spectral radiation intensities were measured for horizontal paths through the flame axis at various heights above the burner exit. An infrared monochromator (Oriel, Model 724) with appropriate gratings and order-sorting filters was used to measure spectral radiation intensities at 2800 and 4500 nm with half-peak bandwidths of 30 and 60 nm, respectively. The present flames radiated strongly at these wavelengths: At 2800 nm, the 2700 nm bands of CO_2 and H_2O are present; and at 4500 nm, the 4300 nm band of CO_2, 4700 nm band of CO, and the broad 6100 nm band of H_2O are present. However, radiation at 2800 and 4500 nm was dominated by radiation from the 2700 and 4300 nm bands of CO_2 for present test conditions. A fast response (flat to 10 kHz) liquid nitrogen cooled InSb detector (Hamamatsu, Model P3357-01) was used for these measurements.

Table 1 Test conditions[a]

Reynolds Number $(\rho u d/\mu)_m$		7400		12700
Richardson Number (ad/u_m^2)		1.72×10^{-4}		5.75×10^{-5}
u_m (m/s)		20.1		34.7
Flow Rates (mg/s)				
Carbon Monoxide		691		1195
Hydrogen		14.3		24.8
x/d	$\bar{f}_c$	$\bar{u}_c$(m/s)	$\bar{f}_c$	$\bar{u}_c$(m/s)
30	0.508	14.8	0.533	22.7
40	0.298	10.5	0.368	16.8
50	0.195	8.0	0.252	12.5

[a]Flow directed vertically upward from a 7.04 mm diameter burner in still air. Initial mixture density of 0.905 kg/m^3, viscosity of 1.738×10^{-5} kg/ms, and stoichiometric mixture fraction of 0.244.

The collimated flame radiance was collected using a focusing lens with a field stop in front of the monochromator. Three fields of view were considered, having diameters of 5, 8, and 10 mm at the flame axis, and field angles of 0.6, 0.95, and 1.2 deg. Effects of the field of view were only significant with respect to the high-frequency end of the power spectral densities of radiation fluctuations; in this region, Richardson extrapolation of the three measurements was used to infer results for an infinitely small diameter path, similar to Sivathanu et al. (1990); see Kounalakis (1990) for example extrapolations. The output of the detector was a-c coupled; therefore, mean and rms values were measured using a chopper/lock-in amplifier system operating at 4 kHz, a 2 kHz low-pass filter, and a sampling frequency of 5 kHz (the a/d converter and computer system were the same as for the mixture fraction measurements). However, temporal power spectral densities and probability density functions were measured without the chopper, using a 6.3 kHz low-pass filter and a sampling frequency of 12.5 kHz.

Wavelength readings were calibrated using narrow line filters and a blackbody source. To assure system linearity, the monochromator/detector system was calibrated at several temperatures of a blackbody source (Infrared Industries, Model 463). Experimental uncertainties (95 percent confidence) of these measurements were dominated by effects of finite sampling times: They were less than 10 percent and were repeatable within this range.

Test Conditions. Test conditions are summarized in Table 1. Two flames were considered, have burner exit Reynolds numbers of 7400 and 12,700. The flow at the burner exit was fully developed turbulent pipe flow so that the flames were turbulent throughout. Burner exit Richardson numbers were less than 2×10^{-4} and the flames were relatively short due to their high stoichiometric mixture fraction; therefore, the flames approximated jet flames with small effects of buoyancy except near the edge of the flow because the surroundings were still, e.g., the outline of the flame was relatively independent of the flow rate for present test conditions. The radiation paths were at $x/d = 30$, 40 and 50; the lowest two positions were below the flame tip (taken as the point where the mean mixture fraction along the axis was stoichiometric) while the highest position was just beyond or near the flame tip for the low and high Reynolds number flames. Centerline velocities (measured using laser velocimetry; see Kounalakis, 1990) at these positions

were generally greater than 10 m/s so that the flow near the axis was dominated by burner exit momentum.

Theoretical Methods

General Description. Radiation statistics were found by stochastic simulations to yield realizations of mixture fraction distributions along the radiation path while satisfying the measured mixture fraction statistics. Scalar properties along the path were found from the mixture fraction distributions using the state relationships illustrated in Fig. 1 (allowing for the 10 percent radiative heat loss from the flame as a whole). Spectral radiation intensities were then found by solving the equation of radiative transfer along the path with a narrow-band model. Finally, the resulting time series of spectral radiation intensities was analyzed to find radiation statistics, similar to the measurements.

Narrow-Band Model. Scattering was ignored for the narrow-band model, which followed the approach of Ludwig et al. (1973). This involves use of the Goody statistical narrow-band model, with the Curtis–Godson approximation to account for absorption along inhomogeneous gas paths. The 2700, 4300, 4700 and the 6300 nm bands of CO, CO_2, and H_2O were considered using the RADCAL algorithm of Grosshandler (1980), as extended by Jeng et al. (1984).

Stochastic Simulation. The stochastic simulations were designed to reproduce the PDFs and spatial and temporal correlations of mixture fraction along the radiation path. Mean properties were known along the path; therefore, the simulation yields the instantaneous fluctuation from the mean. While the general approach was similar to that of Kounalakis et al. (1989), modifications were made to eliminate some unnecessary approximations and the new formulation is described in the following.

Measurements, to be discussed later, indicate that a clipped Gaussian function is a reasonable approximation of the PDF of f. Thus, direct simulation of f is problematical because the fluctuation algorithm cans generate values that are outside of the finite range of the PDF of f. This difficulty can be circumvented, however, by carrying out the simulation in terms of a corresponding Gaussian random variable, z, defined as follows:

$$f=z \quad 0\le z\le 1; \quad f=0, \quad z<0; \quad f=1, \quad z>1 \tag{1}$$

Since the PDFs of the original and transformed variables differ, their correlations between different points differ as well. This was handled by transforming the correlations as described by Sivathanu et al. (1990). Present measurements, to be discussed later, indicated that spatial and temporal correlations could be approximated reasonably well as exponential functions. The specific corrections between exponential temporal correlations for f and z can be found from Faeth et al. (1991).

The stochastic simulation follows the time-series simulation techniques described by Box and Jenkins (1976). It is based on an autoregressive process in time and a moving average in space. A first-order autoregressive process in time (a Markov process) satisfies an exponentially decaying temporal correlation for all times while minimizing memory requirements. Additionally, a moving average process in space is convenient because different points along the path have different fluctuation levels and it is not necessary to specify two-point/two-time correlations.

Numbering points along the radiation path as $i=1, 2, \ldots, N$, the algorithm for $z_k'(t)$ becomes (Box and Jenkins, 1976):

$$z_k'(t)=R_k(\Delta t)z_k'(t-\Delta t)+\sum_{i=1}^{k}\phi_{ik}s_i(t) \tag{2}$$

where $R_k(\Delta t)=\exp(-\Delta t/\tau_{Ik})$ satisfies the exponential temporal correlation at k. The ϕ_{ik} are weighting factors chosen to match the spatial correlations along the radiation path ($\phi_{jj}=1$ by definition), while the $s_i(t)$ are uncorrelated random shocks having Gaussian PDFs with mean values of zero and variances selected to match the PDF of z. The Δt used in the simulation need not be small, except to resolve properly the high-frequency end of the temporal power spectra of radiation fluctuations (using a large Δt implies $R_k(\Delta t)\ll 1$, which just yields a time-independent simulation).

To find the ϕ_{ik} and the variances of the $s_i(t)$, multiply $z_k'(t)$ by $z_p'(t)$, both given by equation (2), and let $p<k$ with no loss of generality. Recalling that the $s_i(t)$ are uncorrelated, the resulting expected values of $\overline{z_k'(t)z_p'(t)}$ become

$$\overline{z_k'z_p'}\ (1-R_kR_p)=\sum_{i=1}^{p-1}\phi_{ik}\phi_{ip}\bar{s}_i^2+\phi_{pk}\bar{s}_p^2 \tag{3}$$

where $\overline{z_k'(t)z_p'(t)}=\overline{z_k'z_p'}$, $R_k(\Delta t)=R_k$, etc., to simplify the notation. Setting $k=p$ in equation (3) and solving for $\bar{s}_k^2$ yields

$$\bar{s}_k^2=\overline{z_k'^2}(1-R_k^2)-\sum_{i=1}^{k-1}\phi_{ik}^2\bar{s}_i^2 \tag{4}$$

Finally, solving for ϕ_{pk} from equation (3) gives

$$\phi_{pk}=\left(\overline{z_k'z_p'}\ (1-R_kR_p)-\sum_{i=1}^{p-1}\phi_{ik}\phi_{ip}\bar{s}_i^2\right)/\bar{s}_p^2 \tag{5}$$

where $\bar{s}_p^2$ can be found by setting $k=p$ in equation (4). Since the temporal and spatial correlations of z are known, equations (4) and (5) can be solved in a sequential manner from $p=1$ to $p=k$, beginning with $k=1$ and proceeding to $k=N$. For the present statistically stationary conditions, the $\bar{s}_k^2$ and ϕ_{pk} can be found once-and-for-all for a particular radiation path. The simulation is initiated as a time-independent simulation, with realizations at subsequent times found using equation (2). The effect of spatial discretization on the simulation of radiation fluctuations was checked using 30, 60, and 90 points along the radiation path for a typical test case, with essentially unaltered results; therefore, present computations were performed using 30 points to control computation times. PDFs and power spectral densities were found from predicted time series 122,880 elements long. Sampling frequencies for the stochastic predictions were 20 kHz so that frequencies up to 10 kHz could be resolved. The present simulations reproduced given values of $\bar{f}$ and $\bar{f}'$ within 1 percent, and given values of spatial and temporal correlations of f' within 10 percent.

Mixture Fraction Statistics

Time-averaged mean and root-mean-squared fluctuations of mixture fractions for the three radiation paths across each flame are illustrated in Figs. 2 and 3. The results are normalized by $\bar{f}_c$ (summarized in Table 1) and are plotted as a function of r/x, which is the similarity variable for nearly constant density turbulent jets and plumes. In terms of these coordinates, $\bar{f}/\bar{f}_c$ is Gaussian in shape, and is relatively independent of position and burner exit Reynolds number. Flow widths, based on radial position where $\bar{f}/\bar{f}_c$ becomes small, are in the range $r/x=0.18$–0.20, which is typical of the flame-containing region of jet flames (see Jeng et al., 1984, Gore et al., 1987, and references cited therein).

Mixture fraction fluctuation distributions illustrated in Figs. 2 and 3 exhibit greater variability with respect to height and burner exit Reynolds number than mean mixture fractions. Below the flame tip ($x/d=30$ and 40), mixture fraction fluctuations decrease near the axis because turbulent production of mixture fraction fluctuations is reduced as the gradient of the mean mixture fraction approaches zero. Beyond the flame tip ($x/d=50$), however, mixture fraction fluctuations are high-

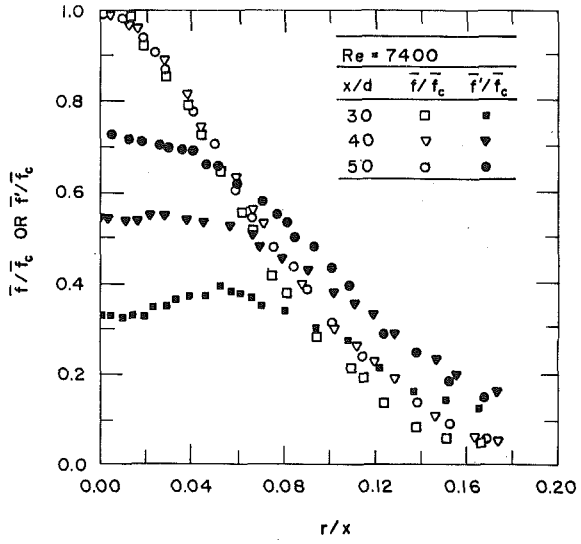

Fig. 2 Radial profiles of mean and fluctuating mixture fractions: Re = 7400

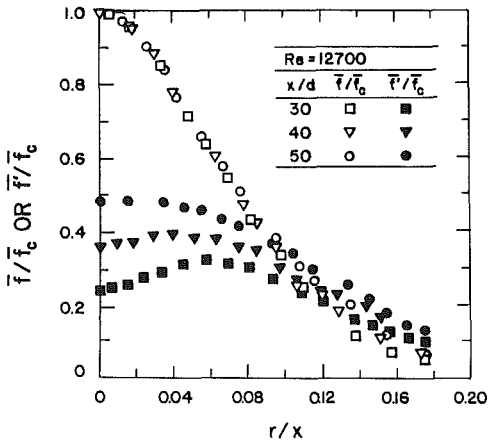

Fig. 3 Radial profiles of mean and fluctuating mixture fractions: Re = 12,700

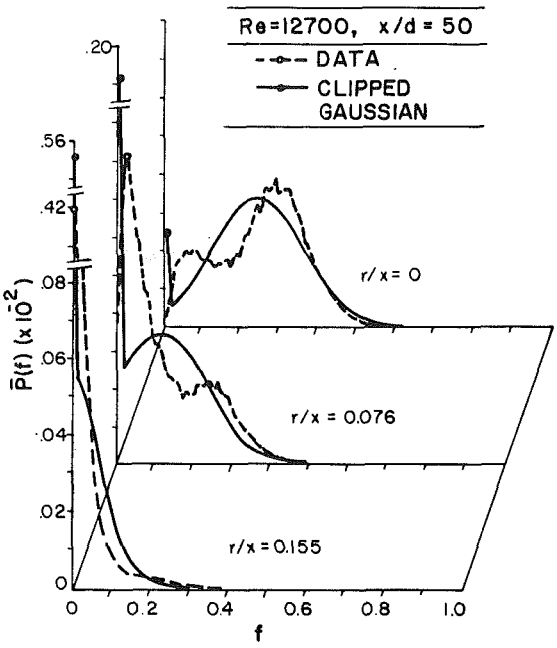

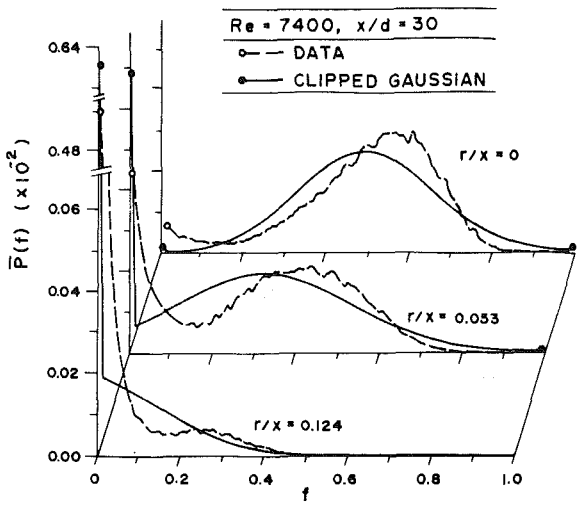

Fig. 4 Typical PDFs of mixture fraction

est at the axis; this behavior is generally not observed in non-buoyant flows and may be caused by instabilities due to effects of buoyancy, i.e., density increases rapidly with vertical distance in this region. Additionally, fluctuations near the axis at $x/d = 50$ are higher for the low Reynolds number flame, which tends to support an effect of buoyancy as the cause of this behavior. The present mixture fraction fluctuation intensities near the axis reach values of roughly 70 and 50 percent for the low and high Reynolds number flames at $x/d = 50$. This is high in comparison to isothermal jets, where Becker et al. (1967) and Birch et al. (1978) observe maximum values near the axis of 20–30 percent. In contrast, other Mie scattering measurements in flames yield values comparable to present findings, e.g., Ebrahimi and Kleine (1977), Kennedy and Kent (1981), and Stårner and Bilger (1983) (for small streamwise pressure gradients) find values in the range 60–90 percent.

Typical PDFs of mixture fraction are plotted for various radial positions in Fig. 4. Results are shown for $x/d = 30$, Re = 7400 and $x/d = 50$, Re = 12,700, which spans the present range of mixture fractions along the axis. Clipped-Gaussian distributions having the same mean and fluctuating values as the measurements are also plotted on the figures so that the capabilities of this PDF expression to fit the data can be evaluated. The general shape of the PDFs is similar to the observations of Kennedy and Kent (1981) in turbulent hydrogen/air flames. Results at $r/x = 0$, Re = 7400 exhibit small spikes at both $f = 0$ and 1; however, the remainder all have relatively large air intermittency spikes at $f = 0$. The air intermittency spikes are broadened, but this is not evidence of a significant viscous superlayer, because the scattering particles have negligible molecular mass diffusion rates; rather, the effect is probably caused by limitations of instrument frequency response and the finite size of the measuring volume (Kennedy and Kent, 1981). Due to their ability to treat the fuel and air intermittency spikes, the clipped-Gaussian PDFs provide a reasonable fit of the data for a two-moment PDF; therefore, this functional form was adopted for the stochastic simulations, as noted earlier.

The functional forms of the temporal and spatial correlations of the two flames were similar (Kounalakis, 1990); therefore, only results for Re = 12,700 will be considered in the following. Measured temporal correlations at various streamwise and radial positions are illustrated in Fig. 5. Exponential fits of the correlations are also shown on the plots. The correlations are essentially independent of radial position at each x/d, but become somewhat sharper near the origin as x/d increases. This behavior is probably caused by improved spatial resolution of the measurements as length scales increase with

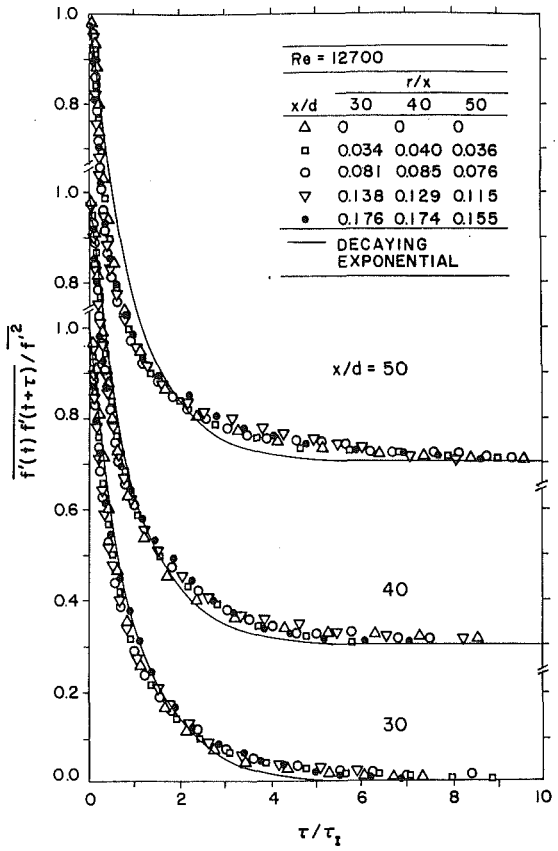

Fig. 5 Autocorrelations of mixture fraction fluctuations: Re = 12,700

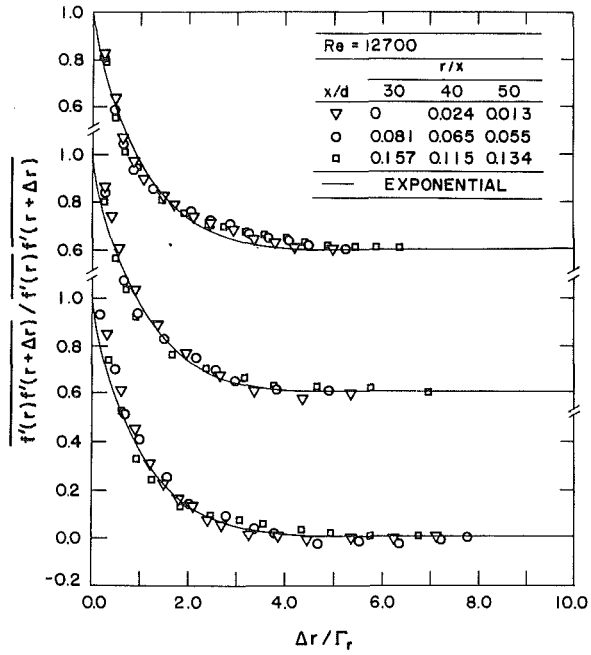

Fig. 6 Spatial correlations of mixture fraction fluctuations: Re = 12,700

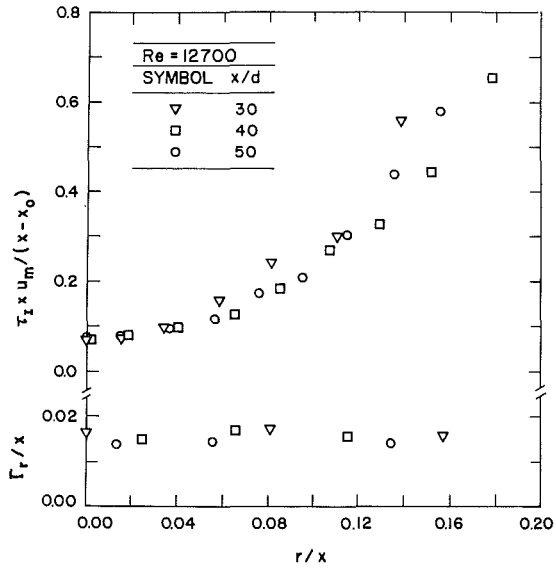

Fig. 7 Integral time and length scales: Re = 12,700

increasing x/d so that results at $x/d=50$ may be more representative of properties throughout the flames. Nevertheless, radiation properties are dominated by the large-scale features of the flow, which are represented reasonably well by an exponential function; therefore, this functional form was used for the simulations, as noted earlier.

Measured spatial correlation of mixture fraction fluctuations along the radiation paths are illustrated in Fig. 6. Exponential fits of the correlations are also shown on the plots. These correlations exhibit little variation with position and are represented very well by exponential functions.

Measured integral length and time scales along the radiation paths are plotted in Fig. 7 for Re = 12,700. When normalized in the manner of Fig. 7, the results for Re = 7400 were essentially the same, including the same virtual origin location, $x_o/d=13$, used in the normalization of the temporal integral scales (Kounalakis, 1990). Within experimental uncertainties, spatial integral scales are proportional to distance from the burner exit and are relatively independent of radial position, yielding a correlation of $\Gamma_r/x=0.016$. The correlations of temporal integral scales show that τ_I is smallest at the axis. This behavior is consistent with Taylor's hypothesis; namely, length scales are relatively uniform across the flow while mean velocities are highest at the axis so that $\tau_I \sim \Gamma_r/\bar{u}$ implies smaller values of τ_I near the axis. The correlations of Fig. 7, and the corresponding correlations for Re = 7400, were used directly in the stochastic simulations for mixture fraction distributions.

Radiation Statistics

Measured and Predicted Results. Measurements and predictions of mean and fluctuating spectral radiation intensities, and the temporal integral scales of radiation fluctuations, are summarized in Table 2. Results are shown for both wavelengths and both flames at $x/d=30$, 40, and 50. The flames were optically thin (transmittance of 90 percent) for $\lambda=2800$ nm and optically thick (transmittance of 30 percent) for $\lambda=4500$ nm. Mean spectral radiation intensities are highest in the region ofthe flame tip, $x/d=40-50$, where high levels of emission associated with high-temperature reaction zones have the longest path lengths through the flow. This region is extended in the streamwise direction for the present flames because temperatures and concentrations of CO_2 and H_2O have broad maxima near stoichoimetric conditions; see Fig. 1. Emission is also greater at 4500 nm than 2800 nm due to the large absorption coefficient of the 4300 nm band of CO_2 (Ludwig et al., 973). The comparison between measured and predicted mean spectral radiation intensities in Table 2 is excellent, with discrepancies generally less than 10 percent. Errors of the predictions are smaller than in past work (Gore et al., 1987; Kounalakis et al., 1989) because uncertainties of mixture fraction statistics have been reduced from predictions based on a turbulence model. Predictions based on mean scalar properties along the radiation paths (not shown in Table 2) were 1.1–4.2

Table 2 Measured and predicted radiation properties

x/d	$\bar{i}_\lambda$ (kW/m^2-sr-μm)		$\bar{i}'_\lambda/\bar{i}_\lambda$(%)		τ_{Ir}(ms)	
	Meas.	Pred.	Meas.	Pred.	Meas.	Pred.
Re=7400, λ=2800 nm:						
30	2.6	2.3	24	23	2.0	0.8
40	2.9	2.7	27	29	2.1	1.1
50	2.8	2.5	35	36	3.0	1.9
Re=7400, λ=4500 nm:						
30	8.7	9.8	20	16	1.7	0.8
40	11.2	10.3	18	19	2.0	1.1
50	11.0	9.7	26	27	2.3	1.4
Re=12700, λ=2800 nm:						
30	2.2	2.5	25	21	1.2	0.6
40	3.3	3.4	22	21	1.6	1.0
50	3.6	3.3	26	27	1.8	1.2
Re=12700, λ=4500 nm:						
30	9.2	10.1	19	15	1.2	0.6
40	11.4	12.0	15	13	1.5	0.9
50	12.4	11.7	18	16	1.9	1.3

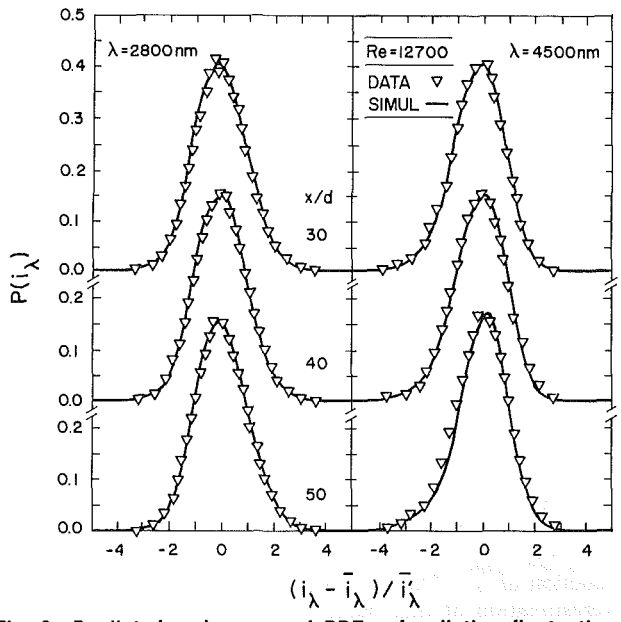

Fig. 8 Predicted and measured PDFs of radiation fluctuations: Re = 12,700

times lower than the measurements (Kounalakis, 1990). This bias of mean property predictions is larger than observed for infrared emission from carbon monoxide/air flames as a whole (see Kounalakis et al., 1989) since only strongly emitting wavelength were considered during the present study.

Measured radiation fluctuation intensities in Table 2 generally increase as x/d increases and are in the range 15–35 percent. These values are similar to observations of Kounalakis et al. (1989) for the same range of x/d in carbon monoxide/air frames. The comparison between measured and predicted radiation fluctuation intensities is excellent, with average discrepancies less than 15 percent.

In contrast to the other properties in Table 2, discrepancies between measured and predicted temporal integral scales of radiation fluctuations are disappointingly large. The predictions underestimate the measurements with errors in the range 30–60 percent, decreasing with increasing x/d and Re. This was surprising because similar stochastic simulations of continuum radiation statistics from soot in luminous flames, based on measured soot statistics, yielded excellent predictions of temporal integral scales of radiation fluctuations (Sivathanu et al., 1990). This behavior suggested that preferential diffusion, which was not a factor for the luminous flame study because only soot particle properties were measured and contributed to continuum radiation, might be the source of the difficulty. Preferential diffusion effects are caused by the relative spread of fuel gases by molecular diffusion in comparison to the seeding particles, which have negligible mass diffusivities, causing length and time scales to be underestimated by Mie scattering measurements. Preferential diffusion errors are small for high Reynolds number gases at room temperature but become significant in the high-temperature gases that dominate radiant emission from flames due to the strong temperature dependence (roughly $T^{3/2}$) of the molecular mass diffusivities of gases. The effect of preferential diffusion on length-scale measurements was estimated by computing the relative diffusion of integral-scale sized gas elements in comparison to particles for typical residence times in the flames (Kounalakis, 1990). The results indicated relative size increases of the gas to particle-containing regions on the order of two—decreasing with increasing x/d and Re—which is sufficient to explain the magnitudes and trends of the errors in Table 2. A corollary of this behavior is that the Mie scattering measurements also overestimate mixture fraction fluctuations in flames, as discussed by Bilger (1989). This helps explain the unusually high mixture fraction fluctuation levels observed using Mie scattering measurements in flames that were discussed earlier. The potential effect of these errors on other aspects of the predictions will be considered later.

Measured and predicted PDFs of spectral radiation intensities are illustrated in Fig. 8 for Re = 12,700; however, results for Re = 7400 were similar (Kounalakis, 1990). The measured PDFs are generally Gaussian in shape, except for increased positive skewness at $\lambda = 4500$ nm and $x/d = 50$. The degree of skewness is not large and the reasons for it were not studied in any detail; however, the predictions are in excellent agreement with the measurements, including correct representation of the skewness at $\lambda = 4500$ nm and $x/d = 50$.

Measured and predicted power spectral densities of spectral radiation intensities for all conditions considered are illustrated in Fig. 9. Measurements for the two flames are plotted separately in order to reduce cluttering; however, they are essen-

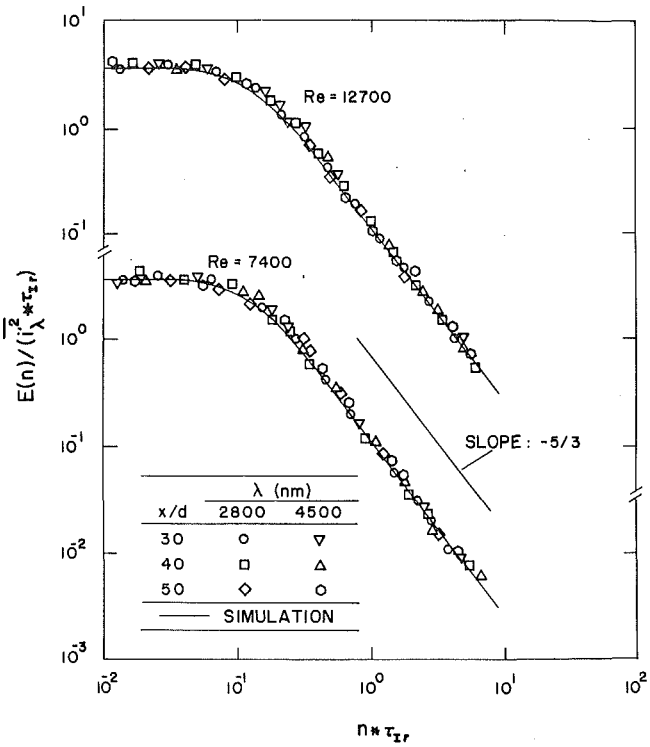

Fig. 9 Predicted and measured temporal power spectral densities of radiation fluctuations

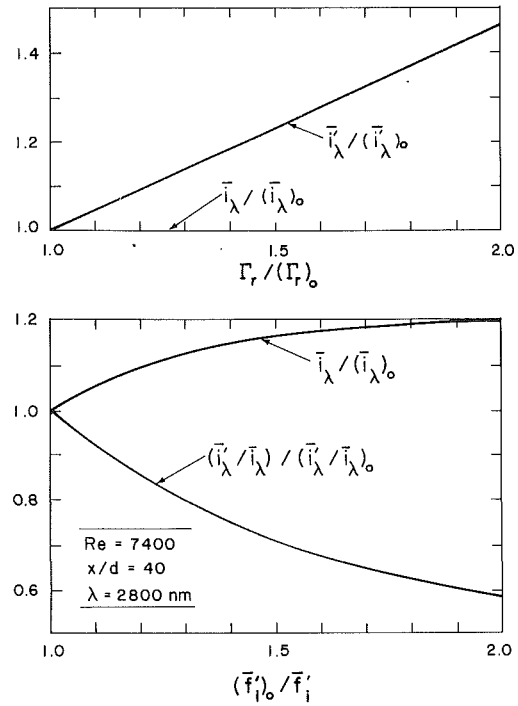

Fig. 10 Sensitivity analysis of the simulation

tially identical. Approach to a high-frequency cut-off, or radiation microscale, cannot be detected in the measurements, due to limited spatial resolution. The comparison between measured and predicted power spectral densities is excellent. The predictions also do not exhibit approach to a radiation microscale; however, this is not surprising, since the exponential temporal correlations of mixture fraction fluctuations used in the stochastic simulations have frequency content extending to infinity. An interesting feature of the predictions is that they exhibit an inertial-like region where the spectra decay proportional to $n^{-5/3}$, similar to the measurements, even though exponential temporal correlations of mixture fraction fluctuations used in the simulation decay according to n^{-2}.

Sensitivity Analysis. Sensitivity computations were undertaken to evaluate two aspects of the predictions of radiation statistics: the effects of approximate functional fits of the PDFs and correlations of mixture fractions, and the effects of potential preferential diffusion errors of the Mie scattering measurements of mixture fraction statistics.

The effect of the clipped-Gaussian PDF and exponential temporal correlation assumptions was examined by computing spectral radiation properties using measured mixture fraction data. Mixture fraction time series for Re = 12,700 and $x/d = 40$ were used, saving results along the radiation path roughly one integral scale apart. These data were then used to generate a time series of spectral radiation intensities based on the statistically independent eddy approach (Kounalakis et al., 1989). It was found that predictions using the measured and simulated mixture fraction time series agreed within 30 percent, including: mean and rms values, PDFs, power spectral densities and integral time scales of spectral radiation intensities. At the same time, similar comparisons for complete and statistically independent eddy simulations yielded differences on the order of 20 percent. Thus, the statistically independent eddy approximation dominated the errors of the computations using measure time series of mixture fractions, and the clipped-Gaussian and exponential functional forms of the PDFs and correlations are not a significant source of error in the simulations.

The main issues with respect to the Mie scattering measurements are the effects of underestimation of integral length and time scales, and overestimation of rms fluctuations of mixture fractions, on predicted radiation statistics. This was examined by parametrically varying these properties in the simulations. Results for $x/d = 40$ and Re = 7400 are illustrated in Fig. 10; however, findings at other conditions were similar. The subscript 0 indicates reference values corresponding to the present Mie scattering measurements. The upper part of the figure illustrates the effect of increasing length scales on $\bar{i}_\lambda$ and $\bar{i}_\lambda'$. It is seen that $\bar{i}_\lambda$ is unaffected while $\bar{i}_\lambda'$ increases as the length scale increases, which is similar to behavior found by Kounalakis et al. (1988, 1989) for ad hoc simulations of mixture fractions to find radiation statistics. The lower part of the figure illustrates the effect of $\bar{f}'$ on $\bar{i}_\lambda$ and $\bar{i}_\lambda'$. In this case, reductions of $\bar{f}'$ increase $\bar{i}_\lambda$ slightly but cause a significant reduction of $\bar{i}_\lambda'$. Thus, underestimation of length scales and overestimation of rms fluctuations by preferential diffusion errors of the Mie scattering measurements of the mixture fraction statistics cause only modest changes of predictions of $\bar{i}_\lambda$ and $\bar{i}_\lambda'$ (the latter since increased length scales and corresponding reduced fluctuation levels compensate for one another). In contrast, varying integral time scales of mixture fraction fluctuations causes a proportional variation of the integral time scales of radiation fluctuations (Kounalakis, 1990). These properties explain present observations where the Mie scattering measurements of mixture fraction statistics yielded excellent predictions of all properties of the radiation statistics, except for underestimating the integral time scale.

Conclusions

The relationships between mixture fraction and radiation statistics were studied for radiation paths through turbulent carbon monoxide/hydrogen jet flames burning in still air. The main conclusions are as follows:

1 Mixture fraction fluctutations in the flames induced radiation fluctuations (with radiation fluctuation intensities in the range 10–40 percent), which caused mean radiation levels

to be biased above estimates based on mean scalar properties (by factors of 1.1–4.2) for both optically thin and thick conditions.

2 The biasing could be explained by computing spectral radiation intensities for simulated mixture fraction distributions through the flames using stochastic time series methods in conjunction with the laminar flamelet concept and a narrow-band radiation model. This approach yielded predictions (of moments, PDFs, and temporal power spectra of spectral radiation intensities) that agreed with measurements within experimental uncertainties.

3 Predicted temporal integral scales of radiation fluctuations underestimated measurements: This discrepancy was due to differential diffusion errors of the Mie scattering technique, which become large in the important region near stoichiometric conditions where molecular diffusivities are large. Because of differential diffusion, Mie scattering is only recommended for measurements of mean mixture fractions in flames unless Reynolds numbers are very high.

4 Present findings show that radiation statistics of nonluminous flames are strongly influenced by mixture fraction statistics (probability density functions and spatial and temporal correlations) through the laminar flamelet approximation. Unfortunately, existing models of turbulent flames generally do not address these properties and existing measurements of them are limited. Thus, a better understanding of flame radiation statistics will require more information about mixture fraction statistics in flames than is now available.

5 Use of the clipped-Gaussian and exponential functional forms for the PDFs and the spatial and temporal correlations of mixture fractions is convenient and introduced errors on the order of 10 percent for present stochastic simulations of radiation statistics.

Acknowledgments

This research was supported by the Center for Fire Research of the National Institute of Standards and Technology, Grant No. 60NANB8D0833, with H. R. Baum serving as Scientific Officer.

References

Becker, H. A., Hottel, H. C., and Williams, G. C., 1967, "The Nozzle Fluid Concentration Field of a Round Turbulent Free Jet," *J. Fluid Mech.*, Vol. 30, pp. 285–303.

Bilger, R. W., 1977, "Reaction Rates in Diffusion Flames," *Combust. Flame*, Vol. 30, pp. 277–284.

Bilger, R. W., 1989, "Turbulent Diffusion Flames," *Ann. Rev. Fluid Mech.*, Vol. 21, pp. 101–135.

Birch, A. D., Brown, D. R., Dodson, M. G., and Thomas, J. R., 1978, "The Turbulent Concentration Field of a Methane Jet," *J. Fluid Mech.*, Vol. 88, pp. 431–449.

Box, G. P., and Jenkins, G. M., 1976, *Time Series Analysis*, Holden-Day, San Francisco, CA, pp. 47–66.

Ebrahimi, I., and Kleine, R., 1977, "The Nozzle Fluid Concentration Field in Round Turbulent Free Jets and Jet Diffusion Flames," *Sixteenth Symposium (International) on Combustion*, The Combustion Institute, Pittsburgh, PA, pp 1711–1723.

Faeth, G. M., and Samuelson, G. S., 1986, "Fast Reaction Non-Premixed Combustion," *Prog. Energy Combust. Sci.*, Vol. 12, pp. 305–373.

Faeth, G. M., Kounalakis, M. E., and Sivathanu, Y. R., 1991, "Stochastic Aspects of Turbulent Combustion Processes," *Chemometrics and Intelligent Lab Syst.*, Vol. 10, pp. 199–210.

Fischer, S. J., Hardouin-DuParc, B., and Grosshandler, W. L., 1987, "The Structure and Radiation of an Ethanol Pool Fire," *Combust. Flame*, Vol. 70, pp. 291–306.

Glass, M., and Kennedy, I. M., 1977, "An Improved Seeding Method for High Temperature Laser Velocimetry," *Combust. Flame*, Vol. 29, pp. 333–335.

Gordon, S., and McBride, B. J., 1971, "Computer Program for Calculation of Complex Chemical Equilibrium Compositions, Rocket Performance, Incident and Reflected Shocks, and Chapman-Jouguet Detonations," NASA SP273.

Gore, J. P., Jeng, S. M., and Faeth, G. M., 1987, "Spectral and Total Radiation Properties of Turbulent Carbon Monoxide/Air Diffusion Flames," *AIAA J.*, Vol. 25, pp. 339–345.

Grosshandler, W. L., 1980, "Radiative Transfer in Nonhomogeneous Gases: A Simplified Approach," *Int. J. Heat Mass Trans.*, Vol. 23, pp. 1447–1457.

Grosshandler, W. L., and Joulain, P., 1986, "The Effect of Large-Scale Fluctuations on Flame Radiation," *Prog. Astro. and Aero.*, Vol. 105, Part II, AIAA, Washington, DC, pp. 123–152.

Jeng, S.-M., Lai, M.-C., and Faeth, G. M., 1984, "Nonluminous Flame Radiation in Buoyant Axisymmetric Flames," *Combust. Sci. Tech.*, Vol. 40, pp. 41–52.

Kennedy, I. M., and Kent, J. H., 1981, "Scalar Measurement in a Co-flowing Turbulent Diffusion Flame," *Combust. Sci. Tech.*, Vol. 25, pp. 109–119.

Kounalakis, M. E., 1990, "Structure and Radiation Properties of Turbulent Diffusion Flames," Ph.D. Thesis, The University of Michigan, Ann Arbor, MI.

Kounalakis, M. E., Gore, J. P., Jeng, S. M., and Faeth, G. M., 1988, "Turbulence/Radiation Interactions in Nonpremixed Hydrogen/Air Flames," *Twenty-Second Symposium (International) on Combustion*, The Combustion Institute, Pittsburgh, PA, pp. 1281–1290.

Kounalakis, M. E., Gore, J. P., and Faeth, G. M., 1989, "Mean and Fluctuating Radiation Properties of Nonpremixed Turbulent Carbon Monoxide/Air Flames," ASME JOURNAL OF HEAT TRANSFER, Vol. 111, pp. 1021–1030.

Ludwig, C. B., Malkmus, W., Reardon, J. E., and Thomson, J. A., 1973, "Handbook of Infrared Radiation From Combustion Gases," NASA SP-3080.

Markstein, G. H., 1981, "Scanning-Radiometer Measurements of the Radiance Distribution of PMMA Pool Fires," *Eighteenth Symposium (International) on Combustion*, The Combustion Institute, Pittsburgh, PA, pp. 537–547.

Porscht, R., 1974, "Studies on Characteristic Fluctuations of the Flame Radiation Emitted by Fires," *Combust. Sci. Tech.*, Vol. 10, pp. 73–84.

Sivathanu, Y. R., Kounalakis, M. E., and Faeth, G. M., 1990, "Soot and Continuum Radiation Statistics of Luminous Turbulent Diffusion Flames," *Twenty-Third Symposium (International) on Combustion*, The Combustion Institute, Pittsburgh, PA, in press.

Stårner, S. H., and Bilger, R. W., 1981, "Measurements of Scalar-Velocity Correlations in a Turbulent Diffusion Flame," *Eighteenth Symposium (International) on Combustion*, The Combustion Institute, Pittsburgh, PA, pp. 921–930.

Stårner, S. H., and Bilger, R. W., 1983, "Differential Diffusion Effects on Measurements in Turbulent Diffusion Flames by the Mie Scattering Technique," *Prog. Astro. and Aero.*, Vol. 88, AIAA, Washington, DC, pp. 81–104.

E. Y. Kwack
Member of Technical Staff.
Assoc. Mem. ASME

C. P. Bankston
Deputy Section Manager.
Assoc. Mem. ASME

P. Shakkottai
Member of Technical Staff (Research).

L. H. Back
Group Supervisor.
Fellow ASME

Jet Propulsion Laboratory,
California Institute of Technology,
Pasadena, CA 91109

On the Reverse Flow Ceiling Jet in Pool Fire-Ventilation Crossflow Interactions in a Simulated Aircraft Cabin Interior

The behavior of the reverse flow ceiling jet against the ventilation flow from 0.58 to 0.87 m/s was investigated in a 1/3 scale model of a wide body aircraft interior. For all tests, strong reverse flow ceiling jets of hot gases were detected well upstream of the fire. The penetration lengths of the reverse flow ceiling jet for the tests agree fairly well with the relation, $l_r/H = 0.6\,[\mathcal{F}-5]$ where $\mathcal{F}$ is the fire-crossflow parameter, $\mathcal{F} = 2gHQ/\rho cT_s A u_a^3$. Both the thicknesses of the reverse flow ceiling jet and the smoke layer increased with the fire-crossflow parameter. The thickness of the smoke layer where the smoke flows along the main flow below the reverse flow ceiling jet was almost twice that of the reverse flow ceiling jet. Detailed spatial and time-varying temperatures of the gas in the test section were measured and velocity profiles were also measured using a temperature-compensated hot film.

Introduction

Postcrash fires in commercial transport aircraft continue to be a subject of public concern. While new materials and control strategies continue to be introduced, fires still occur, especially as a result of the high liquid fuel loading in postcrash situations. In addition, in-flight fires must also be considered. A number of studies on fire in a cabin have been carried out in full-scale or reduced-scale facilities. These studies were reviewed earlier by Bankston and Back (1985). It was found that the major factor affecting fire penetration and spread in an aircraft fuselage is the ambient wind condition. In the postcrash situation, wind is almost always present through openings. Thus, an externally initiated fire may be blown through an opening and interact with the induced flow along the interior of the fuselage. An experimental facility having a one-third scale simulated aircraft cabin geometry was built and instrumented at the Jet Propulsion Laboratory, and detailed temperature, flow, and combustion measurements were made to investigate pool fire and ventilation flow interactions (Bankston and Back, 1985; Bankston et al., 1987) and the response of composite interior panel materials to fire (Bankston and Back, 1986).

To gain some insight into the physics of the transport mechanism in this facility, consider a fuel fire initiated across the floor. For the situation where there is no ventilation crossflow, the fire plume would impinge on the ceiling and spread in either direction along the ceiling. With ventilation crossflow, the fire plume (although blown downstream) can still impinge on the ceiling and spread upstream as well as spread in the expected downstream direction. Earlier, it was observed that the fire plume was strong enough to establish the reverse flow ceiling jet against the ventilation flow, which replicates possible flow conditions in a postcrash wide-body aircraft. Thus, smoke and toxic gases spread upstream against a significant ventilation flow as well as downstream. The JPL pool fire test facility (0.76 m × 1.52 m in cross section) was subsequently extended from 4.25 m to 9.2 m in length to investigate the transport of smoke and combustion products farther upstream of the fire than was previously possible. This paper reports on fire dynamic studies in this extended facility under crossflow conditions.

Contributed by the Heat Transfer Division and presented at the Joint AIAA/ASME Thermophysics and Heat Transfer Conference, Seattle, Washington, June 18–20, 1990. Manuscript received by the Heat Transfer Division March 13, 1990; revision received August 13, 1990. Keywords: Fire/Flames, Stratified Flows, Transient and Unsteady Heat Transfer.

Experimental System and Procedure

The experimental system consists of an inlet section with a flow control damper, a blower, a flow settling section, a test section, and an exhaust stack. The test section (Fig. 1) has a uniform cross section, 0.76 m high by 1.52 m wide, which is approximately 1/3 of the scale of a wide-body transport interior. The test section is composed of 8 interchangeable subsections. The four modules (M1–M4), which were made of 1.6-mm-thick galvanized steel, were added to the original test section (four modules M5–M8) used in the previous studies. The original modules were made of 3.2-mm-thick hot-rolled steel plate and covered with 2.5-cm-thick ceramic fiberboard insulation. Thus, the test section was extended from 4.25 m to 9.2 m in length.

Ventilating air flow was provided by a centrifugal blower (maximum air flow rate = 80 m^3/min or 2800 CFM) and the air flow rate was controlled by a damper upstream of the blower. After exiting the blower the air flow passed through a flow settling chamber, which is composed of a diffuser section, a constant-area section (1.52 m high by 1.83 m wide), and a converging section. A pair of 20 mesh screens and a 10-cm-long honeycomb flow straightener were placed inside of the constant area section to insure uniform air flow at the test section entrance. The vertical hot film anemometer traverses were made at three spanwise locations, center (H1) and 46 cm off the centerline of the test section (H2 and H3) under non-

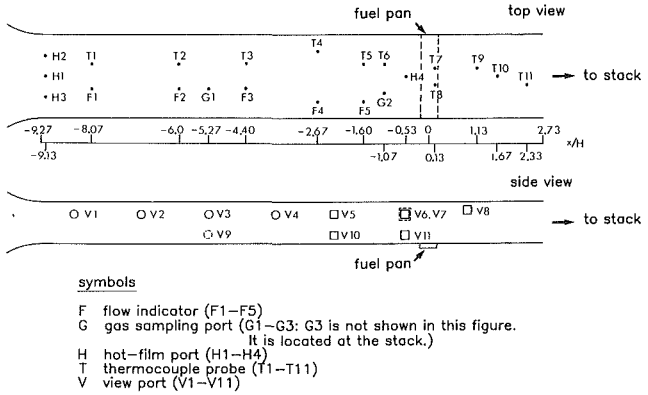

Fig. 1 Schematic diagram of the test section (0.76 m high, 1.52 m wide and 9.2 m long) shows the locations of flow indicators, gas sampling ports, hot-film ports, thermocouple probes, and view ports

Table 1 Summary of test conditions

u_a, m/s	$\dot{Q}_a$, m³/s	T_i, K	T_s, K	ΔO_2	$\dot{Q}$, kW	Re_a	$\mathcal{F}$	l_r/H
0.58	0.67	296	428	0.12	285	37,200	33.5	>9.2
0.68	0.79	294	436	0.10	281	44,300	19.8	8.0
0.80	0.93	303	421	0.105	335	49,300	15.8	5.4
0.87	1.02	301	428	0.07	246	53,400	8.6	4.8

combustion conditions to characterize the flow quality at the entrance of the test section. Uniform velocities were observed along both vertical and spanwise directions.

Approximately 4 liters of Turbojet A was used as the fuel in a water-cooled fuel pan measuring 30 cm in the streamwise direction by 150 cm in the spanwise direction. Thus, the fuel pan provides a 0.3 m "channel" fire across the test section. Prior to ignition of the fuel, the fuel was preheated by a U-shaped resistance heating element on top of the wick blanketing the pan to provide for rapid ignition over the entire fuel surface at the start of the test. After heating at 600 W for 10 min, the fuel was ignited by an external pilot flame inserted through the port V11 in the sidewall of the test section (Fig. 1). It was observed that complete ignition was achieved over the fuel surface in approximately 5 s.

Gases were sampled sequentially at three locations during tests and analyzed for oxygen, carbon monoxide, carbon dioxide, and total hydrocarbon concentrations. One probe was located in the exhaust stack and the remaining two were in the test section (Fig. 1). The oxygen concentration data measured at the exhaust stack were utilized to calculate energy release rates in the steady state by oxygen consumption calorimetry.

Eleven view ports allowed visual observations along the test section (Fig. 1). Five flow direction probes were used to determine the penetration length and the thicknesses of the reverse flow ceiling jet and smoke layers. These were located 23 cm (F1, F2, and F3) and 46 cm (F4 and F5) off the test section centerline and extended 38 cm down from the test section ceiling. The probes are 10-cm-wide rectangles constructed from 3.2 mm steel rod. Thin 0.01-mm-thick Kapton strips were attached loosely at both ends at 2.5-cm intervals along the height of the probe. The strips were spaced closer at 1.27-cm intervals along the top 5.1 cm adjacent to the ceiling. The flow directions indicated by the flow probes were recorded as a function of vertical height by observers during the experiments. The thickness of the smoke layer was also determined by the flow sensor and recorded at the same time. Light was provided through ports 9 and 10 to assist the visual observations. The smoke layer thicknesses were measured accurately because the boundary of the smoke layer is quite sharp. The reverse flow ceiling jet thicknesses are less accurate because of the spacing of the strips, and therefore, error bands are shown in Fig. 3.

The detailed vertical velocity profile measurements were made at the midplane of the test section 36 cm upstream of the fuel pan (H4). A custom-designed temperature-compensated hot-film probe capable of operating at gas temperatures up to approximately 600 K was used. However, the probe vertical length was half the height of the test section so that flow velocities could be measured only in the upper half of the test section.

Gas temperatures in the test section were measured by 46 chromel-alumel (type K) thermocouples having unshielded beaded junctions. Four thermocouples were attached on each probe, at locations 2.5, 19, 38, and 57 cm from the ceiling, respectively. Eleven of these thermocouple probes were located at different axial locations to measure the axial as well as vertical variation of temperature. Two thermocouple probes (T7 and T8) located at the same axial position were used to check the temperature variation in the spanwise direction. Inlet air and exhaust gas temperatures were measured before the blower and in the exhaust stack, respectively. Since the temperature measurements were made with unshielded, beaded junction thermocouples, the measurements are subject to radiation errors. A detailed error estimation was reported in an earlier paper (Bankston and Back, 1985).

Results and Discussion

The behavior of the reverse flow ceiling jet was observed for various ventilation air flow velocities ranging from 0.58 to 0.87 m/s (Table 1). The velocity of the ventilation air flow was determined using the hot-film anemometry traverse upstream of the fuel pan under the noncombustion condition. Reynolds numbers based on values of air properties at the inlet temperatures ranged from 37,200 to 53,400. The total energy release $\dot{Q}$ was calculated by oxygen consumption calorimetry using O_2 depletion measurements in the exhaust stack during the quasi-steady period. The heat of combustion for Turbojet A was 42.8 kJ/g. The dimensionless penetration length of the reverse ceiling jet flow l_r/H was determined by a combination of visual observations and temperature measurements near the ceiling.

For all tests, strong reverse flow ceiling jets of heated gas were detected well upstream of the fire by the flow direction probes (Figs. 2*a*–2*d*). In Figs. 2(*a*–*d*), the upper part of the figures shows the temperature distributions with isothermal lines, which were measured at $t \simeq 180$ s, and in the lower part, the dashed and solid lines indicate that thicknesses of the reverse flow ceiling jet δ_r and the smoke layer δ_s, respectively, which were determined at the same time.

While the flame is blown over downstream significantly by the ventilation air flow, heated gas still reaches the ceiling with

Nomenclature

A = cross-sectional area of test section = 1.16 m²
c = specific heat of combustion gases, J/gK
D_h = hydraulic diameter = $2WH/(W+H)$ = 1.01 m
$\mathcal{F}$ = fire-crossflow parameter = $2gH\dot{Q}/\rho cT_sAu_a^3$
g = gravitational acceleration, m/s²
H = test section vertical height = 0.76 m
l_r = penetration length of ceiling jet flow, m
ΔO_2 = fractional change in oxygen concentration during test = $1 - O_{2,s}/O_{2,i}$
$\dot{Q}$ = energy release rate of the pool fire, kW
$\dot{Q}_a$ = ventilation air flow rate, m³/s
Re_a = Reynolds number = $\rho u_a D_h/\mu$
t = time, s
T = temperature, K
T_i = ventilation air temperature at the inlet of the test section, K
T_s = mixed mean temperature of exhaust gases in the stack, K
u = local gas flow velocity in the x direction, m/s
u_a = averaged ventilation air flow in the x direction, m/s
x = coordinate in the ventilation flow direction, m: positive downstream and negative upstream of the center of the fuel pan
y = coordinate in the vertical direction above floor of the test section, m
W = test section span width, 1.52 m
δ_r = thickness of the reverse flow ceiling jet, m
δ_s = thickness of the smoke layer, m
μ = dynamic viscosity of ventilation air, Ns/m²
ρ = density of ventilation air, kg/m³

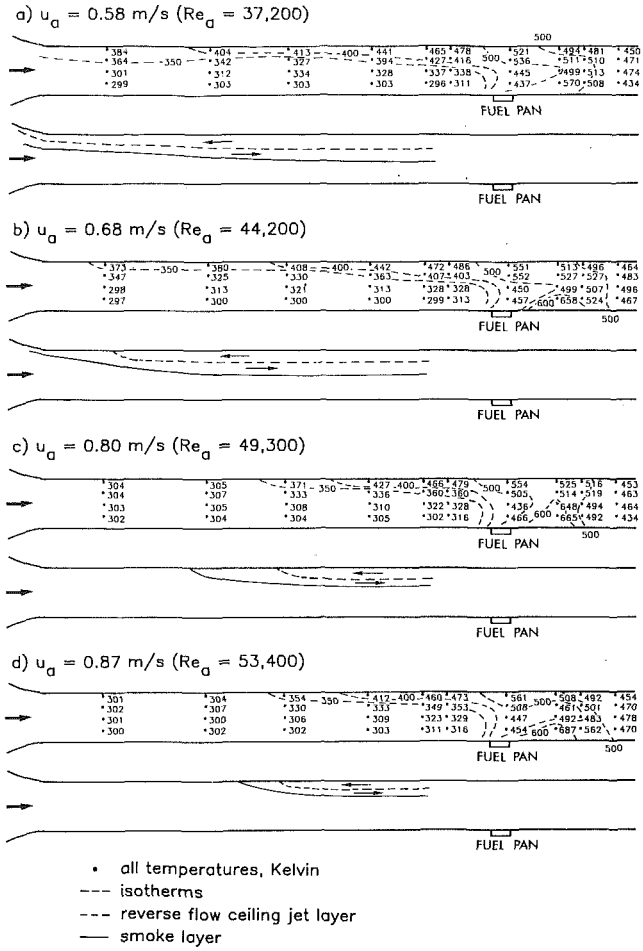

Fig. 2 Profiles of the gas temperature and the reverse flow ceiling jet and the smoke layer for various ventilation air flows: (*a*) $u_a = 0.58$ m/s, (*b*) $u_a = 0.68$ m/s, (*c*) $u_a = 0.80$ m/s, and (*d*) $u_a = 0.87$ m/s at $t \simeq 180$ s

enough momentum to establish the reverse flow jet. It is plausible to assume that during penetration against the cooler ventilation flow, the reverse flow ceiling jet loses its momentum and slows down because of heat loss to the ceiling, momentum exchange with the main ventilation flow at the boundary, and the friction at the ceiling and walls. Eventually, the reverse flow ceiling jet stops and begins to move in the downstream direction when its dynamic pressure becomes less than that of the incoming ventilation flow, forming a thicker smoke layer below the reverse flow ceiling jet layer. Although resolution of the details of the fronts of the ceiling jet and smoke layer are limited by the axial spacing of the measurement locations as well as unsteadiness in the turbulent flow, it does appear that the effective front of the smoke layer extended beyond the ceiling jet, presumably because of turbulent diffusion as depicted in Figs. 2(*a–d*).

For $u_a = 0.58$ m/s, the reverse ceiling jet was strong enough to penetrate all the way upstream of the test section and enter the flow settling section. Eventually, the gases came back into the test section along with the main flow, and filled all of the test section. The thickness of the smoke layer was measured before total loss of visibility. For $u_a = 0.68$ m/s, none of the flow direction strips of sensor F1 indicated reverse flow, but the gas temperature of 373 K near the ceiling (2.5 cm from the ceiling) at this axial location ($T1$) was very close to that at $T2$, 380 K. Therefore, the stagnation point of the reverse ceiling jet must be very close to $F1$. For this test the smoke layer also extended across the test section eventually. For the higher ventilating flows of $u_a = 0.80$ and 0.87 m/s, the stagnation

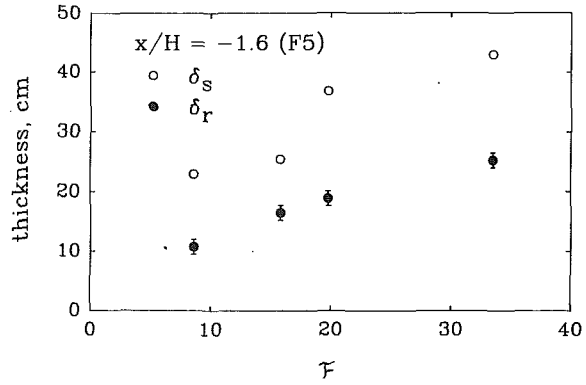

Fig. 3 Thicknesses of the reverse flow ceiling jet and the smoke layer *versus* fire-crossflow parameter at *x/H* = −1.6 (*F5*); δ_s is almost twice as thick as δ_r

points of the reverse ceiling jet were located around $F3$ and the frontal tips of the smoke layer were around $F2$.

The thicknesses of the reverse flow ceiling jet and smoke layer remain relatively constant in the test section, even though they become thinner near the leading edge, forming a wedge shape. Similar smoke layer shapes were observed by Hwang and Wargo (1986). In general, the thicknesses of both layers decreased with increase of the ventilation flow for a fixed energy release rate. Since the energy release rate was not constant in the current experiments (Table 1), the thicknesses of both layers at view port $F5$ were plotted in Fig. 3 as a function of the fire-crossflow parameter proposed by Thomas (1958), which is the ratio of the buoyancy head to the velocity head of the ventilation flow. By using the approximate energy balance $\dot{Q} = \rho u_a c A (T_s - T_i)$, this ratio can be written as

$$\mathcal{F} = 2gH\dot{Q}/\rho c T_s A u_a^3 \tag{1}$$

The thickness of the reverse flow ceiling jet δ_r increased with increasing fire-crossflow parameter. The thickness of the smoke layer shows a similar trend but the data are more scattered. The smoke layer is much thicker, almost twice that of the reverse flow ceiling jet. For $u_a = 0.58$ m/s, the smoke layer was almost half of the height of the test section.

The dimensionless penetration length of the reverse flow ceiling jet l_r/H versus the fire-crossflow parameter is shown in Fig. 4. Figure 4 also includes the experimental data of Thomas (1958) and Eisner and Smith (1954), both related to mine fires, as well as JPL data by Bankston et al. (1984) for comparison. Thomas found that when the fire-crossflow parameter is larger than 5, then a reverse flow ceiling jet will occur. Based on a simple model he proposed the following formula to correlate the reverse flow ceiling jet penetration:

$$\frac{l_r}{H} = 0.6\,[\mathcal{F} - 5] \tag{2}$$

The current data points agree fairly well with equation (2), which is shown as a line in Fig. 4. Data at the lowest ventilation velocity (value of $\mathcal{F}$ of 33.5) where the reverse flow ceiling jet extended into the contraction section upstream a distance of 9.2 ceiling heights from the fire obviously are not shown in Fig. 4.

Although it is difficult to infer scaling relations for flows involving convective and radiant heat transfer, it is worthwhile noting that the correlation between the dimensionless penetration length l_r/H and the fire-crossflow parameter $\mathcal{F}$ applies to cross sections of various sizes and shapes. The data of Eisner and Smith (1954) were obtained in a full-size mine tunnel with a round ceiling of height 2.44 m and width of 2.4 m, while the data of Thomas (1958) were obtained in a smaller 0.33-m square tunnel. Our data in comparison were obtained in an intermediate size rectangular channel of height 0.76 m and width 1.52 m. Of course, caution should be exercised in ex-

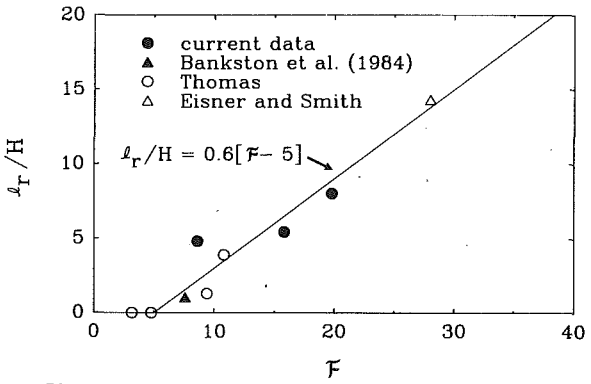

Fig. 4 Dimensionless penetration length of the reverse flow ceiling jet versus fire-crossflow parameter; the data show fairly good agreement with Thomas' correlation

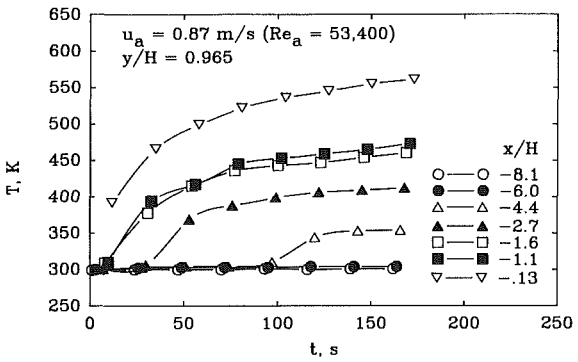

Fig. 5 Gas temperatures 2.5 cm from the ceiling of the test section ($y/H = 0.965$) versus time at various axial locations for $u_a = 0.87$ m/s

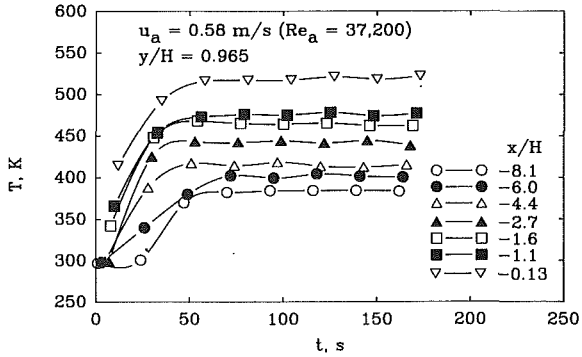

Fig. 6 Gas temperatures 2.5 cm from the ceiling of the test section ($y/H = 0.965$) versus time at various axial locations for $u_a = 0.58$ m/s

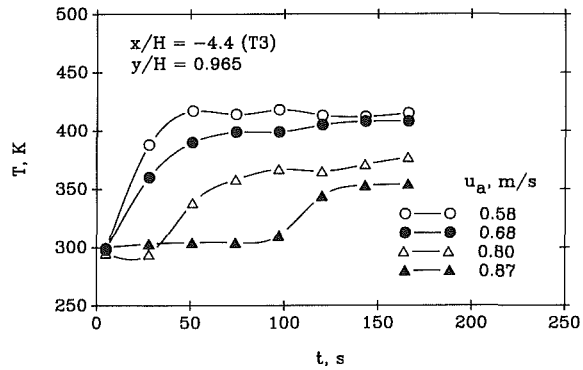

Fig. 7 Gas temperatures 2.5 cm from the ceiling of the test section ($y/H = 0.965$) versus time at $x/H = -4.4$ ($T3$) for various ventilation air flows

trapolating our results for a 1/3-scale model of a wide-body aircraft interior to full scale, which is obviously more complex because of seats, aisles, baggage compartments, partitions, etc.

Gas temperatures at various locations in the test section were measured during the entire test period. Time-varying gas temperatures near the ceiling (2.5 cm from the ceiling) at various axial locations are plotted in Fig. 5 for a ventilation air velocity of 0.87 m/s. The gas temperature measurements started when the flame was observed over all the fuel pan, which usually took 5 s after ignition with the torch through port V11 (Fig. 1). Gas temperatures upstream of the fire increased sharply when the hot reverse ceiling jet passed, then gradually increased and reached nearly steady values, which decrease with distance from the flame because of heat loss to the main flow, the ceiling, and the walls. The reverse ceiling jet reached thermocouple port T5 at $x/H = -1.6$ within 31 s after measurements started and passed $T4$ ($x/H = -2.67$) during the next 22 s. The average velocity of the ceiling jet front in this region was estimated to be of the order of 4 cm/s. The ceiling jet penetrated farther against the main ventilation flow and arrived at $T3$ ($x/H = -4.4$) at $t = 120$ s with a mean frontal velocity of 2 cm/s in the region from $T4$ to $T3$. The reverse ceiling jet continued losing its momentum as described earlier before stopping at thermocouple port $T3$. Downstream of the fire, temperatures increased rapidly with time and reached steady values, which decreased as the distance from the flame increased because of heat loss to the surroundings (not shown).

In the case of $u_a = 0.58$ m/s, in general, similar behavior was observed (Fig. 6). However, the reverse ceiling jet was strong enough to penetrate all the way into the flow settling chamber. It took less than 26 s for the reverse ceiling jet to reach $T2$ ($x/H = -6.0$) and the reverse ceiling jet passed $T1$ ($x/H = -8.07$) within an additional 21 s. The mean velocity of the reverse ceiling jet front was about 8 cm/s in this range. It took about 70 s to obtain steady values of temperature of the hot gas, except in the stack, where it took about 110 s. However, it required about 160 s for $u_a = 0.87$ m/s.

Figure 7 shows the time-varying temperatures at $T3$ ($x/H = -4.4$) for four ventilation air flows. In general, the temperature of the reverse ceiling jet increases with decreasing velocity of the ventilation air flow. It took less than 27 s to reach $T3$ when $u_a = 0.58$ and 0.68 m/s, whereas it took about 50 and 120 s for $u_a = 0.80$ and 0.87 m/s, respectively. The temperature of the reverse ceiling jet at $T3$ became lower as the ventilation air flow increased.

Figure 8 shows the gas axial temperature profiles at 2.5 cm ($y/H = 0.965$) and 19 cm ($y/H = 0.75$) from the ceiling at $t \simeq 180$ s, which are the same as the first and second rows of temperatures in Figs. 2(a-d). The temperature at 2.5 cm from the ceiling has a peak value near the top of the fuel pan and decreases both upstream and downstream from the fuel pan. For $x < 0$, this represents the temperature profiles in the reverse ceiling jet. The temperatures at 19 cm from the ceiling (in the smoke layer moving downstream) are somewhat lower, but show similar trends. However, temperatures at $x/H = -8.07$ ($T1$) are higher than those at $x/H = -6.0$ ($T2$) for $u_a = 0.58$ and 0.68 m/s, which are closer to the fuel pan. This may be explained by the recirculation of the reverse ceiling jet into the main flow at the stagnation point. More detailed time-varying gas temperatures at $y/H = 0.75$ are shown in Fig. 9 for two axial locations, $x/H = -8.07$ ($T1$) and -6.0 ($T2$). The general behavior is similar to that at $y/H = 0.975$ (Fig. 6). However, temperatures at $x/H = -8.07$ ($T1$) are higher than those at $x/H = -6.0$ ($T2$) even though $T1$ is farther away from the fuel pan. The gas temperatures outside of the smoke layer, in the lower portions of the test section, are almost the same as the inlet temperature, except nearer the fuel pan.

The detailed velocity profiles measured 36 cm upstream of the fuel pan ($H4$ in Fig. 1) are shown in Fig. 10, which provides direct readouts from the hot-film bridge output versus vertical height for the four ventilation flow conditions. For comparison, the pretest cold flow profiles are also plotted. In the cold

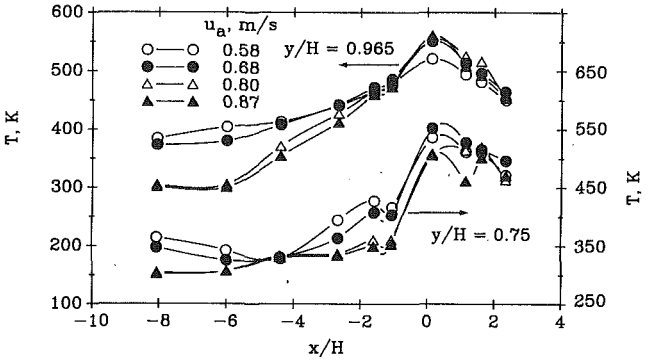

Fig. 8 Axial gas temperature profiles for various ventilation air flows at $t=180$ s: at $y/H=0.965$ (upper) and at $y/H=0.75$ (lower)

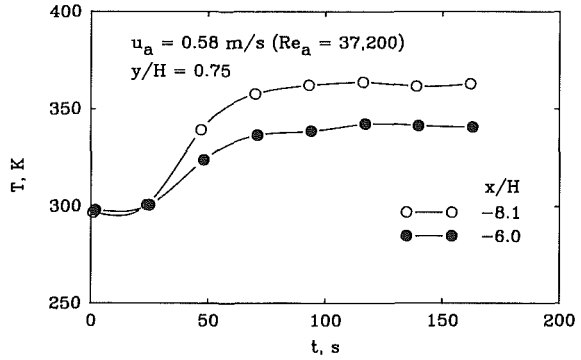

Fig. 9 Gas temperatures 19 cm from the ceiling of the test section ($y/H=0.75$) versus time at various axial locations near the stagnation point of the reverse flow ceiling jet for $u_a=0.58$ m/s

flow measurements, a uniform velocity was observed all the way across the test section except in the ceiling (and floor) boundary layers. With the fire, the hot gas velocity increased in the lower portion of the test section. This is due to the incoming ventilation flow being diverted into a smaller cross-sectional area caused by blockage and due to the effect of increased temperatures and reduced gas density, while ventilation mass flow rate remains fixed. The velocity then dropped off sharply as the flow reversal point was approached. The hot gas near the ceiling moved against the main flow. The thickness of the reverse ceiling jet was almost a quarter of the height of the test section for $u_a=0.58$ m/s, which is consistent with the visual observation (Figs. 2*a* and 3) and decreased as the main flow increased. The maximum velocity of the reverse ceiling jet was over 40 cm/s at this axial location when $u_a=0.58$ m/s and decreased with increasing main flow.

Summary and Conclusions

Interactions between a pool fire and a ventilation flow have been investigated in a 1/3-scale simulated wide-body aircraft cabin interior. Of specific interest in this paper was the behavior of the reverse flow ceiling jet and smoke layer that emanate from part of the fire plume impingement on the ceiling and penetrate upstream against the ventilation flow. The frontal speed of the reverse flow ceiling jet slows down as it moves farther upstream before reaching a terminal location. The time for nearly steady behavior was about 70 and 160 s for ventilation velocities of 0.58 and 0.87 m/s, respectively. A summary of the results for this terminal behavior is as follows:

1 Strong reverse flow ceiling jets of hot gases were detected well upstream of the fire for all tests (whose fire-crossflow parameters were larger than 8).

2 The penetration lengths of the reverse flow ceiling jets agree fairly well with the correlation proposed by Thomas.

3 The thickness of the reverse ceiling jet increases with the fire-crossflow parameter.

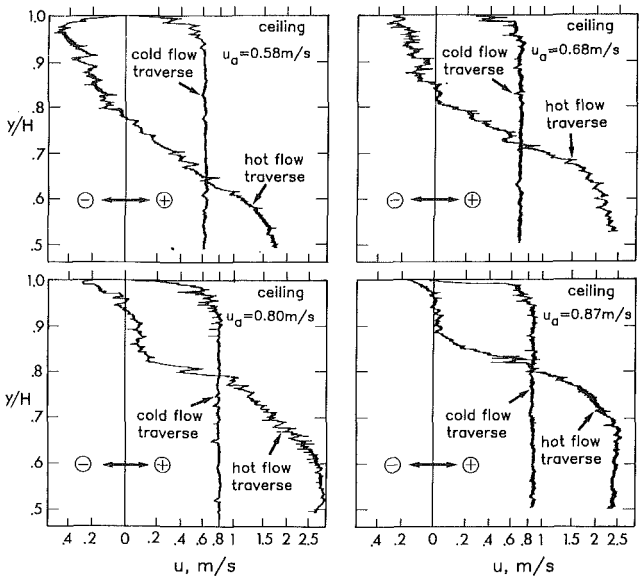

Fig. 10 Detailed velocity profiles in the upper half of the test section were measured 36 cm upstream of the fuel pan for various ventilation air flows; for comparison, pretest cold flow profiles are included

4 The smoke layer thickness shows behavior similar to that of the reverse flow ceiling jet although the smoke layer is twice as thick as the reverse flow ceiling jet.

Thus, smoke and toxic gases carried by the reverse flow ceiling jet impose an additional hazard to passengers even upstream of the fire.

Acknowledgments

The work described in this paper was performed by the Jet Propulsion Laboratory, California Institute of Technology, under contract with the National Aeronautics and Space Administration. The work was supported by the Transport Aircraft Aviation Safety Program, Office of Aeronautics and Space Technology (OAST) of NASA.

The authors thank Messrs. D. C. Schneider and J. J. Godley for their contributions in fabrication, assembly, and instrumentation of the test facility. Assisting in the conduct of the experiments were Messrs. Schneider and Godley and Drs. K. Aaron, G. Fabris, K. Harstad, and T. Luchik. Finally, we gratefully acknowledge the support and suggestions of Dr. Thor Eklund at the FAA Technical Center during the development of the JPL facility.

References

Bankston, C. P., Back, L. H., Cho, Y. I., and Parthasarathy, S. P., 1984, "Measurements of the Flow and Heat Transfer Characteristics for Pool Fires in a Simulated Aircraft Cabin Interior With Ventilation," presented at Fall Technical Meeting, Eastern Section of the Combustion Institute, Clearwater Beach, FL.

Bankston, C. P., and Back, L. H., 1985, "Pool Fire-Ventilation Crossflow Experiments in a Simulated Aircraft Cabin Interior," *J. Aircraft,* Vol. 22, pp. 861–868.

Bankston, C. P., and Back, L. H., 1986, "Measurements of the Response of Transport Aircraft Ceiling Panels to Fuel Fires," *J. Aircraft,* Vol. 23, pp. 207–212.

Bankston, C. P., Back, L. H., Cho, Y. I., and Shakkottai, P., 1987, "Pool Fires in a Simulated Aircraft Cabin Interior With Ventilation," *J. Aircraft,* Vol. 24, pp. 470–472.

Eisner, H. S., and Smith, P. B., 1954, "Convective Effects From Underground Fires: the Backing of Smoke Against the Ventilation," presented at the 8th International Conference of Directors of Safety in Mines Research, Dortmund, Federal Republic of Germany.

Hwang, C. C., and Wargo, J. D., 1986, "Experimental Study of Thermally Generated Reverse Stratified Layers in a Fire Tunnel," *Combustion and Flame,* Vol. 66, pp. 171–180.

Thomas, P. H., 1958, "The Movement of Buoyant Fluid Against a Stream and the Venting of Underground Fires," Fire Research Station, Boreham Wood, United Kingdom, Fire Research Note 351.

A Comparison of Augmentation Techniques During In-Tube Evaporation of R-113

R. S. Reid
Los Alamos National Laboratory,
Los Alamos, NM 87544

M. B. Pate
Iowa State University,
Ames, IA 50011

A. E. Bergles
Rensselaer Polytechnic Institute,
Troy, NY 12180

An experimental study was conducted to determine the potential of three techniques for augmenting in-tube evaporation of refrigerants: high-fin tubes, microfin tubes, and twisted tape inserts. Five tubes with internal fins and one smooth tube with a twisted-tape insert were tested. Additionally, experiments were performed with two reference smooth tubes having diameters similar to the maximum inside diameters of the finned tubes. All experiments involved evaporating Refrigerant 113 (R-113) by direct electrical heating of the tube wall. Local evaporation heat transfer coefficients were measured as a function of quality for a range of mass fluxes and heat fluxes. Enhancement factors were calculated by forming ratios of the heat transfer coefficient for the augmented tube and a smooth tube of the same maximum inside diameter. Mass fluxes, pressure levels, and qualities were fixed when enhancement factors were calculated. For the internally finned tubes the enhancement factors varied from 1.1 to 2.8. An internally finned tube having helical spiral angles of 16 deg produced the largest enhancement of heat transfer. The tube with the twisted-tape insert typically had an enhancement factor of about 1.5. Pressure gradient ratios and enhancement performance ratios are also presented.

Introduction

In-tube evaporators are used in many air conditioning and refrigeration systems. While in-tube evaporation is normally characterized by high heat transfer coefficients relative to those of the fluid flowing on the outside of the tube, this is not always the case. Therefore, whenever in-tube evaporation represents a substantial fraction of the controlling thermal resistance, augmentation of the in-tube flow can offer either improvements in the capacity or reduction in the size of the evaporator.

Various techniques have been used to improve the heat transfer characteristics of in-tube flow. These techniques invariably result in an increase in pumping power. Therefore, an important criterion in the evaluation of augmentation methods is the pressure loss penalty that accompanies the improvement in heat transfer coefficient.

Several experimental studies have investigated evaporation of standard refrigerants inside internally finned tubes (Bergles et al., 1983). Lavin and Young (1965) used Refrigerant 12 (R-12) and Refrigerant 22 (R-22) to study horizontal and vertical flow through electrically heated tubes with fins about 2.54 mm high and spiral angles of 0.0–7.08 deg. The 7.08 deg spiral tube had slightly better performance. The augmentation ratios, h_a/h_s, of both tubes were around 2.3. Here, the augmented transfer coefficient, h_a, is based on the surface area of a smooth tube with the same maximum inside or root diameter, and the ratio is evaluated at constant mass flux, pressure level, and average quality. Lavin and Young did not include pressure drop information in their report.

Kubanek and Miletti (1979) performed tests with R-22 heated with water at high pressure. Three internally finned tubes with spiral angles of 5.15, 10.9, and 13.1 deg were tested. The fin height in the 5.15 and 10.9 deg tubes was 0.635 mm, while in the 13.1 deg tube it was 0.508 mm.

Enhancement factors increased at higher mass fluxes. At a mass flux of 200 kg/m^2-s, the tube with the 10.9 deg spiral had the highest performance, with an enhancement factor around 4.0. The 13.3 deg spiral tube had an enhancement factor of about 2.4. The pressure gradient ratios in these finned tubes, evaluated under similar constraints, ranged from 1.1 to 3.9.

Ito and Kimura (1979) studied heat transfer and pressure drop of R-22 in internally finned horizontal tubes. The tubes tested were one meter long and 11.2 mm i.d. The fins were triangular and numbered between 21 and 37 per tube. The test section was covered with a sheath guard heater. Several spiral angles and variations in fin height from 0.06 mm to 0.40 mm were tested. The heat transfer coefficients were reported highest for the tube with a 7.0 deg spiral. The pressure drop approached that of a smooth tube when fin height was less than 0.2 mm. A later study by Kimura and Ito (1981) used the same apparatus to study heat transfer in 4.75-mm-i.d. tubes at low flow rates. The best heat transfer performance in annular flow was obtained with tubes having 15 deg spiral fins.

Tatsumi et al. (1982) investigated evaporation of R-22 in two 8.72-mm-i.d. tubes. Both tubes had numerous, low fins (hereafter referred to as a microfin tube) with a 7 deg spiral. The first tube had 65 triangular, 0.15-mm-high fins; the second tube had 60 trapezoidal, 0.12-mm-high fins. At a mass flux of 200 kg/m^2-s, the enhancement factor for heat transfer for the first tube was 1.90; for the second tube the enhancement factor was 1.68. Tatsumi reported that heat transfer coefficients were higher with larger fin heights and that the larger coefficients were obtained when the spiral angle was around 10 deg.

Tojo et al. (1984) tested evaporative heat transfer and pressure drop in 8.82-mm-i.d., microfin tubes with R-22. Mass fluxes ranged from 136 to 453 kg/m^2-s and test pressures ranged from 340 to 581 kPa. Three geometries were compared: a tube having 65 sawtooth-shaped fins with a 25 deg spiral, a tube having 48 trapezoidal fins with a 10 deg spiral, and a tube having 48 sawtooth-shaped fins with a 10 deg spiral. Fin height ranged between 0.15 mm and 0.20 mm from base to tip. The test sections were 5 m long and heated with a water jacket. Tojo reported the highest heat transfer coefficients from the tube with sawtooth-shaped fins. Tojo's work indicates that fin geometry has a significant influence on the heat transfer augmentation.

Contributed by the Heat Transfer Division and presented at the ASME Winter Annual Meeting, Boston, Massachusetts, December 13–18, 1987. Manuscript received by the Heat Transfer Division October 11, 1988; revision received February 27, 1990. Keywords: Augmentation and Enhancement, Evaporation, Finned Surfaces.

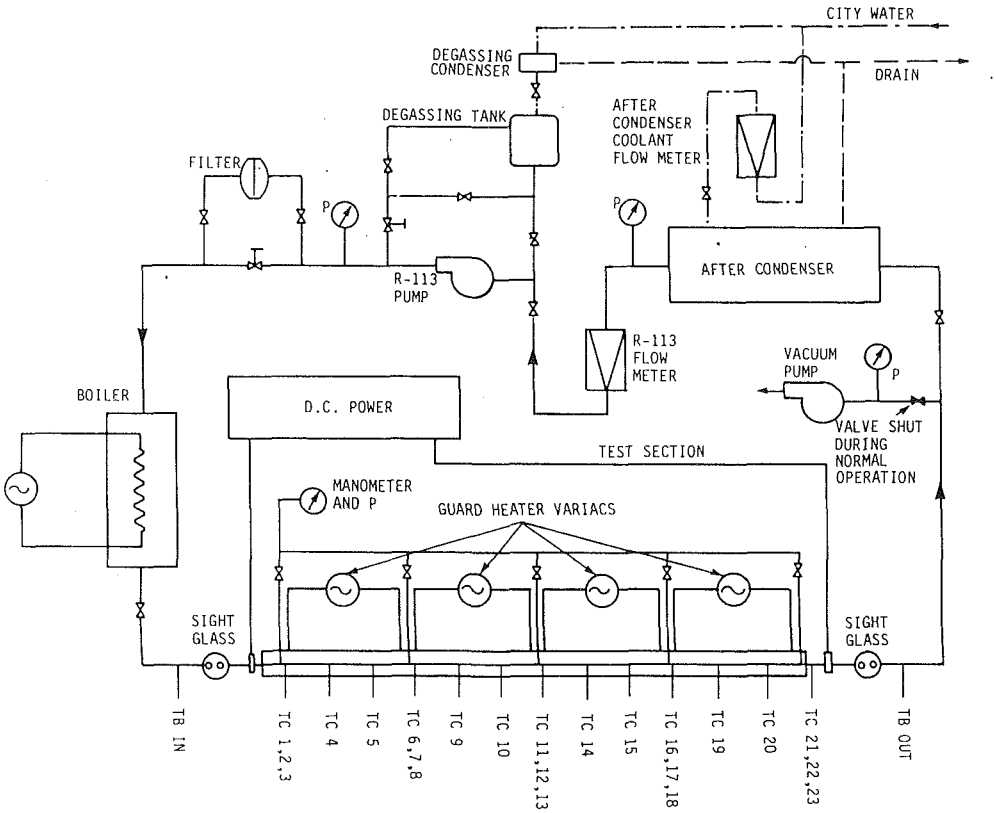

Fig. 1 Schematic of experimental apparatus

Several studies have reported data for refrigerants evaporating inside tubes with twisted-tape inserts. Blatt and Adt (1963) reported correlations for heat transfer and pressure drop of R-11. Both heat transfer coefficients and pressure drop increased as y, the number of tube diameters per 180 deg of tape twist, decreased.

Agarwal et al. (1980) tested R-22 flowing through a horizontal, electrically heated, 10-mm-i.d., 2.1-m-long stainless steel tube. Tapes of five different twists ($y = 3.76$, 5.58, 7.37, 10.15, and 12.00) were tested. The optimal heat transfer was obtained with $y = 7.37$ followed closely by the case when $y = 10.15$. Heat transfer coefficients decreased as the twist was increased below $y = 7.37$. Heat transfer coefficients lower than those with no swirl were obtained with $y = 5.58$ and $y = 3.78$. Heat transfer coefficients were highest at a mass flux of 195 kg/m^2-s.

Jensen and Bensler (1985) used upwardly flowing R-113 in an electrically heated, 8.10-mm-i.d., 1.2-m-long stainless steel tube. Tests were conducted in both single- and two-phase flow by using tapes that were 0.254 mm thick with $y = 3.94$, 8.94, and 13.92. The test section was covered by a guard heater to minimize heat loss. The two-phase heat transfer performance was reported to increase with a tighter twist (as y approached 0).

Although many past studies have examined in-tube evaporative heat transfer augmentation and the associated pressure drop, comparisons of refrigerant evaporation under similar conditions inside high-finned tubes (with fin heights greater than 0.25 mm), low-finned tube (with fin heights less than 0.25 mm and otherwise called microfins), and tubes with twisted-tape inserts have not been conducted. These three approaches to heat transfer augmentation are explored in this study by obtaining experimental data on the same apparatus and using the same procedures.

Experimental Apparatus and Procedure

An existing experimental facility was modified for testing uniformly heated, 3.66-m test sections (Khanpara et al., 1986). The experimental apparatus consisted of a horizontal test section with R-113 flowing in a closed loop as shown in Fig. 1. A more detailed description of the experimental apparatus and procedures is given by Reid (1986).

Flow Loop

The flow loop consisted of a boiler (preheater), test section, after-condenser, and pump. A series of bypasses and restric-

Nomenclature

A = area
D = diameter
E = enhancement performance ratio $= (h_a/h_s)/(\Delta p_a/\Delta p_s)$
G = mass flux
h = heat transfer coefficient
k = thermal conductivity
p = pressure
Q = total heat transfer
r = tube radius
T = temperature
V = tube metal volume
x = quality (flowing mass fraction of vapor)
y = tape twist ratio (length of 180 deg tape twist/D_i)

Subscripts

a = tube modified to augment heat transfer
avg = average
bot = bottom outside of tube wall
i = internal diameter
mid = middle outside of tube wall
o = outside diameter
s = smooth tube
top = top outside of tube wall
tt = twisted tape
w = tube wall

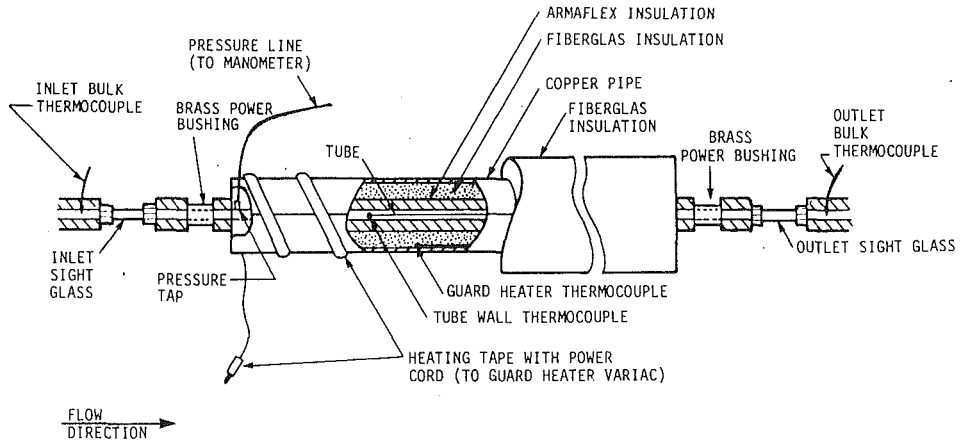

Fig. 2 Test section construction

tions controlled the R-113 flow rate and pressure in the test section. Hydrodynamic stability was obtained by reducing the pressure by about 170 kPa with the inlet throttle valve.

The boiler preheated the R-113 to a subcooled condition, approximately 11°C below the fluid saturation temperature. As R-113 flowed through the test section, it was uniformly heated by direct electrical current passing through the walls of the tube. The direct current, which was provided by a 66-V, 1200-amp capacity d-c rectifier, was conducted through water-cooled copper tubes to bus bars located at the entrance and exit of the test section. Power to the test section was controlled with a remote control box. After exiting the test section, the R-113 passed to the water-cooled condenser where it was condensed and subcooled prior to being returned to the pump to complete the circuit. A degassing tank open to the atmosphere was used to remove dissolved gas from the liquid prior to operating the loop.

Bulk fluid temperatures at the inlet and exit of the test section were measured with 30-gage copper-constantan thermocouples located at midstream. Intermediate bulk fluid temperatures were inferred by measuring the pressure of the saturated R-113 at five locations along the test section. The inlet pressure was measured with a calibrated pressure gage, while the pressure drop between each of the five taps was measured with a vertical mercury manometer. The R-113 flow rate was measured by a rotameter located between the condenser and the pump. The water flow rate in the condenser was measured with a rotameter located at the condenser entrance. Both of the above flow measurements had an experimental uncertainty of approximately ±1 percent.

Figure 2 shows the construction of the test section, which consisted of a 3.66-m tube. Thermocouples measured wall temperature at 23 locations along the test section. One layer of tape was placed between the tube and the thermocouple bead for electrical isolation. Two additional layers of tape were wrapped around the tube to secure the thermocouples. Each thermocouple wire was run along the length of the tube for at least 0.90 m in order to eliminate thermocouple wire lead losses. The tube and thermocouple wires were then covered with insulation and enclosed by a guard heater. The guard heater was constructed from a 6.35-mm-thick wall by 88.9-mm-o.d. copper tube wrapped with heating tape. The outside of the guard heater was insulated to reduce the power required to maintain an adiabatic wall condition at the outer surface of the test tube. Copper-constantan thermocouples were taped to the inside of the copper tube at eight locations along the length of the guard heater to aid in establishing the adiabatic condition.

Bus bar fittings were clamped to bushings soldered to each end of the test tube. The voltage was measured across the bus bars while the current was obtained from the voltage drop across a shunt; both measurements were made with a digital voltmeter. The uncertainties in these measurements led to an uncertainty of ±1 percent in the heat flux.

The dimensions of the tubes tested are shown in Table 1. Also shown in Table 1 is the tube numbering system (i.e., Tubes 1 through 8), which is used throughout this paper to identify each tube.

Data Reduction

Because of current capacity limitations in the rectifier, the 10.92-mm-i.d. copper tubes were tested at lower mass fluxes than the 8.71-mm tubes. Each tube was tested at an inlet pressure of approximately 338 kPa and an inlet temperature of approximately 70°C.

For each test run, 13 axial heat transfer coefficients were calculated on the basis of bulk fluid saturation temperature, tube heat flux, and tube inside wall temperature. Because the temperature difference across the wall of the stainless steel tube was quite large, measured outside wall temperatures were corrected to give the inside tube wall temperatures

$$T_i = T_o + Q/V \cdot k[(r_o^2 - r_i^2)/4 - r_o^2/2\ln(r_o/r_i)] \quad (1)$$

Four thermocouples were mounted just downstream of each pressure tap; hence, the readings were averaged:

$$T_{avg} = (T_{top} + 2T_{mid} + T_{bot})/4 \quad (2)$$

Wall temperatures at all other locations were based on the single measurement, T_{mid}. Circumferential variations in wall temperatures were normally negligible in the forced convection vaporization region, and somewhat larger (but still less than 2.0°C) in the nucleate boiling region. The local heat transfer coefficient at each axial location was then calculated as follows:

$$h = Q/[A(T_{avg} - T_{sat})] \quad (3)$$

When heat transfer coefficients were calculated for augmented tubes, the area used in equation (3) was the area of a smooth tube with the same maximum inside diameter as the augmented tube. Mass flux was also based on a smooth tube cross-sectional area calculated from the maximum inside diameter. Qualities at each axial location were calculated from inlet conditions and energy balances along the tube length. The uncertainties in the heat transfer coefficient and quality calculations were approximately ±10 percent and ±0.02, respectively.

Heat transfer coefficients measured at the first and last axial locations were not considered valid because of heat losses. A problem that arose when the electrically heated twisted-tape inserts were tested was heat generation within the metallic tape. A common solution to this problem in tests with water is to isolate the tape from the tube wall with electrical insulation tape. Unfortunately, the adhesive on common insulating tapes dissolves in R-113. Therefore, heat generation was minimized in this study by using a twisted tape with a small cross-sectional

Table 1 Geometry of tubes tested

Tube No.	1	2	3	4	5	6	7	8
Type	Smooth	Hitachi Thermofin	Noranda T0038	Smooth	Wieland 0°	Wieland 16°	Noranda T0050	Twisted Tape
Augmentation Method	N/A	Helical Micro-Fin	Helical High-Fin	N/A	High-Fin	Helical High-Fin	Helical High-Fin	Twisted Tape
Material	Cu	Cu	Cu	SS	Cu	Cu	Cu	SS
Outside Diameter	9.525	9.525	9.525	12.70	12.58	12.55	12.70	12.70
Inside Diameter	8.712	8.712	8.509	10.92	10.92	10.92	11.43	10.92
Fin Shape	--	Triangle	Rectangle	--	Trapezoid	Trapezoid	Rectangle	--
Number of Fins	--	65	21	--	32	32	26	--
Helix Angle	--	17.5°	30°	--	0°	16°	31°	--
Fin Height	--	0.211	0.381	--	0.551	0.551	0.508	--
Fin Base Width	--	0.290	0.430	--	0.404	0.404	0.430	--
Fin Tip Width	--	~0.0	0.430	--	0.239	0.239	0.409	--
Wall Thickness	0.407	0.407	0.508	0.889	0.760	0.760	0.635	0.889
Tape Thickness	--	--	--	--	--	--	--	0.254
Tape Width	--	--	--	--	--	--	--	9.53
Pitch, Length of 180° Tape Twist/D_i	--	--	--	--	--	--	--	11.6
Area Ratio A_a/A_s	1.00	1.60	1.80	1.00	1.89	1.96	2.10	1.55
Wetted Perimeter	27.37	43.83	49.34	34.31	64.68	67.29	72.08	53.32

All dimensions in mm.

area. The heat generated in the tape was calculated to be approximately 7 percent of the total heat transfer. Since in-tube heat transfer coefficients are based on the heat flux and temperature at the inside tube wall, the wall heat flux was computed by subtracting the computed heat generated in the tape from the total heat transferred to the tube. The local quality was based on the total heat transfer.

Results

The results of the experiments performed on the six different augmented tubes are presented according to the tube diameter. Cross-sectional views of all eight tubes tested are shown in Fig. 3.

The smooth tube data (Tube 1 and Tube 4) are mainly presented through the use of enhancement factors, which are defined as the ratios of measured heat transfer coefficients for an augmented tube and a smooth tube of the same maximum inside diameter as the augmented tube (i.e., the diameter measured from the base of the fins). In some cases, the smooth tube data for heat transfer coefficients have also been plotted with the augmented tube data. A detailed evaluation of the smooth tube data was reported earlier by Reid et al. (1987).

Microfin Tube 2 and High-Fin Tube 3. Two different types of augmented tube with similar diameters were tested. One tube is a microfin tube, manufactured by Hitachi, Inc., and it is hereafter referred to as Tube 2. The second tube is a high-fin tube, manufactured by Noranda Metals Industries, Inc., and it is hereafter referred to as Tube 3. As indicated in Table 1, Tube 2 has many more fins than Tube 3, 65 fins compared to 21 fins; the fin height is much less, 0.211 mm compared to 0.381 mm; and the helix angle is less, 17.5 deg compared to 30 deg.

A plot of experimental heat transfer coefficient versus quality at various heat fluxes for Tube 2 is shown in Fig. 4. Heat transfer coefficients are more dependent on heat flux in regions of lower quality, which represents a nucleate boiling region, as compared to higher quality, which represents a forced convection vaporization region. For each heat flux case, the heat transfer coefficient dips at a certain quality and then increases approximately linearly with quality. This behavior is interesting in that reference smooth tube data taken under similar conditions showed that the heat transfer coefficient was almost independent of quality (Reid et al., 1987).

A comparison of heat transfer coefficients at various mass fluxes at a constant outlet quality is presented in Fig. 5 for

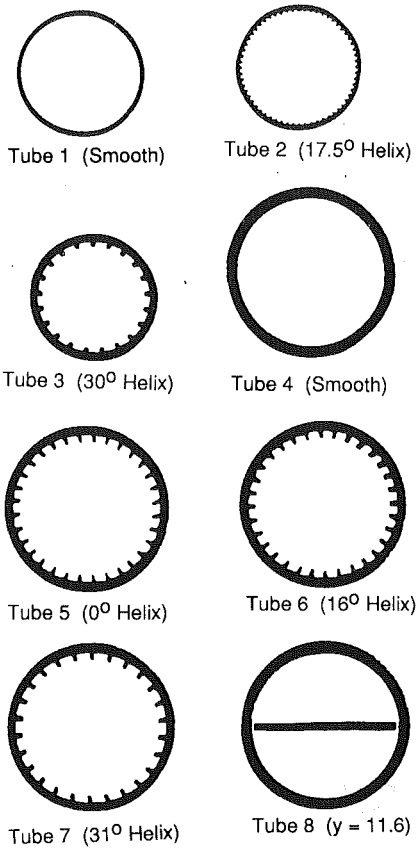

Fig. 3 Cross-sectional views of tubes tested

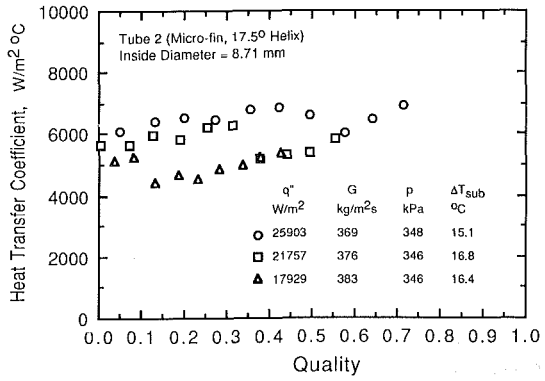

Fig. 4 Evaporative heat transfer coefficients at various heat fluxes for Tube 2

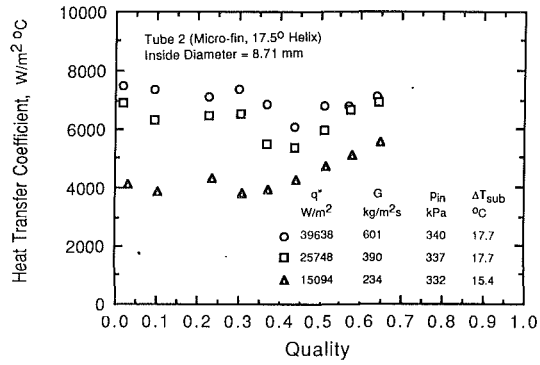

Fig. 5 Evaporative heat transfer coefficients at various mass fluxes for Tube 2

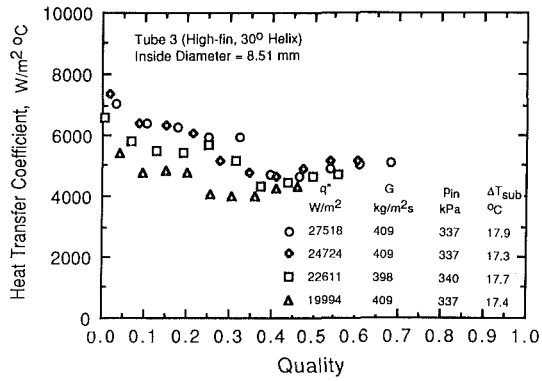

Fig. 6 Evaporative heat transfer coefficients at various heat fluxes for Tube 3

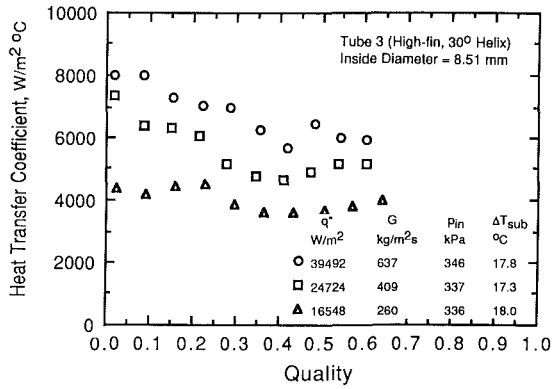

Fig. 7 Evaporative heat transfer coefficients at various mass fluxes for Tube 3

Tube 2. It is difficult to determine the exact effect of mass flux on heat transfer coefficient in Fig. 5 because heat flux is also varying. Comparisons of constant outlet quality with differing conditions may be useful for practical refrigerator or air conditioner design.

Figure 6 presents heat transfer coefficients versus quality at various heat fluxes for Tube 3. As with Tube 2, plotted in Fig. 4, heat transfer coefficients are dependent on heat flux at low qualities, but at higher qualities a common curve representing a forced convection vaporization region is attained. A reduction in heat transfer coefficients is present in the transition region between the nucleate boiling and the forced convection vaporization region, probably because of nucleation suppression.

A comparison of heat transfer coefficients with mass flux as a parameter is shown in Fig. 7 for Tube 3. As with Tube 2 plotted in Fig. 5, heat transfer coefficients increase with mass flux, even though the exact magnitude cannot be determined because of changes in the heat flux.

Of special interest for studies of heat transfer augmentation is the question of how much the heat transfer coefficient is increased relative to an equivalent smooth tube at similar conditions. Local enhancement factors were calculated by forming ratios of experimentally measured heat transfer coefficients for the augmented tube and a smooth tube of the same maximum inside diameter. Heat transfer coefficient data for the augmented and smooth tube were taken at similar values of quality, heat flux, and mass flux. At no time did the measured quality, heat flux, and mass flux for a comparative point between the augmented and smooth tubes deviate by more than 10 percent. As shown in Fig. 8, the enhancement factors for the two augmented tubes are similar. Enhancement factors in the low-quality region are approximately 1.6 for Tube 2 and 1.7 for Tube 3. As quality increases above 0.4, a level that corresponds to a forced convection vaporization region, enhancement factors for both tubes decrease to a value of 1.3. Interestingly, some of these augmentation ratios are less than the area ratios, which are 1.6 for Tube 2 and 1.8 for Tube 3.

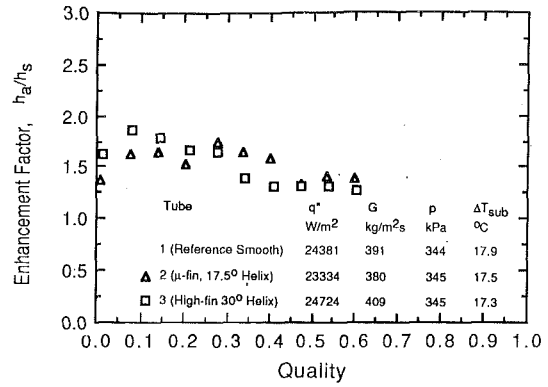

Fig. 8 Heat transfer enhancement factors for Tubes 2 and 3

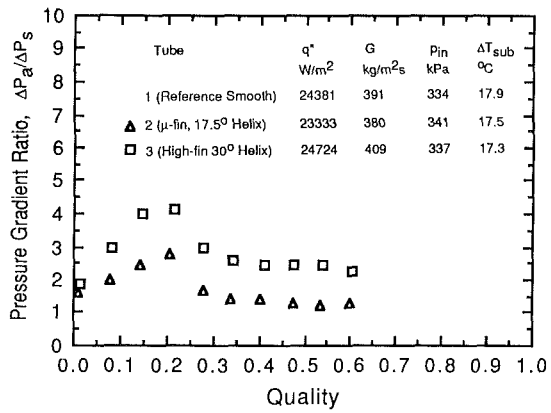

Fig. 9 Pressure gradient ratios for Tubes 2 and 3

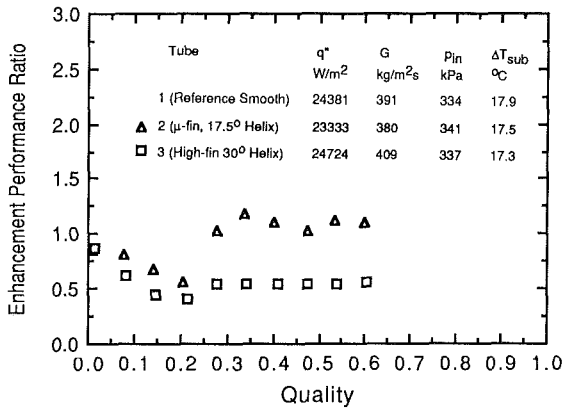

Fig. 10 Enhancement performance ratios for Tubes 2 and 3

It is somewhat surprising that the enhancement factors are similar for the two tubes because they represent very different approaches to in-tube enhancement.

Plots that demonstrate the effects of mass flux and heat flux on enhancement factors, though not presented here, show that the enhancement factors decreased as mass flux increased for both Tube 2 and Tube 3. It was also observed in the forced convection region at high mass fluxes that Tube 2's smaller fins were more effective than the larger fins of Tube 3 in enhancing heat transfer. The larger fins probably result in a thicker liquid film, and therefore, a lower increase in the heat transfer coefficient. This speculation is supported by the work of Reidy (1987). Pressure gradient ratios, $\Delta p_a/\Delta p_s$, for both augmented tubes are shown in Fig. 9. As previously discussed, the pressure of the test fluid was actually measured at only five positions (see Fig. 1) along the test section. Therefore, in order to plot pressure gradient ratios at positions that correspond to the local heat transfer coefficients along the tube, some of the data plotted in Fig. 9 are interpolated values. The

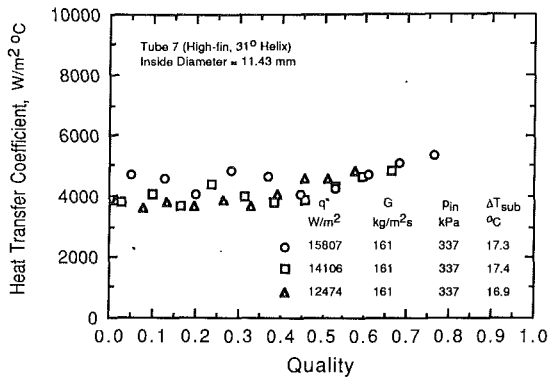

Fig. 11 Evaporative heat transfer coefficients at various heat fluxes for Tube 7

pressure gradient ratios for Tube 2 (microfin tube) are 1.8 to 2.8 at low quality and 1.2 at high quality. The pressure gradient ratio for Tube 3 (high-fin tube) is considerably higher, varying from 4.0 at low quality to 2.2 at high quality.

The effects of heat transfer and pressure drop can be combined into one parameter called the enhancement performance ratio (enhancement factor over the pressure gradient ratio), which is shown in Fig. 10. From the viewpoint of maximizing heat transfer while minimizing pressure drop, higher values are most desirable. Because of the larger pressure gradient ratios for Tube 3 (high-fin tube), the enhancement performance ratio for Tube 2 (microfin tube) is greater over most of the quality range. Specifically, in the high-quality range Tube 2 has an enhancement performance ratio of 1.1 while Tube 3 has a value just slightly greater than 0.5.

High-Fin Tubes 5, 6, and 7. Three augmented tubes with high fins and differing helix angles were tested and compared to each other and to the 10.92-mm-i.d. smooth tube (Tube 4). The comparison with the smooth tube is presented mostly in the form of enhancement factors, as defined previously. Tubes 5 and 6 were manufactured by Wieland-Werke, and they have helix angles of 0 and 16 deg, respectively. Tube 7, manufactured by Noranda Metals Industries, has a significantly larger helix angle of 31 deg. Other parameters for these tubes vary only slightly. For example, Tube 7 has fewer fins (26 compared to 32) and the diameter is slightly larger (11.43 compared to 10.92 mm i.d.) than Tubes 5 and 6. Because of the similarities among the three tubes, the experimental data should give an indication of the effects of helix angle on the performance of high-fin tubes.

The dependence of heat transfer coefficients on quality at various heat fluxes is shown in Fig. 11 for Tube 7. As observed with the data for the smaller diameter tubes presented previously, the heat transfer coefficients increased slightly with heat flux at low quality, which represents a nucleate boiling region. At qualities above 0.4, the usual forced convection vaporization occurred, as evidenced by all three heat fluxes converging to a common curve. A comparison of heat transfer coefficients versus quality with varying mass flux for Tube 7 is presented in Fig. 12. The heat transfer coefficients increased with mass flux. Also, there is evidence of a slight increase with quality at values of quality above 0.3.

The trends observed on both Tubes 5 and 6 were consistent with those observed with Tube 7 presented in Figs. 11 and 12. Specifically, heat transfer coefficients increased with heat flux at low qualities. Therefore, these plots are not repeated here for either Tubes 5 or 6. However, heat transfer for the three finned tubes and the reference smooth tube are compared in Fig. 13 at the same mass flux. Interestingly, heat transfer coefficients for Tubes 5 and 6 show even less dependence on quality than Tube 7. Tube 6 with a 16 deg helix angle generally has the best heat transfer coefficients for these tests.

Enhancement factors based on heat transfer coefficients for

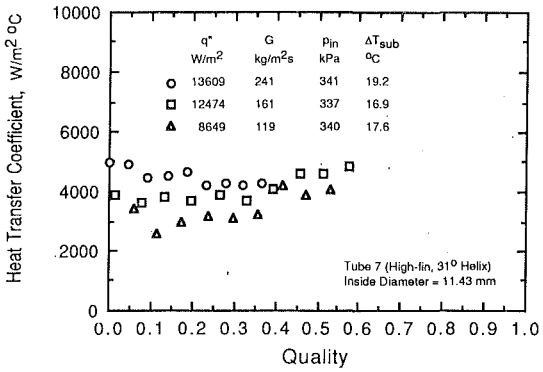

Fig. 12 Evaporative heat transfer coefficients at various mass fluxes for Tube 7

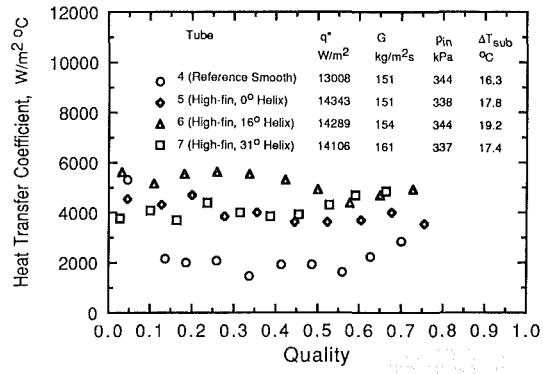

Fig. 13 Comparison of heat transfer coefficients for high-fin Tubes 5, 6, and 7

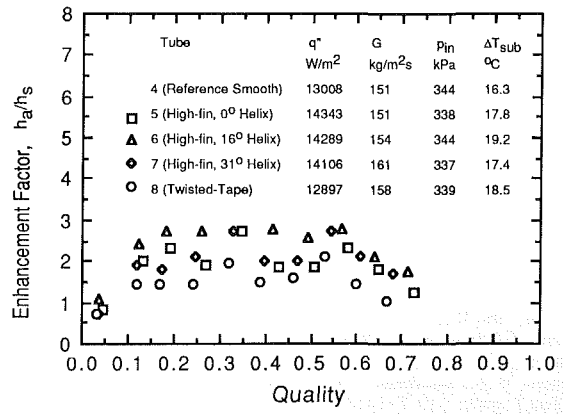

Fig. 14 Heat transfer enhancement factors for high-fin Tubes 5, 6, and 7 and a twisted-tape (Tube 8)

all three high-fin tubes are plotted in Fig. 14. These enhancement factors are reasonably constant over the quality range from 0.05 to 0.6. At all but the highest qualities, Tube 6 with a 16 deg helix angle has the highest enhancement factor, about 2.8. Tube 7 (31 deg) has an enhancement factor slightly higher than Tube 5 (0 deg), 2.2 compared to 2.0, over most of the quality range. At the lowest qualities, all four tubes have enhancement factors approaching unity. In the high-quality range, the performance of Tube 7 with a 31 deg helix angle approaches that of Tube 6. The enhancement factor of Tube 5 above 0.6 quality is slightly lower than that of the other two finned tubes. The trend of higher enhancement factors in tubes with fins having some helical twist agrees qualitatively with Lavin and Young (1965). Similarly, the trend of highest enhancement factors at moderate helix angles agrees with the results of Kubanek and Miletti (1979) and Kimura and Ito (1981).

A plot of pressure gradient ratio versus quality is shown in

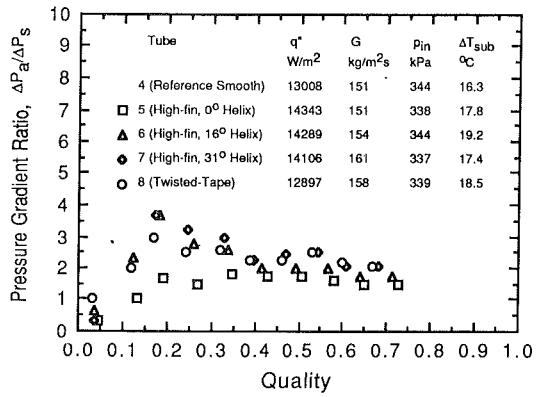

Fig. 15 Pressure gradient ratios for high-fin Tubes 5, 6, and 7 and a twisted-tape (Tube 8)

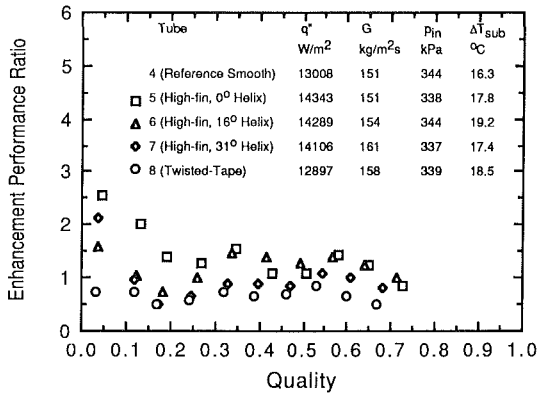

Fig. 16 Enhancement performance ratios for high-fin Tubes 5, 6, and 7 and a twisted tape (Tube 8)

Fig. 15. Of the three high-fin tubes plotted in Fig. 15, Tube 5 with a 0 deg helix angle has the lowest pressure gradient ratio with a value of approximately 1.6 over a wide quality range. Tube 6 has a slightly higher pressure gradient ratio approaching about 2.0, while the pressure gradient ratio for Tube 7 is even higher at about 2.6. It can be concluded that the pressure gradient ratio increases with the helix angle. At the lowest quality, the pressure gradient ratio is 1.0 or even less for all three tubes. This low value may be due to uncertainties in pressure measurements at the point of incipient boiling.

As discussed previously, an enhancement performance ratio can be defined that includes the effects of both heat transfer enhancement and pressure gradient increases, for the three high-fin tubes. Following the general trends of the enhancement factor and the pressure gradient ratio, the enhancement performance ratios are generally constant over most of the quality range plotted. Tubes 5 and 6 are comparable, with enhancement performance ratios of about 1.3. Tube 7 with a 31 deg helix angle has a slightly lower value approaching 1.0. A possible conclusion applicable to high-fin tubes is that enhancement performance ratios can be increased by lowering the helix angle.

Twisted-Tape Insert Tube 8. This test section was assembled by inserting a stainless steel twisted tape, with $y = 11.6$, into a 10.92-mm-i.d. stainless steel tube. Tests were conducted to determine both evaporative heat transfer and evaporative pressure drop. Experimental procedures and test conditions were similar to those for the 10.92-mm-i.d. stainless steel smooth tube without the twisted tape.

A comparison of heat transfer coefficients versus quality with varying heat flux is presented in Fig. 17. The effect of heat flux on heat transfer coefficients diminishes as quality increases; however, the forced convection region, defined by

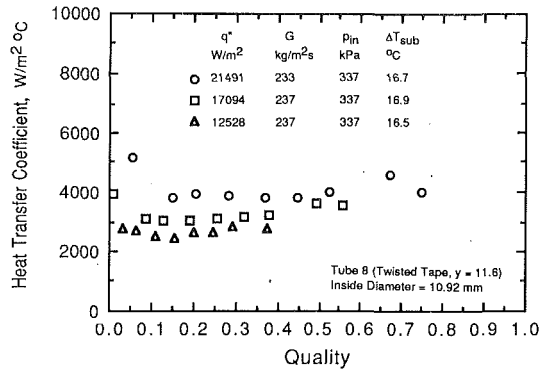

Fig. 17 Evaporative heat transfer coefficients at various heat fluxes for Tube 8 (twisted-tape insert)

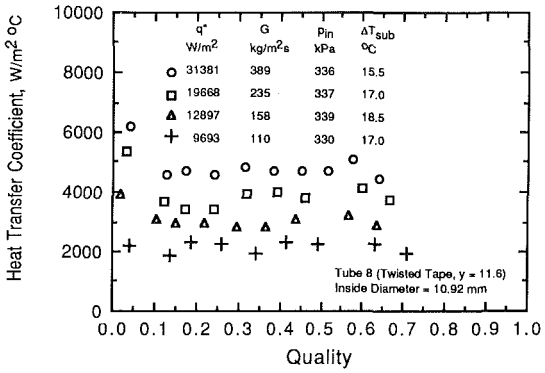

Fig. 18 Evaporative heat transfer coefficients at various mass fluxes for Tube 8 (twisted-tape insert)

a dip and then a steady increase in the heat transfer coefficient, is less obvious than it was for the finned tubes. A plot of heat transfer coefficient versus quality is shown in Fig. 18 for a range of mass fluxes and heat fluxes. Heat transfer coefficients are shown to be independent of quality over a wide range of qualities.

The enhancement factor for Tube 8 is included in Fig. 14. An enhancement factor of about 1.5 is shown for a wide range of qualities. This value is lower than the values that were obtained previously for the high-fin tubes. Even though not shown on Fig. 14, the effects of augmentation were generally less pronounced as the mass flux was increased. As mass flux increased to 237 and 389 kg/m^2-s, the average enhancement factor decreased to 1.2 and 1.0, respectively.

Pressure gradient ratios for Tube 8, as shown in Fig. 15, varied from 2.0 at low quality to 2.75 at high quality. In the low-quality region, the pressure gradient ratio is lower than the values for all of the finned tubes except Tube 5. In the higher quality region, the pressure gradient ratio for Tube 8 tended to be the largest. The enhancement performance ratios for Tube 8, as shown in Fig. 16, varied from 0.8 at low qualities to 0.5 at high qualities. These values are lower than the values for the three high-fin tubes with similar diameters.

Dissimilar test conditions in the Jensen and Bensler (1985) study for vertical flow of R-113 permitted only a limited comparison with the data in the present study. The closest comparison possible was at 233 and 277 kg/m^2-s, 21.5 and 20.0 W/m^2, 0.283 and 0.249 quality, and 345 and 350 kPa inlet pressure for the current study and the Jensen and Bensler study, respectively. At these local conditions the heat transfer coefficient was 3890 W/m^2 K for the current study and 2200 W/m^2 K for Jensen and Bensler, a 46 percent deviation. Jensen and Bensler correlated their vertically flowing twisted tape data with several variations on a correlation by Chen (1966) taking into account the increased fluid flux at the tube wall and using the tube hydraulic diameter. The Chen correlation was among six correlations compared with the reference smooth tube data used in this study (Reid et al., 1987). The Chen correlation was the poorest predictor of the data with deviations typically greater than 30 percent. The Jensen and Bensler correlation yielded deviations similar to those of the current data.

Conclusions

The evaporative heat transfer and pressure drop characteristics of six different augmented tubes were tested in the study. A comparison of a microfin tube and a high-fin tube for the same test conditions showed that they have similar enhancement factors that ranged from 1.3 to 1.7, depending on the quality, for a specific mass flux. However, because of lower pressure gradients, the microfin tube had a much higher enhancement performance ratio (1.1 compared to 0.5), which accounts for both heat transfer and pressure drop effects. A comparison of three high-fin tubes with different helix angles, ranging from 0 to 31 deg, showed that the tube with an intermediate value of 16 deg had the highest enhancement factor, which was 2.8 over most of the quality range. This result is in qualitative agreement with several studies in the literature. Enhancement performance ratios for the three tubes varied from 1.0 to 1.3, with the two smaller helix angle tubes (0 and 16 deg) having the largest values. Compared to the three high-fin tubes, the twisted-tape insert had lower enhancement factors (1.5) and enhancement performance factors (0.6). A systematic comparison between the twisted tape data and data found in the literature was not possible due to dissimilar test conditions.

References

Agarwal, K. N., Varma, H. K., and Lal, S., 1980, "Boiling of R-12 Under Swirl Flow," *Proceedings Fifth National Heat and Mass Transfer Conference*, Hyderabad, India, Feb., pp. 101–106.

Bergles, A. E., Nirmalan, V., Junkhan, F. H., and Webb, R. L., 1983, "Bibliography on Augmentation of Convective Heat and Mass Transfer—II," Heat Transfer Laboratory Report HTL-31, ISU-ERI-Ames-84221, Iowa State University, Ames, IA, Dec.

Blatt, T. A., and Adt, R. R., 1963, "The Effects of Twisted Tape Swirl Generators on the Heat Transfer Rate and Pressure Drop of Boiling Freon 11 and Water," ASME Paper No. 63-WA-42.

Chen, J. C., 1966, "A Correlation for Boiling Heat Transfer to Saturated Fluids in Convective Flow," *I&EC Process Design and Development*, Vol. 5 (3), pp. 322–329.

Ito, M., and Kimura, H., 1979, "Boiling Heat Transfer and Pressure Drop in Internal Spiral-Grooved Tubes," *Bulletin of Japan Society of Mechanical Engineers*, Vol. 22 (171), pp. 1251–1257.

Jensen, M. K., and Bensler, H. P., 1985, "Saturated Forced-Convective Boiling Heat Transfer With Twisted-Tape Inserts," ASME JOURNAL OF HEAT TRANSFER, Vol. 107, pp. 43–47.

Khanpara, J. C., Bergles, A. E., and Pate, M. B., 1986, "Augmentation of R-113 In-Tube Evaporation With Micro-Fin Tubes," *ASHRAE Transactions*, Vol. 92, Pt. 2, pp. 506–524.

Kimura, H., and Ito, M., 1981, "Evaporating Heat Transfer in Horizontal Internal Spiral-Grooved Tubes in the Region of Low Flow Rates," *Bulletin of Japan Society of Mechanical Engineers*, Vol. 24 (195), pp. 1602–1607.

Kubanek, G. R., and Miletti, D. L., 1979, "Evaporative Heat Transfer and Pressure Drop Performance of Internally Finned Tubes With Refrigerant 22," ASME JOURNAL OF HEAT TRANSFER, Vol. 101, pp. 447–452.

Lavin, J. G., and Young, E. H., 1965, "Heat Transfer to Evaporating Refrigerants in Two-Phase Flow," *AIChE Journal*, Vol. 11, (6), pp. 1124–1132.

Reid, R. S., 1986, "Augmented In-Tube Evaporation of Refrigerant 113," M.S. Thesis, Iowa State Univerity, Ames, IA.

Reid, R. S., Pate, M. B., and Bergles, A. E., 1987, "Evaporation of Refrigerant 113 Flowing Inside Smooth Tubes," ASME Paper No. 87-HT-51.

Reidy, L. W., 1987, "Flat Plate Dray Reduction in a Wake Tunnel Using Riblets," Naval Ocean Systems' Center, Technical Report 1169, May.

Tatsumi, A., Oizumi,K., Hayashi, M., Ito, M., and Eng, D., 1982, "Application of Inner Groove Tubes to Air Conditioners," *Hitachi Review*, Vol. 32(1), pp. 55–60.

Tojo, K., Hosokawa, K., Arimoto, T., and Ohta, Y., 1984, "Performance Characteristics of Multi-grooved Tubes for Air Conditioners," *Australian Refrigeration, Air Conditioning and Heating*, Aug., pp. 45–61.

J. C. Passos[1]

D. Gentile[2]

Ecole Nationale Supérieure de Techniques Avancées,
Groupe Phénomène d'Interface,
91120 Palaiseau, France

An Experimental Investigation of Transition Boiling in Subcooled Freon-113 Forced Flow

An experimental study of subcooled boiling in a Freon-113 forced flow is presented. The test section is a short tube (length 50 mm, inner diameter 8 mm, and wall thickness 0.3 mm) heated by the Joule effect. Wall temperature profiles along the tube are presented for different operating points and discussed in terms of the upstream propagation of a temperature front separating regions of nucleate and film boiling. This study emphasizes the effect of axial heat conduction on the boiling processes.

Introduction

Concern about nuclear reactor water safety has led to detailed analyses of accident situations in which different boiling regimes occur.

The quantity and configuration of vapor produced on a heated wall lead to a more or less efficient heat transfer. The periodic growth and detachment of bubbles from the wall in the nucleate boiling regime offers a very effective heat transfer mechanism, while the vapor formed in the film boiling regime when coalescence of bubbles on the surface occurs insulates the wall from the liquid and degrades the heat transfer.

A continuous research effort has been devoted to the understanding of the transition process between these two regimes. In particular, it is of significant practical importance to analyze the vapor flow pattern in geometric configurations, such as a vertical heated tube cooled by internal forced convection. Instabilities in the transition boiling regime (between the nucleate and film boiling regimes) require the use of special experimental systems based on a thermal stability criterion (Stephan, 1965). Among the different techniques that have been used are the transient quenching of a hot patch test section (Cheng et al., 1978; Ragheb et al., 1981; Ueda et al., 1983), and the stabilization of wall temperatures using another external fluid flow (Ramu and Weissman, 1977).

For this study, experiments have been conducted in a vertical tube whose wall has been heated by the Joule effect and cooled by an upward internal forced flow of Freon-113. Stabilization of the wall temperature when the transition boiling regime appears in a region of the tube has been achieved by means of an electronic feedback mechanism, which regulates the electrical current by continuous control of the wall temperature (Gentile et al., 1985). Measurement of the wall temperature along the tube has shown that, under specific test conditions, regions displaying different heat transfer mechanisms coexist and a strong temperature gradient on the wall occurs. For such situations, a local increase of the downstream temperature induces upstream growth of the vapor film. This phenomenon is associated with axial conduction along the tube. The results are discussed in terms of internal and external heat transfer characteristics and are tentatively interpreted by using the equal areas criterion (Maddock et al., 1969).

Experimental Facilities

The experiments have been performed in a loop where Freon-113 has been circulated at pressures between 0.15 and 0.40 MPa, mass flow rates between 400 and 1300 kg/m^{2}s, and degrees of subcooling between 5 and 40 K.

The test section consisted of a thermally insulated Inconel tube, 50 mm long (l), 8 mm in diameter (d), and 0.3 mm in wall thickness, heated by the Joule effect and instrumented with eight chromel-alumel thermocouples (TC) from Pirocoax-Mesurix 0.5 mm in diameter (numbered 4 to 11 in Fig. 1). Similar thermocouples are soldered to the flanges at 0.3 mm from the internal surface (see Fig. 1). Three of them (TC 1, 2, 3) allow measurement of the temperatures at the inlet and the other three (TC 12, 13, 14), at the outlet so that the boundary conditions can be estimated for each operating point, corresponding to a given heat flux, q_e, and the temperature indications of the TC 11. The length of the tube preceding the heated test section was equal to 500 mm, i.e., 62.5 d, and thus allowed for a fully developed turbulent flow (Schlichting, 1979) at the entrance of the test section. In order to visualize the flow at the entrance and exit of the heated section, a Pyrex tube has been installed, before and after the Inconel tube. Moreover, two chromel-alumel thermocouples of 0.2 mm have been installed at the axis of the flow in the exit of the two transparent sections. These thermocouples allow evaluation of the degree of inlet subcooling and the exit temperature of the fluid.

Using Gauss's law, we can prove that the electric fluid inside the heated tube is equal to zero. This result prevents the existence of the known effects of electric fields on the nucleate boiling of Freon-113 (Asch, 1966; Hsu and Grahan, 1976).

The electrical current (or the equivalent electrical power, $q_e = U^2/RS$, where $R = 7.4\ \text{m}\Omega \pm 1$ percent is the tube electrical resistance, U is the voltage at the tube ends, and $S = \pi dl$) delivered to the tube was regulated by an analog electronic feedback control device (Gentile et al., 1985; Gentile, 1987) by means of a driving voltage ranging from -10 V to 0 V, and determined by an error signal to the difference between the wall temperature and a set point temperature (see Fig. 2*b*). The concept behind this control system is based on the stability criterion (Stephan, 1965; Peterson and Zaalouk, 1971), the hypotheses of which are a locally uniform wall temperature (static stability) and a small temperature disturbance (dynamic stability). An electronic safety device cut off the heating when the wall tube temperature indicated for one of three control TCs exceeded 613 K. The external heat losses due to natural convection have been evaluated through the empirical correlation recommended by McAdams (1964) for vertical planes and cylinders and have been considered negligible when compared to the values of q_e required for the boiling process.

[1]Departamento de Engenharia Mecânica, Universidade Federal do Rio de Janeiro, CT, Bloco G, C.P. 68503, 21945 Rio de Janeiro-RJ, Brazil.

[2]Present address: Direction de la Recherche Renault, Avenue du 18 Juin 1940, 92500 Rueil Malmaison, France.

Contributed by the Heat Transfer Division for publication in the JOURNAL OF HEAT TRANSFER. Manuscript received by the Heat Transfer Division January 20, 1989; revision received May 15, 1990. Keywords: Boiling, Multiphase Flows, Phase-Change Phenomena.

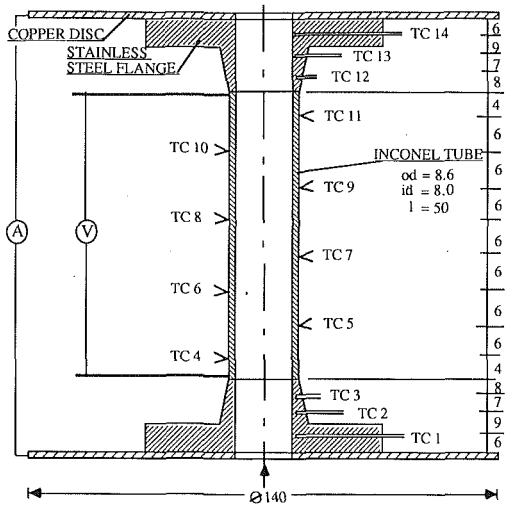

Fig. 1 Test section with thermocouple positions

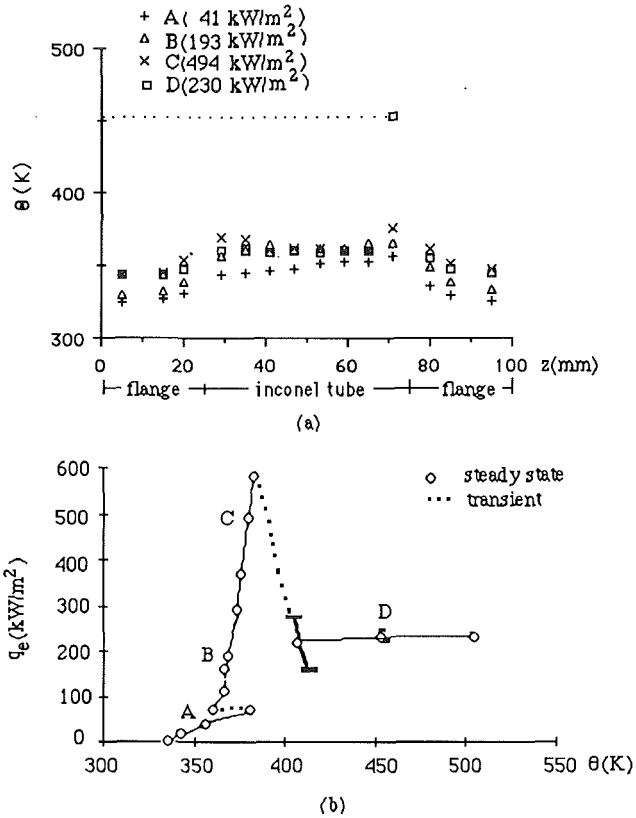

Fig. 2 (*a*) Wall temperatures; (*b*) q_e versus θ (TC 11)

Results

Two significant experimental results are presented below concerning the measurement of the wall temperatures and the propagation of a vapor film upstream on the tube.

1 Temperature Profiles. Figure 2(*a*) shows the wall temperature (θ) along the tube and the flanges for four operating points on the q_e-temperature diagram displayed in Fig. 2(*b*). Point A corresponds to single liquid phase convection, B and C to partial nucleate boiling (because the outlet temperatures of Freon are lower than the saturation temperature (T_{sat})), and D to transition boiling. The tests were performed for a pressure of 0.30 MPa (T_{sat} = 357 K), a mass flow rate of 782 kg/m^{2}s, and a subcooling of 20 K. For operations at A, B, and C the temperatures along the tube are nearly uniform and the maximum temperature difference between cases B and C is only 12 K for an increase in heat flux of 301 kW/m^2. At D, the high temperature of 453K, near the exit of the tube (TC 11), is attributed to a local transition from nucleate to film boiling in spite of the fact that the heat flux density (230 kW/m^2 ± 10 kW/m^2) was well below that of C (494 kW/m^2 ± 18 kW/m^2). Moreover, this temperature rise is very steep because it occurs between two thermocouples separated by only 6 mm, leading to a mean temperature gradient of about 15 K/mm.

2 Development of the Vapor Film Along the Heated Wall. In order to show how the vapor film extends its influence upstream, an experiment has been carried out as follows: For a pressure of 0.20 MPa (T_{sat} = 342 K) a mass flow rate of 402 kg/m^{2}s, and an inlet subcooling of 10 K, the system was brought to the conditions corresponding to case D above. At this point the indication of the thermocouple TC 11 was 416 K (±2 K) while all others were between 343 and 351 K (see profile I of Fig. 3). Then the heat flux was modified very slightly in order to increase the temperature given by the TC 11 to 546 K. At this point, TC 10 indicated 473 K (with fluctuations of about ±5 K) while the other thermocouples still remained at 343 and 351 K (see profile II of Fig. 3). Increasing the temperature indicated by TC 11 to 613 K brought the indication of TC 10 to 603 K and that of TC 9 to 403 K without modifying the others (see profile III of Fig. 3). In this case, the temperature fluctuations of TC 10 and TC 11 were only ±0.5 K while those of TC 9 were ±5 K. This was related to the occurrence of a stable film boiling regime in the vicinity of TC 10 and TC 11, while an unstable transition boiling regime was present near TC 9. It should be pointed out that in this experiment, the heat flux, corresponding to profiles II and III, was 128 kW/m^2, well below the critical heat flux, 451 kW/m^2, and the bulk exit quality was about 0 percent. This indicates that the different heat exchange regimes in the tube corresponded to a localized boiling on the wall, the rest of the flow (in the bulk) being liquid (subcooled boiling). The critical heat flux was also determined without the use of the feedback control, by means of a quasi-steady-state increasing of U, or q_e. Thus, the critical value of the heat flux was characterized by a sharp increase in the local wall temperature (Collier, 1981). In the case of profile I, large fluctuations in the heat flux (±43

Nomenclature

d, id = inner diameter of the heated tube
G = mass flow rate
k = thermal conductivity
l = length of the heated tube
od = outside diameter of the heated tube
p = test pressure
q = heat flux
q_e = heat flux delivered to the tube by the Joule effect
q_i = heat flux transferred to the fluid
q_{min} = heat flux at the Leidenfrost temperature
R = electrical resistance of the heated tube
S = area of the internal surface of the heated tube = πdl
ΔT = inlet subcooling
T_{sat} = saturation temperature
U = electrical voltage
V = volume of the tube
z = axial coordinate
θ = wall temperature
θ_L = Leidenfrost temperature
ϕ = diameter of the copper disk

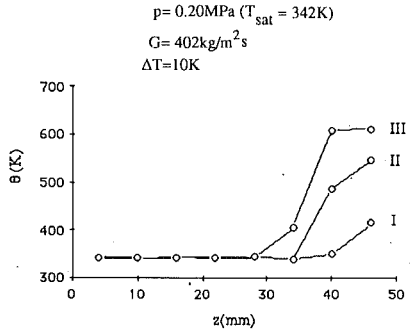

Fig. 3 Wall temperature profiles

kW/m^2), associated with the transition boiling regime at the exit of the tube, occurred. The effect of the feedback control was to prevent the sudden occurrence of vapor in the whole tube, thereby stabilizing the longitudinal temperature profile, which corresponds to the one described by the equal area criterion (see next paragraph).

Figures 4(*a*, *b*, *c*) show the evolution of the heat flux generated by the Joule effect as a function of the temperatures indicated by thermocouples 9, 10, and 11, respectively. Operating point I is reached by TC 11 in the transition boiling regime after transiting through the critical heat, while TC 9 and TC 10 remain in the nucleate boiling regime. For operating point II, TC 10's temperature moved into the transition region, showing the progressive extension of the vapor film upstream the tube. For operating point III, TC 9's temperature increases and enters the transition regime. It is important to note that the points presented in these figures are obtained for steady conditions and that the passage from one operating point to another is achieved with a minimal modification of the electrical current, i.e., at a nearly generated constant heat flux. Transient conditions indicated in Fig. 4(*c*) (or Fig. 2*b*) show that the transition boiling was not stabilized in the region immediately after the peak boiling heat flux. The high wall temperature at the tube exit and the presence of temperature gradients as high as 33 K/mm (profile III of Fig. 3) promoted the axial heat conduction and the extension of the vapor film to the upstream region for a heat flux smaller than the critical value. The peculiar shape of the q_e–θ curves will be discussed later.

The experimental uncertainty computed as shown in Kline (1985) show a maximum of 4.5 percent for q_e and 3.6 percent for temperature measurements.

It is well known that Freon-113 is subject to chemical decomposition for temperatures higher than 573 K. Thus, such a phenomenon may have occurred during the tests performed under the conditions corresponding to profile III in Fig. 3. Examination of the upper portion of the tube did indeed show traces of decomposition.

Discussion of Results

The results presented were obtained using an electronic feedback system allowing us to cover, at nearly constant generated heat flux (q_e), the range of local wall temperatures (for the selected thermocouple, TC 11) between the nucleate and the film boiling regimes (see Fig. 5). In this figure, the internal characteristic, q_i, which represents the heat flux transferred to the fluid, and the external characteristics, q_e, are shown versus the local wall temperature. The θ_L value, known as the Leidenfrost temperature, corresponds to the beginning of the transition between the film and the nucleate regimes and q_{min} is the correspondent heat flux. Once the conditions for steady multiple states were reached, the electronic regulation could be bypassed, provided the local temperature was higher than θ_L. If the temperature was set below θ_L, the operating point moved to the nucleate boiling branch of the curve because it

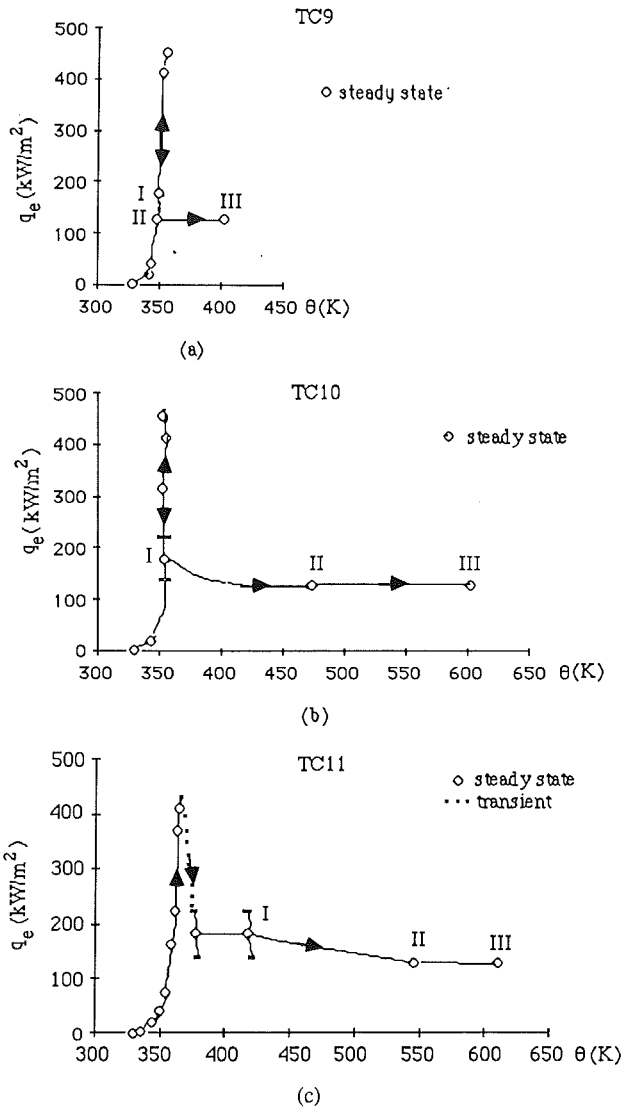

Fig. 4 Operating points on the q_e–θ characteristics

was not possible to achieve stable conditions on the portion of the curve with a negative slope (Stephan, 1965). Under these conditions the Leidenfrost temperature could be determined as shown by Gentile (1987).

It should be pointed out, however, that the initial design of the electronic feedback system did not take into account the possible existence, in the forced convection regime, of an axial conduction effect due to the intense temperature gradients along the tube. As a result the transition boiling was not fully stabilized in this regime while it was in the pool boiling regime over a small heated horizontal plate (Afify, 1986) and around a heated platinum wire (Benejean and Llory, 1981) where temperature gradients, if they exist, are less intense.

Let us now turn our attention to the heat exchange process when axial conduction is present and assume that the temperature profile along the tube presents a sharp change as shown in Fig. 6. This profile does not take into account the temperatures at the flanges, especially the temperature gradient in the upper extremity of the heated tube. It should be observed in Fig. 2(*a*) that the level of the wall temperature along the flanges is nearly independent of the different boiling regimes taking place within the heated tube. On the other hand, this temperature level is only dependent on the electrical power delivered to the test section. Moreover, for D, the slope displayed by the temperature distribution in the upper flange

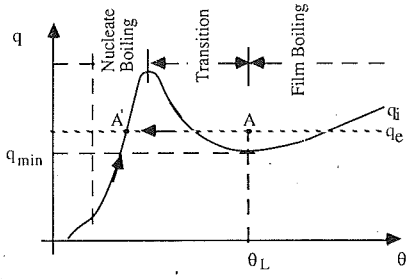

Fig. 5 Trajectory of the working point versus θ

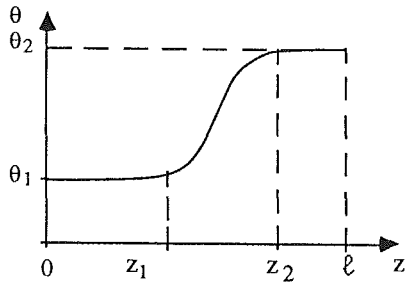

Fig. 6 Idealized temperature profile

represents a temperature gradient in the axial direction, $\Delta\theta/\Delta z$, of about 1.7 K/mm. Thus, the equivalent heat flux is equal to 26 kW/m^2, corresponding to 10 percent of the total heat flux generated in the test section of which the amount delivered to the heated tube is equal to 230 kW/m^2. Of course, the ratio between the amount of heat flux conducted through the flanges and the amount transferred to the fluid would be smaller in a longer tube. However, the hypothesis of zero heat flux has been considered as valid in our case, presenting end effects. Under these assumptions, the heat balance equation is then

$$k\frac{d^2\theta}{dz^2}+\frac{S}{V}(q_e-q_i)=0 \tag{1}$$

where k is the conductivity of the tube material, z the axial coordinate, S the internal surface of the tube, and V the corresponding volume of the tube. This one dimensional equation is valid for steady-state heat conduction, taking into account that the wall thickness is very thin and that a high axial gradient exists in a small portion of the tube. Integrating this equation between θ_1 and θ_2, one obtains

$$\frac{1}{2}\left[k\left(\frac{d\theta}{dz}\right)^2\right]_0^l+\frac{S}{V}\int_{\theta_1}^{\theta_2}(q_e-q_i)d\theta=0 \tag{2}$$

Since $d\theta/dz=0$ for $z=0$, l, the first term is also zero. The assumed hypothesis $q_i=q_e$ for all boiling regimes is no longer acceptable when multiple states coexist along the tube. Thus, the shape of the $q_e(\theta)$ curve differs from that of $q_i(\theta)$. This leads to the peculiar shape of the curves shown in Fig. 4. Figure 7 shows schematically that the areas A^+ and A^-, located between q_i and q_e, are equal in order to satisfy the condition of zero value of the integral (Maddock et al., 1969).

Conclusions

The following conclusions can be drawn from the present work:

(*i*) The coexistence of three different heat transfer boiling regimes on a heated tube 50 mm long was observed for subcooled bulk boiling over the range of mass flow rates tested

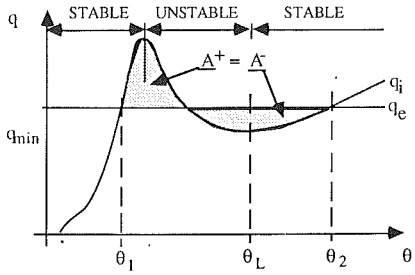

Fig. 7 Internal and external characteristics

(400 to 1300 kg/m^{2}s) since the bulk exit quality was about 0 percent.

(*ii*) The high wall temperature that occurred at the downstream end of the tube when a vapor film was stabilized promoted the axial heat conduction, and, consequently, led to the transition from the nucleate to the film boiling regime farther upstream. This occurred for a heat flux density that was much smaller than the critical value necessary for the first transition from nucleate to film boiling.

Acknowledgments

The authors wish to express their gratitude to Professor D. H. Fruman and referees for their helpful comments and suggestions. This work was partially supported by Electricité de France (EDF) and Centre National de la Recherche Scientifique (CNRS). One of the authors, J. C. P., gratefully acknowledges personal financial support from CAPES, of the Educational Ministry of Brazil.

References

Afify Ali, M. A. M., 1986, "Transfert de Chaleur en Ebullition Stagnante du Fréon-113," Thèse Docteur Ingénieur, ENSTA, Palaiseau, France.

Asch, V., 1966, "Electrokinetic Phenomena in Boiling 'Freon-113'," *Journal of Applied Physics,* Vol. 37, pp. 2654–2658.

Benejean, R., and Llory, M., 1981, "Stabilisation Electronique d'un Processus Thermique non Linéaire," EDF, Bulletin de DER, Série A, No. 3.

Cheng, S. C., Ng, W. W. L., and Heng, K. T., 1978, "Measurements of Boiling Curves of Subcooled Water Under Forced Convective Conditions," *Int. J. Heat Mass Transfer,* Vol. 21, pp. 1385–1392.

Collier, J. G., 1981, *Convective Boiling and Condensation,* 2nd ed., Ch. 8, McGraw-Hill, New York.

Gentile, D., Llory, M., and Benejean, R., 1985, "Stabilization of Freon-113 Subcoooled Boiling in Forced Convection," *Int. Com. Heat Mass Transfer,* Vol. 12, pp. 521–529.

Gentile, D., 1987, "Etude Expérimentale de l'Ebullition du Fréon-113 en Convection Forcée à l'aide d'um Dispositif Eléctronique de Stabilization," Rapport Final ENSTA, Contrat EDF, 2E66099, Avenant No. 1.

Hsu, Y. Y., and Graham, R. W., 1976, *Transport Processes in Boiling and Two-Phase Systems,* 1st ed., Ch. XIII, pp. 414–427, McGraw-Hill, New York.

Kline, S. J., 1985, "The Purposes of Uncertainty Analysis," ASME *Journal of Fluid Engineering,* Vol. 107, pp. 153–160.

Maddock, B. J., James, G. B., and Norris, W. T., 1969, "Superconductive Composites: Heat Transfer and Steady State Stabilization," *Cryogenics,* Vol. 9, pp. 261–273.

McAdams, W. H., 1964, *Transmission de la Chaleur,* Dunod, Paris, pp. 192–196.

Peterson, W. C., and Zaalouk, M. G., 1971, "Boiling Curve Measurements From a Controlled Heat Transfer Process," ASME JOURNAL OF HEAT TRANSFER, Vol. 93, pp. 408–412.

Ragheb, H. S., Cheng, S. C., and Groeneveld, D. C., 1981, "Observations in Transition Boiling of Subcooled Water Under Forced Convective Conditions," *Int. J. Heat Mass Transfer,* Vol. 24, pp. 1127–1137.

Ramu, K., and Weissman, J., 1977, "Transition Flow Boiling Heat Transfer to Water in a Vertical Annulus," *Nucl. Eng. and Design,* Vol. 40, pp. 285–295.

Schlichting, H., 1979, *Boundary-Layer Theory,* 7th ed., Ch. XX, p. 596, McGraw-Hill, New York.

Stephan, K., 1965, "Stabilitat bein Sieden," *Brenust Wärme Kraft,* Vol. 17, pp. 571–578, French transl., EDF-DER No. 1780 CH.

Ueda, T., Tsunenari, S., and Koyanagi, M., 1983, "An Investigation of Critical Heat Flux and Surface Rewet in Flow Boiling Systems," *Int. J. Heat Mass Transfer,* Vol. 26, pp. 1189–1198.

Geometry Effects on Critical Heat Flux for Subcooled Convective Boiling From an Array of Heated Elements

W. R. McGillis
Graduate Research Assistant.

V. P. Carey
Professor of Engineering and Applied Science.

B. D. Strom
Graduate Research Assistant.

Department of Mechanical Engineering, University of California, Berkeley, CA 94720

The critical heat flux (CHF) condition was experimentally determined for subcooled flow boiling from an array of simulated microelectronic devices on one wall of a vertical rectangular passage. A test apparatus was used in these experiments that allowed visual observation of the boiling process while simultaneously measuring the heat flux and surface temperature for ten heat-dissipating elements. Using R-113 as the coolant, the CHF condition was determined for flush and slightly protruding heated elements. As expected, the element farthest downstream was found to reach the CHF condition first in all cases. For both the flush and slightly protruding elements, the trends in the CHF data are similar to those previously reported for subcooled flow boiling on an isolated element. At moderate flow velocities, the critical heat flux predicted by a proposed correlation for subcooled flow boiling from a single element was found to agree well with the multiple-flush-element data if the local fluid subcooling at the last element was used in the correlation. At lower velocities, however, the data deviated from the predicted values. The data for slightly protruding elements were also found to deviate from those for the flush elements at higher velocities. The apparent physical reasons for these trends are discussed in detail.

Introduction

Because high heat transfer coefficients are obtained at high heat flux levels in boiling processes, cooling systems that employ boiling appear to be among the best prospects for high-heat-flux cooling of electronic components. Several recent papers (for example, Oktay et al., 1986; Chu, 1986) have pointed out that projected trends in electronics packaging indicate that future systems will require cooling techniques that can remove heat at heat flux levels significantly higher than those in current system design. As a consequence of the above observations, a number of recent investigations of the application of boiling heat transfer to electronics cooling have been conducted. In particular, several recent studies have examined boiling processes in dielectric fluorocarbon liquids similar to those that may be encountered during direct immersion cooling of electronic components. Park and Bergles (1985) have investigated pool boiling heat transfer from simulated microelectronic chips on vertical flat surfaces. Boiling from an isolated heat source and from a pair of heat sources was studied. The use of ultrasonic enhancement and heat sinks with microholes or microfins were also examined.

In another recent study, Samant and Simon (1986) investigated subcooled boiling heat transfer from a single small high-heat-flux patch in a subcooled turbulent flow. The effects of free-stream subcooling and velocity on the boiling curve and critical heat flux were determined. The use of an impinging jet to enhance the critical heat flux for nucleate boiling from localized heat sources has also been studied (see Lienhard and Hasan, 1979, and Sharan and Lienhard, 1985). Hwang and Moran (1981) reported typical results for pool boiling from an array of microelectronics chip heaters immersed in a motionless fluorocarbon bath with different degrees of subcooling. The effects of the array geometry, however, were not considered by these authors.

Katto and Kurata (1980) and Yagov and Puzin (1984) considered a submerged jet of saturated fluid flowing parallel to a small heater. Mudawar et al. (1987) investigated the performance of falling films of saturated liquid over an array of discrete heaters. The observations of these authors appear to confirm those of Gaertner (1965) who, in his photographic studies, found that the critical heat flux (CHF) was dictated by the transport across a thin liquid sublayer below a vapor blanket, which nearly covers the surface. This vapor blanket is fed by vapor jets on the heated surface, and the liquid sublayer is fed by liquid passing through breaks in the vapor film, or entering at the heater periphery. When the liquid sublayer is vaporized faster than it can be replenished, the system undergoes the transition to film boiling.

Haramura and Katto (1983) developed a model based on the observation of Gaertner (1965) and others for predicting the CHF condition for a finite flush-mounted heater element on an adiabatic wall exposed to a flow of saturated liquid. Mudawar et al. (1987) extended the model to boiling from heated elements on a surface covered by a subcooling falling liquid film. Mudawar and Maddox (1991) developed a modified version of this model from which they derived a method for correlating their CHF data for subcooled convective boiling from a single flush element in a channel flow.

Although the flow boiling characteristics of a discrete chip-sized element have been well documented, knowledge of how the boiling characteristics of one heated element are affected by others in an array of elements is extremely limited. Of particular importance to electronics cooling is the manner in which the critical heat flux condition for one element is affected by the boiling process of the other elements in the array. The studies of Mudawar et al. (1987) and Park and Bergles (1985) provide some insight on this matter. Virtually no information currently exists, however, regarding the critical heat flux conditions for subcooled flow boiling over an array of chip-type elements in a channel.

The purpose of the study described here was to explore experimentally the critical heat flux (CHF) characteristics of

Contributed by the Heat Transfer Division for publication in the JOURNAL OF HEAT TRANSFER. Manuscript received by the Heat Transfer Division January, 26, 1990; revision received October 18, 1990. Keywords: Boiling, Electronic Equipment, Multiphase Flows.

an array of heater elements in subcooled flow boiling. While most previous investigations of flow boiling from discrete sources have considered only flush-mounted heater surfaces, the present study considers both flush heater elements and elements that protrude from the wall. Slightly protruding elements better simulate most real mounted chips.

A ten by ten array of electronic chips, evenly spaced, was chosen as a typical geometry of real electronic chip modules. This array was experimentally modeled in a special test section having a single column of ten evenly spaced heater elements in a vertical channel with adiabatic walls. This experimental model implicitly assumes that each column of chips in a real array would operate under flow boiling without significantly affecting the behavior of chips in the laterally adjacent vertical column. Using R-113 as the coolant, critical heat flux data were obtained for wide ranges of flow rate and subcooling. As described in later sections, the data imply that the protrusion of the elements into the channel can have a significant effect on the critical heat flux condition.

Experimental Apparatus and Procedure

To study the convective boiling process on an array of elements, the special test section shown in Fig. 1 was constructed. One end of the rectangular copper slab was machined to form evenly spaced "fingers," with Teflon spacers and neoprene gaskets between the fingers. This end of the slab fits into the assembly shown in Fig. 1 to form a channel with the ends of the fingers exposed to the coolant on one wall. The side walls of the channel were Teflon and the opposite wall was made of transparent polycarbonate plastic to allow visual observation of the boiling process.

Each one of the square copper fingers measured 6.4 mm on each side. This somewhat unusual test section design allows us to vary the amount by which the heated elements protrude into the channel. Experiments were conducted with both flush and protruding heater elements. The base of the slab was heated by two Tempco 500 W resistance bar heaters clamped to the slab. Heat flowed from the bar heaters through the fingers to the element surfaces, where it was transferred into the fluid by boiling and/or convection. The back of the test section was heavily insulated to minimize heat losses. Thus, the heaters provided an almost uniform heat flux to the heater element surfaces.

Copper constantan thermocouples (AWG 30) were soldered into 0.5 mm dia holes in the copper fingers using a high-melting-point solder. Three thermocouples were placed along each finger as shown in Fig. 1. Two thermocouples were also placed in the flow, one at the channel inlet and one directly behind the downstream heater element. These thermocouples led to a multiplexer, which held two Metra Byte 16 channel multiplexer boards. The multiplexers were driven by an IBMPC/AT with digital/analog converter boards.

The measured temperature gradient in each finger was used to calculate the heat flux dissipated from the exposed surface of each element. Extrapolation of the temperature profile also allowed us to determine the surface temperature of each element. Heat flux is defined as the total heat flow through the copper finger leading to the heater element divided by the total surface area of the heater element exposed to the flow. These results were used to construct the typical boiling curves for each element (surface heat flux versus surface superheat). The surface superheat temperature of an element was determined by subtracting the saturation temperature of the fluid (typically 47.6°C) from the surface temperature of each element.

The system flow loop, shown in Fig. 2, provided a steady flow of subcooled liquid to the test section. Fluorocarbon coolant R-113 stored in the reservoir was pumped through a flow meter and into the test section where heating and partial vaporization occurred. The fluid then passed through the condenser, a countercurrent heat exchanger coil using city water as the coolant. If additional cooling of the test fluid proved necessary, some fluid was directed through a supercooler, consisting of a coil immersed in a cold brine bath. The reservoir, heat exchangers, and all pipes were insulated with 1/2 in. foam rubber. This arrangement made it possible to achieve fluid temperatures corresponding to subcooling levels ranging from 42 to 17°C at the test section inlet.

Depending on the coverplate used, the channel height H could vary from 1.9 mm to 6.4 mm. For the fixed flow rate capacity of the coolant supply system, the variable channel height extended the range of coolant velocities and allowed us to vary the channel geometry, thereby allowing us to evaluate its effect on the boiling process. As noted above, the size of each square surface element L was 6.4 mm on a side. The distance between adjacent elements was also 6.4 mm. The channel width W was 12.7 mm.

Software written for use with the IBM data acquisition boards monitored the thermocouples for indications of achieving steady state and/or the transition to film boiling on the heater elements. When steady state was reached, the temperatures indicated by all the thermocouples were logged into a data file. The applied heat flux was gradually increased by small increments during a given experiment at a given flow rate. The system was allowed to stabilize, and data were recorded after each increment. Eventually, a point was reached where the surface temperature increased continuously without stabilizing after increasing the heat flux. When the surface temperature of a heater element increased faster than 1°C/s, it was assumed that the critical heat flux had been exceeded, and power to the bar heaters was immediately cut off.

The highest heat flux for which the system reached steady state for nucleate boiling was used to determine the critical heat flux. When transition to film boiling occurs, the incremental increase in power input to the heaters produced a run-

Nomenclature

A_e = effective area of protruding elements in nucleate boiling
A_l = area of downstream face of protruding element
A_t = total exposed surface area of heated element
C_o = empirical constant from Kutateladze (1952)
c_{pf} = specific heat at constant pressure of liquid coolant
g = acceleration of gravity
H = channel height
H_e = length of heater element protrusion into channel
h_{fg} = heat of vaporization
L = length and width of a heater element
q'' = heat flux
q''_M = critical or maximum heat flux
$q''_{M,fc}$ = calculated flush element critical heat flux
$q''_{M,pool}$ = maximum heat flux in pool boiling
q^{*}_{M} = nondimensional critical heat flux
T_{sat} = fluid saturation temperature
T_w = heater element surface temperature
T_b = bulk fluid temperature
ΔT_{sub} = liquid subcooling = $T_{sat} - T_b$
U = velocity of liquid in channel
W = channel width
We = Weber number = $\rho_f U^2 L/\sigma$
ρ_g = density of vapor phase
ρ_f = density of liquid phase
σ = liquid surface tension

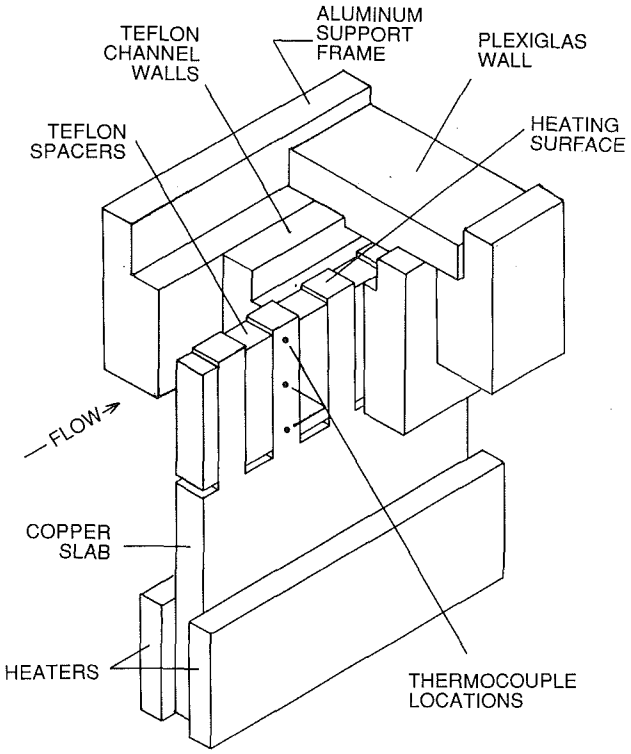

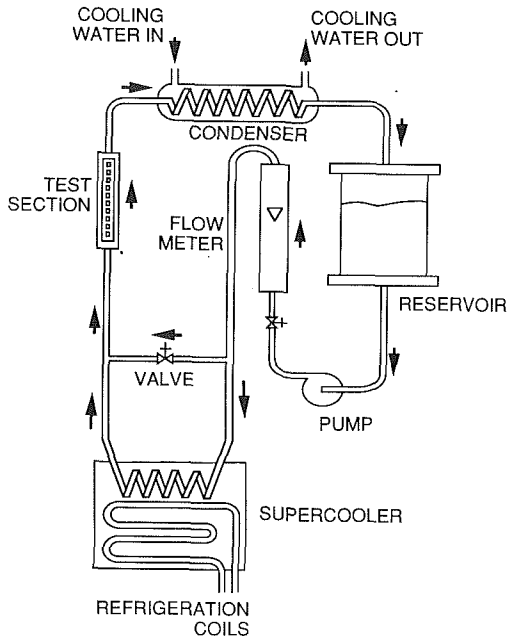

Fig. 2 Test system used in convective boiling experiments

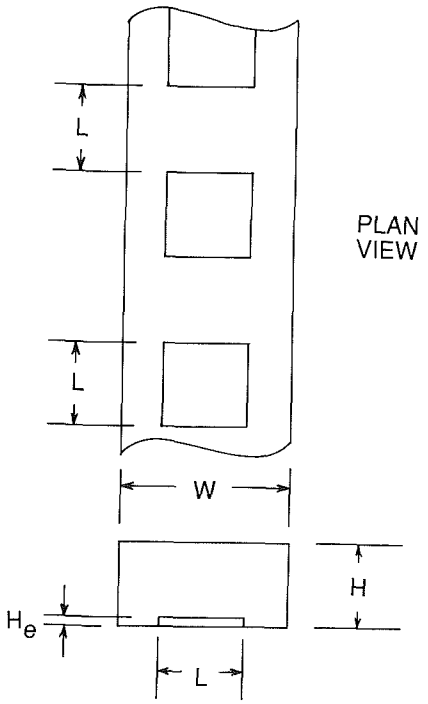

Fig. 1 *(a)* **Cutaway view of test section;** *(b)* **drawing of channel geometry**

away surface temperature making determination of the heat flux impossible. The power input to the heaters that would correspond to the "true" critical heat flux for the element was an intermediate power level, which lay between these two points. Since the power settings were always changed so that the incremental increase in power was at most 7 percent, 3.5 percent was added to the last stable heat flux measured ensuring that the calculated peak heat flux was within 96.5 percent of the true critical heat flux.

Figure 3 shows photographs of subcooled boiling from the

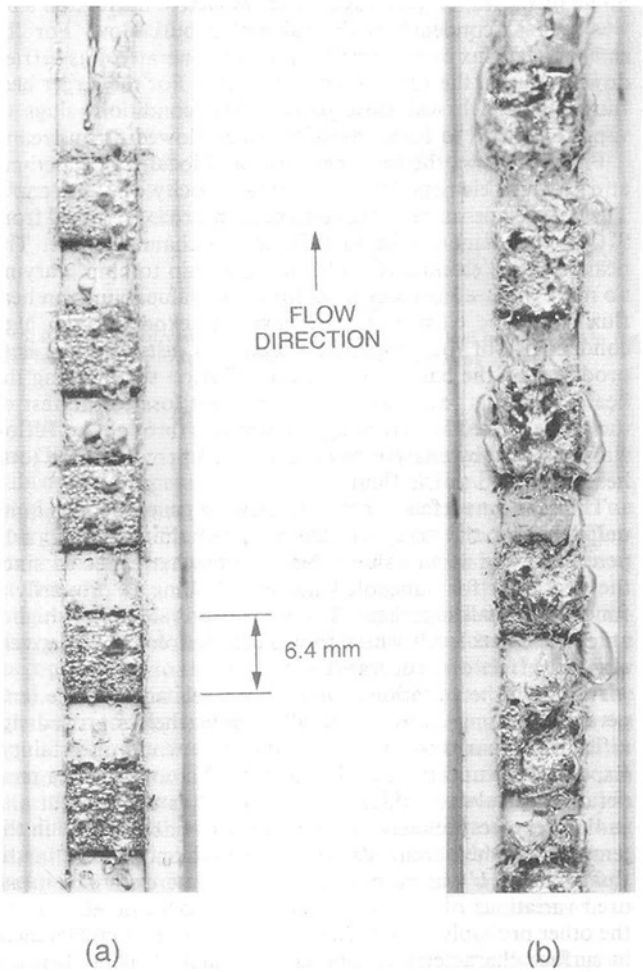

Fig. 3 Photographs of two-phase flow of R-113 in a channel with an array of heated elements. Bulk flow velocity is 44.8 cm/s and the bulk fluid inlet temperature was 23°C. Average heat fluxes were: *(a)* **21 W/cm², (b) 43 W/cm².**

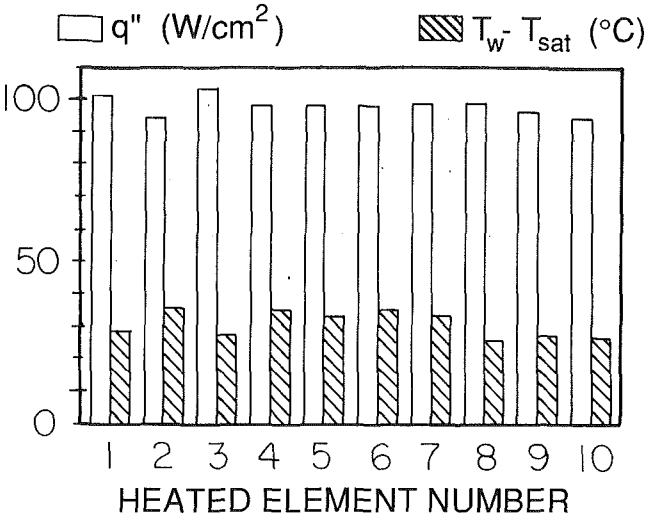

Fig. 4 Local heat flux and local wall superheat at each flush heater element for a bulk flow velocity of 103.9 cm/s and for an inlet bulk fluid temperature of 9°C

five elements nearest the downstream end of the array. Both photos are for an inlet bulk fluid temperature of 23°C and a bulk flow velocity of 44.8 cm/s (the inlet subcooling was therefore 24.6°C in both cases). Figures 3(*a*) and 3(*b*) correspond to mean element heat fluxes of 21 and 43 W/cm^2, respectively. Some of the vapor generated from the active nucleation sites was seen to condense in the subcooled bulk flow. For the smaller heat flux case, part of the vapor generated was carried downstream in the form of small bubbles. For the larger heat flux case, which was close to the CHF condition, slugs of vapor appeared to form, parts of which flowed downstream.

Figure 4 shows the local heat flux and local wall superheat at each flush element for a bulk flow velocity of 103.9 cm/s. The bulk temperature of the coolant in this case increased from 9°C at the channel inlet to 19°C at the channel outlet. The heat flux was essentially uniform from chip to chip, varying no more than ±3 percent from the mean value. Uniform heat flux from one element to the next was expected; the high conductivity of the copper slab served to distribute the heat produced by the bar heaters, and the Teflon surrounding the heater elements restricted conductive heat loss to the rest of the test section. The percentage of heat loss through the Teflon was estimated by analysis to be less than 3 percent of the total heat dissipated to the fluid.

The element surface temperatures were generally also quite uniform over the array of elements, remaining within ±12 percent of the mean value. This is somewhat expected since the heat flux for subcooled nucleate boiling is primarily a function of wall superheat. The variation is somewhat higher at low heat flux levels where forced convection has a relatively stronger effect on heat transfer.

Although the variation in heat flux levels and surface temperatures among chips was small, it nevertheless proved significant compared to the estimated experimental uncertainty. Experimental uncertainties in the heat flux and surface temperature calculated values were estimated as ±2 percent and ±4 percent, respectively, due primarily to uncertainties in the temperature measurements. Experimental uncertainty in the fluid velocity U was estimated to be ±3.5 percent. The measured variations of surface temperature from one element to the other probably cannot be entirely attributed to differences in surface characteristics among the heater elements because the surfaces were, in fact, very similar and Freon, being a highly wetting fluid, would tend to mask any small differences in cavity size distribution that existed.

Air leakage into the test section through the seals is believed to have been eliminated by the seals and the positive system pressure relative to the laboratory ambient. The effectiveness of the seals was evident from the fact that no fluid leakage occurred during the unheated system operation with channel fluid flow. The thermal expansion of the seals that occurs during element heating further served to tighten the seals around the elements. Deaeration of initially entrapped air in the cavities was provided by repeating heating cycles of the same fluid. The above observations suggest that the possible effects of air leakage and/or presence of dissolved air in the coolant should have been small.

Although the uniformity of the heat input to the elements in our test section was not perfect, the amount of variation is not unlike that expected in a real array of chips. Since we determined the heat flux and surface temperature for each chip independently, this nonuniformity does not affect the accuracy of our data. Furthermore, as will be discussed below, the data suggest that the critical heat flux for an element in the array depends mainly on the local conditions at that element, and is not strongly dependent on the distribution of the heat input upstream of it.

Using the test system described above, experiments were performed for both protruding and flush heated elements with the channel oriented vertically and the flow upward. For the protruding-case experiments, the elements extended 0.8, 1.6, and 2.4 mm into the channel; H_e = 0.8, 1.6, and 2.4 mm, respectively. Three different channel geometries were tested with protruding and flush elements. Subcooled flow boiling experiments were conducted using R-113 at nominally atmospheric pressure. The inlet subcooling and mean flow velocities in the channel were varied from 20°C to 40°C and 9.6 to 103.9 cm/s, respectively. The velocity range covered corresponded to channel Reynolds numbers (based on channel hydraulic diameter) between 1993 and 8048.

Discussion of Results

The Boiling Curve. Although the main purpose of the present study was to examine the critical heat flux behavior, some observations regarding the boiling curve data are noteworthy. Heat flux data for the first element in the array at 20°C subcooling for a flush and 0.8 mm protruding element are shown in Figs. 5 and 6, respectively. The first element encountered by the flow is expected to behave essentially as an isolated element. Hence, an approximate fit to the data of Ma and Bergles (1983) for saturated pool boiling of R-113 from a vertical, flush heater element is plotted for comparison in these figures.

Note that the peak heat flux levels presented in Figs. 5 and 6 do not correspond to the critical heat flux for that particular element. In our experiments with the array of elements, the transition to film boiling occurred at the heater element nearest the channel exit first, where the bulk subcooling of the flow was lowest. Whenever this occurred, the test was aborted to avoid damaging the test section. Thus, the upper range of heat flux for any heater element was limited by the transition at the last element.

As shown in Fig. 5 and 6, subcooling and/or flow significantly extends the nucleate boiling range beyond that obtained for pool boiling in a motionless saturated liquid pool. It is apparent from Fig. 6 that the data for different velocities converge to essentially the same boiling curve at higher heat flux levels where nucleate boiling is expected to be fully developed. The same behavior is observed for subcooled flow boiling in round tubes (see, for example, Collier, 1981). It is also apparent from Fig. 6 that the boiling curves for the protruding heaters are in close agreement, within the scatter of the boiling data, with the approximate fit to the data for the flush heaters.

Critical Heat Flux. The primary purpose of this study was

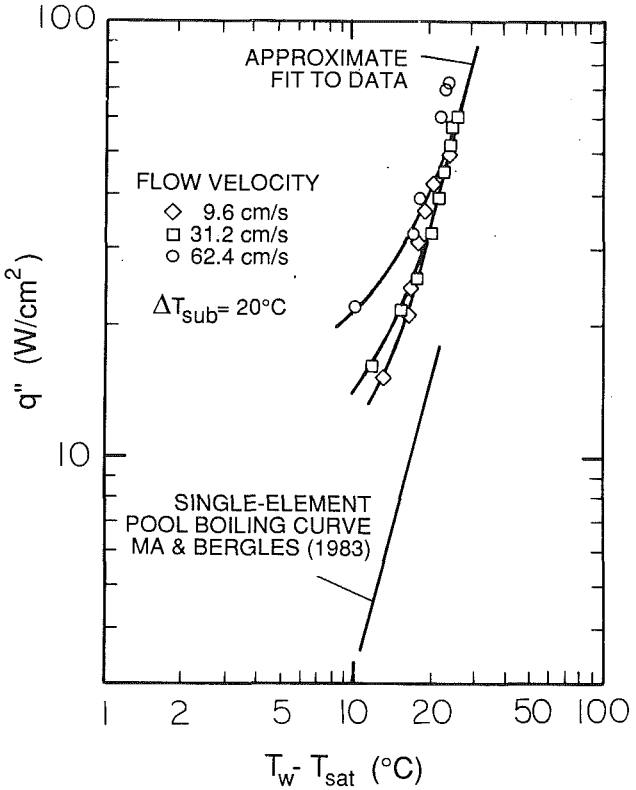

Fig. 5 Boiling data for the leading flush heater element (located farthest upstream)

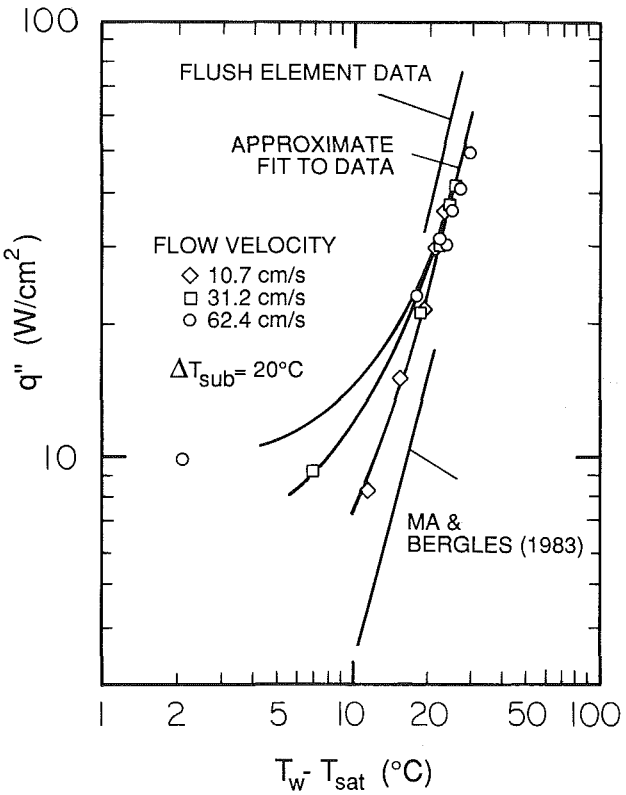

Fig. 6 Boiling data for the leading 0.8 mm protruding heater element (located farthest upstream)

to analyze the combined effects of subcooling and velocity on CHF of an array of simulated microelectronic devices for different elements and channel geometries. The effects of flow velocity and subcooling on the critical heat flux are illustrated

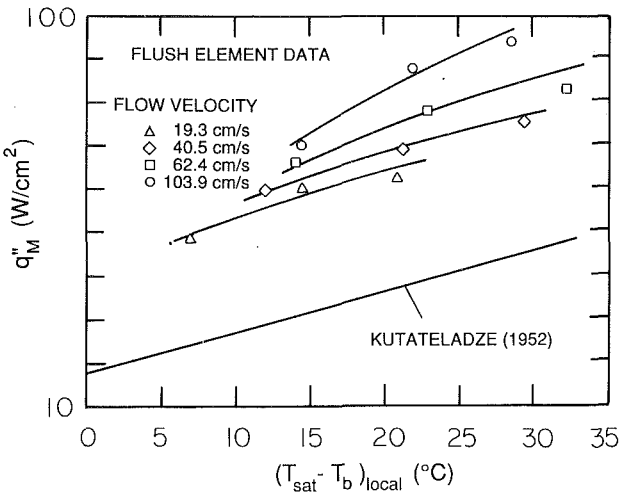

Fig. 7 Effects of velocity and subcooling on critical heat flux data for the last flush heater element in an array

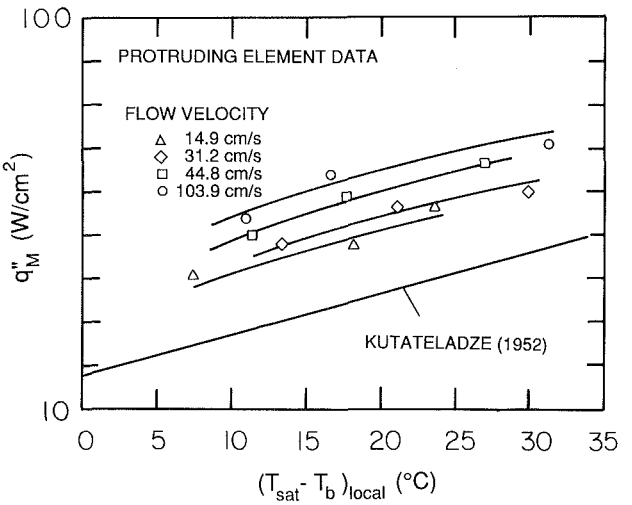

Fig. 8 Effects of velocity and subcooling on critical heat flux data for the last 0.8 mm protruding heater element in an array

by the representative data in Figs. 7 and 8. These figures show the CHF data of the last heater element versus the local fluid subcooling temperatures for different bulk flow velocities. The local subcooling at the last element was determined from an energy balance for the flow using the measured exit temperature and the measured heat input for the last heated element in the array.

Increasing flow velocity and subcooling both serve to increase the critical heat flux. Mechanisms for these effects are incorporated into the subfilm evaporation model of Mudawar et al. (1987) mentioned in the Introduction. In this model, the transition to film boiling is dictated by the evaporation of the liquid sublayer. When flow is induced over the surface, there is a greater flow of liquid into the sublayer from the upstream edge than is present in pool boiling. The evaporating fluid in the sublayer is thus replenished at a higher rate, postponing dryout. When subcooled liquid enters the sublayer, it has a greater capacity for heat absorption than if it were saturated. Thus, subcooled liquid increases the heat flux necessary to achieve a transition to film boiling.

Figure 7 shows the influence of velocity and subcooling on the CHF of the flush-mounted heaters. For any given velocity, CHF increases with increasing subcooling. This trend agrees with that predicted by the correlation for subcooled boiling with zero flow proposed by Kutateladze (1952). For subcooled

pool boiling from an infinte flat, horizontal surface, Kutateladze recommended the following equation for $q''_{M,\text{ pool}}$:

$$q''_{M,\text{ pool}} = 0.16\rho_g h_{fg}\left[\frac{g\sigma(\rho_f-\rho_g)}{\rho_g^2}\right]^{1/4}\left[1 + C_o\left(\frac{\rho_f}{\rho_g}\right)^m \frac{c_{pf}\Delta T_{\text{sub}}}{h_{fg}}\right] \quad (1)$$

where $C_o = 0.065$ and $m = 0.8$. Somewhat later, Ivey and Morris (1962) recommended the same correlation, but proposed constant values $C_o = 0.1$ and $m = 0.75$. For R-113 at atmospheric pressure, the difference between the two correlations ranges from 1–6 percent depending on the degree of subcooling. The line corresponding to equation (1) is plotted in Figs. 7 and 8. As the inlet velocity in this study is reduced, the measured CHF values appear to approach limiting values that are discernibly higher than those given by the pool boiling model.

It is well known that small heater elements may have critical heat flux values significantly higher than that for an infinite flat surface under identical conditions. Lienhard et al. (1973) reported significant deviations from the infinite flat plate for values of $L\sqrt{(g(\rho_f-\rho_g)/\sigma)}$ smaller than 1. For our system, this combination of parameters was about 6.0. This suggests that the significant deviation between our data and the predicted data does not seem to be solely a consequence of the size of our element. The fact that the zero-velocity limit of our critical heat flux data is significantly higher than the infinite surface prediction proposed by Kutateladze (1952) could be at least partly a result of the effect of vapor buoyancy on the flow field. The buoyancy acting on vapor bubbles generated and released from the element surfaces strongly augments the upward flow near the elements. To maintain the same total mass flow that is input upstream of the heaters with the increased upward velocity near the elements, the fluid laterally adjacent to the elements must slow down and/or recirculate. In the limit of the mean flow rate approaching zero, a strong bouyancy-driven upward flow may still exist over the heater elements. When this flow reaches the top of the test section passage, most of the upward flow may then be recirculated downward in the lateral regions of the channel away from the elements. Localized recirculation of the flow may also occur. Hence, even at very low mean velocities in the channel, the buoyancy-induced local velocity enhancement near the elements may act to augment the critical heat flux. Although we have no direct evidence of alterations of the flow in the channel due to bouyancy effects of this type, these arguments strongly suggest that such effects may be present and may contribute to the enhancement of the critical heat flux at low flow rates.

It is useful to compare the trends in the critical heat flux data in Fig. 7 to those predicted by the correlation developed by Mudawar and Maddox (1991).

$$q''^{*}_M = \frac{q''_M/(\rho_g U h_{fg})}{\left(\frac{\rho_f}{\rho_g}\right)^{\frac{15}{23}}\left(\frac{L}{D_h}\right)^{\frac{1}{23}}\left[1+\frac{c_{pf}\Delta T_{\text{sub}}}{h_{fg}}\right]^{\frac{7}{23}}\left[1+0.021\frac{\rho_f}{\rho_g}\frac{c_{pf}\Delta T_{\text{sub}}}{h_{fg}}\right]^{\frac{16}{23}}} \quad (2a)$$

$$= 0.16\ \text{We}^{-\frac{8}{23}} \quad (2b)$$

where the Weber number is defined as:

$$\text{We} = \frac{\rho_f U^2 L}{\sigma} \quad (3)$$

In the above relations, U is the mean (bulk) flow velocity in the channel. Equations (2) and (3) imply that q''_M is proportional to $U^{7/23}$. For the higher velocities investigated in this study, the trend of the experimental data for the flush-mounted heaters is in good agreement with this predicted trend. For a local subcooling of 20°C, the correlation predicts that increasing the bulk flow velocity from 62.4 cm/s to 103.9 cm/s will produce a 17 percent increase in critical heat flux. This increase is about the same for the experimental data of this study.

Although the asymptotic limit of the q''_M versus $(T_{\text{sat}}-T_b)_{\text{local}}$ curves as U is reduced is significantly above that predicted by Kutateladze's (1952) relation, the curves for low velocities do appear to approach a limiting curve having a slope (with respect to the subcooling) that is the same for the pool boiling prediction. As the flow velocity increases, however, the slope of the curves increases somewhat. The correlation represented in equations (2) and (3) also predicts a somewhat stronger variation of q''_M with $(T_{\text{sat}}-T_b)_{\text{local}}$ than is predicted by Kutateladze's correlation (1). This variation of the slope with flow velocity suggests that in the low-velocity regime, a transition from a buoyancy mechanism to a forced-flow effect occurs as the velocity increases. The transition to a forced-flow effect on q''_M appears complete at a velocity of about 40 cm/s.

The effects of subcooling and velocity on the CHF condition for the 0.8 mm protruding heater elements is shown in Fig. 8. As for the flush-heater case, increasing the subcooling and velocity is seen to increase the critical heat flux. However, unlike the data for the flush heater elements, the slope of the curves for this data (with subcooling) is about the same as the slope of the pool boiling correlation even at the highest velocities tested. There appears to be no deviation in slope with increasing velocity for these data. This trend may be an indication that as a result of protrusions into the flow field, hydrodynamic effects on the critical heat flux condition are significantly altered, relative to the flush-heater case. It can also be seen that for a given velocity and subcooling, the critical heat flux is significantly higher for the flush elements relative to the 0.8 mm protruding elements. For example, at 20°C subcooling and 103.9 cm/s, q''_M is about 25 percent greater for the flush-mounted elements.

As in the flush-element case, the data for the 0.8 mm protruding elements do not asymptotically approach the pool boiling line as U is significantly decreased. For the 0.8 mm protruding elements, however, the q''_M versus subcooling curves at low flow velocities are much closer to the pool boiling line than the corresponding curve for the flush elements under identical conditions.

To examine further the combined effects of subcooling and flow velocity on CHF condition, our CHF data obtained were plotted in terms of the dimensionless parameters used in the correlation of Mudawar and Maddox (1991). The resulting plots for the flush and 0.8 mm protruding-element cases are shown in Figs. 9 and 10, respectively. Also shown in these plots is the correlation of Mudawar and Maddox (1991) as specified by equations (2) and (3). Figure 9 shows that the high-velocity data for the flush-element case agree well with the correlation curve. Moreover, as We^{-1} approaches unity, the data approach a steeper slope in the graph of q''^{*}_M versus We^{-1}. This behavior was not observed in the studies of Mudawar and Maddox (1991) because the range of We covered in their experiments was relatively high (>100).

At low velocities, the CHF data approach values specified by the Kutateladze (1952) correlation cast in terms of the dimensionless parameters used in the correlation of Mudawar and Maddox (1991). Curves representing the Kutateladze correlation plotted in Figs. 9 and 10 correspond specifically to pool boiling of R-113 at atmospheric pressure.

It can be seen in Fig. 9 that as We^{-1} increases (flow velocity decreases) beyond $\text{We}^{-1} = 0.01$, the slope of an approximate curvefit through the CHF data for the flush elements increases until the curvefit to the data is parallel to but higher than the curve corresponding to pool boiling. The apparent asymptotic limit of the data corresponds to the curve

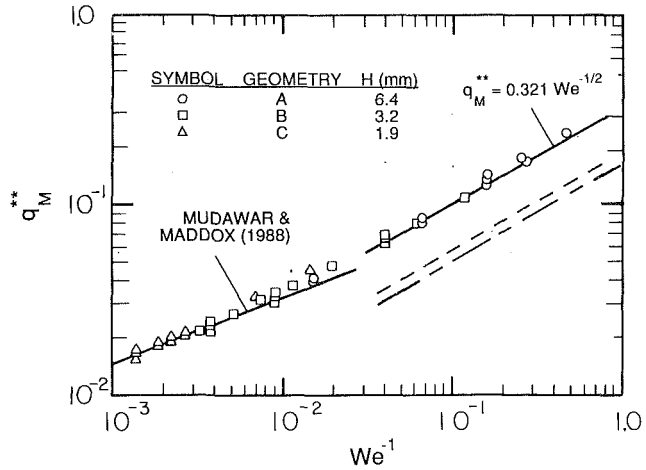

Fig. 9 Nondimensional critical heat flux data for the last flush heater element in an array. The broken lines represent predictions of Kutateladze (1952) considered for ΔT_{sub} = 0°C(——·—— and 20°C (·····).

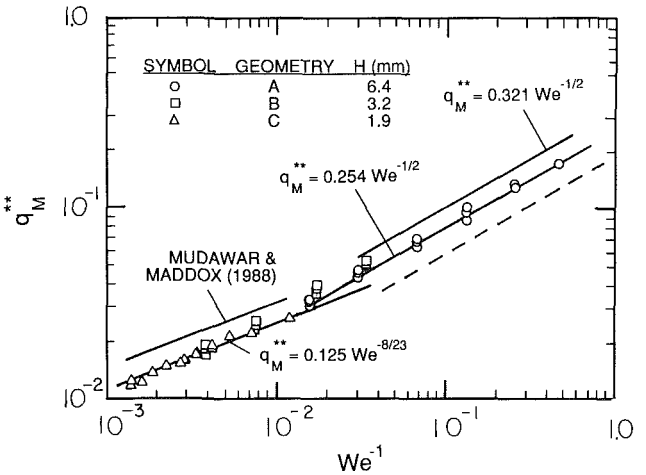

Fig. 10 Nondimensional critical heat flux data for the last 0.8 mm protruding heater element in an array. The broken line represents the prediction of Kutateladze (1952) considered for $\Delta T_{sub} = 20°C$(·····).

$$q_M^{**} = 0.321\ We^{-\frac{1}{2}} \tag{5}$$

As discussed above, the approach of the CHF data to a limiting curve above that specified by pool boiling apparently is due, in part, to added buoyancy-induced recirculating flow.

The foregoing discussion implies that the correlation proposed by Mudawar and Maddox (1991) for predicting the subcooled flow boiling CHF on a single isolated flush element can be successfully applied to an array of flush elements provided that We > 100 and the local subcooling is used in equation (2) to predict the critical heat flux for each element. It also implies, however, that using this correlation in this manner for We < 100 may not yield accurate results. It appears that in the very low We regime (We < 10), the CHF condition is dictated largely by mechanisms similar to those in pool boiling. The range of Weber number between 10 and 100 apparently corresponds to a transition between forced-convection and pool-boiling CHF regimes.

Figure 10 similarly shows the CHF data for the 0.8 mm protruding-heater case, also plotted in terms of q_M^{**} and Weber number. The lines corresponding to equation (2) and pool boiling are also plotted on Fig. 10. It can be seen that relative to the Mudawar and Maddox (1991) correlation, the trend in the 0.8 mm protruding element data is significantly different from that for the flush-element case. At higher velocities (high We), the data for the 0.8 mm protruding case are significantly below the correlation curve, whereas at lower velocity, the data are above the curve. Similar to the trend in the flush element data, there appears to be a subtle transition in the slope of the data for the 0.8 mm protruding element. At low Weber numbers, the slope more closely resembles that of pool boiling, and at high Weber numbers, the data appears to have a similar slope to the model proposed by Mudawar and Maddox (1991).

The model on which the correlation of Mudawar and Maddox (1991) is based does not account for the possible modification of the CHF mechanism due to a complex element geometry. The effects of element protrusion into the flow in the channel may account for the stronger dependence of q_M^{**} on inverse Weber number. In particular, it can be argued that the forced-convection effect in the wake of the protruding heater element is relatively less effective in maintaining adequate liquid flow to the downstream face of the heated element.

Since the liquid motion in the recirculating flow downstream of the element is relatively weak, it is expected that dryout on the downstream face of the element may be dictated by mechanisms similar to those for pool boiling in a motionless pool of liquid. If this surface of the element trips to film boiling first, the heat normally transferred from this surface by nucleate boiling would be diverted to the other surfaces of the element. The resulting higher effective heat flux applied to the other surfaces could promote the onset of critical heat flux condition. This behavior may be responsible for the fact that at higher velocities, the critical heat flux for the 0.8 mm protruding elements is significantly lower than for flush elements under the same conditions. Thus, the downstream face of the heated element may play a critical role in the transition to critical heat flux by serving as the location where the CHF condition is achieved first, thereby precipitating the subsequent dryout of the entire element. While increasing flow rates serve to enhance cooling of the top surface, and probably the leading and side surfaces of the element as well, this may have little effect on postponing local dryout of the trailing surface. These arguments imply that the mechanisms associated with the transition to the CHF condition for protruding elements may differ significantly from those included in the model of the CHF mechanism for flush elements developed by Mudawar and Maddox (1991).

As the flow velocity was decreased, the CHF data for the 0.8 mm protruding elements were found to tend toward a limiting curve parallel to, but higher than the pool boiling limit. The interpretation of the trends in the data for the 0.8 mm protruding-element case was basically the same as that for the flush-element case described above. For We < 10, a pool-boiling-type mechanism apparently dictates the CHF condition, whereas for We > 100 forced-convection effects apparently dominate. For the intermediate range, 10 ≤ We ≤ 100, a transition from one mechanism to the other occurs.

As shown in Fig. 10, the limiting curves that provide a best fit to the 0.8 mm protruding-element CHF data in the high velocity and low velocity ranges are

$$q_M^{**} = 0.125\ We^{-\frac{8}{23}} \text{ for } We > 100 \tag{6}$$

and

$$q_M^{**} = 0.254\ We^{-\frac{1}{2}} \text{ for } We < 10 \tag{7}$$

Also plotted in Fig. 10 are the corresponding limiting curves, which fit the data for the flush-element case. It can be seen that for the 0.8 mm protruding elements, the data are shifted downward, relative to those for the flush elements, by about the same amount in both regimes.

The fluid approaching the last element in the array, where the CHF condition is achieved first, is a two-phase mixture of subcooled liquid and saturated vapor, the vapor having been produced by boiling at the upstream elements. Data taken in

the present study suggest that flow disturbances caused by the presence of vapor in the coolant did not seem to affect the transition to film boiling adversely.

For fluid flowing at 21.3 cm/s and 20°C subcooling, the amount of vapor present over the last heater element was estimated from visual observation to be about 50–60 percent of the total volume. The amount of uncondensed vapor visually appeared to drop with increased subcooling. At 40°C it appeared to have dropped to about 10 percent. This large change in subcooling and the associated change in the amount of vapor present appeared to have no significant effects on the measured critical heat flux other than those already accounted for in the correlation by Mudawar and Maddox (1991) for a single isolated element. In fact, there was no consistent trend between q_M^{**} and ΔT_{sub}, which would indicate that changes in the amount of uncondensed vapor had any influence on the critical heat flux condition for the last element in either the protruding or flush array.

It can also be seen in Figs. 9 and 10 that the variations in the cross-sectional geometry had very little effect on the measured CHF conditions for either the flush or 0.8 mm protruding-element cases. For the flush elements, altering the channel cross section at a given subcooling and flow rate produced no detectable effect on the critical heat flux. For the 0.8 mm protruding-element case, the CHF data for the channel geometry B appear to be slightly higher than those for A, but no significant difference between B and C are observed. The slight difference between data for A and B at the same conditions is almost within the scatter of the data.

Figure 11 shows the CHF data for an increased heater-element protrusion (H_e = 1.6 mm) plotted in terms of q_M^{**} and Weber number. The lines corresponding to the best fit to the CHF data for the flush and 0.8 mm protruding elements are also plotted for comparison. As expected, the trends in the data for the 1.6 mm protruding-element case are consistent with that for both the flush and 0.8 mm protruding-element case. For low velocities, a pool-boiling-type mechanism apparently dicates the CHF condition, whereas for high velocities forced-convection effects apparently dominate. It can be seen in Fig. 11 that there is not a significant deviation for the 1.6 mm protruding element data to that of the 0.8 mm protruding element data.

As noted above, it is expected that dryout occurs on the downstream face of the protruding element at heat flux levels characteristic of the CHF condition for pool boiling. When the downstream face is in an apparent film boiling regime, heat is expected to be diverted to the other exposed element surfaces where nucleate boiling is present. The resulting increase in the effective heat flux for these faces of the element results in a lower critical heat flux because it is based on the total exposed surface area. If the amount of heat removed from the dry downstream face of the protruding element is negligible, this suggests that the heat flux from the other surfaces in nucleate boiling is the same as the heat flux from a flush element in nucleate boiling at the same surface temperature. As a first estimate, the critical heat flux for the protruding element based on the total exposed surface area might be estimated as being equal to the critical heat flux for a flush element multiplied by the correcting area ratio, A_e/A_t. The effective area, A_e, is the portion of the area of the protruding element undergoing nucleate boiling and A_t is the total exposed element surface area. This argument implies that the critical heat flux q''_M obeys the relation

$$\frac{q''_M}{q''_{M,\,fc}} = \frac{A_e}{A_t} \tag{8a}$$

$$= 1 - \frac{A_I}{A_t} \tag{8b}$$

where $q''_{M,\,fc}$ is the calculated critical heat flux for a flush

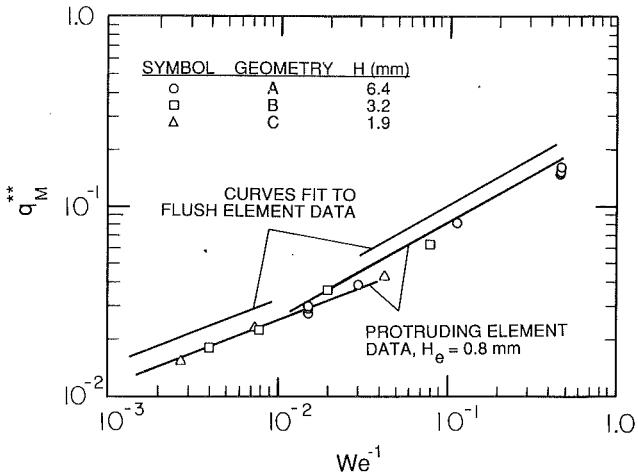

Fig. 11 Nondimensional critical heat flux data for the last 1.6 mm protruding heater element in an array

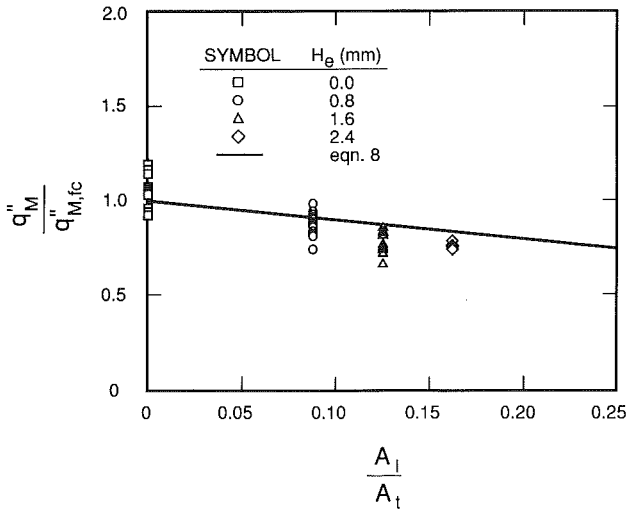

Fig. 12 Critical heat flux data nondimensionalized with the critical heat flux for the calculated flush case

element using the bulk fluid velocity and local fluid subcooling. Equation (8), plotted in Fig. 12, is in fairly good agreement with the experimental dimensionless critical heat flux data for flush elements, 0.8, 1.6, and 2.4 mm protruding elements. The dimensionless critical heat flux is 1 when the elements are flush and as the height of the protrusion, H_e, gets larger, the ratio A_I/A_t trends to the value 1/4, which corresponds to a dimensionless critical heat flux of 3/4.

Conclusions

The results of our experimental study of the crtical heat flux conditions for upward subcooling flow boiling of R-113 over flush and protruding arrays of heated elements imply the following conclusions.

Bubbles flowing downstream apparently did not have a significant effect on critical heat flux for flush elements. For moderate to high flow velocities over flush elements, predictions of the isolated element CHF correlation of Mudawar and Maddox (1991) were found to agree well with the observed CHF conditions at the last heated element in the array if the local subcooling of the flow was used in the correlation.

The critical heat flux data for the protruding elements did not agree well with the predictions of the Mudawar and Maddox (1991) correlation with the local element subcooling. At higher velocities the data were significantly below the predictions of this correlation. The reduction in the critical heat flux

is believed to be associated with premature dryout of the downstream face of the element, which is only weakly washed by the recirculating wake flow. Dryout of this face of the element is believed to increase the heat flux to the other faces, subsequently leading to dryout of the element at a lower overall heat flux.

The results for both the flush and protruding heaters suggest the exsistence of three regimes: a convective CHF regime for $We > 100$ in which the CHF condition is controlled by forced-convective effects; a pool-boiling CHF regime for $We < 10$ in which the CHF condition apparently is dictated by mechanisms similar to those in pool boiling; and a transition regime between the convective and pool boiling regime corresponding approximately to $10 \leq We \leq 100$.

While the data indicate that critical heat flux values of 100 W/cm^2 can be obtained for flush-heated elements using subcooled flow boiling of R-113, the reduction of the critical heat flux associated with the protrusion of the elements is a matter of concern to electronics cooling applications. The best conservative estimate of the CHF condition for protruding electronic devices appears to be provided by the correlations to our data for protruding elements using the local subcooling at that device.

Acknowledgments

The authors gratefully acknowledge support for this research provided by IBM and the National Science Foundation under research grant No. CBT-8451781.

References

Chu, R. C., 1986, "Heat Transfer in Electronic Systems, Keynote Address," *Proceedings, 8th International Heat Transfer Conference*, C. L. Tien et al., eds., Hemisphere Publishing Corp., Washington, D. C., Vol. 1, pp. 383–384.

Collier, J. G., 1981, *Convective Boiling and Condensation*, 2nd ed., McGraw-Hill, New York.

Gaertner, R. F., 1965, "Photographic Study of Nucleate Pool Boiling on a Horizontal Surface," ASME JOURNAL OF HEAT TRANSFER, Vol. 87, pp. 17–29.

Haramura, Y., and Katto, Y., 1983, "A New Hydrodynamic Model of Critical Heat Flux, Applicable Widely to Both Pool and Forced Convective Boiling on Submerged Bodies in Saturated Liquids," *International Journal of Heat and Mass Transfer*, Vol. 26, pp. 389–399.

Hwang, U. P., and Moran, K. P., 1981, "Boiling Heat Transfer of Silicon Integrated Circuits Chip Mounted on a Substrate," *Heat Transfer in Electronic Equipment*, ASME HTD-Vol. 20, pp. 53–59.

Ivey, H. J., and Morris, D. J., 1962, "On the Relevance of the Vapor–Liquid Exchange Mechanism for Subcooled Boiling Heat Transfer at High Pressure," British Report AEEW-R-137, Atomic Energy Establishment, Winfrith, United Kingdom.

Katto, Y., and Kurata, C., 1980, "Critical Heat Flux of Saturated Convective Boiling on Uniformly Heated Plates," *International Journal of Multiphase Flow*, Vol. 6, pp. 575–582.

Kutateladze, S. S., 1952, "Heat Transfer During Condensation and Boiling," translated from a publication of the State Scientific and Technical Publishers of Literature on Machinery, Moscow–Leningrad, as AEC-tr-3770.

Lienhard, J. H., Dhir, V. K., and Riherd, D. M., 1973, "Peak Pool Boiling Heat Flux Measurements on Finite Horizontal Flat Plates," ASME JOURNAL OF HEAT TRANSFER, Vol. 95, pp. 477–482.

Lienhard, J. H., and Hasan, M. Z., 1979, "Correlation of Burnout Data for Disk Heaters Cooled by Liquid Jets," ASME JOURNAL OF HEAT TRANSFER, Vol. 101, pp. 383–384.

Ma, C. F., and Bergles, A. E., 1983, "Boiling Jet Impingement Cooling of Simulated Microelectronic Chips," *Heat Transfer in Electronic Equipment*, ASME HTD-Vol. 28, pp. 3–10.

Mudawar, I. A., Incropera, T. A., and Incropera, F. P., 1987, "Boiling Heat Transfer and Critical Heat Flux in Liquid Films Falling on Vertically-Mounted Heat Sources," *International Journal of Heat and Mass Transfer*, Vol. 30, pp. 2083–2095.

Mudawar, I., and Maddox, D. E., 1991, "Critical Heat Flux in Subcooled Flow Boiling of Fluorocarbon Liquid on a Simulated Electronic Chip in a Vertical Rectangular Channel," *International Journal of Heat and Mass Transfer*, in press.

Oktay, S., Hannemann, R., and Bar-Cohen, A., 1986, "High Heat From a Small Package," *Mechanical Engineering*, Vol. 108, No. 3, pp. 36–42.

Park, K.-A., and Bergles A. E., 1985, "Heat Transfer Characteristics of Simulated Microelectronic Chips Under Normal and Enhanced Conditions," Heat Transfer Laboratory, Department of Mechanical Engineering, Engineering Research Institute, Iowa State University, HTL-35.

Samant, K. R., and Simon, T. W., 1986, "Heat Transfer From a Small Heated Region to R-113 and FC-72," ASME JOURNAL OF HEAT TRANSFER, Vol. 111, pp. 1053–1059.

Sharon, A., and Lienhard, J. H., 1985, "On Predicting Burnout in the Jet-Disk Configuration," ASME JOURNAL OF HEAT TRANSFER, Vol. 107, pp. 398–402.

Yagov, V. V., and Puzin, V. A., 1984, "Critical Heat Fluxes in Forced-Convection Boiling of Refrigerant-12 Under Conditions of Local Heat Sources," *Heat Transfer—Soviet Research*, Vol. 16, No. 4.

An Experimental Study of Laminar Film Condensation With Stefan Number Greater Than Unity

R. L. Mahajan
AT&T-Bell Laboratories,
Princeton, NJ 08540

T. Y. Chu
Sandia Laboratories,
Albuquerque, NM 87185

D. A. Dickinson
AT&T-Bell Laboratories,
Princeton, NJ 08540

Experimental laminar condensation heat transfer data are reported for fluids with Stefan number up to 3.5. The fluid used is a member of a family of fluorinated fluids, which have been used extensively in the electronics industry for soldering, cooling, and testing applications. Experiments were performed by suddenly immersing cold copper spheres in the saturated vapor of this fluid, and heat transfer rates were calculated using the quasi-steady temperature response of the spheres. In these experiments, the difference between saturation and wall temperature varied from 0.5°C to 190°C. Over this range of temperature difference, the condensate properties vary significantly; viscosity of the condensate varies by a factor of nearly 50. Corrections for the temperature-dependent properties of the condensate therefore were incorporated in calculating the Nusselt number based on the average heat transfer coefficient. The results are discussed in light of past experimental data and theory for Stefan number less than unity. To the knowledge of the authors, this is the first reported study of condensation heat transfer examining the effects of Stefan number greater than unity.

1 Introduction

The classical analysis of laminar film condensation on vertical or inclined surfaces is due to Nusselt (1916). In that analysis the condensate film was assumed to be thin, and convective and inertia effects were considered to be negligible. Within the condensate film, gravity was balanced simply by the viscous force, and the temperature profile in the film condensate was assumed to be linear. From the analysis, the local heat transfer rate, Nu_x, was calculated to be

$$\mathrm{Nu}_x = \left[\frac{(\rho_f - \rho_g) g\, h_{fg}\, x^3}{4\, v\, k (T_{\mathrm{sat}} - T_w)}\right]^{1/4} \tag{1}$$

Bromley (1952) performed an analysis using a nonlinear temperature profile. Rohsenow (1956) expanded the calculation to include the effect of liquid crossflow within the film. The analysis, based on a control volume approach, resulted in a differential-integral equation, which was solved by successive approximation. It was shown that the effect of the nonlinear temperature distribution in the film can be accounted for by replacing h_{fg} in equation (1) by h^+_{fg}, given by

$$h^+_{fg} = h_{fg}\left(1 + \frac{3}{8}\,\mathrm{S}\right)(1 - 0.1\mathrm{S} - 0.0328\mathrm{S}^2)/(1 - 0.1\mathrm{S})^2 \tag{2}$$

where S is the Stefan or Jakob number. For the range $0 < \mathrm{S} < 1$, it was shown that equation (2) is very closely approximated by

$$h^+_{fg} \approx h'_{fg} = h_{fg}(1 + 0.68\mathrm{S}) \tag{3}$$

The complete boundary solution, including the inertia and convection effects, was obtained by Sparrow and Gregg (1959). It was shown that except for very low Prandtl number Pr, Rohsenow's approximate analysis was quite adequate.

Koh et al. (1961) applied a boundary layer treatment to include the interfacial shear while Chen (1961) considered analytically the effect of thermal convection, inertia forces, and interfacial shear. The Nusselt–Rohsenow approach was extended by Dhir and Lienhard (1971) to include axisymmetric bodies in nonuniform gravity. For a sphere of diameter D, the Nusselt number based on the average heat transfer coefficient was calculated to be

$$\mathrm{Nu} = 0.785\left[\frac{(\rho_f - \rho_g) g\, h'_{fg} D^3}{v\, k\, (T_{\mathrm{sat}} - T_w)}\right]^{1/4} \tag{4}$$

For a review of these and other earlier studies, see Merte (1973).

A study pertinent to the present investigation is an experimental investigation of quasi-steady laminar film condensation of steam on copper spheres by Dhir (1975). The average heat transfer data were obtained in the range of Stefan number 0.009–0.12 and were shown to be within ±13 percent of the steady-state theoretical results of Dhir and Lienhard (1971) and Yang (1973).

All the studies of condensation heat transfer discussed above are for relatively small sensible heat effects. The contribution of sensible heat is accounted for by correcting the latent heat of vaporization by a sensible heat term in the manner of equation (3). In these studies the correction is considered accurate for Stefan numbers up to 1. The recent study of Sadasivan and Lienhard (1987) showed that the correction factor is weakly dependent on Prandtl number. The conventional view expressed in the literature is that this correction is adequate since Stefan number beyond unity exceeds the range of practical interest (Sadasivan and Lienhard, 1987).

In the last decade, new families of fluorinated fluids having Stefan numbers much greater than 1 in heat transfer applications have become widely used in various industries. Typical applications include cooling of electronic equipment and a mass soldering process called "condensation soldering" or "vapor phase soldering." The process was invented as a method of supplying heat for soldering connector pins to printed circuit boards for telephone switching systems (Chu et al., 1974; Pfahl et al., 1975; Wenger and Mahajan, 1979a, 1979b, 1979c). In this method, articles to be soldered, having predeposited solder at joints, are immersed in a body of saturated vapor of a fluorinated liquid with a typical saturation temperature of 215°C. The basic soldering machine consists of a vessel where vapor of the fluorinated liquid is generated continuously by boiling. The vapor is condensed on a condensing coil near the top opening of the vessel. Because the vapor is much heavier than air, a stable body of saturated vapor can be maintained in the vessel between the boiling fluid and the condensing coil.

Contributed by the Heat Transfer Division and presented at the Joint AIAA/ASME Thermophysics and Heat Transfer Conference, Seattle, Washington, June 18–20, 1990. Manuscript received by the Heat Transfer Division March 19, 1990; revision received August 31, 1990. Keywords: Condensation, Materials Processing and Manufacturing Processes, Phase-Change Phenomena.

The heat transfer to articles immersed in the vapor is rapid and uniform, with absolute control of the maximum temperature. Today, condensation soldering is used throughout the electronics industry.

Ammann and Farkass (1977) measured the heat transfer coefficient h for some of the fluorinated condensation heating fluids using an isothermal transient calorimeter, and compared the results to theoretical values calculated using simply equation (1). The measurements ranged from 125 to 66 percent of the theoretical value, and it was concluded that the agreement was sufficient for engineering purposes. The effects of variable fluid properties (i.e., film temperature) and Stefan number were not examined. Since Stefan numbers as high as 3.5 are encountered during condensation heating, it is of theoretical as well as practical interest to understand the effect of large sensible heat. The present paper reports the results of a series of experiments carried out to observe film condensation for Stefan numbers up to 3.5. Condensation in this experiment is quasi-steady, and heat transfer rate is readily calculated by monitoring the temperature response of copper spheres suddenly immersed in saturated vapor of the fluorinated liquid.

2 Fluid Properties

The condensing fluid used in the present investigation is perfluorotriamylamine, $(C_5F_{11})_3N$, a member of the family of perfluorinated inert liquids manufactured by 3M Co. The fluid is sold as *Fluorinert*[R] liquid and is commercially identified as FC-70. The physical properties of this fluid at 25°C, taken from the 3M Fluorinert Electronic Liquid Product Manual, are given in Table 1.

The properties of this fluid that are of significance in determination of the film condensation heat transfer rate are the kinematic viscosity, thermal conductivity, specific heat, density, and heat of vaporization. Some of these are strongly dependent on temperature. For example, data provided by 3M Co. on measurements of viscosity (Table 2) indicate that for temperature over the range from room temperature to the boiling point of the liquid, the kinematic viscosity varies by a factor of nearly 50. A least-squares fit of the measured data resulted in the correlation of kinematic viscosity as a function of temperature,

$$\log \log (\nu + 0.90825) = (14.1226 - 5.69327 \log T) \quad (5)$$

where T is the temperature (K) and ν is kinematic viscosity (centistokes). The general form of this correlation is that recommended by ASTM Standard D 341-77, "Viscosity-Temperature Charts for Liquid Petroleum Products." The equation fitted the data in Table 2 to an accuracy of ±3 percent.

Table 1 Physical properties of FC-70[R]

Typical boiling point, °C	215
Pour point, °C	-25
Average molecular weight	820
Surface tension, dynes/cm	18
Critical temperature, °C	335*
Critical pressure, atm	10.2*
Vapor pressure, torr	<0.1
Solubility in water, ppm	8
Solubility of air, ml/100 ml	22
Density, g/ml	1.93
Viscosity, centistokes	14.0
Specific heat, cal/g-°C	0.25
Heat of vaporization, cal/g	16
Thermal conductivity, mW/cm²-(°C/cm)	0.69*
Coefficient of expansion, ml/ml-°C	0.0010

*Estimated.
[R]Trademark.

Table 2 Liquid viscosity as a function of temperature

Temperature, °C	Measured value of viscosity, centistokes
24	11.88
30	8.61
40	5.87
60	2.88
80	1.65
100	1.09
110	0.91
120	0.76
130	0.66
140	0.57
150	0.50
173	0.38
216	0.25

The measurements of k, ρ, and c_p as a function of temperature were obtained at AT&T's Thermal Engineering Laboratory at Bell Laboratories, Princeton. The best-fit correlations describing the temperature dependencies of these properties are

$$k = 0.7242718 - 6.353033 \times 10^{-4} T \quad (6)$$

$$c_p = 0.2468938 + 1.51426 \times 10^{-4} T + 1.285630 \times 10^{-7} T^2 \quad (7)$$

Nomenclature

Bi = Biot number $= hD/2k_c$
c_p = specific heat at constant pressure
c_{pc} = specific heat of condensing surface
D = sphere diameter
g = gravitational acceleration
h = average heat transfer coefficient
h_{fg} = latent heat of vaporization
h'_{fg} = $h_{fg}(1 + 0.68\ S)$
k = thermal conductivity of condensate
k_c = thermal conductivity of copper
m_c = mass of condensing surface
Nu = average Nusselt number based on sphere diameter $= hD/k$
Nu_x = local Nusselt number $= hx/k$
Pr = condensate Prandtl number $= \mu c_p/k$
S = Stefan or Jakob number $= c_p \Delta T/h_{fg}$
T = temperature
t = time
x = distance from the upper stagnation point for a sphere or from the leading edge for a plate
ΔT = difference between saturation temperature and sphere surface temperature
ΔT_o = difference between saturation temperature and constant surface temperature
ΔT_w = change in sphere temperature with time
δ = quasi-steady condensate film thickness
δ_{ss} = steady-state condensate film thickness
μ = condensate dynamic viscosity
ν = condensate kinematic viscosity
ρ = density

Subscripts

calc = calculated theoretical value
cp = constant property
exp = experimental
f = condensate
g = vapor
i = initial
m = mean
ref = reference
sat = saturated
vp = variable property
w = surface

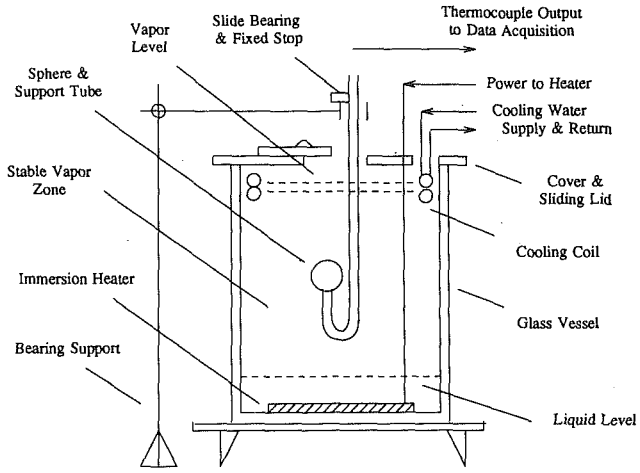

Fig. 1 Experimental apparatus

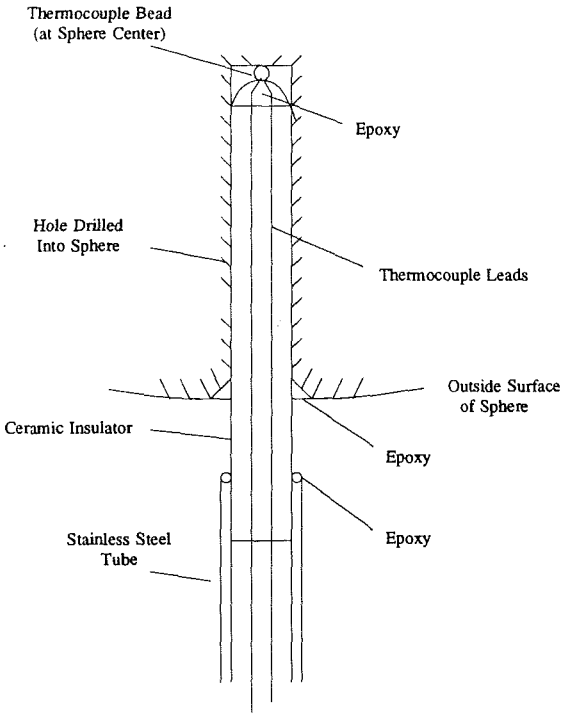

Fig. 2 Details of sphere assembly

$$\rho_f = 1.970381 - 1.829488 \times 10^{-3} T \tag{8}$$

where k, c_p, ρ_f, and T are thermal conductivity in mW/cm-°C, specific heat in cal/g-°C, density in g/ml, and temperature in °C, respectively. The correlations fit the experimental data to an accuracy of ±2 percent.

3 Experimental Apparatus and Procedure

Condensation experiments were conducted using copper spheres with diameters of 25.4 mm and 50.8 mm as the condensing surface. Diagrams of the experimental setup and the sphere assembly are shown in Figs. 1 and 2, respectively. The body of the sphere was machined from copper and finished with a smooth surface. It was supported from the bottom on a stainless steel tube to prevent condensate on the tube surface from running onto the sphere, and a ceramic insulator was used to separate the two pieces. A thermocouple used to measure the sphere temperature was positioned at the sphere center, with the leads running through the ceramic and through the stainless steel tube. Epoxy was used to support the thermocouple bead, which was held in direct contact against the copper by the weight of the sphere. Epoxy also was used as a seal where the ceramic entered both the sphere and the steel tube.

The vessel used to contain the sphere and condensing vapor was a cylindrical glass jar with height 46 cm and diameter 30 cm, as shown in Fig. 1. Electric resistance immersion heaters were used to boil the liquid in the base of the jar and water-cooled coils at the top were used to condense the vapor continuously, so that a region of saturated vapor was set up when the apparatus was fully heated and operating at steady state. Air filled the space above the saturated vapor zone. Power input to the heaters was adjustable using a variac. The jar was fitted with a stainless steel cover, with a smaller removable cover to allow the sphere to be inserted into the vapor. Hence the entire system was at atmospheric pressure. An equipment stand fitted with a slide bearing was used to hold the stainless steel tube supporting the sphere, with a stop clamped to the tube to fix the vertical position of the sphere within the vapor volume. This arrangement allowed manual insertion of the sphere to be fast, smooth, and repeatable. At the beginning of each run a thermocouple was used to read the actual vapor temperature T_{sat} to be used in the data reduction.

To begin an experimental run, steady state was first established in the jar. The heater power was adjusted so that the vapor/air interface was at the top turn of the condensing coils. This allowed the insertion of the sphere and resulting condensation to have a minimal effect on the vapor height, thus minimizing turbulence at the vapor/air interface and any intermixing of air into the vapor zone. Consistent with the past observations of Chu et al. (1975), the interface was observed to be well defined and stable. Temperature measurements were started just as the sphere, normally at room temperature, was lowered through the cover into position and continued until the sphere temperature was within a few degrees of T_{sat}. A data acquisition system was used to read the sphere temperature at preprogrammed time intervals, selected as 0.5 s for both sphere sizes. This interval was long enough to allow negligible error due to variation in the actual time interval used by the acquisition system as well as short enough to allow accurate determination of dT_w/dt at each measured sphere temperature T_w.

Profiles for T_w and dT_w/dt at the start of a run are shown in Fig. 3. A transient period occurs as the sphere enters the vapor and the condensate film is established, followed by the period of quasi-steady condensation, during which a continuous, laminar condensate film was observed. As the run proceeds the temperature asymptotically approaches T_{sat}.

4 Data Reduction and Analysis

4.1 Experimental Nusselt Number. A Fortran program was written to process the experimental data, which consisted simply of the temperature measurements at equal time intervals. The heat transfer coefficient h, at a given measured wall temperature, T_w, was determined using the lumped capacity relation,

$$m_c c_{pc} (dT_w/dt) = hA (T_{sat} - T_w) \tag{9}$$

The experimental Nusselt number Nu_{exp} is then

$$Nu_{exp} = hD/k \tag{10}$$

The error introduced using equation (9) is negligible if Bi is less than 0.4 (Dhir, 1975). For all the data to be presented Bi is less than 0.05, so the temperature of the sphere can be assumed uniform. The rate of temperature rise, $dT_w/dt = \Delta T_w/\Delta t$, was calculated from the sequence of temperature measurements. The sphere surface temperature was taken to be the average of the initial and final temperatures for each interval.

The largest uncertainty in determination of the experimental Nusselt number is due to the measurement of dT_w/dt. At the

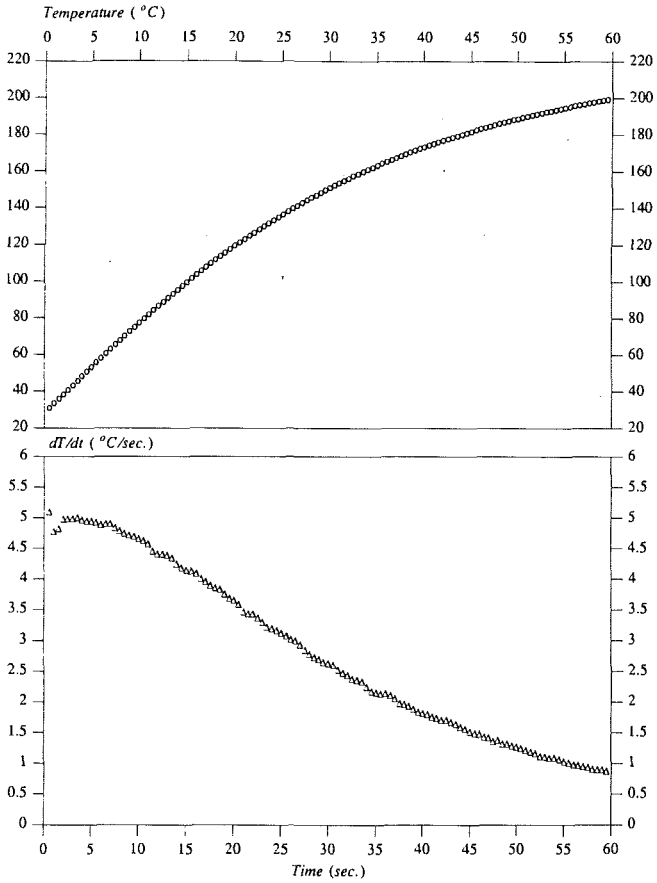

Fig. 3 (*a*) Temperature versus time; (*b*) rate of temperature rise versus time

beginning of a run, $\Delta T_w/\Delta t$ was calculated using two time intervals (1 s) and was about 5°C/s with the 25.4-mm sphere. At higher sphere temperature, with slower heating rate, a sufficient number of time intervals were used to maintain a ΔT_w of at least 2°C. The accuracy of the temperature measurement is ±0.1°C, so the accuracy of the calculation for h and Nu_{exp} is approximately ±2 percent at lower sphere temperature (or higher S) and increases to approximately ±5 percent at higher sphere temperature (or lower S).

Another source of error is due to neglecting the heat transferred to the sphere from the ceramic support. Treating the support as an extended fin, calculations indicate that accounting for the fin effect would decrease Nu_{exp} by 1 percent. Also, in equation (9), the product $m_c c_{pc}$ was calculated using only the mass of the sphere (determined by weighing) and the specific heat of copper. Inclusion of the mass and specific heat of the ceramic located inside the sphere would increase Nu_{exp} by approximately 2 percent. Thus, correcting for these two errors would increase Nu_{exp} by about 1 percent. Poor thermal contact between the copper and ceramic lessens the magnitude of both effects, so the combined resulting error in Nu_{exp} is less than 1 percent.

4.2 Calculated Nusselt Number. In this experimental investigation, the film Reynolds number did not exceed 16, so that laminar film condensation analysis is applicable. For calculation of the theoretical Nusselt number, it must be determined whether the experiment is truly quasi-steady. Furthermore, a relationship between the quasi-steady and steady-state calculations needs to be obtained. Dhir (1975) determined the relative liquid film thicknesses for the quasi-steady and steady-state conditions and estimated the agreement that could be expected between the measured heat transfer coefficients for the two cases. For a vertical flat plate, local steady-state film thickness is

$$\delta_{ss} = \left[\frac{4\nu k \Delta T_0 x}{g(\rho_f - \rho_g) h_{fg}'}\right]^{1/4} \tag{11}$$

It was shown by Dhir that the governing equation for the quasi-steady film thickness δ can be written as

$$\left[\frac{g(\rho_f-\rho_g)h_{fg}'}{\nu k \Delta T(t)}\right]\delta^3 \frac{\partial \delta}{\partial x} = 1 + \left\{\left[\frac{dT_w}{dt}\frac{1}{\Delta T(t)}\frac{\delta^2}{\alpha}\right] \times \left[\frac{5}{8} + \frac{h_{fg}}{4c_p \Delta T(t)}\right]\right\} \tag{12}$$

For a sphere, the term g can be replaced by an effective gravitation as derived by Dhir. If the entire right-hand side is treated as a constant and the left-hand side is integrated, then

$$(\delta/\delta_{ss})^4 = 1 + \left\{\left[\frac{dT_w}{dt}\frac{1}{\Delta T(t)}\frac{\delta^2}{\alpha}\right] \times \left[\frac{5}{8} + \frac{h_{fg}}{4c_p \Delta T(t)}\right]\right\} \tag{13}$$

where δ_{ss} has been substituted using equation (11). The term in the curly brackets is a ratio of dimensionless thermal diffusion constant and the sensible heat capacity of the film (Dhir, 1975). When this ratio is small, quasi-steady film thickness approaches the steady-state value.

It was shown by Dhir that for steam condensing on a copper sphere the ratio δ/δ_{ss} is approximately 1.06 for the minimum value of S = 0.009, so that quasi-steady condensation should result in measured values of heat transfer coefficient within a few percent of those that would be obtained for steady state. For the present case with FC-70 condensing on a 25.4 mm sphere, with $(dT_w/dt)(1/\Delta T)$ approximately 0.035 s^{-1} (from the measured data), an intermediate value of S = 1.5, approximate film thickness of 1.0×10^{-4} m (from equation (11)), and thermal diffusivity of the condensate of 3.3×10^{-8} m^2/s, we have $\delta/\delta_{ss} = 1.008$. The agreement is considerably closer than that with stream, due partly to the slower heat transfer with this fluid, but mainly due to the much larger value of S. Clearly the steady-state calculations can be used to predict accurately the quasi-steady condensation heat transfer rates for the fluid used in this investigation.

For determining the theoretical values of Nusselt number, Nu_{calc}, the full boundary layer solutions of Sparrow and Gregg (1959) can be used. However, as noted there, for Pr > 10, the full boundary layer solutions are very close to the approximate calculations of Rohsenow (1956). For FC-70 condensate, Pr varies from 320 at room temperature (25°C) to approximately 8 at the saturation temperature (215°C). Equations (2) and (4) are therefore appropriate for obtaining theoretical estimates of Nu. Also note that although equation (3) is prescribed in Rohsenow's paper for use in the range $0 < S < 1$, our calculations of h using both equation (2) and equation (3) for values of S much greater than 1 (we performed calculations for S up to 20) indicate that the difference between the two calculations is at the most 0.5 percent. In the results to follow, we have therefore chosen to use the simplified equation (3) in conjunction with equation (4) to calculate Nu_{calc}.

The experimental heat transfer data will be presented relative to the theoretical values calculated in the manner above in terms of the ratio Nu_{exp}/Nu_{calc}. The wall temperature will be presented in terms of the Stefan number, S.

5 Results and Discussion

Results for three runs using the smaller sphere are shown in Fig. 4. The temperature T_{ref} used for calculation of fluid properties was the average of T_w and T_{sat}. The sequence of points measured during the run moves to the left as the sphere is heated. With the sphere initially at room temperature, corresponding to an initial Stefan number of nearly 3.5, it appears that the Nusselt number ratio is fairly constant for Stefan

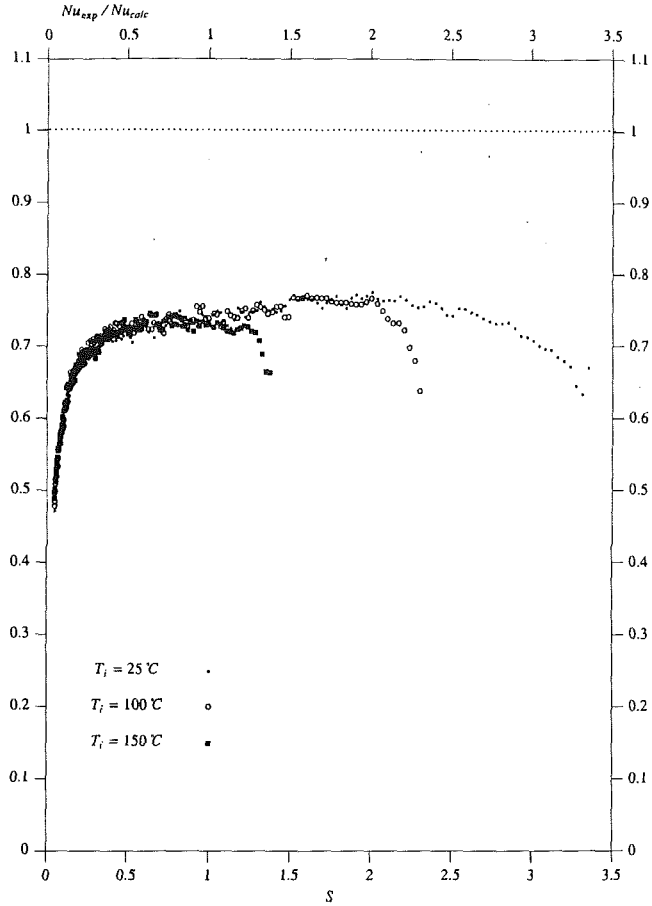

Fig. 4 Comparison of runs and different initial surface temperatures, t_i, with fluid properties evaluated at the mean temperature

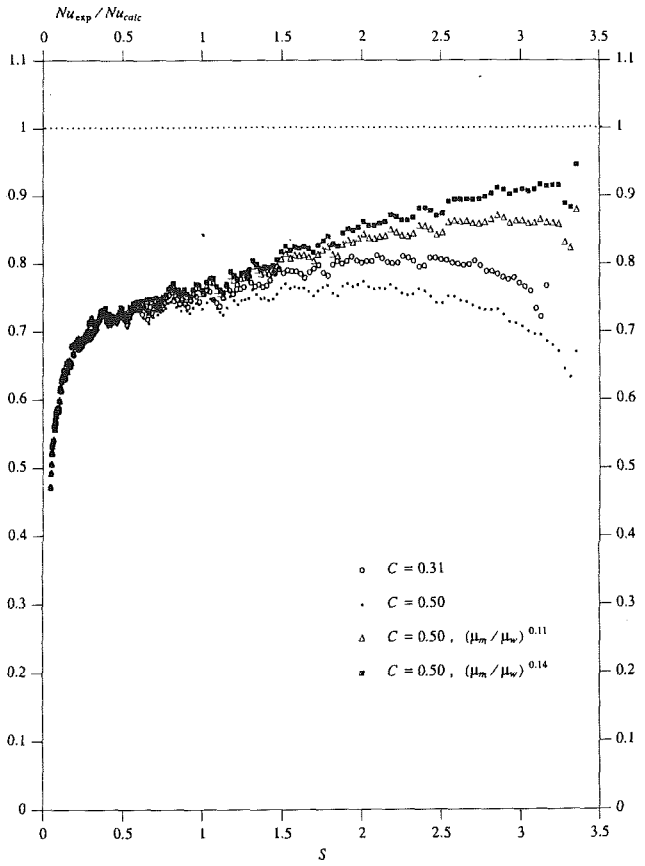

Fig. 5 Effects of reference temperature and viscosity corrections

numbers between approximately 0.3 and 2.3 and drops off at both ends of this range. There are a number of non-ideal effects that contribute to this behavior, including disturbance to the vapor zone due to insertion of the test object, the effect of property variation, and the effect of noncondensable gases. Each of these will be addressed in the following sections.

5.1 Effect of Thermal Transients and Initial Disturbance. The time required to achieve steady state after suddenly reducing the temperature of a sphere already immersed in saturated vapor was obtained by Sparrow and Siegel (1959) as

$$t_{ss} = \left[\frac{h_{fg}\rho_f \mu x}{g(\rho_f - \rho_g)k\Delta T_0}\right]^{1/2} \times \left[1 + \frac{c_p \Delta T_0}{2h_{fg}}\right] \tag{14}$$

For the present case with FC-70, t_{ss} is approximately 0.25 to 0.50 s. However, this accounts for the thermal transient only and does not include the effect of lowering the sphere into the vapor as done in these experiments. The disturbance of the vapor zone results in a transient period that is considerably longer, as discussed below, so that the thermal transient alone cannot be observed in the measured data.

When the interface between the vapor and air is disturbed the vapor and air become intermixed, creating a foglike zone surrounding the entry region. This fog also follows the sphere into the vapor zone. Therefore, for the first few seconds of the experiment the condensation rate is expected to be lowered by the presence of air and possibly water vapor as noncondensable gas. A measure of the disturbance time was obtained by performing runs with elevated initial temperatures and observing the time required for the data to merge into that for the run with ambient initial temperature. Typical results, corresponding to initial sphere temperatures of 100°C and 150°C, are shown in Fig. 4. For both the runs the insertion transients are clearly visible. They occur over a time period of approximately 4 s (8 data points), independent of initial temperature, and exhibit a very steep slope approaching the ambient initial temperature run. The decrease in the Nusselt number ratio at high S for the ambient initial temperature run occurs over a much longer period of time and is not solely an effect of initial transient. This is discussed in detail below.

5.2 Effect of Property Variations. The decline in Nusselt number ratio for Stefan number greater than about 2.3 can be attributed to the effect of viscosity variation in the condensate film. For example, for the test data shown in Fig. 4, S = 2.3 corresponds to $T_w = 96°C$. The viscosity varies across the condensate film by a factor of about 5. For S = 3.35, corresponding to $T_w = 30.8°C$, the variation is a factor of about 34.

The standard way of correcting for property variations is to use a film temperature defined as

$$T_{\text{ref}} = T_w + C\Delta T \tag{15}$$

where the constant C takes on values between 0.23 to 0.33 (Minkowycz and Sparrow, 1966; Poots and Miles, 1967; Denny and Mills, 1969). However, this correction is for water and the associated property variation is relatively small. The correction with $C = 0.31$ is shown in Fig. 5. For larger property variation, the power law correction factor based on viscosity ratio is adapted to correct the calculated Nusselt number

$$\text{Nu}_{vp} = \text{Nu}_{cp}\left(\frac{\mu_m}{\mu_w}\right)^n \tag{16}$$

where the subscript m denotes the mean temperature ($C = 0.5$) across the boundary layer. This method has been successfully used for laminar forced flow in tubes. The exponent n takes on a value of either 0.11 (Yang, 1962) or 0.14 (Deissler, 1951). With the power law correction using $n = 0.11$, the Nusselt num-

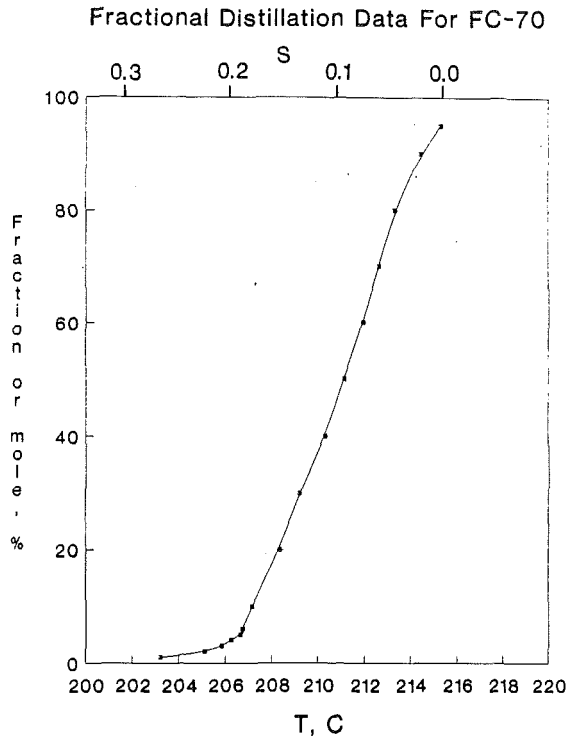

Fig. 6 FC-70 distillate collected (percent of original sample) as a function of temperature and corresponding Stefan number

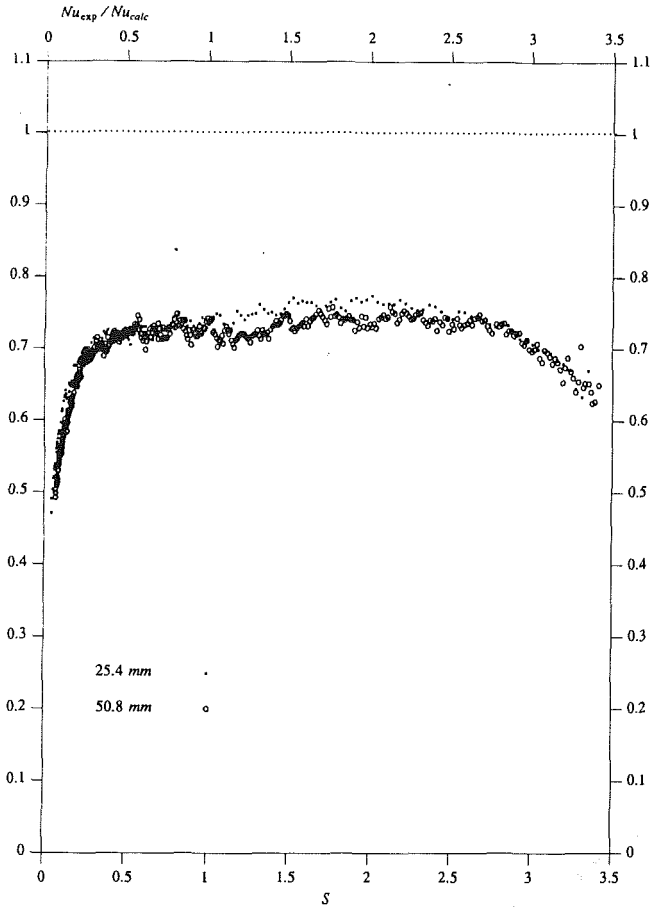

Fig. 7 Comparison of data for 25.4 mm and 50.8 mm spheres, with fluid properties evaluated at the mean temperature

ber ratio approaches asymptotically a maximum value of about 0.87 at high S, as shown in Fig. 5. Using the correction with $n=0.14$, the ratio continues to rise with increasing slope. Note that the data corresponding to the initial disturbance period of 4 s have been included.

5.3 Effect of Noncondensable Components. The difference of about 10 percent between Nu_{exp} and Nu_{calc} using the power law correction (0.11 or 0.14) probably is due mainly to the presence of air, which, as a noncondensable gas, impedes the motion of vapor to the condensing surface and hence reduces the rate of heat transfer. In addition, water vapor present at a concentration even as high as 3 percent will have a condensing temperature less than 25°C and hence also will be noncondensable over the full range of S.

The more or less linear decrease of the Nusselt number ratio with S in the range $0.3<S<3.3$ and the abrupt drop below $S\approx 0.3$ can be attributed to the fact that the working fluid FC-70 is not a single component fluid but a continuum of volatile components that condense over a range of temperatures. The results of distillation of a sample of FC-70 are plotted in Fig. 6 in terms of temperature. The corresponding St is shown, assuming $T_{sat}=215$°C. As the sphere temperature increases during an experimental run, an increasing fraction of the vapor becomes noncondensable, thus decreasing the rate of heat transfer. An inspection of Fig. 6 shows that 1 percent of low temperature volatiles become noncondensable at approximately 203°C. For the sphere at this temperature, the corresponding value of S is 0.22. This is very close to the value of S below which the heat transfer rate drops precipitously. Relatively small amounts of noncondensables can have a significant effect on condensation rates (Rose, 1969; Felicione and Seban, 1973).

Experimental results for the larger sphere, with diameter 50.8 mm, show the same trends as observed with the smaller sphere. Some representative results are compared to those for the smaller sphere in Fig. 7.

6 Concluding Remarks

1 Laminar film condensation results for Stefan numbers greater than unity have been presented. The fluid used, Fluorinert^R FC-70, is one of several similar fluids, which are now routinely used in condensation soldering applications in the electronics industry.

2 For the fluid used, the ratio of dimensionless thermal diffusion time constant and sensible heat capacity is very small so that quasi-steady laminar condensation heat transfer results obtained by immersing copper spheres at room temperature in a body of hot saturated vapor are very close to the steady-state heat transfer calculations.

3 Calculations indicate that for large Prandtl number fluids, the simplified Nusselt–Rohsenow expressions, equation (1) and equation (2), recommended for use for $0<S<1$, can also be used to give accurate predictions of heat transfer rates for larger values of S.

4 At large S, experimental heat transfer rates, when corrected for viscosity variations, are about 10 percent lower than the theoretical values. The deficit increases with decrease in S. This deficit is explained in terms of noncondensable components present in the vapor.

5 Experiments are planned in the future with ultrapure single component distillate of FC-70 to quantify further the effect of the noncondensables on the results reported here.

References

Ammann, H., and Farkass, I., 1977, "On the Applicability of the Nusselt Correlation to Transient Condensation Heating," *Proceedings of NEPCON West*, Anaheim, CA.

Bromley, L. A., 1952, "Effect of Heat Capacity of Condensate," *Ind. and Engr. Chem.*, Vol. 44, No. 12, p. 2966.

Chen, M. M., 1961, "An Analytical Study of Laminar Film Condensation: Part I—Flat Plates," ASME JOURNAL OF HEAT TRANSFER, Vol. 83, p. 48.

Chu, T. Y., Mollendorf, J. C., and Pfahl, R. C., Jr., 1974, "Soldering Using Condensation Heat Transfer," *Proceedings of the Technical Program, NEPCON West*, Anaheim, CA.

Deissler, R. G., 1951, "Analytical Investigation of Fully Developed Laminar Flow in Tubes With Heat Transfer With Fluid Properties Variable Around the Radius," NACA TN 2410.

Denny, V. E., and Mills, A. F., 1969. "Non-similar Solutions for Laminar Film Condensation on a Vertical Surface," *Int. J. Heat Mass Transfer*, Vol. 12, p. 965.

Dhir, V. K., and Lienhard, J. H., 1971, "Laminar Film Condensation on Plane and Axi-symmetric Bodies in Non-uniform Gravity," ASME JOURNAL OF HEAT TRANSFER, Vol. 95, No. 1, p. 97.

Dhir, V. K., 1975, "Quasi-Steady Laminar Film Condensation of Steam on Copper Spheres," ASME JOURNAL OF HEAT TRANSFER, Vol. 97, p. 347.

Felicione, F. S., and Seban, R. A., 1973, "Laminar Film Condensation of a Vapor Containing a Soluble, Non-condensing Gas," *Int. J. Heat Mass Transfer*, Vol. 16, p. 1601.

Koh, J. C. Y., Sparrow, E. M., and Hartnett, J. P., 1961, "The Two Phase Boundary Layer in Laminar Film Condensation," *Int. J. Heat Mass Transfer*, Vol. 2, p. 69.

Merte, H., Jr., 1973, "Condensation Heat Transfer," *Advances in Heat Transfer*, Vol. 9, p. 181, Academic Press.

Minkowycz, W. J., and Sparrow, E. M. 1966, "Condensation Heat Transfer in the Presence of Non-condensables, Interfacial Resistance, Superheating, Variable Properties, and Diffusion," *Int. J. Heat Mass Transfer*, Vol. 9, p. 1125.

Nusselt, W., 1916, "Die Operflachenkondensation des Wasserdampfes," *Z. ver Deutsch. Ing.*, Vol. 60, pp. 541, 569.

Pfahl, R. C., Jr., Mollendorf, J. C., and Chu, T. Y., 1975, "Condensation Soldering," *Welding Journal*, Vol. 54, No. 1, p. 22.

Poots, G., and Miles, R. G., 1967, "Effects of Variable Physical Properties on Laminar Film Condensation of Saturated Steam on a Vertical Flat Plate," *Int. J. Heat Mass Transfer*, Vol. 10, p. 1677.

Rohsenow, W. M., 1956, "Heat Transfer and Temperature Distribution in Laminar Film Condensation," *Trans. ASME*, Vol. 78, p. 1645.

Rose, J. W., 1969, "Condensation of a Vapor in the Presence of a Non-condensing Gas," *Int. J. Heat Mass Transfer*, Vol. 12, p. 233.

Sadasivan, P., and Lienhard, J. H., 1987, "Sensible Heat Correction in Laminar Film Boiling and Condensation," *Int. J. Heat Mass Transfer*, Vol. 109, p. 545.

Sparrow, E. M., and Gregg, J. L., 1959, "A Boundary-Layer Treatment of Laminar-Film Condensation," ASME JOURNAL OF HEAT TRANSFER, Vol. 81, No. 1, p. 13.

Sparrow, E. M., and Siegel, R., 1959, "Transient Film Condensation," ASME *Journal of Applied Mechanics*, Vol. 81, No. 1, p. 120.

Wenger, G. M., and Mahajan, R. L., 1979a, "Condensation Soldering Technology—Part I: Condensation Soldering Fluids and Heat Transfer," *Insulation/Circuits*, Sept., p. 131.

Wenger, G. M., and Mahajan, R. L., 1979b, "Condensation Soldering Technology—Part II: Equipment and Production," *Insulation/Circuits*, Oct., p. 133.

Wenger, G. M., and Mahajan, R. L., 1979c, "Condensation Soldering Technology—Part III: Installation and Application," *Insulation/Circuits*, Nov., p. 13.

Yang, K. T., 1962, "Laminar Forced Convection of Liquids in Tubes With Variable Viscosity," ASME JOURNAL OF HEAT TRANSFER, Vol. 84, p. 353.

Yang, J. W., 1973, "Laminar Film Condensation, on a Sphere," ASME JOURNAL OF HEAT TRANSFER, Vol. 95, No. 2, p. 174.

H. Honda
Institute of Advanced Material Study,
Kyushu University,
Kasuga, Fukuoka 816, Japan

B. Uchima

S. Nozu

H. Nakata

E. Torigoe

Department of Mechanical Engineering,
Okayama University,
Tsushima, Okayama 700, Japan

Film Condensation of R-113 on In-Line Bundles of Horizontal Finned Tubes

Film condensation of R-113 on in-line bundles of horizontal finned tubes with vertical vapor downflow was experimentally investigated. Two tubes with flat-sided annular fins and four tubes with three-dimensional fins were tested. The test sections were 3 × 15 tube bundles with and without two rows of inundation tubes at the top. Heat transfer measurements were carried out on a row-by-row basis. The heat transfer enhancement due to vapor shear was much less for a finned tube bundle than for a smooth tube bundle. The decrease in heat transfer due to condensate inundation was more marked for a three-dimensional fin tube than for a flat-sided fin tube. The predictions of the previous theoretical model for a bundle of flat-sided fin tubes agreed well with the measured data for low vapor velocity and a small to medium condensate inundation rate. Among the six tubes tested, the highest heat transfer performance was provided by the flat-sided fin tube with fin dimensions close to the theoretically determined optimum values.

Introduction

Shell and tube condensers utilizing horizontal finned tubes are commonly used in the refrigeration, air-conditioning, and process industries because of their high heat transfer performance. Numerous experimental and theoretical studies have been reported on the effects of fin geometry and condensing fluid on the condensation heat transfer performance of single horizontal finned tubes. However, a relatively small number of studies have reported on the performance of horizontal finned tube bundles, which are subject to the combined effects of vapor shear and condensate inundation. A comprehensive review of the relevant literature is given by Marto (1988).

Most of the previous studies of horizontal finned tube bundles were concerned with the case of negligible vapor shear. Katz and Geist (1948) and Gogonin et al. (1983) measured the row-by-row heat transfer coefficient for vertical columns of horizontal tubes having flat-sided annular fins (flat-sided fin tube). Mills et al. (1975) and Marto (1986) also obtained row-by-row data for flat-sided fin tubes by using an inundation tube for simulating condensate inundation. These data showed that the effect of the number of vertical tube rows was much smaller than the theoretical prediction of the Nusselt (1916) equation for a vertical column of horizontal smooth tubes. Smirnov and Lukanov (1972) obtained row-by-row data for a 4 × 20 (columns × rows) bundle of flat-sided fin tubes with vertical vapor downflow. Contrary to the foregoing results for vertical columns of horizontal finned tubes, their data showed a sharp decrease in the heat transfer coefficient with the increase of row number up to the sixth row. Thereafter, it decreased gradually, then took a minimum value at the tenth row, and finally increased again with further increasing of the row number. Fujii and Uehara (1973) pointed out that the unique distribution of the heat transfer coefficient measured by Smirnov and Lukanov was probably due to the accumulation of air in the condenser. McNaught and Cotchin (1989) measured the average heat transfer coefficient for R-12 condensation in a shell and tube condenser with a staggered bundle of flat-sided fin tubes. Their data could be satisfactorily predicted by the modified Beatty and Katz (1948) equation that accounted for the effects of condensate retension between fins and condensate inundation from upper tubes.

Honda et al. (1987b) proposed a theoretical model of film condensation on a bundle of horizontal flat-sided fin tubes. This theoretical model took account of the effect of condensate inundation but neglected the effect of vapor velocity. While the predictions of this theoretical model showed a good agreement with row-by-row data by Katz and Geist (1948), Gogonin et al. (1983), and Marto (1986), this theory remains to be verified by experimental data for larger tube bundles. The present study is aimed at obtaining a better understanding of condensate flow and heat transfer in in-line bundles of horizontal finned tubes. Row-by-row heat transfer data are obtained for condensation of R-113 with vertical vapor downflow. Two kinds of flat-sided fin tubes and four kinds of three-dimensional fin tubes are tested and their heat transfer characteristics are compared with each other.

Experimental Apparatus

The experimental apparatus, which consisted of a natural circulation loop of refrigerant R-113 and a forced circulation loop of cooling water, is shown schematically in Fig. 1. It was basically the same as those used in previous studies for single horizontal smooth tubes (Honda et al., 1986) and horizontal smooth tube bundles (Honda et al., 1988a) with the exception of the test section and the cooling water piping. A detailed description of the apparatus is given by Honda et al. (1986).

The test sections were 3 × 15 (columns × rows) in-line bundles of horizontal finned tubes made of copper. The test tubes had diameters at fin tip, d, of 15.6–16.1 mm. Both the longitudinal and transverse tube pitches were 22 mm. The tube bundle was assembled in a vertical duct with inner dimensions of 66 × 100 mm, as shown in Fig. 2. The tube pitches and the duct dimensions of the test section were the same as those for the previous study for horizontal smooth tube bundles (Honda et al., 1988a). The d values of the test tubes were also close to the outer diameter of the smooth tube (= 15.9 mm). This facilitated direct comparison between the finned tube and smooth tube results. The side walls parallel to the tube axis were provided with viewing windows. A gutter for collecting the falling condensate on the duct wall was attached to the duct just downstream of the 15th row. The collected condensate

Contributed by the Heat Transfer Division and presented at the 20th National Heat Transfer Conference, Philadelphia, Pennsylvania, August 6–9, 1989. Manuscript received by the Heat Transfer Division October 17, 1989; revision received May 3, 1990. Keywords: Condensation, Finned Surfaces, Heat Exchangers.

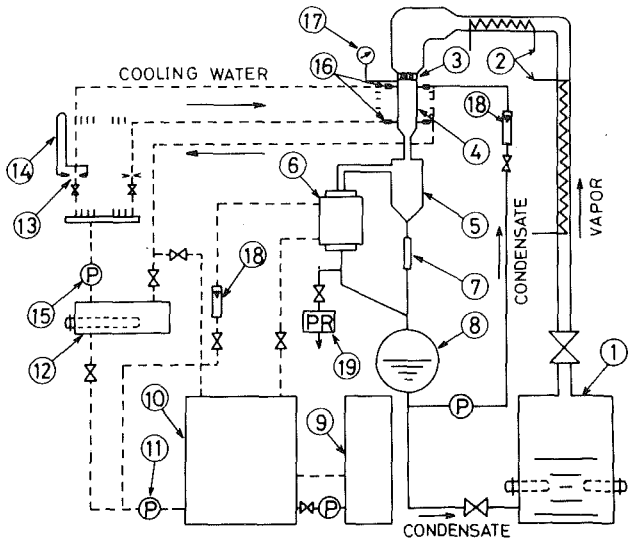

1 Boiler 2 Superheater 3 Calming section
4 Test section 5 Drain separater 6 Dump condenser
7 Condensate measuring tube 8 Condensate receiver
9 Chilling unit 10 Cooling water tank 11 Feed pump
12 Circulation tank 13 Orifice 14 Inverse U-tube manometer
15 Feed pump 16 Mixing chamber
17 Pressure gauge 18 Rotameter 19 Vacuum pump

Fig. 1 Schematic diagram of experimental apparatus

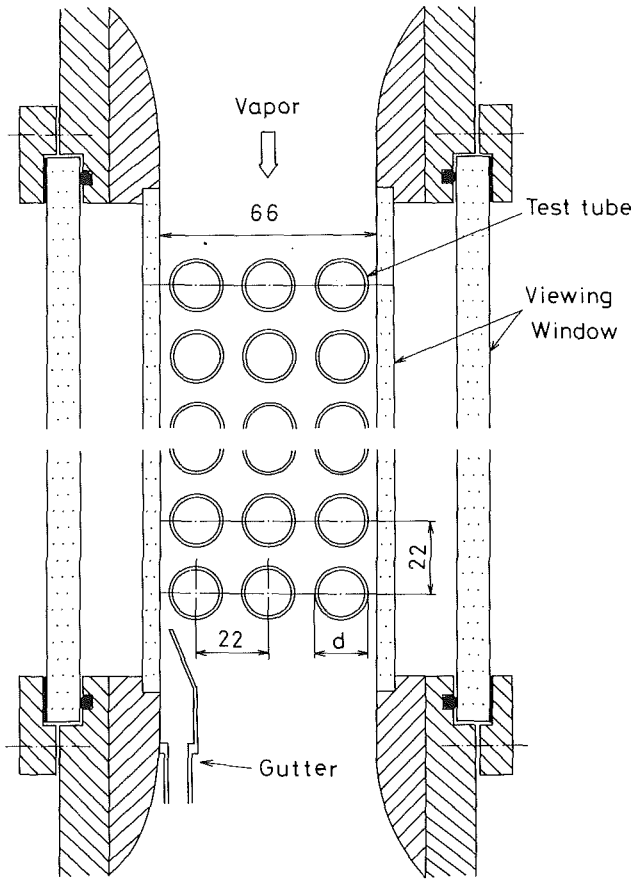

Fig. 2 Schematic diagram of test section

was led outside the duct through a pipe and flowed vertically downward through a measuring glass tube and a stop valve. Then the condensate was returned inside the duct. The test section was connected to a calming section and a convergent section at the upper and lower ends, respectively. The distance between the 15th row and the convergent section was 320 mm.

It should be noted here that dummy half tubes are usually placed on the side walls to simulate a large tube bundle. In the present experiments, however, the dummy half tubes were not placed so as to facilitate visual observation of the condensate flow pattern. Thus, there was a possibility that the heat transfer characteristics of the present tube bundles deviated from those of large tube bundles at a high vapor velocity. Experimental results revealed that the deviation was small, especially for the flat-sided fin tube, because the effect of vapor velocity was small.

Six finned tubes with different fin geometries were tested. The dimensions of the test tubes are listed in Table 1. Tubes A and B had flat-sided annular fins, whereas Tubes C–F had three-dimensional fins. The longitudinal cross section and close-up of the test tubes are shown in Fig. 3. Tube A and Tubes C–F were obtained from several manufacturers. Tube B was machined from a smooth tube. This tube had fin dimensions that were close to the optimum values obtained from the previous theoretical model (Honda et al., 1987b). The procedure for optimizing the fin dimensions is described in detail by Honda and Nozu (1990). It should be mentioned here that the optimum fin dimensions depend on the bundle depth, tube material, and conditions of vapor and coolant.

For Tube A, two types of test section were used. One of the test sections consisted of 45 active tubes. The other had two

Nomenclature

d = diameter at fin tip
g = gravitational acceleration
h = fin height
h_{fg} = specific latent heat of evaporation
l = effective length of tube or surface
n = number of rows counted from top row
Nu = condensation number = $\alpha(\nu_l^2/g)/\lambda_l$
p = fin pitch
Q = heat transfer rate to coolant
Q_l = heat loss to environment
Re = film Reynolds number, equation (5)
T_s = saturation temperature
T_w = tube wall temperature at fin root
T_{wm} = average tube wall temperature at fin root for a tube row
ΔT = average condensation temperature difference for a tube row $= T_s - T_{wm}$
t = fin thickness at fin tip
u = vapor velocity based on minimum free cross section
W = flow rate of condensate leaving a tube row
α = average heat transfer coefficient for a tube row based on equivalent smooth tube area, equation (1)
γ = ratio of condensate transported to duct wall to total condensate leaving a tube row, equation (3)
ϵ = ratio of condensate flow rate on the duct wall to total condensate flow rate at the exit of tube bundle, equation (4)
θ = fin half tip angle
λ_l = thermal conductivity of condensate
μ_l = dynamic viscosity of condensate
ν_l = kinematic viscosity of condensate

Subscripts

N = calculated value by the Nusselt equation for single smooth tube
n = nth row
o = tube bundle inlet

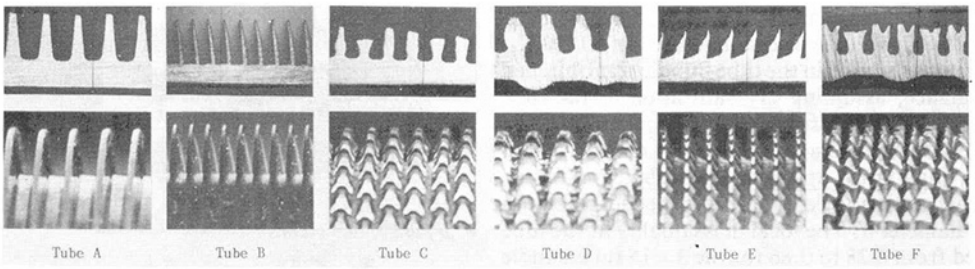

Fig. 3 Longitudinal cross section and close-up of test tubes

Table 1 Dimensions of test tubes

Tube designation			A	B	C	D	E	F
Fin pitch	p	mm	0.96	0.50	0.73	1.00	0.69	0.95
Fin height	h	mm	1.43	1.30	0.99	1.28	1.01	1.14
Fin thickness at fin tip	t	mm	0.24	0.05	----	----	----	----
Fin half tip angle	θ	rad	0.082	0.047	----	----	----	----
Diameter at fin tip	d	mm	15.60	16.10	15.85	15.80	15.86	15.81
Diameter at fin root		mm	12.74	13.50	13.87	13.24	13.84	13.53
Tube inside diameter		mm	11.21	11.80	12.09	11.39	12.22	12.04

rows of inundation tubes at the top and the lower rows consisted of active tubes. The inundation tube was a double tube consisting of Tube A as an outer tube and a 7 mm i.d., 9 mm o.d. inner tube. The outer tube had a 2 mm wide, 100 mm long slit at the bottom of the tube, whereas the inner tube had 1.4 mm dia holes drilled 5–15 mm apart at the top of the tube. The hole spacing was longer near the open end. The condensate was fed from a condensate receiver to the inner tube of each inundation tube by a circulation pump via a rotameter. The condensate exited through the holes on the inner tube and the slit on the outer tube, and was distributed almost uniformly along the tube. For Tubes B to F, experiments were conducted using test sections that had only one or two rows of these tubes at the 12th to 14th rows. The top two rows of the test sections were inundation tubes and the other rows consisted of Tube A.

The vapor gage pressure was measured by a precision Bourdon tube gage, reading to 10^2 Pa, connected to a pressure tap on the duct wall located 100 mm upstream of the first row. The atmospheric pressure was measured by a Fortin barometer. The vapor temperature was measured by two 1 mm o.d. sheathed thermocouples inserted in the test section at 70 mm upstream and 70 mm downstream of the tube bundle, respectively. The condensate temperature returning to the boiler was also measured by a 1 mm o.d. sheathed thermocouple. The cooling water temperatures at the inlet and outlet of each row were measured by two junction thermopiles inserted in mixing chambers. The test tubes were electrically insulated from the duct wall to measure the wall temperature by the resistance thermometry. The test tubes and a standard resistor of 1 mΩ were connected in series by a lead wire to a 40 A d-c power supply. Voltage taps were soldered at both ends of each test tube. The thermocouple and thermopile outputs and the voltage drops of the test tubes and the standard resistor were read ten times consecutively and recorded by a programmable data logger to 1 μV. In order to avoid the effect of parasitic voltage, readings of the voltage drops were repeated by reversing the d-c current and the averages of the two measurements were adopted as the experimental data. The cooling water flow rate for each tube row was measured by an orifice and an inverse U-tube manometer. The flow rate of condensate on the duct wall (collected by the gutter shown in Fig. 2) was measured by using the measuring glass tube and a stop watch.

Experimental Procedure and Data Analysis

The calibration curve of the resistance-temperature relation for each test tube was obtained by preliminary experiments. Prior to the experiments, the test section was evacuated using a vacuum pump to minimize the heat transfer at the tube surfaces. Then water at a prescribed temperature was passed through the test tubes at a high velocity. The wall temperature was assumed to be equal to the average value of the water temperatures in the inlet and outlet mixing chambers. The variation of the water temperature between the two mixing chambers ranged to 0.08 K at the highest temperature of 325 K.

Two kinds of condensation experiments were performed at the vapor pressure of about 0.11 MPa ($T_s \simeq 323$ K). The first experiment was aimed at separating the effect of vapor shear from that of condensate inundation. In this experiment the cooling water was passed through only one row at the lower half of the tube bundle. The second experiment was aimed at obtaining heat transfer data under combined effects of vapor shear and condensate inundation. The experimental procedure was somewhat different between Tube A and Tubes B–F. For Tube A, the row-by-row data were obtained by using the two test sections with and without two rows of inundation tubes at the top. The latter was used to obtain experimental data at higher condensate inundation rates. For Tubes B–F, experimental data covering a wide range of condensate inundation rate were obtained by first increasing the number of upper rows through which the cooling water was passed, and then by increasing the condensate flow rate supplied to the inundation tubes. In both the experiments, the power input to the boiler was changed in six steps form 5 to 45 kW, which corresponded to the vapor velocity (based on the minimum free cross section) at the tube bundle inlet u_o of 3.3 to 18.9 m/s. For each step of the power input, experimental data in the condensation temperature difference range of 1 to 18 K were obtained by changing the cooling water temperature.

During the experiments, the superheater was switched off. Thus, the measured vapor temperatures were assumed to be equal to the local saturation temperatures. Due to the static pressure drop in the tube bundle, the saturation temperature downstream of the tube bundle was lower than the upstream value by a maximum of 0.3 K. The local saturation temperature T_s in the tube bundle was determined by an interpolation procedure taking account of the static pressure drop.

The wall temperature measured by the resistance thermometry was considered to be a kind of average temperature of the test tube. The contribution of fins on the electrical resistance of the tube was estimated by using thermal conductance data for infinite plates with repeated rectangular grooves normal to heat flow (Schneider, 1985). The results indicated that the difference in the electrical resistance between the finned tube and a superficial smooth tube obtained by cutting off the fins was less than 5 percent for Tubes A and B. The difference was supposed to be even smaller for Tubes C–F, because these tubes had three-dimensional fins. Considering the foregoing and the fact that the fin efficiency was greater than 90 percent, the measured wall temperature was considered to be equal to the average temperature of the superficial smooth tube. The tube wall temperature at the fin root T_w was obtained from the measured value, making a small correction (< 0.15 K) for

the wall conduction for one half of the tube thickness. The possible error in the T_w value was estimated to be ± 0.08 K.

The local vapor mass quality in the tube bundle was obtained from the heat balance, assuming dry saturation at the tube bundle inlet and neglecting the subcooling of condensate. The local vapor velocity u in the tube bundle was defined based on the local mass quality just upstream of a tube row and the minimum free cross section for a bundle of superficial smooth tubes with outer diameter d. The local mass quality at the tube bundle exit ranged from 0.28 to 0.86 for the 3×15 tube bundle of Tube A. This value was higher for a higher power input to the boiler and for smaller ΔT.

The average heat transfer coefficient α and the average condensation number Nu for a tube row (consisting of three columns) were, respectively, defined as

$$\alpha = (Q - Q_l)/3\pi dl\Delta T \tag{1}$$

$$\mathrm{Nu} = \alpha(v_l^2/g)^{1/3}/\lambda_l \tag{2}$$

where Q is the heat transfer rate calculated from the temperature rise and flow rate of the cooling water, Q_l is the heat loss to the environment, l is the effective length of the test tube ($=$ 100 mm), $\Delta T = T_s - T_{wm}$ is the average condensation temperature difference, and T_{wm} is the average tube wall temperature at the fin root for the tube row. The temperature rise of the cooling water ranged from 1.0 to 5.5 K. The Q_l value was obtained from a calibration line determined by preliminary experiments. The experimental procedure was basically the same as that for the calibration of resistance-temperature relation for the test tubes except that the cooling water was passed at a slow velocity to obtain a relatively large temperature variation between the inlet and outlet mixing chambers. The measured values of Q_l were plotted versus the temperature difference between the water and ambient air and the data were approximated by a straight line. It was found that $Q_l/Q < 0.04$. The uncertainties in these measurements led to an uncertainty of ± 5 percent in the α value for $\Delta T \geq 3$K. The variation of T_w among three tubes in each row increased with ΔT and u_o, reaching a maximum value of 3 K. This corresponded to the ± 13 percent variation in $(T_s - T_w)$ from ΔT. In the data reduction the physical properties of the condensate were evaluated at the reference temperature $T_{wm} + 0.3\Delta T$.

Experimental Results and Discussion

Behavior of Condensate. Figure 4 shows the condensate flow patterns at the first and thirteenth rows of Tube A for low and high values of u_o. The film Reynolds number Re (defined by equation (5)) for each condensate flow pattern is also shown in the figure. In Fig.4 (a) for $u_o = 3.4$ m/s, the condensate falls from the tube bottom in the forms of droplets and condensate columns at the first and thirteenth rows, respectively. The falling condensate impinges on the lower tube and flows down the tube through a number of grooves between adjacent fins. The other grooves between the impinging points are not affected by the falling condensate. The arrows in Fig. 4 show the flooding level for the latter portion (unaffected region) below which the groove is almost completely flooded with condensate. As expected, this level is independent of the row number. The measured flooding levels for Tubes A and B (flat-sided-fin tubes) agreed well with the theoretical prediction for a stagnant vapor (Honda et al., 1983). While these results are in accord with the previous results for stagnant vapors (Honda et al., 1987a), the Re value at the flow mode transition was considerably different between the two cases. In the previous study the falling condensate of R-113 formed a complete sheet for Re $>$ 400. In the present study, on the other hand, a complete sheet mode was not observed for Tubes A and B within the investigated range of Re ($<$1800). This difference is clearly due to the effect of vapor shear. In Fig.

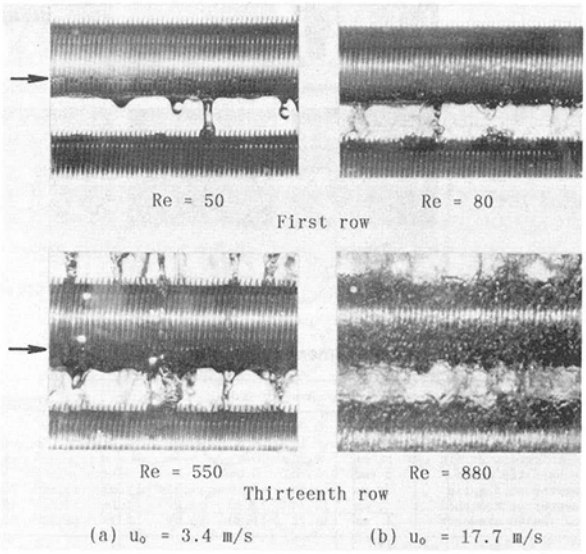

Fig. 4 Comparison of condensate flow patterns; Tube A, ΔT = 3.5 K

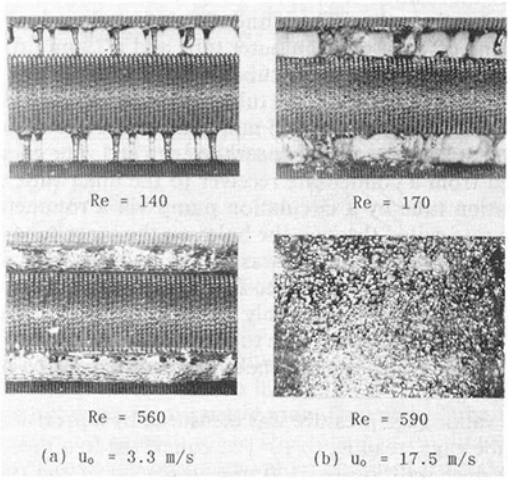

Fig. 5 Comparison of condensate flow patterns; Tube D, ΔT = 5.3 K

4(b) for $u_o = 17.7$ m/s, a part of the falling condensate disintegrates into small droplets by the vapor shear and impinges on the viewing window. As a result, the tubes at the 13th row are obscured by the condensate on the viewing window. It is also seen from the comparison of the first row between Figs. 4(a) and 4(b) that the flooding level is not affected by the vapor shear.

Figure 5 shows condensate flow patterns corresponding to the combination of low and high values of u_o and Re for Tube D. Comparison of Figs. 4 and 5 reveals that the condensate flow patterns for Tubes A and D are basically the same at low Re, but are considerably different at high Re. In Fig. 5(a) for $u_o = 3.3$ m/s, the condensate falls in columns and a complete sheet at Re $= 140$ and 560, respectively. This is in contrast to the case of Tube A where a complete sheet mode was not observed. Formation of a complete sheet at a relatively small Re was also observed for other three-dimensional-fin tubes. This may be ascribed to the existence of longitudinal grooves between the three-dimensional fins, which act to equalize the condensate flow rate along the tube length. In Fig. 5(b) for $u_o = 17.5$ m/s, generation of small droplets is so pronounced at Re $= 590$ that the tubes cannot be observed through the viewing window. Another point to note is that the flooding level, which was clearly observed for Tube A, is not clear for Tube D. This difference is due to the fact that while the condensate film thickness in the groove of a flat-sided fin tube changes sharply at some angular position, that of a three-

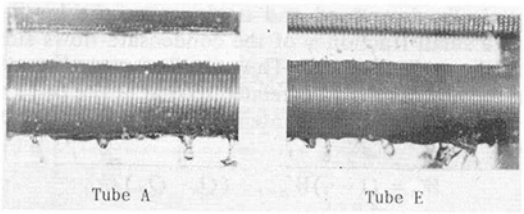

Fig. 6 Condensate flow patterns without condensate inundation; u_o = 17.6 m/s, $\Delta T \simeq 5$ K

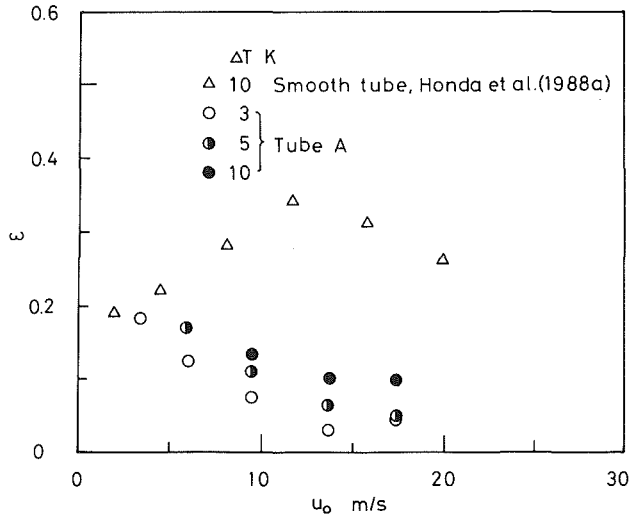

Fig. 7 Variation of ϵ with u_o

dimensional fin tube increases gradually with the angle measured from the tube top (Honda et al., 1983).

Figure 6 shows the condensate flow patterns for Tubes A and E at a high vapor velocity without condensate inundation from the upper tubes. These figures were obtained by passing the cooling water through only one row in the tube bundle. It is seen from Fig. 6 that the condensate is retained in the grooves between adjacent fins near the top and bottom of the tube. This is in contrast to the case of the first row in Fig. 4 where the condensate retention is observed only near the bottom of the tube. The condensate retention observed near the top of the lower tube is due to the presence of maximum pressure points at about 0.7 rad from the top where the impact of the mainstream on the tube surface occurs (Zukauskas, 1972). It is also seen that some of the retained condensate near the top of the tube is entrained in the recirculating vapor flow downstream of the upper tube and impinges on the bottom of the upper tube. These features are characteristic of the in-line tube bundle at a high vapor velocity.

Figure 7 shows the ratio of condensate falling on the duct wall to the total condensate flow rate at the exit of the 3×15 bundle of Tube A, ϵ, plotted as a function of u_o with ΔT as a parameter. The value of ϵ is higher for higher ΔT and decreases monotonically with increasing u_o. Also shown in Fig. 7 are the previous results for the in-line bundle of horizontal smooth tubes (Honda et al., 1988a). Comparison of the present and previous results reveals that both results are in good agreement at $u_o \simeq 3$ m/s, but the present data deviate toward a smaller ϵ with increasing u_o. This indicates that the generation of entrainment due to vapor shear is much less for the flat-sided fin tube than for the smooth tube.

Heat Transfer Results

Effect of Vapor Velocity. Figure 8 shows the heat transfer results for the lower row (12th to 14th row) without condensate inundation from the upper tubes. In Figs. 8(*a*)-8(*f*), experi-

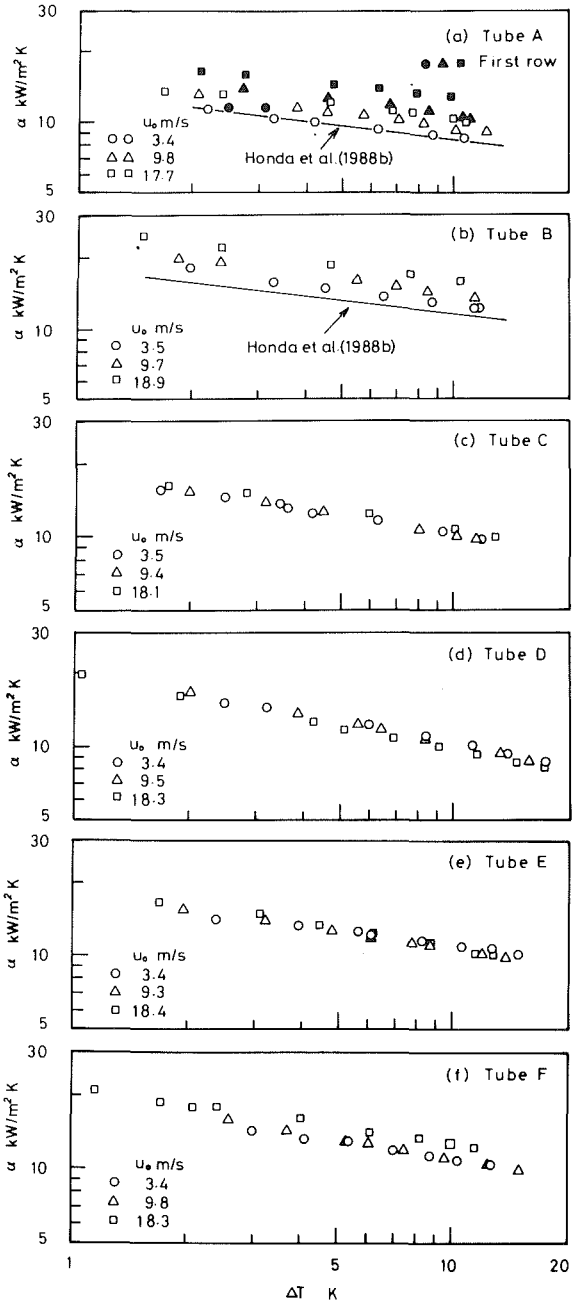

Fig. 8 Variation of α with ΔT for lower row without condensate inundation from upper tubes

mental data for Tubes A–F are plotted on the coordinates of α verses ΔT with u_o as a parameter, respectively. In Fig. 8(*a*) for tube A, the data for the first row are also shown by solid symbols. Generally, the effect of vapor velocity is much less for the finned tubes than for a smooth tube reported in a previous paper (Honda et al., 1988a). This is in accord with the results of Gogonin and Dorokhov (1977) and Michael et al. (1989) for refrigerant condensation on single smooth and flat-sided fin tubes. The enhancement of heat transfer due to the increase of u_o from about 3.3 m/s to 18 m/s is about 20 percent for Tubes A and B, and about 15 percent for Tube F, whereas little enhancement is obtained for Tubes C–E. Comparison of the results for different tubes reveals that Tube B is the best-performing tube. Tubes C–F show the heat transfer performance about 10 percent lower than that for Tube B at $u_o \simeq 3.4$ m/s. Tube A shows the lowest heat transfer performance, which is about 33 percent lower than that for Tube B at

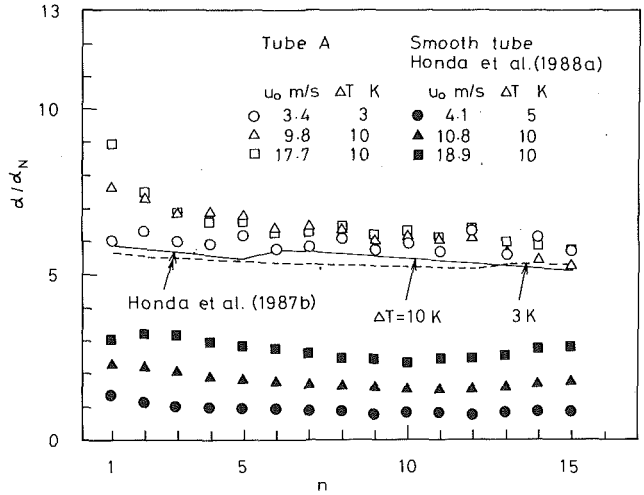

Fig. 9 Variation of α/α_N with n; Tube A

$u_o = 3.4$ m/s. Comparison of the first and lower rows for Tube A reveals that the α value for the former is higher than that for the latter, with the difference increasing with u_o. This is mainly due to the decrease of effective surface area with increasing u_o for the lower row as a result of condensate retention at the upper part of the tube (see Fig. 6).

The solid lines in Figs. 8(*a*) and 8(*b*) show the theoretical predictions for a horizontal flat-sided fin tube with negligible vapor shear (Honda et al., 1988b). The theoretical prediction agrees well with the experimental data for Tube A at $u_o = 3.4$ m/s, whereas the former is about 10 percent lower than the latter for Tube B at $u_o = 3.5$ m/s.

Effect of Row Number. Figure 9 shows the variation of the enhancement ratio α/α_N with the row number n for Tube A, where α_N denotes the Nusselt (1916) solution for smooth tube with the same values of d and ΔT as the finned tube. The experimental data are presented for three values of u_o. At $u_o = 3.4$ m/s, the α/α_N ratio decreases very slowly with increasing n (about 4 percent), which is in accord with the previous results for a vertical column of horizontal finned tubes (Katz and Geist, 1948; Gogonin et al., 1983; Marto, 1986). It should be mentioned here that a small row-by-row variation of the data is due to the experimental uncertainty of ±5 percent. At $u_o = 9.8$ m/s and 17.7 m/s, the α/α_N ratio decreases rather sharply from the first row to the third row. Thereafter it decreases gradually with increasing n. Comparison of the results for different u_o reveals that the effect of u_o is more pronounced for the upper rows. For the first row, the α/α_N ratio increases by about 50 percent with the increase of u_o from 3.4 to 17.7 m/s. For the fifth and lower rows, the increase is within 10 percent.

Also shown in Fig. 9 are the theoretical predictions for a bundle of horizontal flat-sided fin tubes with negligible vapor shear (Honda et al., 1987b) and the experimental data for R-113 condensation in the in-line bundle of horizontal smooth tubes (Honda et al., 1988a). The theoretical predictions show a small increase in α/α_N at the column mode to sheet mode transition (i.e., at $n = 13$ and 6 for $\Delta T = 3$ and 10K, respectively). Generally, the theoretical predictions are smaller than the experimental data. However, the deviation is within 10 percent for $u_o = 3.4$ m/s. Comparison of the Tube A and smooth tube results reveals that the effect of u_o on the α/α_N value is much smaller for Tube A. This reflects the predominant effect of surface tension in enhancing condensation on the finned tube.

Combined Effects of Vapor Shear and Condensate Inundation. The condensate inundation rate was evaluated by the gravity-drained flow model (Honda et al., 1988a). According to this model, most of the condensate leaving the tube bottom falls vertically downward and impinges on the lower tube, whereas a small fraction γ of the condensate flows sideways and falls down the duct wall. Thus, the flow rate of condensate leaving the nth row, W_n, is related to that at the $(n-1)$th row, W_{n-1}, and the heat transfer rate at the nth row, $(Q_n - Q_{ln})$, as follows:

$$W_n = (1-\gamma)W_{n-1} + (Q_n - Q_{ln})/h_{fg} \tag{3}$$

When γ is assumed to be constant for all rows, ϵ is related to γ, W_n, and $(Q_n - Q_{ln})$, as follows:

$$\epsilon = \gamma \sum_{1}^{15} W_n / \sum_{1}^{15} \{(Q_n - Q_{ln})/h_{fg}\} \tag{4}$$

The film Reynolds number for the nth row Re_n is defined as

$$\mathrm{Re}_n = 2W_n/3\mu_l 1 \tag{5}$$

The values of γ and W_n for each experimental run were obtained by substituting the measured values of Q_n, Q_{ln}, and ϵ into equations (3) and (4), and solving the resulting simultaneous equations iteratively. Then Re_n was obtained from equation (5). The γ value ranged form 0.6 to 5.0 percent, whereas the W_n value ranged from 2.5×10^{-3} to 0.21 kg/s. Although the gravity-drained flow model is not correct at high u_o, the difference in the calculated Re_n values between this model and the uniformly dispersed flow model (Honda et al., 1988a) is within 23 percent for the tube bundles tested.

Figure 10 shows the heat transfer results under combined effects of vapor shear and condensate inundation. In Figs. 10(*a*)-10(*f*), the data for Tubes A–F are plotted on the coordinates of Nu versus Re with u_o and ΔT as parameters, respectively. Since the actual ΔT value for each data deviated somewhat from the nominal one, the α value at nominal ΔT was estimated from the measured data assuming a power law $\alpha = c\Delta T^a$, where the exponent a was obtained from the slope of a straight line drawn through the corresponding data points in Fig. 8.

Comparison of Figs. 10(*a*)-10(*f*) reveals that the Nu versus Re distribution is considerably different in trend between Tubes A and B with flat-sided fins and Tubes C–F with three-dimensional fins. For Tubes A and B, Nu decreases very slowly with increasing Re at fixed values of u_o and ΔT. As expected, Nu is higher for higher u_o and smaller ΔT. The effects of u_o and ΔT on Nu are more significant for lower Re. For Tubes C–F, on the other hand, Nu decreases rather sharply with increasing Re at fixed values of u_o and ΔT. Although the effects of u_o and ΔT are qualitatively in accord with the cases of Tubes A and B, they are more significant for higher Re. The foregoing difference in the Nu versus Re distribution between the flat-sided fin and three-dimensional fin tubes is related to the difference in the condensate flow patterns shown in Figs. 4 and 5. For Tube A, the condensate flows down a number of grooves between adjacent fins smoothly without generating much entrainment (Fig. 4). Thus, the effective surface area (i.e., surface area covered with a thin condensate film) is supposed to decrease modestly with increasing Re. For Tube D, on the other hand, the condensate flow pattern at high Re is characterized by the formation of a complete sheet when u_o is low, and by generation of numerous droplets when u_o is high (Fig. 5). These results indicate that the flow resistance of the groove is higher for Tube D than for Tube A, which results in a sharper decrease in the effective surface area for Tube D with increasing Re.

Also shown in Fig. 10 are the experimental data without condensate inundation from the upper tubes. For these data, ΔT increases with Re. Comparison of the data with and without condensate inundation reveals that the slope of the Nu versus Re distribution is more sharp for the latter for Tubes A and B, whereas it is almost unchanged between the two data sets for Tubes C–F.

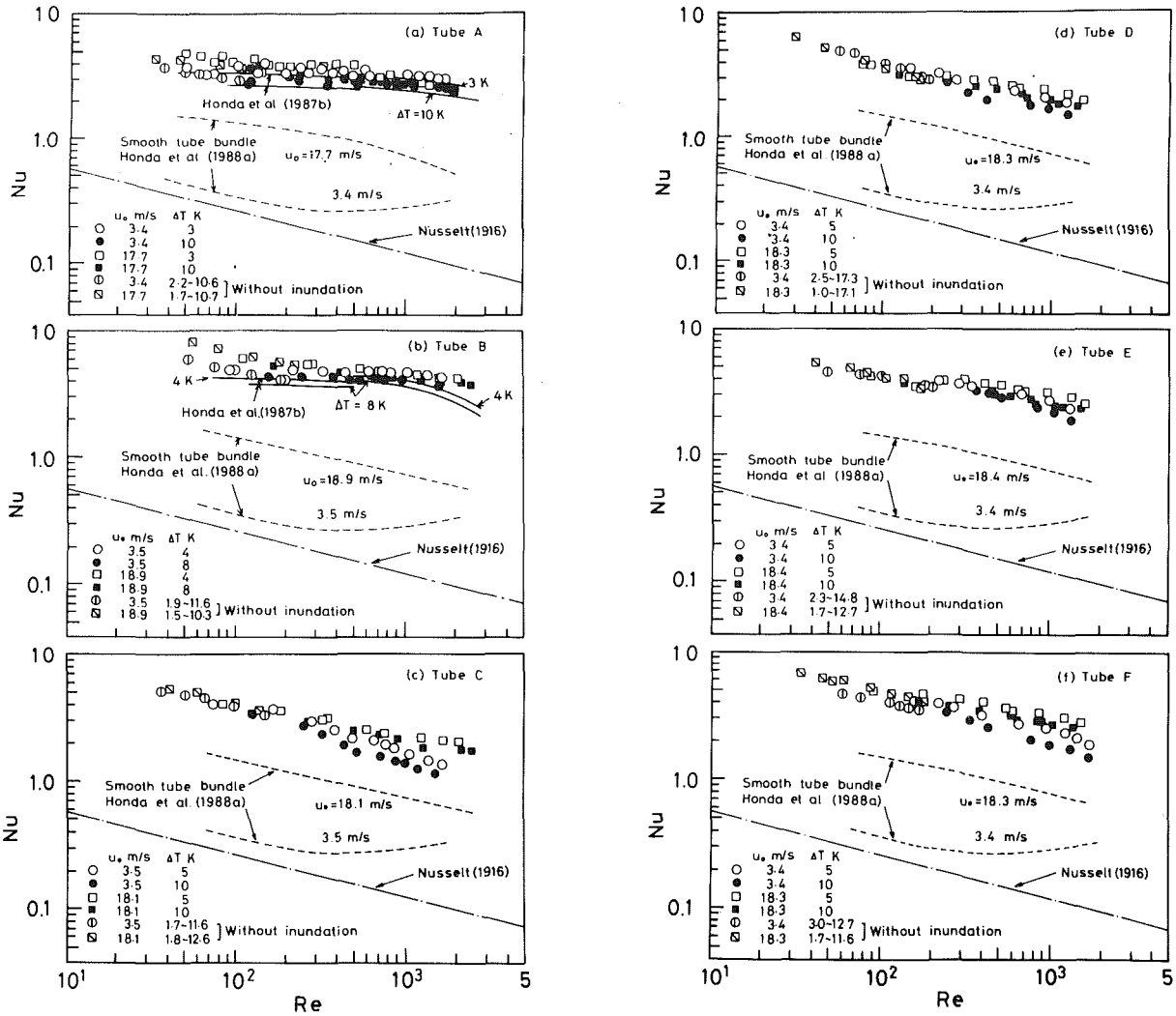

Fig. 10 Variation of Nu with Re

The solid, dotted, and dash-dot lines in Fig. 10, respectively, show the theoretical predictions for a bundle of horizontal flat-sided fin tubes with negligible vapor shear (Honda et al., 1987b), the empirical equation for a bundle of horizontal smooth tubes (Honda et al., 1988a), and the Nusselt equation (1916) for a horizontal smooth tube. The dotted line for each u_o represents the average value of the predictions for different ΔT. Comparison of the theoretical predictions for Tubes A and B with the experimental data reveals that the agreement is good for small u_o and small to medium Re, but the former deviates toward a smaller value with increasing Re. For the data at $u_o = 3.4 \sim 3.5$ m/s, the difference between the two ranges from 5 percent to 10 percent for Tube A in the range $\mathrm{Re} = 50 \sim 1800$, whereas it ranges from 12 percent to 18 percent for Tube B in the Range $\mathrm{Re} = 90 \sim 1800$. The theoretical predictions for Tube B show a rather sharp decrease in Nu for $\mathrm{Re} > 1500$, which is due to the almost complete flooding of grooves between adjacent fins. Such a sharp decrease is not observed for the measured data. This may be ascribed to the effect of momentum of impinging condensate, which acts to thin the condensate film in the grooves between adjacent fins. Comparison of the results for the smooth and finned tube bundles reveals that the heat transfer enhancement due to vapor shear is much less for the finned tube bundle than for the smooth tube bundle. This indicates the predominant effect of surface tension in enhancing condensation on the finned tube bundles. The heat transfer enhancement ratio comparing the measured Nu with the prediction of the Nusselt equation increases with Re for Tubes A and B, whereas it changes modestly with Re for Tubes C–F. It is seen from the comparison Figs. 10(*a*)–10(*f*) that the highest enhancement is provided by Tube B with fin dimensions close to the theoretically determined optimum values. For $u_o = 3.5$ m/s and $\Delta T = 4$K, the maximum value of the enhancement ratio ranges from 18 to 40 in the range $\mathrm{Re} = 90 \sim 1800$.

Figure 11 shows a comparison of the present results for $u_o = 3.4 \sim 3.5$ m/s and $\Delta T = 3 \sim 5$ K with available experimental data for refrigerants condensing on vertical enhanced surfaces (Miyoshi et al., 1977; Mori et al., 1981a, 1981b; Yamashita et al., 1987; Kedzierski and Webb, 1987). In Fig. 11, only the data for a best performing surface in each study are cited. A summary of the experimental data is given in Table 2. It is relevant to note here that for the vertical surfaces, Nu is defined on the projected area basis and Re is evaluated at the lower end on the surface. Consequently, the data for larger Re correspond to larger ΔT. An overall inspection of Fig. 11 reveals that the difference in the heat transfer performance among different tubes and surfaces is more marked for larger Re. The vertical finned surface tested by Mori et al. (1981b) shows almost the same heat transfer performance as Tube B at small Re, but deviate toward a smaller Nu as Re increases. This is partly due to the smaller fin height of this surface than that of Tube B, which results in the flooding of grooves between adjacent fins at smaller Re.

The foregoing results indicate that the numerical method for optimizing fin dimensions described in Honda and Nozu

Table 2 Summary of experimental data for vertical enhanced surfaces cited in Fig. 11

Symbol	Enhancement technique	p mm	h mm	l mm	Fluid	Reference
○	Flute(#3)	1.0	0.5	446	R-11	Miyoshi et al. (1977)
△	Triangular Fin	1.0	0.87	50	R-113	Mori et al. (1981a)
▲	Rectangular Fin	0.71	0.89	160	R-113	Mori et al. (1981b)
●	EHD (18kV)	----	----	1080	R-113	Yamashita et al. (1987)
□	Adamek fin (#3)	1.34	1.47	101.6	R-11	Kedzierski and Webb (1987)

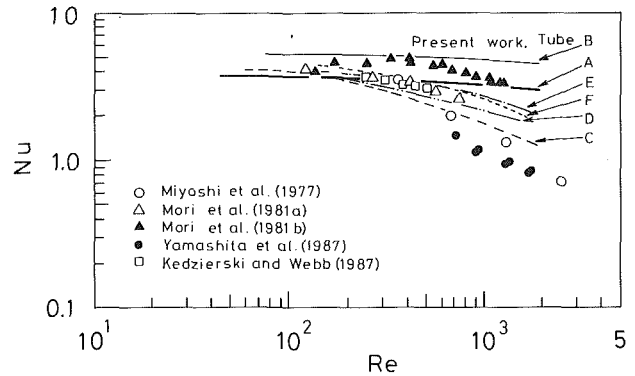

Fig. 11 Comparison of present results for u_o = 3.4~3.5 m/s and ΔT = 3~5 K with available experimental data for vertical enhanced surfaces

(1990) may usefully be applied to improve the design of condensers. However, it should be mentioned that while the present experiments are for downflow condensation on in-line tube bundles, many process condensers are crossflow, segmentally baffled type equipment with staggered tube bundles. Although the experimental results show that the effect of vapor velocity is modest, especially for flat-sided fin tubes, the effect may be more significant for staggered tube bundles than for in-line tube bundles. In this regard, experiments with staggered bundles of Tubes A–F are now under way.

Conclusions

1 The falling modes of condensate for flat-sided and three-dimensional fin tubes were basically the same at small Re, but were considerably different at large Re. Generation of small droplets due to vapor shear was more marked for the three-dimensional fin tube.

2 The flooding level of condensate for the unaffected region of a flat-sided finned tube was independent of u_o. This value agreed well with the theoretical prediction for stagnant vapor. When u_o was high, condensate retention was also observed near the top of tubes in the second and subsequent rows.

3 The heat transfer enhancement due to vapor shear was much less for a finned tube bundle than for a smooth tube bundle. For the flat-sided-fin tubes at low u_o and Re <1500, the measured Nu value agreed well with the prediction of the previous theoretical model for stagnant vapor. However, the theoretical prediction deviated toward a smaller value with increasing Re.

4 The decrease in Nu due to condensate inundation was more marked for a three-dimensional fin tube than for a flat-sided fin tube. The effects of u_o and ΔT on the Nu value were more marked at large Re for the three-dimensional fin tube, whereas the reverse was true for the flat-sided fin tube.

5 Among the six finned tubes tested, the highest heat transfer performance was provided by tube B (flat-sided fin tube) with fin dimensions close to the theoretically determined optimum values. This tube showed a higher heat transfer performance than available data for vertical enhanced surfaces at large Re.

References

Beatty, K. O., and Katz, D. L., 1948, "Condensation of Vapors on Outside of Finned Tubes," *Chem. Eng. Prog.*, Vol. 44, No. 1, pp. 55–70.

Fujii, T., and Uehara, H., 1973, "Film Condensation Heat Transfer," *Advances in Heat Transfer Engineering* [in Japanese], I. Tanasawa, ed., Yokendo, Tokyo, Vol. 1, pp. 1–101.

Gogonin, I. I., and Dorokhov, A. R., 1977, "Heat Transfer in Condensation of Flowing R-21 Vapor on Horizontal Finned Tubes," *Khim. Neft. Mashinostr.*, No. 8, pp. 17–18.

Gogonin, I. I., Kabov, O.A., and Sosunov, V.I., 1983, "Heat Transfer in Condensation of R-12 Vapor on Bundles of Finned Tubes," *Kholodil'naya Tekhnika*, No.1, pp. 26–29.

Honda, H., Nozu, S., and Mitsumori, K., 1983, "Augmentation of Condensation on Horizontal Finned Tubes by Attaching a Porous Drainage Plate," *Proceedings, ASME-JSME Thermal Engineering Joint Conference*, Y. Mori and W-J. Yang, eds., Vol. 3, pp. 289–295.

Honda, H., Nozu, S., Uchima, B., and Fujii, T., 1986, "Effect of Vapor Velocity on Film Condensation of R-113 on Horizontal Tubes in a Crossflow," *Int. J. Heat Mass Transfer*, Vol. 29, No. 3, pp. 429–438.

Honda, H., Nozu, S., and Takeda, Y., 1987a, "Flow Characteristics of Condensate in a Vertical Column of Horizontal Low Finned Tubes," *Proceedings, 2nd ASME-JSME Thermal Engineering Joint Conference*, P.J. Marto and I. Tanasawa, eds., ASME, Vol. 1, pp. 517–524.

Honda, H., Nozu, S., and Takeda, Y., 1987b, "A Theoretical Model of Film Condensation in a Bundle of Horizontal Low Finned Tubes," *Boiling and Condensation in Heat Transfer Equipment*, E. G. Ragi et al., eds., ASME HTD-Vol. 85, pp. 79-85; ASME JOURNAL OF HEAT TRANSFER, Vol. 111, No. 2, 1989, pp. 525–532.

Honda, H., Uchima, B., Nozu, S., Nakata, H., and Fujii, T., 1988a, "Condensation of Downward Flowing R-113 Vapor on Bundles of Horizontal Smooth Tubes," *Trans. Jpn. Soc. Mech. Engrs.* [in Japanese], Ser. B, Vol. 54, No. 502, pp. 1453–1460.

Honda, H., Nozu, S., and Uchima, B., 1988b, "A Generalized Prediction Method for Heat Transfer During Film Condensation on a Horizontal Low-Finned Tube," *JSME Int. J.*, Ser. II, Vol. 31, pp. 709–717.

Honda, H., and Nozu, S., 1990, "Effects of Bundle Depth and Working Fluid on the Optimized Fin Geometry of a Horizontal Low Finned Condenser Tube," *Proceedings, 2nd Int. Symp. Condensers and Condensation*, HTFS, pp. 407–416.

Katz, D. L., and Geist, J.M., 1948, "Condensation on Six Finned Tubes in Vertical Row," *Trans. ASME*, Vol. 70, pp. 907–914.

Kedzierski, M. A., and Webb, R.L., 1987, "Experimental Measurements of Condensation on Vertical Plates With Enhanced Fins," *Boiling and Condensation in Heat Transfer Equipment*, E. G. Ragi et al., eds., ASME HTD-Vol. 85, pp. 87–95.

Marto, D.J., 1986, "Recent Progress in Enhancing Film Condensation Heat Transfer on Horizontal Tubes," *Heat Transfer Engineering*, Vol. 7, Nos. 3-4, pp. 61–71; also private communication.

Marto, P.J., 1988, "An Evaluation of Film Condensation on Horizontal Integral-Fin Tubes," ASME JOURNAL OF HEAT TRANSFER, Vol. 110, No. 4(*b*), pp. 1287–1305.

McNaught, J. M., and Cotchin, C. D., 1989, "Heat Transfer and Pressure Drop in a Shell-and-Tube Condenser With Plain and Low-Fin Tube Bundles," *Chem. Eng. Res. Des.*, Vol. 67, pp. 127–133.

Michael, A. G., Marto, P. J., Wanniarachchi, A. S., and Rose, J. W., 1989, "Effect of Vapor Velocity During Condensation on Horizontal Smooth and Finned Tubes," *Heat Transfer With Phase Change*, I. S. Habib and R. J. Dallan, eds., ASME HTD-Vol. 114, pp. 1–10.

Mills, A. F., Hubbard, G. L., James, R. K., and Tan, C., 1975, "Experimental Study of Film Condensation on Horizontal Grooved Tubes," *Desalination*, Vol. 16, pp. 121–133.

Miyoshi, M., Takahata, T., and Mochida, Y., 1977, "Condensation Heat Transfer of Freon-11," *Proceedings, 14th National Heat Transfer Symposium of Japan* [in Japanese], pp. 247–249.

Mori, Y., Hijikata, K., Hirasawa, S., and Nakayama, W., 1981a, "Optimized Performance of Condensers With Outside Condensing Surface," ASME JOURNAL OF HEAT TRANSFER, Vol. 103, No. 1, pp. 96–102.

Mori,Y., Hijikata, K., and Kondo, T., 1981b, "Fundamental Study of Condenser Tubes for Highest Performance," *Proceedings, 18th National Heat Transfer Symposium of Japan* [in Japanese], pp. 163–165.

Nusselt, W., 1916, "Die Oberflächenkondensation des Wasserdampfes," *Zeit. Ver. Deut. Ing.*, Vol. 60, pp. 541–546, 569–575.

Schneider, P. J., 1985, "Conduction," *Handbook of Heat Transfer Fundamentals*, W. M. Rohsenow et al., eds., McGraw-Hill, New York, pp. 4.1–4.187.

Smirnov, G. F., and Lukanov, I. I., 1972, "Study of Heat Transfer From Freon-11 Condensing on a Bundle of Finned Tubes," *Heat Transfer-Soviet Research*, Vol. 4, No. 3, pp. 51–56.

Yamashita, K., Kumagai, M., Watanabe, Y., Kikuchi, K., Yabe, A., and Taketani, T., 1987, "The Development of an EHD Condenser," *Proceedings, 24th National Heat Transfer Symposium of Japan* [in Japanese], pp. 170–172.

Zukauskas, A., 1972, "Heat Transfer From Tubes in Crossflow," *Advances in Heat Transfer*, T. F. Irvine, Jr. and J. P. Hartnett, eds., Academic Press, New York, Vol. 8, pp. 93–160.

P. E. Phelan[1]
Research Assistant,
Department of Mechanical Engineering,
University of California,
Berkeley, CA 94720

M. I. Flik
Assistant Professor,
Department of Mechanical Engineering,
Massachusetts Institute of Technology,
Cambridge, MA 02139
Mem. ASME

C. L. Tien
A. Martin Berlin Professor,
Department of Mechanical Engineering,
University of California,
Berkeley, CA 94720
Fellow ASME

Radiative Properties of Superconducting Y-Ba-Cu-O Thin Films

Some applications of thin-film high-temperature superconductors, such as bolometers, radiation shielding, and space-cooled electronics, require knowledge of the superconducting-state radiative properties. At present, no general predictive model of the radiative properties has been presented. In this work, reflectance predictions based on two of the major theories of the superconducting state, the classical Drude–London theory and the quantum-mechanical Mattis–Bardeen theory, are compared with the available experimental data to determine the best method for predicting the radiative properties of thin-film Y–Ba–Cu–O. It is seen that the Mattis–Bardeen theory is more successful than the Drude–London theory in predicting the reflectance. Consequently, approximate formulae for the Mattis–Bardeen theory are developed, thus enhancing the theory's usefulness for engineering calculations.

Introduction

The most promising immediate applications of high-temperature superconductors (HTSC) are devices based on thin films. In several of these applications, such as liquid-nitrogen temperature radiation shielding, liquid-nitrogen temperature superconducting bolometers, optically triggered switches, and hybrid semiconductor/superconductor electronics intended for space applications, the radiative properties of thin-film HTSC are of concern. Superconducting radiation shielding is attractive because of the nearly perfect reflectance exhibited by superconductors in the far-infrared region. Radiation absorption is crucial, not only to the operation of superconducting bolometers, which operate in the transition region between their superconducting and normal states, but also to optically triggered switches. Finally, space-based 77-K electronics can conceivably be cooled solely through radiation to the space environment. These examples demonstrate the need for a working knowledge of the radiative properties of HTSC.

Early work on the radiative properties of metallic low-temperature superconductors (LTSC) demonstrated the significance of the *energy gap* (Glover and Tinkham, 1957; Richards and Tinkham, 1960). The energy gap is the energy required to separate a superconducting Cooper pair of electrons into quasiparticles, that is, into excited electrons. Essentially, at zero temperature a superconductor will absorb no radiation if the energy of the incident photons is less than the energy gap, leading to perfect reflectance at long wavelengths. Tinkham (1975) provided an overview of the radiative properties of a superconductor, and discussed both the classical and quantum-mechanical theories of the superconducting state.

The radiative properties of HTSC are fundamentally different from those of LTSC in the following ways: (I) HTSC are ceramics, whereas LTSC are metals, leading to possibly different radiation interaction mechanisms; (II) HTSC exhibit anisotropic properties, while LTSC are generally isotropic. In particular, the *ab*-plane properties of HTSC appear metallic, but the *c*-axis properties are somewhat like those of a dielectric (Timusk and Tanner, 1989); (III) HTSC are operated at liquid-nitrogen temperatures instead of liquid-helium temperatures, resulting in shorter electron mean free paths and higher phonon frequencies; (IV) the energy gap of HTSC appears to be substantially greater than that of LTSC; and (V) the superconducting coherence length ξ of HTSC is very short compared to that of LTSC. The coherence length ξ is analogous to the mean free path of normal-state electrons; ξ can be thought of as the "mean free path" of a Cooper pair (Tinkham, 1975). As a result of these differences, the radiative properties of HTSC can deviate significantly from the established properties of LTSC.

Previous studies concerning the radiative properties of HTSC have been conducted primarily to determine their electron and phonon properties (Timusk and Tanner, 1989). Perhaps the principal motivation for these investigations has been the identification and quantification of the superconducting energy gap. A result of this emphasis is the lack of a complete description of the radiative properties which is appropriate for engineering calculations. A general *predictive* model—one that does not rely on curve-fitting through measured reflectance data—of the superconducting-state properties of thin-film HTSC has not been presented. The emittance, which is the key radiative property for bolometers and radiation-cooled electronics, has mostly been neglected. One study has reported emittance measurements of HTSC (Fletcher et al., 1989), but it examined bulk samples, which exhibit radiative characteristics very different from those of well-ordered thin films. Phelan et al. (1989) showed that the *normal-state* far-infrared reflectance can be adequately described using the Drude free-electron theory, but they did not investigate the superconducting-state properties. It has not been ascertained whether a simple free-electron theory sufficiently describes the superconducting-state radiative properties, or whether a more sophisticated approach is required.

This work addresses these issues by examining two of the major theories of the superconducting state: the classical two-fluid model, which combines the London theory (London, 1961) with the normal-state Drude model, and the quantum-based theory (Mattis and Bardeen, 1958), which is derived from the Bardeen–Cooper–Schrieffer (BCS) theory. The two approaches are used to calculate the normal-incidence specular reflectance of a well-ordered Y–Ba–Cu–O thin film, or single crystal, which is sufficiently thick so as to eliminate any interference or substrate effects. Epitaxial thin films and single crystals are preferred for analysis in order to isolate the *ab*-plane behavior, since bulk radiative properties are a combination of *ab*-plane and *c*-axis properties, and hence are less amenable to analysis. The predictions are compared with ex-

[1]Currently Post Doctoral Fellow, Department of Mechanical Engineering Science, Tokyo Institute of Technology, Ohokayama, Meguroku, Tokyo, 152, Japan.

Contributed by the Heat Transfer Division and presented at the Joint AIAA/ASME Thermophysics and Heat Transfer Conference, Seattle, Washington, June 18–20, 1990. Manuscript received by the Heat Transfer Division March 1, 1990; revision received August 2, 1990. Keywords: Cryogenics, Radiation.

perimental data gathered from the literature. It is demonstrated that the Mattis–Bardeen (MB) theory is more successful than the Drude–London (DL) model in describing the reflectance spectrum. Consequently, approximate formulae for the MB theory are developed that facilitate the use of the theory for engineering calculations.

Drude-London Theory

Basic Physics. The DL theory is a free-electron model that extends the Drude theory to the superconducting state. It assumes that the total number density of electrons N is the sum of the superconducting-state number density N_s and the normal-state number density N_n. Only the normal-state electrons experience a viscous damping force from the crystal lattice; the superconducting-state electrons are able to move freely with no damping. Furthermore, it is assumed that not only do the electrons act independently of one another, but the response of each electron to an incident electric field is independent of the electron's position within the medium. These assumptions lead to inaccuracies, as described in the next subsection.

Applicability Conditions. The DL theory is a "local" theory; it is expected to apply when two conditions are satisfied: (*i*) the superconducting coherence length ξ is much shorter than the London penetration depth λ_L (Newhouse, 1964); and (*ii*) the electron mean free path l is much shorter than the electromagnetic field power penetration depth δ. The London penetration depth λ_L is the zero-frequency (dc) limit of the complex magnetic field amplitude penetration depth and does not vary with frequency.

Condition (*i*) shall be examined first. For Y–Ba–Cu–O, an approximate value for ξ_o, where the subscript o denotes zero temperature, is 2 nm (Cava et al., 1987; Gottwick et al., 1987). Here, the Pippard coherence length is assumed to be of the same order of magnitude as the Ginzburg–Landau coherence length, which is justified since for low temperatures far from T_c they are approximately equal (Tinkman, 1975). The corresponding value for λ_{Lo} is 150 nm (Harshman et al., 1989; Wu et al., 1989). Thus, for temperature $T=0$ K, it follows that

$$\frac{\xi_o}{\lambda_{Lo}} \sim 0.01 \tag{1}$$

and condition (*i*) is satisfied. For higher temperatures, λ_L has been observed to vary with temperature in approximate agreement with the semi-empirical two-fluid relation

$$\frac{\lambda_L(T)}{\lambda_{Lo}} = \left[1 - \left(\frac{T}{T_c}\right)^4\right]^{-1/2} \tag{2}$$

where T_c is the critical temperature (Harshman et al., 1987, 1989; Uemura et al., 1988; Krusin-Elbaum et al., 1989; Wu et al., 1989). The penetration depth therefore increases with temperature and becomes infinite at T_c. Contrarily, if ξ is assumed to obey the Pippard empirical relation (Van Duzer and Turner, 1981)

$$\frac{1}{\xi} = \frac{1}{\xi_o} + \frac{1}{\alpha l} \tag{3}$$

where α is a constant of order one, then ξ will decrease with temperature, since l can be estimated from (Newhouse, 1964)

$$l \sim \frac{h}{N^{2/3} e^2 r_{dc}} \tag{4}$$

where h is Planck's constant, e the magnitude of an electron's charge, and r_{dc} the dc resistivity. In general both N and r_{dc} increase with increasing T, and so from equation (4) l must decrease with increasing T, and consequently from equation (3) ξ must decrease with increasing T. Thus, the ratio ξ/λ_L is maximum at zero temperature, implying condition (*i*) is satisfied for all temperatures for Y–Ba–Cu–O.

Condition (*ii*) will now be examined. The power penetration depth δ is given by (Bohren and Huffman, 1983)

$$\delta \sim \frac{\lambda}{4\pi|\kappa|} \tag{5}$$

where λ is the wavelength of the incident radiation and κ the

Nomenclature

A = gap parameter, equation (15)
c = speed of light in vacuum $= 2.998 \times 10^8$ m s^{-1}
e = magnitude of an electron's charge $= 1.602 \times 10^{-19}$ C
g = dimensionless energy gap, equation (14)
h = Planck's constant $= 6.626 \times 10^{-34}$ J s
i = $\sqrt{-1}$
k_B = Boltzmann constant $= 1.381 \times 10^{-23}$ J K^{-1}
l = electron mean free path, m
m = complex refractive index $= n + \kappa i$
m_e = electron rest mass $= 9.110 \times 10^{-31}$ kg
n = real part of the complex refractive index
N = total electron number density, m^{-3}
N_n = number density of normal-state electrons, m^{-3}
N_s = number density of superconducting-state electrons, m^{-3}
r_{dc} = direct-current resistivity, Ωm
t = time, s
T = temperature, K
T_c = critical temperature, K
α = constant in equation (3)
γ = exponent in equation (19), given by equation (20)
δ = electromagnetic field power penetration depth, m
Δ = energy gap, J
ϵ_∞ = electrical permittivity of free space $= 8.854 \times 10^{-12}$ C V^{-1} m^{-1}
θ = dimensionless temperature $= T/T_c$
κ = imaginary part of the complex refractive index
λ = wavelength of the incident radiation in vacuum, m
λ_g = energy gap wavelength, equation (16), m
λ_L = London penetration depth, m
Λ = dimensionless wavelength $= \lambda/\lambda_g$
μ_∞ = magnetic permeability of free space $= 4\pi \times 10^{-7}$ V s^2 C^{-1} m^{-1}
ξ = superconducting coherence length, m
ρ = normal-incidence specular reflectance
σ = complex conductivity $= \sigma_1 + \sigma_2 i$, Ω^{-1} m^{-1}
σ_n = normal-state conductivity in the Mattis–Bardeen theory, equations (18) and (19), Ω^{-1} m^{-1}
σ_1 = real part of the complex conductivity, Ω^{-1} m^{-1}
σ_2 = imaginary part of the complex conductivity, Ω^{-1} m^{-1}
τ = electron relaxation time, s
ω = angular frequency of the incident radiation in vacuum, rad s^{-1}
ω_{pn} = normal-state plasma frequency, rad s^{-1}
ω_{ps} = superconducting-state plasma frequency, rad s^{-1}

Subscripts

o = zero temperature
∞ = free space

imaginary part of the refractive index m, defined as $m=n+\kappa i$. The penetration depth will increase with λ and with r_{dc}, if the Hagen-Rubens relation $\kappa \propto \sqrt{\lambda/r_{dc}}$, which leads to $\delta \propto \sqrt{\lambda r_{dc}}$, applies for the normal electrons. Thus, δ in the superconducting state, at least with regard to the existing normal electrons, should be maximum at $T=T_c$ and should increase with increasing wavelength.

An evaluation of equation (4) to determine the magnitude of l requires estimates of both N and r_{dc}. Measured values of r_{dc} in the temperature range $T_c < T < 300$ K indicate that r_{dc} increases linearly with temperature (Chaudhari et al., 1987; Roas et al., 1988). With regard to the reflectance data, which will be compared with the results presented here, the relation

$$r_{dc}=(6.0\times 10^{-9})T \tag{6}$$

where T is in K and r_{dc} is in Ω m, represents the extrapolated normal-state resistivity of the samples examined by Schützmann et al. (1989), and is assumed to hold for the *normal* electrons down to zero temperature. Equation (6) is also applied to the single-crystal specimens of Collins et al. (1989), for which no resistivity data are given.

The function $N(T)$ is more difficult to estimate. Hall effect data suggest that above T_c, N also increases linearly with temperature (Chaudhari et al., 1987; Duan et al., 1987), but below T_c there has been no direct measurement of $N(T)$. Note that below T_c, the relation $N(T)=N_s(T)+N_n(T)$ applies. Equation (2), however, can lead to an estimate of $N(T)$ for $T<T_c$, since λ_L is related to N_s through

$$\lambda_L{}^2 \equiv \frac{m_e}{N_s e^2 \mu_\infty} \tag{7}$$

where m_e is the electron rest mass and μ_∞ the magnetic permeability of free space. Thus, equation (2) leads to an expression for $N_s(T)$,

$$\frac{N_s(T)}{N_o}=1-\left(\frac{T}{T_c}\right)^4 \tag{8}$$

where N_o is the total number of electrons at zero temperature and it has been assumed that at that point all the electrons are in the superconducting state.

The derivation of equation (2) requires the assumption that N, the total electron number density, remains constant and equal to its value at 0 K, N_o (Schoenberg, 1962). Thus, the success of equation (2) in fitting penetration depth data suggests $N(T)$ is constant below T_c, and leads to the following assumed temperature dependence for N:

$$N=\begin{cases}(1.6\times 10^{26})T_c+2.7\times 10^{28} & T\le T_c\\ (1.6\times 10^{26})T+2.7\times 10^{28} & T>T_c\end{cases} \tag{9}$$

where N is in m^{-3} and T is in K. The linear function for N above T_c is appropriate for the reflectance data of Schützmann et al. (1989) and has been developed in a procedure described elsewhere (Phelan et al., 1989). Some experimental studies suggest N_o is of the order of 10^{27} to 10^{28} m^{-3} (Gottwick et al., 1987; Harshman et al., 1989; Krusin-Elbaum et al., 1989). For the experiment of Schützmann et al. (1989), $T_c=91$ K, and equation (9) yields a value of $N_o=N(T_c)=4.16\times 10^{28}$ m^{-3}. Since this is the same order of magnitude as has been reported in the other investigations, this value of N_o will be used in all forthcoming calculations.

Estimates of the ratio l/δ, based on equations (4) and (5) and using the DL theory to compute κ, reveal the following:

$$\begin{aligned}&\frac{l}{\delta}\sim 1.4 && \text{for } T=20 \text{ K}, 1\le\lambda\le 200\ \mu\text{m}\\ &\frac{l}{\delta}\sim 0.3 && \text{for } T=77 \text{ K}, 1\le\lambda\le 200\ \mu\text{m}\\ &0.02\lesssim\frac{l}{\delta}\lesssim 0.3 && \text{for } T=100 \text{ K}, 1\le\lambda\le 200\ \mu\text{m}\end{aligned} \tag{10}$$

implying condition (*ii*) may not be satisfied for temperatures far below the critical temperature, but appears to be satisfied for higher temperatures.

Calculation of the Refractive Index and the Reflectance. The derivation of the DL theory will not be given here since it has been presented earlier (Van Duzer and Turner, 1981; Timusk and Tanner, 1989). The complex refractive index m is determined from

$$m^2=(n+\kappa i)^2=1-\frac{\omega_{ps}^2}{\omega^2}-\frac{\omega_{pn}^2}{\omega(\omega+i/\tau)} \tag{11}$$

where ω is the angular frequency of the incident radiation and the electric field is assumed to vary as $\exp(-i\omega t)$, where t is time. The superconducting plasma frequency ω_{ps}, the normal plasma frequency ω_{pn}, and the relaxation time τ are given by

$$\omega_{ps}^2\equiv\frac{N_s e^2}{m_e \epsilon_\infty} \qquad \omega_{pn}^2\equiv\frac{N_n e^2}{m_e \epsilon_\infty} \qquad \tau=\frac{m_e}{N_n e^2 r_{dc}} \tag{12}$$

where ϵ_∞ is the electrical permittivity of free space. This relation for τ is most suitable for long-wavelength radiation where the absorption of energy from incident photons results in *intra*band electronic transitions. As the photon energy, and therefore the frequency, is increased, the absorption mechanisms of the electrons within the medium change, resulting in a frequency-dependent τ. These high-energy absorption mechanisms include *inter*band transitions and other inelastic processes (Timusk and Tanner, 1989). Thus, the DL model as presented here is not expected to apply for short wavelengths where inelastic processes can occur.

The only input parameters required for the DL theory are r_{dc}, N_n, and N_s, which can be determined from equations (6), (8), and (9). The value of m calculated from equation (11) can be inserted into the general expression governing the normal-incidence reflectance ρ at the interface between two semi-infinite media (Bohren and Huffman, 1983):

$$\rho=\left|\frac{m_1-m_2}{m_1+m_2}\right|^2 \tag{13}$$

in which m_1 refers to the complex refractive index of the incident medium (typically vacuum or air, i. e., $m_1=1$) and m_2 refers to the refractive index calculated from equation (11). If the film thickness is much larger than δ, then there is no transmission and the emittance is equal to $1-\rho$, if no diffuse reflection occurs.

Mattis-Bardeen Theory

Basic Physics. The MB theory is based on quantum-mechanical arguments and is an extension of the BCS energy gap theory of superconductivity. It differs from the DL model in at least three major points: (1) It treats electrons as waves instead of classical particles; (2) it allows for a finite energy gap between the normal and superconducting states, whereas the DL model corresponds to an infinite gap; and (3) the electric field is allowed to vary spatially over a distance comparable with ξ_o, instead of requiring the electrons to experience only a constant electric field while traveling a distance ξ_o. This last difference is significant since it permits calculation of the radiative properties even when the superconductor is in the anomalous skin effect regime where $\xi_o >> \delta$. Indeed, the MB theory is strictly valid only in this limit.

Applicability Conditions. Either of two conditions should be satisfied for the MB theory to apply. One is mentioned directly above: The zero-temperature coherence length is much greater than the electric field penetration depth, or $\xi_o >> \delta$, the extreme anomalous limit (Mattis and Bardeen, 1958). The other requires the superconductor to be in the "dirty" limit, where $l << \xi_o$ (Tinkham, 1970). Timusk and Tanner (1989)

state that the MB theory should also be applicable in the clean limit, $l >> \xi_o$, but they do not give a derivation for this criterion. It is in contrast to the statement of Tinkham (1970), who expects the MB theory to yield the greatest error in the clean limit. When comparing l with ξ_o, it appears that Y-Ba-Cu-O is in the "clean" limit, at least for low temperatures. Estimates of l/ξ_o, calculated from equations (4), (6), and (9), are 9, 2, and 2 for $T=$ 20 K, 77 K, and 90 K, respectively. Although the applicability of the MB theory to Y-Ba-Cu-O is not completely established, it is the most frequently used theory for the optical properties of superconductors and the best choice for the high-temperature superconductors at this point.

Calculation of the Refractive Index and the Reflectance. The MB theory in itself does not give a complete description of a superconductor's radiative properties. Instead, it provides the ratio of the complex conductivity in the superconducting state, $\sigma = \sigma_1 + \sigma_2 i$, to the normal-state conductivity σ_n. Since only the conductivity ratio is given, the MB theory cannot be extended into the normal state like the DL model. Under the conditions of the theory, σ_n is assumed to be entirely real and independent of frequency. The results are presented in the form of σ_1/σ_n and σ_2/σ_n as functions of singular integrals (Mattis and Bardeen, 1958; Van Duzer and Turner, 1981).

A parameter required by the MB theory is the ratio of the energy gap at temperature T, $\Delta(T)$, to that at zero temperature, Δ_o. In the case of *weak coupling*, $\Delta(T)$ is much smaller than the characteristic energy of lattice vibrations, which corresponds to T_c being much smaller that the Debye temperature. In the weak-coupling limit, $\Delta(T)/\Delta_o$ is a function only of the dimensionless temperature $\theta \equiv T/T_c$. The BCS theory gives $\Delta(T)/\Delta_o$ in the form of an implicit integral relation. An approximate formula, however, has been developed (Flik and Hijikata, 1990),

$$\frac{\Delta(T)}{\Delta_o} \equiv g \cong [1-\theta^{10/3}]^{1/2} \tag{14}$$

which is accurate to within 5 percent of the weak-coupling expression. Equation (14) is used throughout the present analysis in place of the original BCS expression.

The energy gap at zero temperature, Δ_o, is linearly proportional to T_c,

$$2\Delta_o = Ak_BT_c \tag{15}$$

where A is the constant of proportionality. The BCS theory predicts $A=3.52$, but presently there is some doubt as to whether this value holds for the high-temperature superconductors. Thus, it is beneficial to permit A to be a variable input parameter.

The wavelength corresponding to the energy gap, λ_g, is determined from

$$\lambda_g = \frac{hc}{2\Delta(T)} = \frac{hc}{Ak_BT_c} \cdot \frac{\Delta_o}{\Delta(T)} = \frac{hc}{Ak_BT_cg} \tag{16}$$

where c is the speed of light in vacuum. The significance of λ_g will be demonstrated in the following section.

An appropriate, frequency-independent value for σ_n must be determined. One possibility that has been used in at least one previous study (Collins et al., 1987) is the dc limit ($\omega = 0$) of the Drude conductivity, which is simply the inverse of the measured dc resistivity r_{dc}. This choice is consistent with the MB theory in that it is independent of frequency and is valid for long wavelengths. It should be noted that the equations of the MB theory used here are strictly valid only in the far-infrared where σ_n is close to the real, constant dc conductivity. The theory is therefore expected to become less applicable with decreasing wavelength. All of the results presented in this study are calculated assuming $\sigma_n = 1/r_{dc}$.

The refractive index m, for the magnetic permeability equal to that of free space, is related to σ through

$$m^2 = 1 + \frac{\sigma i}{\epsilon_\infty \omega} \tag{17}$$

where again the electric field is assumed to vary as $\exp(-i\omega t)$. Finally, m can be inserted into equation (13) to determine the reflectance and the emittance. The input required to calculate m consists of three variables: r_{dc}, T_c and the gap parameter A.

Comparison With Experimental Data

The experimental data used in the present study for comparative purposes are near-normal specular reflectance measurements made on epitaxial, c-axis-oriented Y-Ba-Cu-O thin films (Schützmann et al., 1989), and on single crystals (Collins et al., 1989). Schützmann et al. (1989) measured the reflectance with a Fourier-transform infrared spectrometer, and estimated the accuracy of their measurements to be at worst ± 2 percent. Collins et al. (1989) performed their measurements with a scanning interferometer, which had an estimated precision of better than 1 percent. The film thickness in the first study is approximately 0.4 μm (Schützmann et al., 1989), and the crystal thickness in the second is about 50 μm (Collins et al., 1989). The measured wavelength spectrum is roughly $7\ \mu m < \lambda < 160\ \mu m$. The critical temperature T_c is 91 K for the former study and 92 K for the latter, but here T_c shall be taken to be 91 K for all samples.

A direct comparison of the results of both theories with experimental data is given in Fig. 1. The data and theoretical results are presented for $T=20$ K and $T=45$ K. The gap parameter A of the MB theory is taken to be the BCS value, 3.52. It is apparent that the MB theory matches the data more closely than the DL model, which essentially predicts zero reflectance for $\lambda = 0$ and $\rho = 1$ for $\lambda > 0$. A further evaluation of the DL model is given in Fig. 2, where theoretical results are presented for $T=20$ K, 77 K, and 100 K. As expected, with an increase in temperature the electron mean free path becomes sufficiently short compared with the penetration depth to make the theory more valid, although some error still occurs for short wavelengths where δ is small. The DL model appears only marginally useful for liquid nitrogen temperature ($T=77$ K).

A further evaluation of the MB theory is presented in Fig.3. Again, A is taken to be 3.52. The MB theory is not expected to apply to the 100 K and 105 K data, but those data are included to demonstrate the validity of the theory at temperatures near T_c. As both Figs. 1 and 2 indicate, the MB theoretical results are within 12 percent of the experimental data

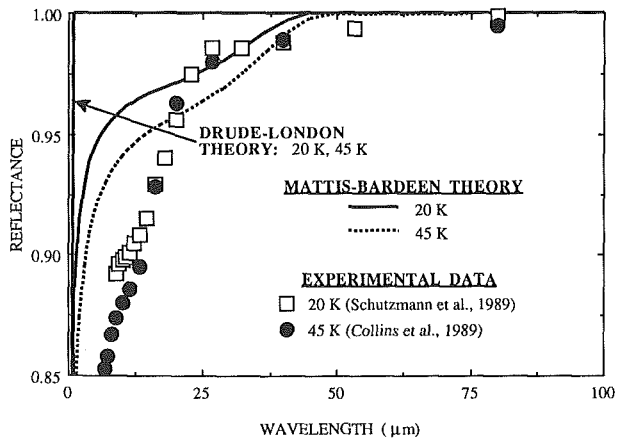

Fig. 1 A comparison between the Drude-London theory, the Mattis-Bardeen theory, and experimental data; the gap parameter A of the Mattis-Bardeen theory is taken to be 3.52

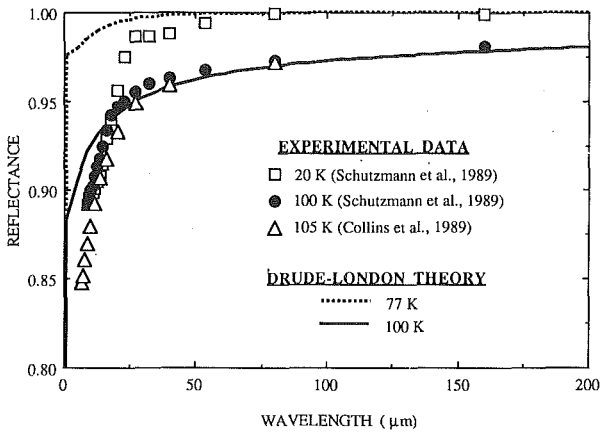

Fig. 2 A comparison between the Drude-London theory and experimental data at various temperatures, including both the superconducting and normal states; the 20 K theoretical curve is coincident with the left ordinate axis and the upper abscissa axis

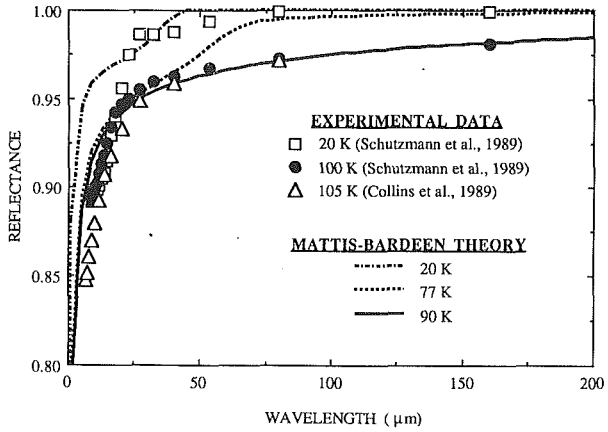

Fig. 3 A comparison between the Mattis-Bardeen theory and both superconducting and normal-state experimental data at various temperatures; the gap parameter A is taken to be 3.52

for the temperature range $20\ \text{K} \le T \le 90\ \text{K}$. The agreement for higher temperatures is somewhat surprising since the decrease in l means the superconductor is not in the anomalous skin effect regime. The greatest error occurs for small wavelengths and is due perhaps to the choice of $\sigma_n = 1/r_{dc}$, which, as mentioned before, should be more valid for long wavelengths. A better value for σ_n at these wavelengths could be determined by fitting the MB theoretical results to the experimentally measured reflectance over the spectrum of interest. This procedure, however, would render the theory less general by requiring a priori reflectance data in addition to stretching the theory beyond its intended limits. A better approach would perhaps be to employ the theory of Leplae (1983) or that of Pöpel (1989), who have extended the MB theory to consider strong-coupling superconductors and short-wavelength radiative behavior, respectively. The deviation of the data from the MB theory could also be due to the fact that Y-Ba-Cu-O is in the clean limit. The theory of Pöpel (1989) is stated to be valid for any electron mean free path and could possibly remove this limitation.

A self-consistency check needs to be provided here to demonstrate the validity of the semi-infinite relationship, equation (13), for calculating the reflectance of a 0.4 μm thin film. Using the MB theory to compute κ, for $1\ \mu\text{m} \le \lambda \le 200\ \mu\text{m}$ and at 20 K, the maximum calculated δ is about 20 nm, and is usually less than 14 nm. For 50 K, the maximum δ is about 32 nm, and is usually less than 24 nm. For 90 K, δ is generally larger than the film thickness (40 nm). The penetration depth calculated from the DL model is always much less than that from the MB theory. Noting that here the theoretical results are directly compared with only 20 K and 45 K superconducting-state data, the influence of the finite film thickness at these temperatures is small. Indeed, Schützmann et al. (1989) reported the substrate had no influence on their measured reflectances. A comparison with thin-film superconducting-state data at higher temperatures near T_c would, however, require the electromagnetic relations appropriate for a finite-thickness thin film.

Finally, the effect of varying A on the MB-calculated reflectance is shown in Fig. 4. The curves and data apply for $T = 20$ K. The values of A are drawn from other studies, which suggest $A = 1.9$ and $A = 5.8$ (Schützmann et al., 1989), and $A = 7.0$ (Olson et al., 1989). It is not clear which choice is best. Until more information about the energy gap is known, it is recommended to use the BCS value of $A = 3.52$.

The influence of the gap parameter A is clearly manifested by the wavelength corresponding to the energy gap, λ_g. For wavelengths above this value, the superconducting film acts as a perfect reflector. In Fig. 4, λ_g varies from about 23 μm

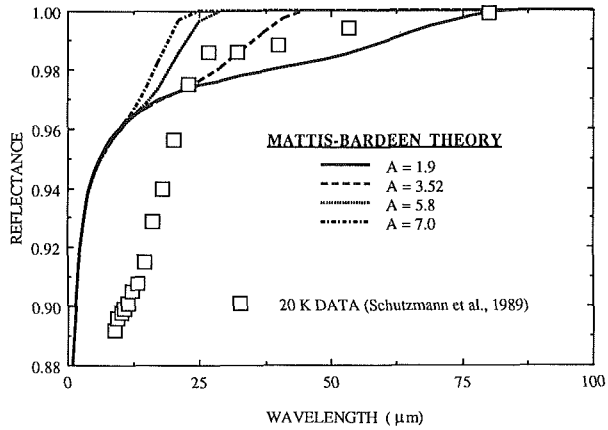

Fig. 4 Effect of varying the gap parameter A on the theoretical reflectance calculated from the Mattis-Bardeen theory; all results are for $T = 20$ K

for $A = 7$ to about 83 μm for $A = 1.9$. This figure clearly demonstrates the potential of thin-film superconductors to serve as radiation shields, in particular for far-infrared radiation emitted at cryogenic temperatures.

Employing the approximate relation given by equation (14) for the gap function g leads to an undetermined error in the MB reflectance predictions. The BCS *weak-coupling-limit* relation for g, which equation (14) was derived to approximate, is itself not rigorously valid for high-temperature superconductors like Y-Ba-Cu-O, due to their high critical temperatures. An evaluation of the *exact* implicit relation for g (Van Duzer and Turner, 1981) for Y-Ba-Cu-O, for which the Debye temperature is about 400 K (Lang et al., 1988) and T_c is 91 K, reveals that the constant A, defined in equation (15), should be 3.66 instead of the usual weak-coupling value of 3.52. The magnitude of A must be increased to make the theory consistent at zero temperature. Regardless of whether the weak-coupling theory is used or not, equation (14) serves as an excellent approximation for the gap function g, since in either case the error is less than 5 percent. In the present analysis, all of the MB calculations, except for those leading to Fig.4, have utilized $A = 3.52$. The success of the MB theory as it is presently formulated demonstrates its validity, and thus a more accurate calculation of g has not been attempted, nor has $A = 3.66$ been substituted for $A = 3.52$.

The assumed dependence of the electron number density on temperature, equation (9), is the most uncertain portion of the present formulation. A considerable amount of effort was involved with determining a credible relationship between N

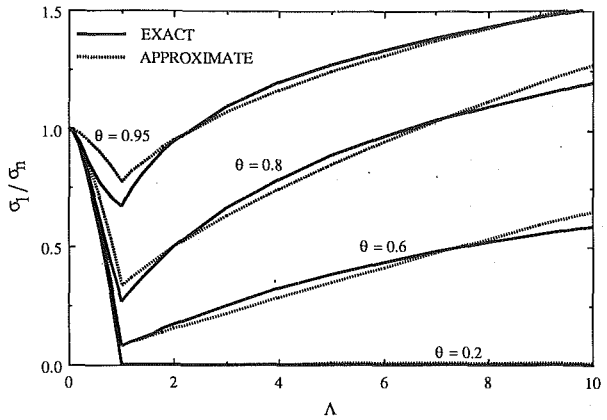

Fig. 5 A comparison between the exact Mattis-Bardeen theory and the approximate expressions, equations (18)-(20); the ratio of the real part of the superconducting conductivity to the normal-state conductivity is plotted as a function of dimensionless wavelength

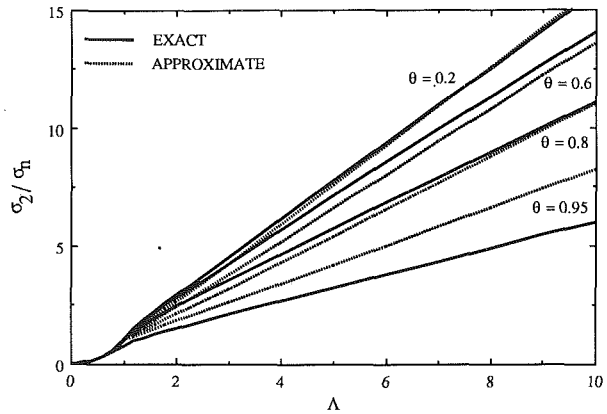

Fig. 6 A comparison between the exact Mattis-Bardeen theory and the approximate expressions, equations (18)-(20); the ratio of the imaginary part of the superconducting conductivity to the normal-state conductivity is plotted as a function of dimensionless wavelength

and T. Both the zero-temperature and normal-state number density have been measured, but little is known about the temperature dependence of N between 0 K and T_c. The assumed constant value is consistent with the derivation of equation (2), and also agrees with measured values of N_o. Also, provided N is of the same order of magnitude as equation (9), the exact form of the N versus T function is not important, since N would have to be substantially altered to change the results significantly. In particular, N has to be decreased by four to five orders of magnitude to make the Drude-London predictions agree better with the experimental data. Thus, equation (9) should be considered a useful approximation rather than an exact expression.

To summarize, the MB theory matches the experimental data more closely than the DL theory. The differences between the two theoretical results are especially apparent for low temperatures ($T \leq 45$ K). The DL model effectively assumes an infinite energy gap (Timusk and Tanner, 1989), which leads to the prediction of perfect reflectance for all wavelengths at low temperatures. Despite its easy evaluation, it is not useful for calculation of the radiative properties of HTSC. On the other hand, the MB theory is more difficult to understand and to calculate. The next section addresses its difficult calculation by presenting approximate formulae to be used in place of the singular integrals of the MB theory.

Approximate Expressions for the Mattis-Bardeen Theory

The complexity of the integral expressions for σ_1/σ_n and σ_2/σ_n hinders their use in engineering calculations. Consequently, approximate relations have been developed for σ_1/σ_n and σ_2/σ_n in terms of dimensionless wavelength $\Lambda \equiv \lambda/\lambda_g$ and temperature $\theta \equiv T/T_c$.

These expressions apply for $\Lambda \leq 1$:

$$\frac{\sigma_1}{\sigma_n} = 1 - (1 - \theta^{4.919})\Lambda^{1.6} \quad \text{and} \quad \frac{\sigma_2}{\sigma_n} = \Lambda^{2.35} \tag{18}$$

These expressions apply for $\Lambda > 1$:

$$\left[\frac{\sigma_1}{\sigma_n} = \theta^{4.919}\Lambda^{\gamma}\right] \text{and}$$

$$\frac{\sigma_2}{\sigma_n} = [-(0.991)\theta^{2.559} + 1.67](\Lambda - 1) + 1 \tag{19}$$

where

$$\gamma \equiv 1.455 - (0.387)\theta - (0.881)\theta^2 \tag{20}$$

Equations (18)-(20) are valid for $0 \leq \theta < 1$ and $0 \leq \Lambda \leq 10$, although the upper limit on Λ can be extended. The approximate expressions are graphed, along with the exact results, in Figs. 5 and 6. The dimensionless temperature θ is varied between 0.2 and 0.95. Note that the $\theta = 0$ curves are coincident with those for $\theta = 0.2$ on this scale. It is seen from both figures that the greatest error occurs for $\theta = 0.95$; for σ_1/σ_n, the error is $\sim$ 20 percent near $\Lambda = 1$, and for σ_2/σ_n the error increases with Λ, reaching $\sim$ 40 percent at $\Lambda = 10$.

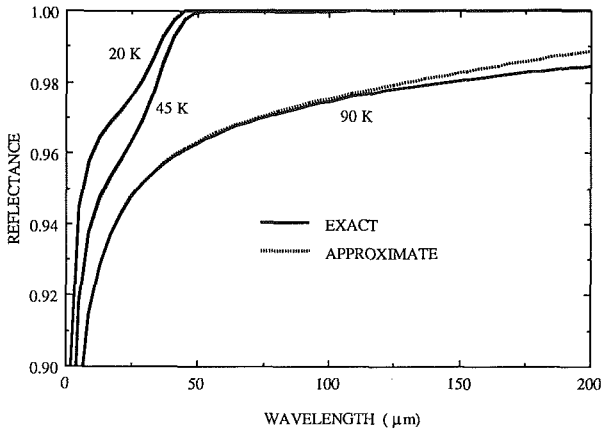

Fig. 7 A comparison between the exact Mattis-Bardeen theory and the approximate expressions, equations (18)-(20); the reflectance at three temperatures is plotted as a function of wavelength; on this scale, the only visible difference between the two is for 90 K

The errors associated with the approximate expressions have little effect, however, on the calculated reflectance. As indicated in Fig. 7, very little difference is seen between the exact ρ curves and the approximate ρ curves. The greatest error again occurs for large temperatures, in this case for $\theta = 90/91 = 0.99$, but for the three curves shown in Fig. 7 the maximum error is less than 0.2 percent. Thus, the approximate relations given in equations (18)-(20), combined with equations (13) and (17), are adequate for reflectance and emittance calculations.

Equations (18)-(20) are derived specifically for the superconducting *ab*-plane properties of Y-Ba-Cu-O, but they should also be valid for the other high-T_c superconductors. The radiative properties of both the bismuth and the thallium-based compounds appear similar to those of Y-Ba-Cu-O (Reedyk et al., 1988; Zetterer et al., 1989; Collins et al., 1989), suggesting equations (18)-(20) can also be applied to describe their *ab*-plane properties. In all cases, the refractive index calculated from the above approximate expressions should be inserted into the proper electromagnetic relations, whether they be for semi-infinite media, as is done here, for a single thin film, or for multiple films.

Conclusions and Recommendations

An evaluation of the classical Drude–London theory and the quantum-mechanical Mattis–Bardeen theory has been carried out to determine which model is more capable of predicting the radiative behavior of well-ordered thin-film or single-crystal Y–Ba–Cu–O. Comparison with experimental reflectance data indicates the Mattis–Bardeen theory is more successful than the Drude–London theory. The theoretical results are within 12 percent of experimental data, and the agreement improves as the wavelength increases. The magnitude of the energy gap is still unclear; hence, at present it is recommended to use the BCS value of the gap parameter A until other data become available.

Approximate formulae for the Mattis–Bardeen theory have been determined. The normal incidence specular reflectance calculated from these formulae matches the exact Mattis–Bardeen reflectance to within 0.2 percent. These approximate relations are recommended for general engineering use.

Acknowledgments

The authors wish to express their appreciation to L. Carr, P. L. Richards, and M. Sherwin for their helpful discussions, and to G. Chen, S. H. Park, and T. Qui for reviewing the manuscript. The official reviewers' comments are much appreciated. One of the authors (M.I.F.) acknowledges the support of the Lynde and Harry Bradley Foundation through a Career Development Chair.

References

Bohren, C. F., and Huffman, D. R., 1983, *Absorption and Scattering of Light by Small Particles*, Wiley, New York, pp. 29–32.

Cava, R. J., Batlogg, B., van Dover, R. B., Murphy, D. W., Sunshine, S., Siegrist, T., Remeika, J. P., Rietman, E. A., Zahurak, S., and Espinosa, G. P., 1987, "Bulk Superconductivity at 91 K in Single-Phase Oxygen-Deficient Perovskite $Ba_2YCu_3O_{9-\delta}$," *Physical Review Letters*, Vol. 58, pp. 1676–1679.

Chaudhari, P., Collins, R. T., Freitas, P., Gambino, R. J., Kirtley, J. R., Koch, R. H., Laibowitz, R. B., LeGoues, F. K., McGuire, T. R., Penney, T., Schlesinger, Z., Segmuller, A. P., Foner, S., and McNiff, E. J., 1987, "Properties of Epitaxial Films of $YBa_2Cu_30_{7-\delta}$," *Physical Review B*, Vol. 36, pp. 8903–8906.

Collins, R. T., Schlesinger, Z., Koch, R. H., Laibowitz, R. B., Plaskett, T. S., Freitas, P., Gallagher, W. J., Sandstrom, R. L., and Dinger, T. R., 1987, "Comparative Study of Superconducting Energy Gaps in Oriented Films and Polycrystalline Bulk Samples of Y–Ba–Cu–O," *Physical Review Letters*, Vol. 59, pp. 704–707.

Collins, R. T., Schlesinger, Z., Holtzberg, F., and Feild, C., 1989, "Infrared Evidence for Gap Anisotropy in $YBa_2Cu_3O_7$," *Physical Review Letters*, Vol. 63, pp. 422–425.

Duan, H. M., Lu, L., Wang, X. M., Lin, S. Y., and Zhang, D. L., 1987, "Hall Effect of the High T_c Superconducting Y–Ba–Cu–O Compound," *Solid State Communications*, Vol. 64, pp. 489–491.

Fletcher, L. S., Peterson, G. P., Pandey, R. K., and Cunnington, G. R., 1989, "Spectral Properties of Selected Superconducting Materials," Paper No. AIAA-1674, presented at the AIAA 24th Thermophysics Conference, Buffalo, NY, June 12–14.

Flik, M. I., and Hijikata, K., 1990, "Approximate Thermal Packaging Limit for Hybrid Superconductor-Semiconductor Electronic Circuits," *Heat Transfer 1990*, G. Hetsroni, ed., Vol. 2, pp. 319–324, Hemisphere, New York.

Glover, R. E., and Tinkham, M., 1957, "Conductivity of Superconducting Films for Photon Energies Between 0.3 and 40 k_BT_c," *Physical Review*, Vol. 108, pp. 243–256.

Gottwick, U., Held, R., Sparn, G., Steglich, F., Rietschel, H., Ewert, D., Renker, B., Bauhofer, W., von Molnar, S., Wilhelm, M., and Hoenig, H. E., 1987, "Transport Properties of $YBa_2Cu_3O_7$: Resistivity, Thermal Conductivity, Thermopower and Hall Effect," *Europhysics Letters*, Vol. 4, pp. 1183–1188.

Harshman, D. R., Aeppli, G., Ansaldo, E. J., Batlogg, B., Brewer, J. H., Carolan, J. F., Cava, R. J., Celio, M., Chaklader, A. C. D., Hardy, W. N., Kreitzman, S. R., Luke, G. M., Noakes, D. R., and Senba, M., 1987, "Temperature Dependence of the Magnetic Penetration Depth in the High-T_c Superconductor $Ba_2YCu_3O_{7-\delta}$: Evidence for Conventional s-Wave Pairing," *Physical Review B*, Vol. 36, pp. 2386–2389.

Harshman, D. R., Schneemeyer, L. F., Waszczak, J. V., Aeppli, G., Cava, R. J., Batlogg, B., Rupp, L. W., Ansaldo, E. J., and Williams, D. L., 1989, "Magnetic Penetration Depth in Single-Crystal $YBa_2Cu_3O_{7-\delta}$," *Physical Review B*, Vol. 39, pp. 851–854.

Krusin-Elbaum, L., Greene, R. L., Holtzberg, F., Malozemoff, A. P., and Yeshurun, Y., 1989, "Direct Measurement of the Temperature-Dependent Magnetic Penetration Depth in Y–Ba–Cu–O Crystals," *Physical Review Letters*, Vol. 62, pp. 217–220.

Lang, M., Lechner, T., Riegel, S., Steglich, F., Weber, G., Kim, T. J., Luthi, B., Wolf, B., Rietschel, H., and Wilhelm, M., 1988, "Thermal Expansion, Sound Velocities, Specific Heat and Pressure Derivative of T_c in $YBa_2Cu_3O_7$," *Zeitschrift fur Physik B*, Vol. 69 pp. 459–463.

Leplae, L., 1983, "Derivation of an Expression for the Conductivity of Superconductors in Terms of the Normal-State Conductivity," *Physical Review B*, Vol. 27, pp. 1911–1912.

London, F., 1961, *Superfluids*, Vol. 1, Dover Publications, Inc. New York, pp. 27–95.

Mattis, D. C., and Bardeen, J., 1958, "Theory of the Anomalous Skin Effect in Normal and Superconducting Metals," *Physical Review*, Vol. 111, pp. 412–417.

Newhouse, V. L., 1964, *Applied Superconductivity*, Wiley, New York, pp. 69, 62–64, 91.

Olson, C. G., Liu, R., Yang, A.-B., Lynch, D. W., Arko, A. J., List, R. S., Veal, B. W., Chang, Y. C., Jiang, P. Z., and Paulikas, A. P., 1989, "Superconducting Gap in Bi–Sr–Ca–Cu–O by High Resolution Angle-Resolved Photoelectron Spectroscopy," *Science*, Vol. 245, pp. 731–733.

Phelan, P. E., Flik, M. I., and Tien, C. L., 1989, "Normal-State Radiative Properties of Thin-Film High-Temperature Superconductors," *Advances in Cryogenic Engineering—Materials*, R. P. Reed and F. R. Fickett, eds., Vol. 36, pp. 479–486, Plenum Press, New York.

Popel, R., 1989, "Surface Impedance and Reflectivity of Superconductors," *Journal of Applied Physics*, Vol. 66, pp. 5950–5957.

Reedyk, M., Bonn, D. A., Garrett, J. D., Greedan, J. E., Stager, C. V., Timusk, T., Kamaras, K., and Tanner, D. B., 1988, "Far-Infrared Optical Properties of $Bi_2Sr_2CaCu_2O_8$," *Physical Review B*, Vol. 38, pp. 11981–11984.

Richards, P. L., and Tinkham, M., 1960, "Far-Infrared Energy Gap Measurements in Bulk Superconducting In, Sn, Hg, Ta, V, Pb, and Nb, "*Physical Review*, Vol. 119, pp. 575–590.

Roas, B., Schultz, L., and Endres, G., 1988, "Epitaxial Growth of $YBa_2Cu_3O_{7-x}$ Thin Films by a Laser Evaporation Process," *Applied Physics Letters*, Vol. 53, pp. 1557–1559.

Shoenberg, D., 1952, *Superconductivity*, Cambridge University Press, Cambridge, United Kingdom, pp. 194–197.

Schützmann, J., Ose, W., Keller, J., Renk, K. F., Roas, B., Schultz, L., and Saemann-Ischenko, G., 1989, "Far-Infrared Reflectivity and Dynamical Conductivity of an Epitaxial $YBa_2Cu_3O_{7-\delta}$ Thin Film," *Europhysics Letters*, Vol. 8, pp. 679–684.

Timusk, T., and Tanner, D. B., 1989, "Infrared Properties of High T_c Superconductors," *The Physical Properties of High-Temperature Superconductors I*, D. M. Ginsberg, ed., World Scientific Publishing Company, Singapore, pp. 339–407.

Tinkham, M., 1970, "Far Infrared Absorption in Superconductors," in: *Far Infrared Properties of Solids*, Plenum Press, New York, pp. 223–246.

Tinkham, M., 1975, *Introduction to Superconductivity*, McGraw-Hill, New York, pp. 1–71.

Uemura, Y. J., Emery, V. J., Moodenbaugh, A. R., Suenaga, M., Johnston, D. C., Jacobson, A. J., Lewandowski, J. T., Brewer, J. H., Kiefl, R. F., Kreitzman, S. R., Luke, G. M., Riseman, T., Stronach, C. E., Kossler, W. J., Kempton, J. R., Yu, X. H., Opie, D., and Schone, H. E., 1988, "Systematic Variation of Magnetic-Field Penetration Depth in High-T_c Superconductors Studied by Muon-Spin Relaxation," *Physical Review B*, Vol., 38, pp. 909–912.

Van Duzer, T., and Turner, C. W., 1981, *Principles of Superconductive Devices and Circuits*, Elsevier, New York, pp. 118–121, 126, 128, 67–69.

Wu, D. H., Kennedy, W. L., Zahopoulos, C., and Sridhar, S., 1989, "Characteristics and Growth of Single Crystals of $Y_1Ba_2Cu_3O_7$ With Superior Microwave Properties," *Applied Physics Letters*, Vol. 55, pp. 696–698.

Zetterer. T., Ose, W., Schutzmann, J., Otto, H. H., Obermayer, P. E., Tasler, N., Lengfellner, H., Lugert, G., Keller, J., and Renk, K. F., 1989, "Preparation, Characterization, and Far-Infrared Study of Ceramic High-T_c Superconductors," *Journal of the Optical Society of America B*, Vol. 6, pp. 420–435.

Journal of Heat Transfer

Technical Notes

This section contains shorter technical papers. These shorter papers will be subjected to the same review process as that for full papers.

Macroscopic Constriction Resistance in Microelectronic Packages

D. Veith,[1,4] G. P. Peterson, [2,4] and L. S. Fletcher[3,4]

Introduction

Because the reliability of semiconductor packages is strongly dependent upon the package operating temperature, the thermal behavior of these packages is a significant factor in determining the mean time between failures. As a result, the package thermal resistance is of great interest to design and development engineers. The internal thermal resistance of a typical dual-in-line (DIP) semiconductor device can be divided into two components: the microscopic resistance (that resistance caused by the imperfect contact between the internal surfaces) and the macroscopic resistance (the resistance resulting from large geometric variations). A typical example of macroscopic resistance is the resistance resulting from the change in shape and size of the heat transfer area as heat flows from the chip to the surrounding package material. The microscopic resistance is the resistance between the chip and package material due to the surface roughnesses.

There have been a number of investigations dealing with the thermal control of electronic devices, but only a limited number consider the effect of geometry on the overall thermal resistance. Ellison (1984) provides an excellent overview of computational techniques for use in evaluating the thermal performance of electronic equipment. Antonetti and Yovanovich (1984), in a review of the thermal management in electronic packages, presented and discussed the many factors contributing to the high internal resistances in semiconductor packages. Yerman et al. (1983) and Mahalingham et al. (1984) experimentally determined the effect of voids or cracks on the thermal conductivity of the bonded interface. These two investigations indicated that small concentrations of random voids have little effect on the overall resistance, but large contiguous voids may result in significant increases in the chip-to-substrate resistance.

Nakayama (1986) presented an excellent summary of the thermal management of electronic equipment and noted that in conventional plastic dual-in-line packages where the chip occupies only a small area, the flying leads play an important role in dissipating the heat. As the chip size increases, however, the flying leads dissipate a proportionately smaller amount of heat, and the thermal conductivity of the mold compound, the surface area of the chip, and the location of the chip within the mold compound become more important.

An experimental investigation of the significance and magnitude of the thermal contact resistance at the bonded joints between the silicon chips and substrate materials in semiconductor devices was conducted by Peterson and Fletcher (1988). Seven conductive epoxies were evaluated, and although the contact resistances were found to be constant with respect to the mean interface temperature, the thermal contact resistance was found to be as much as 40 percent of the overall joint resistance.

The current investigation focuses on the macroscopic resistance, which is typically the larger of the two resistances occurring in a package. Several techniques can be used to determine the macroscopic resistance, including conduction shape factors (such as those reported by Rohsenow and Hartnett, 1973), analytical or numerical procedures, analog methods, and direct heat flux measurements. Most techniques, however, are difficult to use due to the complexity of the boundary conditions and the range of the temperature differences.

In order to determine the macroscopic constriction resistance occurring in a representative microelectronic package, a combined numerical and experimental investigation was conducted. The constriction resistance was determined as a function of the geometric parameters, and an electrolytic analog technique was used to provide experimental data for comparison with the numerical model.

Numerical Investigation

To model the microelectronic package, the spreader material and surrounding mold compound were assumed to form a two-dimensional system in which the influence of the two ends was neglected. To simplify the model further, the influence of the flying leads and pin connectors was neglected, and the chip and spreader material were treated as one unit with a single

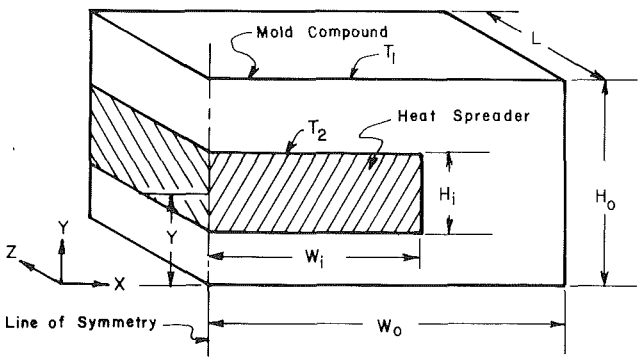

Fig. 1 Electronic package cross section

[1]Graduate Research Assistant.
[2]Professor of Mechanical Engineering; Mem. ASME.
[3]Dietz Professor of Mechanical Engineering; Fellow ASME.
[4]Department of Mechanical Engineering, Texas A&M University, College Station, TX 77843-3123.

Contributed by the Heat Transfer Division for publication in the JOURNAL OF HEAT TRANSFER. Manuscript received by the Heat Transfer Division February 27, 1990; revision received September 14, 1990. Keywords: Analog Techniques, Conduction, Electronic Equipment.

Table 1 Geometric parameters

Parameters	Numerical Investigation (cm)	Experimental Investigation (cm)
W_o	10.16	10.16
H_o	3.81 to 10.16	3.81, 5.08, 7.62, 8.89
H_i	0.64 to 3.81	1.27, 2.54, 3.18
W_i	1.27 to 8.89	2.54, 5.08, 7.62, 8.89
Y	$H_o/2$ to 0.64	$H_i \le Y \le H_o/2$

rectangular cross-sectional area, as shown in Fig. 1. The computational domain is also shown, along with the governing geometric parameters, the half-width of the package, W_o, the height of the package, H_o, the half-width of the chip, W_i, the height of the chip, H_i, and the distance of the chip centerline from the bottom of the package, Y.

Using this configuration, a numerical grid was established, and a finite difference model was developed, in which the thermal resistance, R, was defined as

$$R = \frac{T_2 - T_1}{Q}$$

for a heat flux Q. The boundary conditions were maintained by holding the outer nodes at constant temperature T_1 and the interior nodes of the simulated chip at constant temperature T_2. The symmetry line was treated as an adiabatic boundary, such that $\partial T/\partial x = 0$ (no heat flux).

To determine the effect of grid size, a numerical solution was obtained for a single configuration using several different grid sizes. In this test, the thermal resistance was found to converge to a fixed value. Increasing the number of nodes form 3700 to 6500 resulted in a difference between the calculated resistances of less than 0.015 percent. Using the numerical model, the temperature distribution and thermal resistance per unit length were calculated for the geometric combinations listed in Table 1.

Experimental Investigation

The electrolytic analog is a well-known technique used to simulate field problems, e.g., heat conduction problems that satisfy the Laplace equation. The first investigations using this technique were conducted in the late 1800s by Adams (1875). Later, Karplus (1958) presented detailed information about analog systems in general and the electrolytic analog in particular. More recently, the electrolytic analog has been used to investigate heat transfer in several different configurations including the constriction resistance of single contacts (Yip and Venart, 1968), the constriction resistance of conical bodies (Major and Williams, 1979), and the macroscopic resistance in bolted and riveted joints (Fletcher et al., 1989)

There are several features that must be considered in using an electrolytic analog for thermal resistance measurements. First, the electrolytic tank must be fabricated in such a way that the shape of the electrolyte within the tank provides a scale model of the actual problem. Second, because all the isothermal boundaries in the thermal model are represented as equipotential surfaces in the electrolytic model, all adiabatic boundaries require material with a very low conductivity. Third, to avoid polarization, which allows the deposition of a gaseous layer near the electrodes and increases the cell resistance, a-c voltages with frequencies between 50 to 1500 Hz were used. Finally, because the electrolyte should have no electrical reactance, distilled water was used, and all brass surfaces were polished and coated with graphite.

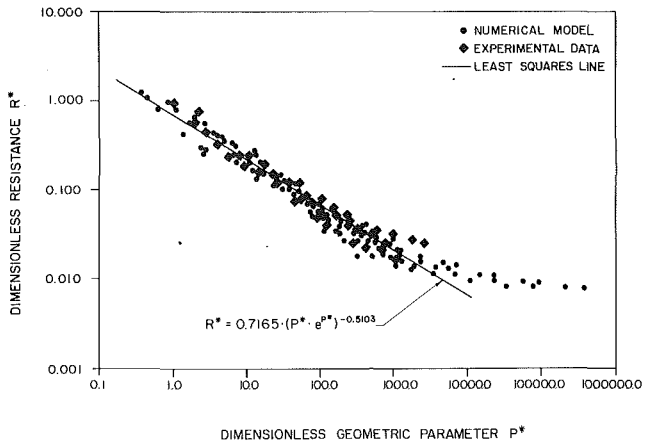

Fig. 2 Dimensionless resistance as a function of dimensionless geometry

In conducting the experimental investigation with the electrolytic tank, various geometric parameters were considered to insure that a wide range of geometric configurations would be tested. To compare the thermal resistance values with the results measured with the electrolytic tank analog, this resistance was calculated as

$$R \cdot \lambda \cdot L$$

where λ is the thermal conductivity, L is the package length, and R is as previously defined.

To measure the conductivity, a digital conductivity meter was used. The electrical conductivity of the distilled water was measured with a dip cell, which had an accuracy of ± 0.1 to ± 0.2 percent. An uncertainty analysis indicated an uncertainty in the resistance of from 1.7 to 8.25 percent. Although several points exhibited relatively large discrepancies between the experimental and numerical results, the average deviation was found to be 5.6 percent.

Numerical data were obtained for all of the parameter combinations shown in Table 1. In addition, over 120 parameter combinations were evaluated experimentally. The influence of the five geometric parameters was determined by varying each parameter individually and observing how these variations affected the resistance. As the width of the simulated chip, W_i, increased, the distance between isotherms decreased, indicating a decrease in the package resistance. Similarly, the resistance decreases as Y, W_o, and H_o decreased and as H_i increased.

In order to compare the numerical and experimental results, a dimensionless thermal resistance, R^*, was defined as

$$R^* = R \cdot L \cdot \lambda \cdot Y$$

which increased or decreased as the corresponding geometric parameters increased or decreased. A geometric dimensionless parameter was established that related the surface areas of the two electrodes to a geometric parameter, P^*, defined as

$$P^* = \frac{1.5 \cdot W_1 + 4.0 \cdot H_i}{2.0 \cdot W_o + H_o} \cdot \frac{L}{Y}$$

An examination of this parameter shows that P^* consists of a ratio between the areas of the simulated heat spreader and the package. Dividing this ratio by Y resulted in a value of P^* that was independent of the location of the chip within the package.

In order to develop an equation that relates the numerical and experimental data, the variation of dimensionless thermal resistance with the dimensionless geometric parameter was compared, as shown in Fig. 2. The data demonstrated a relatively linear dependency between the geometric variables and the dimensionless resistance for values of the dimensionless geometry less than 5000. At dimensionless geometric parameter values greater than 5000, the simulated heat spreader was either nearly as large as the whole package or lies very close to one

surface ($Y \cong 0$). If follows that as the number of grid points between the surfaces gets small, the accuracy of the model is greatly reduced. For these reasons, values beyond this point were not investigated experimentally. This may also partially explain the increasing deviation between the experimental and numerical values at increasing values of dimensionless resistance. Utilizing a least-squares analysis, the following expression was developed for the experimental results:

$$R^* = 0.7165 \cdot (P^* \cdot e^{P^*})^{-0.5103}$$

As shown in Fig. 2, the correlation between this expression, the numerical results, and the experimental data is quite good. Using this expression, the thermal resistance can be calculated for the heat conduction in a given electronic package if the thermal conductivity of the mold compound and the package geometric parameters are known.

Both a numerical and an experimental method were used to investigate the internal thermal resistance of one type of microelectronic package. The comparison between the measured and calculated results shows good agreement and demonstrates that an electrolytic analog can be used to determine the macroscopic resistance in electronic packages. The results indicate that the internal location of the chip and heat spreader can significantly affect the overall package resistance. The results also indicate that the electronic package thermal resistance is relatively insensitive to heat spreader and chip thickness while variations in the outer area, primarily W_i, or chip-to-outside-package area ratio can greatly influence the thermal resistance. The resistance was shown to be very sensitive to the vertical location, Y, of the chip/spreader within the package. A nondimensional expression was developed that permits the internal package resistance to be determined as a function of the package geometry.

Acknowledgments

This investigation was supported by the Texas Higher Education Coordinating Board through the Advanced Technology Program.

References

Adams, W. C., 1875, "On the Forms of Equipotential Curves and Surfaces and Lines of Electric Force," *Proc. Roy. Soc. (London)*, Vol, 23, pp. 280–284.

Antonetti, V. W., and Yovanovich, M. M., 1984, "Thermal Contact Resistance in Microelectronic Equipment," *Thermal Management Concepts in Microelectronic Packaging*, IHSM Tech. Monograph Series, No. 6984-003, pp. 135–151.

Ellison, G. N., 1984, *Thermal Computations for Electronic Equipment*, Van Nostrand Reinhold Company, New York.

Fletcher, L. S., Peterson, G. P., Madhusudana, C. V., and Groll, E., 1990, "Heat Transfer in Bolted and Riveted Joints," ASME JOURNAL OF HEAT TRANSFER, Vol. 112, No. 4, pp. 857–863.

Karplus, W. J., 1958, *Analog Simulation in Field Problems*, McGraw-Hill, New York.

Major, S. J., and Williams, A., 1979, "The Solution of a Steady Conduction Heat Transfer Problem Using an Electrolytic Tank Analog," *Mechanical Engineering Transactions*, The Institute of Engineers, Australia, pp. 7–11.

Mahalingham, M., Nadhuker, M., Lofgran, L., Andrews, J., Olsen, O. R., and Berg, H. M., 1984, "Thermal Effects of Diebond Voids in Metal, Ceramic and Plastic Packages," *Semiconductor Int.*, pp. 71–79.

Nakayama,W., 1986, "Thermal Management of Electronic Equipment: A Review of Technology and Research Topics," *Applied Mechanics Reviews*, Vol, 39, pp. 1874–1868.

Peterson, G. P., and Fletcher, L. S., 1988, "Thermal Contact Resistance of Silicon Chip Bonding Materials," *Cooling Technology for Electronic Equipment*,W. Aung, ed., Hemisphere, Washington, DC, pp. 523–524.

Rohsenow, W. M., and Hartnett, J. P., 1973, *Handbook of Heat Transfer*, McGraw-Hill, New York.

Yerman, A. J., Burgess, J. F., Carlson, R. O., and Neugebauer, C. A., 1983, "Hot Spots Caused by Voids and Cracks in the Chip Mountdown Medium in Power Semiconductor Packaging," *IEEE Tran. Comp. Hybrids, and Manf. Tech.*, Vol. CHMT-6, No. 4, p. 473–479.

Yip, F. C., and Venart, J. E. S., 1968, "Surface Topography Effects in the Estimation of Thermal and Electrical Contact Resistances," *Proc. IMechE*, Vol. 182. Pt. 3K, pp. 81–91.

Shear Flow Over a Wall With Variable Temperature

C. Y. Wang[1]

Introduction

The Leveque solution (Leveque, 1928; see also Knudsen and Katz, 1958) for forced convection due to shear flow over a plate is one of the basic solutions of convective heat transfer. The solution is exact if the fluid velocity is linear, such as that generated by the movement of parallel plates (e.g., Ling, 1963; Kaiping, 1983). The solution is asymptotic if the thermal boundary layer is much thinner than the velocity boundary layer, such that the local velocity profile is approximately linear. This occurs for developing thermal boundary layers (e.g., Newman, 1969; Nakajima et al., 1978).

Although he discussed the general case, Leveque (1928) originally considered shear flow over a plate with a sudden constant temperature change. The problem was subsequently extended to the constant heat flux case by Worsoe-Schmidt (1967). In both instances exact similarity boundary layer solutions are obtained. In this note we shall consider the variable wall temperature case. Both analytic and numerical methods will be used.

Formulation

Let velocity be linear and parallel

$$U = by \tag{1}$$

The governing forced convection boundary layer equation is

$$U(y)\,\frac{\partial T}{\partial x} = a\,\frac{\partial^2 T}{\partial y^2} \tag{2}$$

Here (x, y) are coordinates parallel and normal to the surface at $y = 0$, T is the temperature, and a is the thermal diffusivity. Let the wall temperature difference change suddenly to a power law distribution for $x > 0$

$$T - T_\infty = \begin{cases} 0 & x<0, \quad y=0 \\ cx^\lambda & x>0, \quad y=0 \end{cases} \tag{3}$$

Here λ and c are constants and T_∞ is the free flow temperature. Using the similarity transformation

$$T - T_\infty = cx^\lambda f(\eta), \quad \eta = \left(\frac{b}{ax}\right)^{1/3} y \tag{4}$$

equation (2) becomes

$$\eta\left(\lambda f - \frac{1}{3}\,\eta f'\right) = f'' \tag{5}$$

with the boundary conditions

$$f(0) = 1 \tag{6}$$

$$f(\infty) = 0 \tag{7}$$

Equation (5) reduces to Leveque's original equation when $\lambda = 0$.

Integration of equation (5) from zero to infinity yields the property

$$\left(\lambda + \frac{2}{3}\right) \int_0^\infty \eta f d\eta = -f'(0) \tag{8}$$

[1]Michigan State University, East Lansing, MI 48824.

Contributed by the Heat Transfer Division for publication in the JOURNAL OF HEAT TRANSFER. Manuscript received by the Heat Transfer Division February 27, 1990; revision received September 25, 1990. Keywords: Forced Convection.

surface ($Y \cong 0$). If follows that as the number of grid points between the surfaces gets small, the accuracy of the model is greatly reduced. For these reasons, values beyond this point were not investigated experimentally. This may also partially explain the increasing deviation between the experimental and numerical values at increasing values of dimensionless resistance. Utilizing a least-squares analysis, the following expression was developed for the experimental results:

$$R^* = 0.7165 \cdot (P^* \cdot e^{P^*})^{-0.5103}$$

As shown in Fig. 2, the correlation between this expression, the numerical results, and the experimental data is quite good. Using this expression, the thermal resistance can be calculated for the heat conduction in a given electronic package if the thermal conductivity of the mold compound and the package geometric parameters are known.

Both a numerical and an experimental method were used to investigate the internal thermal resistance of one type of microelectronic package. The comparison between the measured and calculated results shows good agreement and demonstrates that an electrolytic analog can be used to determine the macroscopic resistance in electronic packages. The results indicate that the internal location of the chip and heat spreader can significantly affect the overall package resistance. The results also indicate that the electronic package thermal resistance is relatively insensitive to heat spreader and chip thickness while variations in the outer area, primarily W_i, or chip-to-outside-package area ratio can greatly influence the thermal resistance. The resistance was shown to be very sensitive to the vertical location, Y, of the chip/spreader within the package. A nondimensional expression was developed that permits the internal package resistance to be determined as a function of the package geometry.

Acknowledgments

This investigation was supported by the Texas Higher Education Coordinating Board through the Advanced Technology Program.

References

Adams, W. C., 1875, "On the Forms of Equipotential Curves and Surfaces and Lines of Electric Force," *Proc. Roy. Soc. (London)*, Vol, 23, pp. 280–284.

Antonetti, V. W., and Yovanovich, M. M., 1984, "Thermal Contact Resistance in Microelectronic Equipment," *Thermal Management Concepts in Microelectronic Packaging*, IHSM Tech. Monograph Series, No. 6984-003, pp. 135–151.

Ellison, G. N., 1984, *Thermal Computations for Electronic Equipment*, Van Nostrand Reinhold Company, New York.

Fletcher, L. S., Peterson, G. P., Madhusudana, C. V., and Groll, E., 1990, "Heat Transfer in Bolted and Riveted Joints," ASME JOURNAL OF HEAT TRANSFER, Vol. 112, No. 4, pp. 857–863.

Karplus, W. J., 1958, *Analog Simulation in Field Problems*, McGraw-Hill, New York.

Major, S. J., and Williams, A., 1979, "The Solution of a Steady Conduction Heat Transfer Problem Using an Electrolytic Tank Analog," *Mechanical Engineering Transactions*, The Institute of Engineers, Australia, pp. 7–11.

Mahalingham, M., Nadhuker, M., Lofgran, L., Andrews, J., Olsen, O. R., and Berg, H. M., 1984, "Thermal Effects of Diebond Voids in Metal, Ceramic and Plastic Packages," *Semiconductor Int.*, pp. 71–79.

Nakayama,W., 1986, "Thermal Management of Electronic Equipment: A Review of Technology and Research Topics," *Applied Mechanics Reviews*, Vol, 39, pp. 1874–1868.

Peterson, G. P., and Fletcher, L. S., 1988, "Thermal Contact Resistance of Silicon Chip Bonding Materials," *Cooling Technology for Electronic Equipment*,W. Aung, ed., Hemisphere, Washington, DC, pp. 523–524.

Rohsenow, W. M., and Hartnett, J. P., 1973, *Handbook of Heat Transfer*, McGraw-Hill, New York.

Yerman, A. J., Burgess, J. F., Carlson, R. O., and Neugebauer, C. A., 1983, "Hot Spots Caused by Voids and Cracks in the Chip Mountdown Medium in Power Semiconductor Packaging," *IEEE Tran. Comp. Hybrids, and Manf. Tech.*, Vol. CHMT-6, No. 4, p. 473–479.

Yip, F. C., and Venart, J. E. S., 1968, "Surface Topography Effects in the Estimation of Thermal and Electrical Contact Resistances," *Proc. IMechE*, Vol. 182. Pt. 3K, pp. 81–91.

Shear Flow Over a Wall With Variable Temperature

C. Y. Wang[1]

Introduction

The Leveque solution (Leveque, 1928; see also Knudsen and Katz, 1958) for forced convection due to shear flow over a plate is one of the basic solutions of convective heat transfer. The solution is exact if the fluid velocity is linear, such as that generated by the movement of parallel plates (e.g., Ling, 1963; Kaiping, 1983). The solution is asymptotic if the thermal boundary layer is much thinner than the velocity boundary layer, such that the local velocity profile is approximately linear. This occurs for developing thermal boundary layers (e.g., Newman, 1969; Nakajima et al., 1978).

Although he discussed the general case, Leveque (1928) originally considered shear flow over a plate with a sudden constant temperature change. The problem was subsequently extended to the constant heat flux case by Worsoe-Schmidt (1967). In both instances exact similarity boundary layer solutions are obtained. In this note we shall consider the variable wall temperature case. Both analytic and numerical methods will be used.

Formulation

Let velocity be linear and parallel

$$U = by \tag{1}$$

The governing forced convection boundary layer equation is

$$U(y)\,\frac{\partial T}{\partial x} = a\,\frac{\partial^2 T}{\partial y^2} \tag{2}$$

Here (x, y) are coordinates parallel and normal to the surface at $y = 0$, T is the temperature, and a is the thermal diffusivity. Let the wall temperature difference change suddenly to a power law distribution for $x > 0$

$$T - T_\infty = \begin{cases} 0 & x<0, \quad y=0 \\ cx^\lambda & x>0, \quad y=0 \end{cases} \tag{3}$$

Here λ and c are constants and T_∞ is the free flow temperature. Using the similarity transformation

$$T - T_\infty = cx^\lambda f(\eta), \quad \eta = \left(\frac{b}{ax}\right)^{1/3} y \tag{4}$$

equation (2) becomes

$$\eta\left(\lambda f - \frac{1}{3}\,\eta f'\right) = f'' \tag{5}$$

with the boundary conditions

$$f(0) = 1 \tag{6}$$

$$f(\infty) = 0 \tag{7}$$

Equation (5) reduces to Leveque's original equation when $\lambda = 0$.

Integration of equation (5) from zero to infinity yields the property

$$\left(\lambda + \frac{2}{3}\right) \int_0^\infty \eta f d\eta = -f'(0) \tag{8}$$

[1]Michigan State University, East Lansing, MI 48824.

Contributed by the Heat Transfer Division for publication in the JOURNAL OF HEAT TRANSFER. Manuscript received by the Heat Transfer Division February 27, 1990; revision received September 25, 1990. Keywords: Forced Convection.

From the second law of thermodynamics we expect $0 \le f \le 1$ (i.e., the fluid temperature is increased, but not as much as the wall temperature). Thus, $f'(0) \le 0$. Equation (8) shows that $\lambda \ge -2/3$ in order for the boundary layer to exist.

The local heat transfer rate is

$$q = -\rho c_p a \left.\frac{\partial T}{\partial y}\right|_0 = -\rho c_p a^{2/3} b^{1/3} c x^{\lambda - 1/3} f'(0) \tag{9}$$

The total heat flux across an x = const plane is

$$Q = \rho c_p \int_0^\infty U(T - T_\infty)dy = \rho c_p a^{2/3} b^{1/3} c x^{\lambda + 2/3} \int_0^\infty \eta f d\eta \tag{10}$$

Equation (8) therefore confirms the conservation of thermal energy

$$\int_0^x q dx = Q \tag{11}$$

Exact Solutions

For some specific values of λ, equations (5)–(7) yield exact analytic solutions. For $\lambda = 0$, the constant wall temperature case, Leveque (1928) found

$$f(\eta) = \frac{3^{1/3}}{\Gamma\left(\frac{1}{3}\right)} \int_\eta^\infty \exp\left(-\frac{\eta^3}{9}\right) d\eta \tag{12}$$

Here Γ is the gamma function. Equation (12) yields

$$f'(0) = -\frac{3^{1/3}}{\Gamma\left(\frac{1}{3}\right)} = -0.53837. \tag{13}$$

Equation (9) shows $\lambda = 1/3$ for the constant heat flux case. The exact solution is found by Worsoe-Schmidt (1967)

$$f = \exp\left(-\frac{\eta^3}{9}\right) - \frac{\eta}{3} \int_\eta^\infty \eta \exp\left(-\frac{\eta^3}{9}\right) d\eta \tag{14}$$

$$f'(0) = -3^{-2/3}\Gamma\left(\frac{2}{3}\right) = -0.65099 \tag{15}$$

In this note we introduce two new exact solutions. For $\lambda = -2/3$ equation (10) shows that the total heat flux is independent of distance x. This is the important case of an isolated heat source of strength Q at the origin. Equation (5) gives

$$-\frac{1}{3}(\eta^2 f)' = f'' \tag{16}$$

The solution is

$$f = \exp\left(-\frac{\eta^3}{9}\right) \tag{17}$$

$f'(0) = 0$ can also be obtained from equation (8). Figure 1 shows the isotherms for this new solution.

On the other hand, if the temperature distribution is such that $\lambda = -1/3$, let

$$f = g(\eta)\exp\left(-\frac{\eta^3}{18}\right) \tag{18}$$

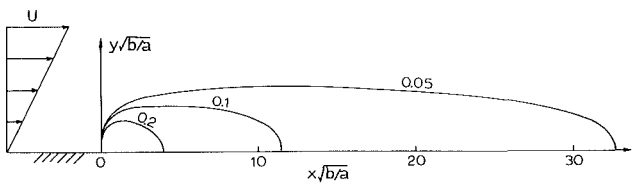

Fig. 1 Isotherm values of $(T - T_\infty)\rho c_p a/Q$ for $\lambda = -2/3$; isolated heat source at origin

Equation (5) becomes

$$g'' - \frac{\eta^4}{36} g = 0 \tag{19}$$

The solution is (Murphy, 1960; Abramowitz and Stegun, 1965)

$$g = \sqrt{\eta}\left[c_1 K_{1/6}\left(\frac{\eta^3}{18}\right) - c_2 I_{1/6}\left(\frac{\eta^3}{18}\right)\right] \tag{20}$$

where K and I are modified Bessel functions.

The boundary conditions yield

$$f = \frac{2^{2/3}}{3^{1/3}\Gamma\left(\frac{1}{6}\right)} \sqrt{\eta} K_{1/6}\left(\frac{\eta^3}{18}\right) \exp\left(-\frac{\eta^3}{18}\right) \tag{21}$$

Using the asymptotic properties of K for small η we find

$$f'(0) = -\frac{\pi 2^{4/3} 3^{1/3}}{\left[\Gamma\left(\frac{1}{6}\right)\right]^2} = -0.36849 \tag{22}$$

Numerical Solution

Numerical integration is necessary for other values of λ. For given λ, we guess $f'(0)$ and integrate equations (5) and (6) as an initial value problem by the Runge-Kutta-Fehlberg algorithm. A step size of 0.02 is found to be adequate for five-digit accuracy. The value of $f'(0)$ is guided by our exact solutions and adjusted such that f decays to zero for large η. Figure 2 shows the results. Our numerical values agree with exact values at $\lambda = -2/3, -1/3, 0, 1/3$. Some numerical values for $\lambda = 1, 2, 3$ are $f'(0) = -0.80754, -0.96906, -1.09019$.

Figure 3 shows the similarity function $f(\eta)$ for various λ

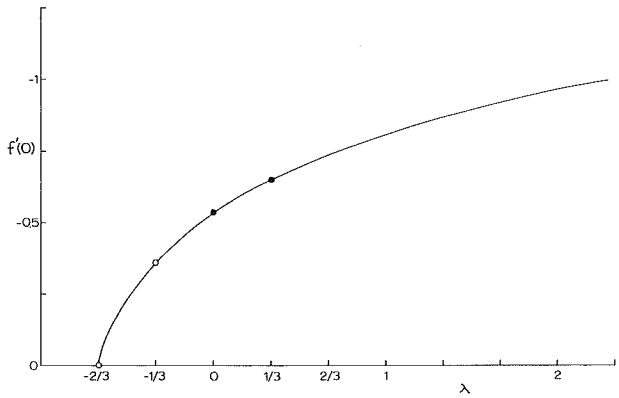

Fig. 2 Initial value $f'(0)$ as a function of λ: • known exact solutions, ○ new exact solutions

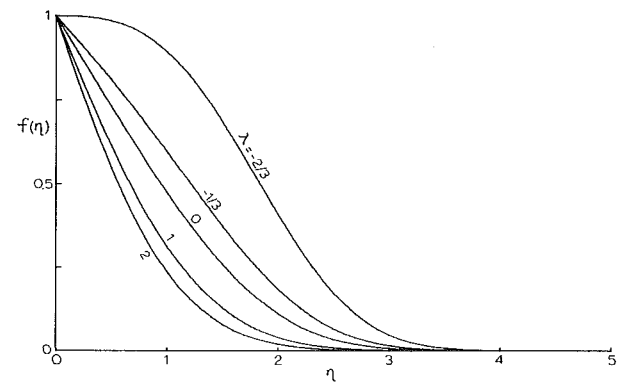

Fig. 3 Similarity function $f(\eta)$ for various λ values

values. All curves decrease monotonically to zero within a thermal boundary layer thickness of $\eta \sim 4$. Inflection points occur for $\lambda \leq 0$.

Arbitrary Temperature Distribution

Suppose the boundary condition is

$$T - T_\infty = \varphi(x) \tag{23}$$

where $\varphi(x)$ is an arbitrary function, defined to be zero when the argument is negative. Leveque (1928) gave the general integral solution

$$T - T_\infty = \left[\int_0^\infty \varphi\left(x - \frac{by^3}{9as^3}\right) e^{-s^3} ds\right] \Bigg/ \left[\int_0^\infty e^{-s^3} ds\right] \tag{24}$$

By taking the Laplace transform (in x) on equation (2), another, albeit more complicated, integral solution may be obtained. In what follows we shall describe an alternate method, which utilizes the power law temperature distributions to approximate the general solution.

Suppose the wall temperature is given as

$$T - T_\infty = \begin{cases} 0 & x < 0 \\ F(x) & 0 < x < l \\ 0 & l < x \end{cases} \tag{25}$$

where $F(x)$ is any continuous differentiable function. Divide the segment $[0, l]$ into N pieces. Due to the linearity of equation (2), one can sum the effect of each piece. Consider the piece $x_i < x < x_{i+1}$. We expand $F(x)$ into a Taylor series about x_i

$$F(x) = F(x_i) + F'(x_i)(x - x_i) + \frac{F''(x_i)}{2}(x - x_i)^2 + \ldots \tag{26}$$

The series is convergent since $F(x)$ is nonsingular. The error due to truncation can be easily estimated by standard methods. Each term on the right-hand side of equation (26) is of the power law form. Our previous results can be applied with $\lambda = 0, 1, 2, \ldots$. Now at $x = x_{i+1}$ the effect of the series is to be cancelled. We add the solutions of $-F(x)$ at x_{i-1}, i.e.,

$$\begin{aligned} -F(x_i) - F'(x_i)(x - x_i) - \frac{F''(x_i)}{2}(x - x_i)^2 + \ldots \\ = -F(x_i) - F'(x_i)(x - x_{i+1} + x_{i+1} - x_i) \\ - \frac{F''(x_i)}{2}(x - x_{i+1} + x_{i+1} - x_i)^2 \\ = \left[-F(x_i) - F'(x_i)(x_{i+1} - x_i) - \frac{F''(x_i)}{2}(x_{i+1} - x_i)^2\right] \\ + [-F'(x_i) + F''(x_i)(x_{i+1} - x_i)](x - x_{i+1}) \\ + \left[-\frac{F''(x_i)}{2}\right](x - x_{i+1})^2 + \ldots \end{aligned} \tag{27}$$

The canceling surface temperature distribution follows equation (27) for $x > x_{i-1}$ and is zero for $x < x_{i+1}$.

In case $F(x)$ is discontinuous or nondifferentiable, one can set the node x_i at the discontinuity. If the singularity is weaker than $x^{-2/3}$, temperature distributions with negative or fractional powers of x may be superposed.

Similarly if heat flux $q(x)$ is given, it is expanded in a Taylor series for each segment. Equation (9) is then used to determine λ, which will now attain noninteger values.

Conclusions

The forced convection problem due to a parallel shear flow is studied analytically. By assuming the thermal boundary layer to be well within the velocity boundary layer, similarity solutions for power law temperature distribution can be obtained.

In practice, a heated boundary is neither at constant temperature nor at constant heat flux. Therefore, the study of intermediate cases is necessary. Using exact and numerical means, the whole range of power law temperatures is obtained. We also illustrated a method to treat any surface distribution. The results are important in modeling developing thermal boundary layers.

References

Abramowitz, M., and Stegun, I. A., 1965, *Handbook of Mathematical Functions*, Dover, New York, Chap. 10.

Kaiping, P., 1983, "Unsteady Forced Convection Heat Transfer From a Hot Film in Nonreversing and Reversing Shear Flow," *International Journal of Heat and Mass Transfer*, Vol. 26, pp. 545-557.

Knudsen, J. G., and Katz, D. L., 1958, *Fluid Dynamics and Heat Transfer*, McGraw-Hill, New York, Chap. 13.

Leveque, M. A., 1928, "Les lois de la transmission de la chaleur par convection," *Annales des Mines*, Vol. 13, pp. 201-299.

Ling, S. C., 1963, "Heat Transfer From a Small Isothermal Spanwise Strip on an Insulated Boundary," ASME JOURNAL OF HEAT TRANSFER, Vol. 85, pp. 230-236.

Murphy, G. M., 1960, *Ordinary Differential Equations and Their Solutions*, Van Nostrand, New Jersey, Chap. B1.

Nakajima, M., Fukui, K., Ueda, H., and Mizushina, T., 1978, "Developing Combined Free and Forced Laminar Convection Between Vertical Parallel Plates With Constant Wall Temperature," *Journal of Chemical Engineering of Japan*, Vol. 11, pp. 19-24.

Newman, J., 1969, "Extension of the Leveque Solution," ASME JOURNAL OF HEAT TRANSFER, Vol. 91, pp. 177-178.

Worsoe-Schmidt, P. M., 1967, "Heat Transfer in the Thermal Entrance Region of Circular Tube and Annular Passages With Fully Developed Laminar Flow," *International Journal of Heat and Mass Transfer*, Vol. 10, pp. 541-551.

Enhanced Heat Transfer/Pressure Drop Measured From a Flat Surface in a Grooved Channel

M. Greiner,[1,4] R.-F. Chen,[2,4] and R. A. Wirtz[3,4]

Nomenclature

- a = groove length (Fig. 1)
- b = groove depth (Fig. 1)
- D_h = minimum channel hydraulic diameter = $2HW/(H + W)$
- E = local heat transfer enhancement factor = $\theta_{\text{flat}}/\theta_{\text{grooved}}$
- f = Fanning friction factor = $(-dp/dx)(D_h/2\rho V^2)$
- H = minimum channel height (Fig. 1)
- L = grooved section length
- k = fluid thermal conductivity
- $Nu(x)$ = local Nusselt number = $q'' D_h/\Delta T(x)k$
- p = pressure
- Pr = fluid Prandtl number
- q'' = heat flux
- Q = fluid volume flow rate
- Re = Reynolds number = VD_h/ν
- Re_c = critical Reynolds number for the onset of unsteady flow
- T_0 = fluid entrance temperature

[1]Assistant Professor.

[2]Research Assistant.

[3]Professor.

[4]Mechanical Engineering Department, University of Nevada, Reno, NV 89557.

Contributed by the Heat Transfer Division for publication in the JOURNAL OF HEAT TRANSFER. Manuscript received by the Heat Transfer Division February 28, 1990; revision received October 1, 1990. Keywords: Augmentation and Enhancement, Flow Instability, Heat Exchangers.

values. All curves decrease monotonically to zero within a thermal boundary layer thickness of $\eta \sim 4$. Inflection points occur for $\lambda \leq 0$.

Arbitrary Temperature Distribution

Suppose the boundary condition is

$$T - T_\infty = \varphi(x) \tag{23}$$

where $\varphi(x)$ is an arbitrary function, defined to be zero when the argument is negative. Leveque (1928) gave the general integral solution

$$T - T_\infty = \left[\int_0^\infty \varphi\left(x - \frac{by^3}{9as^3}\right) e^{-s^3} ds \right] \Bigg/ \left[\int_0^\infty e^{-s^3} ds \right] \tag{24}$$

By taking the Laplace transform (in x) on equation (2), another, albeit more complicated, integral solution may be obtained. In what follows we shall describe an alternate method, which utilizes the power law temperature distributions to approximate the general solution.

Suppose the wall temperature is given as

$$T - T_\infty = \begin{cases} 0 & x < 0 \\ F(x) & 0 < x < l \\ 0 & l < x \end{cases} \tag{25}$$

where $F(x)$ is any continuous differentiable function. Divide the segment $[0, l]$ into N pieces. Due to the linearity of equation (2), one can sum the effect of each piece. Consider the piece $x_i < x < x_{i+1}$. We expand $F(x)$ into a Taylor series about x_i

$$F(x) = F(x_i) + F'(x_i)(x - x_i) + \frac{F''(x_i)}{2}(x - x_i)^2 + \ldots \tag{26}$$

The series is convergent since $F(x)$ is nonsingular. The error due to truncation can be easily estimated by standard methods. Each term on the right-hand side of equation (26) is of the power law form. Our previous results can be applied with $\lambda = 0, 1, 2, \ldots$. Now at $x = x_{i+1}$ the effect of the series is to be cancelled. We add the solutions of $-F(x)$ at x_{i-1}, i.e.,

$$\begin{aligned} -F(x_i) - F'(x_i)(x - x_i) - \frac{F''(x_i)}{2}(x - x_i)^2 + \ldots \\ = -F(x_i) - F'(x_i)(x - x_{i+1} + x_{i+1} - x_i) \\ - \frac{F''(x_i)}{2}(x - x_{i+1} + x_{i+1} - x_i)^2 \\ = \left[-F(x_i) - F'(x_i)(x_{i+1} - x_i) - \frac{F''(x_i)}{2}(x_{i+1} - x_i)^2 \right] \\ + [-F'(x_i) + F''(x_i)(x_{i+1} - x_i)](x - x_{i+1}) \\ + \left[-\frac{F''(x_i)}{2} \right](x - x_{i+1})^2 + \ldots \end{aligned} \tag{27}$$

The canceling surface temperature distribution follows equation (27) for $x > x_{i-1}$ and is zero for $x < x_{i+1}$.

In case $F(x)$ is discontinuous or nondifferentiable, one can set the node x_i at the discontinuity. If the singularity is weaker than $x^{-2/3}$, temperature distributions with negative or fractional powers of x may be superposed.

Similarly if heat flux $q(x)$ is given, it is expanded in a Taylor series for each segment. Equation (9) is then used to determine λ, which will now attain noninteger values.

Conclusions

The forced convection problem due to a parallel shear flow is studied analytically. By assuming the thermal boundary layer to be well within the velocity boundary layer, similarity solutions for power law temperature distribution can be obtained.

In practice, a heated boundary is neither at constant temperature nor at constant heat flux. Therefore, the study of intermediate cases is necessary. Using exact and numerical means, the whole range of power law temperatures is obtained. We also illustrated a method to treat any surface distribution. The results are important in modeling developing thermal boundary layers.

References

Abramowitz, M., and Stegun, I. A., 1965, *Handbook of Mathematical Functions*, Dover, New York, Chap. 10.

Kaiping, P., 1983, "Unsteady Forced Convection Heat Transfer From a Hot Film in Nonreversing and Reversing Shear Flow," *International Journal of Heat and Mass Transfer*, Vol. 26, pp. 545-557.

Knudsen, J. G., and Katz, D. L., 1958, *Fluid Dynamics and Heat Transfer*, McGraw-Hill, New York, Chap. 13.

Leveque, M. A., 1928, "Les lois de la transmission de la chaleur par convection," *Annales des Mines*, Vol. 13, pp. 201-299.

Ling, S. C., 1963, "Heat Transfer From a Small Isothermal Spanwise Strip on an Insulated Boundary," ASME JOURNAL OF HEAT TRANSFER, Vol. 85, pp. 230-236.

Murphy, G. M., 1960, *Ordinary Differential Equations and Their Solutions*, Van Nostrand, New Jersey, Chap. B1.

Nakajima, M., Fukui, K., Ueda, H., and Mizushina, T., 1978, "Developing Combined Free and Forced Laminar Convection Between Vertical Parallel Plates With Constant Wall Temperature," *Journal of Chemical Engineering of Japan*, Vol. 11, pp. 19-24.

Newman, J., 1969, "Extension of the Leveque Solution," ASME JOURNAL OF HEAT TRANSFER, Vol. 91, pp. 177-178.

Worsoe-Schmidt, P. M., 1967, "Heat Transfer in the Thermal Entrance Region of Circular Tube and Annular Passages With Fully Developed Laminar Flow," *International Journal of Heat and Mass Transfer*, Vol. 10, pp. 541-551.

Enhanced Heat Transfer/Pressure Drop Measured From a Flat Surface in a Grooved Channel

M. Greiner,[1,4] R.-F. Chen,[2,4] and R. A. Wirtz[3,4]

Nomenclature

- a = groove length (Fig. 1)
- b = groove depth (Fig. 1)
- D_h = minimum channel hydraulic diameter = $2HW/(H + W)$
- E = local heat transfer enhancement factor = $\theta_{\text{flat}}/\theta_{\text{grooved}}$
- f = Fanning friction factor = $(-dp/dx)(D_h/2\rho V^2)$
- H = minimum channel height (Fig. 1)
- L = grooved section length
- k = fluid thermal conductivity
- $Nu(x)$ = local Nusselt number = $q'' D_h/\Delta T(x)k$
- p = pressure
- Pr = fluid Prandtl number
- q'' = heat flux
- Q = fluid volume flow rate
- Re = Reynolds number = VD_h/ν
- Re_c = critical Reynolds number for the onset of unsteady flow
- T_0 = fluid entrance temperature

[1]Assistant Professor.

[2]Research Assistant.

[3]Professor.

[4]Mechanical Engineering Department, University of Nevada, Reno, NV 89557.

Contributed by the Heat Transfer Division for publication in the JOURNAL OF HEAT TRANSFER. Manuscript received by the Heat Transfer Division February 28, 1990; revision received October 1, 1990. Keywords: Augmentation and Enhancement, Flow Instability, Heat Exchangers.

$T_s(x)$ = local flat surface temperature
$\Delta T(x)$ = local temperature difference between the flat surface and the inlet = $T_s(x) - T_0$
V = average velocity based on minimum channel cross section = Q/WH
W = channel width normal to the plane of Fig. 1
x = axial coordinate
$\theta(x)$ = local dimensionless temperature = $1/\mathrm{Nu}(x)$
ν = kinematic viscosity
ρ = fluid density

Introduction

In the present work, the effect of passive flow destabilization on augmenting the heat transfer/pumping power performance of a rectangular channel is studied experimentally. We consider the passage shown in Fig. 1. Our goal is to determine how shear layers that span transverse grooves on one wall trigger flow instabilities and effect heat transfer from the opposite surface. A fully developed, isothermal air flow at temperature T_0 enters a grooved test section with the same *minimum* wall spacing and lower surface temperature, whose upper surface develops a thermal boundary layer by dissipating a uniform heat flux. The grooved section has geometric parameters $a/b = 2.0$, $b/H = 1.2$, and $W/H = 20.3$. Heat transfer and pressure drop measurements are made along the upper wall, in both the developing and fully developed regimes. These results are compared to measurements in a duct whose lower wall is replaced by a flat surface with the same minimum spacing ($a = b = 0$, $W/H = 20.3$). Measurements are made with air ($\mathrm{Pr} \approx 0.7$) for the Reynolds number range $300 \leq \mathrm{Re} \leq 5000$, where the hydraulic diameter and mean velocity are both based on the minimum cross-sectional area.

This work is an extension of a recent experimental flow visualization and heat transfer study using water ($\mathrm{Pr} = 5.5$) with geometric ratios $a/b = 2.0$, $b/H = 0.60$, and $W/H = 10.2$ (Greiner et al., 1990). That channel was designed so that its periodicity length (a) is one-half the wavelength of the least stable Tollmien-Schlichting mode of a flat channel flow, so that those waves would be excited. At Reynolds numbers above a critical value of $\mathrm{Re}_c = 630 \pm 20$, Kelvin-Helmholtz instabilities of the shear layers trigger the outer channel Tollmien-Schlichting modes (Ghaddar et al., 1986), and a traveling wave structure appears near the channel exit ($L/D_h = 26$). (Our current experiments show that waves would have been observed at even lower Reynolds numbers if the grooved section were longer.) As the Reynolds number increases, the onset location moves upstream and the waves become increasingly three dimensional. While no pumping power measurements were made, these structures were observed to enhance the heat transfer by 65 percent relative to the same axial location in planar ducts for Reynolds numbers between 1200 and 4800. At higher Reynolds numbers, a 10 percent augmentation persists. Other experimental and numerical studies (Ichimiya, 1987; Kozlu et al., 1988; Karniadakis et al., 1988) confirm these levels of augmentation.

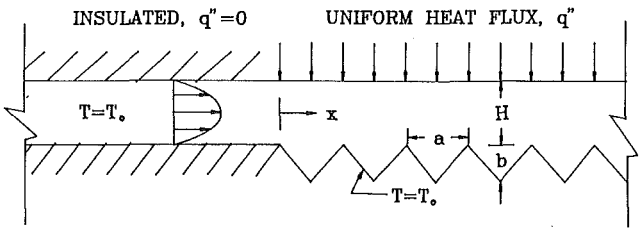

Fig. 1 Thermal and geometric boundary conditions of the grooved, rectangular cross-section channel

This technical note addresses the potential effectiveness of destabilization in gas flows. Pressure drop measurements are made to allow comparisons of different passage configurations on an equal pumping power basis, and measurements are made in the *fully developed* as well as developing thermal regimes.

Experimental Apparatus

Heat transfer and pressure drop experiments are made in an open-loop, induced-draft wind tunnel. Laboratory air, at approximately 26°C and 8.7×10^4 Pa (elevation 1300 m), is drawn through a filter/screen box, an entrance nozzle, and into a flat Plexiglas flow development section with a wall spacing of $H = 10$ mm. For the Reynolds numbers considered, the flow is fully developed by the time it encounters the grooved test section described below. Upon leaving that section, the fluid enters a baffled plenum, flows through calibrated rotameters, and is drawn into the suction end of a variable speed blower.

While the same basic test section used by Greiner et al. (1990) is employed, in an effort to increase the augmentation performance, its minimum wall spacing has been halved to $H = 10$ mm. The current design doubles the groove size compared to the channel dimension, making the channel periodicity length *equal* to the wavelength of the most unstable flow mode and increasing the grooved section dimensionless length to $L/D_h = 55$. Heat transfer measurements from the upper wall are performed at several axial locations using the same techniques reported previously. In the current work, however, the heat transfer results are reported using the inlet temperature T_0, rather than the local bulk value as the reference, and corrections are made to the heat flux for radiation losses.

The axial pressure gradient is measured using eleven 2-mm-diameter taps in the flat surface, starting at $x = 0$ and equally spaced 102 mm apart along its centerline. The pressure difference between the first and the other ten taps is measured with an electronic pressure transducer (±0.5 percent), which is plumbed using a switching valve. The fully developed gradient is determined from the slope of a line fit to the pressure drop versus location data using the least squares technique. An error analysis (Doebelin, 1990) shows that the standard deviation of dp/dx is less than 7 percent of its value for all but the lowest Reynolds number.

Results

Flow visualizations were performed with the current test section installed in the water flow facility described by Greiner et al. (1990). While the grooved duct flow is steady at low Reynolds numbers, at $\mathrm{Re} = 350$ waves appear from $x/D_h = 35$ to the end of the channel. This development length decreases to less than eight hydraulic diameters for $\mathrm{Re} \geq 800$. For a given Reynolds number, the development is shorter than it was in the earlier configuration.

Pressure drop versus location measurements show that the pressure gradient becomes constant after only five hydraulic diameters for $\mathrm{Re} \geq 600$, indicating very rapid flow development. The resulting fully developed grooved and flat channel Fanning friction factors are plotted against Reynolds number in Fig. 2. The flat channel measurements show reasonable agreement with theoretical laminar and turbulent results, and exhibit a kink at roughly $\mathrm{Re} \approx 2800$, in agreement with the parallel plate transitional value for the onset of turbulence (Fox and McDonald, 1985). While the grooved and ungrooved pressure gradients are roughly equal at $\mathrm{Re} = 600$,

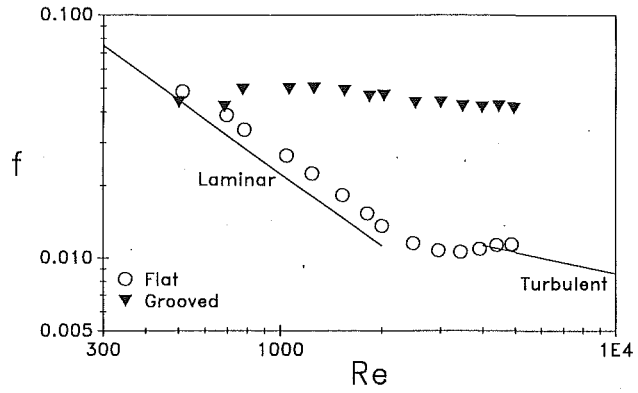

Fig. 2 Fully developed Fanning friction factor versus Reynolds number in the grooved and flat channels; lines indicate laminar (Kays and Crawford, 1980) and turbulent (White, 1974) flat channel correlations

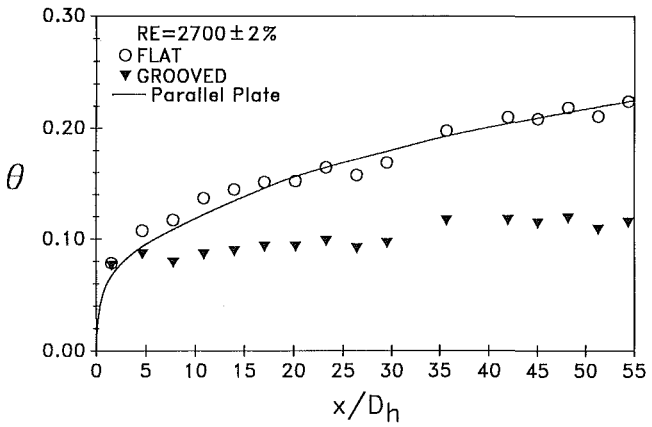

Fig. 3 Dimensionless temperature difference versus channel location for Re = 2700 in flat and grooved channels; the line indicates the theoretical parallel plate solution (Lundberg et al., 1963)

the grooved channel value is significantly larger thereafter due to the enhanced momentum transport in supercritical flow. The supercritical flow friction factor is roughly constant, similar to the behavior of low Reynolds number turbulence. At high Reynolds numbers the grooved channel pressure gradient is approximately three and a half times larger than that of the flat duct.

The dimensionless temperature of the upper, heated surface is plotted in Fig. 3 as a function of location for Re = 2700 in both the flat and grooved channels. The excellent agreement between the flat channel data and the theoretical parallel plate results (Lundberg et al., 1963) confirms the accuracy of the experimental procedure and indicates that the experimental aspect ratio (W/H) is large enough that edge effects are negligible. These results do not reach a plateau by the end of the test section, and theoretical results show that they would not be expected to achieve full development until x/D_h = 0.13RePr = 240, where θ = 0.50.

The dimensionless temperature of the flat surface in the grooved channel is approximately equal to the flat duct value at the inlet. It is seen, however, to reach the fully developed state rapidly, remaining essentially constant downstream. Its fully developed value (determined by averaging the last four measurement locations) is only θ = 0.11. The local heat transfer enhancement factor, $E(x) = \theta_{\text{flat}}(x)/\theta_{\text{grooved}}(x)$, increases with x/D_h and is greater than E = 1.9 at the channel exit. This factor would continue to grow as the flat channel approaches the thermally developed condition, where it would reach E = 0.50/0.11 = 4.5. While this fully developed value is a benchmark of the enhanced *mixing* gained by adding grooves to the lower surface, it is optimistic from a design viewpoint

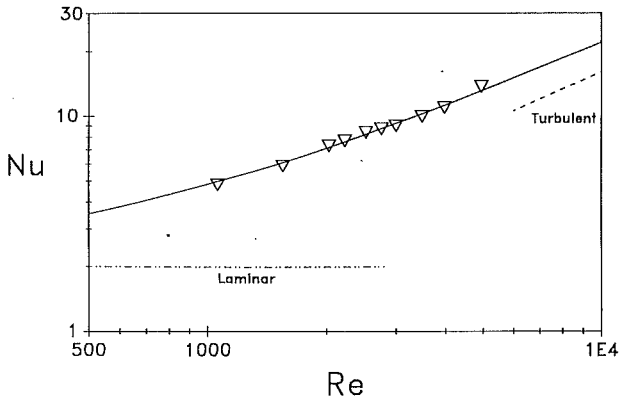

Fig. 4 Nusselt number averaged from x/D = 45 to 55 versus Reynolds number in the grooved channel; lines indicate fully developed laminar and turbulent flat channel theory (Dittus and Boelter, 1930)

since typical exchangers exploit the higher transport associated with developing flows.

Figure 4 is a plot of the fully developed grooved channel Nusselt number averaged from x/D_h = 45 to 55 for 1000 ≤ Re ≤ 5000. Comparison to theoretical, fully developed flat channel results (Dittus and Boelter, 1930) shows significant augmentation. While a maximum transport enhancement of E = 4.6 is observed at Re = 2800, at Re = 5000 the enhancement factor is only E = 1.3. A curve fit of the grooved channel data is shown in Fig. 4 using the asymptotic method of Churchill and Usagi (1972). The low Reynolds number heat transfer is assumed to approach the laminar flat channel value. At high Reynolds numbers the transport is assumed to asymptote to a curve that is 30 percent larger than that predicted for a flat passage (Dittus and Boelter, 1930). The equation for this curve is

$$\text{Nu} = 2(1 + 0.0029\text{Re}^{0.93})^{0.86}$$

This relation is most reliable in the range 1000 ≤ Re ≤ 5000 where its deviation from the data is never more than 5 percent.

Conclusions

This study, in conjunction with our previous results (Greiner et al., 1990), improves the understanding of the mechanisms responsible for enhanced heat transfer gained by introducing spatially periodic disturbances to a channel flow. Specifically, we have seen that grooves lead to free shear layers, which, at supercritical Reynolds numbers, stimulate Tollmien-Schlichting waves. As the Reynolds number is increased, the amplitude of these waves become larger, leading to early three-dimensional transition. This early transition appears to be responsible for the transport enhancement seen in this study.

Grooved channels offer important performance advantages over flat walled passages. The velocity and temperature fields develop much more rapidly than they do in flat ducts. At a given Reynolds number both the fully developed heat transfer and pressure drop are increased. Like the offset strip fin, the present configuration offers large heat transfer enhancement on an equal pumping power basis in the laminar and transitional regimes relative to flat passages.

Acknowledgments

This work is sponsored by the Gas Research Institute under contract number 5087-260-1562.

References

Churchill, S. W., and Usagi, R., 1972, "A General Expression for the Correlation of Rates of Transfer and Other Phenomena," *AIChE Journal*, Vol. 18, pp. 1121-1128.

Doebelin, E. O., 1990, *Measurement Systems Application and Design*, 4th ed., McGraw-Hill, New York, p. 56.

Dittus, F. W., and Boelter, L. M. K., 1930, *University of California, Berkeley Publications on Engineering*, Vol. 2, p. 443.

Fox, R. W., and McDonald, A. T., 1985, *Introduction to Fluid Mechanics*, 3rd ed., Wiley, New York, p. 338.

Ghaddar, N. K., Korczak, K. Z., Mikic, B. B., and Patera, A. T., 1986, "Numerical Investigation of Incompressible Flow in Grooved Channels. Part 1. Stability and Self-sustained Oscillations," *J. Fluid Mech.*, Vol. 163, pp. 99–127.

Greiner, M., Chen, R.-F., and Wirtz, R. A., 1990, "Heat Transfer Augmentation Through Wall-Shape-Induced Flow Destabilization," ASME *Journal of Heat Transfer*, Vol. 112, pp. 336–341.

Ichimiya, K., 1987, "Effects of Several Roughness Elements on an Insulated Wall for Heat Transfer From the Opposite Smooth Heated Surface in a Parallel Plate Duct," ASME *Journal of Heat Transfer*, Vol. 109, pp. 68–73.

Karniadakis, G. E., Mikic, B. B., and Patera, A. T., 1988, "Minimum-Dissipation Transport Enhancement by Flow Destabilization: Reynolds' Analogy Revisited," *J. Fluid Mech.*, Vol. 192, pp. 365–391.

Kays, W. M., and Crawford, M. E., 1980, *Convective Heat and Mass Transfer*, 2nd ed., McGraw-Hill, New York, p. 63.

Kozlu, H., Mikic, B. B, and Patera, A. T., 1988, "Minimum-Dissipation Heat Removal by Scale-Matched Flow Destabilization," *Int. J. Heat Mass Trans.*, Vol. 31, pp. 2023–2032.

Lundberg, R. E., Reynolds, W. C., and Kays, W. M., 1963, "Heat Transfer With Laminar Flow in Concentric Annuli With Constant and Variable Wall Temperature and Heat Flux," NASA TN D-1972.

White, F. M., 1974, *Viscous Fluid Flow*, McGraw-Hill, New York, p. 485.

Laminar Natural Convection From a Vertical Plate With a Step Change in Wall Temperature

S. Lee[1,3] and M. M. Yovanovich[2,3]

Introduction

The study of natural convection heat transfer from a vertical flat plate in a quiescent medium has attracted a great deal of interest from many investigators in the past few decades. The plate with various thermal conditions that allow similarity transformations as well as those that are continuous and well defined have been examined. However, practical problems often involve wall conditions that are arbitrary and unknown a priori. To understand and solve problems involving general nonsimilar conditions at the wall, it is useful to investigate problems subjected to a step change in wall temperature. The problems impose a mathematical singularity and severe nonsimilar conditions at the wall.

An early attempt was made by Schetz (1963) to develop an approximate analytical model for the problems with discontinuous wall temperature conditions. Numerous investigations on the same problem were continued by using an experimental technique (Schetz and Eichhorn, 1964), numerical methods (Hayday et al., 1967), or by using series expansions (Kelleher, 1971; Kao, 1975).

In this paper, a new analytical model that can deal with a discontinuous wall temperature variation is presented. The method results in a set of approximate solutions for temperature and velocity distributions. The validity and accuracy of the model is demonstrated by comparisons with the results of the aforementioned investigators. The agreement is excellent and the results obtained with the solution of this work are remarkably close to existing numerical data of Hayday et al. (1967) and the perturbation series solution of Kao (1975).

[1]Research Assistant Professor; Mem. ASME.

[2]Professor; Fellow ASME.

[3]Microelectronics Heat Transfer Laboratory, Department of Mechanical Engineering, University of Waterloo, Waterloo, Ontario, Canada N2L 3G1

Contributed by the Heat Transfer Division and presented at the ASME Winter Annual Meeting, Boston, Massachusetts, December 13–18, 1987. Manuscript received by the Heat Transfer Division March 26, 1990; revision received July 28, 1990. Keywords: Natural Convection.

Analyis

Governing Equations. The natural convection problem under consideration deals with a two-dimensional vertical plate with a discontinuous temperature variation prescribed along the wall. The plate is located in an ambient fluid, which is maintained at uniform temperature. The conservation of mass, momentum, and energy for steady-state, laminar boundary layer flow yields the usual set of governing differential equations expressed as

$$\frac{\partial u}{\partial x}+\frac{\partial v}{\partial y}=0 \tag{1}$$

$$u\frac{\partial u}{\partial x}+v\frac{\partial u}{\partial y}=\nu\frac{\partial^2 u}{\partial y^2}+g\beta T \tag{2}$$

$$u\frac{\partial T}{\partial x}+v\frac{\partial T}{\partial y}=\alpha\frac{\partial^2 T}{\partial y^2} \tag{3}$$

where x and y are coordinates parallel and normal to the plate, respectively, u and v are corresponding components of the velocity, and T is the local temperature excess over the ambient fluid temperature. The properties α, ν, and β are the thermal diffusivity, kinematic viscosity, and thermal expansion coefficient of the fluid, and g is the gravitational acceleration. In addition to the boundary layer approximations, the assumption of constant fluid properties, except the density in the use of the Boussinesq approximation, is included, and the dynamic pressure work and viscous dissipation terms are neglected in the above equations.

The boundary conditions associated with the foregoing equations are

$$\begin{aligned} &\text{at } y=0, \quad u=v=0, \quad T=T_{w_0} \text{ for } x\le x_0\\ &\qquad\qquad\qquad\quad T=T_{w_1} \text{ for } x>x_0\\ &\text{as } y\to\infty, \ u\to 0, \quad T\to 0\\ &\text{at } x=0, \quad u=0, \quad T=0 \end{aligned} \tag{4}$$

where T_{w_0} and T_{w_1} are constants; $T_{w_0} > 0$ and $T_{w_1} \ge 0$.

Pseudotransient Equations. An approximate method is sought to solve the above set of equations by introducing a pseudotransient coordinate, t. The downstream location x is viewed as $u_c \times t$, where u_c is defined as a characteristic streamwise velocity. With the use of u_c, the original x–y plane is transformed into the t–y plane. An assumption is made such that diffusion is dominant across the boundary layer in the y direction at given time. This implies that the temperature and velocity profiles would take forms of those due to a transient conduction heat transfer into a half space. Subsequently, the convective derivatives in the x–y plane, appearing on the left side of equations (2) and (3), are replaced by transient derivatives, resulting in the following pseudotransient equations:

$$\frac{\partial u}{\partial t}=\nu\frac{\partial^2 u}{\partial y^2}+g\beta T \tag{5}$$

$$\frac{\partial T}{\partial t}=\alpha\frac{\partial^2 T}{\partial y^2} \tag{6}$$

The boundary conditions that are compatible with those prescribed by equation (4) are

$$\begin{aligned} &\text{at } y=0, \quad u=0, \ T=T_{w_0} \text{ for } t\le t_0\\ &\qquad\qquad\quad T=T_{w_1} \text{ for } t>t_0\\ &\text{as } y\to\infty, \ u\to 0, \ T\to 0 \end{aligned} \tag{7}$$

Doebelin, E. O., 1990, *Measurement Systems Application and Design*, 4th ed., McGraw-Hill, New York, p. 56.

Dittus, F. W., and Boelter, L. M. K., 1930, *University of California, Berkeley Publications on Engineering*, Vol. 2, p. 443.

Fox, R. W., and McDonald, A. T., 1985, *Introduction to Fluid Mechanics*, 3rd ed., Wiley, New York, p. 338.

Ghaddar, N. K., Korczak, K. Z., Mikic, B. B., and Patera, A. T., 1986, "Numerical Investigation of Incompressible Flow in Grooved Channels. Part 1. Stability and Self-sustained Oscillations," *J. Fluid Mech.*, Vol. 163, pp. 99–127.

Greiner, M., Chen, R.-F., and Wirtz, R. A., 1990, "Heat Transfer Augmentation Through Wall-Shape-Induced Flow Destabilization," ASME *Journal of Heat Transfer*, Vol. 112, pp. 336–341.

Ichimiya, K., 1987, "Effects of Several Roughness Elements on an Insulated Wall for Heat Transfer From the Opposite Smooth Heated Surface in a Parallel Plate Duct," ASME *Journal of Heat Transfer*, Vol. 109, pp. 68–73.

Karniadakis, G. E., Mikic, B. B., and Patera, A. T., 1988, "Minimum-Dissipation Transport Enhancement by Flow Destabilization: Reynolds' Analogy Revisited," *J. Fluid Mech.*, Vol. 192, pp. 365–391.

Kays, W. M., and Crawford, M. E., 1980, *Convective Heat and Mass Transfer*, 2nd ed., McGraw-Hill, New York, p. 63.

Kozlu, H., Mikic, B. B, and Patera, A. T., 1988, "Minimum-Dissipation Heat Removal by Scale-Matched Flow Destabilization," *Int. J. Heat Mass Trans.*, Vol. 31, pp. 2023–2032.

Lundberg, R. E., Reynolds, W. C., and Kays, W. M., 1963, "Heat Transfer With Laminar Flow in Concentric Annuli With Constant and Variable Wall Temperature and Heat Flux," NASA TN D-1972.

White, F. M., 1974, *Viscous Fluid Flow*, McGraw-Hill, New York, p. 485.

Laminar Natural Convection From a Vertical Plate With a Step Change in Wall Temperature

S. Lee[1,3] and M. M. Yovanovich[2,3]

Introduction

The study of natural convection heat transfer from a vertical flat plate in a quiescent medium has attracted a great deal of interest from many investigators in the past few decades. The plate with various thermal conditions that allow similarity transformations as well as those that are continuous and well defined have been examined. However, practical problems often involve wall conditions that are arbitrary and unknown a priori. To understand and solve problems involving general nonsimilar conditions at the wall, it is useful to investigate problems subjected to a step change in wall temperature. The problems impose a mathematical singularity and severe nonsimilar conditions at the wall.

An early attempt was made by Schetz (1963) to develop an approximate analytical model for the problems with discontinuous wall temperature conditions. Numerous investigations on the same problem were continued by using an experimental technique (Schetz and Eichhorn, 1964), numerical methods (Hayday et al., 1967), or by using series expansions (Kelleher, 1971; Kao, 1975).

In this paper, a new analytical model that can deal with a discontinuous wall temperature variation is presented. The method results in a set of approximate solutions for temperature and velocity distributions. The validity and accuracy of the model is demonstrated by comparisons with the results of the aforementioned investigators. The agreement is excellent and the results obtained with the solution of this work are remarkably close to existing numerical data of Hayday et al. (1967) and the perturbation series solution of Kao (1975).

[1]Research Assistant Professor; Mem. ASME.

[2]Professor; Fellow ASME.

[3]Microelectronics Heat Transfer Laboratory, Department of Mechanical Engineering, University of Waterloo, Waterloo, Ontario, Canada N2L 3G1

Contributed by the Heat Transfer Division and presented at the ASME Winter Annual Meeting, Boston, Massachusetts, December 13–18, 1987. Manuscript received by the Heat Transfer Division March 26, 1990; revision received July 28, 1990. Keywords: Natural Convection.

Analysis

Governing Equations. The natural convection problem under consideration deals with a two-dimensional vertical plate with a discontinuous temperature variation prescribed along the wall. The plate is located in an ambient fluid, which is maintained at uniform temperature. The conservation of mass, momentum, and energy for steady-state, laminar boundary layer flow yields the usual set of governing differential equations expressed as

$$\frac{\partial u}{\partial x}+\frac{\partial v}{\partial y}=0 \tag{1}$$

$$u\frac{\partial u}{\partial x}+v\frac{\partial u}{\partial y}=\nu\frac{\partial^2 u}{\partial y^2}+g\beta T \tag{2}$$

$$u\frac{\partial T}{\partial x}+v\frac{\partial T}{\partial y}=\alpha\frac{\partial^2 T}{\partial y^2} \tag{3}$$

where x and y are coordinates parallel and normal to the plate, respectively, u and v are corresponding components of the velocity, and T is the local temperature excess over the ambient fluid temperature. The properties α, ν, and β are the thermal diffusivity, kinematic viscosity, and thermal expansion coefficient of the fluid, and g is the gravitational acceleration. In addition to the boundary layer approximations, the assumption of constant fluid properties, except the density in the use of the Boussinesq approximation, is included, and the dynamic pressure work and viscous dissipation terms are neglected in the above equations.

The boundary conditions associated with the foregoing equations are

$$\begin{aligned} &\text{at } y=0, \quad u=v=0, \quad T=T_{w_0} \text{ for } x\le x_0\\ &\qquad\qquad\qquad\quad T=T_{w_1} \text{ for } x>x_0\\ &\text{as } y\to\infty, \ u\to 0, \quad T\to 0\\ &\text{at } x=0, \quad u=0, \quad T=0 \end{aligned} \tag{4}$$

where T_{w_0} and T_{w_1} are constants; $T_{w_0} > 0$ and $T_{w_1} \ge 0$.

Pseudotransient Equations. An approximate method is sought to solve the above set of equations by introducing a pseudotransient coordinate, t. The downstream location x is viewed as $u_c \times t$, where u_c is defined as a characteristic streamwise velocity. With the use of u_c, the original x–y plane is transformed into the t–y plane. An assumption is made such that diffusion is dominant across the boundary layer in the y direction at given time. This implies that the temperature and velocity profiles would take forms of those due to a transient conduction heat transfer into a half space. Subsequently, the convective derivatives in the x–y plane, appearing on the left side of equations (2) and (3), are replaced by transient derivatives, resulting in the following pseudotransient equations:

$$\frac{\partial u}{\partial t}=\nu\frac{\partial^2 u}{\partial y^2}+g\beta T \tag{5}$$

$$\frac{\partial T}{\partial t}=\alpha\frac{\partial^2 T}{\partial y^2} \tag{6}$$

The boundary conditions that are compatible with those prescribed by equation (4) are

$$\begin{aligned} &\text{at } y=0, \quad u=0, \ T=T_{w_0} \text{ for } t\le t_0\\ &\qquad\qquad\quad T=T_{w_1} \text{ for } t>t_0\\ &\text{as } y\to\infty, \ u\to 0, \ T\to 0 \end{aligned} \tag{7}$$

where t is currently an unknown function of x, and t_0 is the corresponding time of the discontinuity at x_0.

The solutions to the above transient equations with the specified boundary conditions are obtained by means of either Laplace transforms (Schetz and Eichhorn, 1962; Menold and Yang, 1962), or similarity methods (Lee, 1988). The resulting solutions for $t > t_0$ are

$$T = T_{w_0} \operatorname{erfc} \eta_0 + (T_{w_1} - T_{w_0}) \operatorname{erfc} \eta_1 \tag{8}$$

$$u = 2g\beta[T_{w_0}\, t\, f_u(\eta_0) + (T_{w_1} - T_{w_0})(t - t_0) f_u(\eta_1)] \tag{9}$$

where

$$f_u(\eta) = \begin{cases} \eta \operatorname{ierfc} \eta & \text{for } \Pr = 1 \\ \dfrac{2}{1-\Pr}\left(\mathrm{i}^2\operatorname{erfc}\eta - \mathrm{i}^2\operatorname{erfc}\dfrac{\eta}{\sqrt{\Pr}}\right) & \text{for } \Pr \neq 1 \end{cases} \tag{10}$$

η_0 and η_1 are similarity variables given as

$$\eta_0 = \frac{y}{2\sqrt{\alpha t}} \tag{11}$$

$$\eta_1 = \frac{y}{2\sqrt{\alpha(t - t_0)}} \tag{12}$$

Pr is the Prandtl number, and erfc, ierfc, and i^2erfc are the complementary error functions. These solutions are exact for transient natural convection heat transfer from an infinitely long plate experiencing wall temperature variations given by equation (7). The solutions for $t \leq t_0$ can also be obtained by simply discarding the second term of each equation.

The problem is now reduced to finding a proper characteristic velocity or velocities, u_c, over the boundary layer. Determination of u_c will, in turn, convert the solutions in the t–y plane back into the x–y plane.

t–x Transformations for $x \leq x_0$. The parameters from the steady-state solutions for a uniform temperature plate, and those appearing in the above pseudotransient solutions are compared as follows:

Reference Velocity Group:

$$C_u \sqrt{4g\beta T_{w_0} x} = 2g\beta T_{w_0} t \tag{13}$$

Similarity Variable:

$$C_\eta \left(\frac{\mathrm{Gr}_x}{4}\right)^{1/4} \frac{y}{x} = \frac{y}{2\sqrt{\alpha t}} \tag{14}$$

where $\mathrm{Gr}_x = g\beta T_{w_0} x^3/\nu^2$, and C_u and C_η are dimensionless proportionality constants, functions only of the Prandtl number. The parameters on the left side of the above comparisons are from the similarity analysis of Sparrow and Gregg (1958).

By rearranging equations (13) and (14) for t, one finds, respectively,

$$t = C_u \frac{x}{\sqrt{g\beta T_{w_0} x}} \tag{15}$$

$$t = \frac{\Pr}{2C_\eta^2} \frac{x}{\sqrt{g\beta T_{w_0} x}} \tag{16}$$

Equations (15) and (16) are the t – x transformations sought for $x \leq x_0$. Although they express different relationships between t and x, they both exhibit an identical functional form such that $u_c = \sqrt{g\beta T_{w_0} x}/C$, where

$$C = C_u \tag{17}$$

or

$$C = \frac{\Pr}{2C_\eta^2} \tag{18}$$

The former equation defines the time associated with the reference velocity group and the latter defines the time associated with the similarity variable. The constants C_u and C_η are determined by employing the integral method using the velocity and temperature profiles given by the first terms of equations (8) and (9), with t substituted by equations (15) and (16). It follows that

$$C_u = \left(G_m + \frac{2\sqrt{\Pr}}{1+\sqrt{\Pr}} G_e\right)^{-1/2} \tag{19}$$

$$C_\eta = \sqrt{\Pr C_u G_e} \tag{20}$$

where G_m and G_e are tabulated in Table 1.

t–x Transformations for $x > x_0$. The similarity characteristic of the existing boundary layer, which was initiated at the leading edge, will no longer be maintained at the downstream location at $x > x_0$, as a secondary thermal boundary layer is established from the wall at $x = x_0$. This secondary boundary layer grows quickly into and will eventually engulf the existing one as x approaches infinity, where the solutions become similar once again based on T_{w_1}. Not only would the characteristic streamwise velocity over the existing boundary layer hence be altered, but another distinct characteristic velocity would also evolve over the secondary boundary layer. In the transient solutions, equations (8) and (9), t appearing in the first terms is related to the original boundary layer and $t - t_0$ appearing in the second terms is related to the secondary boundary layer. The t–x transformations are thus defined by

$$t = \frac{x}{u_c} = C\phi \frac{x}{\sqrt{g\beta T_{w_0} x}} \tag{21}$$

$$t - t_0 = \frac{x - x_0}{u_c} = C\psi \frac{x - x_0}{\sqrt{g\beta T_{w_0} x}} \tag{22}$$

where C represents, as previously defined by equations (17) and (18), two different coefficients depending on whether t and $t - t_0$ are associated with the velocity group or the similarity variables. The function ϕ in equation (21) modifies the existing characteristic velocity that would have been attained at the location of interest if the thermal condition at the wall were maintained at T_{w_0}. The other function, ψ in equation (22), represents the ratio of the existing characteristic velocity to the new one that characterizes the flow velocity within the secondary boundary layer initiated at $x = x_0$. These functions are dimensionless and dependent on Pr, θ_{w_1}, and ξ, where $\theta_{w_1} = T_{w_1}/T_{w_0}$ and $\xi = x/x_0$.

By substituting the above t–x transformations, equations (21) and (22), into equations (8) and (9), a set of approximate solutions to the original problem in the x–y plane can be obtained. After nondimensionalization, the resulting set of solutions for $x > x_0$ may be expressed as

$$\theta = \frac{T}{T_{w_0}} = \operatorname{erfc} \eta_0 + (\theta_{w_1} - 1) \operatorname{erfc} \eta_1 \tag{23}$$

Table 1 G_m and G_e

	$\Pr = 1$	$\Pr \neq 1$ ($p = \sqrt{\Pr}$)
G_m	$\dfrac{3\sqrt{2}-4}{4}$	$\dfrac{(1+p^2)^{5/2} - p^5 - (2\sqrt{2}-1)(p^3+p^2) - 1}{1.5\,p^2(1-p^2)^2}$
G_e	$\dfrac{\sqrt{2}-1}{4}$	$\dfrac{(1+p^2)^{3/2} - p^3 - 2(\sqrt{2}-1)p^2 - 1}{2\,p^2(1-p^2)}$

Table 2 h_m and h_e

	Pr = 1	Pr ≠ 1 ($p = \sqrt{\text{Pr}}$)
h_m	$\frac{4(1+\gamma^2)^{5/2} - 10\gamma^2(1+\gamma^2)^{1/2} - 4\gamma^5 - 4}{3\sqrt{2} - 4}$	$\frac{(p^2+\gamma^2)^{5/2} + (1+p^2\gamma^2)^{5/2} - p^2(1+p)(1+\gamma^2)^{5/2} - (1-p^2)(1-p^2)(1+\gamma^2)}{(1+p^2)^{5/2} - p^5 - (2\sqrt{2}-1)(p^3+p^2) - 1}$
h_e	$\frac{(1+\gamma^2)^{3/2} - \gamma^3 - 1}{\sqrt{2} - 1}$	$\frac{(p^2+\gamma^2)^{3/2} + (1+p^2\gamma^2)^{3/2} - 2p^2(1+\gamma^2)^{3/2} - (1+p-p^2)(1-p)(1+\gamma^3)}{(1+p^2)^{3/2} - p^3 - 2(\sqrt{2}-1)p^2 - 1}$

$$u^* = \frac{u}{2\sqrt{g\beta T_{w_0} x}} = C_u \phi [f_u(\eta_0) + (\theta_{w_1} - 1)\gamma f_u(\eta_1)] \quad (24)$$

where

$$\eta_0 = \frac{C_\eta}{\sqrt{\phi}} \left(\frac{\text{Gr}_x}{4}\right)^{1/4} \frac{y}{x} \quad (25)$$

$$\eta_1 = \frac{\eta_0}{\gamma} \quad (26)$$

and γ is related to the modifying functions as follows:

$$\gamma = \sqrt{\left(1 - \frac{1}{\xi}\right) \frac{\psi}{\phi}} \quad (27)$$

In the above solutions, ϕ and γ are the only parameters that are required to complete the solutions. They are determined by solving the following set of first-order ordinary differential equations that are obtained again by employing the integral method:

$$\frac{d\Phi}{d\xi} = \frac{1}{H_m} \left[1 + (\theta_{w_1} - 1)\gamma - \frac{4}{5} \Phi \frac{dH_m}{d\gamma^3} \frac{d\gamma^3}{d\xi}\right] \quad (28)$$

$$\frac{d\gamma^3}{d\xi} = \frac{3}{4} \left[\frac{1 + (\theta_{w_1} - 1)/\gamma - H_e \frac{d\Phi}{d\xi}}{\Phi \frac{dH_e}{d\gamma^3}}\right] \quad (29)$$

with $\Phi = \phi^2 \xi = 1$ and $\gamma^3 = 0$ at $\xi = 1$. Also, the dimensionless functions H_m and H_e are given by

$$H_m = 1 + (\theta_{w_1} - 1)^2 \gamma^5 + (\theta_{w_1} - 1) h_m \quad (30)$$

$$H_e = 1 + (\theta_{w_1} - 1)^2 \gamma^3 + (\theta_{w_1} - 1) h_e \quad (31)$$

where h_m and h_e are tabulated in Table 2. The above equations can be solved numerically for Φ and γ^3, hence ϕ and γ, with specified values of θ_{w_1} and Pr.

An interesting and important observation can be drawn from equation (22). Although t_0, the corresponding pseudotime at fixed x_0, is constant in the t–y plane, it is no longer possible to isolate the fixed t_0 in the x–y plane. This makes the term $t - t_0$ a unique variable, and, therefore, the parameter t in equation (22) is not the same t defined by equation (21). The facts that there are two distinct time-spatial transformations, and the existing characteristic velocity had to be modified by ϕ, are all parts of the conditions that are required if the nonlinearity of the problem was to be reflected through the transformation functions for $x > x_0$.

Results and Discussion

The solutions given in equations (23) and (24) are evaluated for a wide range of Prandtl numbers with various wall temperature ratios θ_{w_1}. Clearly, the solutions to a problem in which the entire wall is at uniform temperature T_{w_0} can also be found from the solutions by discarding the second terms and setting $\phi = 1$. Due to the limited spaces, however, only the cases with a step change in air (Pr = 0.72) will be presented herein to demonstrate the accuracy of the present model. Further comparisons of the results with others can be found from Lee (1988).

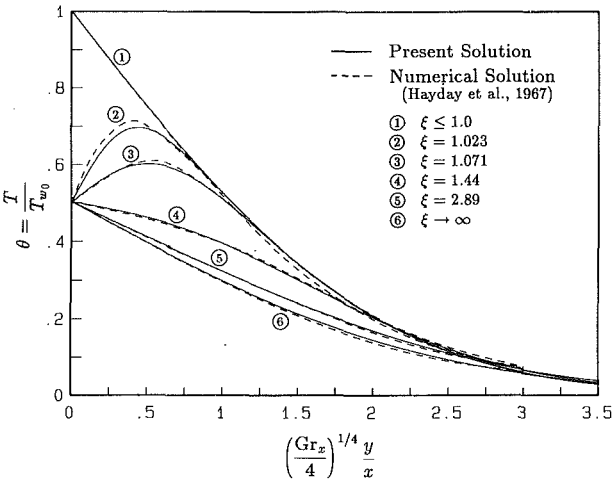

Fig. 1 Comparison of dimensionless temperature field development with a step change in wall temperature: θ_{w_1} = 0.503, Pr = 0.72

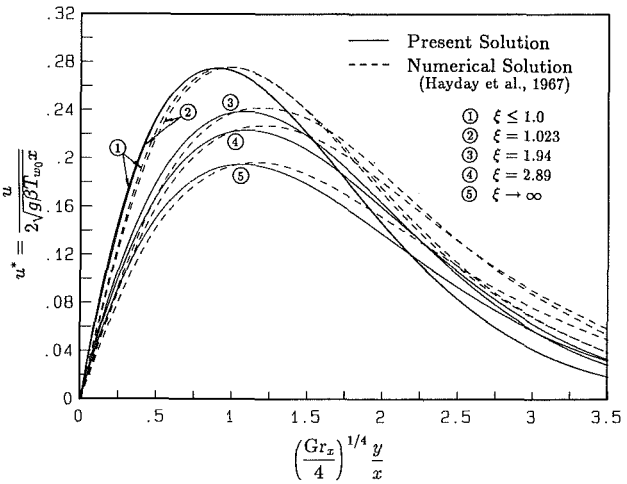

Fig. 2 Comparison of dimensionless velocity field development with a step change in wall temperature: θ_{w_1} = 0.503, Pr = 0.72

Figures 1 and 2 depict the temperature and velocity distributions responding to step changes in wall temperature. Also presented in the figures are the numerical data of Hayday et al. (1967), who solved the boundary layer equations using finite difference methods. Excellent agreement is observed in the temperature distributions, and some discrepancies are found in the velocity distributions over the outer region of the boundary layers. However, the discrepancies are shown to have minimal effects on the surface heat transfer as demonstrated in the following comparison.

From equation (23), the nondimensionalized local wall heat flux at the location $x > x_0$ may be obtained as

$$q^*_{w_1} = \frac{q_{w_1}}{q_{w_0}} = \frac{1}{\sqrt{\phi}} \left[1 + \frac{\theta_{w_1} - 1}{\gamma}\right] \quad (32)$$

where q_{w_0} is the local heat flux at the location of interest with the entire wall maintained at temperature T_{w_0}. The result obtained by using the above equation is plotted and compared with other data in Fig. 3. The values indicated by arrows are the asymptotic values at large ξ, and they are obtained from

$$\lim_{x \to \infty} q^*_{w_1} = \theta^{5/4}_{w_1} \quad (33)$$

The laminar regime is not likely to be maintained at far downstream locations in practice. Nevertheless, it is worthwhile stressing that the resulting solutions satisfy all the limiting

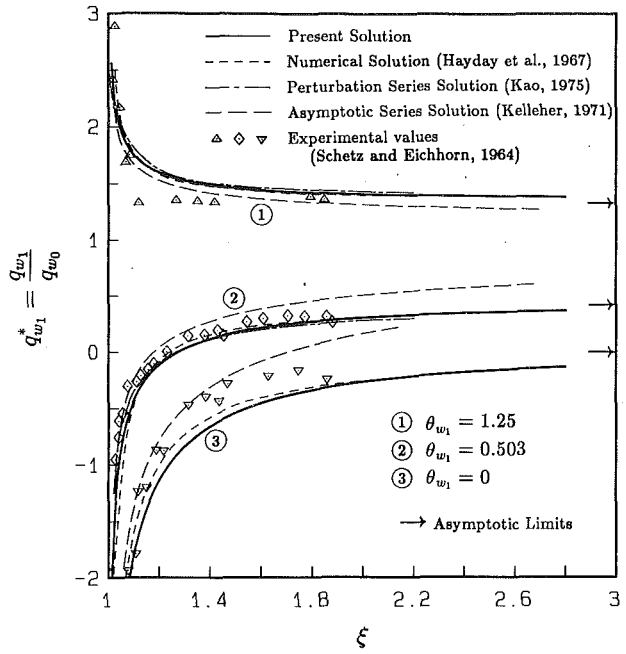

Fig. 3 Comparison of local wall heat-flux variation: Pr = 0.72

conditions at large ξ, as both ϕ and ψ can be shown to become independent of the Prandtl number and approach $\theta_{w_1}^{-1/2}$. Figure 3 exhibits an excellent agreement of the predictions especially with the fully numerical results of Hayday et al. (1967) and the perturbation series solution of Kao (1975). For the case of $\theta_{w_1} = 0$, Kao's solution is unavailable since his perturbation parameter becomes unbounded. Considering the limiting conditions at large ξ, inconsistent deviations are observed in the asymptotic series solution presented by Kelleher (1971).

As with most other approximate solutions, further studies would be needed to validate the use of the solutions for Prandtl numbers and conditions other than those presented. The current methodology is equally applicable for developing a model for problems with a step, as well as multistep changes in surface heat flux (Lee, 1988).

Acknowledgments

The authors wish to acknowledge the financial support of the Natural Sciences and Engineering Research Council of Canada for S. Lee, and the operation grant to M. M. Yovanovich.

References

Hayday, A. A., Bowlus, D. A., and McGraw, R. A., 1967, "Free Convection From a Vertical Flat Plate With Step Discontinuities in Surface Temperature," ASME JOURNAL OF HEAT TRANSFER, Vol. 89, No. 3, pp. 244–250.

Kao, T. T., 1975, "Laminar Free Convective Heat Transfer Response Along a Vertical Flat Plate With Step Jump in Surface Temperature," *Lett. Heat Mass Transfer*, Vol. 2, No. 5, pp. 419–428.

Kelleher, M., 1971, "Free Convection From a Vertical Plate With Discontinuous Wall Temperature," ASME JOURNAL OF HEAT TRANSFER, Vol. 93, pp. 349–356.

Lee, S., 1988, "Laminar Natural Convection From a Vertical Plate With Variations in Thermal Boundary Conditions," Ph.D. Thesis, Department of Mechanical Engineering, University of Waterloo, Waterloo, Ontario, Canada.

Menold, E. R., and Yang, K. T., 1962, "Asymptotic Solutions for Unsteady Laminar Free Convection on a Vertical Plate," ASME *J. Appl. Mech.*, Vol. 29, pp. 124–126.

Schetz, J. A., 1963, "On the Approximate Solution of Viscous-Flow Problems," ASME *J. Appl. Mech.*, Vol. 30, pp. 263–268.

Schetz, J. A., and Eichhorn, R., 1962, "Unsteady Natural Convection in the Vicinity of a Doubly Infinite Vertical Plate," ASME JOURNAL OF HEAT TRANSFER, Vol. 84, pp. 334–338.

Schetz, J. A., and Eichhorn, R., 1964, "Natural Convection With Discontinuous Wall-Temperature Variations," *J. Fluid Mech.*, Vol. 18, part 2, pp. 167–176.

Sparrow, E. M., and Gregg, J. L., 1958, "Similar Solutions for Free Convection From a Nonisothermal Vertical Plate," *Trans. ASME*, Vol. 80, pp. 379–386.

Use of Vortex Generators and Ribs for Heat Transfer Enhancement at the Top Surface of a Uniformly Heated Horizontal Channel With Mixed Convection Flow

J. R. Maughan[1] and F. P. Incropera[2]

Nomenclature

g = acceleration due to gravity
h = heat transfer coefficient
H = channel height or plate separation
k = thermal conductivity
L = channel length
Nu = Nusselt number = hH/k
Nu_{bot} = spanwise-averaged Nusselt number on bottom plate
Nu_{sm} = spanwise-averaged Nusselt number for smooth channel (no attachments)
Nu_{top} = spanwise-averaged Nusselt number on top plate
Pr = Prandtl number
q''_{conv} = convection heat flux
Ra* = modified Rayleigh number = $g\beta q''_{conv}H^4/k\nu\alpha$
Re = Reynolds number = $\overline{w}H/\nu$
$\overline{w}$ = average axial velocity
x, y, z = spanwise, vertical, and axial coordinates
z^* = nondimensional axial coordinate = $z/H\mathrm{RePr}$
z_c = axial coordinate at which secondary flows become evident
α = thermal diffusivity
β = coefficient of thermal expansion
ν = kinematic viscosity

Introduction

Although secondary flows driven by buoyancy forces enhance heat transfer from the bottom surface of a heated, horizontal channel, heat transfer coefficients at the upper surface are known to remain near forced convection levels (Osborne and Incropera, 1985). In situations where performance is limited by the maximum local temperature, such as the cooling of electronic circuitry, enhanced heat transfer at one surface may be of little advantage if approximately equivalent enhancement does not exist at the opposite surface. Hence differences between top and bottom surface conditions may prevent a designer from taking full advantage of buoyancy-

[1] Graduate Research Assistant, Heat Transfer Laboratory, Purdue University, West Lafayette, IN 47907. Current address: General Electric Research and Development Center, Schenectady, NY 12301.

[2] Professor and Head, School of Mechanical Engineering, Purdue University, West Lafayette, IN 47907.

Contributed by the Heat Transfer Division for publication in the JOURNAL OF HEAT TRANSFER. Manuscript received by the Heat Transfer Division June 21, 1990; revision received October 12, 1990. Keywords: Augmentation and Enhancement, Mixed Convection.

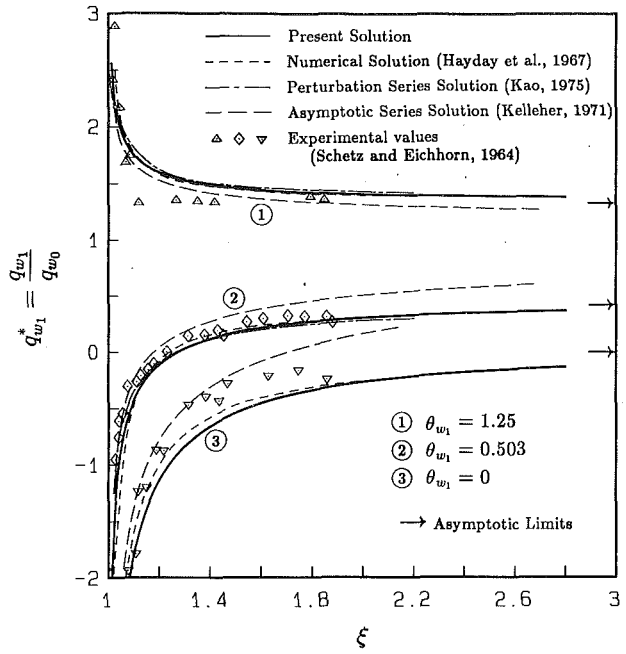

Fig. 3 Comparison of local wall heat-flux variation: Pr = 0.72

conditions at large ξ, as both ϕ and ψ can be shown to become independent of the Prandtl number and approach $\theta_{w_1}^{-1/2}$. Figure 3 exhibits an excellent agreement of the predictions especially with the fully numerical results of Hayday et al. (1967) and the perturbation series solution of Kao (1975). For the case of $\theta_{w_1} = 0$, Kao's solution is unavailable since his perturbation parameter becomes unbounded. Considering the limiting conditions at large ξ, inconsistent deviations are observed in the asymptotic series solution presented by Kelleher (1971).

As with most other approximate solutions, further studies would be needed to validate the use of the solutions for Prandtl numbers and conditions other than those presented. The current methodology is equally applicable for developing a model for problems with a step, as well as multistep changes in surface heat flux (Lee, 1988).

Acknowledgments

The authors wish to acknowledge the financial support of the Natural Sciences and Engineering Research Council of Canada for S. Lee, and the operation grant to M. M. Yovanovich.

References

Hayday, A. A., Bowlus, D. A., and McGraw, R. A., 1967, "Free Convection From a Vertical Flat Plate With Step Discontinuities in Surface Temperature," ASME JOURNAL OF HEAT TRANSFER, Vol. 89, No. 3, pp. 244–250.

Kao, T. T., 1975, "Laminar Free Convective Heat Transfer Response Along a Vertical Flat Plate With Step Jump in Surface Temperature," *Lett. Heat Mass Transfer*, Vol. 2, No. 5, pp. 419–428.

Kelleher, M., 1971, "Free Convection From a Vertical Plate With Discontinuous Wall Temperature," ASME JOURNAL OF HEAT TRANSFER, Vol. 93, pp. 349–356.

Lee, S., 1988, "Laminar Natural Convection From a Vertical Plate With Variations in Thermal Boundary Conditions," Ph.D. Thesis, Department of Mechanical Engineering, University of Waterloo, Waterloo, Ontario, Canada.

Menold, E. R., and Yang, K. T., 1962, "Asymptotic Solutions for Unsteady Laminar Free Convection on a Vertical Plate," ASME *J. Appl. Mech.*, Vol. 29, pp. 124–126.

Schetz, J. A., 1963, "On the Approximate Solution of Viscous-Flow Problems," ASME *J. Appl. Mech.*, Vol. 30, pp. 263–268.

Schetz, J. A., and Eichhorn, R., 1962, "Unsteady Natural Convection in the Vicinity of a Doubly Infinite Vertical Plate," ASME JOURNAL OF HEAT TRANSFER, Vol. 84, pp. 334–338.

Schetz, J. A., and Eichhorn, R., 1964, "Natural Convection With Discontinuous Wall-Temperature Variations," *J. Fluid Mech.*, Vol. 18, part 2, pp. 167–176.

Sparrow, E. M., and Gregg, J. L., 1958, "Similar Solutions for Free Convection From a Nonisothermal Vertical Plate," *Trans. ASME*, Vol. 80, pp. 379–386.

Use of Vortex Generators and Ribs for Heat Transfer Enhancement at the Top Surface of a Uniformly Heated Horizontal Channel With Mixed Convection Flow

J. R. Maughan[1] and F. P. Incropera[2]

Nomenclature

g = acceleration due to gravity
h = heat transfer coefficient
H = channel height or plate separation
k = thermal conductivity
L = channel length
Nu = Nusselt number = hH/k
Nu_{bot} = spanwise-averaged Nusselt number on bottom plate
Nu_{sm} = spanwise-averaged Nusselt number for smooth channel (no attachments)
Nu_{top} = spanwise-averaged Nusselt number on top plate
Pr = Prandtl number
q''_{conv} = convection heat flux
Ra* = modified Rayleigh number = $g\beta q''_{conv}H^4/k\nu\alpha$
Re = Reynolds number = $\overline{w}H/\nu$
$\overline{w}$ = average axial velocity
x, y, z = spanwise, vertical, and axial coordinates
z^* = nondimensional axial coordinate = $z/H\mathrm{RePr}$
z_c = axial coordinate at which secondary flows become evident
α = thermal diffusivity
β = coefficient of thermal expansion
ν = kinematic viscosity

Introduction

Although secondary flows driven by buoyancy forces enhance heat transfer from the bottom surface of a heated, horizontal channel, heat transfer coefficients at the upper surface are known to remain near forced convection levels (Osborne and Incropera, 1985). In situations where performance is limited by the maximum local temperature, such as the cooling of electronic circuitry, enhanced heat transfer at one surface may be of little advantage if approximately equivalent enhancement does not exist at the opposite surface. Hence differences between top and bottom surface conditions may prevent a designer from taking full advantage of buoyancy-

[1] Graduate Research Assistant, Heat Transfer Laboratory, Purdue University, West Lafayette, IN 47907. Current address: General Electric Research and Development Center, Schenectady, NY 12301.

[2] Professor and Head, School of Mechanical Engineering, Purdue University, West Lafayette, IN 47907.

Contributed by the Heat Transfer Division for publication in the JOURNAL OF HEAT TRANSFER. Manuscript received by the Heat Transfer Division June 21, 1990; revision received October 12, 1990. Keywords: Augmentation and Enhancement, Mixed Convection.

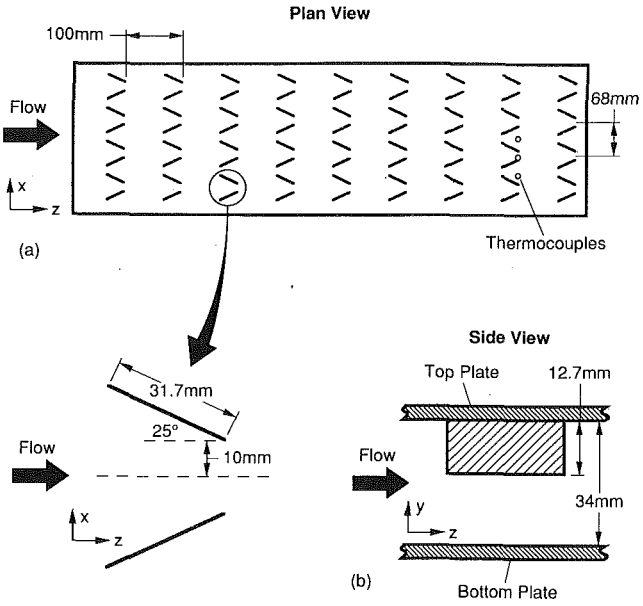

Fig. 1 Geometry and placement of vortex generators on the top surface: (*a*) plan view, (*b*) side view

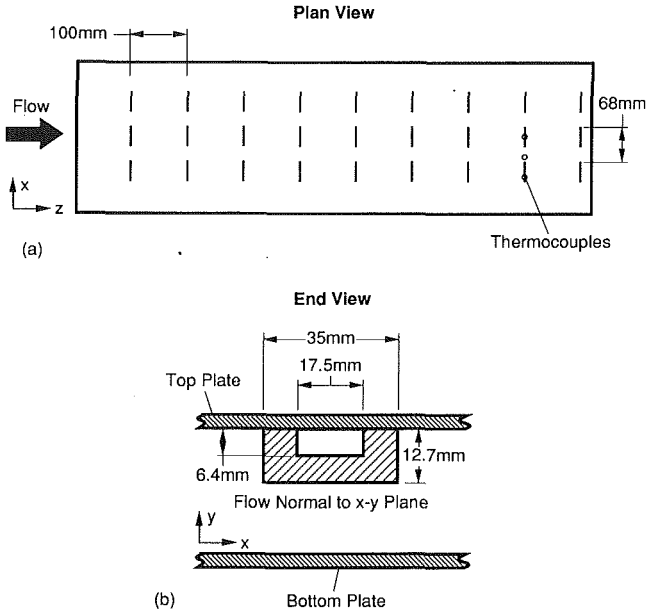

Fig. 2 Geometry and placement of perforated ribs on the top surface: (*a*) plan view, (*b*) end view

driven flows. This note reports on exploratory experiments to assess the feasibility of using mechanical vortex generators or perforated ribs at the top surface of a uniformly heated channel to provide comparable enhancement at both surfaces.

Experimental Procedures

Experiments were performed in a horizontal channel for which top and bottom walls were fabricated by overlaying patch electrical heaters with 3.2-mm-thick Lexan plates (Maughan, 1989). Power dissipation in each heater was independently controlled, and the thermal conductivity of Lexan was sufficiently small to provide approximately uniform heat flux conditions. To confirm this premise, two-dimensional conduction calculations were performed for the Lexan/heater assembly, with imposed longitudinal convection coefficient distributions corresponding to representative conditions with and without surface attachments. In particular, for mixed convection flow over a smooth surface, heat flux nonuniformities were less than 8 percent in the entrance region and negligible in the fully developed region. Moreover, using a longitudinal heat transfer coefficient distribution measured by Tanasawa et al. (1984) for flow over periodically spaced cross ribs, it was determined that surface temperature measurements made in proximity to the ribs could be used with the uniform heat flux approximations to assess accurately the effect of such attachments on local convection conditions.

Two possible approaches to enhancing convection heat transfer at the top surface of the channel were considered. Both approaches seek enhancement by inducing secondary flows, in one case through the use of vortex generators (Fig. 1) and in the other by using perforated ribs (Fig. 2). As demonstrated by Turk and Junkhan (1986), pairs of angled strips can be used to generate longitudinal vortex motion similar to that induced by buoyancy forces at a heated bottom surface. In contrast, ribs placed perpendicular to the flow induce mixing, while perforations disrupt the tendency to form nearly stagnant flow in downstream regions of separation (Tanasawa et al., 1984).

For this study, thin, nonconducting strips were lightly glued to the top surface, thereby enhancing heat transfer through induced secondary flow and not through conduction into extended surfaces (fins). Attachment of the strips was periodic in the longitudinal direction of the test section, which was 917 mm long, 308 mm wide, and of height $H = 34$ mm. To assess

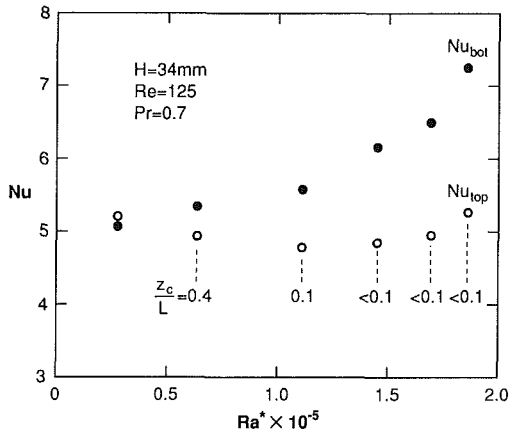

Fig. 3 Effect of Rayleigh number on top and bottom spanwise average Nusselt numbers for smooth surfaces

the effect of the attachments on heat transfer from the base surface, thermocouples were used to monitor surface temperatures at three spanwise locations for $z/L = 0.87$ (Figs. 1 and 2). Without the attachments, this longitudinal position corresponds to fully developed conditions for forced convection when $Re < 160$ and for mixed convection when $Ra^* > 5 \times 10^4$ (Maughan and Incropera, 1990). Temperature measurements were also made at equivalent locations on the bottom plate.

The local Nusselt number at each measurement station was calculated from the measured surface temperature, the measured dissipated flux (corrected for conduction and radiation losses), and the calculated local bulk temperature. Conduction heat losses, calculated from the temperature drop across the insulation underlying the Lexan plates, were approximately 15 percent of the dissipated flux. The net effect of spanwise and longitudinal conduction on the Nusselt number was assumed to be negligible. Radiation losses were minimized by coating each Lexan plate with a layer of aluminum foil. Because of the low emissivity and small temperature difference between the top and bottom plates, radiation losses were small, less than 5 percent of the dissipated flux when estimated from a zonal model of specular radiation exchange between nonisothermal surfaces.

Experiments were performed with the vortex generators and

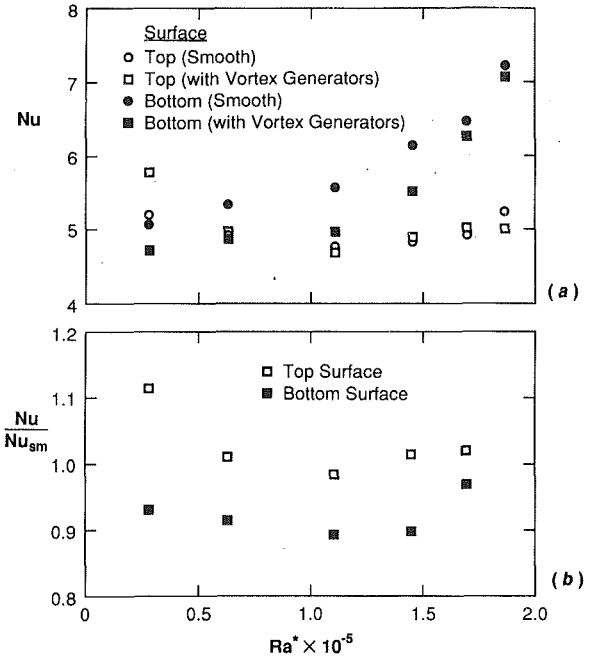

Fig. 4 Effect of vortex generators on top and bottom surface spanwise average Nusselt numbers: (*a*) absolute values, (*b*) relative to values for a smooth surface

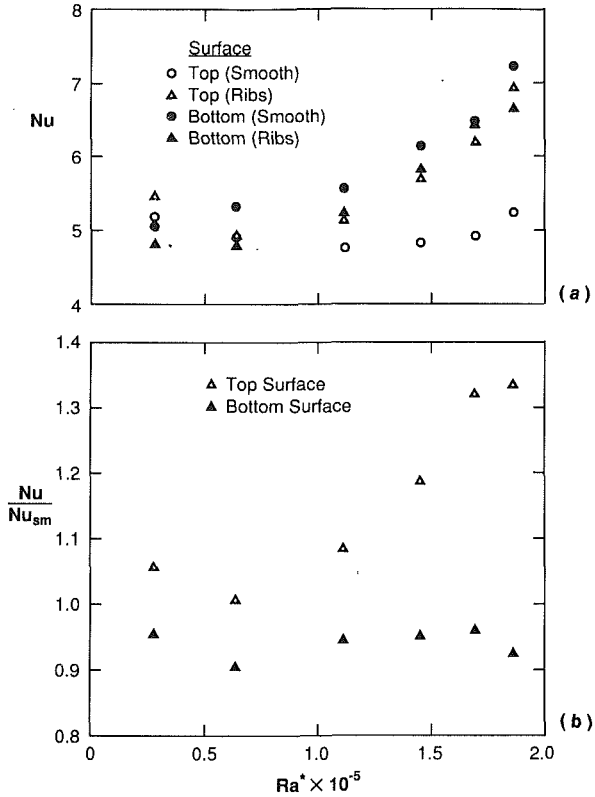

Fig. 5 Effect of perforated ribs on top and bottom surface spanwise average Nusselt numbers: (*a*) absolute values, (*b*) relative to values for a smooth surface

ribs, and results are compared with those obtained for smooth top and bottom surfaces. Experimental conditions correspond to air flow ($Pr = 0.7$), with $Re = 125$ and $3 \times 10^4 < Ra^* < 1.8 \times 10^5$, and reported results represent averages for the three spanwise measurements locations. Although uncertainties have been estimated to be as large as ± 25 percent (Maughan, 1989), differences between Nusselt numbers could be resolved to better than 3 percent.

Results

Figure 3 shows top and bottom plate measurements for smooth surfaces (no vortex generators or ribs). The approximate location for the onset of secondary flow (z_c/L), as determined by flow visualization, is indicated for each Rayleigh number. For $Ra^* = 27{,}800$, no secondary flow was observed and, as expected, top and bottom Nusselt numbers are approximately equal. As the Rayleigh number increases and secondary flows develop on the plate, Nu_{bot} increases and Nu_{top} drops slightly. These trends were also predicted numerically by Maughan (1989). At these Rayleigh numbers, secondary flows develop very slowly and the channel length of these experiments was not long enough to achieve fully developed flow without attachments. The increase in Nu_{top} for $Ra^* > 1.5 \times 10^5$ is atttributed to the onset of buoyancy-induced turbulence in the flow.

Results with the vortex generators are shown in Fig. 4. Nusselt numbers from Fig. 3 are included for comparison, and the ratio Nu/Nu_{sm}, which directly indicates the effect of adding vortex generators, is also included. At low Rayleigh numbers, the attachments augment heat transfer at the top surface and diminish it at the bottom by mechanically inducing vortices. Because of the geometry (Fig. 2*a*), the width of each vortex is equal to the channel height. The situation is analogous to the smooth channel at high Rayleigh numbers, where buoyancy forces induce vortices at the bottom surface. In fact, flow visualization showed the mechanically driven secondary flow at the top surface to be essentially an inverted image of the buoyancy-driven flow at the bottom surface. At higher Rayleigh numbers, the vortex generators lose their relative effectiveness because the flow structure they create to enhance heat transfer would exist even without the attachments. Hence, Nu/Nu_{sm} drops toward unity.

In contrast, perforated ribs result in different, more complicated flow structures that effectively mix flow at the top surface throughout the entire range of Rayleigh numbers. Nusselt numbers at the top surface (Fig. 5) are enhanced to levels corresponding approximately to those of the bottom plate. This result suggests that, if heat transfer coefficients at the top and bottom surfaces are to be comparable, flow patterns that are not normally associated with mixed convection must be created at the top surface.

Summary

This note has reported results from an experimental investigation of fully developed mixed convection in a horizontal channel with nonconducting extended surfaces on the top plate. Without the attachments, Nusselt numbers on the top surface were significantly lower than those at the bottom. Vortex generators mimicked buoyancy-induced flow at low Rayleigh numbers and enhanced heat transfer at the top surface. At higher Rayleigh numbers, vortex generators could not further augment the buoyancy-driven mixing and were no longer effective. Perforated ribs, on the other hand, were effective in increasing top surface Nusselt numbers to levels corresponding approximately to those of the bottom surface. These results, though limited in scope, suggest that further studies could lead to mixed convection conditions for which there is comparable heat transfer at the top and bottom surfaces of the horizontal channel.

Acknowledgments

Support of this work by the National Science Foundation under Grant No. CBT-8316580 is gratefully acknowledged. One author (J.R.M.) is also grateful for fellowships from the

Chevron Corporation, NL Industries Foundation, the Shell Foundation, and the Ingersoll Rand Corporation.

References

Maughan, J. R., 1989, "An Experimental and Numerical Investigation of Mixed Convection in Channels and the Application of Extended Surfaces for Heat Transfer Enhancement," Ph.D. Thesis, School of Mechanical Engineering, Purdue University, West Lafayette, IN.

Maughan, J. R., and Incropera, F. P., 1990, "Regions of Heat Transfer Enhancement for Laminar Mixed Convection in a Parallel Plate Channel," *International Journal of Heat and Mass Transfer,* Vol. 33, pp. 555–570.

Osborne, D. G., and Incropera, F. P., 1985, "Laminar Mixed Convection Heat Transfer for Flow Between Horizontal Parallel Plates With Asymmetric Heating," *International Journal of Heat and Mass Transfer,* Vol. 28, pp. 207–217.

Tanasawa, I., Nishio, S., Takano, K., and Miyazaki, H., 1984, "High Performance Surface for Forced Convection Heat Transfer Using Novel Turbulence Promoters," ASME Paper No. 84-HT-69.

Turk, A. Y., and Junkhan, G. H., 1986, "Heat Transfer Enhancement Downstream of Vortex Generator on a Flat Plate," *Proceedings of the Eighth International Heat Transfer Conference,* C. L. Tien, V. P. Carey, and J. K. Ferrell, eds., Hemisphere Publishing Co., Washington, DC, pp. 2903–2908.

Analysis of Laminar Fully Developed Mixed Convection in a Vertical Channel With Opposing Buoyancy

T. T. Hamadah[1] and R. A. Wirtz[2]

Nomenclature

- b = spacing between channel walls
- g = gravitational acceleration
- Gr = Grashof number, defined in Table 1
- h = heat transfer coefficient
- k = thermal conductivity
- Nu = Nusselt number
- Pr = Prandtl number
- R_q = wall heat flux ratio = q_1''/q_2''
- R_T = wall temperature difference ratio = $(T_1 - T_0)/(T_2 - T_0)$
- Re = Reynolds number based on hydraulic diameter
- T = temperature
- U = dimensionless axial velocity = u/u_{avg}
- X = dimensionless axial coordinate = $x/(b\text{Re})$
- Y = dimensionless transverse coordinate = y/b
- α = dimensionless axial pressure gradient
- β = thermal expansion coefficient
- θ = dimensionless temperature, defined in Table 1
- ν = kinematic viscosity
- ρ = density

Introduction

The problem of laminar fully developed mixed convection in a parallel plate channel is analyzed for the case where buoyancy *opposes* the flow. Complete, closed-form solutions for the velocity and wall heat transfer are obtained for the following cases:

1 Both walls isothermal, with the right wall ($Y = 1$) at T_2 and the left wall ($Y = 0$) at T_1 where $T_2 > T_1$.

2 Both walls at constant heat flux to the fluid, with the right wall at q_2'' and the left wall at q_1'' where $q_2'' > q_1''$.

3 Right wall at constant heat flux, q_2'', while the left wall is maintained at $T_1 = T_0$, the fluid inlet temperature.

Lavine (1988) considered fully developed buoyancy-opposing flow between inclined, constant heat flux plates. Those results, for plates in the vertical orientation, are the same as the present study, Case 2. Kim (1985a, 1985b) considered fully developed buoyancy-aided and opposed laminar flow in vertical concentric tube annuli. Closed-form solutions, which can be superimposed to generate any combination of specified heat flux at the inner and outer tube, are presented. Unfortunately solutions for the case where the inner-to-outer tube radius ratio is one (the parallel plate channel) could not be obtained directly. Aung and Worku (1986a, 1986b, 1987) studied developing and fully developed buoyancy-aided flow between parallel plates with specified plate temperature and heat fluxes. They found that buoyancy enhances heat transfer near the heated wall, and may cause flow reversal near the cooler wall.

In the following, solutions to the fully developed flow energy equation are used to obtain the dimensionless velocity profiles in terms of the Grashof-to-Reynolds number ratio. Criteria for the onset of flow reversal are then developed. Expressions for the mean fluid temperature are developed and used to write wall Nusselt number relations.

Problem Formulation and Solution

Consider a steady, two-dimensional vertical downflow between two parallel walls spaced b apart with X the axial coordinate (positive downward) and Y the transverse coordinate ($Y = 0$ at the left wall). For a fully developed flow with constant properties, and subject to the linear state equation, the dimensionless axial momentum equation is

$$\frac{d^2U}{dY^2} = -\frac{\alpha}{2} + \frac{\text{Gr}}{4\text{Re}}\,\theta \tag{1}$$

where U is the axial velocity, α is the nondimensional dynamic pressure gradient, and Re is the Reynolds number. The definitions of Gr and θ depend on the thermal boundary conditions and are defined in Table 1.

Since θ is independent of X for cases 1 and 3, the energy equation reduces to

$$\frac{\partial^2\theta}{\partial Y^2} = \delta_{k,2}\text{UPr}\,\frac{\partial\theta}{\partial X}, \qquad k = 1, 2, 3 \tag{2}$$

where k is the case number and $\delta_{1,2} = \delta_{3,2} = 0$. The boundary conditions associated with equation (1) are $U = 0$ at $Y = 0$

Table 1 Energy equation, B.C.'s, and definitions of θ, θ_m, and Gr for all cases

			Definitions		
Case	Energy Equation	B.C.'s	θ	θ_m	Gr
1	$\frac{d^2\Theta}{dY^2} = 0$	$\Theta(0) = R_T$ $\Theta(1) = 1$	$\frac{T - T_o}{T_2 - T_o}$	$\frac{T_m - T_o}{T_2 - T_o}$	$\frac{g\beta(T_2 - T_o)(2b)^3}{\nu^2}$
2	$\frac{\partial^2\Theta}{\partial Y^2} = UPr\frac{\partial\Theta}{\partial X}$	$\frac{\partial\Theta}{\partial Y}\Big\|_{Y=0} = -\frac{R_q}{2}$ $\frac{\partial\Theta}{\partial Y}\Big\|_{Y=1} = \frac{1}{2}$	$\frac{T - T_o}{q_2''\frac{(2b)}{k}}$	$\frac{T_m - T_o}{q_2''\frac{(2b)}{k}}$	$\frac{g\beta q_2''(2b)^4}{k\nu^2}$
3	$\frac{d^2\Theta}{dY^2} = 0$	$\frac{\partial\Theta}{\partial Y}\Big\|_{Y=1} = \frac{1}{2}$ $\Theta(0) = 0$	$\frac{T - T_o}{q_2''\frac{(2b)}{k}}$	$\frac{T_m - T_o}{q_2''\frac{(2b)}{k}}$	$\frac{g\beta q_2''(2b)^4}{k\nu^2}$

[1] Digital Equipment Corp., Littleton, MA 01460.

[2] University of Nevada—Reno, Reno, NV 89557.

Contributed by the Heat Transfer Division and presented at the ASME Winter Annual Meeting, Chicago, Illinois, November 28–December 2, 1988. Manuscript received by the Heat Transfer Division November 9, 1989; revision received October 1, 1990. Keywords: Mixed Convection.

Chevron Corporation, NL Industries Foundation, the Shell Foundation, and the Ingersoll Rand Corporation.

References

Maughan, J. R., 1989, "An Experimental and Numerical Investigation of Mixed Convection in Channels and the Application of Extended Surfaces for Heat Transfer Enhancement," Ph.D. Thesis, School of Mechanical Engineering, Purdue University, West Lafayette, IN.

Maughan, J. R., and Incropera, F. P., 1990, "Regions of Heat Transfer Enhancement for Laminar Mixed Convection in a Parallel Plate Channel," *International Journal of Heat and Mass Transfer,* Vol. 33, pp. 555–570.

Osborne, D. G., and Incropera, F. P., 1985, "Laminar Mixed Convection Heat Transfer for Flow Between Horizontal Parallel Plates With Asymmetric Heating," *International Journal of Heat and Mass Transfer,* Vol. 28, pp. 207–217.

Tanasawa, I., Nishio, S., Takano, K., and Miyazaki, H., 1984, "High Performance Surface for Forced Convection Heat Transfer Using Novel Turbulence Promoters," ASME Paper No. 84-HT-69.

Turk, A. Y., and Junkhan, G. H., 1986, "Heat Transfer Enhancement Downstream of Vortex Generator on a Flat Plate," *Proceedings of the Eighth International Heat Transfer Conference,* C. L. Tien, V. P. Carey, and J. K. Ferrell, eds., Hemisphere Publishing Co., Washington, DC, pp. 2903–2908.

Analysis of Laminar Fully Developed Mixed Convection in a Vertical Channel With Opposing Buoyancy

T. T. Hamadah[1] and R. A. Wirtz[2]

Nomenclature

- b = spacing between channel walls
- g = gravitational acceleration
- Gr = Grashof number, defined in Table 1
- h = heat transfer coefficient
- k = thermal conductivity
- Nu = Nusselt number
- Pr = Prandtl number
- R_q = wall heat flux ratio = q_1''/q_2''
- R_T = wall temperature difference ratio = $(T_1 - T_0)/(T_2 - T_0)$
- Re = Reynolds number based on hydraulic diameter
- T = temperature
- U = dimensionless axial velocity = u/u_{avg}
- X = dimensionless axial coordinate = $x/(b\text{Re})$
- Y = dimensionless transverse coordinate = y/b
- α = dimensionless axial pressure gradient
- β = thermal expansion coefficient
- θ = dimensionless temperature, defined in Table 1
- ν = kinematic viscosity
- ρ = density

Introduction

The problem of laminar fully developed mixed convection in a parallel plate channel is analyzed for the case where buoyancy *opposes* the flow. Complete, closed-form solutions for the velocity and wall heat transfer are obtained for the following cases:

1 Both walls isothermal, with the right wall ($Y = 1$) at T_2 and the left wall ($Y = 0$) at T_1 where $T_2 > T_1$.

2 Both walls at constant heat flux to the fluid, with the right wall at q_2'' and the left wall at q_1'' where $q_2'' > q_1''$.

3 Right wall at constant heat flux, q_2'', while the left wall is maintained at $T_1 = T_0$, the fluid inlet temperature.

Lavine (1988) considered fully developed buoyancy-opposing flow between inclined, constant heat flux plates. Those results, for plates in the vertical orientation, are the same as the present study, Case 2. Kim (1985a, 1985b) considered fully developed buoyancy-aided and opposed laminar flow in vertical concentric tube annuli. Closed-form solutions, which can be superimposed to generate any combination of specified heat flux at the inner and outer tube, are presented. Unfortunately solutions for the case where the inner-to-outer tube radius ratio is one (the parallel plate channel) could not be obtained directly. Aung and Worku (1986a, 1986b, 1987) studied developing and fully developed buoyancy-aided flow between parallel plates with specified plate temperature and heat fluxes. They found that buoyancy enhances heat transfer near the heated wall, and may cause flow reversal near the cooler wall.

In the following, solutions to the fully developed flow energy equation are used to obtain the dimensionless velocity profiles in terms of the Grashof-to-Reynolds number ratio. Criteria for the onset of flow reversal are then developed. Expressions for the mean fluid temperature are developed and used to write wall Nusselt number relations.

Problem Formulation and Solution

Consider a steady, two-dimensional vertical downflow between two parallel walls spaced b apart with X the axial coordinate (positive downward) and Y the transverse coordinate ($Y = 0$ at the left wall). For a fully developed flow with constant properties, and subject to the linear state equation, the dimensionless axial momentum equation is

$$\frac{d^2U}{dY^2} = -\frac{\alpha}{2} + \frac{\text{Gr}}{4\text{Re}}\,\theta \tag{1}$$

where U is the axial velocity, α is the nondimensional dynamic pressure gradient, and Re is the Reynolds number. The definitions of Gr and θ depend on the thermal boundary conditions and are defined in Table 1.

Since θ is independent of X for cases 1 and 3, the energy equation reduces to

$$\frac{\partial^2\theta}{\partial Y^2} = \delta_{k,2}\text{UPr}\,\frac{\partial\theta}{\partial X}, \qquad k = 1, 2, 3 \tag{2}$$

where k is the case number and $\delta_{1,2} = \delta_{3,2} = 0$. The boundary conditions associated with equation (1) are $U = 0$ at $Y = 0$

Table 1 Energy equation, B.C.'s, and definitions of θ, θ_m, and Gr for all cases

			Definitions		
Case	Energy Equation	B.C.'s	θ	θ_m	Gr
1	$\frac{d^2\Theta}{dY^2} = 0$	$\Theta(0) = R_T$ $\Theta(1) = 1$	$\frac{T - T_o}{T_2 - T_o}$	$\frac{T_m - T_o}{T_2 - T_o}$	$\frac{g\beta(T_2 - T_o)(2b)^3}{\nu^2}$
2	$\frac{\partial^2\Theta}{\partial Y^2} = UPr\frac{\partial\Theta}{\partial X}$	$\frac{\partial\Theta}{\partial Y}\|_{Y=0} = -\frac{R_q}{2}$ $\frac{\partial\Theta}{\partial Y}\|_{Y=1} = \frac{1}{2}$	$\frac{T - T_o}{q_2''\frac{(2b)}{k}}$	$\frac{T_m - T_o}{q_2''\frac{(2b)}{k}}$	$\frac{g\beta q_2''(2b)^4}{k\nu^2}$
3	$\frac{d^2\Theta}{dY^2} = 0$	$\frac{\partial\Theta}{\partial Y}\|_{Y=1} = \frac{1}{2}$ $\Theta(0) = 0$	$\frac{T - T_o}{q_2''\frac{(2b)}{k}}$	$\frac{T_m - T_o}{q_2''\frac{(2b)}{k}}$	$\frac{g\beta q_2''(2b)^4}{k\nu^2}$

[1] Digital Equipment Corp., Littleton, MA 01460.
[2] University of Nevada—Reno, Reno, NV 89557.

Contributed by the Heat Transfer Division and presented at the ASME Winter Annual Meeting, Chicago, Illinois, November 28–December 2, 1988. Manuscript received by the Heat Transfer Division November 9, 1989; revision received October 1, 1990. Keywords: Mixed Convection.

and $Y = 1$. The boundary conditions associatedwith equation 2 are given in Table 1.

The mixed-mean nondimensional temperature θ_m is given as

$$\theta_m = \int_0^1 U\theta dY \tag{3}$$

where the definitions of θ_m in terms of dimensional values are given in Table 1 for each case.

Conservation of mass at any cross section in the channel gives

$$\int_0^1 UdY = 1 \tag{4}$$

Solution for Case 1

Solving equation (2) and applying the boundary conditions yields the fully developed temperature profile

$$\theta = (1 - R_T)Y + R_T \tag{5}$$

In equation (5), R_T is the ratio of left-to-right wall temperature increase. Substituting into equation (1) yields the velocity profile

$$U = \frac{\mathrm{Gr}}{48\mathrm{Re}}(1 - R_T)(2Y^3 - 3Y^2 + Y) - 6(Y^2 - Y) \tag{6}$$

Equation (6) shows that the velocity profile depends on the parameters Gr/Re and R_T. Note that the equation reduces to the fully developed forced convection velocity profile when Gr/Re = 0. Furthermore, equation (6) gives the forced convection result when $R_T = 1$. This condition is equivalent to the case $T_1 = T_2$, hence no heat transfer. Substituting equations (5) and (6) into equation (3) yields the mixed-mean temperature

$$\theta_m = -\frac{\mathrm{Gr}}{2880\mathrm{Re}}(1 - R_T)^2 + \frac{1}{2}(1 + R_T) \tag{7}$$

The wall heat transfer coefficient is

$$h_i = \frac{q_i''}{T_i - T_m}, \qquad i = 1, 2 \tag{8}$$

where the heat flux q_i'' is given by

$$-q_1'' = q_2'' = k\frac{(T_2 - T_1)}{b} \qquad (T_2 > T_1) \tag{9}$$

so that the Nusselt number based on hydraulic diameter, $h(2b)/k$, is

$$\mathrm{Nu}_1 = 2\left(\frac{T_1 - T_2}{T_1 - T_m}\right) \tag{10a}$$

$$\mathrm{Nu}_2 = 2\left(\frac{T_2 - T_1}{T_2 - T_m}\right) \tag{10b}$$

Utilizing the definition of θ_m, the definition of R_T, and equation (7), results in evaluation of the temperature ratio, hence

$$\mathrm{Nu}_1 = \frac{4}{1 - \dfrac{\mathrm{Gr}}{1440\mathrm{Re}}(1 - R_T)}, \quad R_T < 1 \tag{11a}$$

$$\mathrm{Nu}_2 = \frac{4}{1 + \dfrac{\mathrm{Gr}}{1440\mathrm{Re}}(1 - R_T)}, \quad R_T < 1 \tag{11b}$$

Equation (11) is the fully developed wall Nusselt number for Case 1. It reduces to the fully developed forced convection result when Gr/Re = 0, and when $R_T = 1$.

Solution for Case 2

For this case an energy balance gives

$$\frac{d\theta_m}{dX} = 2(1 + R_q)\mathrm{Pr}^{-1} = \frac{\partial\theta}{\partial X} \tag{12}$$

where the second equality is valid since the flow is fully developed. Substituting equation (12) into equation (2) and combining with equation (1) gives

$$\frac{d^4U}{dY^4} = \frac{\mathrm{Gr}}{2\mathrm{Re}}(1 + R_q)U \tag{13}$$

The general solution is

$$U = C_1\cos(\gamma Y) + C_2\sin(\gamma Y) + C_3e^{\gamma Y} + C_4e^{-\gamma Y} \tag{14}$$

where

$$\gamma = \left[\frac{1}{2}\frac{\mathrm{Gr}}{\mathrm{Re}}(1 + R_q)\right]^{1/4} \tag{15}$$

Substituting equation (14) into equation (1) yields

$$\theta = \frac{1}{\left(\dfrac{1}{4}\dfrac{\mathrm{Gr}}{\mathrm{Re}}\right)}\left\{\frac{\alpha}{2} + \gamma^2[-C_1\cos(\gamma Y) - C_2\sin(\gamma Y) + C_3e^{\gamma Y} - C_4e^{-\gamma Y}]\right\} \tag{16}$$

Table 2 Selected values of C_i for equations (14) and (16)

Gr/Re	C1	C2	C3	C4
		R = 0.0		
100	1.58829	1.54613	-0.21083	-1.56721
200	1.37346	1.45711	0.04183	-1.41529
300	1.37169	1.48892	0.05862	-1.43031
400	1.44100	1.57116	0.06508	-1.50608
		R = 0.5		
100	0.93255	1.67436	-0.03081	-0.90174
200	0.58517	1.57902	0.01270	-0.59787
300	0.45014	1.57448	0.02395	-0.47410
400	0.39388	1.60962	0.02827	-0.42215
500	0.38853	1.67652	0.03036	-0.41889
		R = 1.0		
100	0.48448	1.71185	-.033810	-0.45064
200	0.01544	1.57513	-.000652	-0.01479
400	-.44345	1.44563	0.010320	0.43313
600	-.74183	1.35349	0.011578	0.73025
800	-.98185	1.26968	0.011243	0.97060
1000	-1.1924	1.18713	0.010567	1.18186

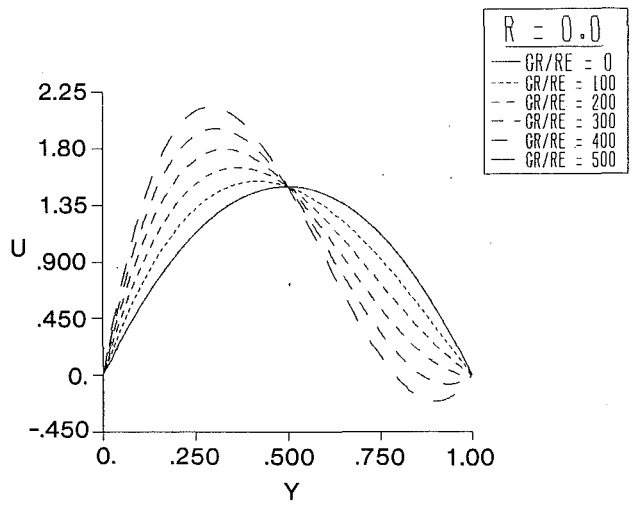

Fig. 1 Velocity profiles, Case 1

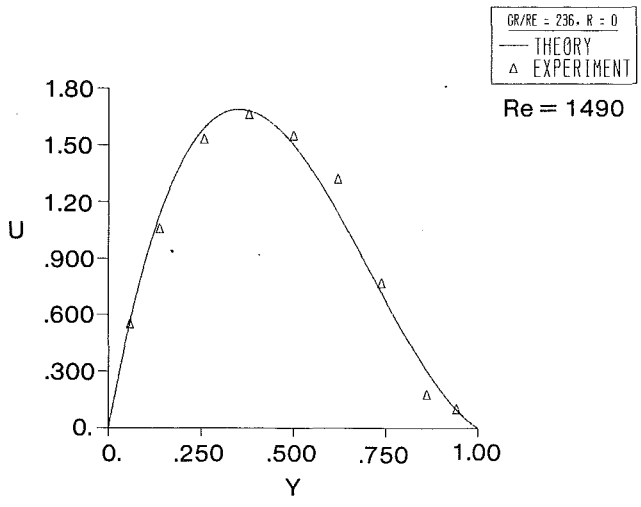

Fig. 2 Comparison between measurements of Wirtz and Hamadah (1987) and present result for Case 1

Applying the boundary conditions to equations (14) and (16) yields the constants C_1, C_2, C_3, and C_4. Selected values of these constants are tabulated in Table 2.

The constant α can be evaluated from

$$\int_0^1 U(\theta-\theta_m)dY=0 \tag{17}$$

where

$$\theta_m=2\mathrm{Pr}^{-1}(1+R_q)X \tag{18}$$

The Nusselt number at the wall can then be expressed as

$$\mathrm{Nu}_1=\frac{1}{\theta_1-\theta_m} \tag{19a}$$

$$\mathrm{Nu}_2=\frac{1}{\theta_2-\theta_m} \tag{19b}$$

Solution for Case 3

The solution for Case 3 parallels that for Case 1. The results are

$$U=\frac{\mathrm{Gr}}{96\mathrm{Re}}(2Y^3-3Y^2+Y)-6(Y^2-Y) \tag{20}$$

$$\theta_m=-\frac{\mathrm{Gr}}{11520\mathrm{Re}}+\frac{1}{4} \tag{21}$$

$$\mathrm{Nu}_1=\frac{4}{1-\dfrac{\mathrm{Gr}}{2880\mathrm{Re}}} \tag{22a}$$

$$\mathrm{Nu}_2=\frac{4}{1+\dfrac{4}{2880\mathrm{Re}}} \tag{22b}$$

Discussion of Results

Case 1. Both Walls Isothermal. Figure 1 shows the effect of increasing Gr/Re on the velocity profile of equation (6) for $R_T = 0$. The results are typical for $-1 \le R_T < 1$ where negative values of R_T correspond to $T_2 > T_0$ and $T_1 < T_0$ while positive R_T is for both walls hotter than T_0. The figure shows that as adverse buoyancy is increased, the flow adjacent to the heated wall is retarded. As a result, the velocity profile becomes inflected in this region and the velocity near the opposite wall increases in order to maintain conservation of mass.

Figure 2 compares the present analytical result with the experimental measurements of Wirtz and Hamadah (1987) for Gr/Re = 236 in a *thermally developing* flow. Their measurements with air in a vertical channel with one isothermal wall heated correspond to the case where $R_T = 0$, i.e., $T_1 = T_0$. The figure (which is typical for measurements over the range $0 < \mathrm{Gr/Re} < 270$) shows that the velocity profiles for the thermally developing flow and the fully developed flow are very similar. The thermally developing velocity profile exhibits stronger inflection near the heated wall and somewhat less skewing of the flow away from the heated wall, probably due to the stronger temperature gradients existing near the heated wall in the thermally developing case.

For sufficiently large Gr/Re, the shear stress at the hotter wall vanishes, and the flow reverses. Differentiation of equation (5) with $dU/dY = 0$ gives a criterion for flow reversal

$$\left(\frac{\mathrm{Gr}}{\mathrm{Re}}\right)_{\mathrm{REV}}=\frac{288}{1-R_T}, \qquad R_T<1. \tag{23}$$

Equation (23) shows that flow reversal occurs at higher Gr/Re as R_T approaches 1.0. Wirtz and Hamadah (1987) report the onset of flow reversal at Gr/Re = 270 for air flow at Re = 1500 for the case where $R_T = 0$, and this is in excellent agreement with equation (23). It is interesting to note that Aung and Worku (1986b) developed a flow reversal criterion, which is identical to equation (23) for the case of buoyancy-aided fully developed mixed convection.

Examination of equation (10) shows that the cold wall heat transfer coefficient Nu_1 increases with increasing Gr/Re and decreasing R_T, while the converse is true for Nu_2. As $\mathrm{Gr/Re} \to 0$, the curves collapse to the fully developed forced convection value. At incipient flow reversal, $\mathrm{Nu}_1 = 5.0$ and $\mathrm{Nu}_2 = 3.33$ for all values of Gr/Re.

Case 2. Both Walls Constant Heat Flux. Velocity profiles for this case are similar to that shown in Fig. 1 for Case 1 when the ratio of wall heat flux $R_q < 1$. On the other hand, when the wall heat fluxes are equal ($R_q = 1$), inflection occurs adjacent to both walls and the velocity profile "pops" in the center of the channel as Gr/Re increases, as shown in Fig. 3.

A criterion for incipient flow reversal may again be developed by recognizing that for sufficiently large Gr/Re, the shear stress at the wall with greater heat flux will vanish. The result is plotted in Fig. 4, where Gr/Re(rev) = 400 at $R_q = 0$ (left wall unheated), and increases rapidly as R_q approaches 1.

Figure 5 shows the fully developed mixed convection heat transfer coefficient for Case 2 as a function of Gr/Re. For $R_q \le 1$, results are plotted up to the point of incipient flow reversal

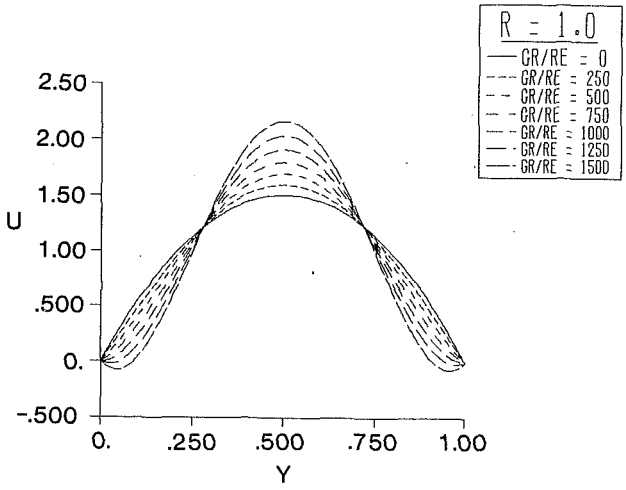

Fig. 3 Velocity profiles for Case 2, R_q = 1.0

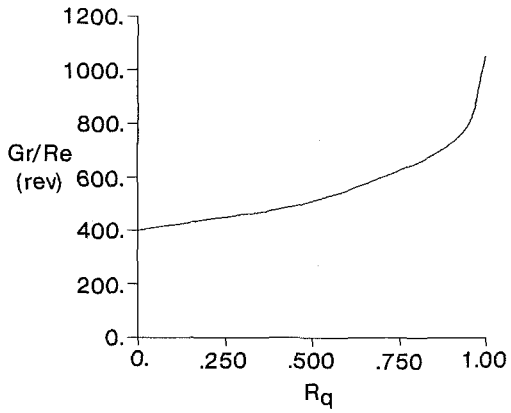

Fig. 4 Incipient flow reversal criteria for Case 2

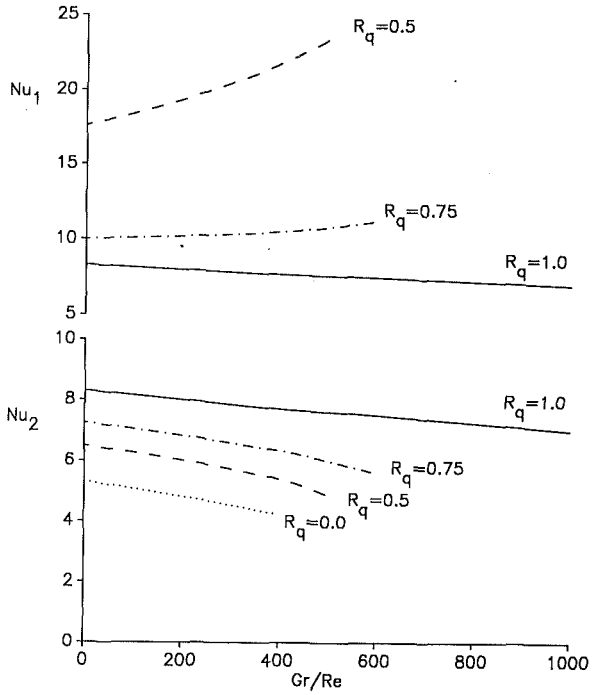

Fig. 5 Heat transfer coefficient for Case 2

given in Fig. 4. When $R_q = 0$, $Nu_1 = Nu_2$ due to the symmetry of the flow shown in Fig. 3. When $R_q < 1$, the hot wall heat transfer coefficient decreases and the cold wall coefficient increases with increasing Gr/Re, similar to the results of Case 1 except that the values do not approach the same numerical value at incipient flow reversal. All quantities approach the forced convection result when Gr/Re = 0.

Case 3. One Wall at Constant Heat Flux. This case is similar to Case 1. The velocity profile becomes inflected near the hot wall with increasing Gr/Re. Incipient flow reversal is predicted to occur at Gr/Re(rev) = 576. The hot wall Nusselt number decreases and the cold wall Nusselt number increases with increasing Gr/Re. At incipient flow reversal, Nu_1(rev) = 5.0, and Nu_2(rev) = 3.33.

Conclusions

Closed-form solutions for fully developed laminar mixed convection in a parallel plane vertical channel with opposing buoyancy are developed for three sets of thermal boundary conditions. Dimensionless velocity profiles and wall heat transfer coefficients are found to depend on the Grashof-to-Reynolds number ratio, and the ratio of wall thermal boundary conditions, R. Criteria for incipient flow reversal are established.

Predicted velocity profiles exhibit inflection near the hotter wall with increasing Gr/Re. At sufficiently high Gr/Re, the flow will reverse. The tendency to reverse increases with decreasing R_T, or R_q. The heated wall Nusselt number decreases with increasing Gr/Re while the cold wall Nusselt number increases.

References

Aung, W., and Worku, G., 1986a, "Developing Flow and Flow Reversal in a Vertical Channel With Asymmetric Wall Temperatures," ASME JOURNAL OF HEAT TRANSFER, Vol. 108, pp. 299–304.

Aung, W., and Worku, G., 1986b, "Theory of Fully Developed, Combined Convection Including Flow Reversal," ASME JOURNAL OF HEAT TRANSFER, Vol. 108, pp.485–488.

Aung, W., and Worku, G., 1987, "Mixed Convection in Ducts With Asymmetric Wall Heat Fluxes," ASME JOURNAL OF HEAT TRANSFER, Vol. 109, pp. 947–951.

Kim, J. H., 1985a, "Analysis of Laminar Mixed Convection in Vertical Tube Annulus With Upward Flow," *Fundamentals of Forced and Mixed Convection*, ASME HTD-Vol. 42, pp. 91–98.

Kim, J. H., 1985b, "Analysis of Laminar Natural Convection Superimposed on Downward Flow in Vertical Tube Annulus," ASME Paper No. 85-WA/HT-13.

Lavine, A. S., 1988, "Analysis of Fully Developed Opposing Mixed Convection Between Inclined Parallel Plates," *Wärme- und Stoffübertragung*, Vol. 23, pp. 249–257.

Wirtz, R. A., and Hamadah, T., 1987, "Transitional Reynolds Number Convection in a Vertical Channel With Opposing Buoyancy Effects," *Proceedings 1987 ASME/JSME Thermal Engineering Joint Conference*, Vol. 1, pp. 443–448.